ILLUMINATING THE UNKNOWN: DEVELOPMENT OF EMISSION-RATIOMETRIC, ZN(II)-SELECTIVE FLUORESCENT PROBES FOR TWO-PHOTON EXCITATION MICROSCOPY

A Dissertation
Presented to
The Academic Faculty

by

Adam Michael McCallum

In Partial Fulfillment
of the Requirements for the Degree
Doctor of Philosophy in the
School of Chemistry & Biochemistry

Georgia Institute of Technology
December 2017

ILLUMINATING THE UNKNOWN: DEVELOPMENT OF EMISSION-RATIOMETRIC, ZN(II)-SELECTIVE FLUORESCENT PROBES FOR TWO-PHOTON EXCITATION MICROSCOPY

Approved by:

Dr. Christoph J. Fahrni, Advisor
School of Chemistry & Biochemistry
Georgia Institute of Technology

Dr. Amit Reddi
School of Chemistry & Biochemistry
Georgia Institute of Technology

Dr. Charles Liotta
School of Chemistry & Biochemistry
Georgia Institute of Technology

Dr. M.G. Finn
School of Biology
Georgia Institute of Technology

Dr. Adegboyega Oyelere
School of Chemistry & Biochemistry
Georgia Institute of Technology

Date Approved: November 02, 2017

Dedicated to my mother, Carolyn Marie Blum, and my grandparents, Ruth and Charles F. Blum, Jr.

ACKNOWLEDGEMENTS

In August of 2005, I stepped foot into Mrs. Vowel's Honors Chemistry class at North Hardin High School in Radcliff, KY, unbeknownst to me, that twelve years later, I would be receiving a Doctor of Philosophy in Chemistry. The path that led me to this moment was one filled with many setbacks, apprehension, and exhaustion, along with ardor, eagerness, commitment, growth, and ultimately pride. As I sit here writing this acknowledgements section, I contemplate all the obstacles that I have encountered on my journey to this moment, and they remind me of all the remarkable people who have made my journey possible. First and foremost, I cannot express enough my gratitude to my advisor, Dr. Christoph J. Fahrni, for his assiduous encouragement and support. I am profoundly grateful for his mentorship concerning my professional and scientific development, his guidance, and his acceptance and understanding of my mistakes and failures.

I am deeply grateful for the love and support from my mother, Carolyn Blum, and my grandparents, Ruth and Charles F. Blum, Jr. to whom my dissertation is dedicated. Their persistent and abiding nurture of my achievements should not be understated because they have made me the person that I am today. I would also like to express my appreciation of my committee members, Drs. Charles Liotta, Amit Reddi, Adegboyega Oyelere, and M. G. Finn, for their overwhelming encouragement and advice throughout my graduate tenure.

My knowledge of and success in organic chemistry would not have been possible without the relentless support of my colleague and mentor, Dr. Thomas Morgan, who taught me innumerable skills that facilitated my scientific accomplishments. In addition, I

cannot thank enough my colleague and friend, Dr. Daisy Bourassa, for her emotional support and friendship since I arrived at Georgia Tech. My success is accredited to her encouragement and altruism. To my fellow graduate students and friends, Dr. Kathryn Lanier, Dr. Haylee Bachman, and those who made my tenure at Georgia Tech nothing but memorable, I thank them very much for their camaraderie, collaboration, and occasional succor. Regarding the remaining members of the Fahrni Lab and members of the Reddi Lab, my five years in graduate school would not have been nearly as enjoyable without their gratification and entertainment. I will deeply miss the laughter, spontaneous singing, and jests.

Lastly, over the past five years, I am truly blessed to have met an amazing group of people (Thomson, Max, Evelyn, Mike, Kyle, Melhim, Tom, Paul, Jonathan, and Corey) with whom I have shared many life experiences, and expressing my gratitude for them cannot be met with words alone. They have been my family away from my family through many ups and downs since I moved to Atlanta, and without them, I would not be the man that I am today.

TABLE OF CONTENTS

LIST OF TABLES

LIST OF FIGURES

LIST OF SCHEMES

LIST OF SYMBOLS AND ABBREVIATIONS

~	Approximately
1PA	One-photon absorption
2PA	Two-photon absorption
Å	Ångström (10^{-10} m)
ADH	Alcohol dehydrogenase
aM	Attomolar
Asp	Aspartic Acid
a.u.	Arbitrary units
br	Broad
BP	Bandpass
CA	Carbonic anhydrase
cAMP	Cyclic adenosine monophosphate
calc'd	Calculated
cGMP	Cyclic guanosine monophosphate
CS1	Coppersensor-1
CS3	Coppersensor-3
CTAP	Copper Triarylpyrazoline
Cu(I)	Monovalent oxidation state of copper bound to unspecified ligand
Cys	Cysteine
d	Doublet
DCM	Dichloromethane
dd	Doublet of doublets
ddd	Doublet of doublet of doublets

DMPC	1,2-dimyristoyl-*sn*-glycero-3-phosphocholine
DMPG	1,2-dimyristoyl-*sn*-glycero-3-phospho-(1'-rac-glycerol)
DMSO	Dimethylsulfoxide
dt	Doublet of triplets
DTDP	2,2'-dithiodipyridine
DTPA	Diethylenetriaminepentaacetic acid
ε	Molar absorptivity coefficient
EC	Enzyme Commission
EDTA	Ethylenediaminetetraacetic acid
EGTA	Ethylene glycol-bis(2-aminoethylether)-*N*,*N*,*N*′,*N*′-tetraacetic acid
EI	Electron ionization
ER	Endoplasmic reticulum
ESI	Electrospray ionization
ESIPT	Excited-state intramolecular proton transfer
ESPT	Excited-state proton transfer
EtOAc	Ethyl acetate
EtOH	Ethanol
eq./equiv.	Molar equivalents
f	Fractional Saturation
F	Fluorescence intensity at a particular metal concentration
fM	Femtomolar
F_{max}	Fluorescence intensity of a metal-saturated fluorescent probe
F_{min}	Fluorescence intensity of a metal-free fluorescent probe
Glu	Glutamic acid
GM	Göppert-Mayer

GSH	Glutathione present in its reduced state
HEDTA	*N*-(2-hydroxyethyl)ethylenediamine-*N*,*N*′,*N*′-triacetic acid
His	Histidine
HOMO	Highest occupied molecular orbital
HRMS	High-resolution mass spectrometry
HSAB	Hard-soft acid-base (theory)
Hz	Hertz
ICT	(Photoinduced) Intramolecular charge transfer
IgE	Immunoglobulin E
iPrOH	Isopropanol
J	Coupling constant used in NMR characterization
K_d	Dissociation constant
K_d'	Apparent dissociation constant at a particular pH
LDBBA	Lithium diisobutyl-*tert*-butoxyaluminum hydride
log*K*	Stability constant
log*K*'	Apparent stability constant
LUMO	Lowest unoccupied molecular orbital
m	Multiplet
M	Molar (concentration term)
MAPK	Mitogen-activated protein kinases
μ	Ionic strength
μL	Microliter
μm	Micrometer
μM	Micromolar
MCL	Monovalent Copper Ligand

MeOH	Methanol
MES	2-(*N*-morpholino)ethanesulfonic acid
mm	Millimeter
mM	Millimolar
mmol	Millimoles
MT	Metallothionein
MTBE	Methyl *tert*-butyl ether
MTF-1	Metal regulatory transcription factor 1
NaAsc	Sodium ascorbate
NIH	National Institutes of Health
nm	Nanometer
nM	Nanomolar
NMR	Nuclear Magnetic Resonance
OD	Optical density
ORTEP	Oak Ridge Thermal Ellipsoid Plot
Φ_F	Fluorescence quantum yield
PET	Photoinduced electron transfer
PIPES	Piperazine-*N*,*N*′-bis(2-ethanesulfonic acid)
PIPBS	Piperazine-*N*,*N*′-bis(2-butanesulfonic acid)
POPC	1-palmitoyl-2-oleoyl-*sn*-glycero-3-phosphocholine
POPG	1-palmitoyl-2-oleoyl-*sn*-glycero-3-phospho-(1'-*rac*-glycerol) sodium salt
pM	Picomolar
pM	–log(metal concentration)
PSP	Phosphine Sulfide-Phosphine
q	Quartet

R	Ratio at a particular metal concentration
R_{max}	Ratio of a metal-saturated fluorescent probe
R_{min}	Ratio of a metal-free fluorescent probe
s	Singlet
S_0	Singlet electronic ground state
S_1	Singlet electronic excited state of n = 1
S_b	Instrument (microscope)-dependent factor for a metal-bound probe
S_f	Instrument (microscope)-dependent factor for a metal-free probe
t	Triplet
TEDTA	Thiobis(ethylenenitrilo)tetraacetic acid
TFA	Trifluoroacetic acid
TMD	Transmembrane domain
TMDTA	Trimethylenediaminetetraacetic acid
TPA	Trispicolylamine
TPEM	Two-photon excitation microscopy
TPEN	*N,N,N',N'*-tetrakis(2-pyridylmethyl)ethylenediamine
TRPS	Tunable Resistive Pulse Sensing
UV-Vis	Ultraviolet-visible light
V	Volts
ZIP	ZRT, IRT-like protein
zM	Zeptomolar
ZnT	Zinc Transporter protein

SUMMARY

Zinc plays critical roles as an essential trace micronutrient in biology by participating in multifarious biological processes that include protein synthesis, gene regulation, metabolic reactions, and DNA repair. While the majority of intracellular Zn(II) is tightly bound to endogenous proteins, there is growing evidence that cells regulate a buffered, kinetically labile pool of Zn(II). At present, the mechanisms that control Zn(II) regulation and distribution during cell growth and development largely remain unexplored, in part due to the challenges associated with phototoxicity and photobleaching of fluorescent probes that are used as indicators for detecting labile Zn(II) when utilized over extended periods of time. Providing an attractive solution over conventional linear optics, two-photon excitation microscopy (TPEM) allows fluorophores to be excited in the near-infrared region, thus offering improved depth penetration combined with reduced phototoxicity and photobleaching, as only fluorophores in the focal plane are excited. In order to take advantage of TPEM, a series of emission-ratiometric two-photon-excitable fluorescent probes that selectively bind Zn(II) with a 1:1 stoichiometry was developed and optimized for TPEM. Designed based on a non-centrosymmetric donor-π-acceptor architecture, the inherent fluorophore platform results in a balanced two photon cross section and a significant chromatic shift upon saturation with Zn(II). Using these optimized probes, the dynamics of labile Zn(II) pools in proliferating 3T3 mouse fibroblast cells using live-cell TPEM were investigated, with potential application in higher organisms, such as zebrafish and mice.

Chapter 1 provides a comprehensive overview of the roles of zinc biology, with emphasis in mammalian cells. This chapter also discusses the advantages of fluorescence microscopy as a powerful microanalytical technique for detecting labile Zn(II) in live

mammalian cells, as well as the photophysical and thermodynamic strategies for designing synthetic, metal-responsive fluorescent probes for facilitating the detection of labile Zn(II). Lastly, the objectives and overall approach to the work performed in this thesis are outlined.

Chapter 2 describes the synthesis and characterization of chromis-1, the first water-soluble, emission-ratiometric, Zn(II)-selective fluorescent probe whose photophysical properties were optimized specifically for TPEM. The inherent chemical properties of the fluorescent probe enabled robust emission-ratiometric capabilities in live 3T3 mouse fibroblast cells using TPEM.

Chapter 3 investigates the intrinsic photobasicity of chromis-1, as well as photophysical strategies to remedy the propensity for its pyridyl acceptor to undergo protonation in the excited state. Through the development of a model compound of chromis-1, the basicity of the pyridyl acceptor was explored, which was found to be 10^7-fold stronger in the excited state compared to the ground state. Rearrangement of the acceptor pyridine led to the development of a constitutional isomer of chromis-1 with a supposed reduced pH sensitivity. While the structural modification did exhibit a reduction in the pH sensitivity compared to chromis-1, the metal-binding ligand was found to play a substantial role in excited-state protonation, which led to the development and synthesis of a brand-new, metal-binding ligand that was incorporated in to the fluorophore core of the isomerized probe to afford the next-generation, pH-insensitive, Zn(II)-responsive ratiometric fluorescent probe chromis-2.

Chapter 4 explores the development of affinity-tuned fluorescent probes that provide a broad dynamic range of affinities for measuring potential changes in buffered Zn(II) present at varying concentrations and in various redistribution processes within the cell. Exploiting the aldehyde functionality of the fluorophore core developed for the synthesis

of chromis-2, the coupling of various metal-binding ligands to the fluorophore afforded a series of fluorophores whose Zn(II) stability constants span ten orders of magnitude from log*K* of 5.4 to 15.1. In addition, these fluorescent probes all demonstrate strong chromatic shifts in both their excitation and emission spectra upon binding Zn(II), as well as excellent metal-ion selectivity for Zn(II).

Chapter 5 investigates the dependence of the emission response on the polarity of the environment in which fluorescent probes, particularly those developed for probing biologically relevant monovalent copper, are characterized. As most fluorescent probes for Cu(I) are significantly lipophilic, their fluorescence behaviors in the aqueous buffer in which they are characterized do not translate well to similar fluorescence signaling responses observed once applied in the cellular environment. By fully characterizing their photophysical and thermodynamic properties in aqueous buffer supplemented with liposomes, the dichotomy between the lower-polarity liposomes and the polar aqueous buffer provides a relevant comparison to the dichotomous environment of the cell. Of the available fluorescent probes for monovalent copper, CS3, CTAP-2, and CTAP-3 represent the three most innovative developments in the Cu(I) fluorescent probe subfield, with CS3 being the most widely employed in imaging labile Cu(I). Therefore, the photophysical properties of these three probes were measured in the presence of liposomes and compared to their properties in aqueous buffer devoid of liposomes. In addition, the photophysical and thermodynamic properties of CTAP-3, as well as a recently developed ratiometric Cu(I) fluorescent probe, were meticulously characterized in both aqueous buffer and in the presence of liposomes.

Chapter 6 serves to discuss the overall conclusions of this work, as well as provide a possible direction in which to steer the design and development of ratiometric fluorescent indicators for probing labile Zn(II) in cellular systems.

CHAPTER 1

INTRODUCTION

1.1 Roles of Transition Metals in Biology

Transition metal ions, especially those of the first-row *d*-block of the periodic table, play an integral role in a myriad of biochemical processes by participating as enzymatic cofactors in reaction catalysis and by acting as structural components of proteins. These metals exist as trace elements in living organisms, but, despite their low abundance, the role that these micronutrients play is of undisputed importance to ensuring proper cellular function. Bioinformatics studies of the proteome have corroborated the importance of metal ions for structure and function. An examination of over 1,300 enzymes whose three-dimensional structures are known has approximated that 47% of these enzymes require metal cofactors, and 41% of these enzymes coordinate a metal ion in the active site.[1] In addition, metal-containing enzymes (metalloenzymes) are present in all six of the Enzyme Commission (EC) classes across all domains of life, demonstrating their importance for a diverse array of functions. Specifically, these functions entail the activation of nucleophiles or the stabilization of intermediates to facilitate catalysis, or they entail the stabilization of the proteins' secondary or tertiary structures, or sometimes both.

The relative affinities of metal-binding ligands, including metalloproteins, for divalent metal ions can be understood using the Irving-Williams Series[2] shown below,

$$Mn^{2+} < Fe^{2+} < Co^{2+} < Ni^{2+} < Cu^{2+} > Zn^{2+}$$

such that Cu^{2+} and Zn^{2+} exhibit a tighter binding to metal-binding ligands than those of the earlier first-row transition metals of biological relevance. However, the degree of metal-ligand complex formation depends on the concentrations of the metal ions available for

binding. The ordering of transition metals based on total intracellular concentrations deviates from the Irving-Williams order of stability of metal complexes, such that:

$$Fe^{2+}, Zn^{2+} > Cu^{2+} > Mn^{2+} > Co^{2+}, Ni^{2+}$$

with iron and zinc being the most abundant and cobalt and nickel being the least abundant in cells. Therefore, cells have evolved to utilize ligands with tighter binding affinities for transition metal ions that are significantly less abundant than the later first-row transition metal ions.

As zinc is the second most abundant transition metal in biological organisms, behind iron, its role in complex biological processes should not be understated. The next section highlights the biological importance of zinc, discussing briefly the key roles that the divalent transition metal ion plays in ensuring proper cellular function, as well as its implications in disease.

1.2 Roles of Zinc in Biology

Zinc is an essential, pervasive micronutrient required for living organisms across all three domains of life.[3] In humans alone, it is predicted that approximately ten percent of the human proteome comprises metalloproteins that require zinc for proper function.[3-4] Zinc is a member of the first-row transitions metals (*3d* level of the *d*-block elements) in the periodic table. With an electron configuration of $[Ar]4s^2 3d^{10}$, zinc is rendered redox-inactive under physiological conditions due to its d^{10} electron configuration, and its coordination chemistry and catalytic properties are governed by its stable 2+ oxidation state.[5] In aqueous solution, Zn(II) forms an octahedral, metal-aquo complex with the formula $[Zn(H_2O)_6]^{2+}$, which is a species of Zn(II) likely present at very low concentrations inside cells when not bound to endogenous ligands. The ability to lose its outer shell $4s^2$ electrons gives rise to its versatile reactivity and its Lewis acidity. Because of its d^{10} electron

configuration, Zn(II) has a ligand field stabilization energy of zero and thus its flexible coordination sphere tolerates a broad range of coordination geometries. With coordination numbers between four and six, Zn(II) complexes adopt various coordination geometries, including tetrahedral, octahedral, and trigonal bipyramidal, of similar energy and stability.[6-7]

According to the Hard-Soft Acid-Base (HSAB) theory, Zn(II) is considered a borderline Lewis acid based on its intermediate polarizability and charge density.[8] The HSAB theory is also used to predict the preference of metal ions, such as Zn(II), for ligands containing various donor groups. Therefore, borderline, intermediate Lewis acids, such as Zn(II), have a donor atom preference for other borderline, intermediate Lewis bases, such as nitrogen-containing heterocycles like pyridine, imidazole, aniline, etc. Given the correlation between donor basicity and metal-ligand coordination, it would seem evident that increasing the basicity of the donor would result in an increase in the metal-ligand affinity. In some instances, however, the increase in the donor basicity leads to an increase in the pK_a, which may invoke a lower affinity of the ligand for the metal cation at a desired pH in aqueous solution (discussed further in Section 1.5), since metal ions and protons compete for binding to the donor same donor atom of a ligand.

Nevertheless, Zn(II)'s Lewis acidity and flexible coordination sphere allow it to form very stable complexes with multifarious ligands, exploiting it as an effective cofactor and structural component of enzymes and proteins in every organism. The roles that Zn(II) plays can be divided into three main categories: as a catalytic cofactor in enzymes, as a structural component in proteins, and as regulatory messenger in signaling mechanisms, of which the former two will be discussed together in the following subsection.

1.2.1 The Catalytic and Structural Roles of Zinc in Enzymes and Proteins

A detailed analysis of the human proteome's zinc-binding proteins (ZBP) estimates that 60% of these metalloproteins utilize Zn(II) as a catalytic cofactor.[4] In addition, of the zinc-containing metalloenzymes, hydrolases, which includes phosphatases and peptidases, represents the most populated of the six EC classes. Both phosphatases and peptidases utilize a Zn(II)-activated water molecule as the nucleophile for hydrolysis of the substrate.[9] Transferases, which largely comprises kinases, make up the second most abundant class of zinc-binding metallonenzymes, where Zn(II) functions more as a structural component rather than a catalytic component. However, a prominent example of a transferase that utilizes Zn(II) as a catalytic cofactor is farnesyltransferase, which displaces a pyrophosphate stabilized by both Zn(II) and Mg(II) via a cysteine-mediated S_N2 attack on the farnesyl diphosphate substrate in the active site of the enzyme.[10]

Two prominent classes of enzymes that utilize Zn(II) in a catalytic role are carbonic anhydrases and alcohol dehydrogenases, whose crystal structures are represented in Figure 1.1. Carbonic anhydrases (CA), a class of enzymes found in erythrocytes, are responsible for catalyzing the hydration of carbon dioxide via the nucleophilic addition of a Zn(II)-activated water molecule to produce bicarbonate, a process necessary for regulating the levels of carbon dioxide in cells. Conserved throughout all isoforms of CA, three histidine residues within the active site are responsible for coordinating and stabilizing the Zn(II) ion, which then coordinates a water molecule as a fourth ligand, thereby activating the water molecule for nucleophilic addition to CO_2.

On the other hand, alcohol dehydrogenases (ADH), which comprise a group of isozymes responsible for catalyzing the interconversion between alcohols and aldehydes/ketones using NAD^+ as a coenzyme, coordinate two Zn(II) ions per subunit, one

involved in catalysis and the other serving as a structural component.[11] In the liver isoform, the active-site Zn(II) is coordinated by one histidine and two cysteine residues. Upon coordination of the alcohol substrate to Zn(II) to generate a tetracoordinate divalent cation, followed by deprotonation of the alcohol hydroxyl group by a serine residue within the active site, produces an alkoxide intermediate that is stabilized by the Zn(II) ion.[12] The Zn(II)-stabilized alkoxide facilitates the collapse of the tetrahedral intermediate and subsequent hydride transfer from the substrate to NAD^+.

Table 1.1 provides a list of additional, selected Zn(II)-dependent enzymes, including their functions, that play a crucial role in carrying out metabolic reactions within the cell. While this list is not comprehensive, it serves to demonstrate how diverse the chemistries that they catalyze are.

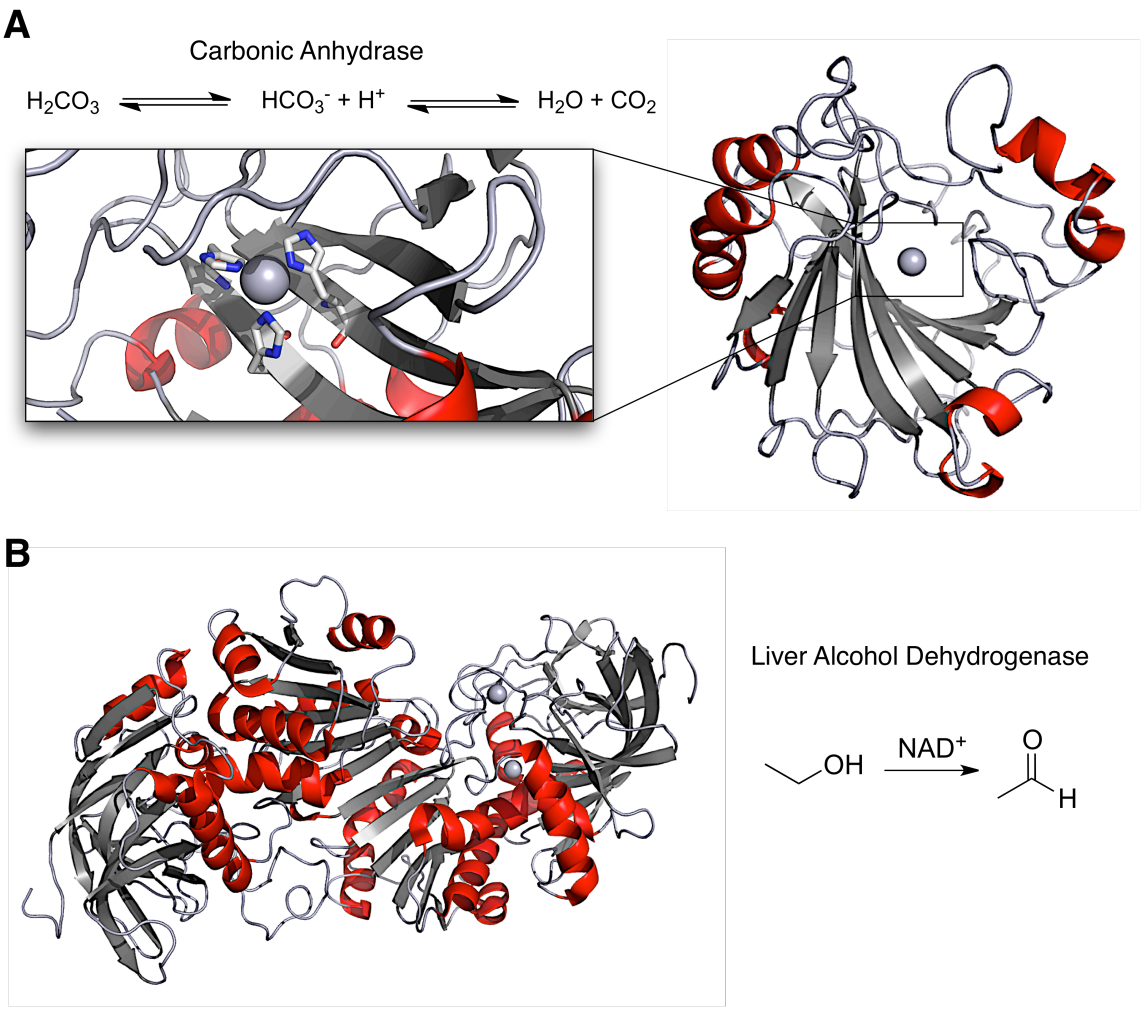

Figure 1.1: PyMol representation of two prominent Zn(II)-binding enzymes, carbonic anhydrase (A) and alcohol dehydrogenase (B). Carbonic anhydrase is responsible for catalyzing the reversible conversion of CO_2 and H_2O to bicarbonate to maintain a balanced pH, and alcohol dehydrogenase is responsible for the interconversion of alcohols and their corresponding aldehydes/ketones.

Table 1.1: Selected list of Zn(II)-dependent enzymes and their functions[a]

Enzyme	Function
Alcohol Dehydrogenase	NAD^+-dependent interconversion between alcohols and their corresponding aldehydes/ketones
D-lactate dehydrogenase	NAD^+/NADH-dependent interconversion of lactate and pyruvate in all living organisms.
Methanol dehydrogenase	Conversion of methanol to formaldehyde
Formaldehyde dismutase	An oxidoreductase that catalyzes the dismutation of two formaldehyde substrates to formate and methanol
Methionine S-methyltransferase	A transferase enzyme that catalyzes the transfer of a methyl group from S-adenosylmethionine to L-methionine to produce S-methyl-L-methionine in amino acid metabolism.
Methionine synthase	Regeneration of methionine from homocysteine.
Farnesyltransferase	Member of the prenyltransferase group that catalyzes the addition of a farnesyl group to a protein through the reaction of a protein's cysteine residue with farnesyl diphosphate
Riboflavin kinase	Transfer of a phosphate group from ATP to riboflavin to produce flavin mononucleotide (FMN)
Phospholipase C	A membrane-assisted enzyme that is responsible for cleaving the C-P bond of phospholipids between the phosphate group and the glycerol group
Amino Acid aminopeptidase family	A family of enzymes responsible for cleaving amino acids from the N-terminus of proteins
Carboxypeptidases	A family of enzymes responsible for cleaving amino acids from the carboxy (C-) terminus of proteins
Deaminases	A family of enzymes that catalyze the removal of an amino group (deamination) from a substrate
Fructose-Biphosphate Aldolase	An enzyme used in both the Calvin Cycle and in Glycolysis that catalyzes the reversible aldol condensation/cleavage of D-fructose 1,6-bisphosphate into glyceraldehyde 3-phosphate (GAP) and dihydroxyacetone phosphate (DHAP)

Table 1.1 continued

Enzyme	Function
Carbonic Anhydrase	Interconversion of CO_2 and H_2O to bicarbonate in red blood cells
Mannose-6-Phosphate Isomerase	Isomerization of mannose-6-phosphate and fructose-6-phosphate.
Pyruvate Carboxylase	The physiologically irreversible carboxylation of pyruvate to produce oxaloacetate to generate intermediates that necessary for the critic acid cycle
Histone Deacetylase	Removal of acetyl groups from *N*-acetyl lysine residues of histone proteins involved in epigenetic regulation

[a]List compiled from ENZYME, the Enzyme Data Bank provided by ExPASy.

Of the metalloenzymes that are known to bind Zn(II), approximately 22% of these enzymes utilize the divalent transition metal for structural purposes.[13] In addition, 86% of Zn(II)-binding enzymes that do not involve Zn(II) in the catalytic reaction utilize the metal as a structural component. Unlike catalytic Zn(II) centers, which tend to form complexes with three active-site ligands consisting of His, Glu, Asp, or Cys, with His being the most predominant, structural Zn(II) sites comprise complexes with four amino acid ligands and do not coordinate water molecules.[14] Moreover, structural Zn(II) sites most commonly prefer Cys residues for coordination, followed by His residues as the second most common. Enzymes that bind Zn(II) for structural purposes, however, do not limit the metal ion solely for structural purposes. The first enzyme that identified Zn(II) as having a structural role and a catalytic role was horse alcohol dehydrogenase, which features a zinc ion coordinated to the thiolate functionalities of four Cys residues in a tetrahedral geometry.[15]

In structural Zn(II) sites, the general role that the metal plays is to maintain the local structure of the protein, which can indirectly affect the activity of a protein through

chemical or conformational changes in the environment of the active-site.[14] One such structural motif of proteins that utilizes Zn(II) for stabilization is the zinc-finger motif, which features a conserved Cys_2His_2 cluster for coordinating the metal cation. This motif has proved to be a ubiquitous structural component of proteins, with gene sequences that code for its expression comprising approximately 3% of the entire human genome.[16] The zinc-finger motif serves a variety of roles that are either vital for maintaining normal cellular function or for facilitating rapid cell proliferation that include transcriptional regulation and activation, DNA replication and repair, RNA packaging, and even facilitating protein folding.[16-19]

1.2.2 Zinc as a Neurotransmitter and Secondary Messenger

Recently, zinc has been found to play a significant role as an extracellular and intracellular signaling factor, facilitating chemical communication between cells by functioning as a potential neurotransmitter, translating extracellular stimuli into intracellular signaling cascades, and participating in the regulation of various intracellular signaling pathways.[20-21] These signaling mechanisms are engendered through fluctuations in zinc concentrations in both the extracellular and intracellular milieu, which leads to the activation of molecular mechanisms that have diverse physiological and pathological implications. For example, zinc that is released from presynaptic neurons into the synaptic cleft has been shown to bind to various membrane-bound receptors and transporters in postsynaptic neurons, thereby modulating neurotransmitter functions.[21-23] Furthermore, glucose-mediated co-release of Zn(II) and insulin from insulin secretory vesicles in pancreatic β-cells produces a signaling response that suppresses further insulin secretion from these cells, thereby acting as a direct regulator of insulin levels in the blood. Extracellular zinc also

has been shown to regulate hepatic insulin secretion through suppression of insulin clearance.[24]

In addition to its role as a neurotransmitter, it has been suggested that zinc functions as a secondary messenger in cells, similar to the roles that calcium, cyclic adenosine monophosphate (cAMP), cyclic guanosine monophosphate (cGMP), and protein phosphatases play in signaling cascades. It has even been well established that Zn(II) acts as an inhibitor of protein tyrosine phosphatase activity, with an inhibition constant in the nanomolar range.[25] In mastocytes, cross-linking of membrane-localized IgE receptors results in a large increase in cytosolic zinc levels emanating from the endoplasmic reticulum (ER), a phenomenon referred to as zinc wave, which is believed to inhibit protein phosphatase activity for MAP kinase (MAPK) activation-induced expression of cytokines.[20, 26-27]

1.3 Regulation of Zinc

Indeed, given the ubiquitous dependence of maintaining proper cellular function on zinc, regulation of zinc both within the cell and between the intracellular and extracellular milieu is achieved through a sophisticated network of metal receptors, transporters, and chaperones (Figure 1.2).[28] One of the keys to maintaining cellular zinc homeostasis lies in the existence and activities of two families of mammalian zinc transporters: the ZIP (Zrt, Irt-like protein, SLC39A family) and the ZnT (SLC30A family). The ZIP family consists of 14 transmembrane proteins that are responsible for shuttling Zn(II) either from the extracellular space into the cytosol or from the organellar lumen into the cytosol.[29] While structures of these metal ion transporters are not known, the 14 ZIP transporters consist of eight predicted transmembrane alpha-helical domains and a His-rich sequence within a variable loop region between domains III and IV, along with the N- and C-termini that

extend into the extracellular space (Figure 1.3, left).[29-30] The highly conserved primary sequences of transmembrane domains (TMDs) III and IV are predicted to form channels through which the metal ions can pass by featuring two His residues that bind the Zn(II).[30-32]

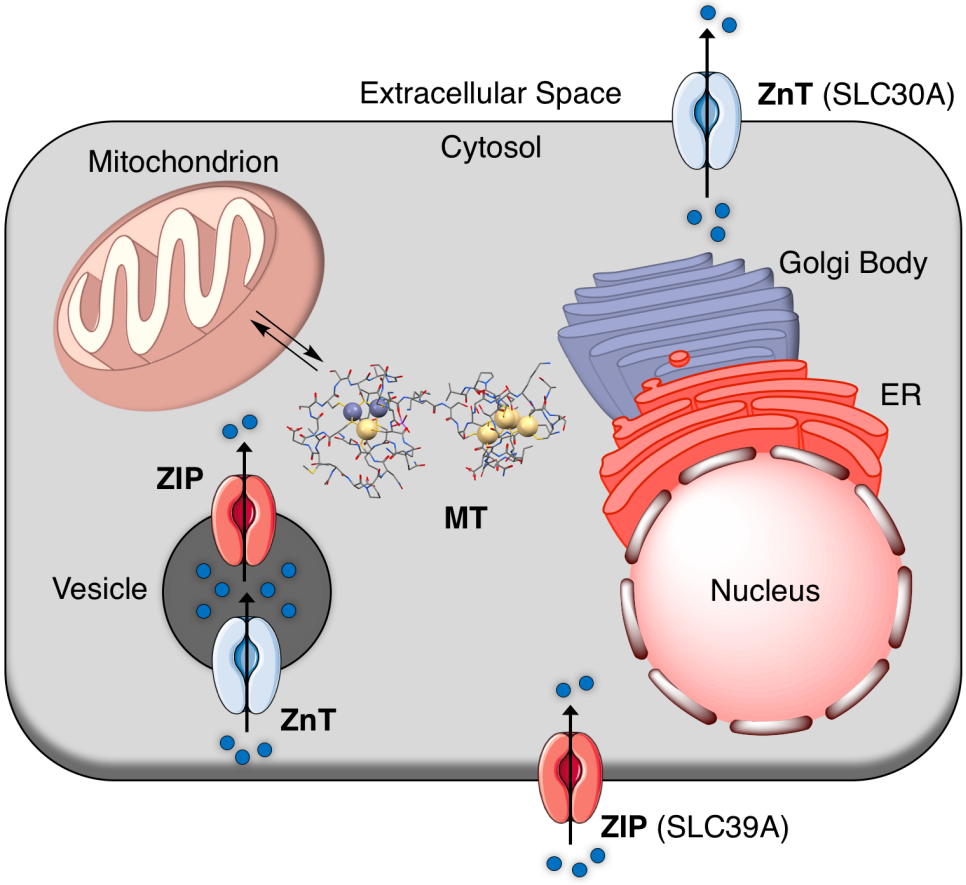

Figure 1.2: Cellular distribution and direction of zinc transport of mammalian zinc transporters. Of the information currently available, zinc transport and redistribution is carried out by a series of membrane-bound ZnT (blue receptors) and ZIP (red receptors) transporters, which are responsible for exporting and importing zinc relative to the cytosol, and metallothionein (MT), a cytoplasmic, soluble metal-binding protein that is capable of binding up to seven Zn(II) ions. Illustrations in figure were provided by ChemBioDraw and Servier Medical Art (www.servier.com).

Changes in expression levels of nearly every ZIP transporter in mammalian tissue have indicated widespread implications in disease due to mistrafficking that leads to either

an accumulation of or a deficiency in cellular zinc.[29] ZIP4, in particular, is highly expressed in tissues responsible for absorption and reabsorption of Zn(II), such as the small intestines, stomach, large intestines, and even the kidney, with localization to the cellular membrane for importing Zn(II) into the cell from the extracellular space.[33] In humans, several mutations in ZIP4 have been identified in acrodermatitis enteropathica (AE) patients, which leads to symptoms such as diarrhea, dermatitis, hair loss, inflammation, and immune deficiency.

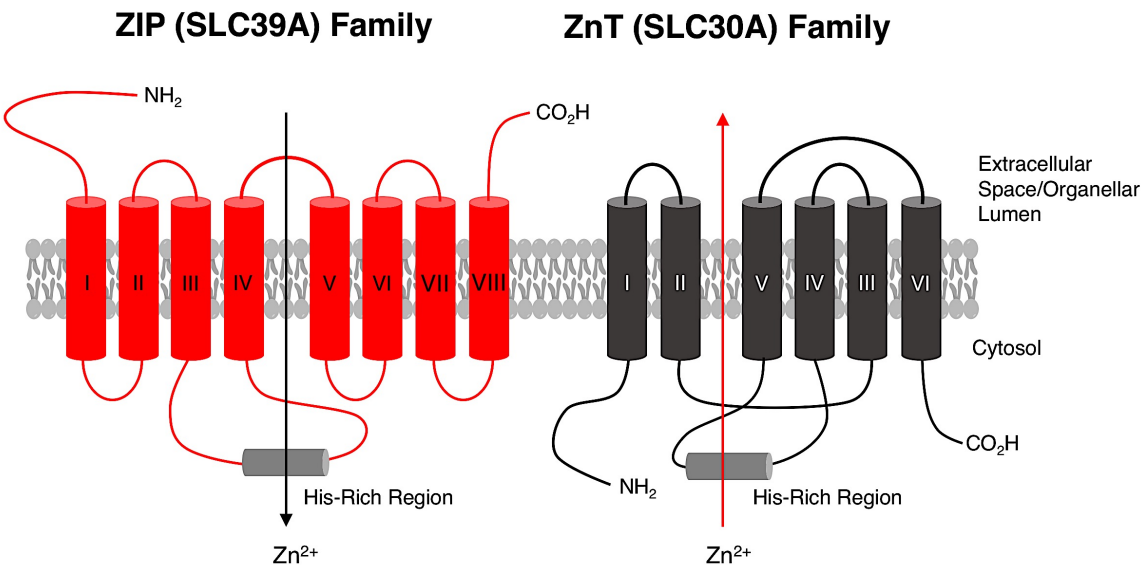

Figure 1.3: Predicted transmembrane topologies and direction of Zn(II) transport of the ZIP and ZnT transporter families. In the ZIP family, there exists a highly conserved His-rich region in the loop between domains 3, and in the ZnT family, the His-rich region lies in the loop between domains 5 and 6. These His-rich regions are predicted to facilitate zinc transport by binding Zn(II) to the histidines, which then allows the transfer of the zinc ion to the amino acid residues within the channel for export from or import into the cytosol. Arrows indicate the direction of travel of Zn(II). Figure adapted from reference [32].

Conversely, the ZnT family of transmembrane transporters is responsible for exporting Zn(II) from the cytosol into the extracellular space or organellar lumen. In mammals, the 10 members of this family of transporters are predicted to consist of six alpha-

helical TMDs, with a highly conserved His-rich sequence within the variable loop between domains IV and V, similar to ZIP proteins (Figure 1.3, right).[29, 31] In addition, ZnT's feature their N- and C-termini on the cytosolic face of the cell membrane rather than the extracellular space/organellar lumen, as is the case with ZIP's. The primary amino-acid sequences of TMDs I, II, and V are highly conserved, which alludes to the function of these domains as potential channels for exporting Zn(II) from the cytosol using Asp (D) and His (H) residues as metal-binding sites within this channel.[34]

Several ZnT's, including ZnT3, 5, 7, and 8, have been shown to play a significant role in insulin regulation with implications in diabetes.[35-40] Recently, ZnT8 has become one of the most rigorously explored zinc transporter associated with diabetes, particular Type-2 (T2D).[40] This metal-ion transporter is exclusively expressed in pancreatic β-cells and functions to export zinc from the cytosol into insulin secretory vesicles for insulin biosynthesis and storage.[24, 41-42] Depending on expression-level regulation, overexpression of ZnT8 has been shown to induce glucose-stimulated insulin secretion,[43] whereas reduced expression has led to reduced insulin secretion in hyperglycemic environments.[44] In ZnT8-KO (knockout) pancreatic β cells, the insulin secretory vesicles of these cells are devoid of insulin that is normally crystallized as its $Insulin_6Zn_2$ hexamer for stabilization and storage *in vivo*, suggesting that ZnT8 is crucial for transporting zinc into these vesicles.[45]

The complex yet inadequately understood mechanisms involved in zinc regulation rely not only on membrane-bound metal-ion transporters, such as ZnT's and ZIP's, but also soluble metal-binding proteins, such as metallothioneins (MTs), that facilitate the transport and distribution of Zn(II) and other biologically relevant transitions metals throughout the cytoplasm. Metallothioneins represent a family of cysteine-rich, metal-binding proteins of low molecular weight (6-7 kDa) that are present in nearly every living

organism.[46] Mammalian MTs consist of a single polypeptide chain of 61-68 amino acids, 18-23 of which are highly conserved cysteine residues that are capable of binding up seven divalent metal ions in a tetrahedral geometry or 12 monovalent copper ions in a trigonal geometry through metal-thiolate cluster formation (Figure 1.4).[46-49] While mammalian MT *in vivo* tends to be present either in the Zn(II)-bound form or as a mixed metal-form, the diversity of metals that have been found to be sequestered by MT, including Cu(I), Cd(II), Pb(II), Ag(I), Hg(II), Bi(II), hints at its role as a possible metal scavenger for controlling heavy-metal toxicity in multifarious organisms.[50-51]

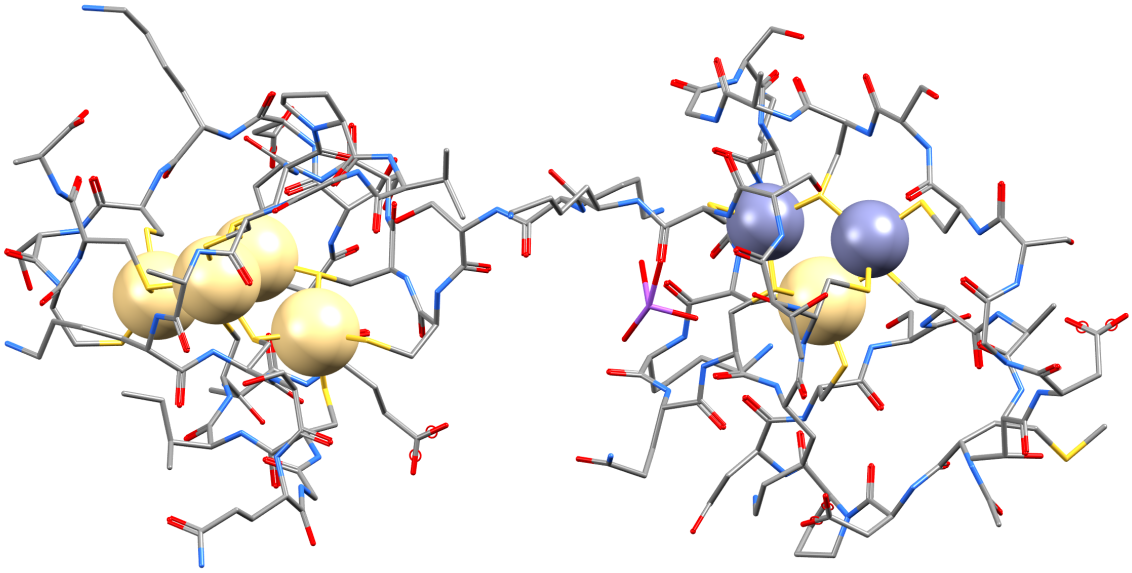

Figure 1.4: Crystal structure of mammalian (rat) metallothionein-2 (MT-2, PDB code: 4MT2), crystallized with 4 Cd^{2+} ions (gold spheres) and 2 Zn^{2+} ions (indigo spheres).[52] Figure was prepared using Mercury version 3.9.

As a cytoplasmic protein, MT engages in metal-binding equilibria with thionein, the metal-free apo-form of MT, which does not feature a defined secondary structure; thus, thionein relies on the coordination of seven transition metals for achieving its three-dimensional fold. Intracellular buffered Zn(II) concentrations, therefore can be regulated through the biosynthesis of thionein, such that, in response to elevated intracellular zinc levels,

binding of the metal regulatory transcription factor (MTF)-1 to the gene sequence that codes for thionein can trigger its expression.[53] Despite the presence of only two Zn(II)-coordinating clusters in human MT, forming a Zn_4S_{11} cluster and a Zn_3S_9 cluster within the α and β domains, respectively, analysis of the Zn(II)-metallothionein complexation equilibria using two known Zn(II)-binding fluorescent probes revealed three different magnitudes of Zn(II)-binding equilibria within these two clusters with stability constants are that separated by four logarithmic units from log*K* of 11.8 to 7.7.[54] The presence of dynamic equilibria between thionein and MT that involve multiple Zn(II)-binding events corroborates the role of MT in zinc buffering within the cell by serving as a cytoplasmic transport vehicle for distributing zinc ions to endogenous cellular ligands, such as other metalloproteins and transcription factors, whose function is vital for cell regulation.[28, 48]

Overall, the interconnected network consisting of 24 mammalian zinc transporters and 2 mammalian MTs that have currently been investigated contribute to the cellular import, export, and redistribution of cellular zinc throughout the various compartments of the cytoplasm and between the intracellular and extracellular milieu. The cellular zinc level, which reflects the total concentration of zinc in the cell (also referred to as the zinc quota), can be divided into three different categories based on its availability: a static fraction that remains tightly bound and therefore unavailable to participate in exchange reactions, a chemically exchangeable fraction that is ligated and participates in homeostatic regulation, and a subpool of labile, aqua-Zn(II) ions that are devoid of coordinated ligands and buffered at very low concentrations. Each of these three components is critical for maintaining zinc homeostasis. While the majority of cellular zinc is tied up in metal complexes with endogenous ligands, the subpool of labile zinc ions, in addition to the ligated yet kinetically exchangeable fraction, comprise the speciation of zinc that is implicated in disease.[55] Because buffered Zn(II) concentrations are orders of magnitude lower than the

zinc quota, the quantitative analysis of these labile Zn(II) pools within the complex cellular environment is very challenging yet critical to understanding how changes in these metal ions pools are correlated to mistrafficking processes that lead to disease. Despite its challenges, various analytical methods that rely on synthetic and genetically encoded Zn(II)-binding ligands have estimated the concentrations of buffered Zn(II) levels in mammalian cells to be in the range of 60-270 picomolar (pM),[55] with higher concentrations ranging from 110-452 pM for certain pancreatic β-cell lines,[37, 56-58] and even as high as 0.614-1.25 nM in proliferating colon cancer cells.[59] Although there exist deviations between specific cell types and tissues, the general consensus is that the exchangeable Zn(II) pool is buffered in the high picomolar to low-nanomolar concentration range.

1.4 Microanalytical Techniques for *in situ* Imaging of Metals in Biology

Elucidating the complex regulatory mechanisms involved in intracellular transition-metal redistribution, trafficking, and storage is imperative for understanding the roles that metal imbalances play in certain diseases. Accomplishing this objective ultimately requires tools for identifying these metals and quantifying their concentrations in cells using analytical instrumentation that offers both high spatial and temporal resolution as well as sufficient sensitivity.[60] Given the small size of a single cell, the *in situ* detection of biologically relevant metal ions requires extremely sensitive microanalytical instrumentation. However, certain conventional analytical techniques for trace-metal analysis, including voltammetry, potentiometry, and X-ray fluorescence, do not deliver the ability to visualize the distribution of metal ions in a spatial manner.[61] Of the currently available microanalytical techniques that permit both the visualization and quantitation of transition metal-ion concentrations at the single-cell level, autometallography, visible light microscopy, and optical fluorescence microscopy are among the most capable methods.[60]

Amid these widely-employed methods, optical fluorescence microscopy offers the best balance between cost-effectiveness and high sensitivity, with submicron spatial resolution and sensitivity down to the single-cell level.[62] Because metal ions themselves are not fluorescent, the utilization of optical fluorescence microscopy requires fluorescent sensors that not only selectively bind the metal analyte of interest, but also induce a change in the emission profile (i.e. through a spectral shift) or intensity to discriminately signal the association of the metal ion with the sensor. While X-ray fluorescence spectroscopy has the capability to measure down to the single-cell level, it only reports on the total metal ion concentration, including those metals that are tied up in endogenous metal-ligand complexes, rather than the pool of kinetically exchangeable metal ions that are important in regulation. Conversely, the use of fluorescent probes in microscopy leads only to the ability to report on the subpopulation of metals that are kinetically and thermodynamically exchangeable, or "labile," within the cell. However, when examining redistribution patterns of metals in proliferating cells over a prolonged period, for example, the use of high-intensity lasers to excite the biological sample can result in photobleaching of the fluorescent probe. For this reason, among others, various microscopy techniques have been developed to enable better sensitivity with deeper sample penetration.[63] One such microscopy technique that has been widely utilized is two-photon fluorescence microscopy, which offers many advantages for imaging live biological samples over prolonged periods of time. The following subsection describes, in detail, the principles of two-photon fluorescence microscopy and its advantages compared to conventional confocal fluorescence microscopy.

1.4.1 Two-Photon Excitation Microscopy (TPEM) and its Application in Biological Imaging

Since the development of the theory of two-photon absorption (2PA) in 1931[64] and the first experimental demonstration of the process in 1961,[65] the invention and further improvement of sub-picosecond pulsed Ti:sapphire lasers to investigate the 2PA process facilitated the evolution of the two-photon fluorescence microscope by Webb and coworkers in the early 1990's.[66] Since then, two-photon excitation microscopy (TPEM) has been widely adopted for the exploration of multiphoton processes not just in biological systems but also in various non-linear optical materials.[67]

Compared to conventional one-photon absorption, two-photon absorption entails the simultaneous absorption of two photons at half the energy, or twice the wavelength (Figure 1.5). Therefore, the probability of two photons interacting with the fluorophore simultaneously increases with the square of the light intensity, whereas one-photon absorption depends only linearly on the intensity of the light.[68] Consequently, two-photon absorption demands lasers of higher, more intense laser power, such as sub-picosecond pulsed lasers, in order to generate a higher photon density that is sufficient for two-photon excitation.

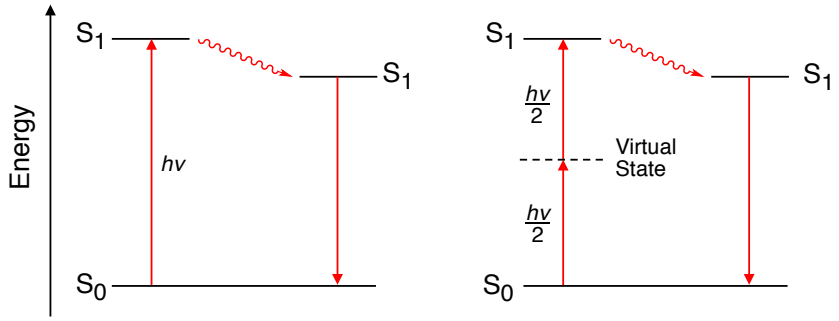

Figure 1.5: Simplified Jabłoński diagram for the comparison between one- (left) and two-photon (right) excitation of a fluorophore.

With respect to the fluorophore employed in TPEM applications, the optical sensitivity of the chromophore is dependent on the fluorophore brightness ($\eta\delta$, also known as the action cross section), which is proportional to the two-photon cross section (δ) and the fluorescence quantum yield (η). Developing and utilizing fluorophores with large 2PA cross sections that lie at or near the two-photon resonance energy is advantageous for increasing the signal-to-noise ratio in microscopy applications. Achieving large 2PA cross sections for fluorophores can be accomplished by incorporation of an electron-rich donor and an electron-deficient acceptor at opposite ends of a conjugated π-system (discussed further in Section 1.5.4.1)

For a simple donor-acceptor model that comprises an electronic transition between only two states, the ground state (S_0) and the lowest vibrational level of the lowest excited state (S_1), the maximum cross section (δ_{max}) of a molecule at the two-photon resonance energy is mathematically related to both the change in the permanent dipole moment ($\Delta\mu$) and the transition dipole moment (M_{01}) via equation 1-1[69] below:

$$\delta_{max} = \frac{2\pi L^4}{5\varepsilon_0^2 n^2 c^2 h}\left(\frac{(\Delta\mu)^2 M_{01}^2}{\Gamma}\right) \quad (1\text{-}1)$$

where Γ represents a damping term associated with the one-photon transition ($S_0 \rightarrow S_1$), which represents the half-width at the half maximum of the two-photon absorption band, and L corresponds to the optical field enhancement compared to that in a vacuum, which is related to the refractive index n of the medium per the relationship $L = (n^2 + 2)/3$.[68-69] Cross section values are reported in units of Göppert-Mayer (GM), named after Maria Göppert-Mayer who theoretically predicted the two-photon absorption process, where 1 GM is equivalent to $1 \cdot 10^{-50}$ $cm^2 \cdot s \cdot photon^{-1}$. Based on equation 1-1, the two-photon cross

section δ increases with increasing excited-state polarization. Therefore, in theory, maximizing the excited-state polarization of the fluorophore should lead to an increase in the two-photon absorption cross section, which in turn will increase the fluorophore brightness for better sensitivity.

The application of two-photon excitation in fluorescence microscopy can be best understood by comparing it to conventional laser-scanning confocal microscopy (LSCM). Both microscopes feature lasers that, at a specific intensity and wavelength, are used to irradiate the focal volume of a sample, and scanning of this focal volume throughout the entire sample, with collection of the emission signal, will result in construction of an emission intensity map.[68] As stated above, for a one-photon process, absorption of a photon is proportional to the intensity of the laser, whereas the photon density of a two-photon absorption is proportional to the square of the light intensity, so the photon density rapidly decreases outside the focal volume. Therefore, the focal volume in two-photon excitation is significantly smaller than in one-photon excitation, resulting in a higher resolution of the microscope.

As illustrated in Figure 1.6, photons produced from the laser travel through an epiluminescence light path and are reflected by a dichroic mirror to the microscope's objective, which focuses the photons on the sample to provide maximum photon density for excitation.[70] Because the photon density of the corresponding two-photon excitation is significantly smaller at the focal volume compared to the focal plane, excitation of the three-dimensional volume (voxel) deep within a sample can be achieved without exciting above or below the focal plane, thereby reducing interference from the surrounding material. Therefore, 2PA generates a very sharp emission point at the focus, whereas 1PA produces an emission stream that follows the direction of the beam path, resulting in a much larger excitation volume (Figure 1.6, inset).[68] Photons emitted from the fluorescent

sample are then collected by the objective and transmitted along the emission path through the dichroic mirror, and before they reach the photomultiplier photon sensor, they are passed through a barrier filter that serves to further attenuate the light.

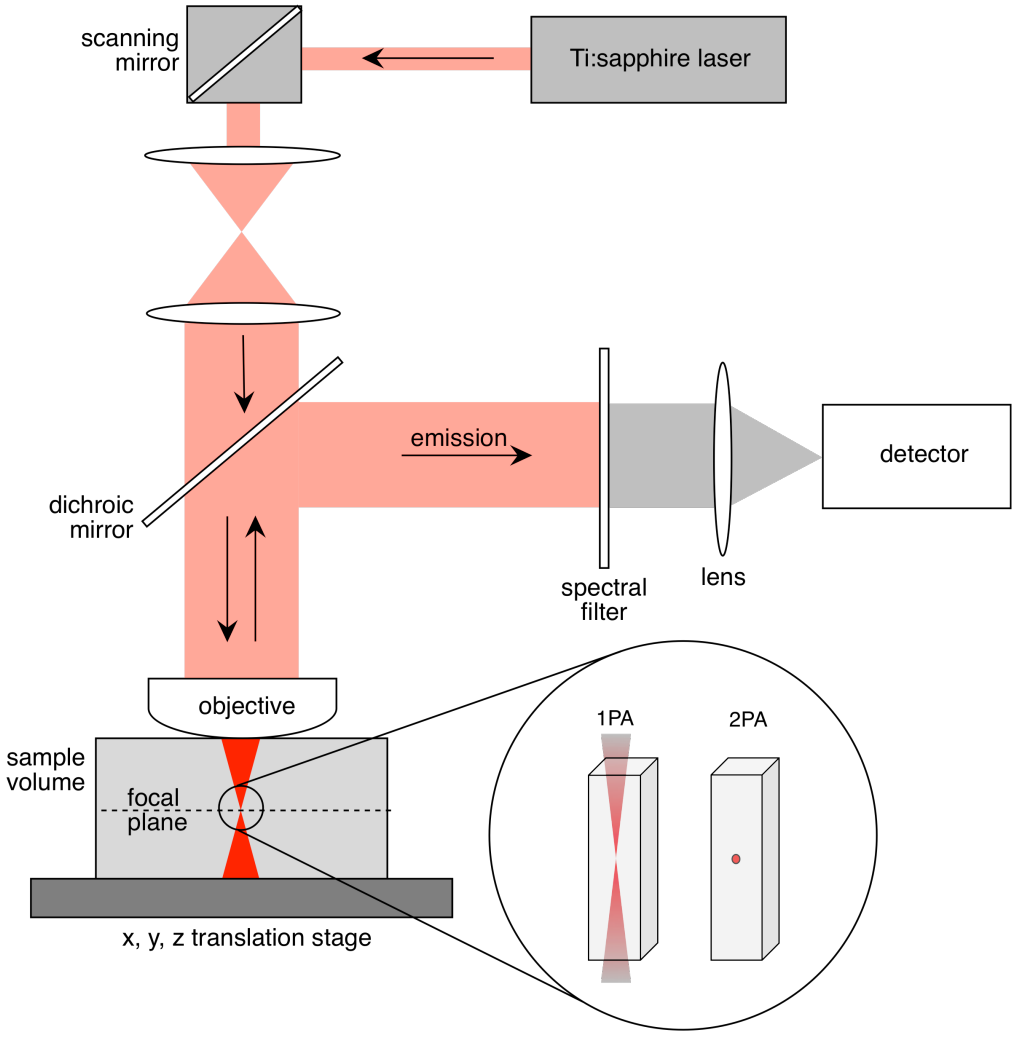

Figure 1.6: Simplified diagram of a two-photon excitation fluorescence microscope. A femtosecond pulsed laser beam is focused on the focal volume of a sample that is then excited by the simultaneous absorption of two photons at half the energy needed to excite the fluorophore. The emission from the focal volume is then passed through a dichroic beam splitter and collected by photomultiplier detectors. The insert depicts the difference between the excitation densities of one- and two-photon microscopes. Figure adapted from reference [68].

Overall, TPEM offers many advantages over conventional confocal fluorescence microscopy for biological imaging. As previously mentioned, by exciting the sample at

longer wavelength (typically 700-1000 nm), the lower-energy photons produced by the laser source make TPEM better suited than one-photon microscopy for imaging biological samples that may be sensitive to UV or shorter-wavelength visible light. This means that samples can be imaged for prolonged periods of time with reduced phototoxicity and photobleaching. In addition, excitation in the near-infrared region results in improved depth penetration, especially in tissues that are prone to intense scattering. TPEM also offers intrinsic 3D imaging capabilities by the ability to acquire equally spaced images along the z-axis of the biological sample. Lastly, the excitation that is restricted to the focal volume using TPEM results in significantly reduced autofluorescence from endogenous intracellular small molecules, such as NADPH and flavins, which is quite attractive for biological imaging. These advantages have promoted the on-going development of fluorescent probes for application in biological imaging using TPEM.[71-72] However, because one-photon and two-photon excitation are inherently different quantum-mechanical processes, fluorescent probes for use in TPEM applications should, therefore, be designed and optimized for two-photon absorption, rather than simply using sensors designed for one-linear processes in two-photon absorbing processes.

1.5 Strategies and Considerations for Designing Metal-Responsive Fluorescent Probes

Small-molecule, synthetic fluorescent probes that can engage in competitive exchanges with endogenous, labile metal “pools” have become indispensable tools for cellular biologists for probing cellular metals due to the ubiquity of fluorescence microscopes. However, the development of effective probes for detecting metals in biology demands an extensive chemical and biological cooperation in an effort to avoid drawing conclusions

based on inadequate or misleading data that arise due to insufficient characterization. For instance, the chemical properties of probes that must be tailored towards the demands of biological experimentation include high selectivity for the metal analyte of interest (as well as preference for oxidation state if the metal analyte of interest is redox-active) over other competitors within the biological environment.[73] Designing cation-selective fluorescent probes, therefore, requires a thorough understanding of coordination chemistry, including coordination geometry and HSAB theory; and photophysical principles to ensure a translation of a metal-binding event into a fluorescence readout that can be detected in the cellular environment using fluorescence microscopy. The following subsections describe the fundamental thermodynamic concepts of metal-ligand interactions and the photophysical principles that lay the foundation for the development of synthetic probes that undergo metal ion-induced fluorescence changes.

1.5.1 The Thermodynamics of Metal-Ligand Interactions

For a probe whose fluorescence readout is modulated by the binding of a metal cation to the metal-coordinating ligand of the probe, which governs both the affinity and selective of the fluorescent probe, the metal cation (M^{n+}) participates in a reversible binding equilibrium with the probe (P) to form a metal-ligand complex (PM^{n+}) with a 1:1 binding stoichiometry. Because these reaction equilibria take place in solution, the solvation of both the metal cation and probe play a critical role in contributing to the stability of the metal-ligand complex. For solution equilibria taking place in water as the solvent, equation 1-2 can be written to describe the equilibrium reaction taking into account solvation effects:

$$M^{n+}_{(aq)} + P_{(aq)} \underset{K_d}{\overset{K_a}{\rightleftharpoons}} PM^{n+}_{(aq)} \qquad (1\text{-}2)$$

The thermodynamic stability of the metal-probe complex (PM^{n+}) can be expressed as either the association equilibrium constant (K_a) or the dissociation constant (K_d) depending on the direction of the equilibrium. Translation of the equilibrium equation 1-2 into an equilibrium constant expression, represented by equation 1-3:

$$K = \frac{[PM^{n+}]}{[M^{n+}][P]} \tag{1-3}$$

Metal-binding fluorescent probes can be designed to engage in coordination with multiple metal cations, or they can be designed such that more than one fluorescent ligand engages in coordination with one metal analyte. These scenarios, however, make the *in-situ* quantification of metal-ion concentrations difficult, in part, because these equilibria may not result in a fluorescence response that is proportional to the output generated from the 1:1 binding stoichiometry.[74]

The equilibrium expressions above consider the activities of the individual species, which are the products of the concentrations of the species and their unit-less activity coefficients, γ. However, analytical measurements to determine the equilibrium constants often report values as concentrations rather than activities. However, the titrations that are performed to determine the thermodynamic constants for a particular equilibrium reaction involve a change in the concentration of the species throughout the titration, which would therefore change the activity of the solution. To ensure that the activity term of the thermodynamic expression remains constant, using a large excess of a chemically inert, non-complexing electrolyte that functions as an ionic background; however, it is important that the concentration of the species of interest does not exceed 5% of the total ionic background to ensure that the activity remains constant.[75] In addition, since the activity

term $\gamma_{ML}/\gamma_M \cdot \gamma_L$ is dependent on both the chemical identity and concentration of the background electrolyte, it is important to not only specify these parameters but also perform calibrations of the probes under identical or similar conditions to enable comparisons between previously conducted metal-ligand interactions.[74]

1.5.2 Protonation as a Competing Pathway in Metal-Ligand Complexation

Metal-ligand complexation equilibria can encounter significant challenges if the ligand engages in protonation equilibria that compete with the metal for binding to the ligand, specifically if the protonation constants lie above the pH of the solution. In such cases, the extent of metal-ligand complex formation is dependent on the pH of the solution; thus, at lower pH, the increase in $[H_3O^+]$ shifts the equilibrium to disfavor the formation of ML. For this reason, the protonation constants of the ligand used in the complexation equilibria should be well-characterized to account for this in the calculation of the equilibrium constants.

Typically, protonation constants are defined with regard to the concentrations of the species in solution rather than the activities, which is comparable to the stability formation constants discussed in the previous section. This means pK_a values are determined based on measuring the hydronium ion concentration p[H] (also commonly written as pH_c). Characterizing either metal-binding ligands, including fluorescent probes, to determine their protonation constants is routinely performed using a combination glass electrode that ideally has been calibrated according to Gran's Method[76-78] or, otherwise, calibrated to a series of standardized solutions of defined pH. To ensure that the pronation constants are expressed in terms of their molar concentrations rather than their activities, the concentration-based protonation constants should be converted to mixed-mode constants by correcting the values upward by 0.11 (for an ionic strength of μ = 0.1 M), which

is recommended by Martell and Smith[79] (for derivation of this correction factor, see reference: Bagchi, P. *et al.*[80]).

To avoid further complications when determining the stability constants of ligands with various protonation states that are pH-dependent, the concept of "apparent" stability constants was introduced,[81] which are equilibrium constants that reflect all significant protonation equilibria of the ligand and metal cation that may influence the metal-ligand interaction. Consider a metal-ligand complexation equilibrium, in which ligand L interacts with metal M to form ML, as described in equation 1-2 (vide supra). Determination of the stability constant ($\log\beta$) of the ligand complex yielded a value of 15.0, and assuming a triprotic equilibrium, the corresponding protonation constants of 9.0, 6.0, and 3.0 indicate that at a neutral pH of 7.0, the ligand is mostly present as the monoprotonated species. Therefore, the presence of a monoprotonated species results in an apparent affinity that is lower at neutral pH as implied by the pH-independent stability constant of 15.0. After correcting the protonation constants upward by 0.11 to account for the ionic strength of the solution, yielding values equal to 9.11, 6.11, and 3.11, respectively, the apparent affinity of the ligand at neutral pH is more than 100-fold lower, yielding a $\log\beta'$ of 12.8. This concept illustrates the significance of protonation equilibria and their implications in determine the stability constants of ligands.

1.5.3 Relating Binding Affinities to Dynamic Ranges

The employment of metal-binding fluorescent probes in a biological environment involves engagement of the probe in competitive binding equilibria with endogenous ligands that, too, bind the metal analyte for which the probe is responsive. In order to effectively engage in competition with these endogenous ligands, the binding affinities of the

fluorescent probes must closely match those of the competitive ligands. Thus, for a meaningful interpretation of biological imaging data, a thorough understanding of all metal-binding equilibria associated with the fluorescent probe is of critical importance.

If the fluorescent probe coordinates the metal cation of interest with a 1:1 binding stoichiometry, equation 1-3 can be used to derive the fractional saturation f of the probe as a function of the buffered metal ion concentration.[74] The fractional saturation is a crucial element for evaluating the dynamic range of the probe response and is defined as the ratio of the concentration of the probe-metal complex [PM^{n+}] to the total probe concentration ($[P]_{total}$) according to equation 1-4:

$$f = \frac{[PM^{n+}]}{[P]_{total}} \tag{1-4}$$

By Combing equations 1-3 and 1-4, the fractional saturation of the probe can be expressed as a function of the free metal ion concentration $[M^{n+}]_{free}$ and the dissociation constant of the ligand ($K_d = 1/K$):

$$f = \frac{[M^{n+}]}{K_d + [M^{n+}]} \tag{1-5}$$

This relationship demonstrates that, within the biological environment, the fractional saturation of the probe is governed by the buffered metal ion concentration, irrespective of the probe concentration, provided that it does not exceed the buffer capacity. At the equivalence point, where the fractional saturation of the probe is 50%, the free metal-ion concentration is equal to the dissociation constant of the metal-ligand complex. A plot of the fractional saturation of probe versus the buffered metal concentration, corresponding to the binding isotherm, graphically illustrates this relationship (Figure 1.7). The slope of the

isotherm is largest within the 90:10% fractional saturation window; thus, the dynamic range of a probe with a 1:1 binding stoichiometry spans approximately two logarithmic units. For example, a probe whose dissociation constant K_d is 1 pM ($K_d = 1 \cdot 10^{-12}$), the ideal dynamic range therefore, would cover metal analyte concentrations between 0.1 to 10 pM (Figure 1.7, grey box). As evident from the shape of the binding isotherm, a change in fractional saturation outside this range yields only small changes in the fluorescence intensity, and these changes would be unsuitable for reliable quantification.

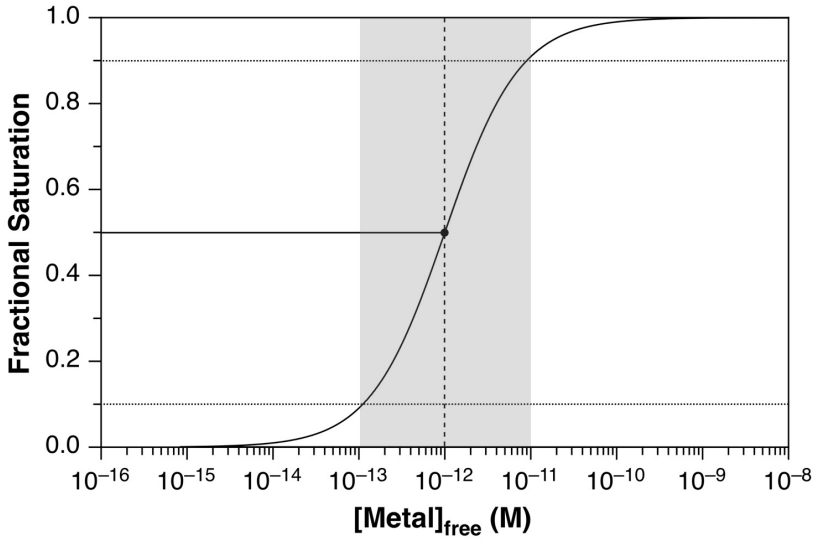

Figure 1.7: Binding Isotherm depicting the relationship between free metal concentrations and the fractional saturation of a fluorescent probe. As the concentration of free metal ion increases, an increase in the fractional saturation of the probe is observed, which leads to an increase in the fluorescence readout. The shaded grey box represents the dynamic range within the 90:10 fractional saturation window, corresponding to two logarithmic decades of free metal concentrations. When the free metal concentration is equivalent to the K_d of the probe, the fractional saturation of the ligand is 50% (dashed vertical line).

The ability for a ligand to engage in complex binding equilibria can also be expressed in terms of the corresponding pM values, which are defined as $-\log[M]_{free}$, at a given total metal ion and ligand concentration.[82] This concept is particularly useful when

comparing ligands with different metal-binding stoichiometries or ligands with basic coordination sites, where a direct comparison of the corresponding stability constants would not be meaningful. Because free-metal concentrations are pH-dependent, the stability constants of ligands can diverge quite dramatically from their respective pM values for the same metal ion because of competing protonation equilibria. In addition, since fluorescent probes usually form metal complexes with a range of metal ions, not just the analyte of interest, careful evaluation of the fluorescence response towards all biologically relevant metal ions is of critical importance.

Overall, a thorough analysis of the coordination chemistry and solution equilibria of a fluorescent probe should be conducted under conditions that mimic the biological environment, including temperature, ionic background, and pH, for a meaningful interpretation of biological imaging data. As the metal exchange kinetics in competition experiments can often be slow, special attention should be given to ensure that full equilibration of the system. Once all relevant species in solution have reached equilibrium, the data can be recorded using a preferred analytical method and analyzed through robust computational data fitting using multivariate data analysis programs, such as Specfit.[83] In addition to the dynamic range, defined by the thermodynamics of the metal-ligand interaction, the fluorescence response of the probe towards analyte binding represents yet another critical parameter that defines the overall detection sensitivity. The following section outlines relevant photophysical concepts and strategies for optimizing the fluorescence response towards metal binding, with an emphasis in TPEM.

1.5.4 Principles for Designing Fluorescent Probes for TPEM

Metal-responsive fluorescent probes can be divided into two general categories based on the change in optical output: intensity-based fluorescent probes that respond

with a fluorescence increase or decrease ("turn-on/off" sensor) and ratiometric sensors that exhibit a chromatic shift in the excitation or emission spectrum upon metal-analyte binding. For the first category, the metal-induced change in emission intensity can be used in conjunction with the experimentally determined dissociation constant to determine the free-metal concentration per equation 1-6:

$$[M^{n+}] = K_d \left(\frac{F - F_{min}}{F_{max} - F} \right) \tag{1-6}$$

where F_{min} and F_{max} are the fluorescence intensities of the free and metal-saturated fluorophores, respectively, determined from an independent calibration experiment with the probe, and F corresponds to the measured fluorescence intensity at a particular metal concentration $[M^{n+}]$.[69] Given the significant variation in probe loading from cell to cell, the limiting fluorescence intensity values may differ quite substantially, thus rendering the quantitative analysis of free metal-ion concentrations within the cell unreliable. Therefore, meaningful interpretations of the fluorescence signal may be compromised due to localization or accumulation of the probe, photobleaching, non-uniform subcellular distributions, or intensity fluctuations from the excitation source.

To overcome these challenges, fluorescent probes can be designed such that they undergo a spectral shift upon binding of the metal analyte, a feature referred to as a ratiometric response. The spectral shift then permits the analysis of the probe response based on the intensity ratio at two distinct excitation or emission wavelengths. For emission-ratiometric measurements, the emission is collected through two bandpass filters, commonly referred to as channels," that function to discriminate either the metal-free or metal-bound probe (Figure 1.8). The intensity ratio is related to the free metal-ion concentration according to equation 1-13, as originally developed by Tsien and coworkers[84]:

$$[M^{n+}] = K_d \left(\frac{R - R_{min}}{R_{max} - R}\right)\left(\frac{S_f}{S_b}\right) \quad (1\text{-}7)$$

where R_{min} and R_{max} are the minimum and maximum intensity ratios determined by an independent calibration of the fluorescence response, R is the calculated ratio at metal concentration $[M^{n+}]$, and S_f and S_b are instrument-dependent calibration factors for the free and metal-bound probe, respectively. From equation 1-7, it is evident that ratiometric analysis does not depend on the concentration of the probe when determining the free metal-ion concentration, providing the concentration of the probe does not exceed the buffered metal concentration. This approach, therefore, allows for the reliable determination of buffered metal-ion concentrations based on cellular imaging data. Nevertheless, despite ratiometric fluorophores boasting particular advantages over intensity-based fluorophores for measuring *in situ* free-metal concentrations, fluorophores of either response mode must rely on efficient two-photon absorption when imaged using TPEM to ensure a robust optical sensitivity.

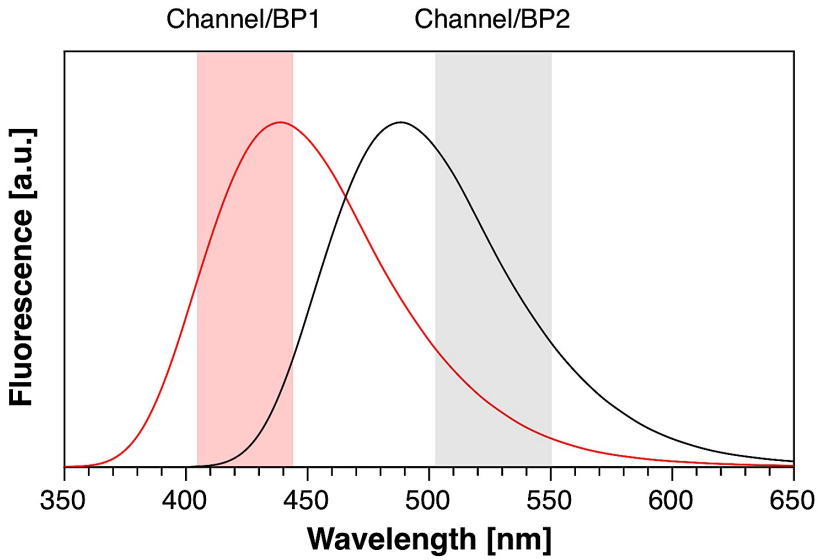

Figure 1.8: Diagram representing the generic principle of a ratiometric emission response upon binding a metal cation to a fluorescent probe. The red curve represents the emission response of the metal-free fluorophore, and the black curve represents the emission response of the metal-bound fluorophore. By choosing two different bandpasses (or channels, red and grey shaded regions), the ratio of the two intensities can be used to calculated the free buffered metal concentrations using equation 1-13.

As alluded to in Section 1.4.1, there exist two potential limitations for applying in TPEM fluorescent probes that are commonly employed in linear, one-photon microscopy. Because the fluorophore brightness is a product of the fluorescence quantum yield and the 2PA cross section, a small cross section may result in a reduced brightness, which may compromise the detection sensitivity within the autofluorescence background of a cell. Optimization of the 2PA cross section, therefore, is crucial for ensuring that fluorophores employed in TPEM demonstrate robust optical sensitivity. Furthermore, most ratiometric fluorophores that are commonly employed in biological imaging undergo a spectral shift in the excitation rather than the emission spectrum, which renders the probes unsuitable for TPEM, as the microscopes utilize a single femtosecond pulsed Ti:sapphire laser. Even if a second laser would be available, the alignment of two lasers at a single focal volume necessary for the scanning acquisition mode is practically unrealistic.

1.5.4.1 Structure-Property Relationships for Maximizing the Two-Photon Absorption Cross Section

Over the past few decades, several design strategies have been developed for maximizing the two-photon absorption cross section of fluorophores.[85-89] In general, these include the combination of three structural elements in the fluorophore: electron-donating (D) and electron-accepting (A) groups at the center and ends of the chromophore that are linked through extended π-conjugated bridges.[68] The spatial arrangement of the these structural elements affects the degree of charge transfer upon photoexcitation and can dictate the two-photon absorption cross section, thus establishing useful structure-property relationships. Preferably, the fluorescent probe should undergo a strong charge-transfer while maintaining a large transition dipole moment upon photoexcitation, both for the metal-free and metal-bound forms. As illustrated in Figure 1.9, depending on the spatial arrangements of the structural elements, three classes of fluorophore architectures that offer large two-photon cross sections have emerged: asymmetric dipolar (A), symmetrical quadrupolar (B), and branched octupolar structures (C).[68, 90-94] Because the structural complexity of non-centrosymmetric octupolar and centrosymmetric quadrupolar architectures, only dipolar systems were considered for the development of metal-responsive fluorescent probes for biological imaging.

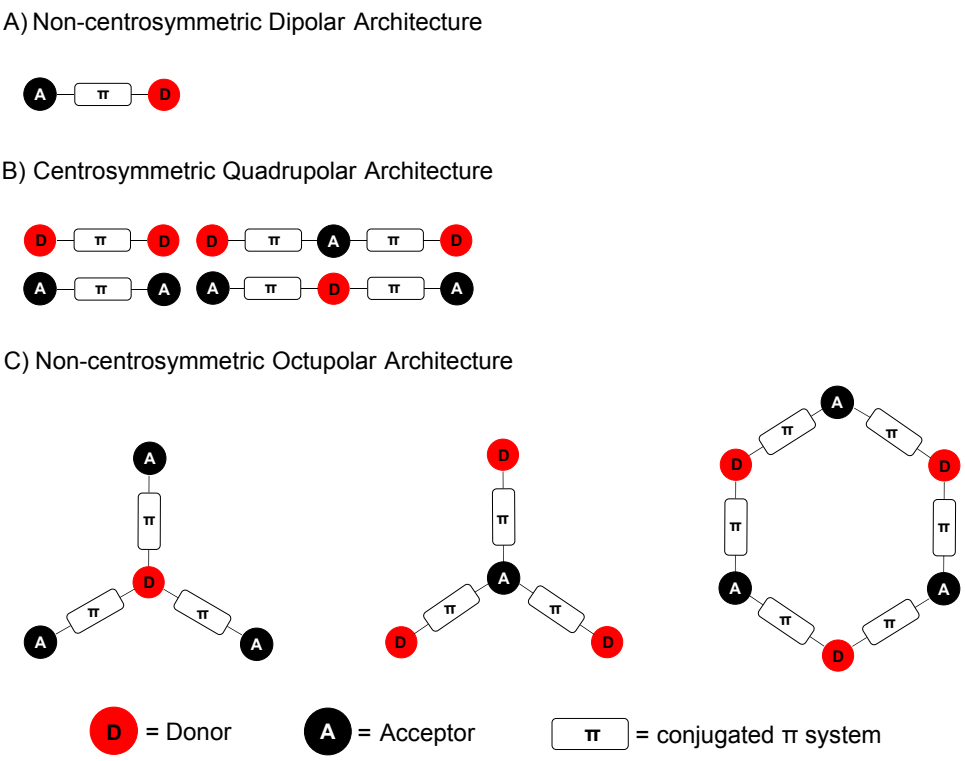

Figure 1.9: Molecular architectures for designing fluorophores with large two-photon cross-sections. Adapted with permission from Reference [69]. © 2011 American Chemical Society.

In general, dipolar fluorophore architectures are characterized by a photoinduced intramolecular charge transfer (ICT) upon photoexcitation, which entails a significant charge redistribution from the electron-rich donor to the electron-deficient acceptor. Promotion of the fluorophore from the ground state leads to the formation of a nonpolarized, local excited state (^{1}LE), which precedes the highly polarized charge-transfer state ^{1}CT (Figure 1.10, center).[75] The resulting ^{1}CT state can then undergo radiative deactivation to the ground state. In the presence of an electron-deficient metal ion, interaction of the metal cation with the electron-rich donor moiety induces a reduction in the degree of charge transfer and yields a higher-energy ^{1}CT state from the resulting δ^+ charge on the donor upon binding the metal cation (Figure 1.10, right). The reduced charge transfer, therefore, is expected to produce blue-shifted emission and excitation spectra relative to

the metal-free probe. On the other hand, interaction of an electron-deficient metal cation with an electron-deficient acceptor increases the degree of ICT and lowers the energy of the ^{1}CT state, resulting in red-shifted excitation and emission spectra compared to the metal-free probe (Figure 1.10, left). Typically, electron-deficient acceptors do not make strong Lewis bases for metal coordination, which renders them less suitable for use in metal-binding probe design. However, heteroaromatic groups, such as pyridine, imidazole, pyrimidine, and coumarins, can function simultaneously as sigma (σ)-donors and π-acceptors, making them attractive components for the design of metal binding probes for two-photon absorption.

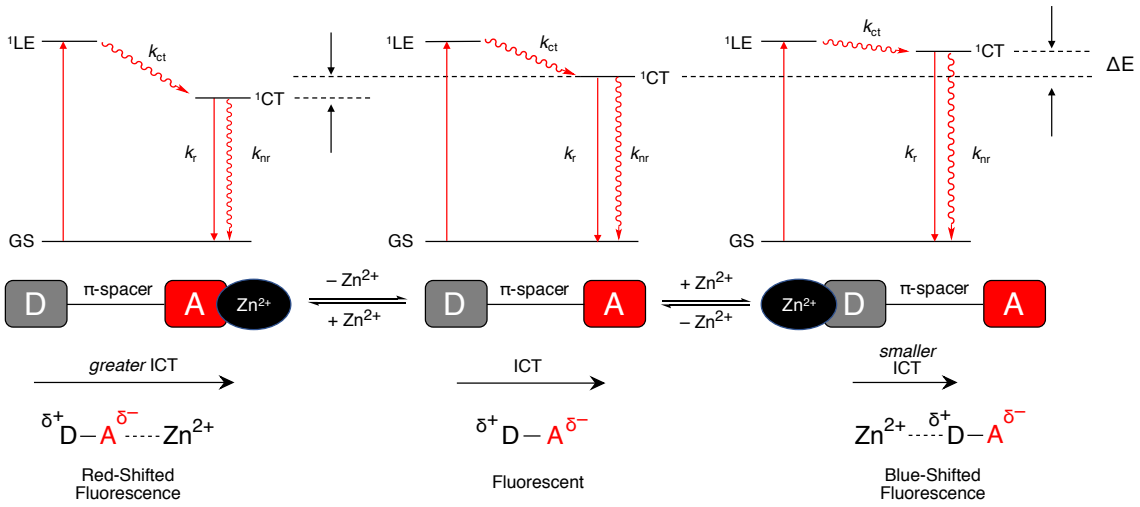

Figure 1.10: Simplified Jabłoński diagram, depicting the change in degree of intramolecular charge transfer-based upon binding the metal to either the donor or acceptor site of a push-pull fluorophore. Upon binding of the metal to the donor, the charge-transfer (CT) energy of the excited state increases, and thus a smaller intramolecular charge transfer (ICT) and blue-shifted fluorescence are observed. However, binding the metal to the acceptor decreases the energy of the charge-transfer (CT) state, and thus a larger intramolecular charge transfer (ICT) is and red-shifted fluorescence are observed. Abbreviations: D, electron donor; A, electron acceptor; GS, ground state; ^{1}LE, local excited state (n = 1); ^{1}CT, charge transfer excited state (n = 1); k_r, rate of radiative deactivation; k_{nr}, rate of non-radiative deactivation; k_{ct}, rate of charge transfer. Adapted with permission from reference [75].

The simplest system featuring a donor and acceptor moiety that are electronically coupled through a linear π-conjugated bridge is the noncentrosymmetric dipolar architecture, depicted in Figure 1.9A. In the ground state, the fluorophore platform exhibits an uneven charge distribution by virtue of resonance stabilization from the electron-rich donor, thus resulting in a considerable dipole moment (Figure 1.11). In the excited state, the dipolar fluorophore undergoes a charge redistribution to produce an even-more-polarized charge-transfer state with an increased dipole moment compared to the corresponding ground state. As mentioned above, according to equation 1-1, greater donor and acceptor group strengths lead to an increase in the charge transfer upon photoexcitation, which in turn yields an increased 2PA cross section. However, it is important to find the optimal combination of donor-acceptor strength for dipolar architectures when attempting to maximize the 2PA cross section, as various factors, such as the degree of bond-order alteration[86] and solvent-solute interactions, can lead to a reduction in action cross sections (fluorophore brightness).[69]

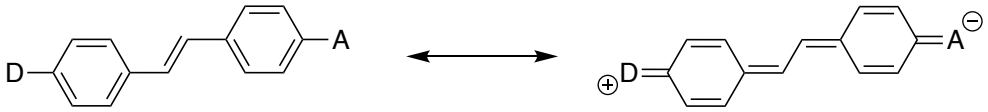

Figure 1.11: Resonance contributors for a simple D–A-substituted stilbene system, depicting the charge distribution throughout the π-system. Adapted with permission from reference [69].

Centrosymmetric quadrupolar molecules (Figure 1.9B) comprise a slightly more complex fluorophore-architecture class that exhibits very large 2PA cross sections, often with δ_{max} values (in GM units) in the hundreds to thousands.[69] However, the utilization of the quadrupolar architecture in the construction of cation-responsive fluorescent probes has proved to be quite challenging for several reasons.[95-97] In polar solvents, such as water or DMSO, strong solute-solvent interactions are further amplified by the formation

of highly polarized excited states and hamper the otherwise large 2PA cross sections and can also significantly reduce the fluorescence quantum yields. These effects can result in a more-than-10-fold-lower action cross section compared to a less-polar environment of an organic solvents.[95-96, 98] The 2PA cross sections and action cross sections are compromised even further by coordination of the metal analyte to the donor moiety, which reduces the degree of ICT to the acceptor group. Lastly, centrosymmetric fluorophores with D-π-A-π-D architectures boast two electron-rich donors that serve as metal-binding sites, which complicate solution equilibria by the formation of 1:1 and 1:2 metal-ligand stoichiometries that further complicate ratiometric analysis.

While the cross sections of dipolar D-A architectures are typically lower than centrosymmetric quadrupolar architectures, the unsymmetrical dipolar arrangement is better suited for the design of ICT-based fluorescent probes with a single metal-binding site, which can be tethered to either the donor or the acceptor terminus of the fluorophore. These strategies can be applied to developing ratiometric metal-responsive fluorescent probes for detecting a wide variety of biologically relevant metals, but consideration of metal-selective chelating ligands should be made when designing metal-selective fluorescent probes. For Zn(II), while a variety of ratiometric fluorescent probes have been reported for the detection of Zn(II), none of the designs were optimized for TPEM. The following section provides a glimpse into the ratiometric fluorescent probes developed for probing biological Zn(II) by conventional fluorescence microscopy.

1.6 Survey of Zn(II)-Responsive Ratiometric Fluorescent Probes Developed for Biological Imaging

Currently, there are only a small number of ratiometric probes available for Zn(II) sensing (Table 1.1). Despite these probes exhibiting ratiometric behavior, the majority of these fluorescent probes experience a ratiometric shift of the excitation rather than the emission spectrum upon binding Zn(II), which precludes them from use in two-photon excitation microscopy.

Table 1.2: Synthetic ratiometric fluorescent probes for Zn(II)

	Free	+ Zn(II)	Free	+ Zn(II)		
Compound	**λ_{ex} (nm)**	**λ_{ex} (nm)**	**λ_{em} (nm)**	**λ_{em} (nm)**	**K_d[a]**	**R_{max}/R_{min}[b]**
FuraZin[99]	378	330	510	510	$2.1 \cdot 10^{-6}$	9.0
IndoZin[99]	350	350	480	395	$3.0 \cdot 10^{-6}$	n.d.
ZnAF-R2[100]	365	335	495	495	$2.8 \cdot 10^{-7}$	7.0
DPA-COUM-4[101]	400	431	481	502	$5.0 \cdot 10^{-7}$	n.d.
ZNP-1[102]	499	499	528/624	528/624	$5.5 \cdot 10^{-10}$	17.8
Zinbo-5[103]	337	376	407	443	$2.2 \cdot 10^{-9}$	33
CZ1[104]	451/526[c]	449/518[c]	488/534[c]	488/534[c]	$2.5 \cdot 10^{-10}$	8.0
CZ2[104]	450/526[c]	448/521[c]	590/535[c]	590/535[c]	n.d.	1.7[d]
DIPCY[105]	627	671	758	765	$2.3 \cdot 10^{-8}$	1.5
ZnIC[106]	513	513	543	558	$1.3 \cdot 10^{-12}$	2.4
RF3[107]	514	495	540	523	$2.2 \cdot 10^{-5}$	2.4

[a]Dissociation constant; [b]dynamic range according to equation 1-13; [c]wavelengths corresponding to the two independent fluorophores; [d]value measured *in vivo*

As illustrated by the corresponding structures in Figure 1.12, the majority of these ratiometric fluorescent probes bind the metal analyte to the donor moiety of the π-conjugated system rather than the acceptor; thus, metal coordination interferes with the intramolecular charge transfer and results in either insignificant spectral changes or a blueshift of the emission maximum. In addition to the lack of emission shift necessary for emission-

ratiometric two-photon imaging, none of these probes, regardless of the spatial arrangement of the fluorophore core, have been optimized for TPEM. Lack of optimization for two-photon excitation complicates matters even further because of hampered 2PA cross sections that result in either reduced fluorophore brightness or complete fluorescence quenching when applied to TPEM.

Although not originally developed for two-photon imaging, the first fluorescent probe developed for the ratiometric detection of calcium, Fura-2,[84] was independently found to have a 2PA cross section of 12 GM in aqueous buffer using two-photon excitation (λ_{ex} = 700 nm), which decreased to 11 GM upon saturation with Ca(II).[108-109] Despite being based on a donor-π-acceptor fluorophore architecture, integration of the metal-binding site into the donor moiety results in a reduced intramolecular charge transfer upon photoexcitation, impacting the 2PA cross section of the fluorophore. In addition, the emission shift was too small for emission-ratiometric imaging using TPEM. Based on the same fluorophore core as Fura-2, FuraZin (Figure 1.12) features a weaker iminodiacetic acid metal-binding ligand integrated into the donor moiety of the push-pull fluorophore, which boasts too weak an affinity to engage in competition with endogenous ligands for Zn(II).[99] While FuraZin has not been employed in TPEM, the decrease in the 2PA cross section of Fura-2 would likely be observed with FuraZin upon binding Zn(II). On the other hand, while Zinbo-5 has been employed in emission-ratiometric imaging of labile Zn(II) pools using TPEM,[103] the limited 28% increase in the ratio upon saturation with Zn(II), in addition to a very narrow dynamic range, renders this probe unsuitable for robust emission-ratiometric, two-photon imaging.

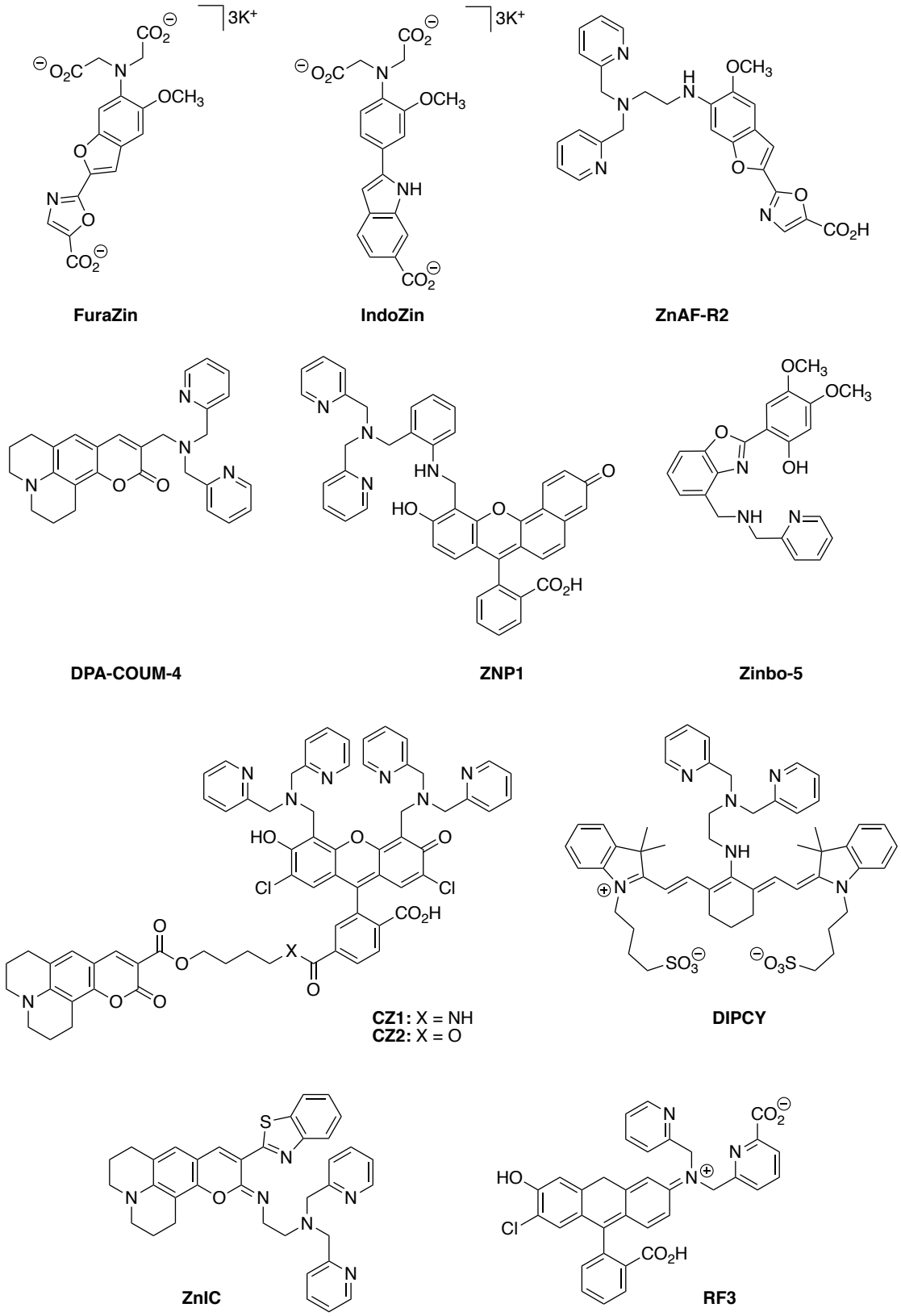

Figure 1.12: Ratiometric fluorescent sensors for Zn(II) as shown in Table 1.1

1.7 Thesis Objectives

Over the past few decades, there has been a surge in the development of both organic fluorophores and engineered fluorescent proteins as tools to investigate the role of metal ions, including Zn(II), in cellular processes.[110-111] In addition, rapidly evolving innovations in microscope design and functionality have delivered advanced technological methods and resources to explore complex bioinorganic processes. In particular, TPEM, as a consequence of exciting the focal volume of a sample in the near-infrared range, offers significantly reduced photobleaching and phototoxicity, improved sample depth penetration, and reduced autofluorescence compared to conventional fluorescence microscopy; thus, this technique enables the imaging of delicate biological samples over prolonged periods of time. The lack of available Zn(II)-selective, emission-ratiometric fluorescent probes designed for TPEM prompted the optimization of a dipolar donor-π-acceptor fluorophore architecture for the development of an emission-ratiometric fluorescent probe with a balanced 2PA cross section, in which the metal-analyte binding site is electronically coupled to the acceptor moiety of the fluorophore rather than the donor.

The work in this thesis aims to broaden the availability of chemical tools for probing labile Zn(II) pools in mammalian cells, with further potential application in higher organisms, such as zebrafish or mice. The majority of this work focused on the optimization and characterization of emission-ratiometric, water-soluble, Zn(II)-selective fluorescent probes optimized for TPEM. The underlying molecular-design approach is based on a donor-acceptor motif that was previously developed[112] as the first emission-ratiometric fluorescent probe with a noncentrosymmetric donor-acceptor platform where the metal cation binds to the acceptor rather than the donor moiety. Further improving the design ap-

proach, chromis-1 was developed as a photophysically optimized probe to yield an improved absorption cross section and red-shifted wavelength of excitation that is well-suited for excitation with Ti:sapphire laser of commercial TPEM instruments. To improve the water solubility in aqueous buffer, hydrophilic groups were also incorporated into the structure of metal chelator moiety to provide relief from aggregation-induced fluorescence artifacts.

Chromis-1 was strategically designed so that the hydrophilic groups of the metal-binding ligand were first present as ester functionalities to enable plasma-membrane diffusion for cellular imaging studies. Upon internalization of the fluorescent probe into the cytoplasm, it was hypothesized that non-specific esterases would then hydrolyze the ester functionalities carboxylic acids to enable water solubility. Quantitative determination of the buffered Zn(II) concentration from cellular staining data, however, negated the estimated values in the literature by nearly 100-fold when calculated using the measured Zn(II) stability constant of the acid form of chromis-1, which suggested that the esters were not being hydrolyzed into their corresponding carboxylic acids as expected. In addition, there were several inconsistencies in both the previous synthesis and characterization of chromis-1. Therefore, the first step on this journey entailed an overhaul of the synthesis and characterization of the photophysical and thermodynamic properties of chromis-1. Because cells were incubated with the ester form of chromis-1, the Zn(II) stability constant of chromis-1 ester needed to be measured. However, its lipophilicity precluded conducting the measurements in aqueous buffer due to potential aggregation-induced fluorescence changes; therefore, liposomes were employed to solubilize the lipophilic probe yet enable characterization in an aqueous medium.

The main body of this work was devoted to a knowledge-driven optimization of the photophysical and thermodynamic properties of the first-generation probe for developing

the next generation of Zn(II)-responsive fluorescent sensors that enable robust emission-ratiometric imaging capabilities by TPEM. During the characterization of chromis-1, it became evident that the probe was undergoing excited-state protonation, which could interfere with ratiometric imaging by virtue of the varying pH of the cytoplasm. Reduction in the senstivity of chromis-1 to fluctuations in pH, which ultimately led to eradicating its propensity for excited-state protonation, furnished chromis-2 as a water-soluble yet cell-permeable fluorescent probe that showed remarkable cellular staining patterns in 3T3 mouse fibroblasts and mouse hippocampal brain tissue. The novel metal-binding ligand, which consists of a symmetrical bis(2-pyrimidylmethyl)amine, lowered the probe's binding affinity by ~ two logarithmic units compared to chromis-1 but resulted in nearly perfectly balanced emission intensities between the metal-free and metal-bound species.

Because Zn(II) is present at varying concentrations in cells and between cell types, the development of fluorescent probes that offer a range of Zn(II) binding affinities would be advantageous to study changes in kinetically and thermodynamically exchangeable Zn(II) pools. The substantial decrease in the binding affinity of chromis-2 compared to its bispicolylamine-containing predecessors served as an impetus to develop a series of affinity-tuned fluorescent probes using a modular synthetic approach to chemically tether various metal-binding ligands to the fluorophore core. This approach generated a series of Zn(II)-selective, affinity-tuned fluorescent probes whose binding affinities span 10 orders of magnitude, potentially enabling a better understanding of Zn(II) buffering and storage mechanisms.

The discrepancies in the photophysical properties between the acid and ester forms of chromis-1 suggested that the polarity of the environment in which fluorescent probes are characterized may have a drastic effect on the fluorescence signaling behav-

iors, especially since most fluorescent probes are lipophilic and therefore localize to cellular membranes and lipid droplets rather than being evenly distributed throughout the cytoplasm. Most often, however, lipophilic probes are characterized *ex vivo* in aqueous buffer rather than in an environment that not only mimics the dichotomy of the cell but also precludes aggregation of the probes, which only leads to misleading conclusions due to the fluorescence dependence on the polarity of the environment in which fluorescent probes are tested. To overcome these potential inaccuracies, lipophilic probes should be characterized in aqueous buffer supplemented with liposomes. Departing from Zn(II)-responsive fluorescent probes, several intensity-based and ratiometric fluorescent probes developed for sensing Cu(I), including ones developed by members of the Fahrni group, were fully characterized to determine their photophysical and thermodynamic properties in aqueous buffer supplemented with liposomes and compare them to the properties in aqueous buffer devoid of liposomes.

1.8 References

1. Andreini, C.; Bertini, I.; Cavallaro, G.; Holliday, G. L.; Thornton, J. M. Metal Ions in Biological Catalysis: From Enzyme Databases to General Principles. *J. Biol. Inorg. Chem.* **2008**, *13* (8), 1205-1218.

2. Irving, H.; Williams, R. J. P. Order of Stability of Metal Complexes. *Nature* **1948**, *162* (4123), 746-747.

3. Andreini, C.; Banci, L.; Bertini, I.; Rosato, A. Zinc Through the Three Domains of Life. *J. Proteome Res.* **2006**, *5* (11), 3173-3178.

4. Andreini, C.; Banci, L.; Bertini, I.; Rosato, A. Counting the Zinc-Proteins Encoded in the Human Genome. *J. Proteome Res.* **2006**, *5* (1), 196-201.

5. Atkins, P. W. *Shriver & Atkins Inorganic Chemistry*. 4th ed.; Oxford University Press: New York, NY, USA, 2006.

6. McCall, K. A.; Huang, C. C.; Fierke, C. A. Function and Mechanism of Zinc Metalloenzymes. *J. Nutr.* **2000**, *130* (5), 1437S-1446S.

7. Huheey, J. E. K., E. A.; Keiter, R. L. *Inorganic Chemistry: Principles of Structure And Reactivity*. 3rd ed.; Harper & Row: 1983.

8. Haas, K. L.; Franz, K. J. Application of Metal Coordination Chemistry To Explore and Manipulate Cell Biology. *Chem. Rev.* **2009**, *109* (10), 4921-4960.

9. Coleman, J. E. Zinc Enzymes. *Curr. Opin. Chem. Biol.* **1998**, *2* (2), 222-234.

10. Sousa, S. F.; Fernandes, P. A.; Ramos, M. J. Unraveling the Mechanism of the Farnesyltransferase Enzyme. *J. Biol. Inorg. Chem.* **2005**, *10* (1), 3-10.

11. Al-Karadaghi, S.; Cedergrenzeppezauer, E. S.; Hovmoller, S.; Petratos, K.; Terry, H.; Wilson, K. S. Refined Crystal-Structure of Liver Alcohol Dehydrogenase-NADH Complex At 1.8-Ångstrom Resolution. *Acta Crystallogr., Sect. D: Biol. Crystallogr.* **1994**, *50*, 793-807.

12. Hammes-Schiffer, S.; Benkovic, S. J. Relating Protein Motion to Catalysis. In *Annual Review of Biochemistry*, Annual Reviews: Palo Alto, 2006; Vol. 75, pp 519-541.

13. Andreini, C.; Bertini, I. A Bioinformatics View of Zinc Enzymes. *J. Inorg. Biochem.* **2012**, *111*, 150-156.

14. Auld, D. S. Zinc Coordination Sphere in Biochemical Zinc Sites. *Biometals* **2001**, *14* (3-4), 271-313.

15. Eklund, H.; Samama, J. P.; Wallen, L.; Branden, C. I.; Akeson, A.; Jones, T. A. Structure of a Triclinic Ternary Complex of Horse Liver Alcohol Dehydrogenase at 2.9 Å Resolution. *J. Mol. Biol.* **1981**, *146* (4), 561-587.

16. Klug, A. The Discovery of Zinc Fingers and Their Applications in Gene Regulation and Genome Manipulation. In *Annual Review of Biochemistry, Vol 79*, Kornberg, R. D.; Raetz, C. R. H.; Rothman, J. E.; Thorner, J. W., Eds. Annual Reviews: Palo Alto, 2010; Vol. 79, pp 213-231.

17. Vallee, B. L.; Coleman, J. E.; Auld, D. S. Zinc Fingers, Zinc Clusters, and Zinc Twists in DNA-Binding Protein Domains. *Proc. Natl. Acad. Sci. U.S.A.* **1991**, *88* (3), 999-1003.

18. Laity, J. H.; Lee, B. M.; Wright, P. E. Zinc Finger Proteins: New Insights into Structural and Functional Diversity. *Curr. Opin. Struct. Biol.* **2001**, *11* (1), 39-46.

19. Krishna, S. S.; Majumdar, I.; Grishin, N. V. Structural Classification of Zinc Fingers. *Nucleic Acids Res.* **2003**, *31* (2), 532-550.

20. Murakami, M.; Hirano, T. Intracellular Zinc Homeostasis and Zinc Signaling. *Cancer Sci.* **2008,** *99* (8), 1515-1522.

21. Kambe, T., Introduction: "Zinc Signaling"–The Blossoming Field of Zinc Biology. In *Zinc Signals in Cellular Functions and Disorders*, Fukada, T.; Kambe, T., Eds. Springer Japan: Tokyo, 2014; pp 1-5.

22. Frederickson, C. J.; Koh, J. Y.; Bush, A. I. The Neurobiology of Zinc in Health and Disease. *Nat. Rev. Neurosci.* **2005**, *6* (6), 449-462.

23. Sensi, S. L.; Paoletti, P.; Bush, A. I.; Sekler, I. Zinc in the Physiology and Pathology of the CNS. *Nat. Rev. Neurosci.* **2009**, *10* (11), 780-791.

24. Chistiakov, D. A.; Voronova, N. V. Zn2+-Transporter-8: a Dual Role in Diabetes. *Biofactors* **2009**, *35* (4), 356-363.

25. Maret, W.; Jacob, C.; Vallee, B. L.; Fischer, E. H. Inhibitory Sites in Enzymes: Zinc Removal and Reactivation by Thionein. *Proc. Natl. Acad. Sci. U.S.A.* **1999**, *96* (5), 1936-1940.

26. Yamasaki, S.; Sakata-Sogawa, K.; Hasegawa, A.; Suzuki, T.; Kabu, K.; Sato, E.; Kurosaki, T.; Yamashita, S.; Tokunaga, M.; Nishida, K.; Hirano, T. Zinc is a Novel Intracellular Second Messenger. *J. Cell Biol.* **2007**, *177* (4), 637-645.

27. Hojyo, S.; Fukada, T. Roles of Zinc Signaling in the Immune System. *J Immunol. Res.* **2016**, 21.

28. Fukada, T.; Yamasaki, S.; Nishida, K.; Murakami, M.; Hirano, T. Zinc Homeostasis and Signaling in Health and Diseases. *J. Biol. Inorg. Chem.* **2011**, *16* (7), 1123-1134.

29. Lichten, L. A.; Cousins, R. J. Mammalian Zinc Transporters: Nutritional and Physiologic Regulation. *Annu. Rev. Nutr.* **2009**, *29*, 153-176.

30. Eide, D. J. The SLC39 Family of Metal Ion Transporters. *Pfluegers Arch.* **2004**, *447* (5), 796-800.

31. Eide, D. J. Zinc Transporters and the Cellular Trafficking of Zinc. *Biochim. Biophys. Acta, Mol. Cell Res.* **2006**, *1763* (7), 711-722.

32. Kambe, T.; Tsuji, T.; Fukue, K. Zinc Transport Proteins and Zinc Signaling. In *Zinc Signals in Cellular Functions and Disorders*, Fukada, T.; Kambe, T., Eds. Springer Japan: Tokyo, 2014; pp 27-53.

33. Wang, K.; Zhou, B.; Kuo, Y. M.; Zemansky, J.; Gitschier, J. A Novel Member of a Zinc Transporter Family is Defective in Acrodermatitis Enteropathica. *Am. J. Hum. Genet.* **2002**, *71* (1), 66-73.

34. Liuzzi, J. P.; Bobo, J. A.; Cui, L.; McMahon, R. J.; Cousins, R. J. Zinc Transporters 1, 2 and 4 Are Differentially Expressed and Localized in Rats During Pregnancy and Lactation. *J. Nutr.* **2003**, *133* (2), 342-351.

35. Smidt, K.; Jessen, N.; Petersen, A. B.; Larsen, A.; Magnusson, N.; Jeppesen, J. B.; Stoltenberg, M.; Culvenor, J. G.; Tsatsanis, A.; Brock, B.; Schmitz, O.; Wogensen, L.; Bush, A. I.; Rungby, J. SLC30A3 Responds to Glucose- and Zinc Variations in beta-Cells and Is Critical for Insulin Production and In Vivo Glucose-Metabolism During beta-Cell Stress. *PLoS One* **2009**, *4* (5), 12.

36. Huang, L. P.; Yan, M.; Kirschke, C. P. Over-Expression of ZnT7 Increases Insulin Synthesis and Secretion in Pancreatic beta-Cells by Promoting Insulin Gene Transcription. *Exp. Cell Res.* **2010**, *316* (16), 2630-2643.

37. Bellomo, E. A.; Meur, G.; Rutter, G. A. Glucose Regulates Free Cytosolic Zn2+ Concentration, SLC39 (ZIP), and Metallothionein Gene Expression in Primary Pancreatic Islet beta-Cells. *J. Biol. Chem.* **2011**, *286* (29), 25778-25789.

38. Huang, L. P.; Kirschke, C. P.; Lay, Y. A. E.; Levy, L. B.; Lamirande, D. E.; Zhang, P. H. Znt7-null Mice Are More Susceptible to Diet-Induced Glucose Intolerance and Insulin Resistance. *J. Biol. Chem.* **2012**, *287* (40), 33883-33896.

39. Myers, S. A.; Nield, A.; Chew, G. S.; Myers, M. A. The Zinc Transporter, SLC39a7 (ZIP7) is Implicated in Glycaemic Control in Skeletal Muscle Cells. *PLoS One* **2013**, *8* (11), 1-15.

40. Myers, S. A. Zinc Transporters and Zinc Signaling: New Insights into Their Role in Type 2 Diabetes. *Int. J. Endocrinol.* **2015**, 1-7.

41. Chimienti, F.; Favier, A.; Seve, M. ZnT-8, a Pancreatic Beta-Cell-Specific Zinc Transporter. *Biometals* **2005**, *18* (4), 313-317.

42. Nicolson, T. J.; Bellomo, E. A.; Wijesekara, N.; Loder, M. K.; Baldwin, J. M.; Gyulkhandanyan, A. V.; Koshkin, V.; Tarasov, A. I.; Carzaniga, R.; Kronenberger, K.; Taneja, T. K.; Xavier, G. D.; Libert, S.; Froguel, P.; Scharfmann, R.; Stetsyuk, V.; Ravassard, P.; Parker, H.; Gribble, F. M.; Reimann, F.; Sladek, R.; Hughes, S. J.; Johnson, P. R. V.; Masseboeuf, M.; Burcelin, R.; Baldwin, S. A.; Liu, M.; Lara-Lemus, R.; Arvan, P.; Schuit, F. C.; Wheeler, M. B.; Chimienti, F.; Rutter, G. A. Insulin Storage and Glucose Homeostasis in Mice Null for the Granule Zinc Transporter ZnT8 and Studies of the Type 2 Diabetes-Associated Variants. *Diabetes* **2009**, *58* (9), 2070-2083.

43. Chimienti, F.; Devergnas, S.; Pattou, F.; Schuit, F.; Garcia-Cuenca, R.; Vandewalle, B.; Kerr-Conte, J.; Van Lommel, L.; Grunwald, D.; Favier, A.; Seve, M. In vivo Expression and Functional Characterization of the Zinc Transporter ZnT8 in Glucose-Induced Insulin Secretion. *J. Cell Sci.* **2006**, *119* (20), 4199-4206.

44. Fu, Y.; Tian, W.; Pratt, E. B.; Dirling, L. B.; Shyng, S. L.; Meshul, C. K.; Cohen, D. M. Down-Regulation of ZnT8 Expression in INS-1 Rat Pancreatic Beta Cells Reduces Insulin Content and Glucose-Inducible Insulin Secretion. *PLoS One* **2009**, *4* (5), 1-9.

45. Tamaki, M.; Fujitani, Y.; Hara, A.; Uchida, T.; Tamura, Y.; Takeno, K.; Kawaguchi, M.; Watanabe, T.; Ogihara, T.; Fukunaka, A.; Shimizu, T.; Mita, T.; Kanazawa, A.; Imaizumi, M. O.; Abe, T.; Kiyonari, H.; Hojyo, S.; Fukada, T.; Kawauchi, T.; Nagamatsu, S.; Hirano, T.; Kawamori, R.; Watada, H. The Diabetes-Susceptible Gene SLC30A8/ZnT8 Regulates Hepatic Insulin Clearance. *J. Clin. Invest.* **2013**, *123* (10), 4513-4524.

46. Coyle, P.; Philcox, J. C.; Carey, L. C.; Rofe, A. M. Metallothionein: The Multipurpose Protein. *Cell. Mol. Life Sci.* **2002**, *59* (4), 627-647.

47. Maret, W. Zinc Coordination Environments in Proteins as Redox Sensors and Signal Transducers. *Antioxid. Redox Signal.* **2006**, *8* (9-10), 1419-1441.

48. Maret, W. Redox Biochemistry of Mammalian Metallothioneins. *J. Biol. Inorg. Chem.* **2011**, *16* (7), 1079-1086.

49. Babula, P.; Masarik, M.; Adam, V.; Eckschlager, T.; Stiborova, M.; Trnkova, L.; Skutkova, H.; Provaznik, I.; Hubalek, J.; Kizek, R. Mammalian Metallothioneins: Properties and Functions. *Metallomics* **2012**, *4* (8), 739-750.

50. Kägi, J. H. R.; Vasak, M. Chemistry and Biochemistry of Metallothionein. *Highlights Mod. Biochem.* **1989**, *1-2*, 299-308.

51. Nath, R.; Kambadur, R.; Gulati, S.; Paliwal, V. K.; Sharma, M., Molecular Aspects, Physiological-Function, and Clinical-Significance of Metallothioneins. *CRC Critical Reviews in Food Sci. Nutr.* **1988**, *27* (1), 41-85.

52. Robbins, A. H.; McRee, D. E.; Williamson, M.; Collett, S. A.; Xuong, N. H.; Furey, W. F.; Wang, B. C.; Stout, C. D. Refined Crystal-Structure of Cd, Zn Metallothionein at 2.0 Å Resolution. *J. Mol. Biol.* **1991**, *221* (4), 1269-1293.

53. Rink, L.; Maywald, M. Zinc Signals in Immunology. In *Zinc Signals in Cellular Functions and Disorders*, Fukada, T.; Kambe, T., Eds. Springer Japan: Tokyo, 2014; pp 197-226.

54. Krezel, A.; Maret, W. Dual Nanomolar and Picomolar Zn(II) Binding Properties of Metallothionein. *J. Am. Chem. Soc.* **2007**, *129* (35), 10911-10921.

55. Maret, W. Analyzing Free Zinc(II) Ion Concentrations in Cell Biology with Fluorescent Chelating Molecules. *Metallomics* **2015**, *7* (2), 202-211.

56. Vinkenborg, J. L.; Nicolson, T. J.; Bellomo, E. A.; Koay, M. S.; Rutter, G. A.; Merkx, M. Genetically Encoded FRET Sensors to Monitor Intracellular Zn2+ Homeostasis. *Nat. Methods* **2009**, *6* (10), 737-U10.

57. Qin, Y.; Miranda, J. G.; Stoddard, C. I.; Dean, K. M.; Galati, D. F.; Palmer, A. E. Direct Comparison of a Genetically Encoded Sensor and Small Molecule Indicator: Implications for Quantification of Cytosolic Zn2+. *ACS Chem. Biol.* **2013**, *8* (11), 2366-2371.

58. Chabosseau, P.; Tuncay, E.; Meur, G.; Bellomo, E. A.; Hessels, A.; Hughes, S.; Johnson, P. R. V.; Bugliani, M.; Marchetti, P.; Turan, B.; Lyon, A. R.; Merkx, M. Rutter, G. A., Mitochondrial and ER-Targeted eCALWY Probes Reveal High Levels of Free Zn2+. *ACS Chem. Biol.* **2014**, *9* (9), 2111-2120.

59. Krezel, A.; Maret, W. Zinc-Buffering Capacity of a Eukaryotic Cell at Physiological pZn. *J. Biol. Inorg. Chem.* **2006**, *11* (8), 1049-1062.

60. McRae, R.; Bagchi, P.; Sumalekshmy, S.; Fahrni, C. J. In Situ Imaging of Metals in Cells and Tissues. *Chem. Rev.* **2009**, *109* (10), 4780-4827.

61. Brown, R. J. C.; Milton, M. J. T. Analytical Techniques for Trace Element Analysis: An Overview. *Trends Anal. Chem.* **2005**, *24* (3), 266-274.

62. Lord, S. J.; Lee, H. L. D.; Moerner, W. E. Single-Molecule Spectroscopy and Imaging of Biomolecules in Living Cells. *Anal. Chem.* **2010**, *82* (6), 2192-2203.

63. Combs, C. A. Fluorescence Microscopy: A Concise Guide to Current Imaging Methods. In *Current Protocols in Neuroscience*, John Wiley & Sons, Inc.: 2001.

64. Goppert-Mayer, M. Elementary File with Two Quantum Fissures. *Ann. Phys. - Berlin* **1931**, *9* (3), 273-294.

65. Kaiser, W.; Garrett, C. G. B. 2-Photon Excitation in CaF2 - Eu2+. *Phys. Rev. Lett.* **1961**, *7* (6), 229-231.

66. Denk, W.; Strickler, J. H.; Webb, W. W. 2-Photon Laser Scanning Fluorescence Microscopy. *Science* **1990**, *248* (4951), 73-76.

67. Marder, S. R. Organic Nonlinear Optical Materials: Where We Have Been and Where We are Going. *Chem. Commun.* **2006**, (2), 131-134.

68. Pawlicki, M.; Collins, H. A.; Denning, R. G.; Anderson, H. L. Two-Photon Absorption and the Design of Two-Photon Dyes. *Angew. Chem., Int. Ed.* **2009**, *48* (18), 3244-3266.

69. Sumalekshmy, S.; Fahrni, C. J. Metal-Ion-Responsive Fluorescent Probes for Two-Photon Excitation Microscopy. *Chem. Mat.* **2011**, *23* (3), 483-500.

70. So, P. T. C. Two-Photon Fluorescence Light Microscopy. In *eLS*, John Wiley & Sons, Ltd: 2001; pp 1-5.

71. Zipfel, W. R.; Williams, R. M.; Webb, W. W. Nonlinear Magic: Multiphoton Microscopy in the Biosciences. *Nat. Biotechnol.* **2003**, *21* (11), 1368-1376.

72. Helmchen, F.; Denk, W. Deep Tissue Two-Photon Microscopy. *Nat. Methods* **2005**, *2* (12), 932-940.

73. Cotruvo, J. A.; Aron, A. T.; Ramos-Torres, K. M.; Chang, C. J. Synthetic Fluorescent Probes for Studying Copper in Biological Systems. *Chemical Society Reviews* **2015**, *44* (13), 4400-4414.

74. Fahrni, C. J. Probing Biological Trace Metals with Fluorescent Indicators. In *Metals in the Brain*, 1 ed.; White, A. R., Ed. Humana Press: 2017; pp 71-107.

75. Fahrni, C. J. Design of Cation-Selective Synthetic Fluorescent Indicators. In *Chemosensors*, Wang, B.; Anslyn, E. V., Eds. John Wiley & Sons, Inc.: Hoboken, NJ, USA, 2011; pp 371-394.

76. Gran, G. Determination of the Equivalent Point in Potentiometric Titrations. *Acta Chem. Scand.* **1950**, *4* (4), 559-577.

77. Gran, G. Determination of the Equivalence Point in Potentiometric Titrations. *Anal. Chem.* **1952**, *24* (9), 1519-1519.

78. Gran, G. Determination of the Equivalence Point in Potentiometric Titrations 2. *Analyst* **1952**, *77* (920), 661-671.

79. Smith, R. M.; Martell, A. E.; Motekaitis, R. J., NIST Critically Selected Stability Constants of Metal Complexes Database. Standard Reference Data Program, National Institute of Standards and Technology, U.S. Dept. of Commerce: Gaithersburg, MD, 2004.

80. Bagchi, P.; Morgan, M. T.; Bacsa, J.; Fahrni, C. J. Robust Affinity Standards for Cu(I) Biochemistry. *J. Am. Chem. Soc.* **2013**, *135* (49), 18549-18559.

81. Schwarzenbach, G., *Complexometric Titrations*. 2 ed.; Methuen: 1957; Vol. 45, p 132.

82. Harris, W. R.; Raymond, K. N. Ferric Ion Sequestering Agents 3. Spectrophotometric and Potentiometric Evaluation of 2 New Enterobactin Analogs - 1,5,9-N,N',N''-Tris(2,3-Dihydroxybenzoyl)-Cyclotriazatridecane and 1,3,5-N,N',N''-Tris(2,3-Dihydroxybenzoyl)Triaminomethylbenzene. *J. Am. Chem. Soc.* **1979**, *101* (22), 6534-6541.

83. Binstead, R. A., Zuberbühler, A. D. *SPECFIT Global Analysis System*, 2001.

84. Grynkiewicz, G.; Poenie, M.; Tsien, R. Y. A New Generation of Ca2+ Indicators with Greatly Improved Fluorescence Properties. *J. Biol. Chem.* **1985**, *260* (6), 3440-3450.

85. Albota, M.; Beljonne, D.; Bredas, J. L.; Ehrlich, J. E.; Fu, J. Y.; Heikal, A. A.; Hess, S. E.; Kogej, T.; Levin, M. D.; Marder, S. R.; McCord-Maughon, D.; Perry, J. W.; Rockel, H.; Rumi, M.; Subramaniam, C.; Webb, W. W.; Wu, X. L.; Xu, C. Design of Organic Molecules with Large Two-Photon Absorption Cross Sections. *Science* **1998**, *281* (5383), 1653-1656.

86. Kogej, T.; Beljonne, D.; Meyers, F.; Perry, J. W.; Marder, S. R.; Bredas, J. L. Mechanisms for Enhancement of Two-Photon Absorption in Donor-Acceptor Conjugated Chromophores. *Chem. Phys. Lett.* **1998**, *298* (1-3), 1-6.

87. Reinhardt, B. A.; Brott, L. L.; Clarson, S. J.; Dillard, A. G.; Bhatt, J. C.; Kannan, R.; Yuan, L. X.; He, G. S.; Prasad, P. N. Highly Active Two-Photon Dyes: Design, Synthesis, and Characterization Toward Application. *Chem. Mat.* **1998**, *10* (7), 1863-1874.

88. Barzoukas, M.; Blanchard-Desce, M. Molecular Engineering of Push-Pull Dipolar and Quadrupolar Molecules for Two-Photon Absorption: A Multivalence-Bond States Approach. *J. Chem. Phys.* **2000**, *113* (10), 3951-3959.

89. Rumi, M.; Ehrlich, J. E.; Heikal, A. A.; Perry, J. W.; Barlow, S.; Hu, Z. Y.; McCord-Maughon, D.; Parker, T. C.; Rockel, H.; Thayumanavan, S.; Marder, S. R.; Beljonne, D.; Bredas, J. L. Structure-Property Relationships for Two-Photon Absorbing Chromophores: Bis-Donor Diphenylpolyene and Bis(styryl)benzene Derivatives. *J. Am. Chem. Soc.* **2000**, *122* (39), 9500-9510.

90. Strehmel, B.; Strehmel, V., Two-Photon Physical, Organic, and Polymer Chemistry: Theory, Techniques, Chromophore Design, and Applications. In *Advances in Photochemistry*, Neckers, D. C.; Jenks, W. S.; Wolff, T., Eds. John Wiley & Sons, Inc.: Hoboken, NJ, USA, 2006; pp 111-354.

91. Terenziani, F.; Katan, C.; Badaeva, E.; Tretiak, S.; Blanchard-Desce, M. Enhanced Two-Photon Absorption of Organic Chromophores: Theoretical and Experimental Assessments. *Adv. Mater.* **2008**, *20* (24), 4641-4678.

92. Rumi, M.; Barlow, S.; Wang, J.; Perry, J. W.; Marder, S. R. Two-Photon Absorbing Materials and Two-Photon-induced Chemistry. In *Photoresponsive Polymers I*, Marder, S. R.; Lee, K. S., Eds. Springer-Verlag Berlin: Berlin, 2008; Vol. 213, pp 1-95.

93. He, G. S.; Tan, L. S.; Zheng, Q.; Prasad, P. N. Multiphoton Absorbing Materials: Molecular Designs, Characterizations, and Applications. *Chem. Rev.* **2008**, *108* (4), 1245-1330.

94. Kim, H. M.; Cho, B. R. Two-Photon Materials with Large Two-Photon Cross Sections: Structure-Property Relationship. *Chem. Commun.* **2009**, (2), 153-164.

95. Pond, S. J. K.; Tsutsumi, O.; Rumi, M.; Kwon, O.; Zojer, E.; Bredas, J. L.; Marder, S. R.; Perry, J. W. Metal-Ion Sensing Fluorophores with Large Two-Photon Absorption Cross Sections: Aza-Crown Ether Substituted Donor-Acceptor-Donor Distyryl Benzenes. *J. Am. Chem. Soc.* **2004**, *126* (30), 9291-9306.

96. Ahn, H. C.; Yang, S. K.; Kim, H. M.; Li, S. J.; Jeon, S. J.; Cho, B. R. Molecular Two-Photon Sensor for Metal Ions Derived from Bis(2-pyridyl)amine. *Chem. Phys. Lett.* **2005**, *410* (4-6), 312-315.

97. Huang, C. B.; Peng, X. J.; Lin, Z. Y.; Fan, J. L.; Ren, A. X.; Sun, D. X. A Highly Selective and Sensitive Two-Photon Chemosensor for Silver Ion Derived from 3,9-Dithia-6-azaundecane. *Sens. Actuators B, Chem.* **2008**, *133* (1), 113-117.

98. Bozio, R.; Cecchetto, E.; Fabbrini, G.; Ferrante, C.; Maggini, M.; Menna, E.; Pedron, D.; Ricco, R.; Signorini, R.; Zerbetto, M. One- and Two-Photon Absorption and Emission Properties of a Zn(II) Chemosensor. *J. Phys. Chem. A* **2006**, *110* (20), 6459-6464.

99. Gee, K. R.; Zhou, Z. L.; Ton-That, D.; Sensi, S. L.; Weiss, J. H. Measuring Zinc in Living Cells: A New Generation of Sensitive and Selective Fluorescent Probes. *Cell Calcium* **2002**, *31* (5), 245-251.

100. Maruyama, S.; Kikuchi, K.; Hirano, T.; Urano, Y.; Nagano, T. A Novel, Cell-Permeable, Fluorescent Probe for Ratiometric Imaging of Zinc Ion. *J. Am. Chem. Soc.* **2002**, *124* (36), 10650-10651.

101. Lim, N. C.; Bruckner, C. DPA-Substituted Coumarins as Chemosensors for Zinc(II): Modulation of the Chemosensory Characteristics by Variation of the Position of the Chelate on the Coumarin. *Chem. Commun.* **2004**, (9), 1094-1095.

102. Chang, C. J.; Jaworski, J.; Nolan, E. M.; Sheng, M.; Lippard, S. J. A Tautomeric Zinc Sensor for Ratiometric Fluorescence Imaging: Application to Nitric Oxide-Induced Release of Intracellular Zinc. *Proc. Natl. Acad. Sci. U.S.A.* **2004**, *101* (5), 1129-1134.

103. Taki, M.; Wolford, J. L.; O'Halloran, T. V. Emission Ratiometric Imaging of Intracellular Zinc: Design of a Benzoxazole Fluorescent Sensor and its Application in Two-Photon Microscopy. *J. Am. Chem. Soc.* **2004**, *126* (3), 712-713.

104. Woodroofe, C. C.; Won, A. C.; Lippard, S. J. Esterase-Activated Two-Fluorophore System for Ratiometric Sensing of Biological Zinc(II). *Inorg. Chem.* **2005**, *44* (9), 3112-3120.

105. Kiyose, K.; Kojima, H.; Urano, Y.; Nagano, T. Development of a Ratiometric Fluorescent Zinc Ion Probe in Near-Infrared Region, Based on Tricarbocyanine Chromophore. *J. Am. Chem. Soc.* **2006**, *128* (20), 6548-6549.

106. Komatsu, K.; Urano, Y.; Kojima, H.; Nagano, T. Development of an Iminocoumarin-Based Zinc Sensor Suitable for Ratiometric Fluorescence Imaging of Neuronal Zinc. *J. Am. Chem. Soc.* **2007**, *129* (44), 13447-13454.

107. Tomat, E.; Lippard, S. J. Ratiometric and Intensity-Based Zinc Sensors Built on Rhodol and Rhodamine Platforms. *Inorg. Chem.* **2010**, *49* (20), 9113-9115.

108. Xu, C.; Zipfel, W.; Shear, J. B.; Williams, R. M.; Webb, W. W. Multiphoton Fluorescence Excitation: New Spectral Windows for Biological Nonlinear Microscopy. *Proc. Natl. Acad. Sci. U.S.A.* **1996**, *93* (20), 10763-10768.

109. Wokosin, D. L.; Loughrey, C. M.; Smith, G. L. Characterization of a Range of Fura Dyes with Two-Photon Excitation. *Biophys. J.* **2004**, *86* (3), 1726-1738.

110. Carter, K. P.; Young, A. M.; Palmer, A. E. Fluorescent Sensors for Measuring Metal Ions in Living Systems. *Chem. Rev.* **2014**, *114* (8), 4564-4601.

111. Chen, Y. C.; Bai, Y.; Han, Z.; He, W. J.; Guo, Z. J. Photoluminescence Imaging of Zn2+ in living Systems. *Chem. Soc. Rev.* **2015**, *44* (14), 4517-4546.

112. Sumalekshmy, S.; Henary, M. M.; Siegel, N.; Lawson, P. V.; Wu, Y.; Schmidt, K.; Bredas, J. L.; Perry, J. W.; Fahrni, C. J. Design of Emission Ratiometric Metal-Ion Sensors with Enhanced Two-Photon Cross Section and Brightness. *J. Am. Chem. Soc.* **2007**, *129* (39), 11888-11889.

CHAPTER 2

DEVELOPMENT OF CHROMIS-1, A WATER-SOLUBLE, ZN(II)-SELECTIVE, EMISSION-RATIOMETRIC FLUORESCENT PROBE FOR DYNAMIC IMAGING OF LABILE ZN(II) FLUXES IN THE CELL BY TWO-PHOTON EXCITATION MICROSCOPY

All experiments and data encompassing this chapter were submitted for publication per reference [28]

2.1 Introduction

As discussed in Chapter 1, ratiometric fluorescent probes represent powerful tools for discerning and understanding biological processes with a wide range of complexity. Because biological samples are often very delicate, the use of high-intensity lasers with which conventional linear confocal microscopes are equipped can pose deleterious effects, such as phototoxicity and photobleaching, that are manifested by the application of fluorescent probes in cells. Two-photon excitation microscopy (TPEM), which utilizes an ultrafast (femtosecond) pulsed Ti:sapphire laser that leads to the simultaneous absorption of two photons at half the energy relative to the linear, one-photon transition in conventional fluorescence microscopy, resulting in not only reduced phototoxicity and photobleaching but also increased sample depth penetration, reduced autofluorescence, and intrinsic 3D imaging resolution.[1-3]

Despite a wealth of literature surrounding the application of both small-molecule and genetically-encoded fluorescent indicators for use in metal-ion sensing,[4] most metal-

selective fluorophores employed for cell imaging have been designed for linear, one-photon microscopy and have not been optimized for two-photon excitation. As discussed in Chapter 1, Section 1.4.1, employment of fluorophores in TPEM that have not been optimized for two-photon absorption can exhibit reduced brightness compared to their brightness in one-photon microscopy, which can decrease even further upon binding of the metal cation.[5] Moreover, most ratiometric metal-ion fluorophores currently available boast a large shift in the excitation peak but not in the emission. Not only are the Ti:sapphire lasers employed in commercial two-photon microscopes not suitable to alternate between different excitation energies in rapid succession, but also the physical alignment of two excitation lasers to the same focal volume of a sample is unrealistic due to its laser-scanning mode for data acquisition. Therefore, ratiometric TPEM imaging requires sensors that offer not only sufficient relative brightness but also undergo a spectral shift of the emission profile,[6] which are requirements that are currently not fulfilled by most ratiometric probes.[3] Designing emission-ratiometric fluorophores that exhibit chromatic shifts in the emission rather than the excitation is, however, significantly more difficult, and as a result, there exists a lack of suitable emission-ratiometric fluorophores for cellular imaging of metals, particularly Zn(II).

2.1.1 Designing Zn(II)-Selective, Emission-Ratiometric Sensors with Enhanced 2PA Cross Sections and Brightness

To address these challenges, Sumalekshmy *et al.* devised a fluorophore design strategy that yields large 2PA cross sections as well as strong bathochromic shifts in the fluorescence emission upon binding of the cationic metal analyte.[7] By electronically coupling the analyte binding site to the acceptor moiety, rather than the donor moiety, of a linear noncentrosymmetric donor-acceptor (D-A) fluorophore architecture, coordination of

the metal cation elicits an increased intramolecular charge transfer (ICT) upon photoexcitation. Inspired by the design and characterization of ratiometric pH probes,[8] the emission-ratiometric, Zn(II)-selective probe featured an anisole donor moiety and a trispicolylamine acceptor moiety that was bridged by an oxazole ring to prevent cis-trans isomerization that could otherwise lead to undesirable fluctuations in the emission response. This fluorescent probe was the first implementation of a noncentrosymmetric D-A architecture for developing an emission-ratiometric, Zn(II)-responsive fluorescent probe. Due to aggregation in aqueous solution, the photophysical properties of the probe were evaluated in methanol, and upon saturation with Zn(II), the probe revealed a red-shifted fluorescence emission and a more favorable 2PA cross section. The two-photon action cross section (δη) increased 5-fold from 11 GM to 55 GM upon binding Zn(II), which exceeded the brightness of traditional fluorophore platforms, including BODIPY, fluorescein, and GFP, that are widely employed in biological imaging.[5, 9]

Large chromatic shifts in the absorption and emission spectra of 24 and 56 nm, respectively, as well as a 5-fold enhancement in brightness, made the probe well-suited for ratiometric metal sensing using TPEM. Despite these advantages, the excitation wavelength at which the 2PA cross sections for both the metal-free and Zn(II)-saturated forms are most similar resided below the 700-nm lower limit off the Ti:sapphire laser with which commercial two-photon microscopes are equipped; therefore, excitation of the probe using standard TPEM lasers would result in hampered brightness. To overcome this challenge, it was hypothesized that substitution of the oxazole ring with a thiazole ring would lower the HOMO-LUMO gap, thus producing a red shift in both the two-photon excitation spectrum, as well as the fluorescence emission spectrum, resulting in a more balanced TPA cross section residing above the 700-nm cut off. In addition, in order to achieve

improved water-solubility, efforts were made to install hydrophilic groups on the bispicolylamine chelator moiety.

Building on the prior development of the newly optimized probe design, this chapter is devoted to the synthesis and characterization of a Zn(II)-selective indicator, chromis-1, that features a balanced 2PA cross section upon saturation with Zn(II) combined with a large emission shift suitable for emission-ratiometric TPEM imaging. The following sections describe the synthesis and complete characterization of the fluorescent probe, including its application in visualizing dynamic changes in labile Zn(II) in live NIH 3T3 mouse fibroblast cells.

2.2 Synthesis and Characterization of Chromis-1, a Water-Soluble, Zn(II)-Selective, Emission-Ratiometric Fluorescent Probe Optimized for TPEM

*2.2.1 Synthesis of Chromis-1 Acid (**2.1b**)*

Following a convergent synthetic approach, chromis-1 was assembled from three building blocks, the Fmoc-protected amino acid **2.3**, α-amino ketone **2.4**, and isonicotinic acid derivative **2.10** (Scheme 2.1). While the latter two building blocks were synthesized based on modified literature procedures,[7, 10] Fmoc-protected acid **2.3** was accessible in two steps from inexpensive isonicotinic acid *N*-oxide. *O*-alkylation of the *N*-oxide starting material with diethylsulfate, followed by a vicarious nucleophilic substitution with NaCN at the 2-position with at the 2-position yielded 2-cyanoisonicotinic acid **2.2**. This intermediate was then converted to the Fmoc-protected acid **2.3** via a one-pot procedure, which proceed first by the reduction of the nitrile to the primary amine via hydrogenation with Pd/C as a catalyst in glacial acetic acid, followed by protection of the primary amine using Fmoc-

succinimidyl carbonate, with a 79% yield overall. The bridging thiazole unit of the fluorophore π-system was constructed by an EDCI-mediated condensation of acid **2.3** and primary amine **2.4**, followed by tandem thionation-cyclization of the coupling intermediate **2.5** with Lawesson's reagent without any adverse reactivity towards the protecting group. Deprotection of **2.6** to yield the primary amine **2.7** without the need for chromatographic purification was effected by employing an ethanethiolate as the nucleophile in lieu of piperidine, which is commonly employed for Fmoc removal; this allowed the non-basic dibenzofulvalene scavenger to be efficiently separated from the amine product by acid-base extraction. The syntheses of these intermediates were optimized to circumvent chromatographic purification, which is advantageous when considering the scalability of a multistep synthesis. The synthesis was concluded by nucleophilic substitution of amine **2.7** with bromide **2.10** (after converting the hydrobromide salt to the free base) to afford crystalline chromis-1 ester (**2.1a**), a portion of which was saponified with aqueous NaOH to afford chromis-1 acid **2.1b** as the corresponding water-soluble disodium salt.

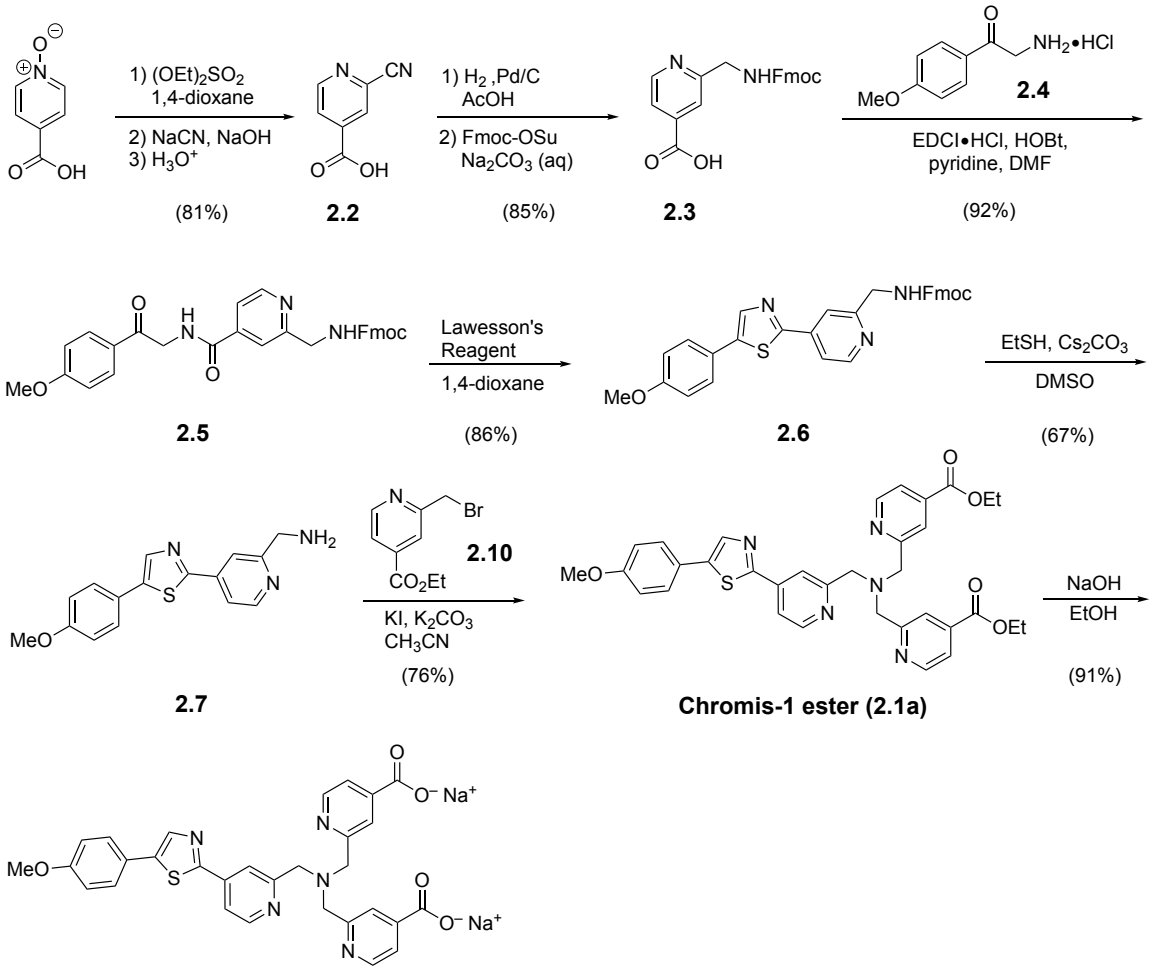

Scheme 2.1: Synthesis of chromis-1 ester (**2.1a**) and chromis-1 acid (**2.1b**).

As mentioned above, the synthesis of bromide **2.10** (Scheme 2.2) was accomplished through modification of a literature procedure.[10] Starting with 2,4-pyridinedicarboxylic acid, both carboxylic acids underwent transesterification reactions to produce the corresponding ethyl dicarboxylate **2.8** by refluxing with concentrated sulfuric acid in EtOH. The ethyl ester in the 2-position was selectively reduced to the corresponding primary alcohol **2.9** by reaction with $NaBH_4$ in EtOH in the presence of $CaCl_2$ as a Lewis acid; typically, $NaBH_4$ is not reactive enough to reduce esters, however, the Lewis-acidic Ca^{2+} activates the ester in alcoholic solvents to permit sufficient reactivity. Finally, alcohol **2.9**

underwent S_N2 substitution with thionyl bromide ($SOBr_2$) to afford 2-(bromomethyl)isonicotinic acid ethyl ester (**2.10**) in pure form. The pure compound (as an oil) had the propensity to turn black in a short period of time, but the decomposed product could be easily purified by filtering the compound dissolved in organic solvent through basic alumina. To circumvent this issue entirely, the neutral pyridine derivative was converted to the corresponding hydrobromide salt by protonation from the HBr generated *in situ* from the reaction of $SOBr_2$ with EtOH. Analytically pure material was then isolated as colorless crystals after recrystallization from boiling EtOH/MTBE.

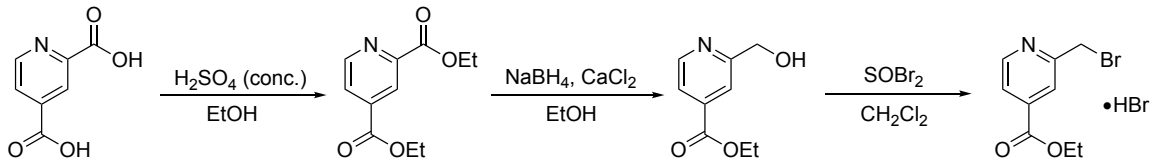

2.8 **2.9** **2.10**

Scheme 2.2: Synthesis of the hydrobromide salt of ethyl 2-(bromomethyl)isonicotinate (**2.10**).

2.2.2 X-Ray Crystal Structure Determination of the Zn(II) Complex of Chromis-1 Acid

The Zn(II) complex of chromis-1 acid was crystallized *in situ* from a mixture of aqueous KCl (0.1 M), DMF, and MeOH to produce individual plate-like triclinic crystals suitable for X-ray crystallographic analysis. A list of selected bond angles and distances is provided in Appendix A., Table A.2. As illustrated in Figure 2.1 below, the Zn(II)-complex adopts a trigonal-bipyramidal coordination geometry with a chlorine atom coordinated to the Zn(II) center in the axial position. Compared to previously published structures of unsubstituted, C3-symmetric [trispicolylamine-Zn(II)Cl]$^+$ complexes,[11-13] the equatorial Zn-N bonds are elongated by an average of 0.03 ± 0.01 Å. The slightly weaker interaction between the zinc atom and the pyridine ligands can be attributed to the electron-withdrawing character of both the thiazole and carboxylic acid substituents. In contrast, there are

no significant differences for the axial Zn-Cl and Zn-N bonds, which adopt a uniform bond distance of 2.26 ± 0.01 Å in all three structures.

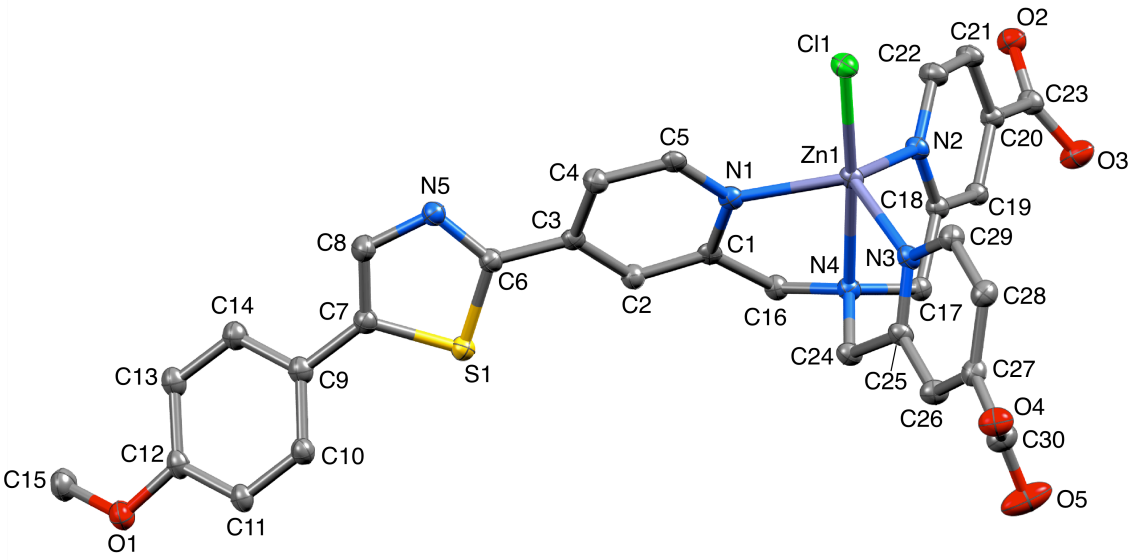

Figure 2.1: ORTEP representation and atom numbering scheme for the crystal structure of the chromis-1-Zn(II) complex [(**2.1b**)Zn(II)]. Ellipsoids shown represent 50% probability. Hydrogen atoms and counter ions have been omitted for clarity. Detailed crystallographic data are provided in Section #. Colored ellipsoids represent the following atoms: Gray, carbon; red, oxygen; blue, nitrogen; yellow, sulfur; light purple, zinc; green, chlorine. Image was generated using the software suite Mercury, version 3.9.

The unit cell of the triclinic crystals contained two conformers with notable structural differences (Figure 2.2). In both conformers, the fluorophore architecture exhibits some deviation from planarity as evident from the dihedral angles of the corresponding aryl-aryl bonds. The largest difference is observed for the anisole ring, which is rotated out of plane by 35 degrees relative to the thiazole; however, this large dihedral angle is apparent in only one of the two conformers, whereas the other conformer features a near-planar dihedral angle of 14.7 degrees, suggesting that the distortion is associated with a soft potential and likely due to packing forces.

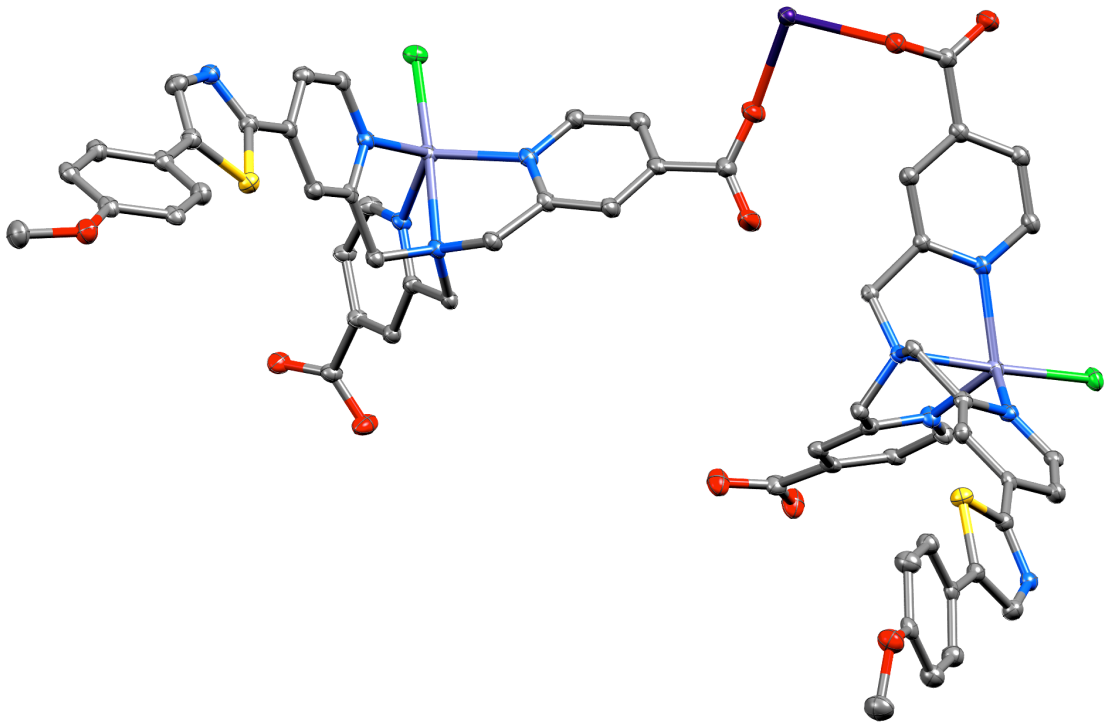

Figure 2.2: ORTEP representation for the crystal structure of chromis-1-Zn(II) complex [(**2.1b**)Zn(II)], depicting the structurally different conformers within the unit cell. Ellipsoids shown represent 50% probability. Hydrogen atoms and counter ions have been omitted for clarity. Colored ellipsoids represent the following atoms: Gray, carbon; red, oxygen; blue, nitrogen; yellow, sulfur; light purple, zinc; green, chlorine; dark purple, calcium. Image was generated using the software suite Mercury, version 3.9.

2.2.3 Steady-State Absorption and Fluorescence Properties of Chromis-1 Acid

Molar ratio titrations of chromis-1 acid (**2.1b**) with Zn(II) in neutral aqueous buffer (pH 7.0, 10 mM PIPES 0.1 M KCl, 25°C) revealed strong chromatic shifts in both the absorption and emission spectra together with sharp saturation at equimolar metal and ligand concentrations. Consistent with Zn(II)-coordination to the pyridyl acceptor moiety of the fluorophore, the absorption maximum at 349 nm ($\varepsilon \sim 22{,}000\ M^{-1}\ cm^{-1}$) is red-shifted by 17 nm upon saturation with Zn(II) (Figure 2.3A). The appearance of clean isosbestic points at 285 and 353 nm combined with equimolar saturation are indicative of a well-defined solution equilibrium involving only free probe and a Zn(II)-complex with 1:1 metal-

ligand stoichiometry. Similarly, the fluorescence emission maximum of the probe is red-shifted from 483 to 520 nm upon binding Zn(II) (Figure 2.3B). By exciting the probe at the isosbestic point, the observed emission intensities are a direct reflection of the quantum yield, which increases more than 2-fold from 0.32 to 0.71 upon coordination of Zn(II) (Table 2.1). Overall, the Zn(II)-induced fluorescence changes are well suited for emission-ratiometric measurements. For example, the ratio of the integrated fluorescence intensities between 510-570 nm and 440-495 nm increases from 0.7 to 2.6 upon saturation with Zn(II), corresponding to a large dynamic range with an R_{max}/R_{min} ratio of 3.7.

Table 2.1: One and two-photon photophysical properties of chromis-1 ester (**2.1a**) and acid (**2.1b**) in aqueous buffer at pH 7.0.[a]

	2.1a[b,c]	[**2.1a**-Zn(II)][b]	**2.1b**[c]	[**2.1b**-Zn(II)]
Abs λ_{max} (nm)[d]	351	378	349	366
ε (10^4 $M^{-1}cm^{-1}$)[e]	2.20	2.86	2.19	2.41
λ_{max} (nm)[f]	n.d.	n.d.	720	740
δ_{max} (GM)[g]	n.d.	n.d.	19	25
Em λ_{max} (nm)[h]	438	495	483	520
Φ_F[i]	0.26	0.56	0.32	0.71

[a] 10 mM PIPES, 0.1 M KCl, 25°C. [b] buffer supplemented with 100 μM liposomes (4:1 DMPC:DMPG). [c] supplemented with 20 μM EDTA to sequester adventitious Zn(II). [d] lowest-energy band of the one-photon absorption spectrum. [e] molar extinction coefficient at λ_{max}. [f] maximum two-photon absorption. [g] two-photon absorption cross section. [h] maximum fluorescence emission. [i] fluorescence quantum yield, referenced to quinine sulfate (Φ_F = 0.546).[14]

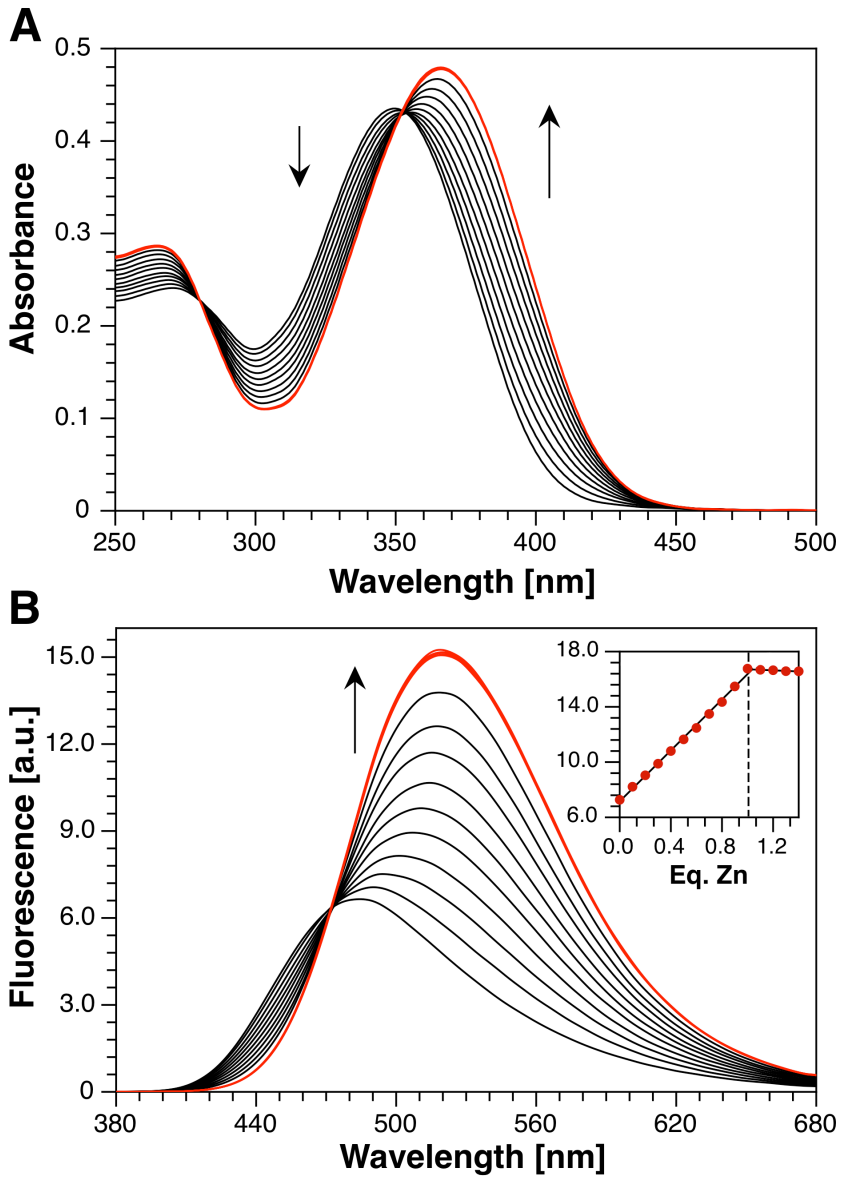

Figure 2.3: Spectral changes of chromis-1 acid (**2.1b**) upon binding Zn(II) in neutral aqueous buffer (pH 7.0, 10 mM PIPES, 0.1 M KCl, 25°C). (A) UV-Vis absorption spectral changes upon stepwise saturation with Zn(II). (B) Fluorescence emission response upon stepwise saturation with Zn(II) (excitation at 353 nm). Red curves indicate the spectra after complete saturation (1.0 eq.) with Zn(II) is achieved. Inset: fluorescence integration over the entire spectral window as a function of molar equivalents of Zn(II).

Analogous to the UV-vis spectral properties, the two-photon absorption (2PA) cross section[15] revealed a red-shifted maximum, which increased from 720 to 740 nm upon Zn(II)-coordination (Figure 2.4). Consistent with greater excited state polarization,[16]

the 2PA cross section of the Zn(II)-bound form is significantly increased compared to the free form. Nevertheless, in the range between 710-740 nm the probe offers balanced cross sections, thus allowing for excitation of the free and Zn(II)-bound probe with similar efficiency.

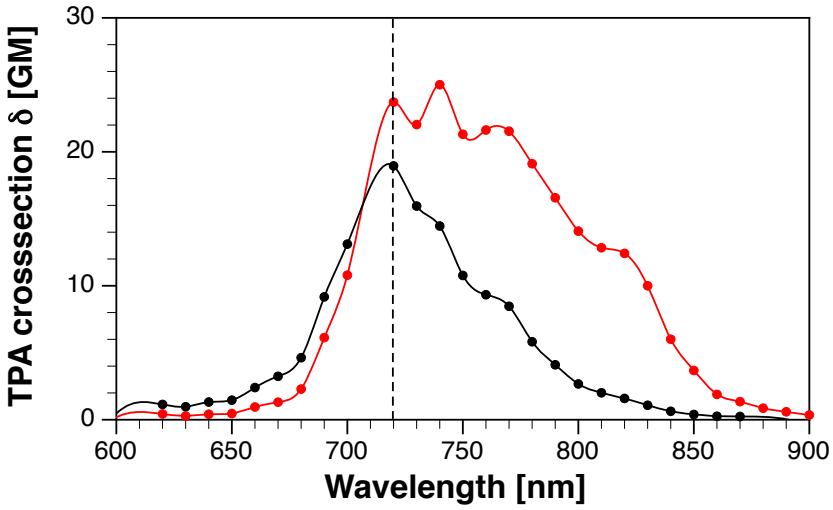

Figure 2.4: Two-photon absorption cross section of the free (black trace) and Zn(II)-bound (red trace) form of chromis-1 acid (**2.1b**). Vertical dashed line corresponds to the wavelength of excitation used to image the fluorophore in live cells using the two-photon microscope, visualizing the balanced TPA cross section of both forms. *Data acquired by Nisan Siegel, Ph.D., Joseph Perry, Ph.D.* Figure adapted with permission from reference [28].

2.2.4 Metal-Ion Selectivity of Chromis-1 Acid

To determine the selectivity of chromis-1 acid (5 μM) in response to biologically relevant divalent metal ions, the fluorescence response of the metal-probe was measured in the presence of an excess of biologically relevant divalent metal ions. To ensure that adventitious metals, including Zn(II), did not interfere with the fluorescence spectrum of metal-free chromis-1 acid, EDTA (ethylenediaminetetraacetic acid, 10 μM) was added before the spectrum of the free form was acquired. To fully saturate chromis-1 acid, as well as the sequestrant (EDTA), 20 μM and 40 μM aliquots of the interfering divalent metals

were added, and emission spectra were acquired after each aliquot. Excluding Zn(II), addition of all other biologically relevant divalent metal ions invoked either no change in the emission response (Mg(II) and Ca(II), Figure 2.5A, B) or resulted in complete fluorescence quenching (Fe(II), Co(II), Ni(II), and Cu(II), Figure 2.5D-G).

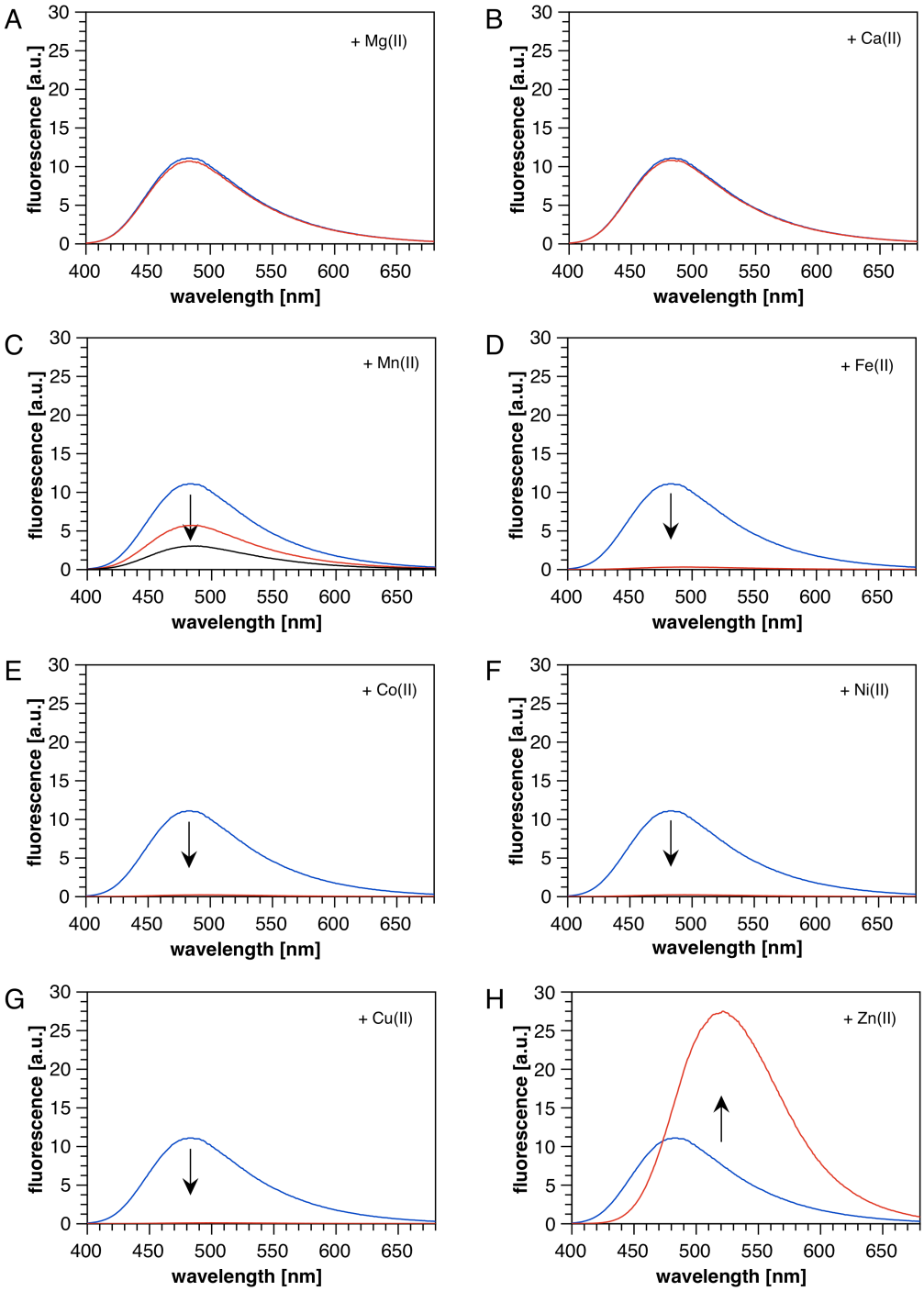

Figure 2.5: Fluorescence response of chromis-1 (**2.1b** 5 μM) in the presence of 4.0 equivalents (20 μM) of interfering divalent metal ions. A-H) Blue traces represent free chromis-1 (5 μM) in pH 7.0 buffer (10 mM PIPES, 0.1 M KCl, 25°C) supplemented with 10 μM EDTA. Red and black traces represent the addition of 20 μM and 40 μM, respectively, of interfering divalent transition metals. Black arrows indicate the change in fluorescence after addition of the interfering divalent metals. Excitation: 358 nm. *Data were acquired by Pritha Bagchi, Ph.D., and the figure was prepared by Christoph Fahrni, Ph.D.* Figure reproduced with permission from reference [28].

Since both the fluorescent probe and its Zn(II) complex are brightly fluorescent, the quenched emission does not translate to an emission-ratiometric response, thus binding of these metal ions results only in a masking effect by competing with Zn(II) for coordination to the probe. For this reason, the ratiometric response of the probe was evaluated in the presence of 0.8 molar equivalents (80% fractional saturation) of the interfering metal ion (Figure 2.6, black bars). Under these conditions, the emission ratio of the remaining 20% of free probe was unaffected by any of the quenching metal ions, thus addition of Zn(II) still produced the emission ratiometric response of the [(chromis-1)Zn(II)] complex observed in the molar ratio titration (Figure 2.6, red, patterned bars).

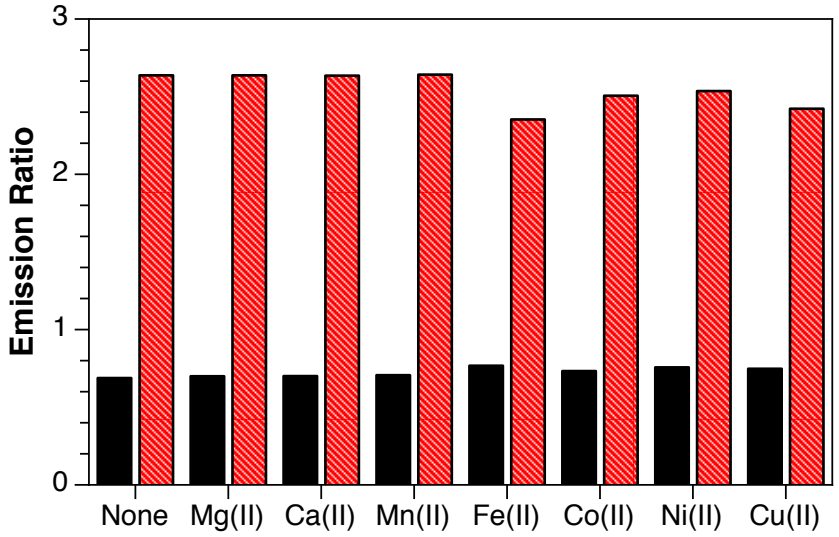

Figure 2.6: Emission-ratiometric response towards selected divalent metal cations at 80% fractional saturation (calculated based on ratio of the integrated fluorescence intensity between 510-570 nm (channel 2) and 440-495 nm (channel 1)). The black bars represent the ratio at 80% fractional saturation, and the corresponding red patterned bars represent the ratio after saturating the remaining 20% of free fluorophore with Zn(II). Excitation: 358 nm.

Of all the biologically relevant transition metals tested, Mn(II) was the only metal that did not bind to chromis-1 with near unity fractional saturation. Therefore, the binding affinity of chromis-1 for Mn(II) was measured via a fluorimetric, metal-addition titration to

determine a stability constant for the Mn(II) complex of chromis-1 acid. Chromis-1 acid (**2.1b**, 5 μM) was titrated with $MnSO_4 \cdot H_2O$ from 0-50 μM, and non-linear, least-squares fitting of the emission spectral data yielded an apparent stability constant of $\text{Log}K_{\text{Mn(II)L}}$ = 5.04 ± 0.004 at pH 7.0 and 0.1 M KCl ionic background, corresponding to an apparent dissociation constant of K_d' = 9.12 μM (Figure 2.7). However, the micromolar affinity of chromis-1 for Mn(II), the ability for Zn(II) to immediately and irreversibly outcompete Mn(II), and the low concentration of Mn(II) in mammalian cells (typically < 10 μM)[17-18] absolve Mn(II) as a potential interference in ratiometric imaging of chromis-1.

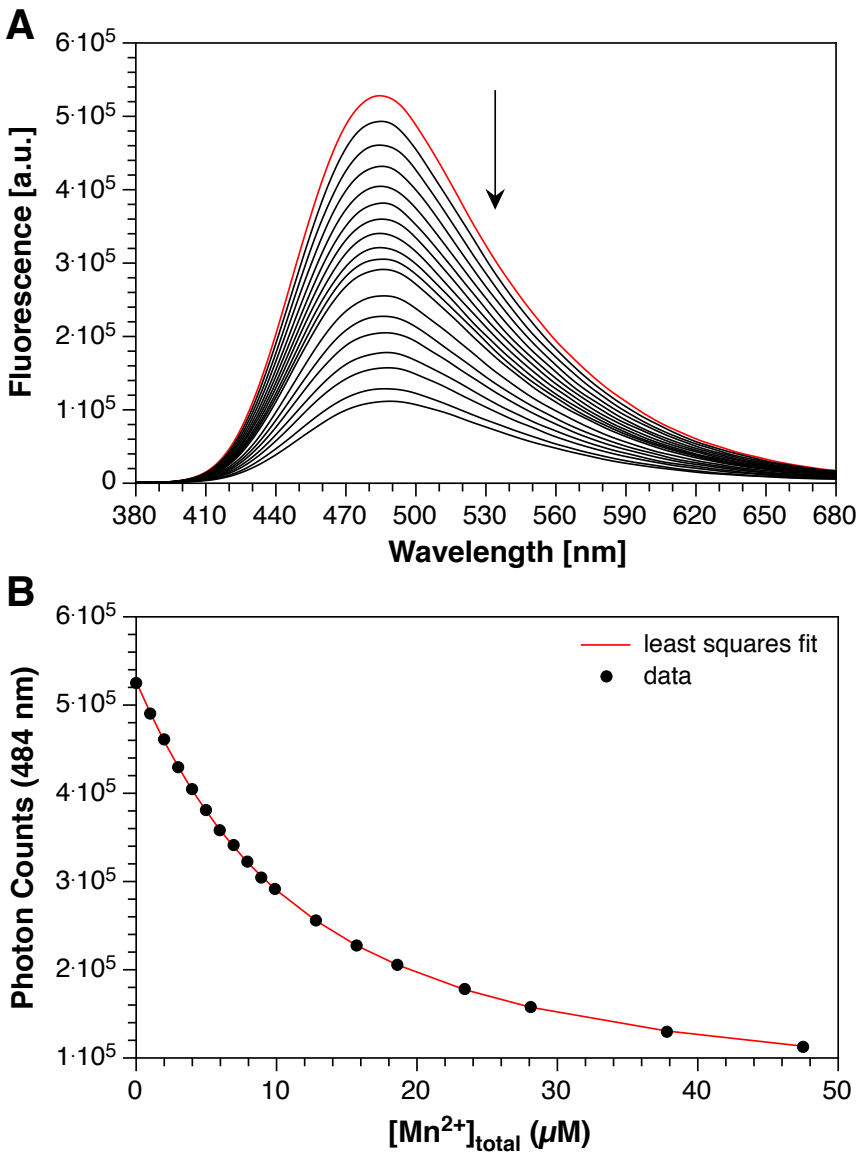

Species	Mn(II)	chromis-1	H	log β
Zn(II)	1	0	0	0.0
Chromis-1	0	1	0	0.0
[(Chromis-1)Mn(II)]	1	1	0	*5.04 ± 0.004*

Figure 2.7: A) Fluorimetric determination of the stability constant of chromis-1 acid for Mn(II) via a direct, metal-addition titration. Chromis-1 (**2.1b**, 5 μM) was equilibrated in aqueous buffer (10 mM PIPES, 0.1 M KCl, pH 7.0, 25ºC) treated with Chelex (1% (w/v), Biorad) and titrated with $MnSO_4 \cdot H_2O$ from 0-50 μM. A fluorescence spectrum (excitation: 358 nm) was acquired after the addition of each aliquot of Mn(II). The red curve indicates free chromis-1 before supplementation with Mn(II). Spectra were analyzed by non-linear least squares fitting to provide a $\text{Log}K_{\text{Mn(II)L}} = 5.04 \pm 0.004$ ($n = 1$). B) Change in fluorescence response at 484 nm with corresponding fit to the equilibrium system model.

2.2.5 Determination of the Zn(II)-Binding Affinity of Chromis-1 Acid

The linear emission increase, along with a sharp, equimolar saturation point observed in the molar ratio titration shown in Figure 2.3, indicates tight Zn(II) binding with near unity fractional saturation throughout the entire titration range. Because the determination of reliable stability constants demands conditions where complex formation is incomplete, ideally within a 10-90% fractional saturation window,[19] both spectrophotometric and fluorimetric titrations were performed in the presence of EGTA (ethylene glycol-bis(β-aminoethyl ether)-*N*,*N*,*N*',*N*'-tetraacetic acid) as a competing ligand with matching affinity (apparent K_d = 4.0 nM at pH 7.0, calculated from published pK_a's and logβ values).[20]

Previous titrations to determine the binding affinity of chromis-1 acid (**2.1b**) in neutral aqueous buffer (10 mM PIPES, pH 7.0) supplemented with 100 mM $KClO_4$ as an ionic background yielded an average apparent stability constant of Log$K_{Zn(II)L} \approx 9.9$, corresponding to an apparent dissociation constant of ~ 120 pM.[21] Attempts to verify this value through repeated spectroscopic titrations using 100 mM KCl as an ionic background in neutral aqueous buffer (10 mM PIPES, pH 7.0, 25°C) resulted in an average, uniform apparent stability constant of Log$K_{Zn(II)L}$ = 10.31 ± 0.13, corresponding to an apparent dissociation constant of K_d' = 49 ± 13 pM (Figure 2.8). These thermodynamic stability constants were obtained regardless of whether the preformed Zn(II)-complex of chromis-1 acid (**2.1b**) was titrated with EGTA or whether Zn(II) was added to a mixture of the probe and EGTA.

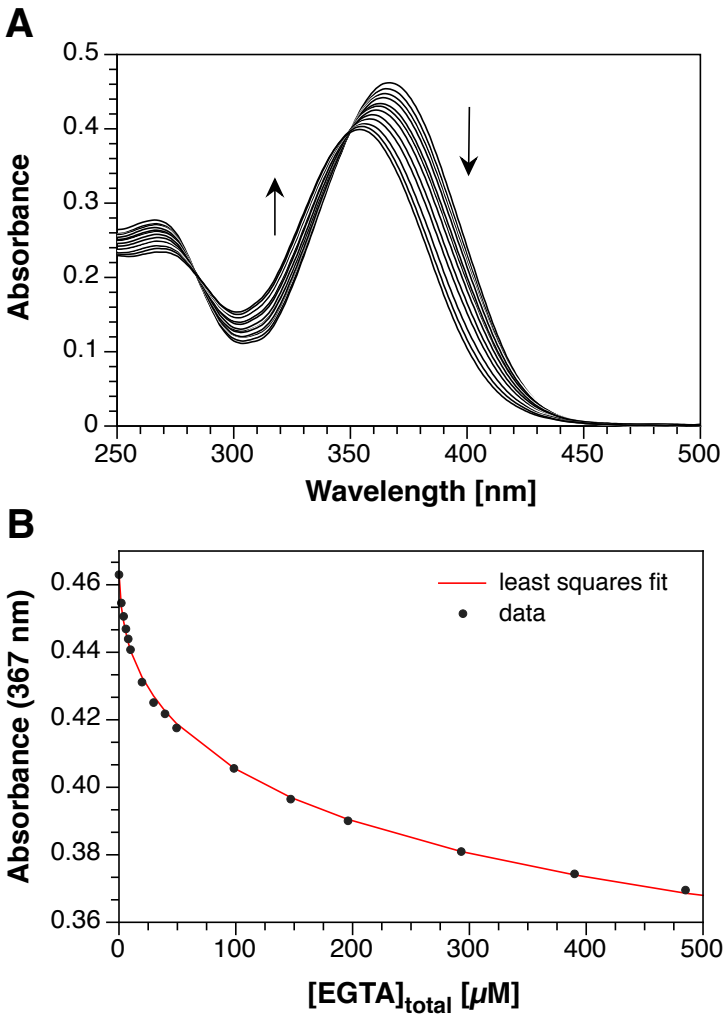

Definition of the Equilibrium System:

Species	Zn(II)	EGTA	chromis-1 acid	H	log β
Zn(II)	1	0	0	0	0.0
EGTA	0	1	0	0	0.0
Chromis-1 acid	0	0	1	0	0.0
EGTA(H)	0	1	0	1	9.51
EGTA(H_2)	0	1	0	2	18.25
EGTA(H_3)	0	1	0	3	21.06
[(EGTA)Zn(II)]	1	1	0	0	12.6
[(chromis-1)Zn(II)]	1	0	1	0	*10.31 ± 0.13*

Figure 2.8: A) Spectrophotometric determination of the stability constant of chromis-1 via a competition titration with EGTA. Chromis-1 (20 μM) was equilibrated with $ZnSO_4 \cdot 7H_2O$ (20 μM) in chelexed aqueous buffer (10 mM PIPES, 0.1 M KCl, pH 7.0, 25°C) and titrated with EGTA to a final concentration of 500 μM. The absorbance spectra were analyzed by non-linear least squares fitting to give an average $\text{Log}K_{Zn(II)L}$ of 10.31± 0.13 (n = 8). B) Change in fluorescence response at 367 nm with corresponding fit to the equilibrium system model.

The discrepancy between the two stability constants corresponds to a ~ 0.6 log-unit difference in the binding affinity or an ~ 80-pM difference in the apparent dissociation constant. To verify the previous value obtained using $KClO_4$ as the background electrolyte, a repeat competition titration of chromis-1 acid in neutral (pH 7.0) aqueous buffer containing $KClO_4$ (100 mM) was performed by a fluorimetric titration of EGTA to a solution containing the preformed [(**2.1b**)Zn(II)] complex. Fitting of the fluorescence data to the equilibrium model described above in Figure 2.8, yielded an apparent stability constant of $\mathrm{Log}K_{Zn(II)L} = 9.51 \pm 0.04$, corresponding to an apparent dissociation constant 310 pM (Figure 2.9), which more closely agrees with the dissociation constant of ~ 120 pM determined initially.

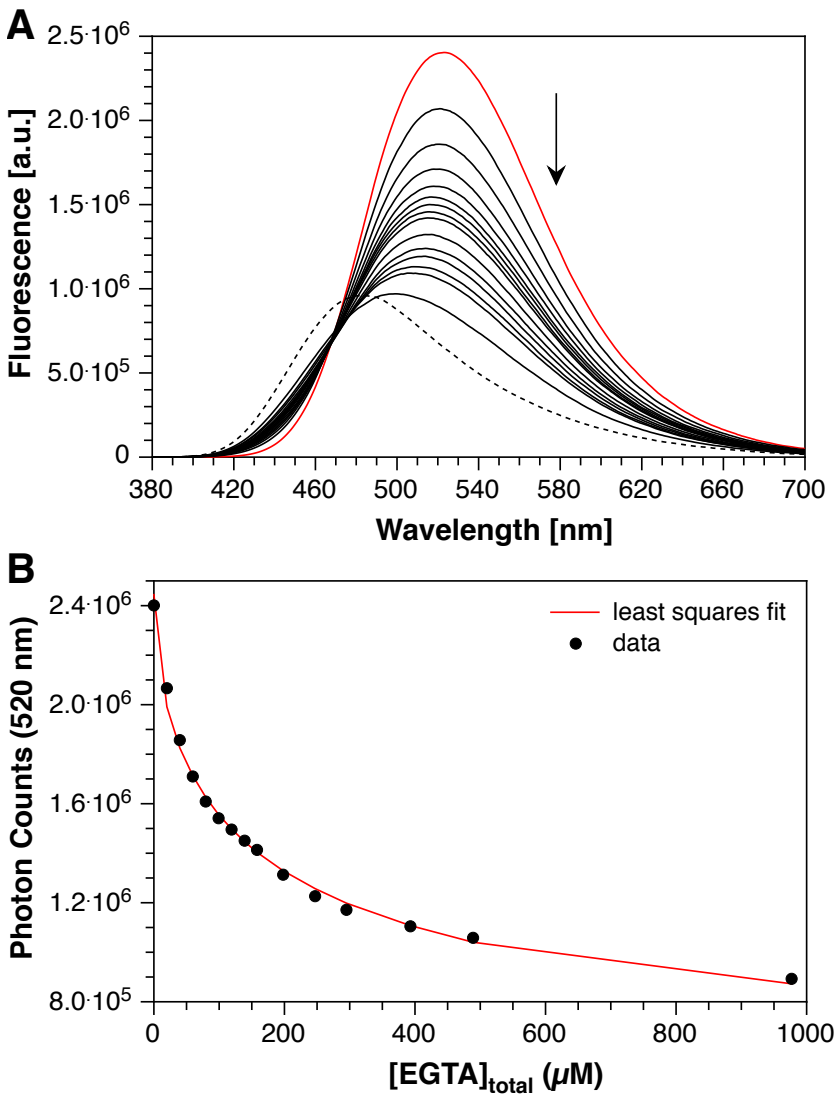

Figure 2.9: A) Fluorimetric determination of the stability constant-dependence of chromis-1 acid (**2.1b**) on the ionic background via competition with EGTA. Chromis-1 (10 μM) was equilibrated with $ZnSO_4 \cdot 7H_2O$ (10 μM) in chelexed aqueous buffer (10 mM PIPES, 0.1 M $KClO_4$, pH 7.0, 25ºC) and titrated with EGTA to a final concentration of 1 mM. The fluorescence spectra (excitation: 358 nm) were analyzed by non-linear, least-squares fitting to give an apparent $Log K_{Zn(II)L}$ of 9.51 ± 0.04 (n = 1). The dashed black curve corresponds to free **2.1b**, and the red curve corresponds to Zn(II)-saturated **2.1b** before the addition of EGTA. B) Change in fluorescence response at 520 nm with corresponding fit to the equilibrium system model described in Figure 2.8.

Analysis of the crystal structure of chromis-1 acid (Figures 2.1, 2.2) provided insight into the ionic background-dependent discrepancy between the two stability constants of chromis-1 acid. While the flexible coordination sphere of Zn(II) allows the metal to

achieve various coordination numbers between four and six when forming metal-ligand complexes, coordination of a 5th ligand to the Zn(II) center of a 4-coordinate Zn(II)-ligand complex should provide greater stability than its 4-coordinate analog. Although metal complexes with perchlorate have been prepared, their stability constants are low due to perchlorate's poor coordinating capability by virtue of its delocalized charge density over each of its four oxygen atoms.[22] On the other hand, chloride is a much more effective donor for coordinating metals, including Zn(II). Therefore, the likelihood of perchlorate binding to Zn(II) as a fifth, auxillary ligand in the chromis-1-Zn(II) complex is less favorable than chloride, and the stability constants for the formation of the chromis-1-Zn(II) complex are direct reflections of this.

The use of KCl(*aq*) as an ionic background in the aqueous buffer used for spectroscopic characterization provides a valuable comparison to the ionic nature of the cell, as $[Cl^-]_{total}$ can range between 5 and 100 mM in mammalian cells.[23] Conversely, the lack or negligible presence of perchlorate ions in mammalian cells due to its toxicity makes the use of the counteranion as a background electrolyte ineffective when best simulating intracellular conditions. On the other hand, the poor coordinating ability of perchlorate makes it an effective background electrolyte in situations when the electrolyte may otherwise engage in metal complexation. In situations when the background electrolyte may influence the thermodynamic properties of the probe being tested, such as chromis-1, it is advantageous to use an ionic background that is most representative of cellular conditions, provided that high concentrations of the electrolyte do not interfere with the fluorescence response of the probe.

2.3 Exploring Dynamic Zinc Fluxes in Ratiometric Imaging of Chromis-1 Ester (2.1a)

Note: All microscopy methods and data in Section 2.3 were gratefully conducted and acquired by Daisy Bourassa, Ph.D. They are included in this thesis to demonstrate the robust application of the fluorescent probe in cellular imaging for which it was designed and intended.

2.3.1 Deriving A Relationship to Calculate the Fractional Saturation of a Probe Using Ratios Determined from Live-Cell Imaging

For a metal-binding fluorophore with a 1:1 binding stoichiometry, the dissociation constant (K_d) for the equilibrium between the metal (M^{n+}) and the probe (P), forming a complex PM^{n+}, is defined as:

$$K_d = \frac{[M^{n+}][P]}{[PM^{n+}]} \tag{2-1}$$

The Fractional saturation *f* of the probe can be expressed as the ratio of the concentration of the metal-bound probe $[PM^{n+}]$ to the total probe concentration $[P]_{total}$. For fluorescent indicators that either exhibit 1:1 binding stoichiometries between the probe and the metal or that bind multiple metals to one probe molecule, the ratiometric response of the probe does not depend on the concentration of the probe. Therefore, the fractional saturation f can be expressed according to the following equation:

$$f = \frac{[M^{n+}]}{K_d[M^{n+}]} \tag{2-2}$$

Solving for $[M^{n+}]$ yields the relationship:

$$[M^{n+}] = \frac{f \cdot K_d}{1 - f} \tag{2-3}$$

For ratiometric imaging, which utilizes fluorescence indicators that undergo a spectral shift in the emission upon binding the metal analyte, the concentration of intracellular labile M^{n+} can be calculated using the dissociation constant (K_d), the ratio of the fluorescence intensities R, and the instrument-dependent factors S_f an S_b that can be obtained from an independent microscope calibration. This relationship[24] is shown below:

$$[M^{n+}]_f = K_d \left(\frac{R - R_{min}}{R_{max} - R}\right)\left(\frac{S_f}{S_b}\right) \tag{2-4}$$

If the instrument-dependent factor is approximated to be 1, equation 2-3 can be substituted into equation 2-4 and solved for f to provide a relationship (2-5) between the fractional saturation of the probe and the ratios determined by fluorescence microscopy.

$$f = \frac{R - R_{min}}{R_{max} - R_{min}} \tag{2-5}$$

The fractional saturation f from equation 2-5 can be substituted into equation 2-3 to calculate a free metal concentration $[M^{n+}]_{free}$. Quantitative imaging analysis software packages, such as ImageJ[25], can then be used to analyze the changes in the emission ratio of fluorescent probes, including chromis-1, over time.

*2.3.2 Ratiometric Imaging of Dynamic Zinc Fluxes in Mouse Fibroblast Cells Using Chromis-1 Ester (**2.1a**)*

Because the anionic dicarboxylate salt of chromis-1 acid (**2.1b**) is not membrane permeable, cellular imaging studies were performed with the ester form of chromis-1 (**2.1a**). To evaluate the Zn(II)-dependent ratiometric response of chromis-1 ester in live cells, perfusion experiments were performed using NIH 3T3 mouse fibroblasts as a model mammalian model (Figure 2.10). As evident from the differential interference contrast (DIC) intensity micrographs (Figure 2.10, middle), chromis-1 ester (**2.1a**) was readily internalized into cells and partitioned into the cellular membranes, demonstrating bright fluorescence throughout the cytoplasm except cellular nuclei, from which it appeared to be excluded. Although the distribution of fluorescence intensities demonstrates uneven and distinct punctate localizations, the processed ratio images display a uniform fractional saturation with an average ratio $R = 0.60 \pm 0.16$. Upon exposure of the cells to exogenous zinc pyrithione, a membrane-permeable ionophore for Zn(II),[26] the ratio swiftly increased by more than 4-fold to yield an average ratio of $R = 2.53 \pm 0.56$, indicative of saturation of chromis-1 ester with Zn(II) (Figure 2.10B). Subsequent incubation of the cells with the high-affinity, membrane-permeable chelator TPEN invoked a ratiometric response that yielded an average ratio of $R = 0.54 \pm 0.13$, which was slightly lower compared to basal-level (resting) conditions. For comparison purposes, a similar ratio value of 0.52 ± 0.14 was calculated when TPEN was supplemented to the adherent cells grown in basal medium without exposure to exogenous zinc pyrithione. As demonstrated by the plot of the intensity ratio versus time, the binding and dissociation events between chromis-1 ester and Zn(II) occurred with very rapid dynamics (Figure 2.10B, right).

To investigate whether chromis-1 is capable of following large, dynamic fluctuations in endogenous Zn(II), NIH 3T3 cells were exposed to 2,2′-dithiodipyridine (DTDP), a reagent that is used to oxidize the sulfhydryl functionalities of Cys residues of endogenous ligands, such as metallothionein, [27] and stimulate the dissociation of Zn(II) ions coordinated to these sulfhydryl groups. Adherent 3T3 cells grown under basal conditions were treated with chromis-1 ester and displayed similar basal-level ratios ~ 0.5 (Figure 2.10C, left), which progresively increased following the addition of DTDP (100 μM) and culminated at a maximum ratio of R_{max} ~ 1.3 after 40 min (Figure 2.10, middle). Interestingly, the elevated ratio that manifested from the release of endogenous Zn(II) after addition of DTDP led to a gradual decrease in the ratio without the assistance of any exogenously added reagents. The observation was accompanied by a re-equilibration of cytoplasmic Zn(II) levels to re-equilibrate to basal-level conditions, reaching intensity ratio of R ~ 0.5 after ~120 minutes.

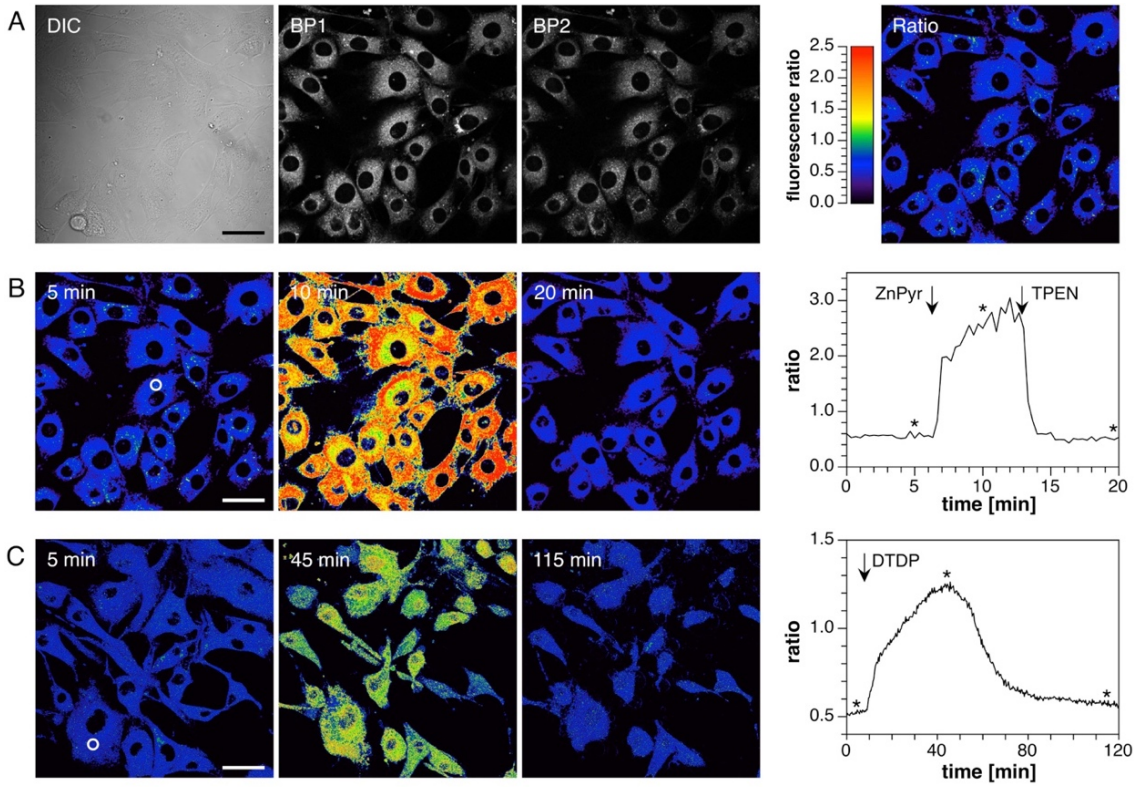

Figure 2.10: Ratiometric imaging of labile Zn(II) in live NIH 3T3 mouse fibroblasts with chromis-1 ester (**2.1a**) by TPEM. A) Left: DIC and fluorescence intensity images respectively. Right: ratio image according to the equation: R = BP2/BP1. B) Left: Ratio images prior to and after the addition of 50 μM $ZnSO_4$ and 5 μM pyrithione (at 10 min). Supplementation of TPEN (100 μM) resulted in a sharp decrease in the fluorescence intensity ratio. Right: Time trace of the change in the average intensity ratio for the ROI indicated by the white circle in the left panels. The asterisks correspond to the time points at which the respective ratio images shown to the left were acquired. C) Left: Ratio images prior and after addition of DTDP (100 μM). Treatment with DTDP resulted in first an increase in the fluorescence ratio that peaked around 40 minutes followed by a gradual decrease back to basal levels. Right: Plot of the time versus average fluorescence intensity ratio for the ROI indicated by the white circle. The asterisks designate the times corresponding to the three fluorescence ratio images on the left. Scale bars: 40 μm. Excitation: 720 nm. *Data were acquired and analyzed, and the figure was prepared, by Daisy Bourassa, Ph.D.*[28] Figure and figure caption were reproduced with permission from author of the paper corresponding to this chapter.

Using the limiting intensity ratio values from perfusion experiments with chromis-1 ester and the measured Zn(II) stability constant of 10.3 for chromis-1 acid (Figure 2.8) led to a calculated intracellular buffered Zn(II) concentration that is inconsistent with estimated values previously reported.[29] In addition to the punctate staining patterns observed during

perfusion experiments with live NIH 3T3 mouse fibroblasts, the discrepancies between the average calculated buffered Zn(II) concentrations would be manifested by incomplete hydrolysis of the ethyl ester functionalities of chromis-1 ester, as the more electron-withdrawing ester groups should yield a weaker binding affinity compared to the anionic carboxylate groups of chromis-1 acid. This understanding furnished momentum to determine the stability constant of chromis-1 ester to elucidate the impact of the substituent effect on the binding affinities of chromis-1 ester and chromis-1 acid.

2.3.3 Determination of the Binding Affinity of Chromis-1 Ester and Comparison to Chromis-1 Acid

To determine the apparent stability constant of **2.1a** under conditions that mimic the cellular environment, fluorimetric titrations were carried out in the presence of liposomes composed of a 4:1 ratio of zwitterionic dimyristoyl phosphatidylcholine (DMPC) and anionic dimyristoyl phosphatidylglycerol (DMPG) as model membranes. Upon dilution from a DMSO stock solution into pH 7.0 buffer containing 100 μM liposomes (freshly extruded) and 1.0 mM EGTA as competing ligand with matching affinity, diester **2.1a** was titrated with $ZnSO_4 \cdot 7H_2O$ up to a total concentration of 1 mM. Non-linear least-squares fitting of the fluorescence titration data over the entire spectral range yielded an average apparent $\text{Log}K_{Zn(II)L} = 8.62 \pm 0.07$, corresponding to an apparent K_d of 2.4 ± 0.4 nM at pH 7.0 (Figure 2.11). Consistent with a stronger electron withdrawing character of the neutral ester groups in **2.1a** compared to the anionic carboxylate substituents in **2.1b**, chromis-1 ester exhibits a Zn(II) affinity that is 1.5 orders of magnitude lower, with the two probes covering a total dynamic range of nearly four orders of magnitude within the 90:10 fractional saturation window (Figure 2.12). Using the ratios in the presence of TPEN and

Zn(II)-pyrithione as the limiting R_{min} and R_{max} values, respectively, NIH 3T3 mouse fibroblast cells that were grown under basal conditions displayed a fractional saturation of ~ 3-6%, corresponding to an average buffered [Zn(II)] = 50-100 pM using the dissociation constant of chromis-1 ester rather than chromis-1 acid.

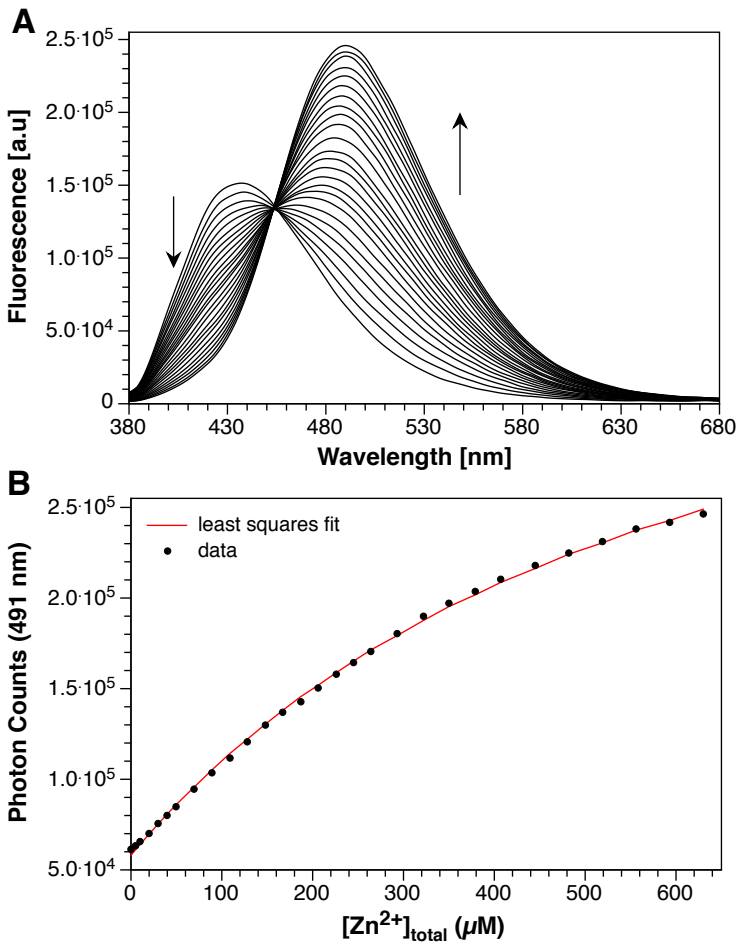

Definition of the Equilibrium System:

Species	Zn(II)	EGTA	chromis-1 ester	H	log β
Zn(II)	1	0	0	0	0.0
EGTA	0	1	0	0	0.0
Chromis-1 ester (**2.1a**)	0	0	1	0	0.0
EGTA(H)	0	1	0	1	9.51
EGTA(H_2)	0	1	0	2	18.41
EGTA(H_3)	0	1	0	3	21.22
[(EGTA)Zn(II)]	1	1	0	0	12.6
[(**2.1a**)Zn(II)]	1	0	1	0	*8.62 ± 0.07*

Figure 2.11: A) Fluorimetric determination of the stability constant of chromis-1 ester (**2.1a**) via a Zn(II)-addition titration in the presence of EGTA. Chromis-1 ester (2 μM) was equilibrated with EGTA (1 mM in diH_2O) in aqueous buffer (20 mM PIPES, 0.1 M KCl, pH 7.0, 25ºC) supplemented with 100 μM 4:1 DMPC:DMPG liposomes and titrated with $ZnSO_4$•$7H_2O$ to a final concentration of 620 μM. Arrows indicate the change in fluorescence after each aliquot of Zn(II) added. The fluorescence spectra (excitation: 358 nm) were analyzed by non-linear least squares fitting to give an average log$K_{Zn(II)L}$ of 8.62 ± 0.07 (n = 2). B) Change in fluorescence response at 500 nm with corresponding fit to the equilibrium system model described in Figure 2.8 above.

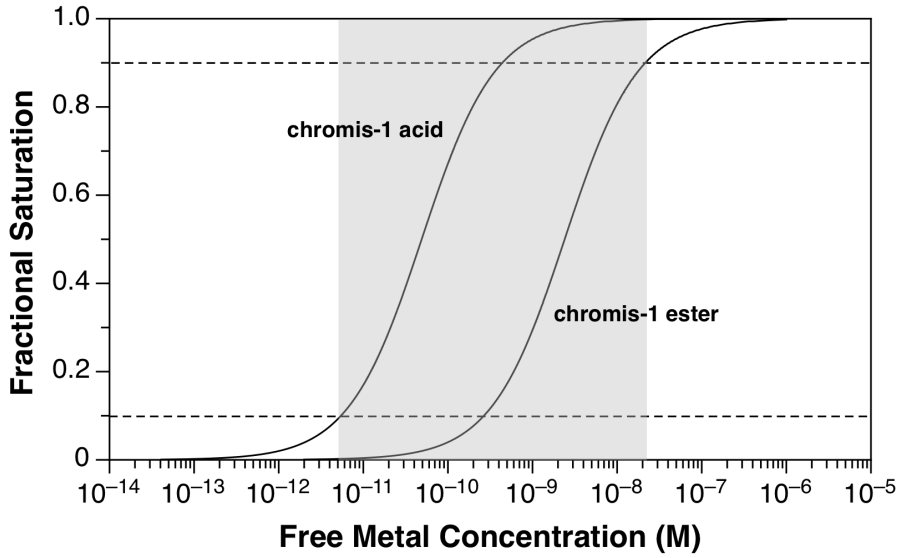

Figure 2.12: Binding isotherms for the formation of the Zn(II) complexes of chromis-1 ester (**2.1a**) and chromis-1 acid (**2.1b**) with 1:1 stoichiometries. The grey region displays the combined dynamic range for the two metal-binding fluorophores within the 90:10 fractional saturation window.

2.3.4 Sensitivity of Chromis-1 Ester to Intracellular pH Fluctuations

To examine the ratiometric response of chromis-1 ester to changes in intracellular pH, live 3T3 mouse fibroblasts cells were exposed to the reagent bafilomycin A_1 (900 nM), a selective inhibitor of vacuolar-type H^+-ATPases.[30-31] Fibroblasts were incubated with both chromis-1 ester and LysoTracker Red, which is used to visualize acidic subcellular compartments. LysoTracker Red functions as an acidotropic fluorophore that is rendered membrane impermeable upon protonation, leading to the selective accumulation within the acidic subcellular compartments. As illustrated in Figure 2.13, the fluorescence intensity of LysoTracker Red was immediately reduced upon addition of bafilomycin A_1, indicating a rapid equilibration of the pH of the stained cytoplasmic components. Conversely, the ratiometric response of chromis-1 ester was negligibly affected under analogous conditions (Figure 2.13). These results are consistent with *in vitro* measurements of the fluorescence dependence of chromis-1 on pH using liposomes as model membranes, where

only minimal changes in the emission intensity and profile were observed between pH 7 to pH 5 (Figure 2.14).

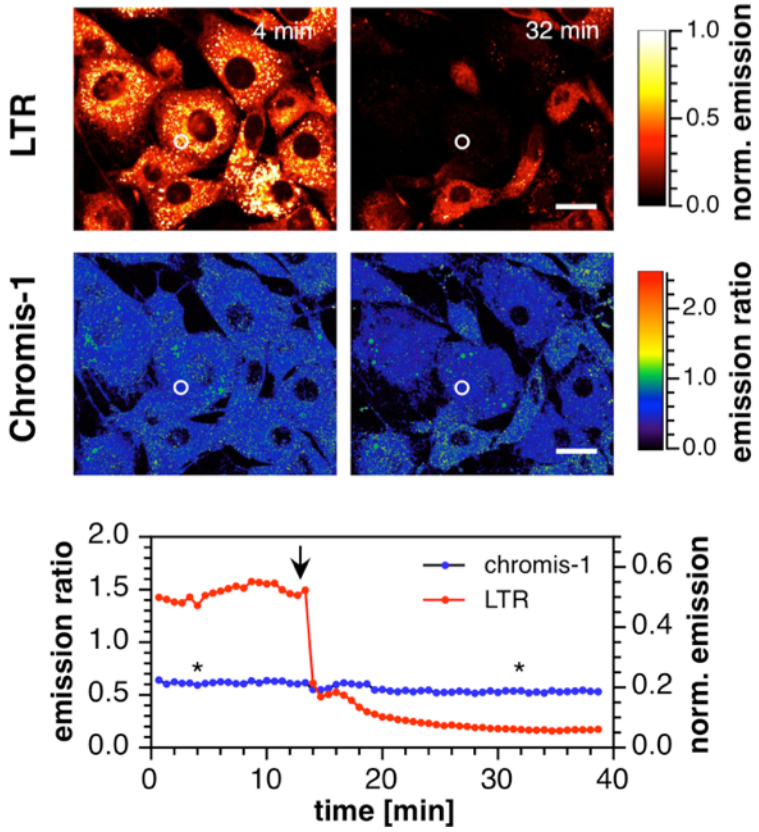

Figure 2.13: Emission ratiometric response of chromis-1 to changes in the intracellular pH. Top panel: Live NIH 3T3 mouse fibroblast cells were co-incubated with Lysotracker Red (LTR, 50 nM) and chromis-1 ester (2 μM), and images were acquired simultaneously to evaluate changes in the LTR fluorescence and chromis-1 emission ratio upon the addition of bafilomycin A_1 (900 nM) at 14 min. Scale bar: 20 μm. Bottom: time-dependent changes of the average emission intensity of LTR (red trace) and intensity ratio of chromis-1 fluorescence (blue trace) for the ROI that is indicated by the white circles in the above images. Asterisks indicate the time points associated with the images in the above micrographs, and the arrow demonstrates the time corresponding to the addition of bafilomycin A_1. *Data were acquired and analyzed, and the figure was prepared, by Daisy Bourassa, Ph.D.*[28] Figure and figure caption were reproduced with permission from author of the paper corresponding to this chapter.

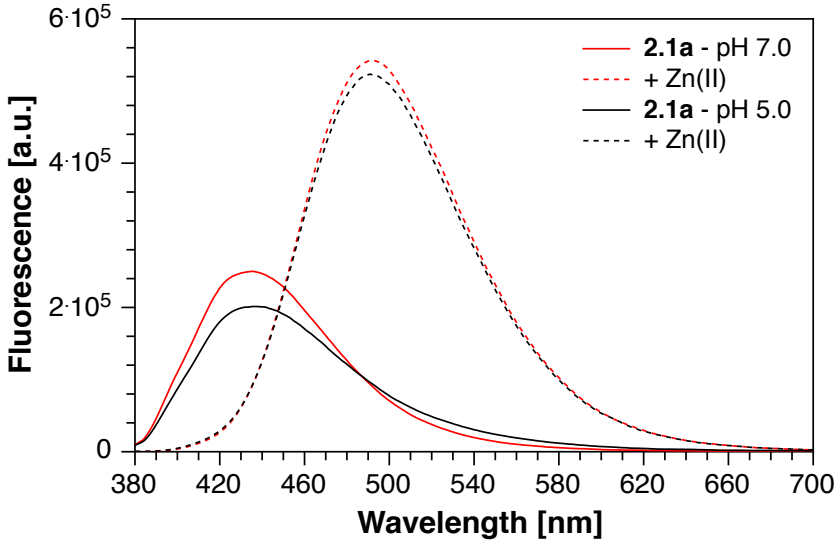

Figure 2.14: Fluorescence dependence of chromis-1 ester (**2.1a**) on pH. Chromis-1 ester (2 μM) was equilibrated in aqueous buffer (10 mM PIPES, 100 mM KCl, 25°C) at pH 7.0 and 5.0, both supplemented with 4:1 DMPC:DMPG liposomes (100 μM), and then saturated with $ZnSO_4 \cdot 7H_2O$ (3 μM). Red traces (solid and dashed) represent the fluorescence response of chromis-1 at pH 7.0, and the black traces (solid and dashed) represent the fluorescence response at pH 5.0. Excitation: 358 nm. Figure and caption were reproduced with permission from reference [28].

2.4 Conclusions

The design of emission-ratiometric fluorescent probes for the detection of trace metal ions in biology by TPEM remains a significant challenge. By incorporating the metal-binding site into the acceptor moiety of a donor-acceptor fluorophore platform, large chromatic shifts of both the excitation and emission maxima were achieved while maintaining balanced action cross sections derived from similar 2PA cross sections between the free and Zn(II)-bound probe. The latter is a vital prerequisite to ensure a robust quantitative analysis of ratiometric images. Because the signal-to-noise ratio is amplified in the derived ratio image compared to the raw fluorescence micrographs, the intensities of the individual emission channels should remain balanced. Although a large R_{max}/R_{min} ratio may seem advantageous for achieving a wide dynamic range, the differences in brightness between

the two emission channels would be difficult to resolve due to the limited absolute dynamic range of the detection system, and thus a large gain in R_{max}/R_{min} would be offset by a decreased signal-to-noise ratio.

Implemented in the form of a Zn(II)-selective fluorescent probe, chromis-1 ester displayed robust emission-ratiometric imaging capabilities in live cells using TPEM. Initially, however, using the measured Zn(II) stability constant of the acid form of chromis-1, cellular staining data with chromis-1 ester generated discrepancies in the calculated buffered Zn(II) levels when compared to the previously published estimations, suggesting that the ester functionalities were not undergoing hydrolysis to their corresponding carboxylic acids by means of non-specific esterases, as expected. Comparison of the Zn(II) stability constants of chromis-1 acid chromis-1 ester, which required the presence of liposomes to enable sufficient solubility for conducting the independent measurements, observed a two-logarithmic difference between the two values. The establishment of limiting R_{min} and R_{max} values provided from *in situ* calibration measurements in 3T3 mouse fibroblast cells, in addition to the Zn(II)-binding affinity value of chromis-1 ester, enabled the determination of estimated buffered cytosolic Zn(II) levels between 50-100 pM under basal-level conditions. This value agrees well with previous reports using genetically encoded ratiometric fluorescence probes,[29] which indicated buffered levels of 80 pM in HeLa cells,[32] 270 pM in HEK293 cells,[33] and 400 pM in pancreatic β cells INS-1cells.[33] Furthermore, the calculation of this estimated buffered Zn(II) range confirmed that, indeed, the ester functionalities were not hydrolyzed upon internationalization into the cytoplasm.

As ratiometric image analysis reports only estimated buffered Zn(II) concentrations by determining the fractional saturation of the probe, absolute buffered Zn(II) levels must be derived from an independent calibration of the probe most often carried out *in vitro*.

Variations in the calibration conditions, including pH, temperature, and background electrolyte composition and concentration, not to mention the reliability of previously measured protonation constants and Zn(II)-binding affinities of the employed competitor ligands and metal ion buffers, only support the notion that the calculated cellular Zn(II) levels should serve as estimated values rather than absolute concentrations. Nevertheless, quantitative ratiometric imaging enabled by the employment of metal-responsive fluorescent probes, including chromis-1, is particularly valuable when discerning relatively subtle changes in buffered Zn(II) concentrations within a particular environment.

2.5 Experimental Section

2.5.1 Synthesis

Materials and Reagents. 2-amino-4'-methoxyacetophenone (**2.4**) was synthesized according to a previously published procedure.[7] Fmoc-succinimidyl carbonate (Oakwood Chemicals), isonicotinic acid *N*-oxide (Alfa Aesar), 2,4-pyridine dicarboxylic acid (Alfa Aesar), and 2-bromo-4'-methoxyacetophenone (Alfa Aesar) were purchased from commercial sources and used without further purification. NMR: ^{1}H NMR spectra were recorded at 400 MHz and referenced to an internal TMS standard (0 ppm) for all NMR solvents excluding D_2O, which was referenced to sodium 3-trimethylsilylpropionate-2,2,3,3-d_6 (0 ppm). ^{13}C spectra were acquired at 100 MHz and referenced to the known chemical shift of the solvent peak ($CDCl_3$: 77.2 ppm; DMSO-d_6: 39.5 ppm; CD_3OD: 49.0 ppm; Acetone-d6: 206.3, 29.8 ppm).

2-Cyanoisonicotinic acid (2.2): *Synthesized and optimized by M. Thomas Morgan, Ph.D.* Isonicotinic acid *N*-oxide (87.7 mmol, 12.2 g), diethyl sulfate (1.2 eq., 105

mmol, 12.2 mL) and dioxane (15 mL) were added to a 100 mL round bottom flask containing a large stir bar. The flask was covered with a fritted adapter to minimize evaporation, and the mixture was stirred at 90°C overnight to produce a biphasic liquid. This was diluted with ice water (100 mL) and washed with an equal volume of ethyl acetate to remove tarry material and unreacted Et_2SO_4. The aqueous phase was neutralized with Na_2CO_3 (1.0 eq., 96.5 mmol, 9.3 g) under stirring, and NaCN (1.1 eq., 96.5 mmol, 4.73 g) was added. After 2 hours, the mixture was slowly acidified with concentrated HCl (2.1 eq., 184 mmol, 15 mL), and the product was collected by filtration and dried by suction overnight to give a red-orange powder, which was recrystallized from boiling acetonitrile-water gave the purified product as a light yellow solid. Yield: 10.67 g (82%). ^{1}H NMR (400 MHz, Acetone-d6) δ 8.19 (dd, *J* = 5.0, 1.6 Hz, 1H), 8.35 (dd, *J* = 1.6, 0.9 Hz, 1H), 8.96 (dd, *J* = 5.0, 0.9 Hz, 1H). ^{13}C NMR (100 MHz, Acetone-d6) δ 117.7, 127.5, 128.7, 135.4, 140.5, 153.2, 164.8.

2-((((((9*H*-fluoren-9-yl)methoxy)carbonyl)amino)methyl)isonicotinic acid (2.3). A solution of **2.2** (6.76 mmol, 1.0 g) in acetic acid (5 mL) was hydrogenated for 2 hours at 20 psi in the presence of Pd/C (5 mol %, 500 mg) as a catalyst. The reaction mixture was filtered through a pad of Celite and the solvent was removed under reduced pressure to give 950 mg (93%) of 2-(aminomethyl)isonicotinic acid. Without further purification, the isolated product (1.32 mmol, 200 mg) was dissolved in 10% aq. Na_2CO_3 (1.5 mL) and a solution of 9-fluorenylmethylsuccinimidyl carbonate (0.91 eq., 1.2 mmol, 405 mg) in 1,4-dioxane (1 mL) was added. After stirring the reaction mixture at room temperature for 12 hours, the solvent was evaporated and the residue was treated with 1 M aq. HCl (1.5 mL). The precipitated product was filtered off, washed with water and a small

amount of methanol, and dried under vacuum to afford 420 mg (85%) of the Fmoc derivative **2.3** as a white solid. ^{1}H NMR (400 MHz, DMSO-d_6, T = 373K) δ 4.22 (t, *J* = 6.9 Hz, 1H), 4.34 (d, *J* = 6.9 Hz, 2H), 4.39 (d, *J* = 6.1 Hz, 2H), 7.29 (t, *J* = 7.4 Hz, 2H), 7.38 (t, *J* = 7.4 Hz, 2H), 7.55 (s, br, 1H), 7.63-7.67 (m, 3H), 7.77 (s, 1H), 7.83 (d, *J* = 7.5 Hz, 2H), 8.66 (d, *J* = 5.0 Hz, 1H), 13.01 (s, br, 1H). Note: Due to the presence of a dynamic conformer equilibrium, the room temperature ^{1}H NMR spectrum displayed an additional set of weak signals which merged with the main set upon heating to 100 °C). Furthermore, the dynamic exchange precluded the recording of a suitable ^{13}C NMR spectrum. MS (ESI) *m/z* 375 (100, $[M+H]^+$). HRMS (ESI) *m/z* calculated for $C_{22}H_{19}N_2O_4$ $[M+H]^+$ 375.1345, found 375.1356.

Fmoc-protected Amide 2.5. A mixture of the Fmoc-protected amino acid **2.3** (9.62 mmol, 3.60 g), 2-amino-1-(4'-methoxyphenyl)ethanone hydrochloride **2.4** (1.1 eq., 10.6 mmol, 2.22 g), EDCI•HCl (1.5 eq., 14.4 mmol, 2.87 g), and 1-hydroxybenzotriazole (HOBt, 0.5 eq., 4.81 mmol, 675 mg) was stirred in DMF (12 mL) until it turned homogeneous (10 min). Pyridine (1.0 eq., 815 μL) was added, and the mixture was stirred overnight. The mixture was diluted sequentially with water (5 mL), methanol (60 mL) and water (20 mL) under rapid stirring. The resulting precipitate was collected by filtration, washed with water, dried under vacuum, and recrystallized from a solution in THF-acetonitrile by boiling until the temperature rose to the boiling point of pure CH_3CN. After cooling to room temperature, the product was collected by filtration and dried under high vacuum to afford a colorless crystalline powder. Yield: 4.59 g (8.80 mmol, 92%). ^{1}H NMR (400 MHz, DMSO-d_6, T = 293 K) δ 3.86 (s, 3H), 4.26 (t, *J* = 5.0 Hz, 1H), 4.34 (d, *J* = 7.0 Hz, 2H), 4.39 (d, *J* = 6.0 Hz, 2H), 4.78 (d, *J* = 5.6 Hz, 2H), 7.09 (d, *J* = 8.8 Hz, 2H), 7.33 (t, *J* = 7.5 Hz, 2H), 7.41 (t, *J* = 7.4 Hz, 2H), 7.70-7.76 (m, 4H), 7.90 (d, *J* = 7.5 Hz, 2H), 8.01-8.05 (m, 3H),

8.69 (d, J = 5.1 Hz, 1H), 9.09 (t, broad, J = 5.6 Hz, NH). ^{13}C NMR (100 MHz, DMSO-d_6) δ 45.8, 46.1, 46.7, 55.6, 65.7, 114.1, 118.5, 119.5, 120.1, 125.3, 127.1, 127.7, 127.8, 130.3, 140.7, 141.7, 143.9, 149.6, 156.5, 160.0, 163.5, 165.2, 193.1. MS (ESI) *m/z* 522 (100, $[M+H]^+$), 177 (18); HRMS (ESI) *m/z* calculated for $C_{31}H_{28}N_3O_5$ $[M+H]^+$ 522.2029, found 522.2066.

Fmoc-protected Thiazole 2.6. Amide **2.5** (2.01 mmol, 1.046 g) and Lawesson's reagent (1.2 eq., 2.41 mmol, 973 mg) were added to a 25 mL round bottom flask equipped with a magnetic stir bar. The flask was clamped above a 120°C oil bath and fitted with a reflux condenser, which was topped with a T-shaped adapter leading to an argon supply and bubbler. The joint between the condenser and flask was pulled apart to leave a gap of a few mm, and the system was flushed with argon. Anhydrous 1,4-dioxane (4 mL) was added from a syringe through the gap in the joint. The joint was quickly seated, and the flask was lowered into the oil bath. After 30 minutes, the reaction was complete by TLC (5:1 CH_2Cl_2-MTBE). Water (~0.5 mL) was added while stirring, and the mixture was cooled to room temperature. The resulting orange slurry was dissolved in CH_2Cl_2 (12 mL) and stirred with 5% aqueous NaOH (6 mL, 4 equiv.) for 20 min. The resulting yellow emulsion was partitioned between water (50 mL) and CH_2Cl_2 (50 mL) and the organic layer was collected. The aqueous layer was extracted with CH_2Cl_2 (10 mL) and the combined organic layers were dried with $MgSO_4$, diluted with MTBE (10 mL), and filtered through a bed of sand (~4 cm) on top of silica gel (~6 cm). The filter was washed with 3:1 CH_2Cl_2-MTBE until the effluent was no longer yellow, and the combined filtrate and washings were concentrated to dryness. The residue was recrystallized from ethyl acetate/2,2,4-trimethylpentane to give pure **2.6** as light yellow fibrous crystals. Yield: 891 mg (1.72 mmol, 86%). ^{1}H NMR (400 MHz, $CDCl_3$) δ 3.86 (s, 3H), 4.27 (t, J = 7.1 Hz, 1H), 4.44 (d, J = 7.1

Hz, 2H), 4.61 (d, *J* = 5.4 Hz, 2H), 5.96 (t, broad, *J* = 4.9 Hz, 1H), 6.96 (d, *J* = 8.8 Hz, 2H), 7.31 (t, *J* = 7.4 Hz, 2H), 7.39 (t, *J* = 7.4 Hz, 2H), 7.53 (d, *J* = 8.8 Hz, 2H), 7.64 (d, *J* = 7.4 Hz, 2H), 7.71 (dd, *J* = 5.2, 1.4 Hz, 1H), 7.76 (d, *J* = 7.5 Hz, 2H), 7.79 (s, br, 1H), 7.99 (s, 1H), 8.64 (d, *J* = 5.1 Hz, 1H). ^{13}C NMR (100 MHz, $CDCl_3$) δ 46.0, 47.2, 55.4, 67.0, 114.7, 118.1, 118.9, 119.9, 123.3, 125.1, 127.0, 127.7, 128.2, 139.0, 141.3, 141.4, 141.7, 144.0, 149.9, 156.5, 157.9, 160.3, 162.5. MS (ESI) *m/z* 520 (100, $[M+H]^+$); HRMS (ESI) *m/z* calculated for $C_{31}H_{26}N_3O_3S$ $[M+H]^+$ 520.1695, found 520.1719.

Primary amine 2.7. A 50-mL round bottom flask was charged with **2.6** (2.02 mmol, 1.049 g), crushed cesium carbonate (2 eq., 4.04 mmol, 1.315 g) and DMSO (15 mL). Ethanethiol (2 eq., 4.04 mmol, 291 μL) was added drop-wise to the stirred mixture. After 1.5 hours, the reaction was complete by TLC (neat EtOAc). The mixture was transferred to a 250-mL Erlenmeyer flask, partitioned between diH2O (50 mL) and toluene (25 mL), and heated gently until two homogeneous liquid phases could be separated. The mixture was acidified with 1 M aq. HCl (1 eq., ~ 2 mL), and the orange aqueous layer was collected, washed with toluene to remove non-basic byproducts, and then made basic (pH ~ 9) by the addition of 5% aq. NaOH. The product was extracted with toluene (2 x 25 mL), and the combined extracts were dried over $MgSO_4$, filtered, and concentrated to afford **2.7** as a pure, pale yellow solid. Yield 454 mg (1.53 mmol, 76%). ^{1}H NMR (400 MHz, $CDCl_3$) δ 3.87 (s, 3H), 4.07 (s, 2H), 6.97 (d, *J* = 8.9 Hz, 2H), 7.55 (d, *J* = 8.9 Hz, 2H), 7.68 (dd, *J* = 5.2, 1.7 Hz, 1H), 7.82-7.83 (m, 1H), 8.00 (s, 1H) 8.65 (dd, *J* = 5.2, 0.8 Hz, 1H). ^{13}C NMR (100 MHz, $CDCl_3$) δ 47.7, 55.4, 114.6, 117.4, 118.2, 123.3, 128.1, 138.8, 140.9, 141.3, 150.1, 160.1, 162.9, 163.0. MS (EI) *m/z* 297 (100, $[M]^+$), 268 (45), 149 (10); HRMS (EI) *m/z* calculated for $C_{16}H_{15}N_3OS$ $[M]^+$ 297.0936, found 297.0921.

Chromis-1 ester (2.1a). A mixture of **2.7** (0.67 mmol, 200 mg), ethyl 2-(bromomethyl)isonicotinate hydrobromide (**2.10**, 2.5 eq., 1.68 mmol, 459 mg), crushed anhydrous potassium carbonate (2.5 eq., 1.68 mmol, 232 mg), and potassium iodide (2.5 eq., 1.68 mmol, 280 mg) in acetonitrile (12 mL) was stirred at room temperature under an argon atmosphere for 12 hours. The reaction mixture was diluted subsequently with EtOAc (10 mL) followed by diH_2O (10 mL). The organic layer was separated, dried over anhydrous Na_2SO_4, and evaporated under reduced pressure. The resulting residue was purified by column chromatography (silica gel, 1:1 dichloromethane/acetone). The oily column product was crystallized by redissolving in a minimal amount of EtOAc and slowly diluting with MTBE until cloudy, after which the mixture was heated to boiling to become homogeneous and concentrated until crystallization began to initialize. The crystals were isolated by suction filtration, washed with MTBE and dried under vacuum to give diester **2.1a** as a light yellow solid. Yield 320 mg (0.513 mmol, 76%). ^{1}H NMR (400 MHz, $CDCl_3$) δ 1.37 (t, J = 7.2 Hz, 6H), 3.88 (s, 3H), 4.03 (s, 2H), 4.07 (s, 4H), 4.37 (q, J = 7.1 Hz, 4H), 6.98 (d, J = 8.9 Hz, 2H), 7.59 (d, J = 8.9 Hz, 2H,), 7.69-7.72 (m, 3H), 7.99 (s, 1H), 8.12-8.14 (m, 3H), 8.61 (dd, J = 5.2, 0.7 Hz, 1H), 8.69 (dd, J = 5.0, 0.8 Hz, 2H). ^{13}C NMR (100 MHz, $CDCl_3$) δ 14.1, 55.4, 60.08, 60.14, 61.6, 114.5, 118.1, 119.6, 121.3, 122.4, 123.4, 128.1, 138.2, 138.8, 141.0, 141.3, 149.76, 149.78, 160.10, 160.14, 160.2, 163.2, 165.1. MS (EI) *m/z* 623 (5, $[M]^+$), 459 (100), 342 (77), 282 (48), 137 (10). HRMS (EI) *m/z* calculated for $C_{34}H_{33}N_5O_5S$ $[M]^+$ 623.2202, found 623.2193.

Chromis-1 acid (2.1b). Sodium hydroxide (2.5 eq., 0.40 mmol, 80.4 μL of a 20 % (w/v) aqueous solution) was added to a stirred solution of **2.1a** (1 eq., 0.16 mmol, 100 mg) in EtOH (4 mL), and the resulting mixture was refluxed under stirring for 2 hours. After cooling to room temperature, the product was filtered and dried under reduced pressure

to afford 90 mg (0.15 mmol, 92% yield) of **2.1b** as pale yellow crystals. ^{1}H NMR (400 MHz, CD_3OD): δ 3.85 (s, 3H), 3.95 (s, 2H), 4.00 (s, 4H), 7.03 (d, *J* = 8.9 Hz, 2H), 7.65-7.68 (m, 4H), 7.75 (dd, *J* = 5.3, 1.8 Hz, 1H), 7.97-8.0 (m, 3H), 8.10 (s, 1H) 8.53 (d, *J* = 5.1 Hz, 3H). HRMS (ESI) *m/z* calculated for $C_{30}H_{24}N_5Na_2O_5S$ $[M+H]^+$ 612.1294, found 612.1287.

Ethyl 2,4-pyridinedicarboxylate (2.8). Adapted from a previously published procedure.[10] 2,4-pyidinedicarboxylic acid (1 eq., 29.9 mmol, 5.0 g) was suspended in absolute ethanol (50 mL), and concentrated H_2SO_4 (1.5 eq., 47.1 mmol, 2.62 mL) was added dropwise to the stirred mixture. After refluxing overnight, the EtOH was removed under reduced pressure, and the resulting oily residue was partitioned between $CHCl_3$ (50 mL) and saturated Na_2CO_3 (20 mL). The organic layer was removed, and the aqueous layer was extracted with $CHCl_3$ (2 x 50 mL). The combined organic layers were dried over anhydrous $MgSO_4$, filtered, and concentrated to a yellow oil. The yellow oil was slowly dissolved in boiling cyclohexane and crystallized while cooling to room temperature under constant stirring. The product was collected by suction filtration, washed with cyclohexane, and dried under vacuum to afford **2.8** as a white crystalline solid. Yield 5.52 g (24.7 mmol, 83%). ^{1}H NMR (400 MHz, $CDCl_3$) δ 1.44 (t, *J* = 6.5 Hz, 3H), 1.48 (t, *J* = 6.5 Hz, 3H), 4.46 (q, *J* = 7.1 Hz, 2H), 4.53 (q, *J* = 7.1 Hz, 2H), 8.05 (dd, *J* = 4.9, 1.6 Hz, 1H), 8.65 (dd, *J* = 1.6, 0.8 Hz, 1H), 8.92 (dd, *J* = 4.9, 0.9 Hz, 1H). ^{13}C NMR (100 MHz, $CDCl_3$) δ 14.3. 14.4, 62.3, 62.4, 124.4, 126.1, 139.2, 149.3, 150.8, 164.4, 164.7. MS (EI) *m/z* 223 (4, $[M]^+$), 179 (35), 178 (40), 152 (33), 151 (100), 150 (45), 123 (30), 78 (18), 77 (21). HRMS (EI) *m/z* calculated for $C_{11}H_{13}NO_4$ $[M]^+$ 223.0845, found 223.0842.

Ethyl 2-(hydroxymethyl)isonicotinate (2.9). Adapted from a previously published procedure.[10] To a solution of ethyl 2,4-pyridinedicarboxylate (**2.8**, 1 eq., 24.6 mmol, 5.50 g) in EtOH (50 mL) at 0˚C was added crushed anhydrous $CaCl_2$ (1 eq., 24.6 mmol,

2.73 g). While stirring under argon, $NaBH_4$ (1 eq., 24.6 mmol, 932 mg) was added slowly to the slightly opaque mixture, and upon the complete addition of $NaBH_4$, the color of the mixture turned bright pink. The reaction mixture was stirred for 2.5 hours at 0˚C when TLC (3:7 EtOAc:hexanes) determined that the reaction was complete. The reaction was quenched with the addition of 6 N HCl (1 eq., 4.1 mL), the white precipitate that formed was filtered off, and filtrate was concentrated under reduced pressure to remove most of the EtOH. The product was portioned between dichloromethane (50 mL) and saturated Na_2CO_3 to neutralize the HCl, followed by the addition of 1 M aq. disodium citrate to dissolve the inorganic salts that precipitated upon basification of the aqueous phase. The aqueous phase was extracted with dichloromethane (2 x 50 mL), and the combined organic layers were dried over anhydrous Na_2SO_4, filtered, and concentrated to a colorless oil. Residual CH_2Cl_2 was removed azeotropically with hexanes under reduced pressure, and the compound was dried under high vacuum to afford **2.9** as colorless crystals. Yield: 4.47 g (24.7 mmol, 72%). ^{1}H NMR (400 MHz, $CDCl_3$) δ 1.48 (t, J = 7.2 Hz, 3H), 4.12 (s, broad, 1H), 4.42 (q, J = 7.2 Hz, 2H), 4.85, (s, 2H), 7.77 (ddt, J = 5.1, 1.6, 0.7 Hz, 1H), 7.87 (ddt, J = 1.6, 0.8, 0.7 Hz, 1H), 8.69 (dd, J = 5.1, 0.9 Hz, 1H). ^{13}C NMR (100 MHz, $CDCl_3$) δ 14.3, 62.0, 64.4, 120.0, 121.6, 138.5, 149.4, 160.9, 165.1. MS (EI) *m/z* 182 (20), 181 (85, $[M]^+$), 180 (100), 178 (40), 153 (45), 152 (95), 151 (34), 136 (54), 124 (58), 123 (29), 108 (20), 78 (44), 51 (44). HRMS (EI) *m/z* calculated for $C_9H_{11}NO_3$ $[M]^+$ 181.0749, found 181.0736.

Ethyl 2-(bromomethyl)isonicotinate (2.10). A 25-mL round bottom flask equipped with a stir bar was charged with **2.9** (1 eq., 5.52 mmol, 1.0 g), fitted with a rubber septum, evacuated under high vacuum, and backfilled with argon. Anhydrous dichloromethane (10 mL) was added via an argon-flushed syringe, and the flask was cooled to

0˚C in an ice bath. Under rapid stirring, thionyl bromide (3 eq., 16.6 mmol, 1.28 mL) was added, and the solution was stirred for 1.5 hours at 0°C. Unreacted thionyl bromide was quenched by the addition of EtOH (20 mL), followed by stirring for an addition 20 min. After concentrating the solution under reduced pressure, the residue was redissolved in a minimal amount of EtOH, and then diluted slowly with methyl *tert*-butyl ether (MTBE) until the solution became cloudy. The compound was then crystallized from boiling EtOH/MTBE to afford hydrobromide **2.10** as a white crystalline solid. Yield 1.46 g (4.5 mmol, 81%). ^{1}H NMR (400 MHz, $CDCl_3$) δ 1.48 (t, J = 7.2 Hz, 3H), 4.54 (q, J = 7.2 Hz, 2H), 5.19 (s, 2H), 8.48 (dd, J = 5.9, 1.5 Hz, 1H), 8.55 (s, 1H), 9.14 (d, J = 5.9 Hz, 1H). ^{13}C HMR (100 MHz, $CDCl_3$) δ 14.1, 24.1, 63.9, 125.9, 128.0, 142.6, 146.3, 153.4, 161.4. Note: ^{1}H and ^{13}C NMRs were acquired of the hydrobromide salt of **2.10** in $CDCl_3$ because of stability issues with the free base. MS (EI) *m/z* 244 (20), 243 (20, $[M]^+$), 165 (19), 164 (100), 120 (33), 82 (18), 80 (20), 64 (19). HRMS (EI) *m/z* calculated for $C_9H_{10}NO_2Br$ $[M]^+$ 242.9895, found 242.9889.

2.5.2 X-Ray Crystallography Methods

2.5.2.1 Crystallization of the Zn(II) Complex of Chromis-1 Acid

Chromis-1 acid (**1b**, 20 mg) was reacted with a stoichiometric quantity of $ZnCl_2$ (4.46 mg) in a mixture of DMF, 0.1 M KCl in H_2O, and HPLC-grade MeOH (2 mL). The precipitated Zn(II) complex was then redissolved by gentle heating, and the resulting solution was supplemented with crushed anhydrous $CaCl_2$ (0.5 eq., 1.8 mg) and filtered through a 0.2 μm nylon filter into a clean vial. Slow evaporation of the corresponding solution afforded X-ray-quality crystals of the [(chromis-1)Zn(II)]Cl_2 complex.

2.5.2.2 Crystallographic Determination of the Chromis-1-Zn(II) Complex

A single suitable plate-shaped crystal (0.22 x 0.09 x 0.03 mm) of the [(**2.1b**)Zn(II)] complex formed by slow evaporation from DMF, H_2O, and MeOH was selected and mounted on a loop with paratone oil on a Bruker APEX-II CCD diffractometer. The selected crystal was cooled to T = 100(2) K (Oxford Cryosystems low-temperature device) during data collection. Data were measured using ω scans of 0.5° per frame for 60.0 s using MoK_α radiation (fine-focus sealed X-ray tube, 45 kV, 35 mA). The total number of runs and images was based on the APEX2 (Bruker) program (2015). The structure was solved and the space group P-1 (#2) was determined by the ShelXT-2014/4 structure solution program[34] using combined Patterson and dual-space recycling methods and by using Olex2[35] as the graphical interface. The crystal structure was refined with version 2014/7 of ShelXL[36] using least-squares minimization, and all hydrogens were refined anisotropically.

2.5.3 Steady-State Absorption and Fluorescence Spectroscopy

2.5.3.1 General Spectroscopic Methods

All buffers and stock solutions used for spectroscopic measurements were prepared using either HPLC-grade water (JT Baker) or 18.2 MΩ•cm Mili-Q water and filtered to remove interfering dust particles or fibers. UV-Vis measurements were performed on a Varian Cary Bio50 spectrophotometer with a constant temperature accessory (Peltier) at 25°C. Fluorescence measurements were performed with a PTI fluorimeter equipped with a 75 W xenon arc lamp excitation source and model 814 photomultiplier detection

system (PMT voltage was 1100 V for all experiments). Fluorescence spectra were corrected for the spectral response of the detection system and for the spectral irradiance of the excitation source (via a calibrated photodiode). For all experiments, both UV-Vis and fluorescence, a 1-cm path length quartz cuvette was used, except for quantum yield determinations, which were performed with a 10-cm path length quartz cuvette for absorbance measurements.

2.5.3.2 Fluorescence Quantum Yield Measurements of Chromis-1 Ester and Chromis-1 Acid

Fluorescence quantum yields of **2.1a** were determined in aqueous buffer (10 mM PIPES, 0.1 M KCl) at pH 7.0 by a 4-point measurement over an OD range of 0.1-0.4 at 365 nm. The solution containing the free form of chromis-1 was supplemented with 20 μM EDTA (30 mM stock solution in diH_2O) to sequester adventitious Zn(II), whereas the Zn(II)-bound form was supplemented with 20 μM $ZnSO_4 \cdot 7H_2O$ to fully saturate the fluorophore. Fluorescence quantum yields were determined using quinine sulfate (Φ_f = 0.546 in 1.0 N H_2SO_4). To determine the quantum yield of **2.1b**, single-point measurements were performed in aqueous buffer (10 mM PIPES, 0.1 M KCl, pH 7.0) supplemented with 100 μM 4:1 DMPC:DMPG liposomes and a probe concentration of 2 μM. The quantum yields were also referenced to quinine sulfate with an OD matching that of **2.1a** (2 μM) in liposomes.

2.5.3.3 Determination of Stability Constants

A) Determination of Zn(II)-Binding Affinity of Chromis-1 Acid (2.1b). The Zn(II) stability constant for **2.1b** was measured via a spectrophotometric competition titration against ethylene glycol-bis(2-aminoethyl-ether)-*N*,*N*,*N′*,*N′*-tetraacetic acid (EGTA).

Chromis-1 (20 μM) in chelexed aqueous buffer (10 mM PIPES, 0.1 M KCl, pH 7.0, 25°C) was saturated with 1 eq. (20 μM) Zn(II) (6 mM $ZnSO_4 \cdot 7H_2O$ in diH_2O) and then titrated with EGTA from 20 μM to 7 mM (using 20 and 300 mM EGTA stock solutions in diH_2O). Absorbance spectra were acquired after each aliquot over the range of 250-500 nm. The data were analyzed by non-linear least squares fitting using Specfit.

B) Determination of Zn(II)-Binding Affinity of Chromis-1 Ester (2.1a) in Presence of 4:1 DMPC:DMPG Liposomes

I. **Preparation of Liposomes.** A 2 mM solution of a 4:1 mixture of 1,2-dimyristoyl-*sn*-glycero-3-phosphocholine (DMPC): 1,2-dimyristoyl-*sn*-glycero-3-phospho-(1'-rac-glycerol) (DMPG) was prepared according to the thin film hydration method. DMPC (32.3 mg) and DMPG (8.21 mg) were dissolved in 4:1 dichloromethane:methanol (20 mL), and the solvent was removed under reduced pressure (rotary evaporator) to afford a thin film of lipids. The thin film was then dried via high vacuum for 2 hours to remove traces of residual solvent. The thin film was then hydrate by the addition of 29.8 mL of aqueous buffer (20 mM PIPES, 0.1 M KCl, pH 7.0). The aqueous lipids were sonicated for 5 minutes and left to hydrate for 5 hours. The resulting solution was diluted to a concentration of 500 μM and passed 21 times through an extruder (Liposofast, Avestin) that was equipped with a polycarbonate membrane (200 nm pore size). Freshly extruded lipids were used immediately for the experiments described below.

II. **Determination of Liposome Size Distribution.** Liposome particle sizes were determined based upon the Tunable Resistance Pulse Sensing (TRPS) principle using the Izon qNano particle analyzer (Izon Science, Ltd., Burnside, New Zealand). Per the manufacturer's recommendations, the liposomes were calibrated against monodisperse carboxylated polystyrene particles (Izon, 200-nm diameter). Liposomes and calibration particles were passed through a Nanopore membrane (NP150) with a pore stretch of 46.00 mm,

an electric potential of 0.50 V, and a pressure of 20 mm Hg using a variable pressure module. Each measurement was conducted by detecting a minimum of 1000 particles. The data were analyzed using the Izon Control Suite 3.0 software to determine the mean diameter and size distribution of the liposomes. The mean diameter of the liposomes was determined to be 122 nm.

III. **Competition Titration.** The Zn(II) stability constant for chromis-1 ester was measured via a fluorimetric competition titration against EGTA. A freshly extruded 2 mM 4:1 DMPC:DMPG liposome solution in aqueous buffer (20 mM PIPES, 0.1 M KCl, pH 7.0, chelexed) was diluted into PIPES buffer containing 1.0 mM EGTA (from 300 mM stock solution in diH_2O) in a 1-cm quartz cuvette to yield a final concentration of 100 μM of liposomes. To ensure liposomes were solely in the gel phase, the solution (3.0 mL) was gently stirred at 25°C for a minimum of 10 minutes. To the buffered liposomes was added chromis-1 ethyl ester (3 mM stock solution in DMSO) to yield a final concentration of 2 μM, and the solution was stirred at 25°C for another 10 minutes. The solution was then titrated with Zn(II) (from 15 mM and 60 mM $ZnSO_4 \cdot 7H_2O$ stock solutions in diH_2O). After each aliquot of Zn(II), solution was equilibrated for 5 minutes, and a fluorescence spectrum was acquired over the spectral window of 380-680 nm with excitation at 358 nm. The data were analyzed by non-linear least squares fitting using Specfit.

2.5.3.4 Fluorescence Dependence of Chromis-1 Ester on pH

Two batches of 2 mM 4:1 DMPC:DMPG liposomes were prepared according to the procedure described above, with one batch being prepared in pH 5.0 buffer (10 mL of 10 mM PIPES, 0.1 M KCl) and the other being prepared in pH 7.0 buffer (10 mL of 10 mM PIPES, 0.1 M KCl). After freshly extruding through polycarbonate membranes (200 nm diameter), the resulting unilamellar liposomes (500 μM) were diluted into a 1-cm path

length quartz cuvette containing aqueous buffer of respective pH to a final concentration of 100 μM. The buffered liposome solution (3.0 mL total) was equilibrated for 15 minutes by stirring at 25°C (Peltier), after which EDTA (3 mM stock solution in diH_2O at pH 7.0) was added to achieve a final concentration of 1 μM to sequester an adventitious Zn(II). The solution was then supplemented with chromis-1 ester (3 mM stock solution in DMSO) to yield a final concentration of 2 μM, followed by an additional 10-minute equilibration period to ensure the dye was fully dissolved in the liposomes. A fluorescence spectrum was acquired of the free form of chromis-1 ester in liposomes over the spectral window of 380-700 nm with excitation at 358 nm. To fully saturate the probe, $ZnSO_4 \cdot 7H_2O$ (3 mM stock solution in diH_2O) was added to yield a final concentration of 4 μM. A fluorescence spectrum of the Zn(II)-bound form of the probe was then acquired. This experiment was performed identically at pH 7.0 and pH 5.0 for comparison purposes.

2.5.3.5 Metal-Ion Selectivity Measurements of Chromis-1 Acid

In a 1-cm quartz cuvette, a 5 μM solution of chromis-1 acid (3.0 mL) was prepared in 10 mM PIPES-K^+ pH 7.0 buffer that had been previously treated with Chelex® (1% w/v) overnight and filtered through a 0.2 μm membrane filter. A fluorescence spectrum was acquired over the spectral window of 380-680 nm with excitation at 358 nm. For each divalent transition metal tested, chromis-1 acid was titrated with the divalent metal ion until 80% of the free fluorophore (4 μM) was saturated with the metal, and a fluorescence spectrum was acquired after each addition and a one-minute equilibration. To saturate with remaining 20% of free probe, 1 μM (0.2 eq.) of Zn(II) was added to the solution, and a fluorescence spectrum was acquired. Responses to Mg(II) and Ca(II) were measured in the presence of 2 mM of each metal (from 1 M stock solutions in H_2O). Metal cations were supplied as aqueous stock solutions (1 mM for all metals excluding Mg(II) and Ca(II),

which were 1 M) of the following metal salts: Mn(II), Fe(II), Cu(II), and Zn(II) as sulfates; Co(II), and Ni(II) as nitrates; Mg(II) and Ca(II) as chlorides. Emission intensities were integrated in two bandpass channels: channel 1 (440-495 nm) and channel 2 (510-570 nm). The ratio of the two channels was plotted for each metal tested, including the response to Zn(II).

To show the fluorescence response of chromis-1 upon complete quenching of the fluorophore, chromis-1 acid (5 μM) was prepared in pH 7.0 buffer (3.0 mL, 10 mM PIPES, 0.1 M KCl, 25°C) supplemented with EDTA (10 μM) in a 1-cm path length quartz cuvette. A fluorescence spectrum was acquired over the spectral window of 400-700 nm with excitation at 358 nm. The fluorophore was saturated with interfering divalent metal ions (20 μM), and a fluorescence spectrum was acquired. For Mn(II), because the fluorescence response was not completely quenched, a second 20 μM aliquot of Mn(II) was added to the cuvette, and another fluorescence spectrum was acquired.

2.6 References

1. Kim, D.; Ryu, H. G.; Ahn, K. H. Recent Development of Two-Photon Fluorescent Probes for Bioimaging. *Org. Biomol. Chem.* **2014**, *12* (26), 4550-4566.

2. Sarkar, A. R.; Kang, D. E.; Kim, H. M.; Cho, B. R. Two-Photon Fluorescent Probes for Metal Ions in Live Tissues. *Inorg. Chem.* **2014**, *53* (4), 1794-803.

3. Kim, H. M.; Cho, B. R. Small-Molecule Two-Photon Probes for Bioimaging Applications. *Chem. Rev.* **2015**, *115* (11), 5014-5055.

4. Carter, K. P.; Young, A. M.; Palmer, A. E. Fluorescent Sensors for Measuring Metal Ions in Living Systems. *Chem. Rev.* **2014**, *114* (8), 4564-4601.

5. Xu, C.; Webb, W. W., Measurement of Two-Photon Excitation Cross Sections of Molecular Fluorophores with Data from 690 to 1050 nm. *J. Opt. Soc. Am. B* **1996,** *13* (3), 481-491.

6. Yellen, G.; Mongeon, R. Quantitative Two-Photon Imaging of Fluorescent Biosensors. *Curr. Opin. Chem. Biol.* **2015**, *27*, 24-30.

7. Sumalekshmy, S.; Henary, M. M.; Siegel, N.; Lawson, P. V.; Wu, Y.; Schmidt, K.; Bredas, J. L.; Perry, J. W.; Fahrni, C. J. Design of Emission Ratiometric Metal-Ion Sensors with Enhanced Two-Photon Cross Section and Brightness. *J. Am. Chem. Soc.* **2007**, *129* (39), 11888-11889.

8. Charier, S.; Ruel, O.; Baudin, J. B.; Alcor, D.; Allemand, J. F.; Meglio, A.; Jullien, L.; Valeur, B. Photophysics of a Series of Efficient Fluorescent pH Probes for Dual-Emission-Wavelength Measurements in Aqueous Solutions. *Chem. Eur. J.* **2006**, *12* (4), 1097-1113.

9. Xu, C.; Zipfel, W.; Shear, J. B.; Williams, R. M.; Webb, W. W. Multiphoton Fluorescence Excitation: New Spectral Windows for Biological Nonlinear Microscopy. *Proc. Natl. Acad. Sci. U.S.A.* **1996**, *93* (20), 10763-10768.

10. Kojima, T.; Hayashi, K. I.; Iizuka, S. Y.; Tani, F.; Naruta, Y.; Kawano, M.; Ohashi, Y.; Hirai, Y.; Ohkubold, K.; Matsuda, Y.; Fukuzumi, S. Synthesis and Characterization of Mononuclear Ruthenium(III)-Pyridylamine Complexes and Mechanistic Insights into their Catalytic Alkane Functionalization with m-Chloroperbenzoic Acid. *Chem. Eur. J.* **2007**, *13* (29), 8212-8222.

11. Allen, C. S.; Chuang, C.-L.; Cornebise, M.; Canary, J. W. Electrospray Mass Spectrometry and X-Ray Crystallography Studies of Divalent Metal Ion Complexes of Tris(2-pyridylmethyl)amine. *Inorg. Chim. Acta* **1995**, *239* (1), 29-37.

12. Adams, H.; Bailey, N. A.; Fenton, D. E.; He, Q.-Y. Mononuclear Zinc (II), Homodinuclear Zinc (II) and Heterodinuclear Zinc (II)--Copper (II) Complexes

Derived from Tris[(2-pyridyl)methyl]amine. *J. Chem. Soc. Dalton Trans.* **1997**, (9), 1533-1540.

13. Duboc, C.; Phoeung, T.; Jouvenot, D.; Blackman, A. G.; McClintock, L. F.; Pécaut, J.; Collomb, M.-N.; Deronzier, A. High-field EPR Investigation of a Series of Mononuclear Mn(II) Complexes Doped into Zn(II) Hosts. *Polyhedron* **2007**, *26* (18), 5243-5249.

14. Brouwer, A. M. Standards for Photoluminescence Quantum Yield Measurements in Solution (IUPAC Technical Report). *Pure Appl. Chem.* **2011**, *83* (12), 2213-2228.

15. Two-Photon Cross Section Data of Chromis-1 Acid were acquired by Siegel, N.; Perry, J. W.

16. Sumalekshmy, S.; Fahrni, C. J. Metal-Ion-Responsive Fluorescent Probes for Two-Photon Excitation Microscopy. *Chem. Mater.* **2011**, 823-830.

17. Culotta, V. C.; Yang, M.; Hall, M. D. Manganese Transport and Trafficking: Lessons Learned from Saccharomyces cerevisiae. *Eukaryot. Cell* **2005**, *4* (7), 1159-1165.

18. Bowman, A. B.; Aschner, M. Considerations on Manganese (Mn) Treatments for In Vitro Studies. *Neurotoxicology* **2014**, *41*, 141-142.

19. Hansen, L. D.; Fellingham, G. W.; Russell, D. J. Simultaneous determination of Equilibrium Constants and Enthalpy Changes by Titration Calorimetry: Methods, Instruments, and Uncertainties. *Anal. Biochem.* **2011**, *409* (2), 220-229.

20. Martell, A. E.; Smith, R. M.; Motekaitis, R. J. *NIST standard reference database 46 version 8.0: NIST critically selected stability constants of metal complexes*, National Institute of Standards and Technology: 2004.

21. Competition Titrations of Chromis-1 Acid (2.1b) were performed by S. Sumalekshmy, Georgia Institute of Technology, 2008.

22. Brown, G. M.; Gu, B. The Chemistry of Perchlorate in the Environment. In *Perchlorate: Environmental Occurrence, Interactions and Treatment*, Gu, B.; Coates, J. D., Eds. Springer US: Boston, MA, 2006; pp 17-47.

23. Valdivieso, A. G.; Clauzure, M.; Massip-Copiz, M.; Santa-Coloma, T. A. The Chloride Anion Acts as a Second Messenger in Mammalian Cells - Modifying the Expression of Specific Genes. *Cell. Physiol. Biochem.* **2016**, *38* (1), 49-64.

24. Grynkiewicz, G.; Poenie, M.; Tsien, R. Y. A New Generation of Ca2+ Indicators with Greatly Improved Fluorescence Properties. *J. Biol. Chem.* **1985**, *260* (6), 3440-3450.

25. Schneider, C. A.; Rasband, W. S.; Eliceiri, K. W. NIH Image to ImageJ: 25 Years of Image Analysis. *Nat. Methods* **2012**, *9* (7), 671-675.

26. Forbes, I. J.; Zalewski, P. D.; Hurst, N. P.; Giannakis, C.; Whitehouse, M. W. Zinc Increases Phorbol Ester Receptors in Intact B-Cells, Neutrophil Polymorphs and Platelets. *FEBS Lett.* **1989**, *247* (2), 445-7.

27. Aizenman, E.; Stout, A. K.; Harnett, K. A.; Dineley, K. E.; McLaughlin, B.; Reynolds, I. J. Induction of neuronal apoptosis by thiol oxidation: Putative role of intracellular zinc release. *J. Neurochem.* **2000**, *75* (5), 1878-1888.

28. Bourassa, D. M.; Ellit, C. M.; McCallum, A. M.; Sumalekshmy, S.; Mcrae, R. L.; Morgan, M. T.; Siegel, N.; Perry, J. W.; Rosenberg, P. A.; Fahrni, C. J., Chromis-1, A Ratiometric Fluorescent Probe Optimized for Two-Photon Microscopy Reveals Dynamic Changes in Labile Zn(II) in Differentiating Oligodendrocytes. *Submitted for publication.*

29. Maret, W. Analyzing Free Zinc(II) Ion Concentrations in Cell Biology with Fluorescent Chelating Molecules. *Metallomics* **2015**, *7* (2), 202-211.

30. Yoshimori, T.; Yamamoto, A.; Moriyama, Y.; Futai, M.; Tashiro, Y. Bafilomycin A1, a Specific Inhibitor of Vacuolar-Type H(+)-ATPase, Inhibits Acidification and Protein Degradation in Lysosomes of Cultured Cells. *J. Biol. Chem.* **1991**, *266* (26), 17707-12.

31. Umata, T.; Moriyama, Y.; Futai, M.; Mekada, E. The Cytotoxic Action of Diphtheria Toxin and its Degradation in Intact Vero Cells are Inhibited by Bafilomycin A1, a Specific Inhibitor of Vacuolar-Type H(+)-ATPase. *J. Biol. Chem.* **1990**, *265* (35), 21940-5.

32. Qin, Y.; Dittmer, P. J.; Park, J. G.; Jansen, K. B.; Palmer, A. E. Measuring Steady-State and Dynamic Endoplasmic Reticulum and Golgi Zn2+ with Genetically Encoded Sensors. *Proc. Natl. Acad. Sci. U.S.A.* **2011**, *108* (18), 7351-6.

33. Vinkenborg, J. L.; Nicolson, T. J.; Bellomo, E. A.; Koay, M. S.; Rutter, G. A.; Merkx, M. Genetically Encoded FRET Sensors to Monitor Intracellular Zn2+ Homeostasis. *Nat. Meth.* **2009**, *6* (10), 737-740.

34. Sheldrick, G. M. SHELXT - Integrated Space-Group and Crystal-Structure Determination. *Acta Crystallogr. A, Foundation and Advances* **2015**, *71*, 3-8.

35. Dolomanov, O. V.; Bourhis, L. J.; Gildea, R. J.; Howard, J. A. K.; Puschmann, H. OLEX2: a Complete Structure Solution, Refinement and Analysis Program. *J. Appl. Crystallogr.* **2009**, *42*, 339-341.

36. Sheldrick, G. M., Crystal Structure Refinement with SHELXL. *Acta Crystallogr. C, Struc. Chem.* **2015**, *71*, 3-8.

CHAPTER 3

SUPPRESSING EXCITED-STATE PROTONATION OF THE PYRIDYL ACCEPTOR OF CHROMIS-1 DRIVEN BY ACCEPTOR-MODIFIED DESIGN STRATEGIES

3.1 Introduction

In the previous chapter, the synthesis and characterization of chromis-1, a water-soluble, emission-ratiometric, Zn(II)-selective fluorescence sensor based on a noncentrosymmetric donor-π-acceptor architecture, which coordinates the metal analyte to the acceptor moiety rather than the donor moiety, was reported. This design strategy, compared to other molecular architectures, permits larger bathochromic shifts in both the absorption and emission, as well as large and balanced TPA cross sections, by inducing an increased intramolecular charge transfer upon photoexcitation when the metal analyte is bound.

Because protonation of the fluorophore can interfere with ratiometric imaging by distorting the ratiometric readout, the macroscopic protonation constants of chromis-1 acid were measured based on spectrophotometric and fluorimetric titrations[1] to ensure that the probe was suitable for ratiometric imaging in the complex cellular environment. During the fluorimetric pH titration of chromis-1 acid, as the pH was incrementally lowered from 7.0 to 5.2, the fluorescence intensity was reduced by 50% compared to the intensity at pH 7.0, manifesting a fluorescence profile with two emission maxima, one at 483 nm and the other at 560 nm, suggesting the presence of two species in solution (Figure 3.1A). As the pH was lowered further from 5.2 to 2.0, the emission band with a maximum at 483 nm

completely disappeared, and the 560-nm emission maximum shifted to ~ 580 nm. However, in the equivalent spectrophotometric pH titration, as the pH was incrementally lowered from 7.0 to 5.2, the absorbance maximum of the spectrum corresponding to pH 5.2 was negligibly red-shifted, and the intensity was reduced only slightly compared to the spectrum at pH 7.0 (Figure 3.1B). Significant changes in the absorption were not observed until the pH was lowered below 3.0, when the formation of a species with a red-shifted absorption maximum was manifesting, consistent with the protonation of the pyridine of the chromophore.

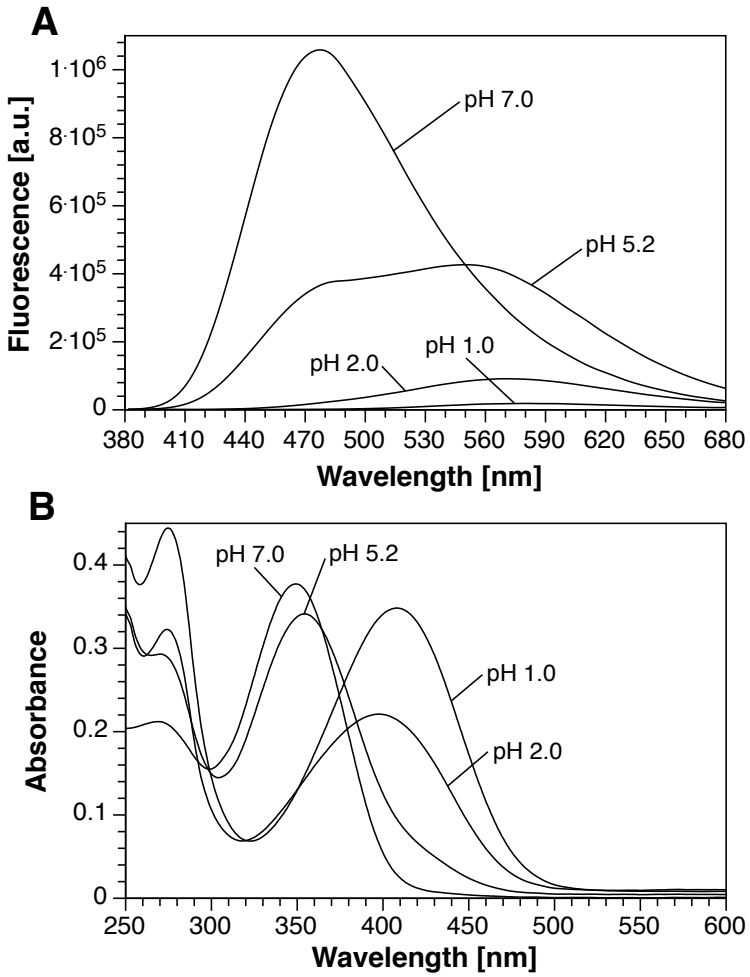

Figure 3.1: Fluorimetric (A) and UV-Vis spectrophotometric (B) spectra at selected pH values to illustrate the change in fluorescence and absorbance of chromis-1 acid (**2.1b**) as the pH of the solution is lowered. Data acquired by Dr. S. Sumalekshmy, and figure prepared by the author.

Deconvolution of the spectrophotometric data to obtain absorbance spectra corresponding to each protonation state (Figure 3.2A) demonstrated that the minimal spectral changes between the dianionic (LH^{2-}) and the monoanionic (L^{-}) species is likely a result of an electrostatic effect from protonation of the one of the pyridines of the chelator moiety. However, generation of the zwitterionic (LH_2) species by protonation of the second pyridine, whose pK_a is two orders of magnitude lower than the other pyridine of the chelating ligand, gives rise to an absorbance spectrum that boasts a molar absorptivity that is nearly 50% lower than that of LH^{-} species. Least-squares fitting of the spectrophotometric data to a triprotic equilibrium model using the Specfit® software package[2] yielded pK_a's for chromis-1 acid of 1.1, 3.4 and 5.5 (Figure 3.2B).

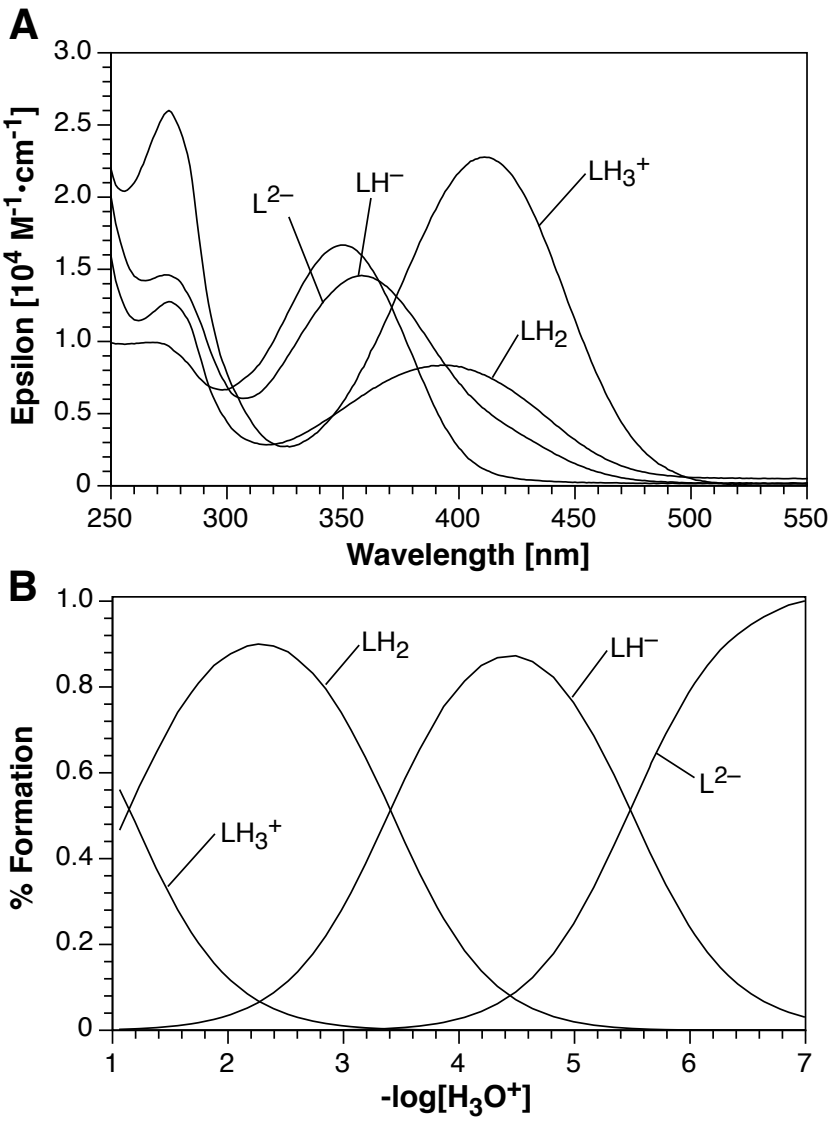

Figure 3.2: Protonation equilibria of chromis-1 acid (**2.1b**) in aqueous solution. (A) Deconvoluted spectra of UV-Vis titration data, depicting the absorbance spectra corresponding to each protonation state. B) Species distribution diagram for the protonation equilibria of chromis-1 acid. L: ligand, chromis-1. Data acquired by Dr. S. Sumalekshmy, and figure prepared by the author.

It should be noted that the protonation constants obtained from fitting of the spectrophotometric data yield only the macroscopic pK_a's rather than microscopic pK_a's. As illustrated in Figure 3.3A, protonation of the monoanionic (L^-) species leads to two protonation equilibria between two different species with the same overall charge, by protonat-

ing either the carboxylate group or the pyridine nitrogen. However, the uncertainty in discerning the spectrophotometric or potentiometric differences between the two LH species present in equilibrium precludes the ability to determine microscopic pK_a's, or the precise protonation site of the species. In fact, the neutral (LH) species that results from protonating the monoanionic species is most likely a mixture of the zwitterionic species and the neutral carboxylic acid that too has its own equilibrium constant. Therefore, the protonation constants are considered macroscopic pK_a's, in which only the protonation state is taken into consideration rather than the protonation site (Figure 3.3B).

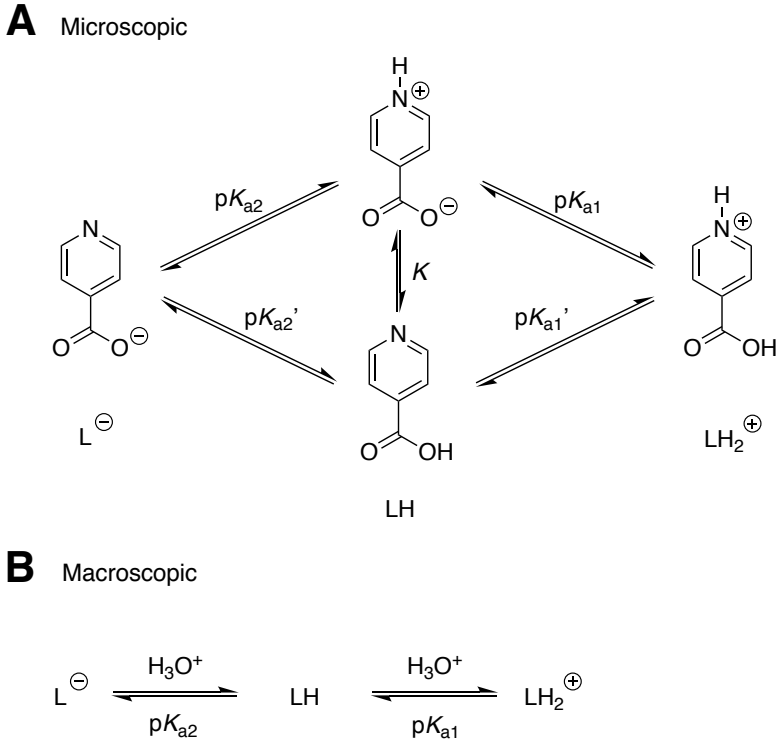

Figure 3.3: Schematic illustrating the difference between determining microscopic (A) and macroscopic (B) protonation constants.

However, ^{14}N and ^{15}N NMR analysis of trispicolylamine (TPA) was able to determine the microscopic pK_a's of the tripodal ligand, discovering that the most basic sites are, in fact, the pyridine rings rather than the tertiary aliphatic amine.[3] Interestingly, all three

pyridines were protonated before the tertiary amine, suggesting that the three pyridine rings induce enough of an electron-withdrawing effect to significantly reduce the pK_a of the aliphatic amine. Upon analysis of the spectrophotometric pH titration data of chromis-1 acid (**2.1b**) and comparison to the NMR data of TPA, the third pK_a of 5.5 is likely associated with protonation of the pyridine of the bispicolylamine chelator (Figure 3.4). Protonation of the first pyridine of the chelator moiety results in a pK_a perturbation that lowers the pK_a of the second pyridine by two log units due to an electrostatic repulsion from the existing positive charge. In order to protonate the chromophore pyridine, the presence of the two positive charges derived from protonation of both bispicolylamine pyridines results in an electrostatic repulsion that lowers the pK_a of the pyridine more than four orders of magnitude from 5.5 to 1.1, relative to the first pyridine. The pK_a of 1.1 that is associated with protonation of the fluorophore pyridine is also supported by the manifestation of a strong red-shift of more than 60 nm in the absorbance relative to the dianionic species and is a colorimetric indication that is consistent with protonation of an electron-deficient chromophore.

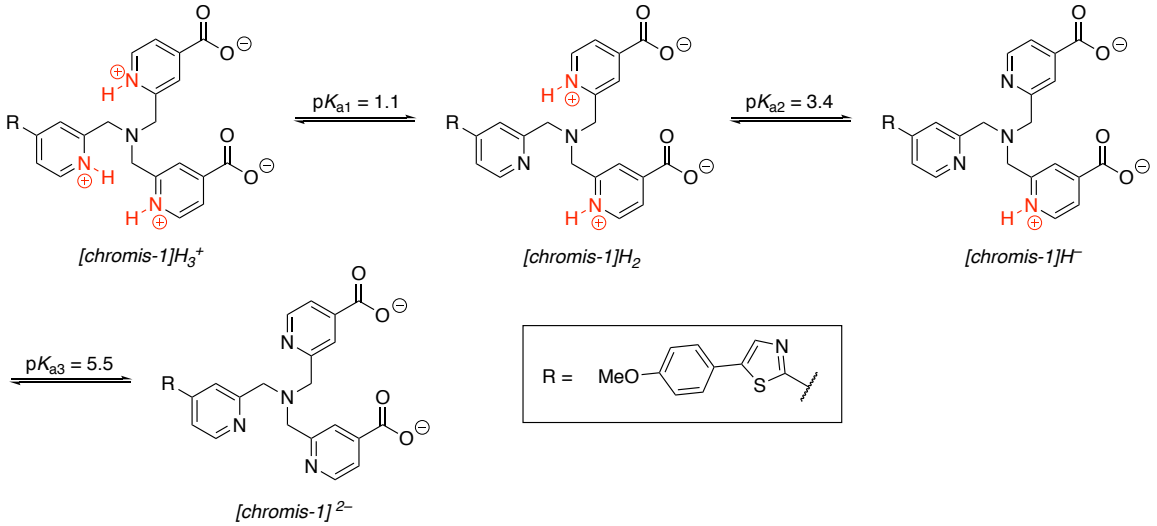

Figure 3.4: Protonation equilibria of chromis-1 acid (**2.1b**) and the predicted species that correspond to the three individual protonation constants determined from the UV-Vis pH titration. Data acquired by Dr. S. Sumalekshmy, and figure prepared by the author.

Comparing the absorption data to the fluorescence data, the spectrum with an emission maximum at 580 nm is consistent with the formation of the monoprotonated species, in which all three pyridines of the trispicolylamine acceptor unit are protonated, whereas the emission maximum at 481 nm is representative of the dianionic chromis-1 acid. However, not only does the emergence of a second emission maximum at 560 nm within the emission spectrum at pH 5.2 not complement the spectral changes observed in the absorption between pH 7.0 and 5.2, but also the emission maximum is blue shifted by 20 nm relative to the monoprotonated species that is not formed until the pH drops below 2.

The discrepancies between the absorption and fluorescence measurements are likely the result of protonation of the chromophore's pyridine nitrogen in the excited state, producing a species that is not present in the ground state, regardless of pH (Figure 3.5). It was hypothesized that as the pH is lowered to ~ 5, the increase in [H_3O^+] results in protonation of pyridyl moiety of the fluorophore core in the excited state, leading to partial quenching of the fluorescence through increased radiationless decay to the ground state.

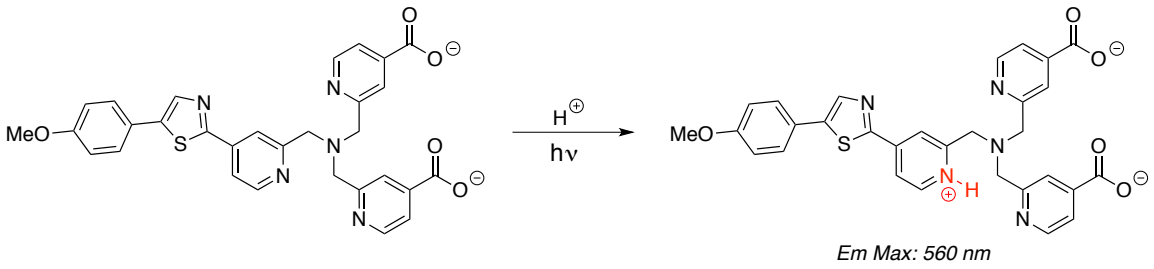

Figure 3.5: Schematic depicting the protonation of the pyridyl acceptor of chromis-1 (**2.1b**) in the excited state to produce a monoanionic species that is not produced in the ground-state.

Even at neutral pH, fluorimetric measurements of chromis-1 acid in aqueous buffer revealed a broadening of the fluorescence emission profile on the red edge, which alluded to the presence of a second emissive species at higher wavelength in the excited state

(Figure 3.1A). It was hypothesized that the second emissive species at pH 7.0 was the same species with the emission maximum at 560 nm that is distinctly present at pH ~ 5.0. To further corroborate that the emission band at 560 nm is due to excited-state protonation, solvent deuterium isotope effect studies were conducted to compare the shapes and intensities of the fluorescence profiles of chromis-1 acid in deuterated versus non-deuterated buffer (10 mM PIPES, 100 mM KCl, pH/D 7.0, 25°C). In deuterated buffer, a 16% fluorescence enhancement was observed relative to the fluorescence intensity in non-deuterated buffer (Figure 3.6A). In addition, upon normalization of the fluorescence spectra of fully deprotonated chromis-1 in both buffers, a sharpening of the fluorescence profile of chromis-1 acid in deuterated buffer relative to non-deuterated buffer was observed, alluding to inhibition of formation of the second emissive species that emits at longer wavelength (Figure 3.6B).

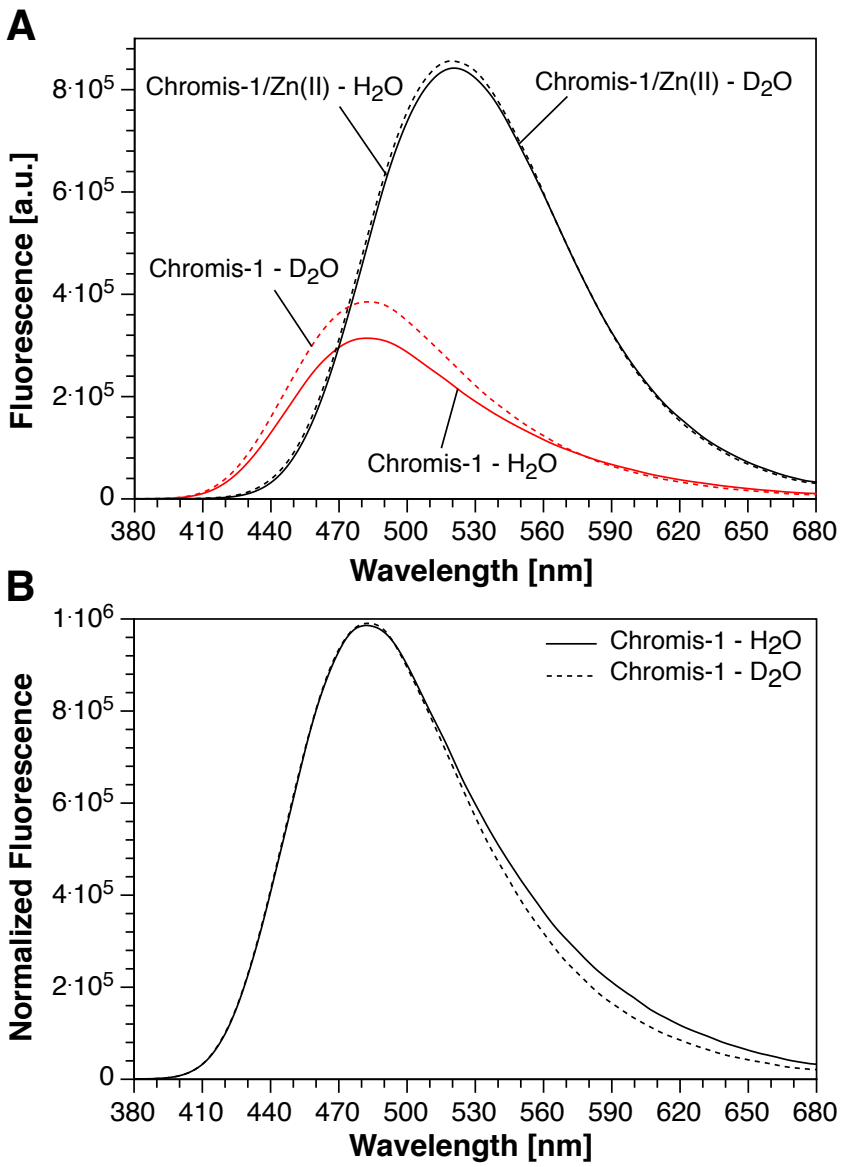

Figure 3.6: A) Solvent deuterium isotope effect for chromis-1 acid (**2.1b**) in deuterated versus non-deuterated buffer (10 mM PIPES, 0.1 M KCl, pH/D 7.0) at 25°C. Solid lines represent the fluorescence spectra in non-deuterated buffer, whereas the dashed lines represent the fluorescence spectra in deuterated buffer. B) Normalization of the emission intensities for the metal-free form of chromis-1 as shown in (A).

Because the intracellular pH varies between the cytosol and subcellular compartments and organelles,[4] fluorescent probes, such as chromis-1, should not respond to fluctuations in pH when imaging live cells. Despite the development of chromis-1 as a water-soluble, Zn(II)-selective fluorescent probe that demonstrated robust emission-ratiometric

imaging capabilities in live cells using TPEM, the sensitivity towards fluctuations in pH could prove challenging for studying biological processes where changes in Zn(II) levels are also accompanied by a change in pH. Therefore, this chapter serves to address the challenges encountered by the undesired emission response of chromis-1 upon acidification by exploring optimizations in the design of the D-π-A architecture of the fluorophore core to reduce the driving force for excited-state protonation while maintaining an increased ICT necessary for inducing large bathochromic shifts in the emission upon binding of Zn(II), thus maintaining its robust emission-ratiometric imaging capabilities.

3.2 Elucidating the Intrinsic Photobasicity of the Donor-Acceptor Fluorophore Platform of Chromis-1

Although the pyridyl acceptor moiety of chromis-1 acid has a very low ground-state pK_a (~ 1.1), the excited-state polarization of chromis-1 places an increased localized charge density on the pyridine nitrogen of the fluorophore, promoting an excited-state protonation of the pyridine nitrogen at a pH significantly higher than its pK_a. It was expected that the ground-state pK_a of the fluorophore pyridine without the bispicolylamine chelator moiety attached would be higher due to the absence of the two additional protonation sites, resulting in an electrostatic repulsion that would otherwise increase the acidity of the chromophore pyridine. To explore the intrinsic photobasicity of the fluorophore core, a model compound of chromis-1, lacking the bispicolylamine chelating group, was synthesized and characterized for its photophysical and thermodynamic properties. To ensure sufficient solubility at micromolar concentrations necessary to perform these characterizations in aqueous buffer, a sulfonate group was tethered to the anisole donor of the fluorophore. To minimize interferences with the ICT strength of the donor, the sulfonate group

was separated from the oxygen donor via a trimethylene bridge. The result was the generation of model compound **3.1** (Scheme 3.1).

*3.2.1 Synthesis of Model Compound **3.1***

Model compound **3.1** was assembled in 4 steps from commercially available, inexpensive starting materials with an overall yield of 29% (Scheme 3.1). Using an EDCI-mediated condensation reaction, 2-amino-4'-methoxyacetophenone hydrochloride **2.4** was coupled to isonicotinic acid to form the amide intermediate **3.6**, which was then subjected to a tandem thionation-cyclization reaction using Lawesson's reagent to form the corresponding thiazole **3.7** in relatively good yield. To functionalize the fluorophore with a water-solubilizing group, the anisole's methoxy group was demethylated using BBr_3 to form the corresponding phenol **3.8**, which was then deprotonated by sodium *tert*-butoxide in THF and subsequently alkylated using 1,3-propanesultone to afford the water-soluble sodium sulfonate salt of **3.1**.

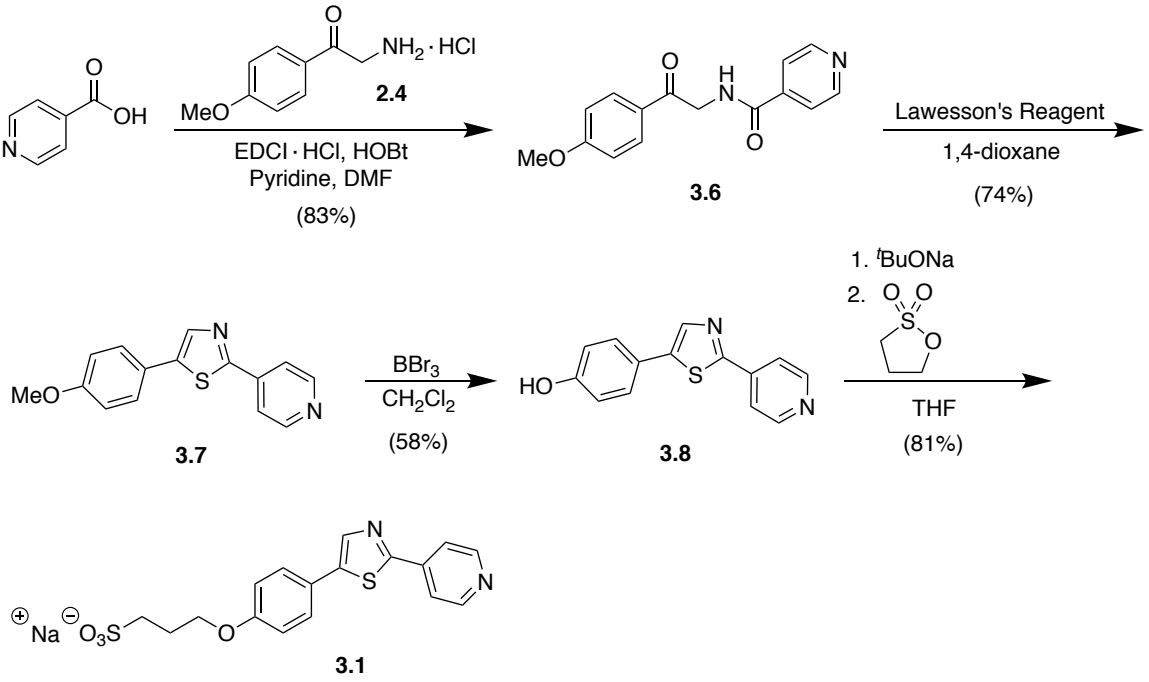

Scheme 3.1: Synthesis of Model Compound **3.1**, with an overall yield of 29% after four steps.

*3.2.2 Photophysical Properties of Model Compound **3.1***

Upon protonation of the pyridyl acceptor, the absorption maximum of model compound **3.1** is red-shifted by 51 nm from 346 nm (ε = 18,000 M^{-1}•cm^{-1}) to 397 nm (ε = 19,600 M^{-1}•cm^{-1}) for the fully protonated pyridine (Table 3.1). The presence of two clean isosbestic point at 288 and 370 nm are indicative of a well-defined solution equilibrium between the neutral and monoprotonated species. Similarly, the emission maximum of **3.1** in pH neutral buffer (10 mM PIPES, 0.1 M KCl, pH 7.0, 25°C) is red-shifted 93 nm from 489 nm to 582 nm when fully protonated, consistent with the 580-nm emission maximum of observed for the triprotonated species (LH_3^+) of chromis-1 acid (Figure 3.2A). The lack of the dicarboxylate-substituted bispicolylamine has a substantial effect on the fluorescence quantum yield of **3.1**, increasing two-fold from 0.32 to 0.65.

Table 3.1: Photophysical and thermodynamic properties of model compound **3.1**

	Neutral[a]	**Protonated**[b]
Absorbance λ_{max} (nm) [c]	346	397
ε (10^4 $M^{-1}cm^{-1}$)[d]	18.0	19.6
Emission λ_{max} (nm)[e]	489	582
Φ_F [f]	0.65	n.d.
pK_a	-	4.49
pK_a*[g]	-	11.7

[a]10 mM PIPES, 0.1 M KCl, 25°C. [b]0.1 N HCl (*aq*). [c]lowest-energy band of the one-photon absorption spectrum. [d]molar extinction coefficient at λ_{max}. [e] maximum fluorescence emission. [f] fluorescence quantum yield, referenced to quinine sulfate (Φ_F = 0.546).[5] [g]excited-state pK_a. n.d. = not determined.

*3.2.3 Determination of the Protonation Constant of the Pyridine Moiety of Model Compound **3.1***

The presence of an electron withdrawing group (thiazole) in the para position relative to the heterocyclic nitrogen was expected to lower the pK_a of the pyridine nitrogen in model compound **3.1** relative to unsubstituted pyridine (pK_a = 5.2)[6]. Taking advantage of the colorimetric shift upon protonation of the fluorophore pyridine, the protonation constant of model compound **3.1** was measured by a spectrophotometric pH titration where the solution pH was varied between 3.3 and 5.6. Spectral deconvolution through non-linear, least-squares fitting of the absorption and potentiometric data to a monoprotic equilibrium model yielded a pK_a = 4.49 ± 0.002 (Figure 3.7). While this value agrees more closely to the pKa of unsubstituted pyridine, it is more than three logarithmic units higher than the pK_a of the pyridyl acceptor of chromis-1.

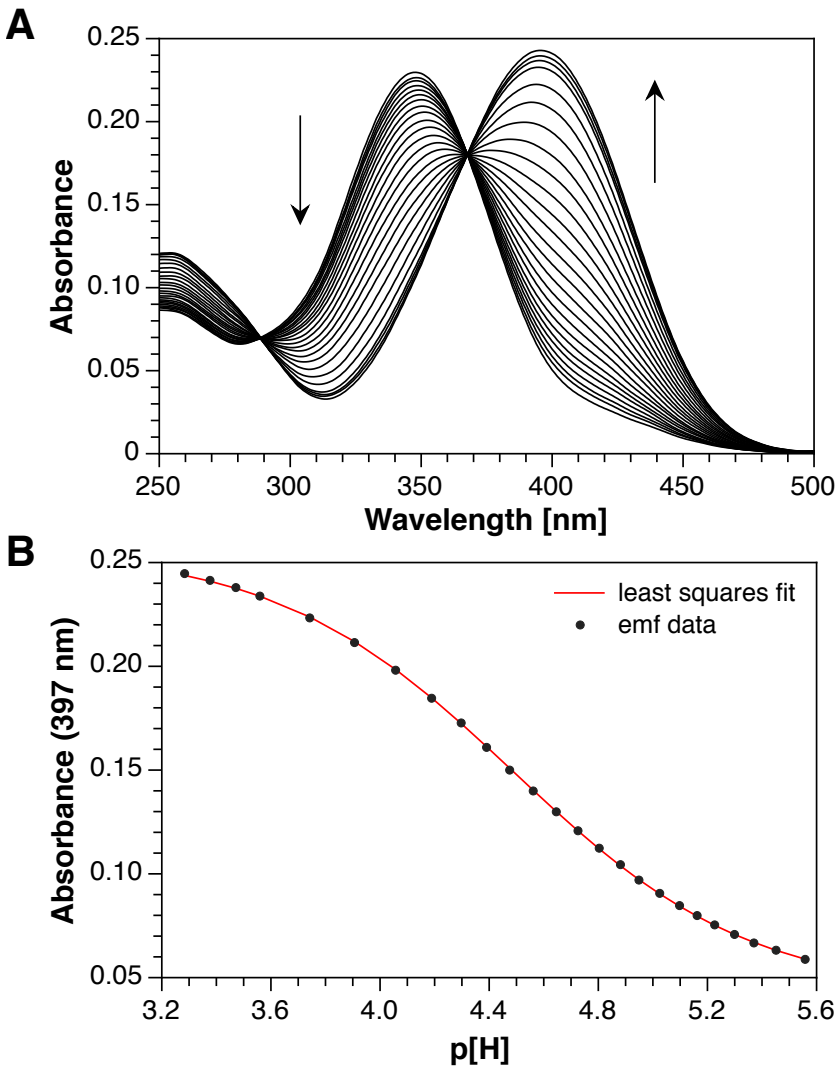

Figure 3.7: Spectrophotometric pH titration of model compound **3.1** (10 μM) at 25 °C in aqueous buffer (5 mM PIPBS, 0.1 M KCl, 5 mM KOH, pH 5.6). Black arrows indicate the change in absorbance after each aliquot of HCl was added. The absorbance from 250-500 nm was recorded as a function of pH_c ($-\log[H_3O^+]$), and the data were analyzed by non-linear least squares fitting to a single protonation model to yield an average $pK_{H1} = 4.49 \pm 0.002$ ($n = 3$).

3.2.4 Employing the Förster Cycle to Estimate the Photobasicity of Model Compound 3.1

For a given chromophore, the Brønsted-Lowry basicity in the ground state can be vastly different than the corresponding basicity in the excited state because of greater

excited-state polarization derived from charge redistribution upon excitation. It was hypothesized that the increase in localized charge density on the pyridyl acceptor of model compound **3.1** upon excitation renders the pyridine as a much stronger base in the excited-state compared to the ground state. Therefore, it was important to determine the excited-state pK_a of model compound **3.1** to establish the degree of photobasicity of the pyridyl acceptor of the fluorophore core and compare it to its ground-state basicity.

The thermodynamic values that represent protonation and the change in energy due to electronic excitation of a fluorophore are related in both the ground state and excited state by a thermodynamic cycle, known as the Förster cycle, that can be used to estimate the driving force for protonation of a species in the electronically excited state.[7-8] In solution, model compound **3.1** behaves as a weak base (denoted as B) in the excited-state, forming the corresponding conjugate acid (denoted as BH^+) and a hydroxide ion. The formation of the protonated species results in an increase in enthalpy in both the ground state and the excited state, denoted as ΔH and ΔH^*, respectively (Figure 3.8). Both the free base and its corresponding conjugate acid in the ground state can be promoted to their respective excited states by the absorption of photons $h\nu_B$ and $h\nu_{BH^+}$, respectively. These electronic transitions between the ground state and the excited state are referred to as 0-0 (zero-zero) transitions after vibrational relaxation to the v_0 vibrational level of either state.

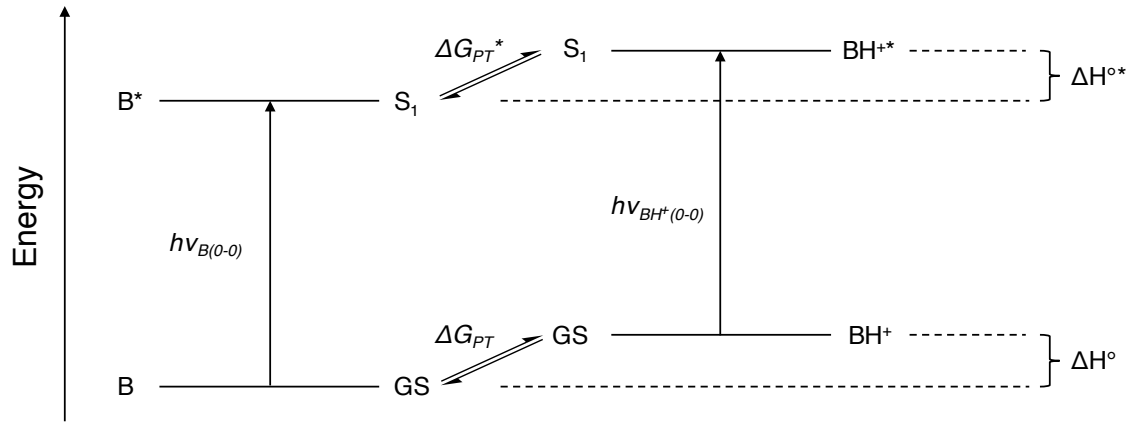

Figure 3.8: Generalized Förster cycle diagram for estimating the excited-state pK_a from the ground-state pK_a and the energies corresponding to the excitation of both the free base (B) and its conjugate acid (BH^+). ΔG_{PT} refers to the free energy of proton transfer.

Considering the Förster Cycle as a sum of each thermodynamic event (absorption, protonation in the excited state, emission, and deprotonation in the ground-state), the following relationship[9] can be derived under the assumption that the molar entropies of dissociation are equal:

$$N_A\, h\nu_B + \Delta H^* - N_A\, h\nu_{BH^+} - \Delta H = 0 \qquad (3\text{-}1)$$

where N_A is Avogadro's constant and $h\nu_B$ and $h\nu_{BH^+}$ correspond to the energy differences of the 0-0 electronic transitions. Rearrangement of equation 3-1 provides the following relationship:

$$\Delta H^{\circ *} - \Delta H^\circ = N_A(h\nu_B - h\nu_{BH^+}) \qquad (3\text{-}2)$$

Using equation 3-2, the differences in the protonation constants of the excited-state and ground-state can be related to the energy differences between the two electronic transitions:

$$pK_a{}^* - pK_a = N_A(\tilde{\nu}_B - \tilde{\nu}_{BH^+}) \quad (3\text{-}3)$$

Under the assumption that the entropies (ΔS and ΔS*) of dissociation for the ground state and excited state of BH^+ to B are equal,[9] the difference between enthalpies (ΔH* – ΔH) can be replaced by the difference in Gibb's free energies, ΔG* – ΔG, for the excited-state and ground-state protonation equilibria, respectively, yielding the following equation after considering the relationships between Gibbs free energy and pK_a:

$$pK_a{}^* = pK_a - \left(\frac{N_A hc\Delta\tilde{\nu}}{2.303RT}\right) \quad (3\text{-}4)$$

Where R is the universal gas constant, T is the temperature (absolute, in Kelvin), and c is the speed of light, which are incorporated into the expression to convert the 0-0 electronic transition frequencies (ν_B and ν_{BH^+}) into wavenumbers ($\tilde{\nu}_B$ and $\tilde{\nu}_{BH^+}$). The experimental determination of these values in wavenumbers are difficult to accurately determine. Most often, these values are estimated as the average energy (in wavenumbers) corresponding to the absorption and emission maximum, such that:

$$\tilde{\nu}_{00} = \left(\frac{\tilde{\nu}_{abs}^{max} + \tilde{\nu}_{em}^{max}}{2}\right) \quad (3\text{-}5)$$

However, the values can also be estimated by the energy, in wavenumbers, corresponding to the intersection between the normalized excitation and emission spectra. If the Stokes shift is too large to accurately approximate this value, the average of the energy corresponding to half the intensities of the excitation and emission bands.

Nonetheless, experimental measurements of the 0-0 energetic transitions between the ground state and the excited state for both the free base and its conjugate acid of the

pyridyl acceptor of model compound **3.1**, as well as the pK_a corresponding to the protonation of the pyridine in the ground state, were used to estimate the K_a in the excited state (K_a*) from the three experimental measurements. Using this Förster cycle, an excited-state pK_a (pK_a*) of 11.7 was calculated, a value that is seven orders of magnitude higher than the ground-state pK_a. However, it should be noted that not only is the Förster cycle an estimation, but also the use of the thermodynamic cycle should be taken with caution, as at an excitation wavelength of 300 nm, a 4-nm error in the wavelength corresponds to a one-unit-discrepancy in the pK_a.[10]

*3.2.5 Solvent Deuterium Isotope Effect of Model Compound **3.1***

The solvent deuterium isotope effect of model compound **3.1** was evaluated in deuterated versus non-deuterated buffers (10 mM PIPES, 0.1 M KCl, pH/D 7.0, 25°C), and integration of the emission spectra revealed an 18% increase in fluorescence in D_2O relative to H_2O buffer (Figure 3.9A). Furthermore, upon normalization of the two spectra (Figure 3.9B), the spectrum of model compound **3.1** in D_2O is narrower and features less of a red-edge tail, alluding to the presence of excited-state protonation as a competitive deactivation pathway.

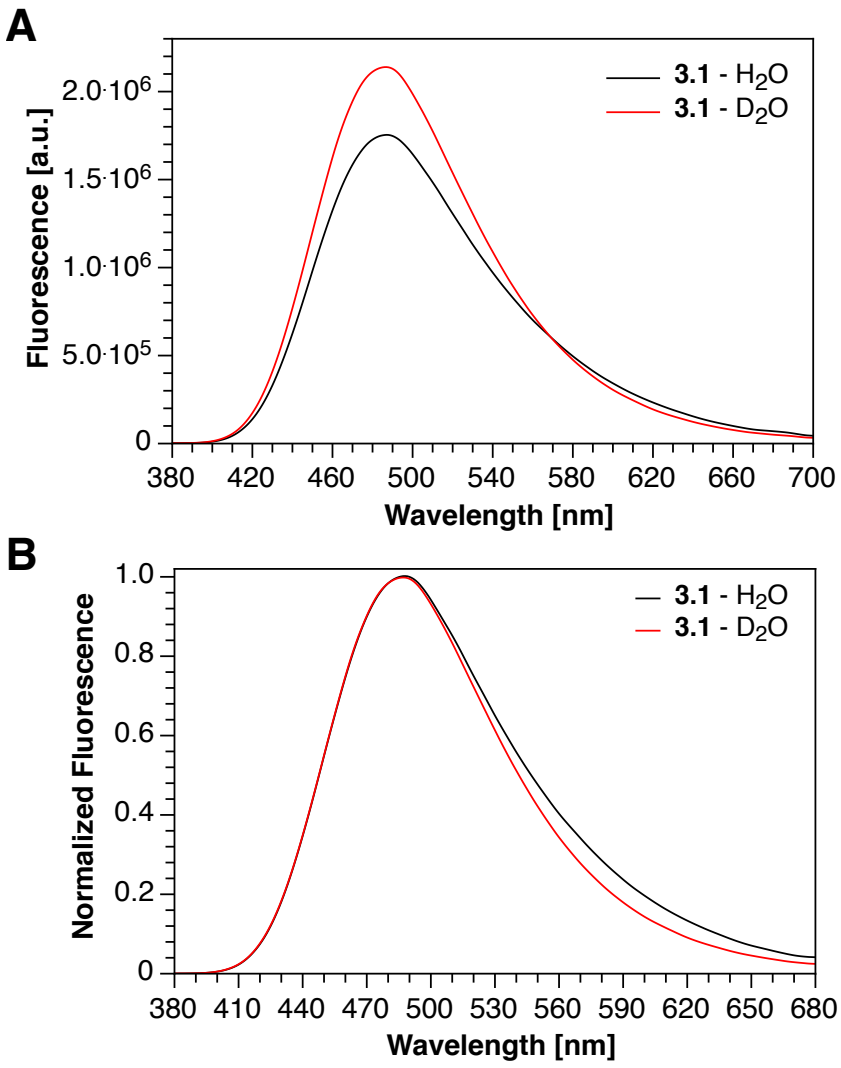

Figure 3.9: Solvent deuterium isotope effect of **3.1** (10 μM) in deuterated versus non-deuterated buffer (10 mM PIPES, 0.1 M KCl, pH/D 7.0) at 25°C. (A) Effect of buffer composition on the fluorescence intensity and profile of model compound **3.1**. (B) Normalization of fluorescence spectra of model compound **3.1** shown in (A). Excitation: 346 nm

3.3 Optimization of the Fluorophore Design for Reducing the Basicity of the Pyridyl Acceptor

Previously published literature data of oxazolyl-pyridine fluorophores bearing structural similarities to model compound **3.1** revealed that isomerization of the pyridine from the 4-position to the 2-position relative to the oxazole ring reduced the ground-state

pK_a from 4.3 to 2.6, a nearly 2 log-unit reduction in the proton basicity of the pyridine.[11] Although the substitution of the oxazole with a thiazole ring was implemented to shift the wavelength of excitation further into the red to be more useful for TPEM, this literature precedent served as a design strategy for decreasing the basicity and ultimately the photobasicity of chromis-1 by isomerizing the pyridyl acceptor from the 4-position to the 2-position relative to the thiazole ring. Assuming the additional π-electron donation from the thiazole sulfur would not have a large effect on the polarization of the fluorophore compared to the oxazole, it was hypothesized that this isomerization would lower the basicity of the pyridine by a comparable ~ 2 log units. This rationale led to the synthesis of model compound **3.2** for spectroscopic characterization.

*3.3.1 Synthesis of Model Compound **3.2***

Model compound **3.2** was synthesized identically to **3.1**, except that amide **3.9** was prepared using picolinic acid rather than isonicotinic acid, and the overall yield for the 4-step synthesis was 48%, almost double that of **3.1** (Scheme 3.2). Despite the structural similarities, including the identical counterion (Na^+) used, the ^1H and ^{13}C NMR spectra of **3.2** could be acquired in MeOD, whereas **3.1** required DMSO-d6 for sufficient solubility at concentrations required to achieve a suitable signal-to-noise ratio.

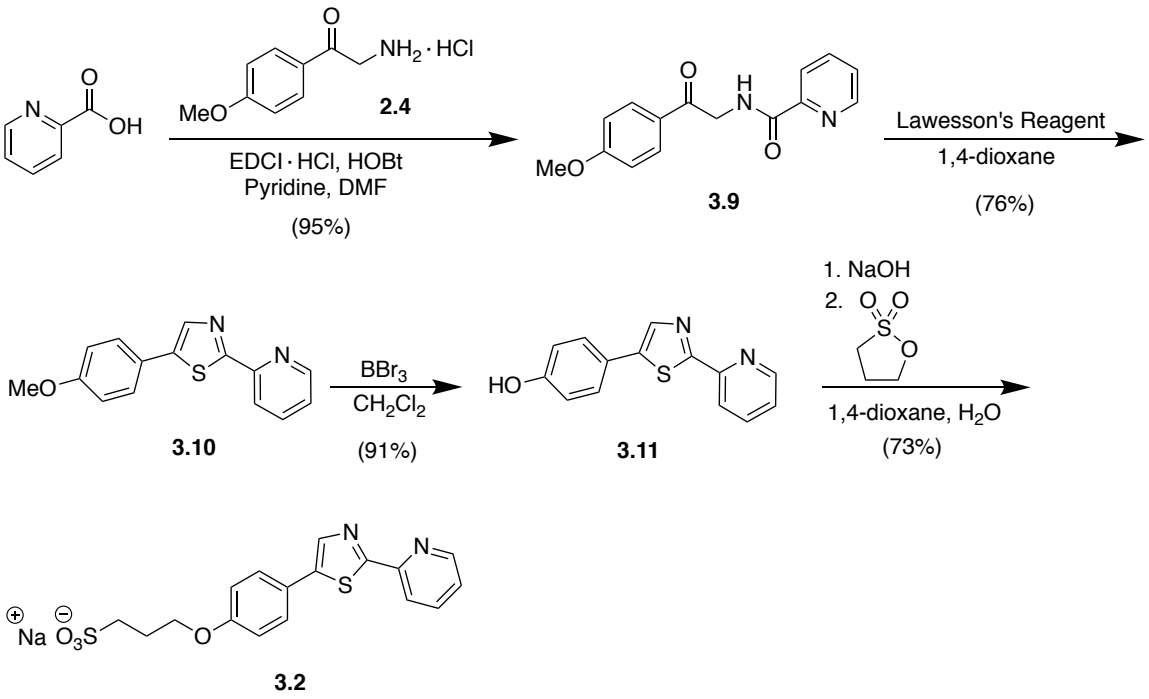

Scheme 3.2: Synthesis of model compound **3.2**, with an overall yield of 48% after four steps.

*3.3.2 Steady-State Absorption and Fluorescence Measurements of Model Compound **3.2***

Fluorescence quantum yield measurements of **3.2** yielded an astounding $\Phi_F = 0.80$ when referenced to quinine sulfate ($\Phi_F = 0.546$ in 1N H_2SO_4)[5], up 15% from that of **3.1** ($\Phi_F = 0.65$) (Table 3.2). The absorbance maximum of the neutral molecule was not shifted relative to **3.1**, but upon protonation, **3.2** demonstrated an 11-nm blue shift in the absorption compared to its constitutional isomer. In the emission, however, **3.2** displayed a 22-nm blue shift in the emission of the neutral form and a 17-nm blue shift for the protonated form.

Table 3.2: Photophysical and thermodynamic properties of model compound **3.2**.

	Neutral[a]	**Protonated**[b]
Absorbance λ_{max} (nm) [c]	345	386
ε (10^4 $M^{-1}cm^{-1}$)[d]	2.25	2.05
Emission λ_{max} (nm)[e]	467	565
Φ_F [f]	0.80	n.d.
pK_a	-	2.34
pK_a*	-	9.4

[a]10 mM PIPES, 0.1 M KCl, 25°C. [b]0.1 N HCl (*aq*). [c]lowest-energy band of the one-photon absorption spectrum. [d]molar extinction coefficient at λ_{max}. [e]maximum fluorescence emission. [f]fluorescence quantum yield, referenced to quinine sulfate (Φ_F = 0.546 in 1N H_2SO_4).[5] n.d. = not determined.

*3.3.3 Model Compound **3.2** Boasts a 100-Fold Decrease in the Ground-State and Excited-State Basicity of the Pyridyl Acceptor*

Spectrophotometric pH titrations of **3.2** analogous to **3.1** demonstrated a more than two logarithmic-unit decrease in the ground-state pK_a of the pyridyl acceptor from 4.49 ± 0.002 for the 4-thiazolyl isomer to 2.34 ± 0.002 for the 2-thiazolyl isomer, consistent with the nearly two logarithmic-unit decrease observed with the oxazolyl fluorophores reported previously (Figure 3.10). Using the Förster Cycle, the calculated excited-state pK_a of **3.2** also dropped more than two log units from 11.7 to 9.4, which indicated a substantial reduction in the photobasicity of the pyridine nitrogen due to the isomerization from the 4-position to the 2-position.

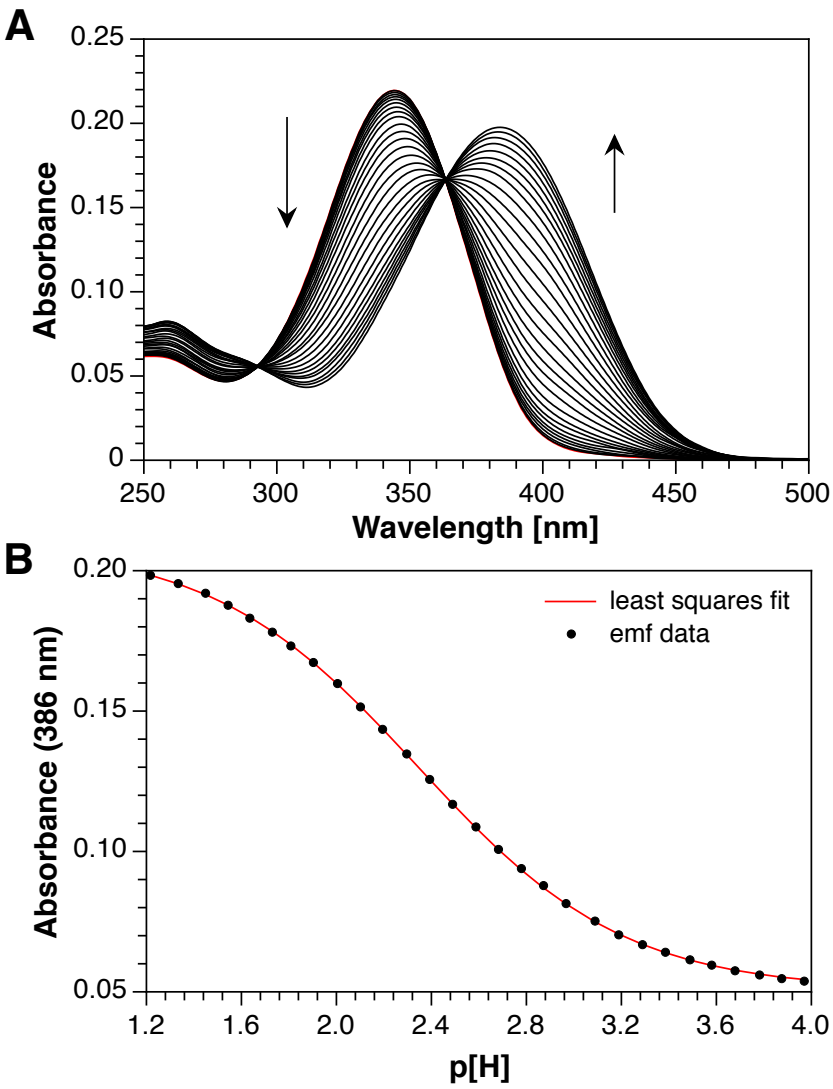

Figure 3.10: Spectrophotometric pH titration of model compound **3.2** (10 μM) at 25 °C in 0.1 M KCl. Black arrows indicate the change in absorbance after each aliquot of HCl was added. The absorbance (250-500 nm) was recorded as a function of pH_c ($-\log[H_3O^+]$), and the data were analyzed by non-linear least squares fitting to a single protonation model to yield an average pK_{H1} = 2.34 ± 0.002 (n = 3).

3.4 Confronting the pH Sensitivity of Chromis-1 through the Implementation of the Isomerized Fluorophore Core

Solvent deuterium isotope studies of model compound **3.2** revealed identical overlapping emission spectra when comparing the fluorescence response in deuterated versus non-deuterated buffers, alluding to the potential eradication of ESPT (Figure 3.11).

These findings, in addition to the reduced ground- and excited-state basicity, as well as the significant increase in quantum yield of **3.2** compared to **3.1**, provided promising insight into the development of a chromis-1 analog that is less sensitive to fluctuations in pH. Therefore, the isomerized pyridyl acceptor moiety was incorporated into the design of a new Zn(II)-selective, emission-ratiometric fluorescent probe (**3.3a/b**) for use in two-photon excitation microscopy.

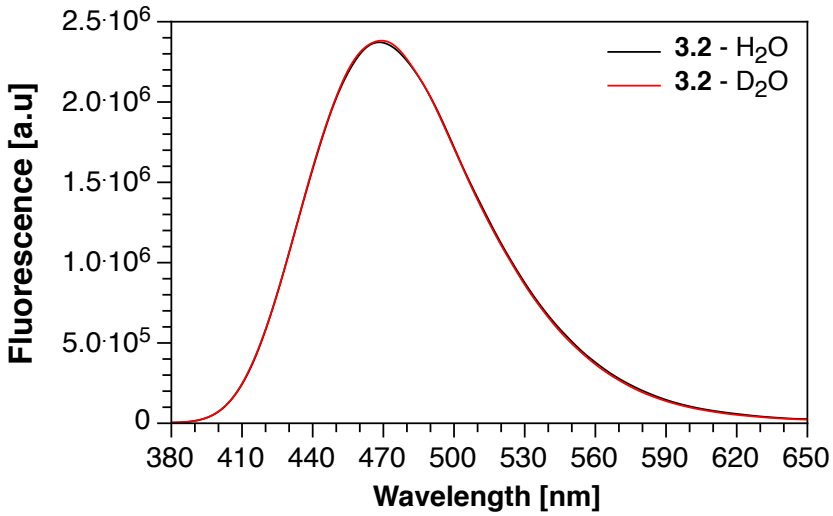

Figure 3.11: Solvent deuterium isotope effect of model compound **3.2** (10 μM) in deuterated and non-deuterated buffer (10 mM PIPES, 0.1 M KCl, pH/D 7.0, 25°C). Excitation: 345 nm

*3.4.1 Synthesis of the 2-Thiazolyl, Zn(II)-Binding Probe **3.3b***

Compound **3.3b** was synthesized in 8 steps from commercially available starting materials with an overall yield of 10% (Scheme 3.3). Beginning with ethyl 6-bromopicolinate, a Rosenmund-von Braun reaction[12-13] with cuprous cyanide (CuCN) in pyridine selectively substituted the bromine with a nitrile group, followed by selective hydrolysis of the ethyl ester **3.12** in boiling 1N $HCl_{(aq)}$ to afford the corresponding carboxylic acid **3.13**. EDCI-mediated condensation of the nitrile acid **3.13** with 2-amino-4'-methoxyacetophenone hydrochloride (**2.4**) yielded amide **3.14**, which was isolated by precipitating the product with

the addition of H_2O, leaving the byproducts and other reagents solubilized in the DMF/H_2O. Amide **3.14** underwent a tandem thionation-cyclization reaction to the corresponding thiazole nitrile **3.15** using Lawesson's reagent. In contrast to **3.15**, the thionation-cyclization reaction to afford Fmoc-protected thiazole **2.6** in the synthesis of chromis-1 (Chapter 2) did not result in side-reactivity with the Fmoc-protected amine. However, the nucleophilic nature of Lawesson's reagent, in combination with the high temperature and increased electrophilicity of the 2-picolylnitrile moiety, created a time-dependent functional group interconversion of the expected thiazole nitrile product to a thioamide. The thioamide was first discovered by TLC, by which the Mn-Zn complex present as the UV-active in fluorescent TLC plates converted the thioamide to the nitrile directly on the TLC plate, sparking motivation to explore literature methods for converting thioamides to nitriles in high yield. Using a modification of a literature procedure to convert aromatic thioamides to nitriles,[14] the thioamide was converted back to the nitrile within ~ 10 minutes by reacting the crude isolated mixture with potassium permanganate in acetone, which surprisingly did not oxidize the fluorophore during the reaction time. Upon recrystallization to afford the pure nitrile **3.15**, lithium diisobutyl-*tert*-butoxyalumunium hydride (LDBBA)[15] was used to selectively reduce the aromatic nitrile to the aldehyde **3.16** at room temperature. Although DIBAL is often used for reductions of nitriles to aldehydes, reaction with DIBAL afforded exclusively the corresponding primary amine, suggesting that the pyridine nitrogen could act as a Lewis base for coordinating the aluminum and augmenting its reactivity.

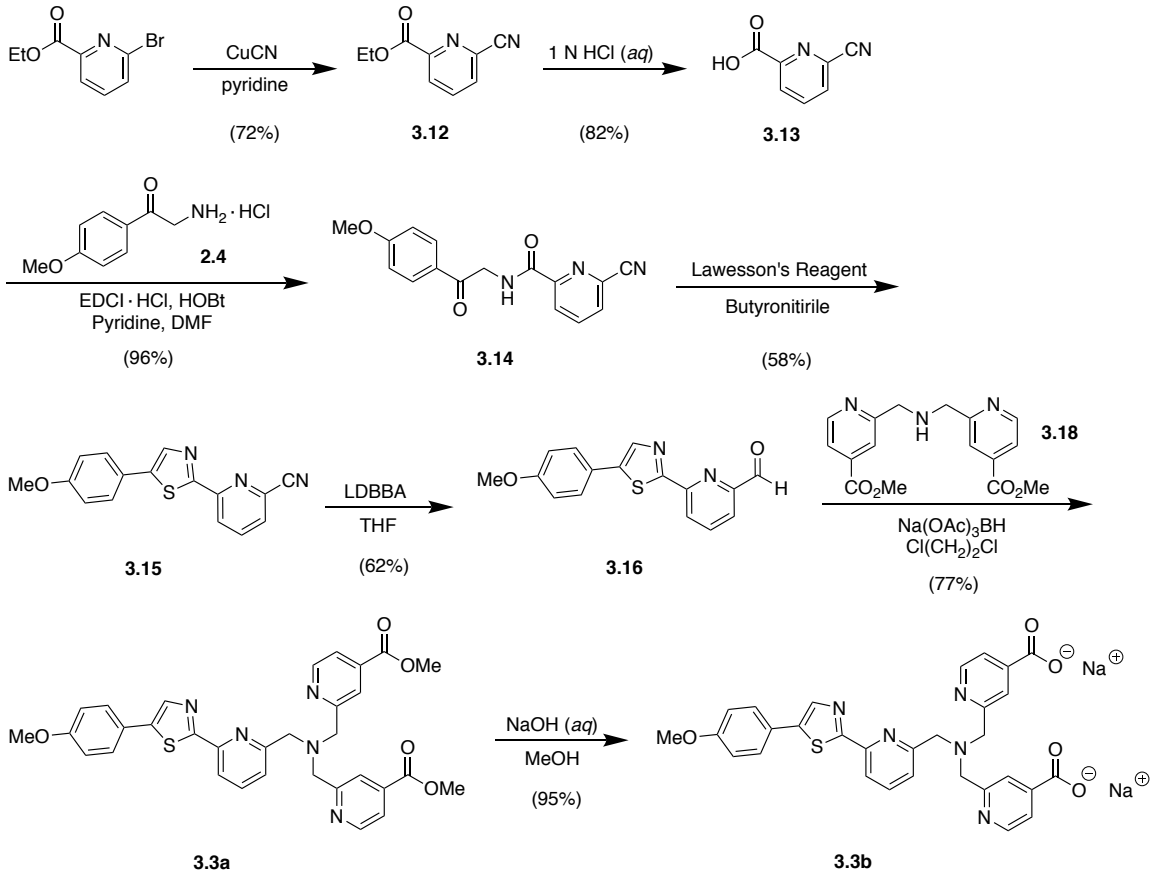

Scheme 3.3: Synthesis of **3.3a** and **3.3b**.

In the synthesis of chromis-1 ester (**2.1a**), assembly of the final probe was achieved by double alkylation of primary amine **2.7** with the brominated isonicotinic acid derivative **2.10**. However, in the synthesis of **3.3a**, the aldehyde functionality of **3.16** required the availability of a secondary amine in order to attach the metal-binding ligand. Therefore, synthesis of a bispicolylamine chelator that bears water-solubilizing carboxylic acids was accomplished by a one-pot dimerization of 2-cyanoisonicotinic acid (**2.2**) in ethanol:water, which is believed to proceed through a palladium-catalyzed hydrogenation of the nitrile to the primary amine, followed by a reductive coupling of the primary amine with the 2-formylisonicotinic acid that was generated from the *in situ* hydrolysis of the imine intermediate (Scheme 3.4). Although the reaction conditions do not result in the complete

formation of the reductively coupled product, the pK_a discrepancies between the fully reduced primary amine and the secondary amine of bispicolylamine dicarboxylic acid **3.17** was exploited to selectively extract **3.17** into the organic layer using 1 M citrate buffer, thus washing out the primary amine that remained protonated in the aqueous layer.

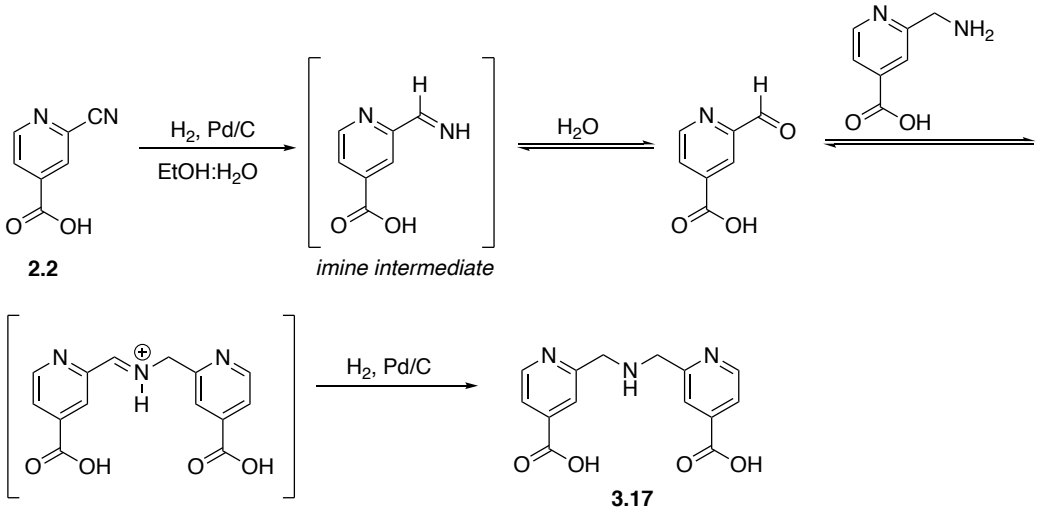

Scheme 3.4: One-pot synthesis and proposed mechanism for the reductive coupling of 2-cyanoisonicotinic acid (**2.2**) to prepare the bispicolylamine derivative **3.17**.

After preparation of **3.17**, the carboxylic acids were esterified using trimethylsilyl chloride (TMSCl) in MeOH to afford the dimethyl ester-substituted bispicolylamine **3.18** (Scheme 3.5) for solubility in organic solvents when coupling the chelator to the fluorophore core.

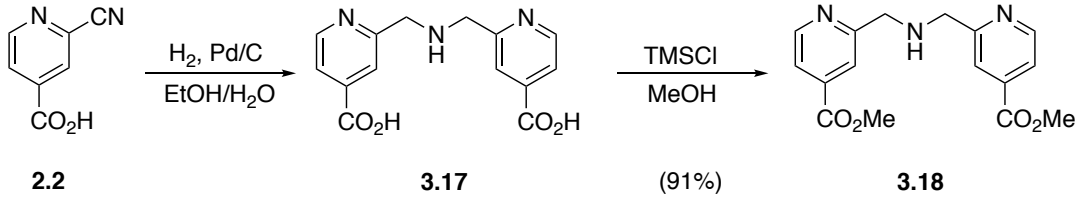

Scheme 3.5: Synthesis of dimethyl ester-substituted bispicolylamine **3.18**.

Exploiting aldehyde **3.16** as a versatile scaffold, fluorophore **3.3a** was assembled via reductive amination with the dimethyl ester-substituted **3.18** in anhydrous 1,2-dichloroethane to afford a glassy yellow solid in 77% yield. A portion of **3.3a** was saponified to the corresponding sodium dicarboxylate salt **3.3b** by refluxing with $NaOH_{(aq)}$ in MeOH, followed by recrystallization from a MeOH:EtOH mixture, to provide an analytical-grade, water-soluble analogue for spectroscopic measurements.

3.4.2 X-Ray Crystallographic Characterization of the 2-Thiazolyl Fluorophore

Due to the availability of only 4 donor atoms for coordination in the structure of chromis-1 acid, the coordination of a chloride ion to the zinc center as an auxillary ligand manifested a characteristic trigonal bipyramidal geometry of Zn(II) complexes often observed in biological complexes as a result of Zn(II)'s flexible coordination sphere.[16-17] However, the presence of the carboxylic acids of chromis-1 made it difficult to obtain high-quality crystals due to a Ca^{2+} ion-mediated dimerization of chromis-1 acid. To avoid this when attempting to crystallize probe **3.3b**, a derivative of **3.3b** lacking the carboxylic acids on the metal-binding ligand was synthesized through a reductive amination coupling of aldehyde **3.16** with di(2-pyridylmethyl)amine (Scheme 3.6), which afford probe **3.3c** for use in crystallizing the corresponding Zn(II) complex of the 2-thiazolyl isomer.

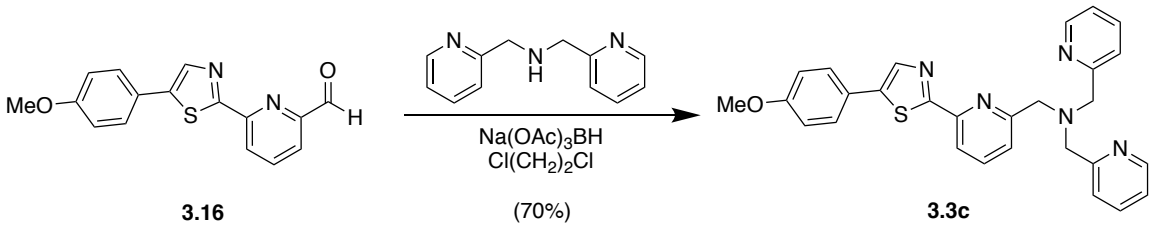

3.16 (70%) **3.3c**

Scheme 3.6: Synthesis of probe **3.3c** for use in crystallizing the Zn(II) complex of the 2-thiazolyl fluorophore of **3.3b**.

As originally hypothesized, isomerization of the pyridyl acceptor moiety from the 4-position to the 2-thiazolyl position resulted in the engagement of the thiazole nitrogen in Zn(II) binding, permitting the formation of a five-coordinate Zn(II) that does not entail ternary complex formation with an auxillary ligand, as observed with chromis-1 acid (**2.1b**, Figure 2.1). The Zn(II) complex of **3.3c** was crystallized *in situ* from a mixture of DMSO and H_2O by reacting with a stoichiometric amount of $Zn(ClO_4)_2$ to generate triclinic colorless crystals suitable for X-ray crystallography. As illustrated in Figure 3.12A, the [(**3.3c**)Zn(II)] complex adopts a trigonal bipyramidal coordination geometry about the Zn(II) center. Given the Hammett parameter of isonicotinicate (σ_p = 0.0), it was hypothesized that the lack of the anionic carboxylates would not distort the N-Zn bond lengths of the bispicolylamine chelator moiety. To assess this, the N-Zn bond lengths for the bispicolylamine pyridines of the [(**3.3c**)Zn(II)] complex were compared to [(chromis-1)Zn(II)] complex. Analysis of the two bispicolylamine N-Zn bonds of both conformers in the [(chromis-1)Zn(II)] complex's unit cell yields an average N-Zn bond length of 2.099 ± 0.01 Å. The analogous N-Zn bonds of the [(**3.3c**)Zn(II)] complex displayed an average bond length 2.038 ± 0.001 Å, corresponding to a bond elongation of 0.06 Å compared to chromis-1. This bond elongation suggests that the carboxylic acids render the pyridine(N)-Zn bonds of chromis-1 less basic, thus translating to a weaker interaction with the Zn(II) ion. In addition, comparison of the pyridyl acceptor N-Zn bond of chromis-1 (2.100 ± 0.002 Å) and **3.3c** (2.044 Å) demonstrates a stronger interaction between the pyridine and the zinc ion due to the shortened (by 0.56 Å) bond distance. In contrast to chromis-1, the unit cell of the triclinic crystals of [(**3.3c**)Zn(II)] displayed well-ordered packing, as evidenced by Figure 3.12B. Analysis of each of the four molecules within the unit cell indicated identical bond distances angles between the nitrogen donors and Zn(II) center (Table 3.6). in addition, the fluorophore core displayed identical torsional angles, which deviated negligibly

from planarity, in contrast to chromis-1, in which the anisole moiety of one of the two conformers was rotated out of plane by 35° relative to the thiazole ring. For further information regarding the structural properties of the [(**3.3c**)Zn(II)], see Tables A.4-A.6 in Appendix A.

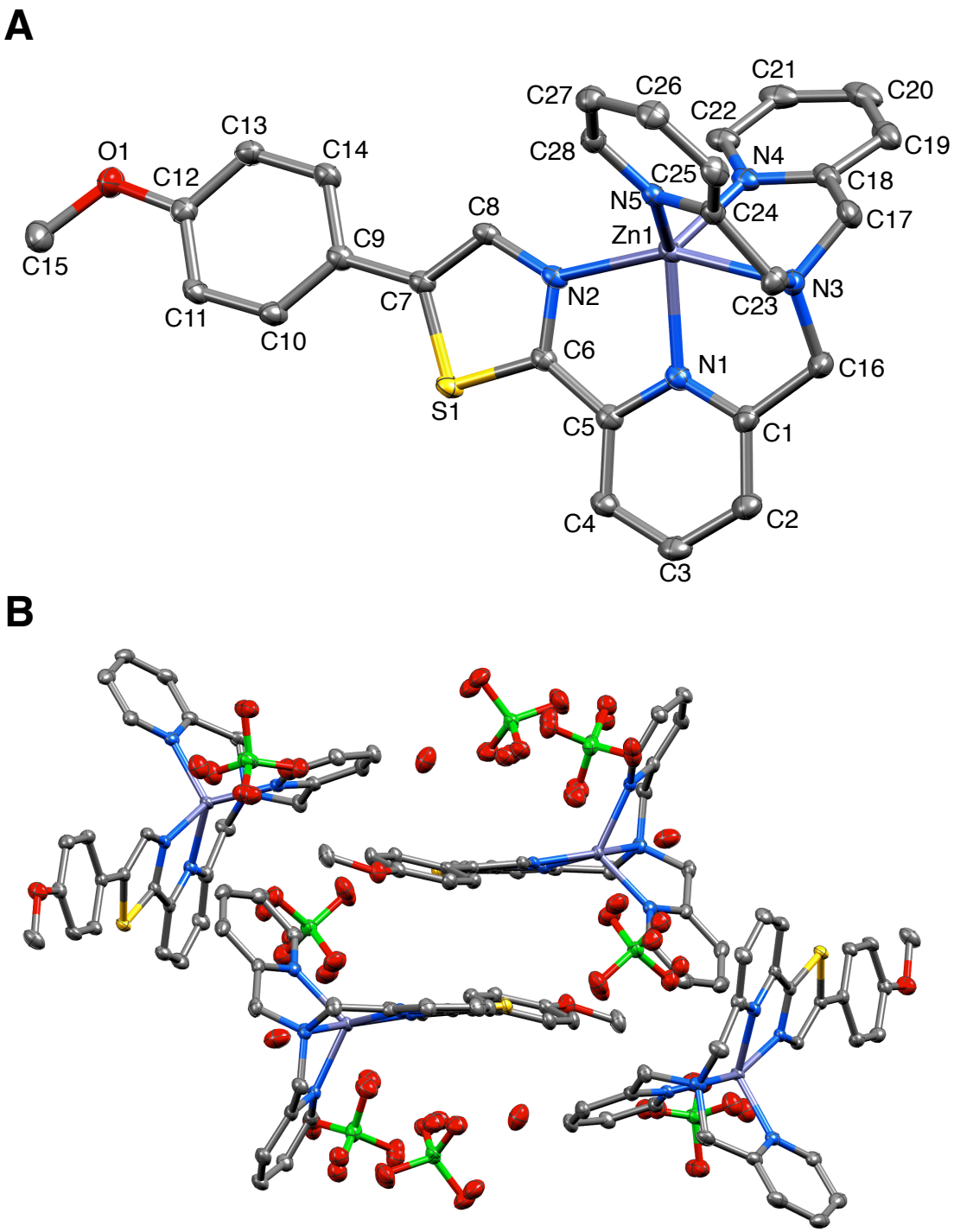

Figure 3.12: (A) ORTEP representation and atom number scheme for the Zn(II) complex of **3.3c**: [(**3.3c**)Zn(II)]. Ellipsoids shown represent 50% probability. Hydrogen atoms and counter ions have been omitted for clarity. (B) ORTEP presentation of the unit cell packing for [(**3.3c**)Zn(II)], showing the symmetry within the crystal. Hydrogen atoms have been omitted for clarity.

*3.4.3 Steady-State Absorption and Fluorescence Properties of Probe **3.3b***

Analogous to chromis-1 acid (**2.1b**), the anionic carboxylates of **3.3b** permitted the preparation of aqueous stock solutions at millimolar concentrations without the need for organic solvents as cosolvents. When diluted into aqueous buffer (10 mM PIPES, 100 mM KCl, 25°C, pH 7.0) at micromolar concentrations, the coordination of Zn(II) resulted in large bathochromic shifts in both the absorption and emission, as evidenced by the molar ratio titration of **3.3b** with Zn(II) (Figure 3.13). Consistent with a strong intramolecular charge transfer upon coordination of Zn(II) to the pyridyl acceptor, the absorbance maximum of 348 nm (ε = 23,600 M^{-1} cm^{-1}) is red-shifted by 17 nm when fully saturated with Zn(II) to 365 nm (ε = 21,700 M^{-1} cm^{-1}) (Table 3.3). While the absorbance spectra of free and Zn(II)-saturated **2.1b** and **3.3b** have nearly identical absorbance maxima, the absorbance maximum of Zn(II)-saturated chromis-1 acid (**2.1b**) increases relative to free chromis-1, whereas the absorbance maximum of Zn(II)-saturated **3.3b** decreases relative to free **3.3b**. The presence of clean isosbestic points at 284 and 361 nm, in addition to equimolar saturation of the probe with Zn(II), indicated an unambiguous equilibrium between free **3.3b** and its corresponding Zn(II) complex with a 1:1 binding stoichiometry.

Comparably, the emission maximum of free **3.3b** undergoes a 50-nm bathochromic shift from 465 to 515 nm, 12 nm larger than chromis-1, with a single isosbestic point at 466 nm. By exciting the fluorophore at its isosbestic point, the effected emission intensities are a direct reflection of the quantum yield, which increases more than 2-fold from 0.25 to 0.69. The isomerization of the pyridyl acceptor from the 4-position to the 2-position realized a modest decrease in the quantum yield from 0.32 to 0.25, despite the significant increase in quantum yield from 0.65 to 0.80 for model compounds **3.1** and **3.2**,

respectively, whereas [(**3.3b**)Zn(II)] only decreased 2% from the corresponding Zn(II) complex of chromis-1.

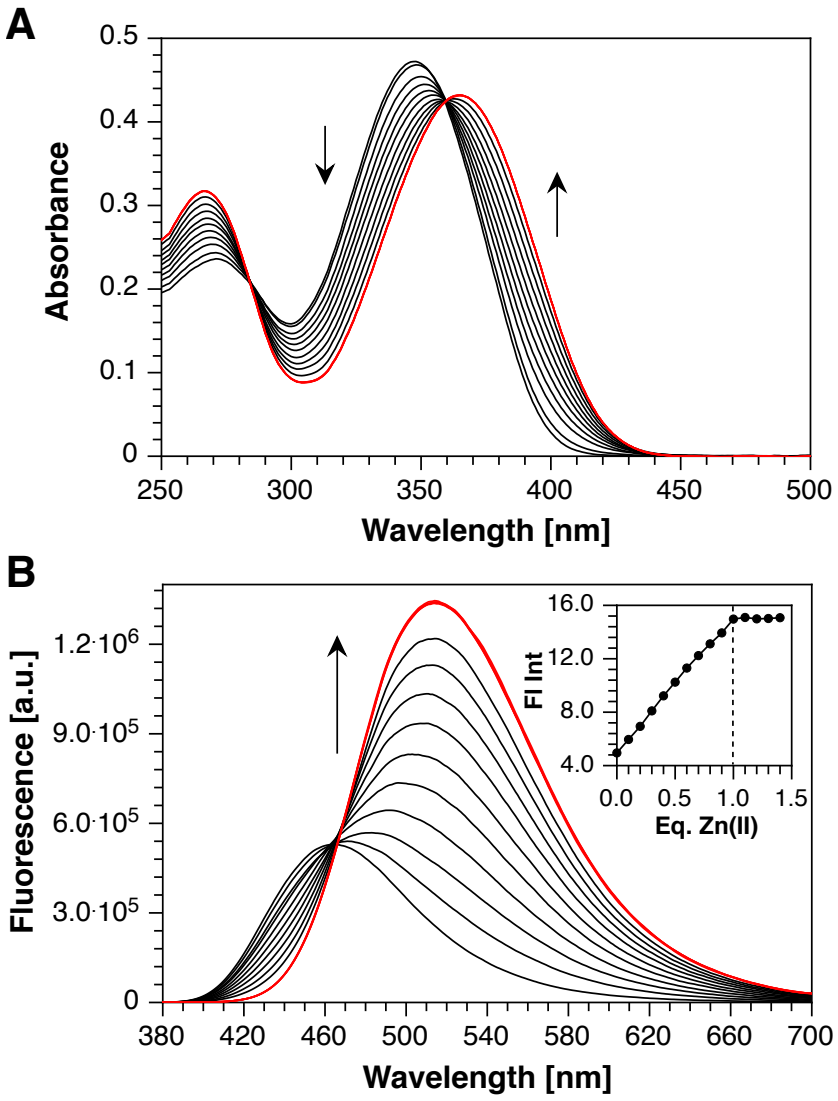

Figure 3.13: Spectral changes of **3.3b** (20 μM) in neutral aqueous buffer (10 mM PIPES, 100 mM KCl, 25°C, pH 7.0) upon stepwise saturation with Zn(II). (A) Absorption (UV-Vis) spectral changes upon saturation with Zn(II). (B) Fluorescence emission response upon saturation with Zn(II) (excitation at 361 nm). Red curves indicate the spectra after complete saturation (1.0 eq.) with Zn(II) is achieved. Inset: fluorescence integration over the entire spectral window as a function of molar equivalents of Zn(II).

Table 3.3: One- and two-photon photophysical properties of **3.3a** and **3.3b** in aqueous buffer at pH 7.0.[a]

	3.3a[b,c]	[(**3.3a**)Zn(II)][b]	**3.3b**[c]	[(**3.3b**)Zn(II)]
Absorbance λ_{max} (nm)[d]	351	367	348	365
ε (10^4 $M^{-1}cm^{-1}$)[e]	2.11	2.22	2.36	2.17
Emission λ_{max} (nm)[f]	434	480	465	515
δ_{max} (GM)[g]	n.d.	n.d.	n.d.	n.d.
λ_{max} (nm)[h]	n.d	n.d.	n.d.	n.d.
Φ_F [i]	0.20	0.27	0.25	0.69

[a]10 mM PIPES, 0.1 M KCl, 25°C. [b]buffer supplemented with 100 μM liposomes (4:1 DMPC:DMPG). [c]supplemented with 20 μM EDTA to sequester adventitious Zn(II). [d]lowest-energy band of the one-photon absorption spectrum. [e]molar extinction coefficient at λ_{max}. [f]maximum fluorescence emission. [g]two-photon absorption cross section. [h]maximum two-photon absorption. [i]fluorescence quantum yield, referenced to quinine sulfate (Φ_F = 0.546 in 1N H_2SO_4).[5] n.d. = not determined.

In an effort to mimic the lipid-rich environment of the cell, as well as to provide a medium in which to dissolve **3.3a**, spectroscopic analysis of the dimethyl ester was performed in the presence of 100 μM liposomes composed of anionic dimyristoyl phosphatidylglycerol (DMPG) lipids. Initial attempts to obtain absorption and emission spectra of free and metal-bound **3.3a** in a 4:1 mixture of zwitterionic dimyristoyl phosphatidylcholine (DMPC) and anionic dimyristoyl phosphatidylglycerol (DMPG) observed a 17-nm red-shift in the absorption upon binding of Zn(II), consistent with the bathochromic absorption shift of **3.3b** in aqueous buffer without liposomes (Figure 3.14A). However, in the emission, binding of Zn(II) to methyl ester **3.3a** demonstrated a dramatic decrease in the fluorescence intensity as well as a vivid broadening of the emission band, which may be indicative of the Zn(II) complex of the probe dissociating from the lipid bilayer (Figure 3.14B). The behavior observed in the emission is most likely attributed to reduced phospholipid solvation due to a smaller lipophilic surface area that can interact with the fatty acid chains. It was hypothesized that increasing the overall anionic charge density of the liposomes

may help stabilize the Zn(II) complex of **3.3a** without adversely affecting the fluorescence response of the free form. Therefore, the absorbance and fluorescence properties of **3.3a** were acquired in 100% DMPG liposomes.

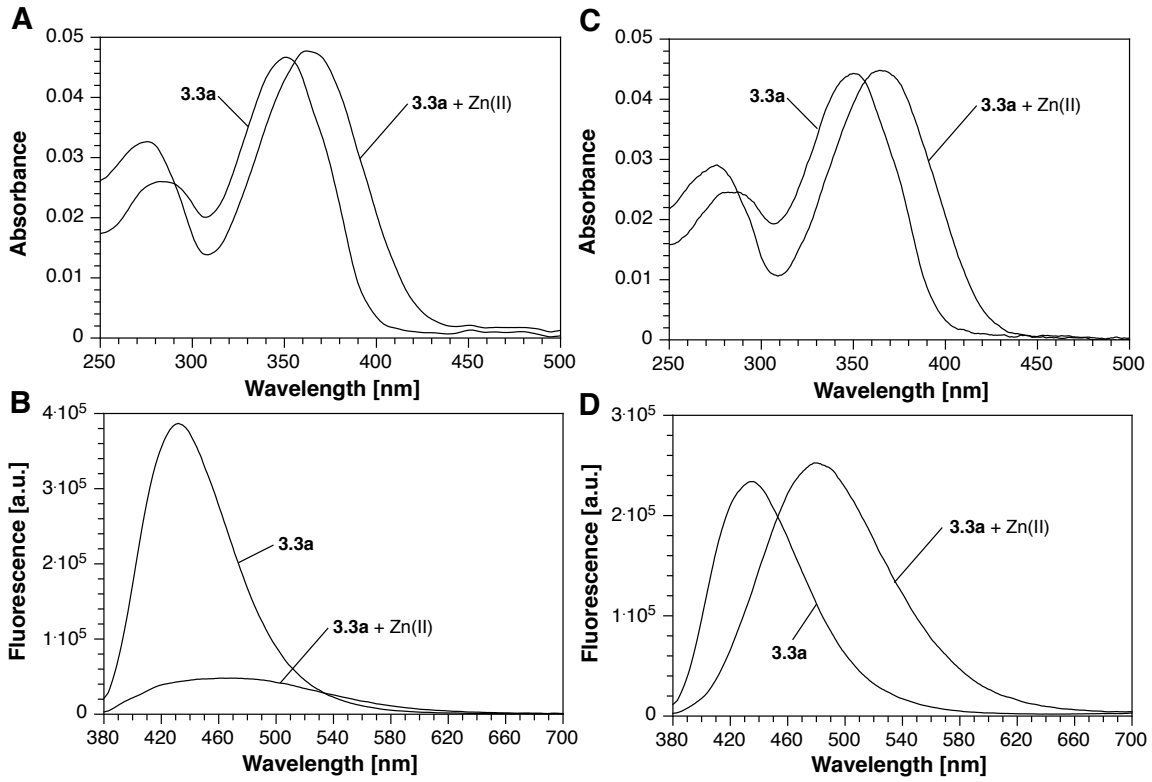

Figure 3.14: Comparison of the absorbance and emission spectral changes of probe **3.3a** upon saturation with Zn(II) between a 4:1 DMPC:DMPG (A,B) lipid mixture and 100% anionic DMPG lipids (C,D) in aqueous buffer (10 mM PIPES, 100 mM KCl, 25°C, pH 7.0). Excitation: 361 nm.

Surprisingly, the anionic liposomes did not induce any absorption shifts of either the free or metal-bound **3.3a** relative to the absorbance maxima in the 4:1 DMPC:DMPG mixture (Figure 3.14C), observing absorbance maxima of 351 nm (ε = 21,100 M^{-1} cm^{-1}) and 367 nm (ε = 22,200 M^{-1} cm^{-1}) for the free- and Zn(II)-bound forms, respectively, in the anionic liposomes (Table 3.3). Conversely, the emission maxima of **3.3a** are blue shifted relative to **3.3b**, demonstrating a 31-nm hypsochromic shift from 465 nm to 434 nm for the free form and a 35-nm blue shift from 515 to 480 nm for the Zn(II)-bound form. In contrast

to the 4:1 DMPC:DMPG liposome mixture, the fluorescence response of Zn(II)-saturated **3.3a** displayed very balanced emission intensities in the anionic liposomes (Figure 3.14D). The presence of the *para*-methyl esters decreased, albeit negligibly, the fluorescence quantum yield of the free form of **3.3a** from 25% (free form of **3.3b**) to 20%, whereas the quantum yield of the Zn(II) significantly decreased to 27%, down 42% relative to the Zn(II)-bound form of **3.3b** (69%).

*3.4.4 The Thiazole Nitrogen of Probe **3.3b** Engages in Zn(II) Coordination to Yield a Higher Affinity than Chromis-1 Acid*

As illustrated in Figure 3.13B (inset) above, a linear fluorescence increase, in conjunction with a sharp saturation at 1.0 equivalent of Zn(II) relative to **3.3b**, indicates Zn(II) binding with near unity fractional saturation over the entire titration range. As mentioned in Chapter 2, reliable stability constants must be determined within a 10-90% fractional saturation window. The additional coordination of the fluorophore's thiazole nitrogen was expected to increase the stability constant for the formation of the Zn(II) complex, therefore demanding a competing ligand with higher affinity for Zn(II) to compete with **3.3b** for coordination. Spectrophotometric and fluorimetric titrations were initially performed using HEDTA (2-(hydroxyethyl)ethylenediaminetriacetic acid) as a competing ligand with an apparent formation constant of logβ = 11.60 at pH 7.0, μ = 0.1 M (calculated from published pK_a's and logβ values).[18] However, the unmatched affinity of HEDTA resulted in a subpar data fit, so a ligand with a slightly weaker apparent affinity for Zn(II) (TMDTA: trimethylenedinitrilotetraacetic acid; logβ = 10.76 at pH 7.0, calculated from published pK_a's and logβ values)[18] was also used to confirm the apparent stability constant of **3.3b**. However, no matter whether EGTA, TMDTA, or HEDTA were titrated against the preformed [(**3.3b**)Zn(II)] complex, non-linear, least-squares fitting of all spectroscopic data afforded

a uniform apparent stability constant of $\log K_{Zn(II)L} = 10.8 \pm 0.05$, equivalent to an apparent dissociation constant of 16 pM at pH 7.0 and $I = 0.1$ M KCl (Figure 3.15).

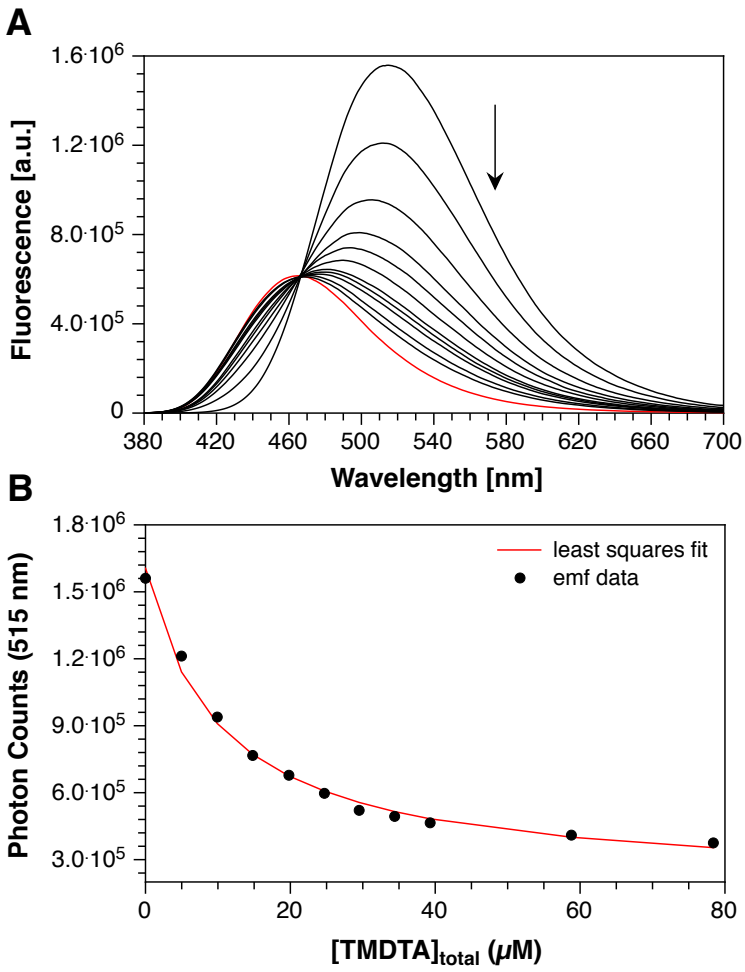

Definition of Equilibrium System:

Species	Zn(II)	TMDTA	**3.3b**	H	log β
Zn(II)	1	0	0	0	0
TMDTA	0	1	0	0	0
3.3b	0	0	1	0	0
TMDTA(H)	0	1	0	1	10.41
TMDTA(H_2)	0	1	0	2	18.42
TMDTA(H_3)	0	1	0	3	21.16
[(TMDTA)Zn(II)]	1	1	0	0	15.22
[(**3.3b**)Zn(II)]	1	0	1	0	*10.8 ± 0.05*

Figure 3.15: A) Fluorimetric determination of the Zn(II) stability constant of **3.3b** via a competition titration with TMDTA. Probe **3.3b** (10 μM) was equilibrated $ZnSO_4 \cdot 7H_2O$ (10 μM) in aqueous buffer (10 mM PIPES, 0.1 M KCl, pH 7.0, 25ºC, treated with Chelex (1% (w/v), Biorad) and titrated with TMDTA to a final concentration of 80 μM. The fluorescence spectra (excitation: 361 nm) were analyzed by non-linear least squares fitting to give an average $\log K_{Zn(II)L}$ of 10.8 ± 0.05 (n = 3). Red curve corresponds to free **3.3b** before saturation with Zn(II). B) Change in fluorescence response at 515 nm with corresponding fit to the equilibrium system model.

Because the anionic carboxylate groups render **3.3b** cell membrane-impermeable, live-cell, two-photon microscopy was performed with the dimethyl ester derivative **3.3a**, which is readily internalized into the cell. Compared to **2.1a**, it was hypothesized that substitution of the ethyl esters with methyl esters would enable faster rates of hydrolysis of the esters to the corresponding water-soluble carboxylic acids by means of non-specific intracellular esterases. However, incubation and subsequent imaging studies with **3.3a** showed punctate staining patterns indicative of membrane partitioning, demonstrating that hydrolysis of the methyl esters did not occur within the time frame of cellular imaging. Therefore, it was imperative that the apparent stability constant of **3.3a** be determined to correlate the ratio values calculated directly from the live-cell imaging data with the fractional saturation. Upon incubation (~ 10 minutes) in pH 7.0 buffer (20 mM PIPES, 100 mM KCl, 25°C) supplemented with 200 μM EGTA and 100 μM of the liposome mixture used with **2.1a**, fluorophore **3.3a** (2 μM) was titrated with $ZnSO_4 \cdot 7H_2O$ from 0-180 μM. Non-linear least squares fitting of the fluorimetric emf data (3 titrations) yielded an average $\log K_{Zn(II)L} = 9.57 \pm 0.05$, corresponding to an apparent K_d of 309 ± 0.3 nM (Figure 3.16). Due to the presence of the stronger electron-withdrawing ester substituents relative to the anionic dicarboxylate substituents in **3.3b**, **3.3a** exhibits a $\log K$ that is ~ 1.5 log units lower than **3.3b**.

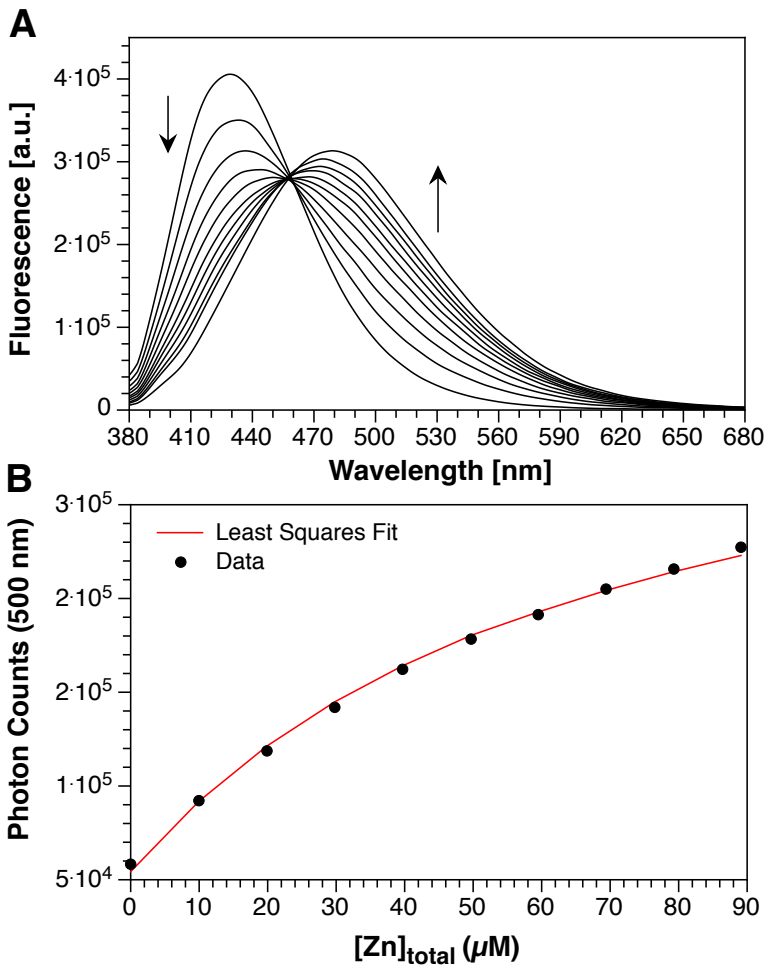

Definition of Equilibrium System:

Species	Zn(II)	EGTA	**3.3a**	H	log β
Zn(II)	1	0	0	0	0
EGTA	0	1	0	0	0
3.3a	0	0	1	0	0
EGTA(H)	0	1	0	1	9.51
EGTA(H_2)	0	1	0	2	18.41
EGTA(H_3)	0	1	0	3	21.22
[(EGTA)Zn(II)]	1	1	0	0	12.6
[(**3.3a**)Zn(II)]	1	0	1	0	*9.57 ± 0.05*

Figure 3.16: A) Fluorimetric determination of the Zn(II) stability constant of **3.3a** via a metal-addition titration in the presence of EGTA in liposomes. Methyl ester **3.3a** (2 μM) was equilibrated with EGTA (100 μM) in aqueous buffer (20 mM PIPES, 0.1 M KCl, pH 7.0, 25ºC and supplemented with DMPG liposomes (100 μM) and titrated with $ZnSO_4 \cdot 7H_2O$ to a final concentration of 90 μM. The fluorescence spectra (excitation: 361 nm) were analyzed by non-linear least squares fitting to give an average $\log K_{Zn(II)L}$ of 9.57 ± 0.05 (n = 3). B) Change in fluorescence response at 500 nm with corresponding fit to the equilibrium system model described above.

*3.4.5 Metal-Ion Selectivity of Probe **3.3b***

As observed with chromis-1 acid (**2.1b**), the addition of an excess (4.0 and 8.0 eq.) of biologically relevant divalent metals resulted in no change in the fluorescence response (with Mg(II) and Ca(II), Figure 3.17A, B) or elicited a complete quenching of the fluorescence response (with all transition metals excluding Zn(II), Figure 3.17C-G) of **3.3b**. Therefore, to evaluate the metal-ion selectivity of **3.3b**, the 80:20 fractional saturation method developed for determining the metal-ion selectivity of chromis-1 (Chapter 2) was employed for **3.3b**. The ratiometric response of the probe was evaluated in the presence of 0.80 molar equivalents (80% fractional saturation) of the interfering divalent transition metal ions (Figure 3.18, black bars), which resulted in quenching of the probe's fluorescence stoichiometrically, while the remaining 20% of free probe remained unaffected by any of the quenching metal ions. Saturation of the remaining 0.2 molar equivalents of the probe with Zn(II) produced a ratiometric readout consistent with the emission response of the [(**3.3b**)Zn(II)] complex that was observed in the molar ratio titration (Figure 3.18, red patterned bars).

Despite the lack of influence of 20 and 40 μM Ca(II) on the emission response of **3.3b** (Figure 3.17B), the addition of 2 mM Ca(II) resulted in an increase in and broadening of the emission profile of the probe (Figure 3.19B) and engendered a slight increase in the emission ratio compared to the probe before the addition of Ca(II). While the response of the probe to millimolar concentrations of Ca(II) could be attributed to the engagement of the thiazole nitrogen in coordinating the metal cation, supplementation of 1.0 equivalent of Zn(II) immediately outcompeted the Ca(II) and restored the fluorescence to the [(**3.3b**)Zn(II)] complex, as expected. The higher affinity of **3.3b** derived from metal coordination to the thiazole nitrogen resulted in a stoichiometric quenching of Mn(II) similar to

the other divalent transition metals tested, whereas chromis-1 acid did not observe stoichiometric quenching by Mn(II). Despite the appearance of tight Mn(II) binding with near unit fractional upon the addition of Mn(II), supplementation of 1 μM Zn(II) to saturate the remaining 20% of free **3.3b** did not indicate a complete shift to the emission maximum of the Zn(II) complex in the absence of any interfering metal ions, suggesting that the affinity of the probe for Mn(II) is weak enough for Zn(II) to outcompete Mn(II). Therefore, in the presence of 0.8 molar equivalents of Mn(II), the addition of 5 μM Zn(II) immediately restored the emission response to that of the [(**3.3b**)Zn(II)] complex (Figure 3.19C). Fe(II) displayed similar effects, although the kinetics for exchange were significantly slower and required ~ 30 to reach equilibrium (Figure 3.19D)

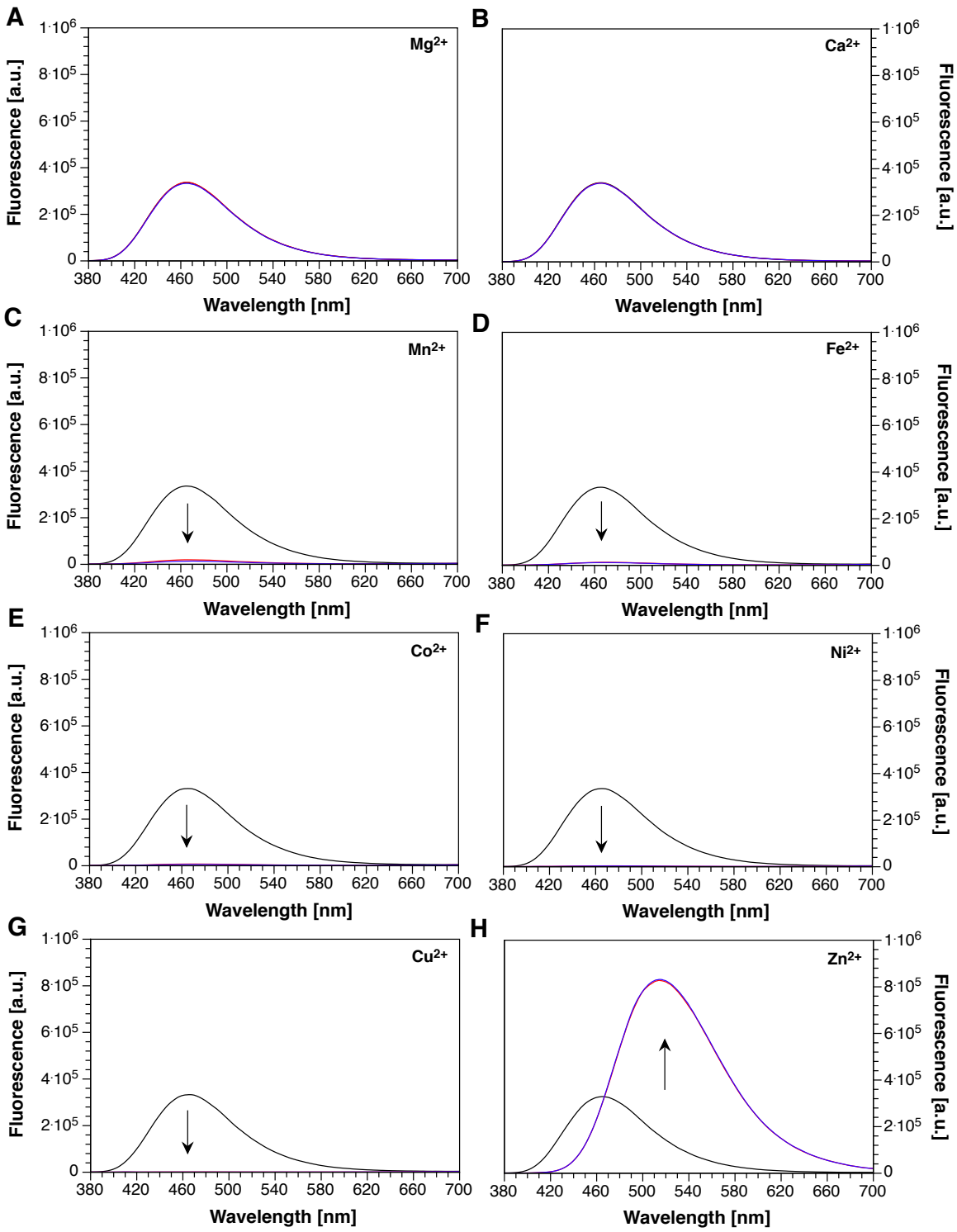

Figure 3.17: Fluorescence response of **3.3b** in the presence of an excess (4.0 and 8.0 equivalents) of interfering divalent metal ions. A-H) Black traces represent free **3.3b** (5 μM) in pH 7.0 buffer (10 mM PIPES, 0.1 M KCl, 25°C) supplemented with 10 μM EDTA. Red and blue traces represent the addition of 20 μM and 40 μM, respectively, of divalent metal ions. Excitation: 361 nm.

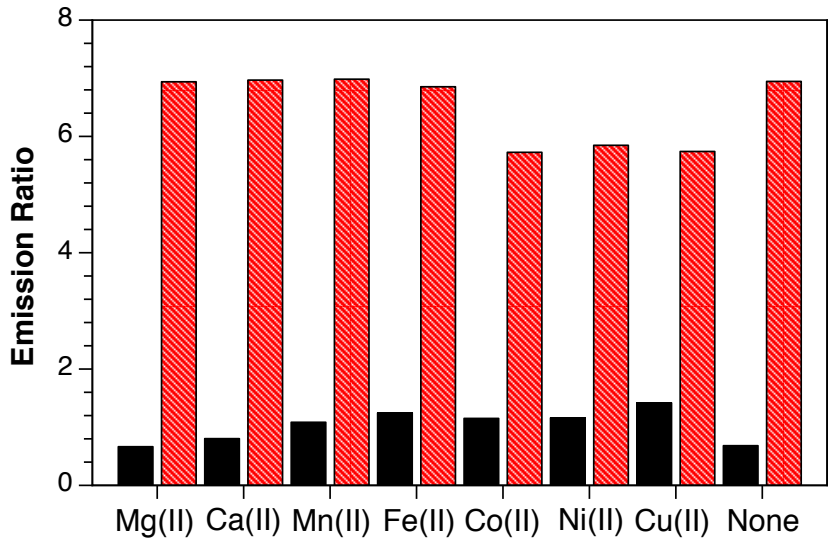

Figure 3.18: Emission-ratiometric response of **3.3b** (5 μM) towards selected divalent metal cations at 80% fractional saturation (calculated based on the ratio of the integrated fluorescence intensity between 510-570 nm (channel 2) and 440-495 nm (channel 1)). The black bars represent the ratio at 80% fractional saturation, and the corresponding patterned red bars represent the ratio after saturating the remaining 20% of free probe with Zn(II). Excitation: 361 nm.

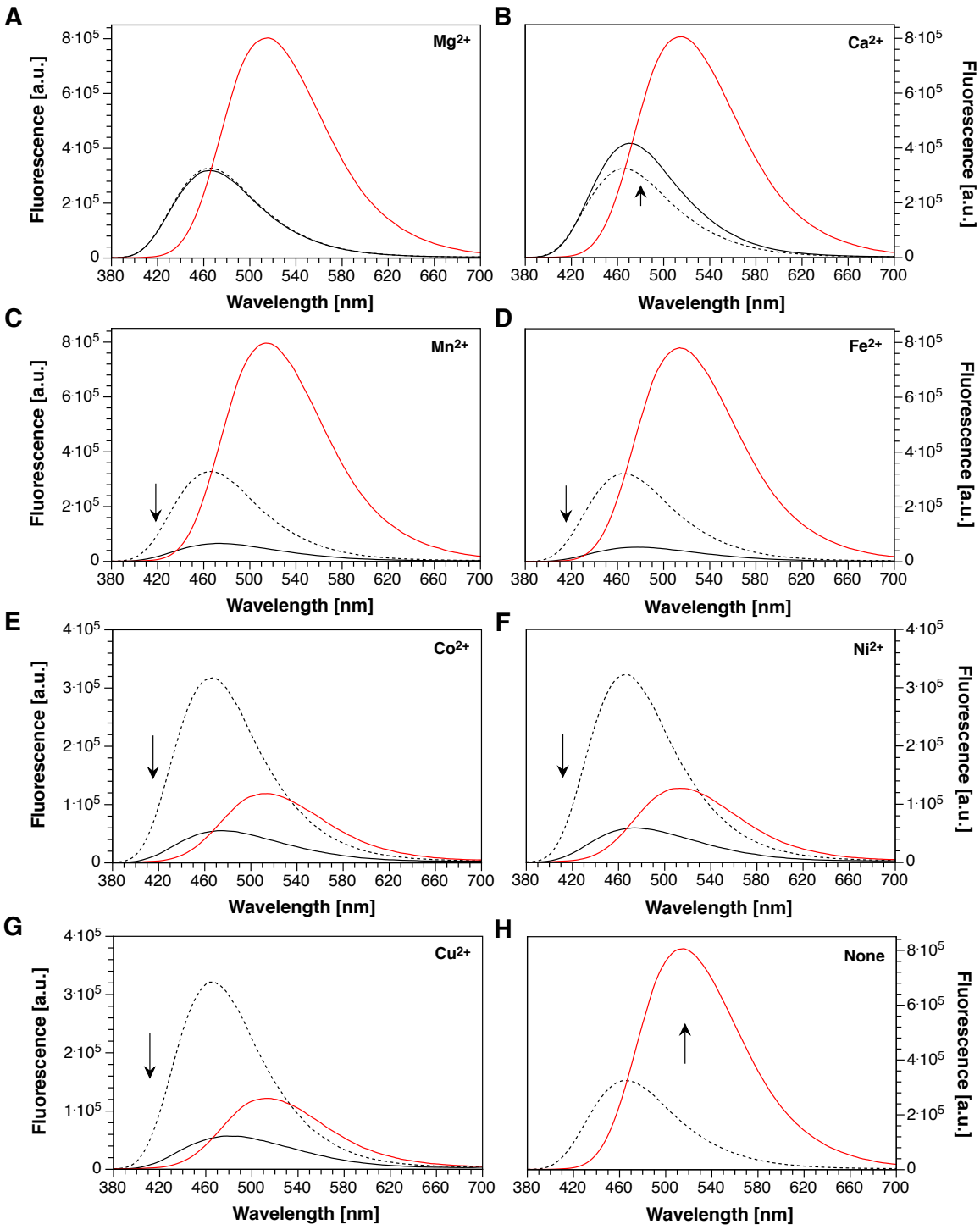

Figure 3.19: Fluorescence spectral response of **3.3b** (5 μM) to selected interfering divalent metal ions in aqueous buffer (10 mM PIPES, 0.1 M KCl, pH 7.0 25°C). A-H) Black dashed traces represent free **3.3b**, and the corresponding solid black traces indicate the response upon incremental supplementation with interfering divalent metal ions. Upon quenching 80% of **3.3b** with interfering metal ions (C-G), the remaining 20% of **3.3b** was saturated with Zn(II) (red traces). Excitation: 361 nm.

*3.4.6 Spectrophotometric Determination of the Protonation Constants of Probe **3.3b***

Analogous to the 3.4 log-unit difference in the ground-state pK_a of the pyridyl acceptor between chromis-1 acid and its corresponding model compound (**3.1**), the presence of the bispicolylamine chelator of **3.3b** was expected to significantly decrease the pK_a of its pyridyl acceptor by several orders of magnitude compared to that of model compound **3.2**. However, since the pK_a of the pyridyl acceptor of chromis-1 acid already has a significantly acidic pKa (pK_a = 1.1), the structural change between chromis-1 and **3.3b** was not expected to manifest a pK_a difference comparable to the two log-unit decrease between model compound (**3.1**) and its corresponding 2-thiazolyl isomer **3.2**.

Spectrophotometric and fluorimetric pH titrations of **3.3b** to determine the protonation constants of the probe observed quite different spectroscopic properties upon incremental acidification of the solution. As illustrated in Figure 3.20A below, as the pH was lowered from 7.0 to 5.0, minimal changes in the absorbance were observed with **3.3b**, which is consistent with those observed with chromis-1 acid. Interestingly, while the absorbance spectra of both **3.3b** and chromis-1 acid had similar molar absorptivity coefficients at pH 2.0, **3.3b** observed a minimal ~ 8-nm red shift between pH 7.0 and pH 2.0, whereas chromis-1 acid demonstrated a significant 50-nm red-shift from 350 nm at pH 7.0 to 400 nm at pH 2.0. Further acidification from pH 2.0 to 1.0 revealed a ~ 50% increase in the absorbance yet a negligible 2-nm red shift of the absorption maxima from 356 to 358 nm. In the emission, however, while the analogous pH change from 7.0 to 5.0 observed a similar ~ 50% decrease in the emission intensity compared to chromis-1 acid, the intensity of the emission band at 560 nm was significantly reduced compared to the fluorescence intensity of the same emission band in the titration with chromis-1 acid (Fig-

ure 3.20B). Nevertheless, fitting of the spectrophotometric emf data to a triprotic equilibrium model and spectral deconvolution (Figure 3.20C) yielded pK_a values for **3.3b** of 0.9, 3.1 and 5.9 (Figure 3.20D). Using previously discussed rationale, the pK_a of 0.9 most likely corresponds to the pK_a of the pyridyl acceptor of **3.3b**, revealing a negligible 0.2 log-unit reduction in the pK_a compared to the pyridyl acceptor chromis-1 acid (Figure 3.20E). Otherwise, the two macroscopic pK_a's that most likely correspond to protonation of the two chelator pyridines agree well with those of chromis-1 acid.

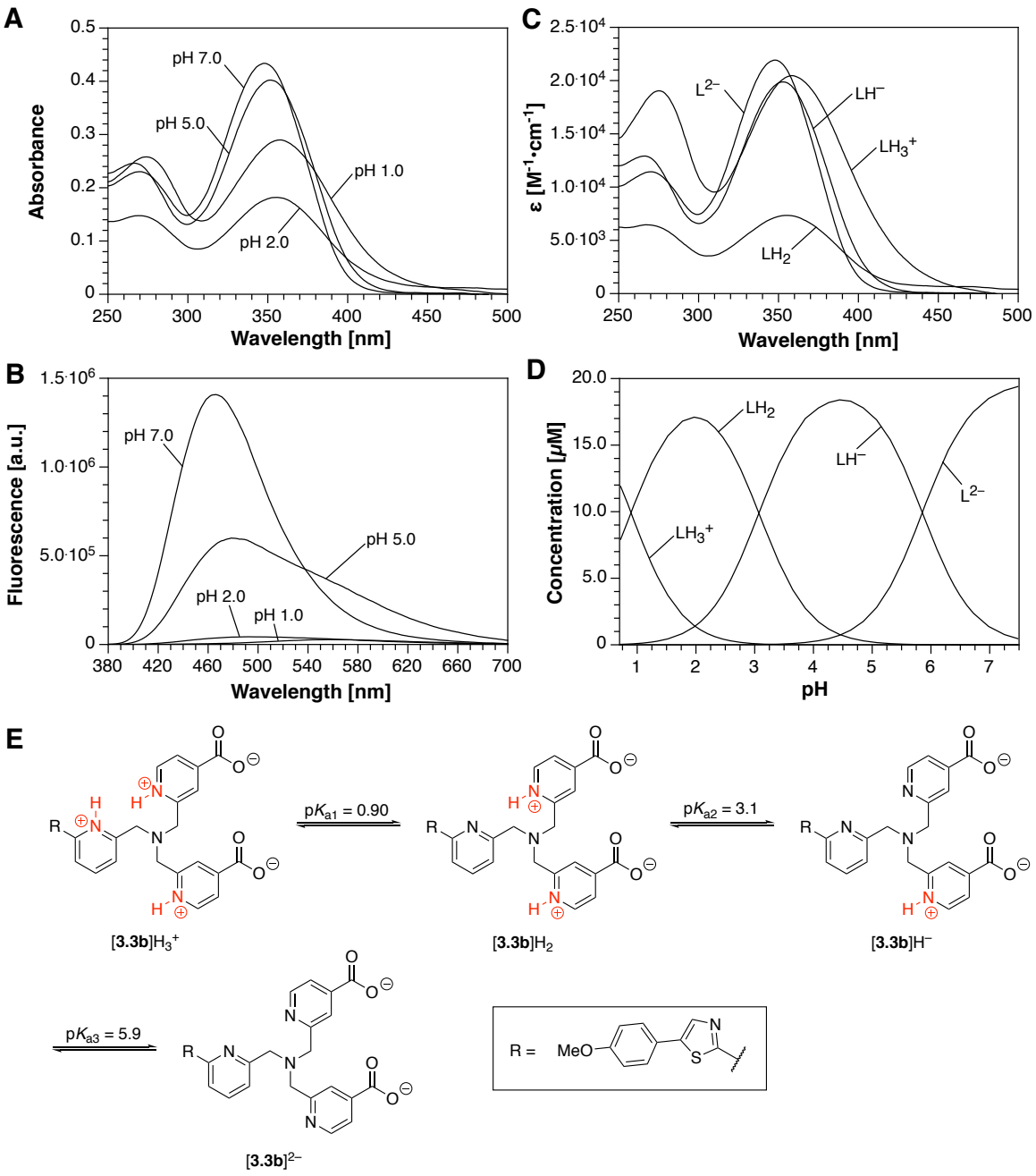

Figure 3.20: Spectrophotometric determination of the macroscopic protonation constants of **3.3b** (20 μM). A) Spectrophotometric (UV-Vis) and B) fluorimetric spectral changes over the pH range of 7.0-1.0. C) Species distribution of chromis-1 throughout the spectrophotometric (UV-Vis) titration. D) Deconvoluted spectra of UV-Vis titration data, depicting the absorbance spectra of each species shown in (A). E) Schematic representing the species corresponding to the three individual protonation constants, determined from the UV-Vis spectrophotometric titration shown in (A). L: ligand, **3.3b**.

*3.4.7 Solvent Deuterium Isotope Effect of Probe **3.3b***

The elimination of a deuterium isotope effect with model compound **3.2**, in addition to a reduction in both the ground-state basicity and photobasicity as a consequence of isomerization of the acceptor pyridine, demonstrated auspicious rationale for incorporating the new fluorophore design into the development of **3.3b** as a fluorescent probe with reduced pH sensitivity. However, when the fluorescence response of the probe was compared in both deuterated and non-deuterated buffers, **3.3b** saw a 10% increase in the fluorescence intensity of free **3.3b** in deuterated buffer compared to non-deuterated buffer, despite identical emission intensities of the Zn(II)-saturated species to rule out pipetting error (Figure 3.21A). Not only was the increase in fluorescence intensity of **3.3b** lower than that of chromis-1 (10% compared to 16%) between deuterated and non-deuterated buffers, but also normalization of both the two spectra of metal-free **3.3b** revealed superimposable spectra, unlike chromis-1, which displayed a more-narrow emission band in D_2O relative to H_2O (Figure 3.21B).

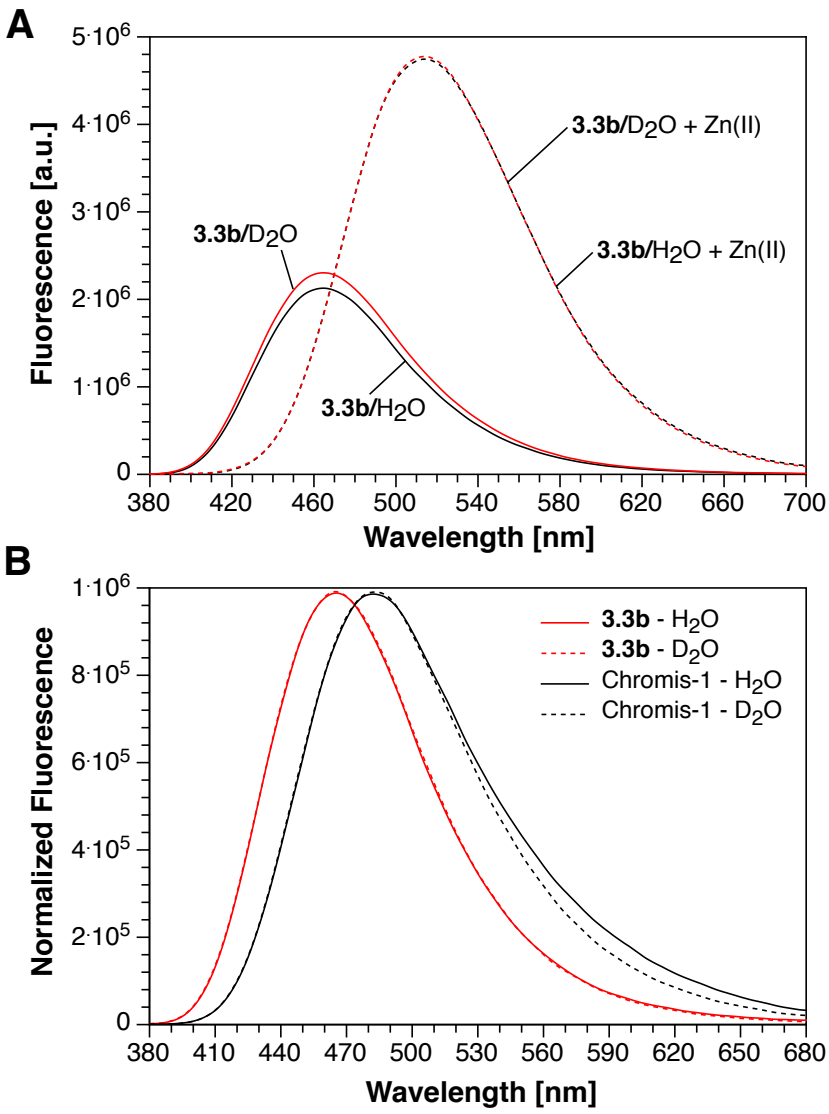

Figure 3.21: A) Solvent deuterium isotope effect of **3.3b** (5 μM) in deuterated versus non-deuterated buffer (10 mM PIPES, 100 mM KCl, pH/D 7.0, 25°C). B) Comparison of the normalized emission spectra of the free form of **3.3b** in (A) to chromis-1 acid from Figure 3.6B. Excitation: 361 nm.

Based on these observations, it was deduced that isomerization of the pyridyl acceptor of chromis-1 to the 2-thiazolyl position did not fully eliminate the excited-state protonation. The discrepancies between the deuterium isotope effects of fluorophore **3.3b** and model compound **3.2** furnished speculation that the excited-state protonation was, in fact, a proton-transfer phenomenon that was manifested from partial protonation of one of

the bispicolylamine pyridines even at neutral pH, inducing an excited-state intramolecular proton transfer (ESIPT) rather than direct protonation of the fluorophore pyridine from the aqueous buffer. This hypothesis led to examining the effect of the chelator moiety on ESPT.

3.5 Suppressing Excited-State Proton Transfer with The Development of Chromis-2

The electron-withdrawing capacity of the both the *p*-ester and the *p*-carboxylate substituents of the bispicolylamine chelator can have a dramatic effect on the basicity of the pyridine nitrogens, which are hypothesized to play a role in ESPT to the pyridyl acceptor of the fluorophore. Considering the differences in the Hammett parameters (σ_p)[19] between the *para*-ethyl ester (σ_p = 0.45) and the anionic carboxylate (σ_p = 0.0) substituents, the more strongly electron-withdrawing methyl esters render the pyridine nitrogens less basic and thus less likely to be protonated at or near neutral pH. To put this into perspective, analysis of the emission spectral response of chromis-1 ester (**2.1a**) in liposomes displayed more balanced emission intensities for the free and metal-bound species (Figure 2.11) compared to those of chromis-1 acid (**2.1b**), even with excitation at the isosbestic point to ensure that the emission intensities directly reflected the quantum yields of both species in solution.

The more balanced emission intensities for the free and metal-bound species of chromis-1 ester (**2.1a**) compared to chromis-1 acid (**2.1b**) can be attributed to the less basic nitrogens of **2.1a** resulting in a less-favorable ESPT process, thus increasing the emission intensity of the metal-free species. Because the fluorescence intensity of **3.3a** significantly decreases upon saturation with Zn(II) relative to the metal-free species in the

4:1 DMPC:DMPG liposome mixture used previously, which is most likely attributed to reduced phospholipid solvation due to a smaller lipophilic surface area for interacting with the lipid bilayer, the comparison of the emission responses of both free and Zn(II)-saturated **3.3a** is less convincing than **2.1a**. Nonetheless, the emission spectra responses between the ester and acid derivatives furnished momentum to explore less-basic, nitrogen-containing heterocycles to replace the bis(2-pyridylmethyl)amine in the chelator moiety, while still permitting the selective binding of Zn(II) with sufficient affinity to be applicable for imaging live cells.

The search for nitrogen-containing heteroaromatic groups with significantly lower basicities than pyridine led to exploring the effect of substituting the pyridine rings of the bispicolylamine chelator with pyrimidine (pK_a = 1.3).[20] Since a pyrimidine analog of bispicolylamine had neither been previously synthesized nor used as a Zn(II) chelator, the methods implemented in the synthesis of **3.17** from 2-cyanoisonicotinic acid were adopted, albeit modified, for the synthesis of a bis(2-pyrimidylmethyl)amine chelator that was coupled to the aldehyde of the 2-thiazolyl fluorophore core to generate a Zn(II)-selective probe for elucidating the mechanism of ESPT.

3.5.1 Synthesis of Chromis-2

Aldehyde **3.16** was designed to serve as a platform to facilitate the facile synthesis of various Zn(II)-binding fluorophores through trivial reductive couplings with primary or secondary amine-containing chelators. Because the envisioned bis(2-pyrimidylmethyl)amine chelator had not been synthesized before, a similar dimerization method used in the preparation of the dimethyl ester-substituted bispicolylamine **3.17** was adopted and further optimized to be applicable for the preparation of the new chelator moiety. Synthe-

sis of the bis(2-pyrimidinylmethyl)amine chelator **3.19** was accomplished by a one-pot dimerization of 2-pyrimidinecarbonitrile in 1:1 dioxane:water (Scheme 3.7). Despite using EtOH:H_2O as the solvent mixture in the assembly of **3.17**, adoption of these reaction conditions for the preparation of **3.19** furnished a significant amount of the imine ethyl ester, suggesting that the kinetics of nucleophilic addition of EtOH to 2-pyrimidinecarbonitrile are faster than the reduction of the nitrile to the corresponding imine. It was hypothesized that the addition of a weak acid, such as AcOH, would facilitate the hydrolysis of the imine intermediate to the corresponding aldehyde, thus shifting the equilibrium towards the reductively coupled intermediate. Interestingly, the addition of 1.0 equivalent of AcOH resulted in a modest 13% yield of bis(2-pyrimidinylmethyl)amine, whereas the absence of any weak acid resulted in a 45% yield, suggesting that the AcOH may favor reduction of the imine intermediate to the primary amine before reductive coupling can occur.

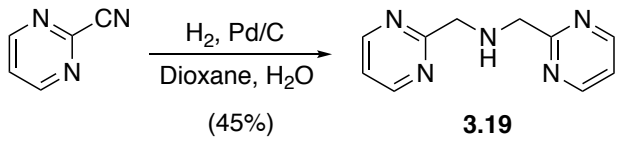

Scheme 3.7: One-pot synthesis of bis(2-pyrimidylmethyl)amine **3.19** from commercially available 2-pyrimidylcarbonitrile.

Upon preparation of bis(2-pyrimidylmethyl)amine **3.19**, reductive amination with aldehyde **3.16** afforded in analytical purity chromis-2 (**3.4**) in 70% yield after recrystallization from boiling cyclohexane:MTBE (Scheme 3.8).

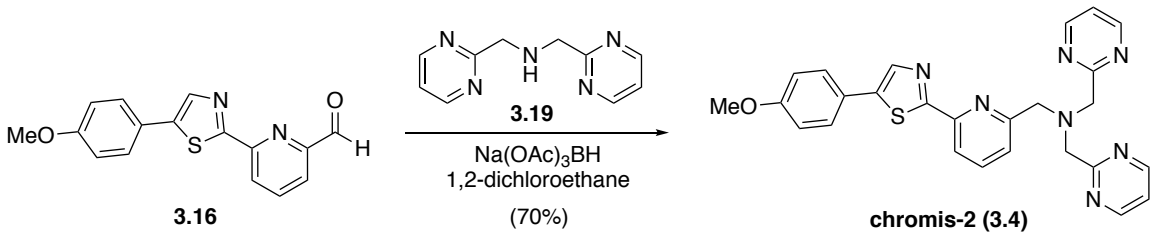

Scheme 3.8: Synthesis of chromis-2 (**3.4**) from aldehyde **3.16**.

3.5.2 Chromis-2 Demonstrates the Absence of a Solvent Deuterium Isotope Effect

To experimentally determine whether the Zn(II)-binding ligand of the probe participated in ESPT to the pyridyl acceptor of the fluorophore, the emission response of chromis-2 was measured in deuterated versus non-deuterated buffer (10 mM PIPES, 100 mM KCl, 25°C, pH/D 7.0) and compared to the emission responses of **3.3b** under identical conditions. While **3.3b** exhibited a 10% increase in the fluorescence intensity in deuterated compared to non-deuterated buffer (Figure 3.22A), substitution of bis(2-pyridylmethyl)-amine with bis(2-pyrimidylmethyl)amine in the development of chromis-2 (**3.4**) engendered no change in the emission intensity or profile between deuterated and non-deuterated buffer (Figure 3.22B). In addition, examination of the emission intensities of the free- and Zn(II)-bound species in aqueous buffer revealed a nearly completely balanced emission response (blue/purple solid/dashed curves). These observations corroborated the eradication of the ESPT phenomenon.

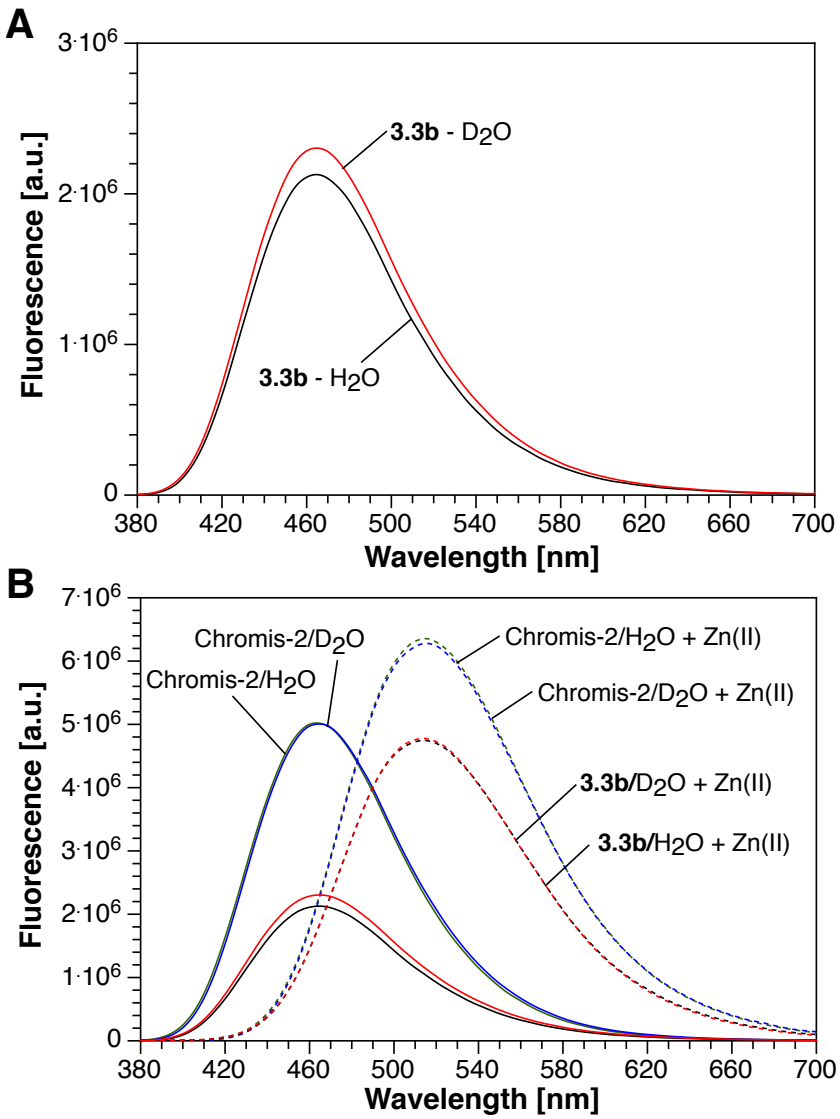

Figure 3.22: Comparison of the solvent deuterium isotope effects between **3.3b** and chromis-2 (**3.4**). (A) Measurement of the fluorescence intensity of **3.3b** (5 μM) in deuterated and non-deuterated aqueous buffer (10 mM PIPES, 0.1 M KCl, pH/D 7.0, 25°C). (B) Comparison between chromis-2 and **3.3b** (5 μM each) in deuterated and non-deuterated aqueous buffer, demonstrating the increase in quantum yield of free and Zn(II)-saturated chromis-2, as well as the eradication of the solvent isotope effect for chromis-2 and its balanced emission intensities.

3.5.3 X-Ray Crystallographic Characterization of Chromis-2

The [(chromis-2)Zn(II)] complex was crystallized *in situ* as the tetrafluoroborate adduct from a mixture of water and methanol to produce monoclinic crystals with the formula $[(\text{chromis-2})\cdot\text{Zn(II)}](BF_4)_2\cdot 2H_2O$. A list of selected bond angles and distances is

listed Table A.8 of Appendix A. As illustrated in Figure 3.23A, crystallization of the [(chromis-2)Zn(II)] complex revealed a heteroleptic ternary complex with a water molecule coordinated to the Zn(II) center in the axial position, resulting in a six-coordinate Zn(II) that adopts a slightly distorted octahedral geometry about the metal ion. Unlike the [(**3.3c**)Zn(II)] complex (Figure 3.12), which displayed a binary ligand-metal complex with a 5-coordinate Zn(II), the coordination of a water molecule to Zn(II) in the [(chromis-2)Zn(II)] complex suggests that the less-basic pyrimidine nitrogens that contribute to a lower affinity for Zn(II) result in a ligand-metal complex with higher metal coordination numbers, as is the case with $[Zn(OH_2)_6]^{2+}$.

The absence of any aromatic substituents on the bispicolylamine chelator of **3.3c** provides an excellent comparison of the crystallographic data of its Zn(II) complex to those for the [(chromis-2)Zn(II)] complex. Analysis of the pyrimidine N-Zn bond distances of [(chromis-2)Zn(II)] shows an average bond elongation of 0.60 ± 0.007 Å relative to the corresponding pyridine N-Zn bonds in the [(**3.3c**)Zn(II)] complex, signifying a weaker metal-ligand interaction as a consequence of pyrimidine's reduced basicity compared to the pyridine nitrogen donors. In addition, the aliphatic tertiary amine N-Zn bond distance is elongated by 0.13 Å compared to the analogous N-Zn bond in **3.3c**, which provides evidence that the electron-withdrawing character of the pyrimidines has a substantial effect on the basicity of the tertiary amine. Surprisingly, the N-Zn bond distances for both the fluorophore pyridine and the thiazole nitrogen are elongated by 0.07 Å and 0.05 Å, respectively, in the [(chromis-2)Zn(II)] complex compared to the [(**3.3c**)Zn(II)] complex. The unit cell of the [(chromis-2)Zn(II)] complex also displayed textbook symmetry, as evident from the packing diagram shown in Figure 3.23B.

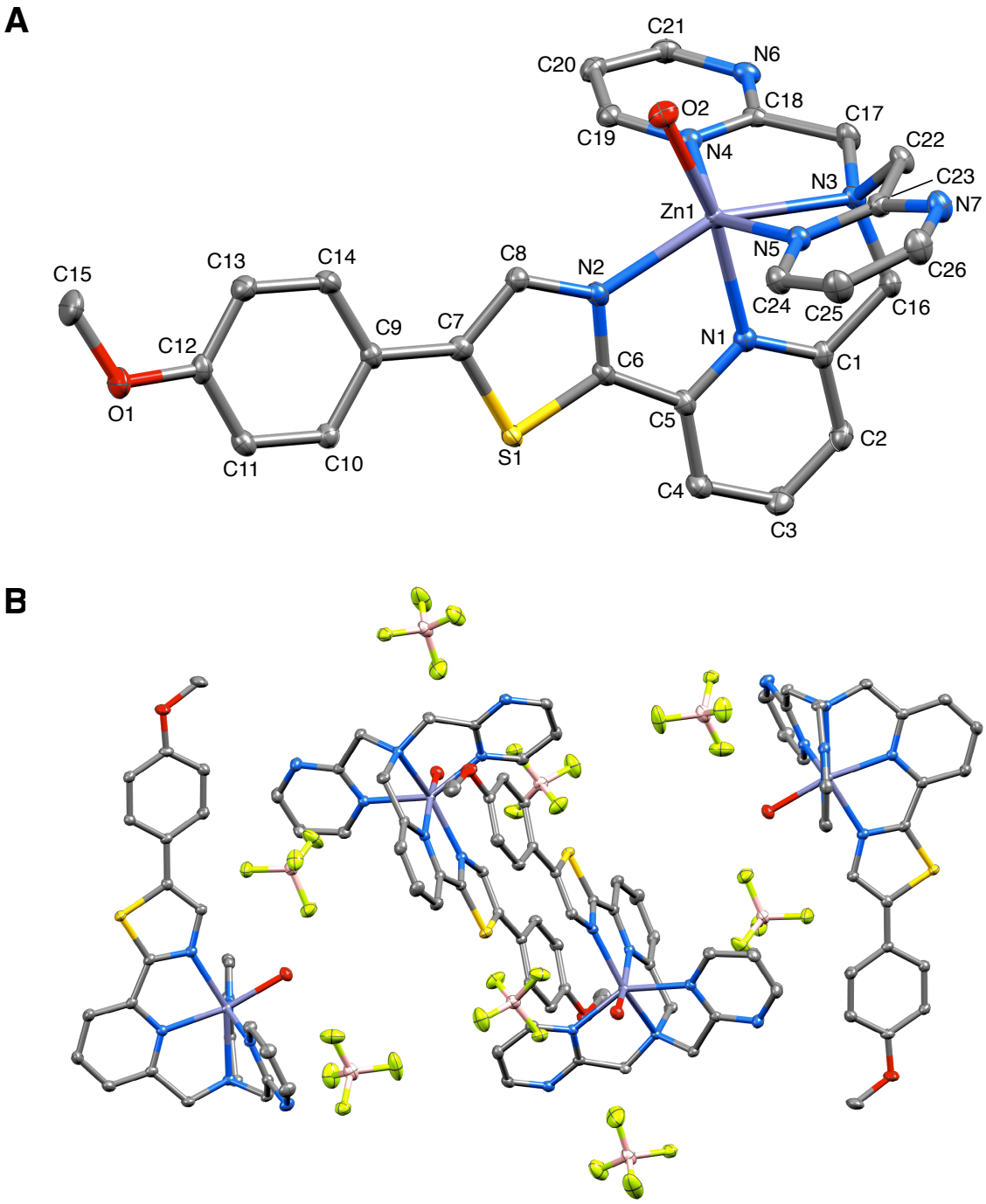

Figure 3.23: (A) ORTEP representation and atom number scheme for the Zn(II) complex of chromis-2: [(**3.4**)Zn(II)]. Ellipsoids shown represent 50% probability. Hydrogen atoms and counter ions have been omitted for clarity. (B) ORTEP presentation of the unit-cell packing for [(**3.4**)Zn(II)], showing the symmetry within the crystal. Hydrogen atoms have been omitted for clarity.

3.5.4 Steady-State Absorption and Fluorescence Properties of Chromis-2

The lack of water-solubilizing carboxylic acid groups in the structure of chromis-2 was a potential issue when investigating the spectroscopic properties of the ligand in aqueous buffer. Because concentrated (millimolar concentrations) stock solutions of fluorescent probes are often diluted to micromolar concentrations into aqueous buffer, it was necessary to ensure that the spectroscopic responses of chromis-2 were not affected in the concentration regime employed for characterization in either aqueous buffer or in cellular media. Spectral overlap experiments of chromis-2 conducted under dilute and concentrated conditions (1 μM versus 10 μM) confuted any potential aggregation-induced fluorescence and absorbance changes in the concentration range used for any experiment involving the probe.

Chromis-2 exhibited large bathochromic shifts in both the absorption and emission upon the coordination of Zn(II), with molar ratio titrations demonstrating a sharp saturation of the probe at equimolar concentrations of probe and metal being indicative of a clean 1:1 binding stoichiometry (Figure 3.24A&B). Consistent with metal coordination to the acceptor moiety of the fluorophore, chromis-2 underwent a 20-nm spectral shift from an absorbance maximum at 348 nm for the free form (ε = 23,400 M^{-1}•cm^{-1}) to 368 nm (ε = 20,800 M^{-1}•cm^{-1}) upon the binding of Zn(II) (Table 3.4). In addition, the emission maximum of the free form of chromis-2 underwent a 50-nm red shift from 465 nm to 515 nm upon saturation with Zn(II). Comparing the emission-ratiometric shift of chromis-2 to that of chromis-1 acid, the free form of chromis-2 is blue-shifted by 18 nm, whereas the Zn(II)-saturated form is blue-shifted by only 5 nm. Therefore, the metal binding-induced bathochromic shift of chromis-2 is 13 nm larger than that of chromis-1 acid, which facilitates

better species discrimination when selecting optimal bandpass ranges for ratiometric imaging using two-photon microscopy. Substitution of the bis(2-pyridylmethyl)amine chelator with bis(2-pyrimidylmethyl)amine in chromis-2 led to an almost 2-fold increase in the fluorescence quantum yield of the free form from 0.25 to 0.47, while the Zn(II)-saturated form increased only 8% from 0.61 to 0.69 (Table 3.4). The 22% increase in the quantum yield of the free form of chromis-2 can be attributed to the suppression of ESPT-mediated fluorescence quenching.

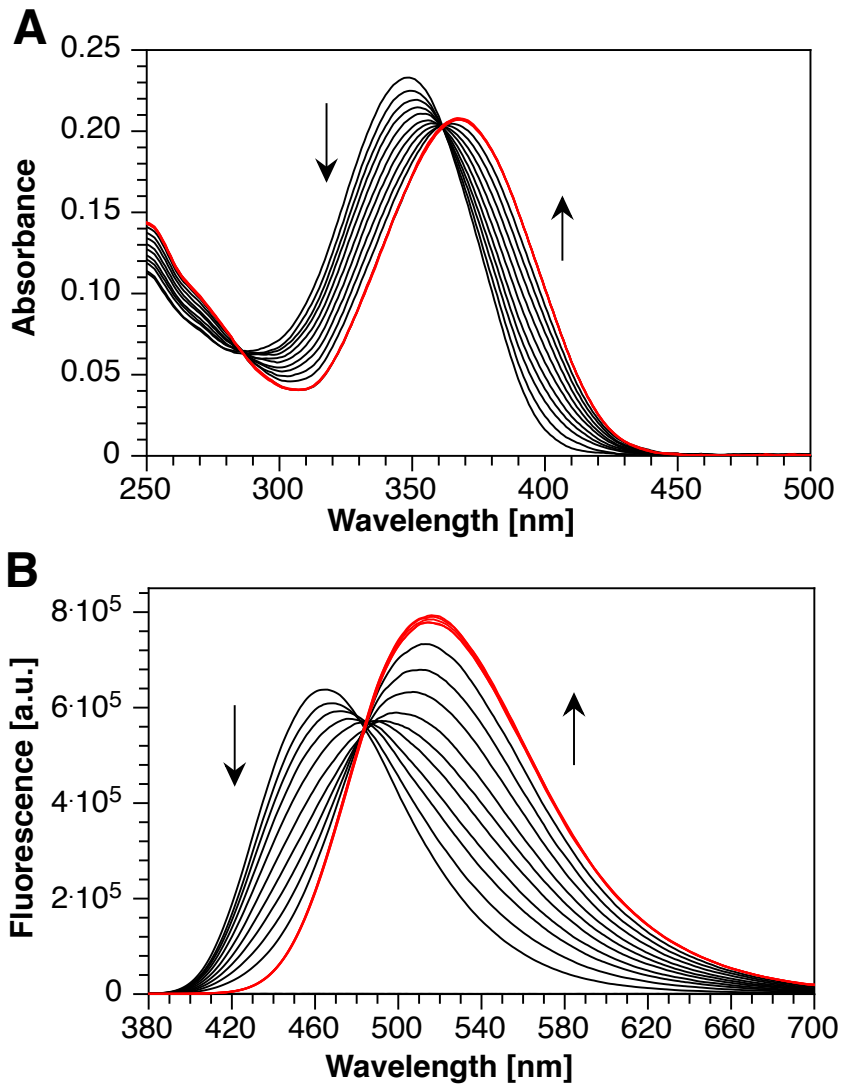

Figure 3.24: Spectral changes of chromis-2 (10 μM) in neutral aqueous buffer (10 mM PIPES, 100 mM KCl, 25°C, pH 7.0) upon stepwise saturation with Zn(II). (A) Absorption (UV-Vis) spectral changes upon saturation with Zn(II). (B) Fluorescence emission response upon saturation with Zn(II) (excitation at 361 nm). Red curves indicate the spectra after complete saturation (1.0 eq.) with Zn(II) is achieved. Inset: fluorescence integration over the entire spectral window as a function of molar equivalents of Zn(II).

Table 3.4: One and two-photon photophysical properties of chromis-2 (**3.4**) in aqueous buffer at pH 7.0.[a]

	Chromis-2 (**3.4**)	[(**3.4**)Zn(II)]
Abs λ_{max} (nm)[b]	348	368
ε (10^4 M^{-1} cm^{-1})[c]	2.34	2.08
Em λ_{max} (nm)[d]	465	515
δ_{max} (GM)[e]	n.d.	n.d.
Φ_F[g]	0.47	0.69

[a]10 mM PIPES, 0.1 M KCl, 25°C. [b]lowest-energy band of the one-photon absorption spectrum. [c]molar extinction coefficient at λ_{max}. [d]maximum two-photon absorption. [e]two-photon absorption cross section. [f]maximum fluorescence emission. [g]fluorescence quantum yield, referenced to quinine sulfate (Φ_F = 0.546 in 1N H_2SO_4).[5]

3.5.5 Metal-Ion Selectivity of Chromis-2

As illustrated in Figure 3.25, supplementation of chromis-2 with excess biologically relevant divalent transition metal ions, except Zn(II) and Mn(II), also revealed either no change in the emission response (with Mg(II) and Ca(II), Figure 3.25A, B) or a complete quenching of the probe's fluorescence response (with all transition metals excluding Zn(II), Figure 3.25C-G). Because binding of the interfering metals did not elicit a ratiometric response, which is consistent with both **3.3b** and chromis-1 acid (**2.1b**), the quenching of the fluorescence serves only as a masking effect by competing with Zn(II) for binding. By evaluating the metal-ion selectivity of the probe in the presence of 0.80 molar equivalents of the interfering metal ions, the emission ratio of the remaining 20% of free probe was left unaltered (Figure 3.26, black bars); therefore, saturation of the 0.20 equivalents of probe with Zn(II) produced an emission ratio that was consistent with the emission ratio of the [(chromis-2)Zn(II)] complex in the absence of any interfering metal ions (Figure 3.26, red patterned bars).

Interestingly, the addition of millimolar Mg(II) produced a slight decrease in the fluorescence intensity of the probe (Figure 3.27B). Consistent with observations of the metal-ion selectivity of **3.3b**, millimolar Ca(II) produced a slight increase and red-edge broadening of the emission profile, which negligibly increased the calculated emission ratio (Figure 3.27C). Despite the additional nitrogen donor from the thiazole, the lower affinity manifested by the less basic pyrimidines of chromis-2 also resulted in a non-quantitative fluorescence quenching with Mn(II). The lower affinity for Mn(II) enabled it to be immediately outcompeted by supplementation of 1.0 equivalent of Zn(II) to restore the emission response to that of the [(chromis-2)Zn(II)] complex in the absence of any interfering metals (Figure 3.27D). Analogous to **3.3b**, despite initial observations of tight Fe(II) binding with near unity fractional saturation, the 0.8 molar equivalents of Fe(II) was outcompeted by Zn(II) over the course of ~ 30 minutes at 25°C (Figure 3.27E). Therefore, the emission response of the probe to the addition of Zn(II) was measured in the presence of 1.0 molar equivalent of Zn(II). Furthermore, the addition of Ni(II) resulted in a time-dependent fluorescence quenching (Figure 3.27G, Insert) that reached equilibrium after ~ 10 minutes.

To evaluate the stability constant for the formation of the Mn(II) complex of chromis-2, a fluorimetric titration was performed by the direct addition of $MnSO_4 \cdot H_2O$ to a solution containing chromis-2. Fitting of the fluorimetric titration data from the metal-addition titration resulted in a stability constant of $\mathrm{Log}K_{\mathrm{Mn(II)L}} = 5.87 \pm 0.01$ (Figure 3.28), corresponding to an apparent dissociation constant of 1.36 μM, which is nearly one log-unit higher than Mn(II) stability constant of chromis-1 acid (**2.1b**).

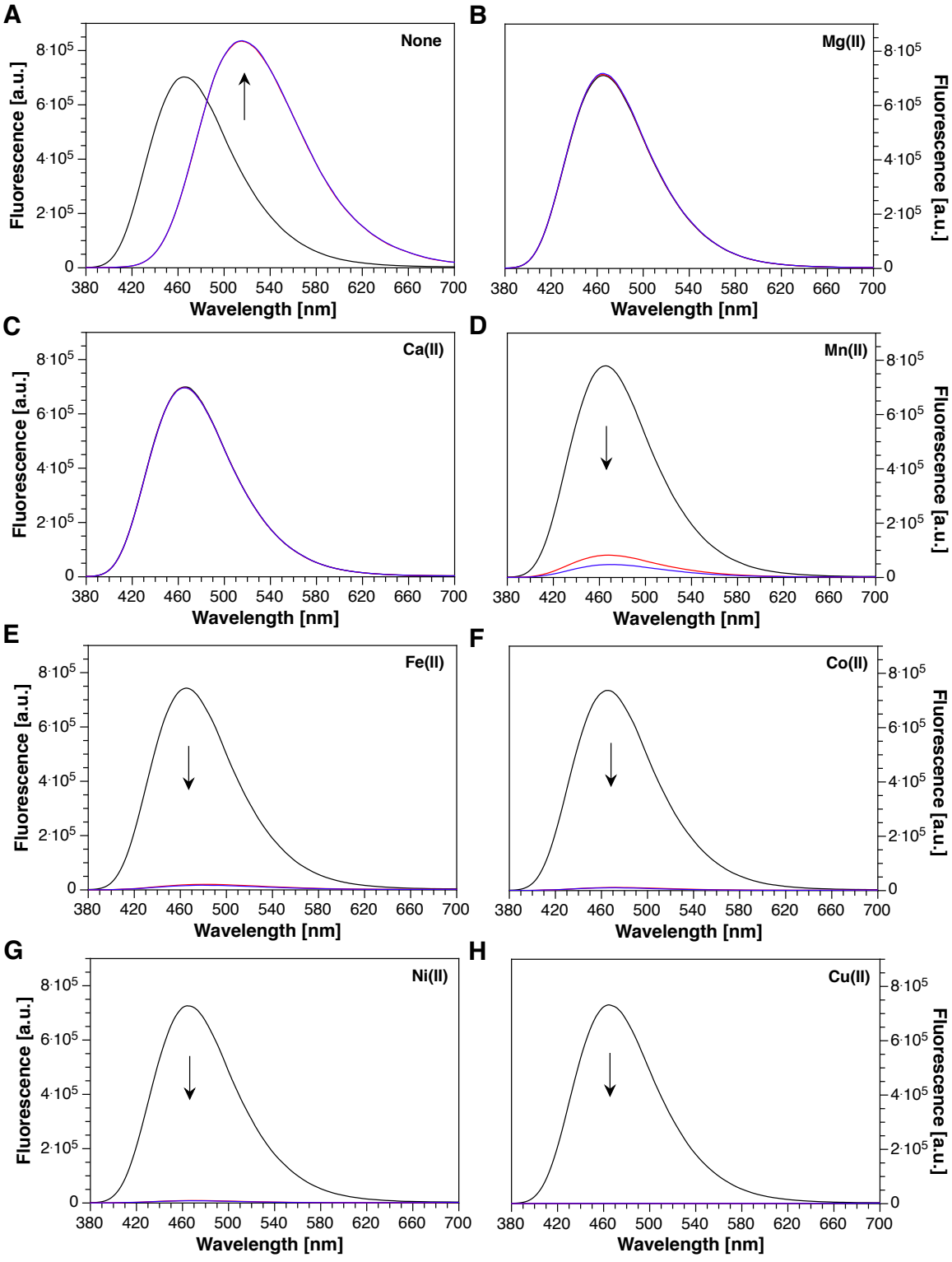

Figure 3.25: Fluorescence response of chromis-2 in the presence of excess (4.0 and 8.0 equivalents) of interfering divalent metal ions. A-H) Black traces represent free chromis-2 (5 μM) in pH 7.0 buffer (10 mM PIPES, 0.1 M KCl, 25°C) supplemented with 10 μM EDTA. Red and blue traces represent the addition of 20 μM and 40 μM, respectively, of divalent metal ions. Excitation: 361 nm.

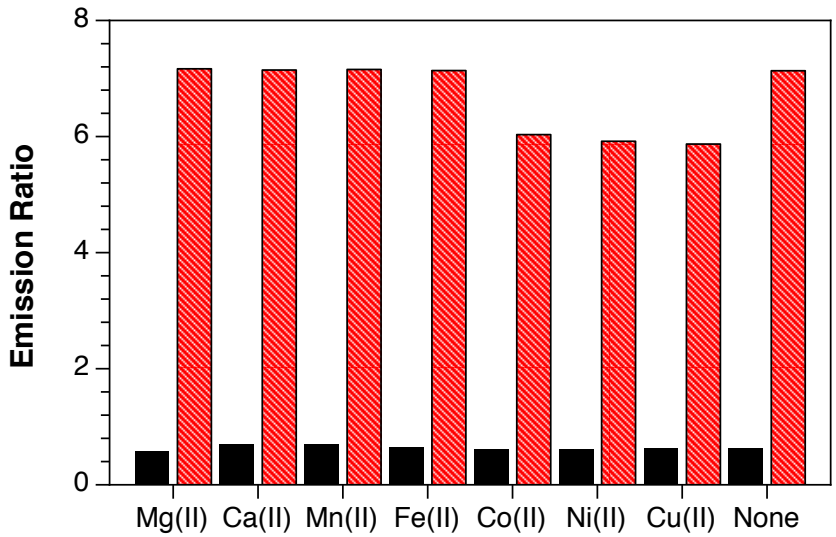

Figure 3.26: Emission-ratiometric response of chromis-2 (5 μM) towards selected divalent metal cations at 80% fractional saturation (calculated based on ratio of the integrated fluorescence intensity between 510-570 nm (channel 2) and 440-470 nm (channel 1)). The red bars represent the ratio at 80% fractional saturation, and the corresponding red patterned bars represent the ratio after saturating the remaining 20% of free fluorophore with Zn(II). Excitation: 361 nm.

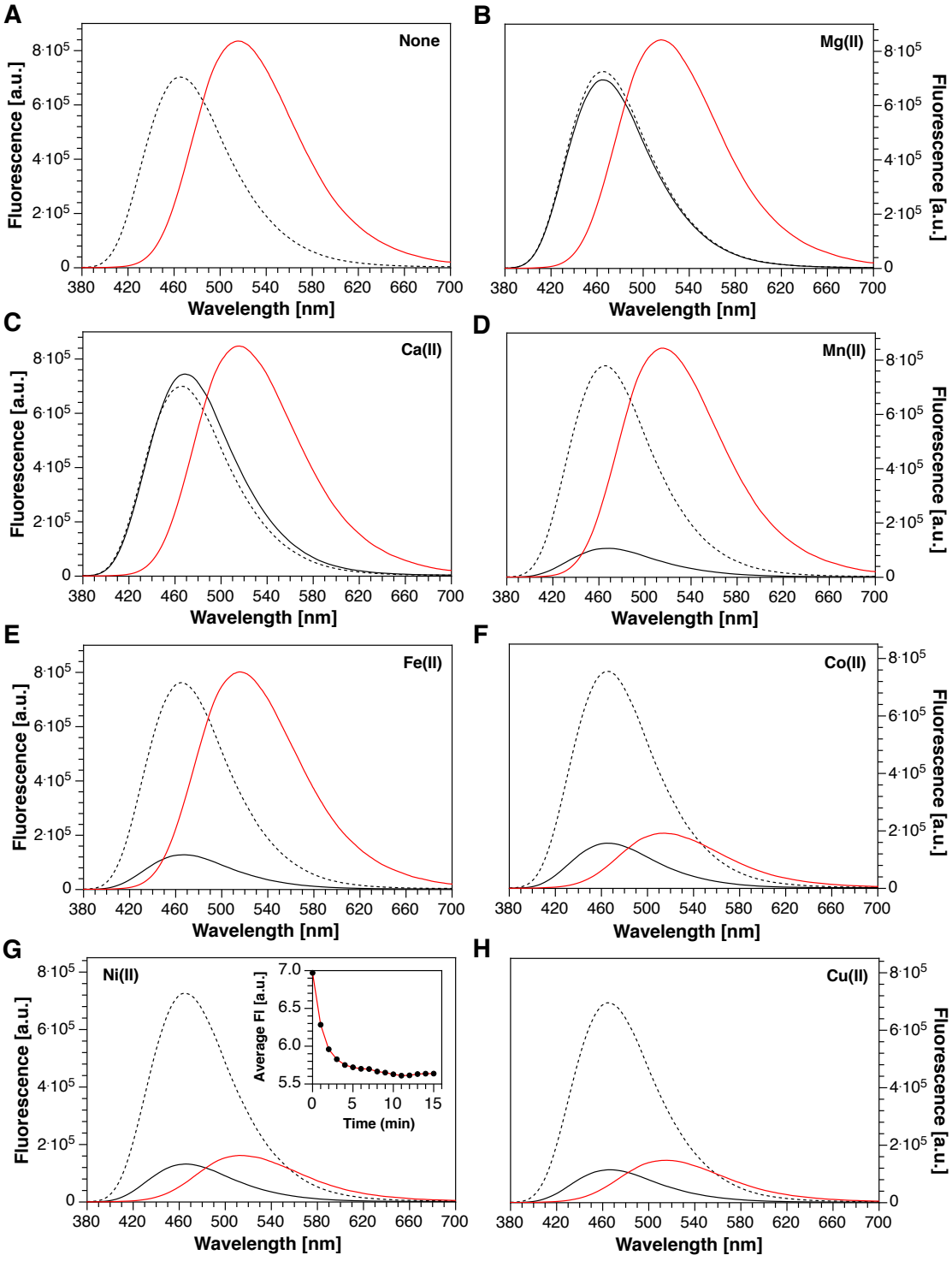

Figure 3.27: Emission spectral response of chromis-2 towards selected divalent metal cations at 80% fractional saturation. A,B) Fluorescence response of chromis-2 (5 μM) in pH 7.0 buffer (10 mM PIPES, 100 mM KCl, 25°C) in the presence of 2 mM alkaline earth metals, with corresponding saturation of probe with 1.0 eq. Zn(II). C-H) Fluorescence response of chromis-2 in the presence of 80% fractional saturation (solid black curves) of interfering divalent metal ions, with corresponding saturation of remaining 20% probe with Zn(II) (red curves). Inset: Kinetics of equilibration of chromis-2 with Ni(II). Excitation: 361 nm.

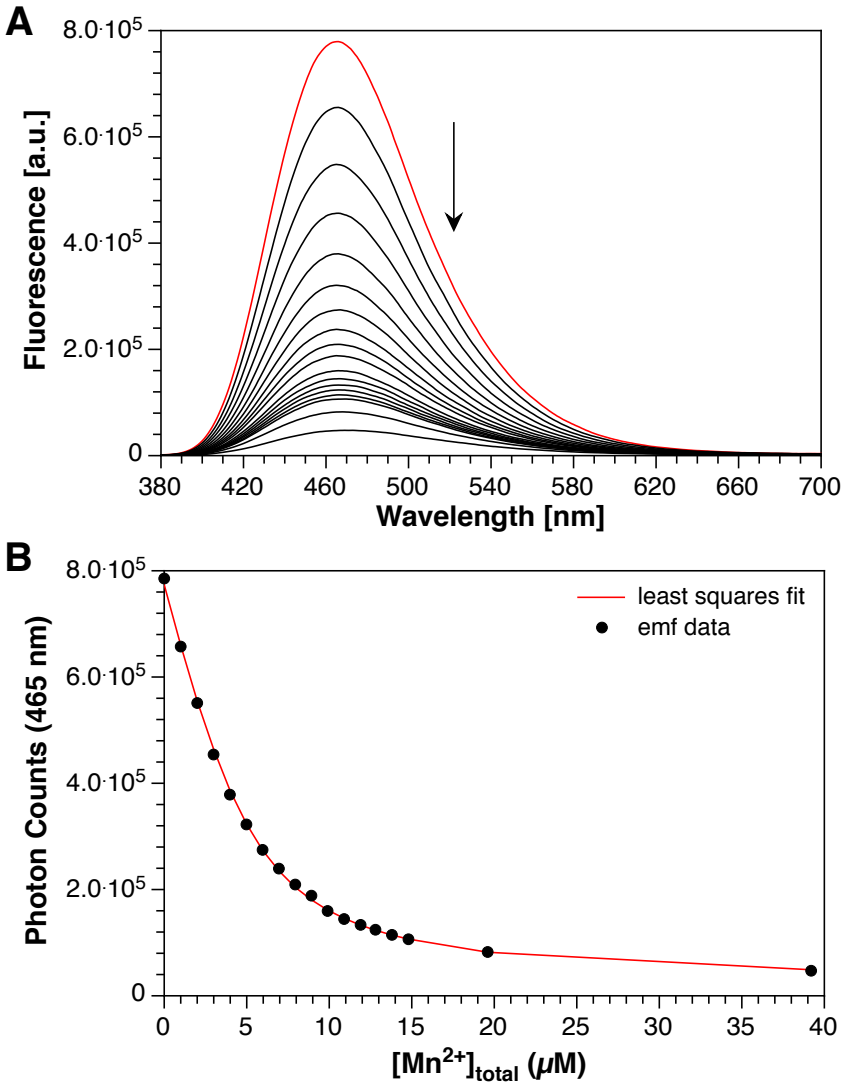

Definition of Equilibrium System:

Species	Mn(II)	chromis-2	H	log β
Zn(II)	1	0	0	0.0
Chromis-2	0	1	0	0.0
[(Chromis-2)Mn(II)]	1	1	0	*5.87 ± 0.01*

Figure 3.28: Fluorimetric determination of the apparent Mn(II) stability constant of chromis-2 (**3.4**) via a direct, metal-addition titration. Chromis-2 (5 μM) was equilibrated in chelexed pH 7.0 buffer (10 mM PIPES, 0.1 M KCl, 25ºC) and titrated with $MnSO_4 \cdot H_2O$ in aliquots from 0-40 μM. The red curve indicates free chromis-2 before the addition of Mn(II). The fluorescence spectra were analyzed by non-linear least squares fitting to yield an average $\log K_{Zn(II)L}$ of 5.87 ± 0.01 (n = 1). B) Change in fluorescence response at 465 nm with corresponding fit to the equilibrium system model.

3.5.6 Zn(II)-Binding Affinity Measurements of Chromis-2

Despite the inherent correlation between the binding affinity and proton basicity, the statistical effect associated with coordinating Zn(II) to either of the two pyrimidine nitrogens provides an additional 0.6 log units (0.3 log units per pyrimidine ring) to the stability constant. In addition, eradication of ESPT effectively permits emission spectral data, that would otherwise be of concern due to potential distortions in emission intensity or spectral shape, to be analyzed in determining robust stability constants. To reliably determine the stability constant of chromis-2, spectrophotometric and fluorimetric titrations were performed in the presence of EGTA as a competing ligand with matching affinity ($\mathrm{Log}K_{\mathrm{EGTA\cdot Zn(II)}}$ = 8.34, K_d = 4.6 nM at pH 7.0, μ = 0.1 M, 25°C). However, initial efforts to determine the Zn(II) stability constant of chromis-2 via a fluorimetric competition titration in the presence of EGTA at pH 7.0 revealed a slight mismatch in the affinity between the two ligands.

As will be discussed more extensively in Chapter 4, the two protonation constants of EGTA that lie above 7.0 produce a strong pH dependence on the stability constant of EGTA, with a 0.5 log-unit change in pH corresponding to a one log-unit change in the affinity. On the other hand, given the expectedly low pK_a's of chromis-2, changes in the pH of the solution are not expected to considerably affect the apparent stability constant of chromis-2. Therefore, fluorimetric determination of the stability constant of chromis-2 was performed at pH 6.5, reducing the affinity of EGTA by one log unit and providing a better matching affinity between the two components to provide a more reliable equilibrium constant. Non-linear least-squares fitting of the fluorimetric titration data provided an apparent stability constant of 7.97 ± 0.03, corresponding to an apparent dissociation constant of K_d' = 10.7 ± 1 nM at pH 6.5 with an ionic background of 0.1 M (KCl) at 25°C (Figure

3.29). In spite of thiazole's propensity to engage in coordinating Zn(II), as well as the statistical effect associated with Zn(II) binding to either of the two pyrimidine nitrogens, the significantly reduced basicity of chromis-2's pyrimidine rings results in a binding affinity that is three log units lower than its predecessor **3.3b** and that is comparable to that of chromis-1 ester (**2.1a**).

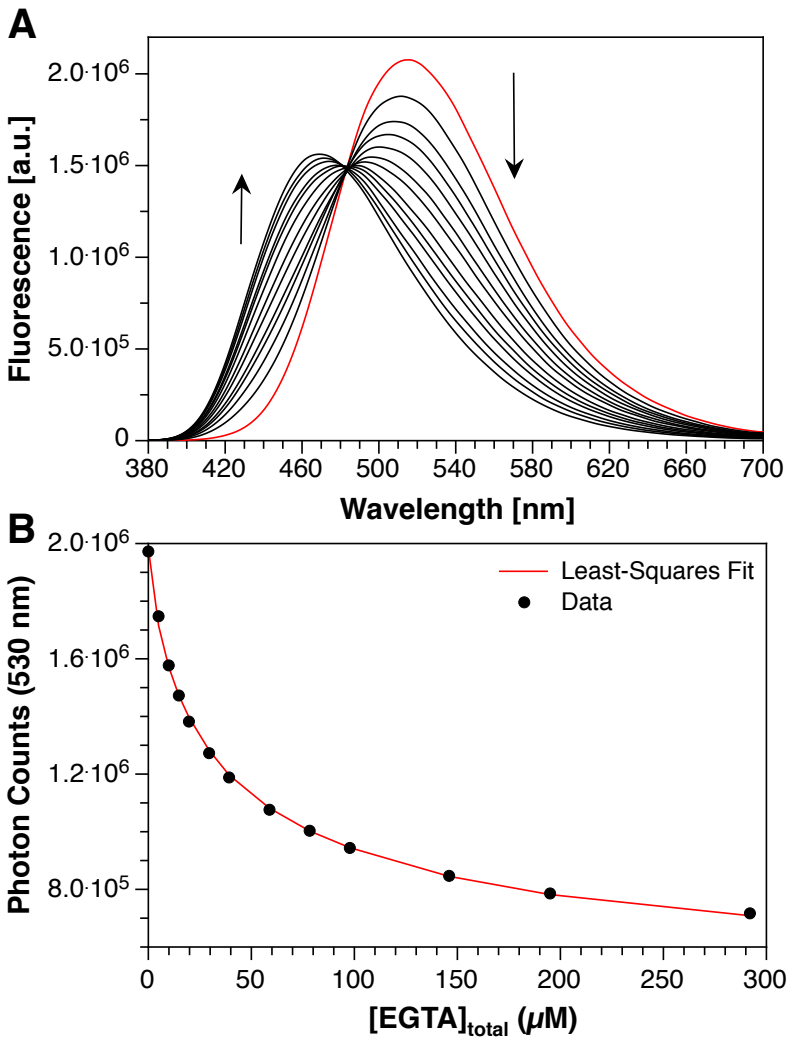

Definition of Equilibrium System:

Species	Zn(II)	EGTA	Chromis-2 (**3.4**)	H	log β
Zn(II)	1	0	0	0	0
EGTA	0	1	0	0	0
3.4	0	0	1	0	0
EGTA(H)	0	1	0	1	9.51
EGTA(H_2)	0	1	0	2	18.41
EGTA(H_3)	0	1	0	3	21.22
[(EGTA)Zn(II)]	1	1	0	0	12.6
[(**3.4**)Zn(II)]	1	0	1	0	*7.97 ± 0.03*

Figure 3.29: A) Fluorimetric determination of the Zn(II) stability constant of chromis-2 (**3.4**) via a competition titration with EGTA. Chromis-2 (10 μM) was equilibrated with $ZnSO_4 \cdot 7H_2O$ (10 μM) in chelexed aqueous buffer (10 mM MES, 0.1 M KCl, pH 6.5, 25°C) and titrated with EGTA to a final concentration of 300 μM. The fluorescence spectra (excitation: 361 nm) were analyzed by non-linear least squares fitting to give an average $\log K_{Zn(II)L}$ of 7.97 ± 0.03 (n = 2). B) Change in fluorescence response at 530 nm with corresponding fit to the equilibrium system model.

3.5.7 Development of Chromis-2-Ctrl as a Non-Zn(II)-Binding Fluorescent Probe for Elucidating the Fluorescence Dependence of Chromis-2 on the Polarity Environment of the Cell

The structure of lipophilic fluorescent probes can dictate their fluorescence signaling behaviors within the lipid-rich environment of a cell, such that the signaling behaviors may differ quite dramatically from those observed in the aqueous buffer in which they are analyzed spectroscopically. While this phenomenon will be discussed more in detail in Chapter 5, the cellular employment of ratiometric fluorescent sensors for probing labile metal pools can often result in a ratiometric readout under disparate conditions, namely oxidation, change in pH, and/or a change in the polarity environment, such as varying compositions of phospholipids that compose the lipid bilayers of cells. While this phenomenon is profoundly unexplored, Deleers et. al. observed that changes in the lipid composition of liposomes containing varying concentrations of phosphatidylserine, ethanolamine, and inositol affected the fluorescence response of the fluorescent probe 3,3-dipropylthiodicarbocyanine due to the changes in the membrane potential.[21] Therefore, the development of a control compound that not only displays the same ratio as the free form of the metal-responsive fluorescent probe, but also does not coordinate the metal analyte of interest is imperative for determining whether the lipid environment of a particular cell line is interfering with the fluorescence properties of the indicator. Because chromis-2 does not boast hydrophilic groups for increase water-solubility, thus likely resulting in an association with lipid membranes, to ensure that the fluorescence properties in the cell match those in aqueous buffer, a control compound that does not bind Zn(II) was synthesized and characterized in aqueous buffer, as well as in mammalian cells and brain tissue.

3.5.7.1 Synthesis of Chromis-2-Ctrl

Exploiting the commercial availability of 5-formylpyrimidine, chromis-2-ctrl was synthesized via a double reductive amination using amine **3.20** that was synthesized via DIBAL (diisobutylaluminum hydride) reduction of nitrile **3.15** (Scheme 3.9). Typically, DIBAL is not used to reduce aromatic nitriles to amines, as the reduction stops at the imine intermediate after 1.0 equivalent of DIBAL reacts. However, upon the addition of 2.0 equivalents of DIBAL, the nitrile was reduced to the corresponding primary amine, which then reacted as a crude mixture with 2.0 equivalents of 5-formylpyrimidine to furnish chromis-2-ctrl in only 13% yield. The low yield was most likely due to the lack of purification of the primary amine.

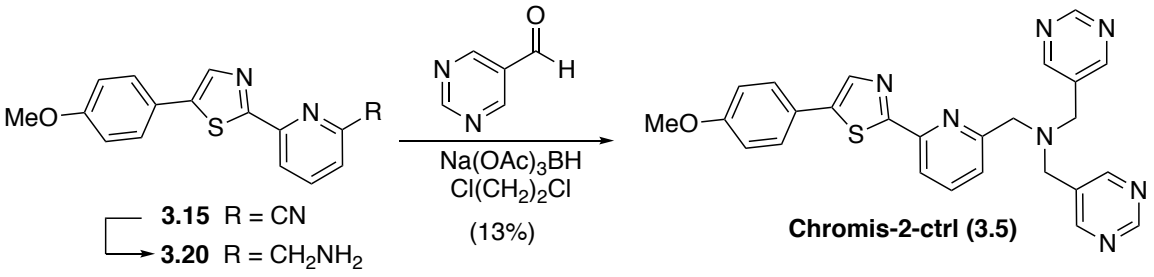

Scheme 3.9: Synthesis of chromis-2-ctrl (**3.5**)

3.5.7.2 Absorbance and Fluorescence Properties of Chromis-2-Ctrl

Analysis of the spectral properties of chromis-2-ctrl showed surmised similarities to the spectral response of chromis-2. In the absorption, the absorbance maximum shifts a negligible 2 nm from 348 nm (chromis-2) to 350 nm, an effect most likely due to a change in the dipole moment of the molecule as a result of the change in polarity of the pyrimidine rings. The emission maximum, however, does not change relative to chromis-2, with a slight increase in the fluorescence intensity of chromis-2-ctrl relatively to chromis-2 (Figure

3.30A). Interestingly, when the two emission spectra are normalized, the fluorescence emission profile of the control compound is slightly narrower than that of chromis-2, which could be the result of a potentially lower acidity due to the isomerization of the pyrimidine rings (Figure 3.30B). The result is a negligible 5% decreased in the calculated ratio from 0.45 to 0.40 between chromis-2 and chromis-2-ctrl based on spectroscopic measurements in aqueous buffer. Given the likelihood that the probe will partition into cellular membranes, the modest ratio discrepancy between chromis-2 and its control compound will potentially be even narrower.

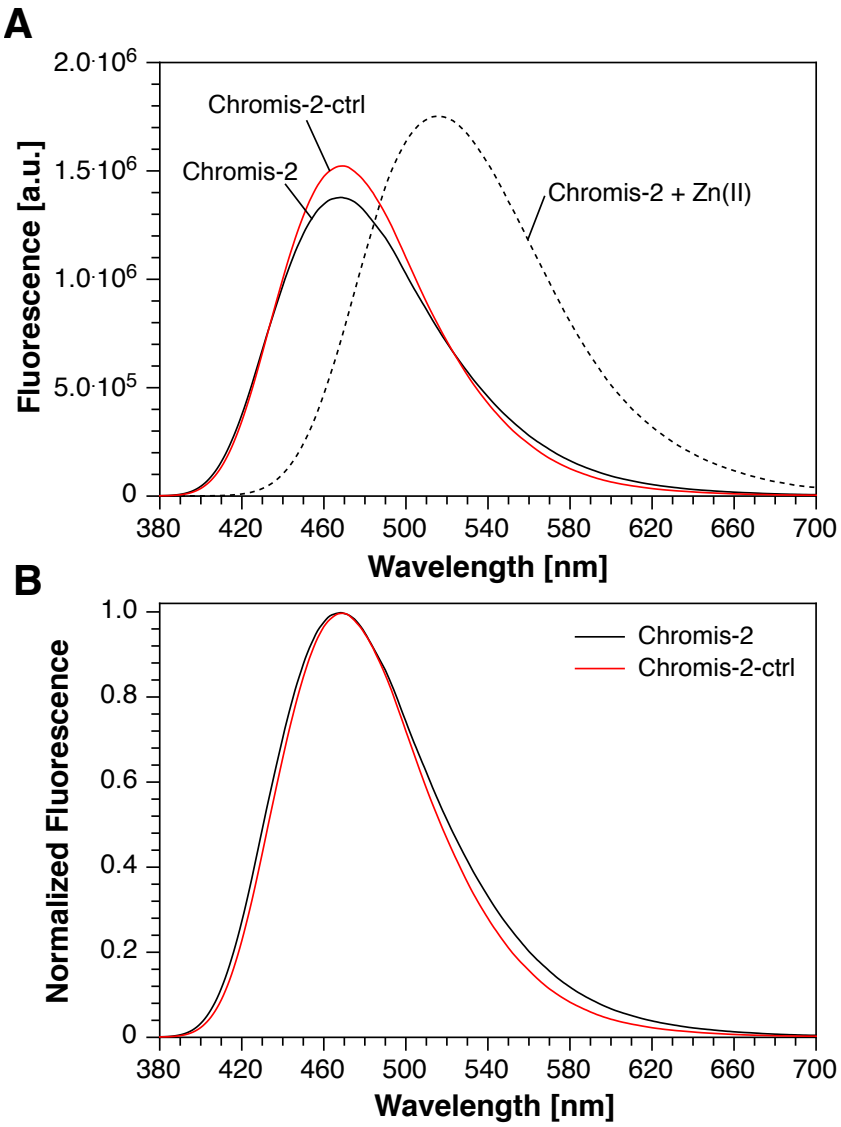

Figure 3.30: A) Emission spectral comparison between chromis-2 (10 μM) and chromis-2-ctrl (10 μM) in pH 7.0 buffer (10 mM PIPES, 100 mM KCl, 25°C). B) Normalized emission spectra of free chromis-2 and chromis-2-ctrl to reveal the spectral change between the two compounds.

To ensure that the control compound does not coordinate Zn(II), spectrophotometric and fluorimetric titrations were performed in aqueous buffer (10 mM PIPES, 100 mM KCl, 25°C, pH 7.0), in which Zn(II) was titrated from 500 μM to 2 mM. Under these conditions, chromis-2-ctrl did not bind Zn(II) up to 2 mM, thus no ratiometric readout was observed in the absorption (Figure 3.31A) or the emission (Figure 3.31B).

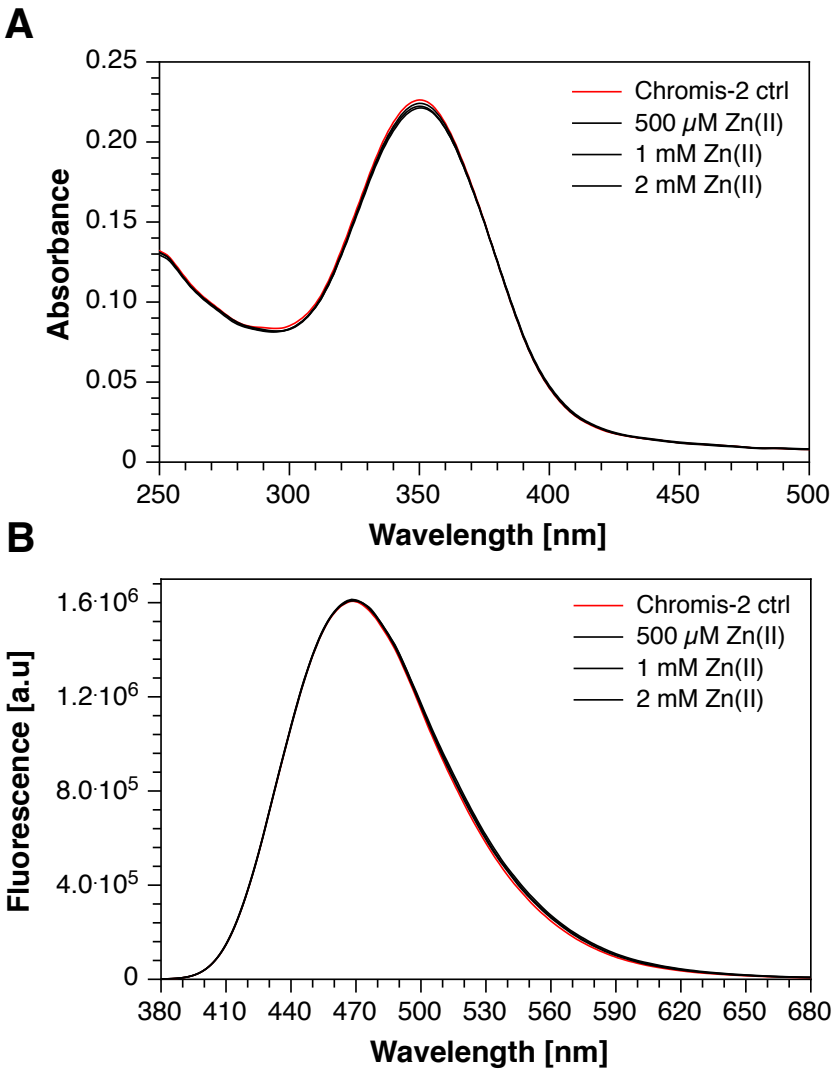

Figure 3.31: Spectrophotometric (A) and fluorimetric (B) titration of chromis-2-ctrl (10 μM) with Zn(II) in pH 7.0 aqueous buffer (10 mM PIPES, 100 mM KCl, 25°C). The red curves depict the free probe in solution, and the corresponding black curves indicate the incremental addition of Zn(II). Excitation: 350 nm.

3.6 Conclusions

Designing emission-ratiometric fluorescent probes for detecting trace metals in biological systems requires a thorough understanding of the underlying photophysical properties of the probe and how the fluorescence properties are affected once employed in the cell. One particular property is the change in the fluorescence properties upon protonation

of the fluorophore. The highly-compartmentalized environment of eukaryotic cells enables protection from rapid, dynamic fluctuations in pH between the localized pH buffering capacity of organelles and vesicles and the cytosol.[4] Dramatic deviations in the pH of the cell, by virtue of compartmentalization, can have deleterious effects on ratiometric imaging should the fluorescent probe be sensitive to changes in pH. The localized charge density on the pyridyl acceptor of chromis-1 acid facilitated an excited-state protonation, which not only led to fluorescence quenching but also led to a broadening of the emission profile on the red edge of the emission. The development of a model compound (**3.1**) for chromis-1 established a profound effect of the metal-binding ligand on the pK_a of the pyridyl acceptor of chromis-1 by the observation of a three logarithmic-unit perturbation compared its model compound. The localized charge density of the pyridyl acceptor of model compound **3.1** is only exacerbated in the excited state by behaving as a 10 million-fold stronger base than in the ground state. be

The rearrangement of the pyridyl acceptor of chromis-1 demonstrated a substantial decrease in the ground-state basicity and photobasicity based on the photophysical and thermodynamic characterization of model compound **3.2**. The reduction in basicity, as well as the eradication of a deuterium isotope effect with model compound **3.2**, provided an impetus to incorporate the new fluorophore design into a metal-binding fluorescent probe. However, incorporation of a metal-binding ligand into the new fluorophore enabled the reappearance of a deuterium isotope effect studies with **3.3b**, which revealed a 10% increase in the fluorescence intensity of the probe in D_2O compared to H_2O, as well as only a minute 0.2 pH-unit decrease in the ground-state pK_a of the pyridyl acceptor compared to chromis-1 acid.

To gauge the role of the metal-binding ligand on the excited-state protonation of the fluorophore pyridine, a pyrimidine-containing analog of bispicolylamine was synthesized and incorporated into the structure of a new 2-thiazolyl metal-binding fluorophore (chromis-2). This subtle modification in the structure of the chelating group resulted in a nearly 2-fold increase in the fluorescence quantum yield of the metal-free fluorophore and almost perfectly balanced fluorescence intensities of the free and metal-bound forms, corroborating the chelator's role in promoting an excited-state intramolecular proton transfer to the pyridyl acceptor of the fluorophore core. The significantly lower proton basicity of pyrimidine compared to pyridine also demonstrated a three logarithmic-unit decrease in the stability constant of chromis-2 from log*K* of 10.8 to 8.0 relative to **3.3b**, despite the statistical effect associated with coordinating Zn(II) to either of the two nitrogens of pyrimidine. Nevertheless, the development of chromis-2 as an emission-ratiometric, water-soluble, Zn(II)-selective fluorescent probe that is insensitive to fluctuations in pH represents a remarkable effort in tailoring the photophysical properties of the indicator to the environment in which it will be employed. The comparable affinity to chromis-1 ester enabled remarkable emission-ratiometric imaging of 3T3 mouse fibroblast cells, as well as of mouse hippocampal brain tissue, where Zn(II) is present in significantly higher concentrations compared to other regions of the brain.[22-23] Indeed, the outlook of chromis-2 in helping to elucidate the roles of Zn(II) in neuroscience, therefore, is quite promising based on these studies.

3.7 Experimental Section

3.7.1 Synthesis

Materials and Reagents. Intermediates 2-cyanoisonicotinic acid (**2.2**) and 2-amino-4'-methoxyacetophenone (**2.4**) were synthesized according to procedures available in Chapter 2. Picolinic acid (Chem-Impex Int'l, Inc.), isonicotinic acid (Eastman), ethyl 6-bromo-picolinate (Combi-Blocks, Inc.), 2-pyrimidinecarbonitrile (Oxchem Corp.) and 5-pyridinecarbaldehyde (Ark Pharm, Inc.) were purchased commercially and used without further purification. Flash chromatography purification was performed on general purpose silica gel (60 Å pore size, 250 mesh, Sorbent Technologies). NMR: ^{1}H NMR spectra were recorded at 400 MHz at ambient temperature (20-23°C), unless state otherwise, and referenced to an internal TMS standard (0 ppm) for all solvents except D_2O, which was referenced to externally added sodium 3-trimethylsilylpropionate-2,2,3,3-d_6 (0 ppm). ^{13}C spectra were acquired at 100 MHz and referenced to the known chemical shift of the solvent peak ($CDCl_3$: 77.0 ppm; DMSO-d_6: 39.5 ppm; CD_3OD: 49.0 ppm; Acetone-d6: 206.3, 29.8 ppm), excluding D_2O, which was referenced to sodium 3-trimethylsilylpropionate-2,2,3,3-d_6 (0 ppm). NMR spectra are provided in Appendix A.2. Mass spectra were recorded by the Georgia Tech Mass Spectrometry Facility.

***N*-(2-(4-methoxyphenyl)-2-oxoethyl)isonicotinamide (3.6)**. A 250 mL round bottom flask equipped with a stir bar was charged with 2-amino-4'-methoxyacetophenone hydrochloride **2.4** (1.1 eq., 4.96 mmol, 1.00 g), isonicotinic acid (1 eq., 4.51 mmol, 555 mg), EDCI·HCl (1.5 eq., 6.77 mmol, 1.30 g), and HOBt (0.5 eq., 2.26 mmol, 305 mg). The contents were dissolved in DMF (15 mL), pyridine (1 eq., 4.51 mmol, 0.363 mL) was added to the reaction solution via a syringe, and the solution was allowed to stir magnetically overnight. The product was crystallized from the solution by the slow addition of 60 mL of

diH_2O, after which the contents of the flask were filtered through a glass frit, washed with cold diH_2O, and dried over vacuum to afford pure **3.6** as a white crystalline solid. Yield: 1.01 g (3.75 mmol, 83%). ^{1}H NMR ($CDCl_3$, 400 MHz) δ 3.91 (s, 3H), 4.90 (d, *J* = 4.2 Hz, 2H), 7.01 (d, *J* = 9.0 Hz, 7.49 (s, 1H), 7.73 (dd, *J* = 4.5, 1.5 Hz, 2H), 8.01 (d, *J* = 9.0 Hz, 2H), 8.79 (d, *J* = 4.9 Hz, 2H). ^{13}C NMR ($CDCl_3$, 100 MHz) δ 46.3, 55.5, 114.1, 121.0, 127.0, 130.3, 141.0, 150.5, 163.4, 165.3, 192.0. EI-MS *m/z* 270 ($[M]^+$, 5%), 241 (45%), 135 (100%), 77 (20%). EI-HRMS *m/z* calc'd for $C_{15}H_{14}N_2O_3$ 270.1006, found 270.1004.

5-(4-methoxyphenyl)-2-(pyridin-4-yl)thiazole (3.7). To an oven-dried 2-neck 100 mL round bottom flask equipped with a stir bar was added isonicotinamide **3.6** (1 eq., 3.36 mmol, 908 mg) and Lawesson's Reagent (1.3 eq., 4.37 mmol, 1.77 g). The flask was connected to a reflux apparatus, and using a glass frit connected to the top of the reflux condenser, the system was flushed with argon for several minutes to remove moisture. Using an argon-filled syringe, butryonitrile (15 mL, dried over 0.4 Å molecular sieves and filtered) was added through the top of the reflux condenser. The flask was lowered into an oil bath at 140°C and allowed to magnetically stir under reflux for 30 min. After cooling to room temperature, saturated $NaHCO_3$ (*aq*) solution (2 mL) was added to the deep red solution under stirring, and the mixture was diluted with ethyl acetate (40 mL), transferred to a separatory funnel, and washed with additional 5% (w/v) NaOH (*aq*) and brine. The organic layer was dried over $MgSO_4$, filtered, and concentrated under reduced pressure to afford a yellow solid residue. The crude solid was recrystallized from a 1:1 mixture of 2,2,4-trimethylpentane:toluene, collected by suction filtration, washed with hexanes, and dried under vacuum to afford **3.7** as an pale-yellow solid. Yield: 670 mg (2.50 mmol, 74%). ^{1}H NMR ($CDCl_3$, 400 MHz) δ 3.83 (s, 3H), 6.94 (d, *J* = 8.8 Hz, 2H), 7.54 (d, *J* = 8.8 Hz, 2H) 7.77 (dd, *J* = 4.6, 1.6, 2H), 7.97 (s, 1H), 8.69 (dd, *J* = 4.6, 1.6 Hz, 2H). ^{13}C NMR ($CDCl_3$, 100 MHz) δ 55.3, 114.6, 119.8, 123.2, 128.1, 138.8, 140.3, 141.3, 150.5, 160.1,

162.7. EI-MS *m/z* 268 ($[M]^+$, 100%), 253 (40%), 164 (23%), 149 (43%), 121 (33%), 77 (25%). EI-HRMS *m/z* calc'd for $C_{15}H_{12}N_2OS$ 268.0670, found 268.0670.

4-(2-(pyridin-4-yl)thiazol-5-yl)phenol (3.8). Thiazole **3.7** (1 eq., 0.373 mmol, 100 mg) was added to a 10 mL round bottom flask equipped with a stir bar. The flask was sealed with a rubber septum, evacuated under high vacuum, and backfilled with argon. Via an argon-filled syringe, anhydrous dichloromethane (2 mL) was transferred to the flask to dissolve the starting material. The flask was then lowered into an ice bath at 0°C, and upon thermal equilibration (~10 minutes), boron tribromide (3 eq., 1.12 mmol, 1.12 mL of a 1 M solution in dichloromethane) was added drop-wise to the stirred solution. After stirring at 0°C for 6 hours, the mixture was diluted with ethyl acetate (10 mL), quenched with diH_2O (10 mL), and the pH was adjusted to ~7 to neutralize the excess HBr using saturated aqueous $NaHCO_3$. The aqueous layer was then extracted with ethyl acetate (2 x 10 mL), and the combined organic layers were dried over $MgSO_4$, filtered, and concentrated to a blood orange solid. The crude solid was recrystallized from boiling methanol afford **3.8** as a burnt orange solid. Yield: 55 mg (0.216 mmol, 58%).%). ^{1}H NMR (DMSO-d6, 400 MHz) δ 6.88 (d, *J* = 8.6 Hz, 2H), 7.58 (d, *J* = 8.6 Hz, 2H), 7.86 (dd, *J* = 4.6, 1.5 Hz, 2H), 8.27 (s, 1H), 8.71 (dd, *J* = 4.6, 1.5 Hz, 2H). 9.92 (s, 1H). ^{13}C NMR (DMSO-d6, 100 MHz) δ 116.1, 119.6, 121.1, 128.2, 138.9, 139.6, 141.5, 150.7, 158.4, 161.4. EI-MS *m/z* 254 ($[M]^+$, 100%,), 150 (73%), 121 (28%). EI-HRMS *m/z* calc'd for $C_{14}H_{10}N_2OS$ 254.0514, found 254.0511.

Sodium 3-(4-(2-(pyridin-4-yl)thiazol-5-yl)phenoxy)propane-1-sulfonate (3.1). In a 10 mL round bottom flask equipped with stir bar, phenol **3.8** (1 eq., 0.236 mmol, 60 mg) was suspended in anhydrous THF (5 mL) under argon. Sodium *tert*-butoxide (NaO^tBu, 1.0 eq., 0.236 mmol, 22.7 mg) was added to a separate, 4-mL vial sealed with

a septum, and the vial was evacuated and backfilled with argon to remove potential moisture. The NaO^{t}Bu was suspended in anhydrous THF (2 mL), transferred to an argon-flushed syringe body, and the suspension was added dropwise to the stirred solution containing phenol **3.8**, which immediately precipitated the phenolate anion intermediate. After 30 minutes of stirring, 1,3-propanesultone (1.1 eq., 0.260 mmol, 32 mg) was added, and the solution stirred vigorously overnight. The THF was removed under reduced pressure to yield a crude yellow solid, which was purified by column chromatography (silica gel, 4:1 dichloromethane:methanol) to afford sulfonate **3.1** as a yellow crystalline solid. Yield: 76 mg (0.201 mmol, 81%). ^{1}H NMR (DMSO-d6, 500 MHz) δ 2.02-2.1 (m, 2H), 2.61 (t, *J* = 7.3 Hz, 2H), 4.17 (t, *J* = 6.6 Hz, 2H), 7.09 (d, *J* = 8.8 Hz, 2H), 7.73 (d, *J* = 8.8 Hz, 2H), 7.93 (dd, *J* = 4.5, 1.7 Hz, 2H), 8.38 (s, 1H), 8.75 (dd, *J* = 4.5, 1.6 Hz, 2H). ^{13}C NMR (DMSO-d6, 100 MHz) δ 25.2, 47.8, 66.9, 115.3, 119.7(2), 119.7(3), 128.1, 139.4(9), 139.5(6), 141.0, 150.7, 159.3, 161.8. ESI-HRMS *m/z* calc'd for $C_{17}H_{15}N_2O_4S_2$ 375.0479, found 375.0478.

***N*-(2-(4-methoxyphenyl)-2-oxoethyl)picolinamide (3.9)**. A 250 mL round bottom flask equipped with a stir bar was charged with 2-amino-4'-methoxyacetophenone hydrochloride **2.4** (1.1 eq., 14.9 mmol, 3.00 g), picolinic acid (1 eq., 13.5 mmol, 1.66 g), EDCI·HCl (1.5 eq., 20.3 mmol, 3.89 g), and HOBt (0.5 eq., 6.76 mmol, 913 mg). After dissolving the contents in 40 mL of DMF, pyridine (1 eq., 13.5 mmol, 1.09 mL) was added to the reaction solution via a syringe, and the solution was allowed to stir magnetically overnight. The product was crystallized out of solution by the slow addition of 100 mL of diH_2O, after which it was filtered by suction filtration, washed with cold diH_2O, and dried over vacuum to afford **3.9** as a white crystalline solid. Yield: 3.48 g (12.9 mmol, 95%). ^{1}H NMR ($CDCl_3$, 400 MHz) δ 3.88 (s, 3H), 4.92 (d, *J* = 4.76 Hz, 2H), 6.98 (d, *J* = 8.8 Hz, 2H), 7.45 (ddd, *J* = 7.6, 4.8, 1.2 Hz, 1H), 7.85 (td, *J* = 7.7, 1.0 Hz, 1H), 8.02 (d, *J* = 8.8 Hz, 1H),

8.20 (dt, *J* = 7.8, 1.0 Hz, 1H), 8.63 (ddd, *J* = 4.8, 1.7, 0.9 Hz, 1H), 8.97 (s, 1H). ^{13}C NMR ($CDCl_3$, 100 MHz) δ 45.9, 55.5, 114.0, 112.1, 126.2, 127.6, 130.2, 137.1, 148.3, 149.6, 164.1, 164.5, 192.1. EI-MS *m/z* 270 ([M]$^+$, 5%), 135 (100%), 78 (23%). EI-HRMS *m/z* calc'd for $C_{15}H_{14}N_2O_3$ 270.1004, found 270.1002.

5-(4-methoxyphenyl)-2-(pyridin-2-yl)thiazole (3.10). To an oven-dried 2-neck 100 mL round bottom flask equipped with a stir bar was added picolinamide **3.9** (1 eq., 6.66 mmol, 1.80 g) and Lawesson's Reagent (1.3 eq., 8.65 mmol, 3.50 g). The flask was connected to a reflux apparatus, and using a glass frit connected to the top of the reflux condenser, the system was flushed with argon for several minutes to remove moisture. Using an argon-filled syringe, butryonitrile (40 mL, dried over 0.4 Å molecular sieves and filtered) was added through the top of the reflux condenser. The flask was lowered into an oil bath at 140°C and allowed to magnetically stir under reflux for 20 min. After cooling to room temperature, saturated $NaHCO_3$ (*aq*) solution (2 mL) was added to the deep red solution under stirring, and the mixture was diluted with ethyl acetate (40 mL), transferred to a separatory funnel, and washed with additional saturated $NaHCO_3$ and brine. The organic layer was dried over $MgSO_4$, filtered, and concentrated under reduced pressure to afford a yellow solid. The crude solid was purified via column chromatography (silica gel) using 7:2:1 hexanes:dichloromethane:MTBE as the elution solvent to afford pure **3.10** as a yellow solid. Yield: 1.36 g (5.07 mmol, 76%). ^{1}H NMR ($CDCl_3$, 400 MHz) δ 3.83 (s, 3H), 6.94 (d, *J* = 8.8, 2H), 7.29 (ddd, *J* = 7.7, 5.0, 1.3 Hz, 1H), 7.56 (d, *J* = 8.9 Hz, 2H), 7.78 (td, *J* = 7.8, 1.7 Hz, 1H), 7.97 (s, 1H), 8.16 (dt, *J* = 8.0, 1.0, 1H), 8.61 (ddd, *J* = 4.9, 1.6, 0.9, 1H). ^{13}C NMR ($CDCl_3$, 100 MHz) δ 55.3, 114.5, 119.2, 124.0, 124.1, 127.9, 136.9, 138.5, 141.5, 149.4, 151.5, 159.8, 166.9. EI-MS *m/z* 268 (100%, [M]$^+$), 253 (40%), 149 (25%), 121 (20%). EI-HRMS *m/z* calc'd for $C_{15}H_{12}N_2OS$ 268.0670, found 268.0668.

4-(2-(pyridin-2-yl)thiazol-5-yl)phenol (3.11). Thiazole **3.10** (1 eq., 0.373 mmol, 100 mg) was added to a 10 mL round bottom flask equipped with a stir bar. The flask was sealed with a rubber septum, evacuated under high vacuum, and backfilled with argon. Via an argon-filled syringe, anhydrous dichloromethane (2 mL) was transferred to the flask to dissolve the starting material. The flask was then lowered into a dry ice/acetone bath at -78°C, and upon thermal equilibration (~20 minutes), boron tribromide (3 eq., 1.12 mmol, 1.12 mL of a 1 M solution in dichloromethane) was added drop-wise to the stirred solution. The mixture was allowed to stir at -78°C for 5 minutes followed by 2.5 hours at room temperature. The mixture was diluted with ethyl acetate (10 mL), washed with diH_2O (10 mL), and the pH was adjusted to 7 to neutralize the excess BBr_3 using saturated Na-HCO_3. The aqueous layer was then extracted with ethyl acetate 2x more (10 mL each), and the combined organic layers were dried over $MgSO_4$, filtered, and concentrated to an orange-yellow crude solid. The crude solid was then purified via column chromatography (silica gel) using 1:1 ethyl acetate:hexanes, followed by recrystallization from 1:1 toluene:cyclohexane to afford **3.11** as a yellow crystalline solid. Yield: 73 mg (0.287 mmol, 77%). ^{1}H NMR (MeOD, 400 MHz) δ 6.86 (d, *J* = 8.8, 2 H), 7.41 (ddd, *J* = 7.5, 4.9, 1.2 Hz, 1H), 7.53 (d, *J* = 8.9, 2H), 7.90 (ddd, *J* = 7.9, 7.6, 1.7 Hz, 1H), 8.00 (s, 1H), 8.13 (dt, *J* = 8.0, 1.1 Hz, 1H), 8.56 (ddd, *J* = 4.9, 1.7, 1.0 Hz, 1H). ^{13}C NMR (MeOD, 100 MHz) δ 117.0, 120.3, 123.7, 125.7, 129.1, 138.6, 139.0, 143.7, 150.5, 152.4, 159.5, 167.7. EI-MS *m/z* 254 (100%, $[M]^+$), 150 (45%), 121 (20%). EI-HRMS *m/z* calc'd for $C_{14}H_{10}N_2OS$ 254.0514, found 254.0513.

Sodium 3-(4-(2-(pyridin-2-yl)thiazol-5-yl)phenoxy)propane-1-sulfonate (3.2). To a 10 mL round bottom flask equipped with a stir bar was added phenol **3.11** (1 eq., 0.248 mmol, 63 mg) and 1,4-dioxane (2 mL). Under magnetic stirring, NaOH (75 µL of a 20% (w/v) aqueous solution) was added to the solution, precipitating the phenolate anion

intermediate. The precipitate was redissolved by adding a few drops of water to the stirred mixture. After 15 minutes, 1,3-propanesultone (1 eq., 0.248 mmol, 30.3 mg) was added, and the solution was allowed to stir vigorously for 4 hours. The 1,4-dioxane/water mixture was removed by gentle evaporation, and the product was crystallized from a 3:1 isopropanol:methanol mixture to afford **3.2** as a yellow crystalline solid. Yield: 72 mg (0.181 mmol, 73%). ^{1}H NMR (DMSO-d6, 400 MHz) δ 2.00-2.06 (m, 2H), 2.58 (t, *J* = 7.4 Hz, 2H), 4.13 (t, *J* = 6.6 Hz, 2H), 7.03 (d, *J* = 8.8 Hz, 2H), 7.49 (ddd, *J* = 7.5, 4.8, 1.2 Hz, 1H), 7.69 (d, *J* = 8.8 Hz, 2H), 7.97 (td, *J* = 7.7, 1.7 Hz, 1H), 8.13 (dt, *J* = 7.9, 1.0 Hz, 1H), 8.27 (s, 1H), 8.64 (ddd, *J* = 4.8, 1.6, 1.0 Hz, 1H). ^{13}C NMR (DMSO-d6, 100 MHz) δ 25.2, 47.8, 66.9, 115.2, 118.8, 123.1, 124.9, 127.9, 137.7, 139.2, 140.9, 149.7, 150.6, 159.1, 166.0. ESI-HRMS *m/z* calc'd for $C_{17}H_{15}N_2O_4S_2$ ($[M+H]^+$) 375.0479, found 375.0476.

6-cyanopicolinic acid ethyl ester (3.12). Solid ethyl 6-bromopicolinate (1 eq., 65.2 mmol, 15.0 g) and cuprous cyanide (2 eq., 130.4 mmol, 11.68g) were added to a 250-mL round bottomed flask equipped with a stir bar. To the round bottomed flask was added anhydrous pyridine (60 mL). Under rapid stirring, the mixture was refluxed under argon for 6 hours. The flask was removed from the hot oil bath, and the black tarry mixture that remained in the flask was diluted with hot toluene (100 mL). To the diluted mixture was added celite powder (~20 g), and the mixture was allowed to stir for ~20 minutes to allow the toluene to penetrate the tarry residue, then the celite/tar was filtered through a bed of celite and washed with hot toluene (50 mL). The filtrate was decanted into a 500-mL round bottom flask, and the solvents were removed under reduced pressure to yield a thick, black residue. The residue was redissolved in ethyl acetate (400 mL), and the solution was transferred to a separatory funnel, diluted with 1 M citric acid (300 mL), and the aqueous layer was extracted with ethyl acetate (2 x 200 mL). The combined organic layers were dried over $MgSO_4$ and filtered, and concentrated under reduced pressure to yield

an orange solid, which was recrystallized from boiling hexanes to yield a white crystalline solid. The white solid was collected by suction filtration, washed with cold hexanes, and dried under high vacuum to give. Yield: 8.23 g (46.7 mmol, 72%). ^{1}H NMR ($CDCl_3$, 400 MHz) δ 1.46 (t, *J* = 7.1 Hz, 3H), 4.52 (q, *J* = 7.1 Hz, 2H), 7.90 (dd, *J* = 7.8, 1.1 Hz, 1H), 8.06 (t, *J* = 7.9 Hz, 1H), 8.34 (dd, *J* = 8.0, 1.1 Hz, 1H). ^{13}C NMR ($CDCl_3$, 100 MHz) δ 14.2, 62.6, 116.3, 127.9, 131.1, 133.9, 138.4, 149.7, 163.5. ESI-MS *m/z* 177 ($[M+H]^+$, 46%), 149 (90%). ESI-HRMS *m/z* 177 calc'd for $C_9H_9O_2N_2$ ($[M+H]^+$) 177.0659, found 177.0656.

6-cyanopicolinic acid (3.13). To a 100-mL round bottom flask was added 40 mL of 1N HCl (*aq*). The flask was lowered into a 100°C oil bath until the aqueous solution began to boil. While rapidly stirring, solid ethyl 6-cyanopicolinate (**3.12**, 28.95 mmol, 5.10 g) was added to the boiling solution, and a vacuum adapter equipped with a glass frit was inserted into the top joint to limit the rate of water evaporation but allow for the removal of ethanol as the starting material was hydrolyzed. Because of the low melting point of the starting material, the reaction mixture was initially biphasic, but the biphasic mixture was slowly converted to a homogeneous solution as the starting material was consumed. The solution was stirred for one hour, and then the flask was removed from the oil bath and allowed to cool to room temperature under medium stirring to permit crystallization of the product. To complete crystallization, the mixture was stirred at 0°C for another hour. The white precipitate was collected by suction filtration, washed with ice cold water (30 mL), followed by one portion (30 mL) of hot hexanes and one portion (30 mL) of 1:1 hexanes:dichloromethane. The white solid was then recrystallized from boiling toluene, collected by vacuum filtration, washed with additional toluene, and dried under vacuum. Yield: 3.50 g (23.63 mmol, 82%). ^{1}H NMR (Acetone-d6, 400 MHz) δ 8.22 (dd, *J* = 7.7, 1.2 Hz, 1H), 8.34 (t, *J* = 7.8 Hz, 1H), 8.42 (dd, *J* = 8.0, 1.2 Hz, 1H), 11.96 (s, br, 1H). ^{13}C NMR (Acetone-

d6, 100 MHz) δ 117.4, 128.7, 132.6, 133.9, 140.5, 150.2, 164.6. ESI-HRMS *m/z* 149 calc'd for $C_7H_5O_2N_2$ ($[M+H]^+$) 149.0346, found 149.0342.

6-cyano-*N*-(2-(4-methoxyphenyl)-2-oxyethyl)picolinamide (3.14). To a clean, dry 100-mL round bottom flask was added 6-cyanopicolinic acid **3.13** (1 eq., 19.93 mmol, 2.95 g), 2-amino-4'-methoxyacetophenone hydrochloride **2.4** (1.1 eq., 21.92 mmol, 4.42 g), 1-ethyl-3-(3-dimethylaminopropyl)carbodiimide hydrochloride (EDCI·HCl, 1.5 eq., 29.9 mmol, 5.73 g), and 1-hydroxybenzotriazole (HOBt, 0.5 eq., 9.97 mmol, 1.35 g) with a stir bar. The starting materials and reagents were dissolved in *N,N*-dimethylformamide (DMF, 60 mL), and upon dissolution (~ 5 min), pyridine (1 eq., 19.93 mmol, 1.61 mL) was added drop-wise to the stirring solution, and the solution was allowed to stir for 6 hours. The solution was then decanted into a 250-mL round bottom flask, diluted with 100 mL of de-ionized water to precipitate the product. The product was then collected by suction filtration, washed with cold deionized water and allowed to dry under vacuum. Yield: 6.47 (21.91 mmol, 68%). ^{1}H NMR ($CDCl_3$, 400 MHz) δ 3.90 (s, 3H), 4.93 (d, *J* = 4.8 Hz, 2H), 7.00 (d, *J* = 8.9 Hz, 2H), 7.87 (dd, *J* = 7.7, 1.1 Hz, 1H), 8.02 (d, *J* = 8.9 Hz, 2H), 8.06 (t, *J* = 7.8 Hz, 1H), 8.44 (dd, *J* = 8.0, 1.1 Hz, 1H), 8.75 (t, *J* = 4.6 Hz, 1H). ^{13}C NMR ($CDCl_3$, 100 MHz) δ 46.0, 55.6, 114.1, 116.5, 125.5, 127.3, 130.3, 130.6, 132.4, 138.7, 151.0, 162.5, 164.2, 191.6. EI-MS *m/z* 295 ($[M]^+$, 1%), 135 (100%). EI-HRMS *m/z* calc'd for $C_{16}H_{13}N_3O_3$ 295.0957, found 295.0954.

6-(5-(4-methoxyphenyl)thiazol-2-yl)picolinonitrile (3.15). To a round-bottomed flask containing vacuum-dried picolinamide **3.14** (1 eq., 14.97 mmol, 4.42 g) and Lawesson's Reagent (1.3 eq., 19.46 mmol, 7.87 g) was added to an oven-dried 100-mL round bottom flask equipped with a stir bar. The flask was connected to a reflux condenser, and the system was flushed with argon for several minutes to remove moisture. Through the top of the reflux condenser was added butryonitrile (60 mL) that had been previously dried

over 0.4 Å molecular sieves and filtered. The apparatus was flushed further with argon and then capped with a glass frit. The flask was lowered into an oil bath at 130°C, and the mixture was refluxed for 30 minutes. The solution was then removed from the oil bath, allowed to cool to room temperature, and the butryonitrile was removed under reduced pressure to yield a dark orange solid residue. The residue was transferred to a 500-mL flask and dissolved in reagent-grade acetone (400 mL). In a 2-L round bottom flask was dissolved 23.7 g of potassium permanganate in acetone (600 mL). The crude residue solution was decanted into a 1-L flask, and the dark purple solution was allowed to stir vigorously for 10 minutes to convert the thioamide byproduct back to the desired nitrile. The reaction was quenched by the addition of 1 M citric acid (aq) (500 mL). The teal-colored solution was filtered through a pad of celite, and the filtrete was concentrated under reduced pressure. The resulting solution was neutralized with saturated aqueous $NaHCO_3$ and extracted with dichloromethane (3 x 300 mL). The combined organic layers were dried over $MgSO_4$, filtered, and concentrated under reduced pressure to yield a yellow solid. The solid was then redissolved in a minimal amount of dichloromethane, loaded onto a 5-cm bed of silica gel, and purified over silica gel using dichloromethane as the eluent. The column product was recrystallized from boiling *n*-dibutyl ether (purified by stirring with crushed KOH pellets to remove any potential peroxide contamination, followed by filtration through a glass frit), collecting the pure yellow crystals by suction filtration and washing with addition *n*-dibutyl ether. Yield 2.55 g (8.68 mmol, 58%). ^{1}H NMR ($CDCl_3$, 400 MHz) δ 3.87 (s, 3H), 6.98 (d, J = 8.9 Hz, 2H), 7.59 (d, J = 8.9 Hz, 2H), 7.69 (dd, J = 7.6, 1.1 Hz, 1H), 7.93 (t, J = 8.1 Hz, 1H), 8.00 (s, 1H), 8.38 (dd, J = 8.1 Hz, 1.1 Hz, 1H). ^{13}C NMR ($CDCl_3$, 100 MHz) δ 55.4, 114.7, 116.8, 122.5, 123.6, 128.2, 128.3, 133.4, 138.0, 138.9, 143.3, 153.2, 160.2, 164.2. EI-MS *m/z* 293 ($[M]^+$, 100%), 278 (30%), 250 (10%),

149 (15%), 121 (16%), 77 (12%). EI-HRMS *m/z* calc'd for $C_{16}H_{11}N_3OS$ 293.0623, found 293.0623.

6-(5-(4-methoxyphenyl)thiazol-2-yl)picolinaldehyde (3.16). Solid picolinonitrile **3.15** (1 eq., 8.37 mmol, 2.46 g) was added to a 250-mL round bottom flask equipped with a stir bar. Via a rubber septum, the flask was evacuated and backfilled with argon several times to ensure exclusion of moisture. Once the starting material was nearly completely dissolved in anhydrous THF (80 mL), lithium diisobutyl *tert*-butoxyaluminum hydride (LDBBA, 1.5 eq., 12.56 mmol, 25.12 mL of a freshly prepared 0.5 M solution), that was prepared according to a published literature procedure,[15] was added dropwise to the rapidly stirred suspension. The deep blue solution that emerged after complete addition of the LDBBA reagent was stirred for 1 hour at room temperature. The reaction was quenched with the addition of 30 mL of 1 M citric acid and stirred for 20 minutes. The turbid mixture was extracted with EtOAc (3 x 50 mL), and the combined organic layers were dried over $MgSO_4$, filtered, and concentrated to afford a yellow-orange solid. The solid residue was purified by column chromatography (silica gel) using 1:1 EtOAc:hexanes as the eluent. The yellow column product was then recrystallized from boiling cyclohexane, and the pale yellow crystals were collected by suction filtration, washed with cold cyclohexane and dried over vacuum. Yield: 1.54 g (5.20 mmol, 62%). ^{1}H NMR ($CDCl_3$, 400 MHz) δ 3.87 (s, 1H), 6.98 (d, *J* = 8.9 Hz, 2H), 7.60 (d, *J* = 8.9 Hz, 1H), 7.95-8.01 (m, 2H), 8.02 (s, 1H), 8.39 (dd, *J* = 6.7, 2.3 Hz, 1H), 10.14 (s, 1H). ^{13}C NMR ($CDCl_3$, 100 MHz) δ 55.4, 114.6, 121.6, 123.3, 123.8, 128.1, 138.0, 138.8, 142.5, 152.2, 152.4, 160.1, 165.4, 193.0. EI-MS *m/z* 296 ($[M]^+$100%), 281 (33%), 149 (27%), 121 (26%). EI-HRMS *m/z* calc'd for $C_{16}H_{12}N_2O_2S$ 296.0619, found 296.0624.

2,2'-[iminobis(methylene)]diisonicotinic acid (3.17). *Synthesis and optimization performed by M. Thomas Morgan, Ph.D.* 2-cyanoisonicotinic acid (21.7 mmol, 3.21 g)

and 50% water wet 10% Palladium on activated carbon (1 mol%, 0.217 mmol, 461 mg) were stirred together in water (10 mL) in a 100 mL round-bottom flask. Methanol (20 mL) was added, followed by trimethylamine (1.2 eq., 26.0 mmol, 3.62 mL), and the flask was connected to a 3-way stopcock adapter, evacuated, and quickly back-filled with hydrogen gas from a 1-L gas burette. The burette was refilled to 1000 mL, and the mixture was vigorously stirred. After 250 mL of H_2(g) had been consumed, a further 50 mL of hydrogen was added to the burette to provide the full theoretical amount required (1040 mL at 22°C and 1 atm). H_2(g) consumption proceeded steadily for approximately 3 hours, then abruptly stopped with 35 mL remaining in the burette, corresponding to consumption of 98% of the theoretical amount. The flask was purged with argon, the mixture was filtered through celite, and the filter cake was washed with ethanol. The combined filtrate was concentrated to a viscous residue, which was taken up in ethanol (100 mL), diluted with toluene (50 mL), and concentrated again. The resulting partially solidified material was taken up in ethanol, filtered through a glass frit to remove the precipitated primary amine byproduct, and concentrated to dryness. The residue from the filtration was taken up in water (25 mL) and the product was precipitated by addition of 90% formic acid, collected by filtration, washed with ice water, and dried by suction overnight. Yield: 1.44 mg (5.01 mmol, 44%). Note: to dissolve in MeOD, two drops of potassium deuteroxide (KOD, 40% w/v in D_2O) were added, the solution was blown dry under a stream of argon to remove the D_2O, and the compound was redissolved in MeOD. ^{1}H NMR (MeOD, 400 MHz) δ 3.98 (s, 4H), 7.72 (dd, *J* = 5.1, 1.4 Hz, 2H), 7.90 (s, 2H), 8.54 (d, *J* = 5.5 Hz, 2H). ^{13}C NMR (MeOD, 100 MHz) δ 54.9, 123.2, 123.5, 148.4, 150.0, 160.5, 172.7. ESI-HRMS *m/z* 288 calc'd for $C_{14}H_{14}O_4N_3$ ($[M+H]^+$) 288.0979, found 288.0980.

2,2'-[iminobis(methylene)]diisonicotinic acid dimethyl ester (3.18). To a 25 mL round bottom flask equipped with a magnetic stir bar was added the starting dicarboxylic acid **3.17** (1 eq., 2.78 mmol, 800 mg) and methanol (12 mL). While stirring under a gentle stream of argon, trimethylsilyl chloride (TMSCl, 3 eq., 8.35 mmol, 1.06 mL) was added drop-wise into the mixture at room temperature, followed by vigorous stirring under reflux overnight. The following day, the methanol was removed under reduced pressure, the residue was reconstituted in dichloromethane (25 mL), washed with saturated $NaHCO_3$ (25 mL), and the organic layer was dried over $MgSO_4$, filtered, and concentrated to an amber-colored oil. The pure oil was crystallized by the addition of cyclohexane and subsequently recrystallized from boiling cyclohexane to afford **3.18** as yellow solid. Note: the crystallization was relatively insufficient, so the remainder of the pure compound was kept as an oil. Yield: 800 mg (2.54 mmol, 91%). ^{1}H NMR ($CDCl_3$, 400 MHz) δ 3.96 (s, 6H), 4.06 (s, 4H), 7.23 (dd, *J* = 5.1, 1.6 Hz, 2H), 7.91 (s, 1H), 8.72 (d, *J* = 5.1 Hz, 2H). ^{13}C NMR ($CDCl_3$, 100 MHz) δ 52.5, 54.1, 121.1, 121.3, 137.6, 149.9, 160.4, 165.4. EI-MS *m/z* 165 (53%), 151 (100%,), 137 (12%), 92 (10%). EI-HRMS *m/z* calc'd for $C_{16}H_{17}N_3O_4$ 315.1219, found 315.1208.

Fluorophore dimethyl ester 3.3a. To an oven-dried 10-mL round bottom flask equipped with a stir bar was added aldehyde **3.16** (1 eq., 0.506 mmol, 150 mg), bispicolylamine dimethyl ester **3.18** (1.07 eq., 0.542 mmol, 171 mg), and $Na(OAc)_3BH$ (1.5 eq., 0.759 mmol, 161 mg). Via a rubber septum, the flask was evacuated for several minutes and backfilled with argon to exclude moisture, and through an argon-filled needle was added 2 mL of anhydrous 1,2-dichloroethane to dissolve the reagents. The reaction was allowed to stir at room temperature for 24 hours. The reaction was quenched by the addition of 2 mL of diH_2O and allowed to stir for ~ 20 minutes. The organic layer was removed, dried over $MgSO_4$, filtered, and concentrated under reduced pressure to afford

a yellow oily residue. The residue was purified by column chromatography (neutral alumina) using 9:1 dichloromethane:methanol to afford **3.3a** as a glassy yellow solid. Yield: 232 mg (0.39 mmol, 77%). ^{1}H NMR ($CDCl_3$, 400 MHz) δ 3.86 (s, 3H), 3.92 (s, 6 H), 3.98 (s, 2H), 4.07 (s, 4H), 6.96 (d, *J* = 8.8 Hz, 2H), 7.51 (d, *J* = 7.7 Hz, 1H), 7.60 (d, *J* = 8.7 Hz, 2H), 7.70 (dd, *J* = 5.0, 1.5 Hz, 2H), 7.76 (t, *J* = 7.8 Hz, 1H), 7.97 (s, 1H), 8.01 (d, *J* = 7.7 Hz, 8.18 (s, 2H), 8.69 (d, *J* = 5.0 Hz, 2H). ^{13}C NMR ($CDCl_3$, 100 MHz) δ 52.6, 55.4, 59.7, 60.1, 114.5, 117.5, 121.2, 122.2, 123.7, 124.1, 128.0, 137.7, 137.8, 138.5, 141.5, 149. 9, 150.8, 158.7, 159.8, 160.5, 165.7, 167.4. ESI-HRMS *m/z* calc'd for $C_{32}H_{30}O_5N_5S$ ($[M+H]^+$) 596.1956, found 596.1962.

Fluorophore dicarboxylate 3.3b. Fluorophore dimethyl ester **3.3a** (1 eq., 0.167 mmol, 100 mg) was added to a 10 mL round bottom flask and dissolved in methanol (3 mL). While stirring, NaOH (2.8 eq., 0.468 mmol, 62 μL of a 30% (w/v) solution in H_2O) was pipetted into the solution, and the mixture was refluxed for 1 hour. The solution was cooled to room temperature, and the methanol was removed under a gentle stream of argon. Absolute ethanol (6 mL) was added to the flask, the mixture was heated until concentrated enough to allow for crystallization of the product. The crystals were collected by vacuum filtration, washed with ethanol, and dried over vacuum to afford dicarboxylate **3.3b** as a yellow crystalline solid. Yield: 97.3 mg (0.159 mmol, 95%). ^{1}H NMR (MeOD, 400 MHz) δ 3.83 (s, 3H), 3.92 (s, 2H), 3.99 (s, 4H), 7.00 (d, *J* = 8.9 Hz, 2H), 7.56 (dd, *J* = 7.7, 0.9 Hz, 1H), 7.63 (d, *J* = 8.9 Hz, 2H), 7.68 (dd, *J* = 5.1, 1.5 Hz, 2H), 7.82 (t, *J* = 7.7 Hz, 1H), 7.90 (dd, *J* = 7.8, 0.9 Hz, 1H), 8.01 (s, 2H), 8.05 (s, 1H), 8.53 (dd, *J* = 5.1, 0.7 Hz, 2H). ^{13}C NMR (MeOD, 100 MHz) δ 55.9, 60.3, 61.7, 115.8, 118.9, 123.2, 124.5, 125.0, 125.5, 129.1, 139.1, 139.4, 143.1, 148.6, 150.0, 151.6, 160.1, 160.6, 161.7, 168.5, 172.7. ESI-HRMS *m/z* calc'd for $C_{30}H_{24}N_5O_5S$ ($[M+H]^+$) 566.1504, found 566.1506.

Fluorophore 3.3c. A 10-mL round-bottom flask containing aldehyde **3.16** (1 eq., 0.675 mmol, 200 mg) and a stir bar was charged with $Na(OAc)_3BH$ (1.5 eq., 1.01 mmol, 215 mg) and bispicolylamine (1.2 eq., 0.81 mmol, 161 mg). After sealing with a rubber septum, the flask was evacuated under high vacuum and backfilled with argon. The contents of the flask were dissolved in anhydrous 1,2-dichloroethane (2 mL), and the reaction mixture was vigorously stirred overnight at room temperature. The following day, the reaction mixture was quenched with 1 M citric acid (1 mL) for ~ 10 minutes, the aqueous phase as made basic by the addition of saturated $NaHCO_3$(aq), and the product was extracted with dichloromethane (2 x 10 mL). The combined organic layers were dried over Na_2SO_4, filtered, and concentrated to a light brown solid residue. The product was dissolved in dichloromethane and purified by column chromatography (silica gel) using 3:10 acetone:DCM as the eluent, affording the product as a pure oil, which was crystallized and subsequently recrystallized from MTBE to yield **3.3c** as off-white, fibrous crystals. Yield: 226 mg (0.471 mmol, 70%). ^{1}H NMR ($CDCl_3$, 400 MHz) δ 3.84 (s, 3H), 3.93 (s, 2H), 3.95 (s, 4H), 6.95 (d, *J* = 8.8 Hz, 2H), 7.12-7.16 (m, 2H), 7.53 (d, *J* = 7.6 Hz, 1H), 7.57 (d, *J* = 8.9 Hz, 2H), 7.64-7.68 (m, 4H), 7.40 (t, *J* = 7.8 Hz, 1H), 7.95 (s, 1H), 8.00 (d, *J* = 7.8 Hz, 1H), 8.54 (d, *J* = 4.8 Hz, 2H). ^{13}C NMR ($CDCl_3$, 100 MHz) δ 55.4, 59.5, 60.2, 114.5, 117.4, 122.0, 122.9, 123.4, 124.2, 128.0, 136.4, 137.3, 138.5, 141.4, 149.1, 150.8, 159.3, 159.4, 159.8, 167.4. ESI-HRMS *m/z* calc'd for $C_{28}H_{26}N_5OS$ ($[M+H]^+$) 480.1844, found 480.1853.

Bis(2-pyrimidylmethyl)amine (3.19). In a 250 mL round-bottom flask, 2-cyanopyrimidine (1 eq., 57.1 mmol, 6.00 g) was dissolved in a 1,4-dioxane:diH_2O (3:1) mixture, and to the solution was added palladium (10%) on activated carbon (50% wet by H_2O, 2 mol %, 2.43 g). The flask was equipped with a 3-way stopcock adapter connected to an H_2 burette, which was filled with 1000 mL of H_2 (g). After repeated evacuation and backfilling with H_2 from the gas burette, the mixture was rapidly stirred while H_2 (2 eq., 114.2

mmol, 2.762 L) consumption from the gas burette proceeded steadily over the course of 48 hours. After complete consumption of the 2.8 L of H_2, the hydrogen-filled flask was carefully purged with argon, the palladium was filtered through a celite filter cake, washed with additional 1,4-dioxane, and the 1,4-dioxane/H_2O was removed under reduced pressure to leave an amber-colored oil residue. The residue was purified by column chromatography (silica gel, 1:4 EtOH:DCM) to afford **3.19** as an amber-colored oil. Yield: 2.58 g (12.83 mmol, 45%). Note: For $^{1}H/^{13}C$ NMR characterization, the oxalate salt of **3.19** was crystallized from MeOH/EtOH by the addition of 2.0 eq. of oxalic acid, followed by subsequent recrystallization from the boiling mixture. The product was filtered, dried under argon, and then redissolved in D_2O for NMR characterization. ^{1}H (D_2O, 400 MHz) δ 3.98 (s, 4H), 7.72 (dd, *J* = 5.1, 1.5 Hz, 2H), 7.90 (s, 2H), 8.54 (dd, *J* = 5.1, 0.7 Hz, 2H). ^{13}C NMR (D_2O, 100 MHz) δ 54.9, 123.2, 123.5, 148.4, 150.0, 160.5, 172.7. EI-MS *m/z* 201 (10%, $[M]^+$), 122 (23%,), 108 (100%), 94 (98%). EI-HRMS *m/z* calc'd for $C_{10}H_{11}N_5$ 201.1014, found 201.1004.

Chromis-2 (3.4). To a 10-mL round-bottom flask containing bis(2-pyrimidylmethyl)amine (**3.19**, 1.2 eq., 0.956 mmol, 193 mg) was added aldehyde **3.16** (1 eq., 0.797 mmol, 236 mg), $Na(OAc)_3BH$ (1.5 eq., 1.20 mmol, 253 mg) and a stir bar. The flask was sealed with a rubber septum, evacuated under high vacuum, and backfilled with argon. The contents were dissolved in anhydrous 1,2-dichloroethane (5 mL), and the reaction was stirred vigorously at room temperature for 24 hours. The reaction mixture was quenched with 1 M disodium citrate (2 mL), followed by extraction with dichloromethane (2 x 10 mL). The combined organic layers were dried over Na_2SO_4, filtered, and concentrated to an amber color oil residue, which was purified by column chromatography (silica gel) using 1:1 acetone:DCM as the eluent. The pure column product (pale yellow oil) was

crystallized by the addition of MTBE, followed by recrystallization from boiling MTBE:cyclohexane to afford **3.4** as an off-white crystalline solid. Yield: 270 mg (0.561 mmol, 70%). ^{1}H NMR ($CDCl_3$, 400 MHz) δ 3.85 (s, 3H), 4.26 (s, 2H), 4.35 (s, 4H), 6.95 (d, *J* = 8.8 Hz, 2H), 7.16 (t, *J* = 4.9 Hz, 2H), 7.56 (d, *J* = 8.7 Hz, 2H), 7.71-7.76 (m, 2H), 7.94 (s, 1H), 7.97 (dd, *J* = 5.9, 3.0 Hz, 1H), 8.72 (d, *J* = 4.9 Hz, 4H). ^{13}C NMR ($CDCl_3$, 100 MHz) δ 55.4, 59.9, 60.4, 114.5, 117.2, 119.1, 123.8, 124.2, 128.0, 137.2, 138.4, 141.2, 150.5, 157.0, 159.6, 159.8, 167.6, 168.5. EI-MS *m/z* 481 ($[M]^+$, 6%), 388 (40%,), 282 (100%), 200 (73%). EI-HRMS *m/z* calc'd for $C_{26}H_{23}N_7OS$ 481.1685, found 481.1699.

Primary amine 3.20. A 25-mL round-bottom flask containing nitrile **3.15** (1 eq., 1.1 mmol, 327 mg) and a magnetic stir bar was sealed with a rubber septum and evacuated under high vacuum to remove any residual moisture. After backfilling with argon, anhydrous THF (10 mL) was added to the flask through an argon-flushed syringe and needle. The flask was lowered into an ice bath and left to thermally equilibrate to 0°C, after which DIBAL-H (2.1 eq., 2.12 mmol, 1.77 mL of a 1.2 M solution in toluene) was added dropwise into the rapidly stirred mixture. After complete addition, the resulting dark amber-colored solution was stirred for 3 hours at 0°C until TLC analysis (9:1 CH_2Cl_2:MeOH) confirmed the complete consumption of the starting nitrile. The reaction was quenched by the addition of 1M citric acid, and after stirring for 20 minutes, the citric acid was neutralized by the addition of saturated Na_2CO_3 (aq) until the pH was above 8. The mixture was diluted with diH_2O and extracted with DCM (3 x 50 mL), and the combined organic layers were dried over Na2SO4, filtered, and concentrated to an amber-colored solid. The crude product was used in the next synthetic step without further purification. Yield: 284 mg (0.834 mmol). ESI-HRMS *m/z* calc'd for $C_{28}H_{26}N_5OS$ ($[M+H]^+$) 480.1844, found 480.1853.

Chromis-2-Ctrl (3.5). To a 10-mL round-bottom flask containing crude amine **3.20** (1 eq., 0.834 mmol, 248 mg) was added 5-formylpyrimidine (2.1 eq., 1.75 mmol, 189 mg), $Na(OAc)_3BH$ (2.5 eq., 2.09 mmol, 442 mg) and a stir bar. The flask was sealed with a rubber septum, evacuated under high vacuum, and backfilled with argon. The contents were suspended in anhydrous 1,2-dichloroethane (5 mL), and the reaction was stirred vigorously at room temperature overnight. The reaction mixture was quenched with 1 M disodium citrate (1 mL) for ~ 15 minutes, followed by extraction with dichloromethane (3 x 10 mL). The combined organic layers were dried over Na_2SO_4, filtered, and concentrated to an amber-colored oil. The oily residue was purified by column chromatography (silica gel) using 7:3 acetone:DCM as the eluent. The pure column product (pale yellow oil) was crystallized by the addition of MTBE, followed by recrystallization from boiling MTBE:cyclohexane to afford **3.5** as an off-white solid. Yield: 54 mg (0.112 mmol, 13%). ^{1}H NMR ($CDCl_3$, 400 MHz) δ 3.82 (s, 4H), 3.84 (s, 2H), 3.86 (s, 3H), 6.97 (d, *J* = 8.8 Hz, 2H), 7.30 (dd, *J* = 7.7, 0.8 Hz, 1H), 7.60 (d, *J* = 8.8 Hz, 2H), 7.79 (t, *J* = 7.8 Hz, 1H), 7.99 (s, 1H), 8.09 (dd, *J* = 7.8, 0.8 Hz, 1H), 8.82 (s, 4H), 9.17 (s, 2H). ^{13}C NMR ($CDCl_3$, 100 MHz) δ 53.1, 55.4, 58.1, 114.6, 118.1, 123.5, 124.0, 128.1, 131.7, 137.7, 138.7, 141.8, 151.3, 157.6, 158.1, 160.0, 166.8. EI-MS *m/z* 481 ($[M]^+$, 3%), 282 (100%,). EI-HRMS *m/z* calc'd for $C_{26}H_{23}N_7OS$ 481.1685, found 481.1676.

3.7.2 X-Ray Crystallographic Methods

3.7.2.1 Crystallization of the Zn(II) Complexes of Probes **3.3c** and Chromis-2 (**3.4**)

[(3.3c)Zn(II)] Complex: A solution of probe **3.3c** (20 mg) in a DMSO:acetone mixture (1.0 mL) was supplemented with a stoichiometric amount of $ZnClO_4 \cdot 7H_2O$ (15.5 mg), precipitating the Zn(II) complex of **3.3c**. The mixture was supplemented with ~ 0.5 mL of

water, and the mixture was gently heated to dissolve the metal-ligand complex. The solution was cooled to room temperature, and the heating and cooling procedure was repeated once more. The solution was filtered through a 0.2 μm nylon filter into a clean vial, and the complex was left to crystallize by slow evaporation to afford single, colorless, prism-shaped crystals suitable for X-ray crystallographic analysis.

[(Chromis-2)Zn(II) Complex: Chromis-2 (20 mg) was dissolved in HPLC-grade MeOH (2.0 mL), and the resulting solution was supplemented with a stoichiometric amount of $ZnBF_4 \cdot xH_2O$ (9.9 mg), precipitating the Zn(II) complex of chromis-2. The mixture was supplemented with ~ 0.5 mL of water, and the mixture was gently heated to dissolve the metal-ligand complex. After the solution cooled to room temperature, the solution was filtered through a 0.2 μm nylon filter into a clean vial, and the complex was left to crystallize by slow evaporation to afford single, colorless crystals suitable for X-ray crystallographic analysis.

3.7.2.2 X-Ray Crystal Structure Determination

[(3.3c)Zn(II)] Complex: a single, prism-shaped crystal (0.40 x 0.37 x 0.18 mm^3) was selected using a loop with paratone oil and mounted on a Bruker D8 diffractometer with an APEX2 detector. The crystal was cooled to T = 100(2) K during data collection. Data were measured using ω scans of 1.0° per frame for 25.0 s using MoK_α radiation (fine-focus sealed X-ray tube, 45 kV, 35 mA). The total number of runs and images collected was based on the strategy calculation from the APEX2 program (Bruker). The maximum resolution that was achieved was Θ = 30.508°C. The structure was solved and the space group $P2_1/c$ (#14) was determined by the ShelXT-2014/4 structure solution program[24] using Intrinsic Phasing and refined by least-squares minimization using ShelXL-2014/7.[25] All

non-hydrogens were refined anisotropically, and hydrogen atoms were calculated geometrically and refined using the riding model.

[(3.4)Zn(II)] Complex: a single crystal (0.265 x 0.246 x 0.206 mm^3) was selected using a loop with paratone oil and mounted on an XtaLAB Synergy Dualflex (Rigaku) diffractometer with a HyPix HPC detector. The crystal was cooled to T = 100(2) K during data collection. Data were measured using using CuK_α radiation. The structure was solved and the space group $P2_1/c$ (#14) was determined by the ShelXT-2014/4 structure solution program[24] using Intrinsic Phasing and refined by least-squares minimization using the ShelXL-2014/7 refinement package.[25] All non-hydrogens were refined anisotropically, and hydrogen atoms were calculated geometrically and refined using the riding model.

3.7.3 Determination of Protonation Constants

3.7.3.1 Glass Electrode Calibration

The protonation equilibrium constants were measured as concentration constants ($\log K_H$) based on potentiometric titrations using a combination double junction glass electrode. The double-junction electrode was calibrated via the titration of a strong acid (5 mM HCl, prepared by dilution of a 0.1 M standardized solution, Sigma-Aldrich) with a strong base (0.1 M KOH, standardized solution, Sigma-Aldrich) in a solution of 0.1 M KCl in a water-jacketed, temperature-controlled titration vessel (Metrohm) at 25°C under an argon atmosphere. From the experimental emf data, the endpoint, electrode potential, and slope were calculated according to Gran's Method using the GLEE software package (pK_w = 13.78, μ = 0.1 M KCl).[26] This calibration procedure was performed, on the same day, prior to the potentiometric titration of each compound, and the experimental electrode potential

and slope used to calculate the experimental p[H] were the result of the average of the emf data from the three independent acid-base calibration titrations.

3.7.3.2 Determination of the Protonation Constant of Model Compound **3.1**

A 10 μM solution of model compound **3.1** (diluted from a 3 mM stock solution in diH_2O) was prepared in 3.0 mL of aqueous buffer (5 mM PIPBS, 0.1 M KCl, 5 mM KOH, 25°C, pH 5.6) in a quartz fluorescence cuvette with a 1-cm pathlength. A combined potentiometric and spectrophotometric titration was carried out in the cuvette by the addition of HCl(*aq*) using various aliquot volumes and concentrations with absorption spectra acquired of the compound in ~ 0.1 pH-unit increments over the pH window between 5.6 and 3.8 (thermostat accessory set to 25°C). After the addition of each aliquot of acid, the solution was equilibrated by magnetic stirring until the pH electrode stabilized, the potential was recorded (in mV), and an absorbance spectrum was acquired over the spectral window of 250-500 nm. After correcting for dilution, the absorbance data were analyzed by non-linear least-squares fitting to a monoprotic equilibrium model. The protonation constant for model compound **3.1** was calculated based on the average calculated monoprotic equilibrium constant of three independent titrations.

3.7.3.3 Determination of the Protonation Constant of Model Compound **3.2**

A 10 μM solution of model compound **3.2** (diluted from a 3 mM stock solution in diH_2O) was prepared in 3.0 mL of aqueous 0.1 M KCl (filtered through a 0.2 μm filter) in a quartz fluorescence cuvette with a 1-cm pathlength, and the pH was adjusted to 4.0 using aqueous HCl (0.05 M). A combined potentiometric and spectrophotometric titration was carried out in the cuvette by the addition of HCl using various aliquot sizes and concentrations with absorption spectra acquired of the compound in ~ 0.1 pH-unit increments

over the pH window between 4.0 and 1.2 (thermostat accessory set to 25°C). After addition of each aliquot acid, the solution was equilibrated via magnetic stirring until the pH electrode stabilized, the potential was recorded (in mV), and an absorbance spectrum was acquired over the spectral window of 250-500 nm. After correcting for dilution, the absorbance data were analyzed by non-linear least-squares fitting to a monoprotic equilibrium model. The protonation constant for model compound **3.2** was calculated based on the average calculated monoprotic equilibrium constant of three independent titrations.

3.7.3.4 Determination of the Protonation Constants of Probe **3.3b**

A 20 μM solution of probe **3.3b** (diluted from a 3 mM stock solution in diH_2O) was prepared in 3.0 mL of aqueous buffer (10 mM PIPES, 0.1 M KCl, 25°C, pH 7.0) in a quartz fluorescence cuvette with a 1-cm pathlength. A combined potentiometric and spectrophotometric titration was carried out in the cuvette by the addition of HCl(*aq*) using various aliquot volumes and concentrations with absorption spectra acquired of the compound in ~ 0.2 pH-unit increments over the pH window between 7.0 and 0.70 (thermostat accessory set to 25°C). After the addition of each aliquot of acid, the solution was equilibrated by magnetic stirring until the pH electrode stabilized, the potential was recorded (in mV), and an absorbance spectrum was acquired over the spectral window of 250-500 nm. After correcting for dilution, the absorbance data were analyzed by non-linear least-squares fitting to a triprotic equilibrium model.

3.7.4 Steady-State Absorption and Fluorescence Spectroscopy

3.7.4.1 General Spectroscopic Methods

All buffers and stock solutions used in spectroscopic measurements were prepared using HPLC-grade water (JT Baker) or 18.2 MΩ•cm Mili-Q water and filtered to remove interfering particles or fibers. UV-Vis absorption measurements were performed on a Varian Cary Bio50 spectrophotometer equipped with a thermostat accessory (Peltier) at 25°C. Fluorescence spectroscopy measurements were performed using a Photon Technology International (PTI) fluorimeter equipped with a 75 W xenon arc lamp excitation source and a photomultiplier detection system (PMT voltage set to 1100 V for all experiments). Fluorescence spectra were corrected for the spectral response of the detection system and for the spectral irradiance of the excitation source (via a calibrated photodiode). For both UV-Vis absorption and fluorescence measurements, a 1-cm path length quartz fluorescence cuvette was utilized, except for fluorescence quantum yield determinations, which used a 10-cm path length quartz cuvette when collecting absorbance measurements.

3.7.4.2 Determination of Fluorescence Quantum Yields

Fluorescence quantum yields of compounds **3.1**, **3.2**, **3.3b** and chromis-2 (**3.4**) were determined in aqueous buffer (10 mM PIPES, 0.1 M KCl) at pH 7.0 by a 4-point measurement over an OD range of 0.1-0.4 using a 10-cm cuvette, with fluorimeter excitation at 365 nm. For probes **3.3b** and **3.4**, the solutions containing the free forms were supplemented with 20 μM EDTA (from a 30 mM stock solution in diH_2O) to sequester adventitious Zn(II), whereas to determine the Zn(II)-bound forms, the solutions were sup-

plemented with 20 μM $ZnSO_4 \cdot 7H_2O$ to ensure complete saturation of the fluorophore. Fluorescence quantum yields for all fluorophores were determined using quinine sulfate (Φ_f = 0.546 in 1.0 N H_2SO_4) as a fluorescence standard.[5] To determine the quantum yield of **3.3a**, single-point measurements were performed in aqueous buffer (10 mM PIPES, 0.1 M KCl, pH 7.0) supplemented with 100 μM 4:1 DMPC:DMPG liposomes and at a probe concentration of 2 μM. The fluorescence quantum yields reported were calculated as an average of two independent measurements for both the metal-free and metal-saturation species. The quantum yields were also referenced to quinine sulfate with an OD matching that of **3.3a** (2 μM) in liposomes.

3.7.4.3 Measurements of the Solvent Deuterium Isotope Effects

Comparison of the fluorescence intensities of model compounds **3.1** and **3.2** were conducted in deuterated and non-deuterated buffer (10 mM PIPES, 100 mM KCl, pH/D 7.0, 25°C). A 3.0 mL solution of aqueous buffer was supplemented with 10 μM of each compound (diluted from 3 mM stock solutions in H_2O), and after thorough mixing via magnetic stirring, fluorescence spectra of model compound **3.1** were acquired over the spectral window of 380-700 nm with excitation at 346 nm, while analogous fluorescence spectra of **3.2** were acquired over the spectral window of 380-650 nm with excitation at 345 nm. This procedure was repeated identically using deuterated buffer (10 mM PIPES, 100 mM KCl, pD 7.0, 25°C).

Comparison of the fluorescence intensities of probes **3.3b** and **3.4** were also performed in deuterated and non-deuterated buffer (10 mM PIPES, 100 mM KCl, pH/D 7.0, 25°C). A 3.0 mL solution of aqueous buffer was supplemented with 5 μM of each compound (diluted from 3 mM stock solutions in either H_2O (**3.3b**) or DMSO (**3.4**)), and after

thorough mixing via magnetic stirring, fluorescence spectra of each compound were acquired over the spectral window of 380-700 nm with excitation at 361 nm. This procedure was repeated identically using deuterated buffer (10 mM PIPES, 100 mM KCl, pD 7.0, 25°C).

3.7.4.4 Molar Ratio Titrations of Probes **3.3b** and **3.4**

A 20 μM solution of **3.3b** in pH 7.0 buffer (3.0 mL, 10 mM PIPES, 0.1 M KCl, 25°C) prepared in a quartz fluorescence cuvette with a 1-cm pathlength was titrated with $ZnSO_4 \cdot 7H_2O$ (from a 3 mM aqueous stock solution) in 2 μM (0.1 eq.) increments. After each aliquot of Zn(II), the solution was equilibrated for 30 seconds by magnetic stirring, and an absorbance (spectral window: 250-500 nm) and fluorescence spectrum (excitation: 361 nm, spectral window: 380-700 nm) were acquired.

For chromis-2 (**3.4**), a 10 μM solution of the probe in pH 7.0 buffer (3.0 mL, 10 mM PIPES, 0.1 M KCl, 25°C) prepared in a quartz fluorescence cuvette with a 1-cm pathlength was titrated with $ZnSO_4 \cdot 7H_2O$ (from a 3 mM aqueous stock solution) in 1 μM (0.1 eq.) increments. After each aliquot of Zn(II), the solution was equilibrated for 30 seconds by magnetic stirring, and an absorbance (spectral window: 250-500 nm) and fluorescence spectrum (excitation: 361 nm, spectral window: 380-700 nm) were acquired.

3.7.4.5 Metal-Ion Selectivity Measurements of Probes **3.3b** and **3.4**

A 5 μM solution (30 mL) of each probe was prepared in pH 7.0 aqueous buffer (10 mM PIPES, 100 mM KCl, 25°C) that had been previously equilibrated overnight with Chelex® to sequester adventitious metal ions, after which the Chelex settled to the bottom and the supernatant was filtered through a 0.2 μm filter. An aliquot (2.0 mL) of the solution

was transferred to a quartz fluorescence cuvette with a 1-cm path length, and a fluorescence spectrum was acquired over the spectral window of 380-700 nm with excitation at 361 nm. Under magnetic stirring, the solution was supplemented with each divalent metal cation (4 μM for transitions metals, corresponding to 80% fractional saturation of the probes, or 2 mM Ca(II) and Mg(II)), and a fluorescence spectrum was immediately acquired. The solution was then supplemented with $ZnSO_4 \cdot 7H_2O$ (from a 1 mM stock solution in H_2O) to yield a final concentration of 1 μM (with Co(II), Ni(II), and Cu(II)) or 5 μM (with all other metals: Mg(II), Ca(II), Mn(II), Fe(II)), and a fluorescence spectrum was immediately acquired. With Fe(II), the fluorescence spectrum was acquired after a 30-min equilibration to ensure complete formation of the [(**3.3b**)Zn(II)] complex, as Zn(II) slowly outcompeted Fe(II). The emission spectra corresponding to 80% fractional saturation of the probes by the interfering metal ions, as well as those corresponding to the addition of Zn(II), were integrated over the ranges of 440-495 nm (CH1) and 510-570 nm (CH2), and the resulting intensities were computed as a ratio of CH2/CH1 (CH1 for chromis-2 was 440-470 nm). Metal cations were supplied as aqueous stock solutions of the following salts: Mg(II), Ca(II) as chlorides (1 M stocks); Co(II) as $Co(NO_3)_2$ (1 μM stock); Mn(II), Fe(II), Cu(II), and Zn(II) as sulfates (1 μM stocks). To avoid aerial oxidation of Fe(II), the stock solution was freshly prepared in 10 mM H_2SO_4 before use.

To measure the fluorescence responses of each probe upon complete saturation of the probe, a 5 μM solution (15 mL) of the probe was prepared in aqueous buffer (10 mM PIPES, 100 mM KCl, 25°C, pH 7.0) that had been supplemented with 2.0 equivalents (10 μM, from a 30 mM stock solution in H_2O) of EDTA. A fluorescence spectrum was acquired of the free probe over the spectral window of 380-700 nm with excitation at 361 nm. The solution was supplemented with interfering divalent metal ions (30 mM stocks

solutions of each metal in H_2O) to yield final concentrations of 20 and 40 μM, with a fluorescence spectrum acquired immediately after each aliquot.

The stability constant for the formation of the chromis-2-Mn(II) complex was determined through a fluorimetric titration by direct addition of Mn(II). A 5 μM solution of chromis-2 was titrated with $MnSO_4 \cdot H_2O$ from 0-40 μM, with a fluorescence spectrum acquired immediately after each aliquot of Mn(II) added. The fluorescence data were analyzed by non-linear least-squares fitting using the Specfit software package.[2]

3.7.4.6 Zn(II)-Binding Affinity Measurements of Probe **3.3a**

The Zn(II) stability constant of **3.3a** was determined through a fluorimetric titration in the presence of EGTA as a competing ligand. A freshly extruded solution (500 μM) of DMPG liposomes (prepared according to the protocol described in the experimental section of Chapter 2) in neutral aqueous buffer (20 mM PIPES, 100 mM KCl, pH 7.0) was equilibrated at 25°C for 10 minutes. The liposome solution was supplemented with 100 μM EGTA (from a 300 mM stock solution in water at pH 7.0), and after a 10 minute equilibration, probe **3.3a** was diluted into the buffer from a 3 mM stock solution in DMSO to a final concentration of 2 μM. After another 20-minute equilibration to dissolve the probe in the liposomes, the solution was titrated with $ZnSO_4 \cdot 7H_2O$ from 0-90 μM by dilution from 3 and 15 mM stock solutions in H_2O. The fluorimetric data were analyzed by non-linear, least-squares fitting using the Specfit software package.[2]

3.7.4.7 Zn(II)-Binding Affinity Measurements of Probe **3.3b**

The Zn(II) stability constant of **3.3b** was determined through a fluorimetric titration using TMDTA (trimethylenedinitrilotetraacetic acid] as the competing ligand. A 10 μM solution of **3.3b** (from a 3 mM stock solution in H_2O) was equilibrated with 10 μM

$ZnSO_4 \cdot 7H_2O$ (from a 5 mM analytical stock solution in H_2O) in 3.00 mL of aqueous buffer (10 mM PIPES, 0.1 M KCl, pH 7.0) at 25°C. The *in situ*-generated [(**3.3b**)Zn(II)] complex was then titrated with TMDTA (from 3 and 20 mM analytical stocks solution in H_2O) from 0-80 μM. After the addition of each aliquot of TMDTA, the solution was equilibrated by magnetic stirring for 50 minutes, and a fluorescence spectrum was acquired over the spectral window of 250-500 nm. The fluorescence data were analyzed by non-linear least-squares fitting using Specfit.[2]

3.7.4.8 Zn(II)-Binding Affinity Measurements of Chromis-2 (**3.4**)

The Zn(II) stability constant of chromis-2 was determined via a fluorimetric titration using EGTA [Ethylene glycol-bis(2-aminoethylether)-*N,N,N′,N′*-tetraacetic acid] as the competing ligand. A 10 μM solution of chromis-2 (from a 3 mM stock solution in DMSO) was equilibrated with 10 μM $ZnSO_4 \cdot 7H_2O$ (from a 5 mM analytical stock solution in H_2O) in 3.00 mL of aqueous buffer (10 mM PIPES, 0.1 M KCl, pH 7.0) at 25°C. The *in situ*-generated [(chromis-2)Zn(II)] complex was then titrated with EGTA (from 3, 20, and 300 mM analytical stock solutions in H_2O) from 0-300 μM. After the addition of each aliquot of EGTA, the solution was equilibrated by magnetic stirring, and a fluorescence spectrum was acquired over the spectral window of 380-700 nm with excitation at 361 nm. The fluorescence data were analyzed by non-linear least-squares fitting using the Specfit software package.[2]

3.7.4.9 Fluorescence Comparison of Probes **3.3b** and Chromis-2

Fluorescence comparison measurements of **3.3b** and chromis-2 were conducted in deuterated and non-deuterated buffer (10 mM PIPES, 100 mM KCl, pH/D 7.0, 25°C).

A quartz cuvette with a 1-cm path length containing 3.0 mL of aqueous buffer was supplemented with 5 μM of **3.3b** (from a 3 mM stock solution in H_2O), and after a 30-second equilibration via magnetic stirring, a fluorescence spectrum was acquired over the spectral window of 380-700 nm with excitation at 361 nm. The probe was then saturated with 5 μM $ZnSO_4 \cdot 7H_2O$ (from a 3 mM stock solution in H_2O), and a fluorescence spectrum was acquired. This was repeated for **3.3b** in deuterated buffer, but with supplementation of 5 μM $ZnSO_4 \cdot 7H_2O$ from a 3 mM stock solution prepared in D_2O (Cambridge Isotopes). To compare the fluorescence intensities and profiles of **3.3b** to chromis-2, these procedures were repeated, except that the buffers were supplemented with 5 μM chromis-2 from a 3 mM stock solution in DMSO.

3.7.4.10 Absorbance and Fluorescence Response of Chromis-2-Ctrl (**3.5**) to Zn(II)

The absorbance and fluorescence response of chromis-2 ctrl (3.5) to Zn(II) was measured by a tandem fluorimetric and spectrophotometric titration. A 10 μM solution of chromis-2 (from a 3 mM stock solution in DMSO) was equilibrated in 3.00 mL of aqueous buffer (10 mM PIPES, 0.1 M KCl, pH 7.0, filtered through a 0.2 μM filter) at 25°C in a quartz cuvette with a 1-cm pathlength. Both a fluorescence spectrum (spectral window of 380-700 nm with excitation at 361 nm) and an absorbance spectrum (spectral window of 250-500nm) were acquired. The solution was titrated with $ZnSO_4 \cdot 7H_2O$ (from a 500 mM stock solution in H_2O) from 0.5-2 mM, and after the addition of each aliquot of $ZnSO_4 \cdot 7H_2O$, the solution was equilibrated by magnetic stirring for 5 minutes, and fluorescence and absorbance spectra were acquired.

3.7.4.11 Fluorescence Spectral Comparison of Chromis-2 (**3.4**) and Chromis-2-Ctrl (**3.5**)

A 10 μM solution of each probe (from 3 mM stock solutions in DMSO) was equilibrated in 3.00 mL of aqueous buffer (10 mM PIPES, 0.1 M KCl, pH 7.0, filtered through a 0.2 μM filter) at 25°C in a quartz fluorescence cuvette with a 1-cm pathlength. A fluorescence spectrum (spectral window of 380-700 nm with excitation at 361 nm) was acquired of the probe in solution. With chromis-2, the solution supplemented with 10 μM $ZnSO_4 \cdot 7H_2O$ (from a 3 mM stock solution in H_2O), and equilibration by magnetic stirring for 1 minute, a fluorescence spectrum was acquired.

3.8 References

1. Spectrophotometric pH Titration of Chromis-1 Acid (2.1b) was performed by S. Sumalekshmy, Georgia Institute of Technology, 2008

2. Binstead, R. A., Zuberbühler, A. D. *SPECFIT Global Analysis System*, 2001.

3. Anderegg, G.; Popov, K.; Pregosin, P. S. Nitrogen-NMR Studies on the Protonation of 2-(aminomethyl)pyridine and Tris(2-pyridylmethyl)amine. *Helv. Chim. Acta* **1986**, *69* (2), 329-332.

4. Casey, J. R.; Grinstein, S.; Orlowski, J. Sensors and Regulators of Intracellular pH. *Nat. Rev. Mol. Cell Biol.* **2010**, *11* (1), 50-61.

5. Brouwer, A. M. Standards for Photoluminescence Quantum Yield Measurements in Solution (IUPAC Technical Report). *Pure Appl. Chem.* **2011**, *83* (12), 2213-2228.

6. Pearson, R. G.; Williams, F. V. Rates of Ionization of Pseudo Acids 5: Steric Effects in the Base-Catalyzed Ionization of Nitroethane. *J. Am. Chem. Soc.* **1953**, *75* (13), 3073-3075.

7. Grabowski, Z. R.; Rubaszewska, W. Generalized Förster Cycle - Thermodynamic and Extrathermodynamic Relationships Between Proton Transfer, Electron Transfer and Electronic Excitation. *J. Chem. Soc. Faraday Trans.* **1977**, *73*, 11-28.

8. Forster, T. Die pH-Abhangigkeit der Fluoreszenz von Naphthalinderivaten. *Z. Elektrochem.* **1950**, *54* (7), 531-535.

9. Valeur, B.; Berberan-Santos, M. N. Structural Effects on Fluorescence Emission. In *Molecular Fluorescence: Principles and Applications*, Wiley-VCH Verlag GmbH & Co. KGaA: 2012; pp 75-107.

10. Lakowicz, J. R. *Principles of Fluorescence Spectroscopy*. 3rd Ed. ed.; Boston, MA: Springer US: 2006.

11. Charier, S.; Ruel, O.; Baudin, J. B.; Alcor, D.; Allemand, J. F.; Meglio, A.; Jullien, L.; Valeur, B. Photophysics of a Series of Efficient Fluorescent pH Probes for Dual-Emission-Wavelength Measurements in Aqueous Solutions. *Chem. Eur. J.* **2006**, *12* (4), 1097-1113.

12. Rosenmund, K. W.; Struck, E. Halogen Formed from Ring Carbon and its Replacement by Other Substitutes I. Announcement: Replacement of Halogen by the Carboxyl Group. *Berichte der Deutschen Chemischen Gesellschaft* **1919**, *52*, 1749-1756.

13. Julius von Braun, E. A. Fluoranthen und Seine Derivate, V. Mitteil.: Substitutions-Verhältnisse beim Alpha-Phenyl-Naphthalin. *Berichte der Deutschen Chemischen Gesellschaft* **1934**, *67* (6), 1051-1056.

14. Yamaguchi, K.; Yajima, K.; Mizuno, N. Facile Synthesis of Nitriles via Manganese Oxide Promoted Oxidative Dehydrosulfurization of Primary Thioamides. *Chemical Communications* **2012**, *48* (91), 11247-11249.

15. Choi, Y. M.; Choi, S. J.; Eom, K. Y.; Hwang, H.; An, D. K. Partial and Chemoselective Reduction of Nitriles with Metal Diisobutyl-t-butoxyaluminum Hydrides. *Bull. Korean Chem. Soc.* **2008**, *29* (11), 2303-2304.

16. McCall, K. A.; Huang, C. C.; Fierke, C. A. Function and Mechanism of Zinc Metalloenzymes. *J. Nutr.* **2000**, *130* (5), 1437S-1446S.

17. Huheey, J. E. K., E. A.; Keiter, R. L. *Inorganic Chemistry: Principles of Structure And Reactivity*. 3rd ed.; Harper & Row: 1983; p 936.

18. Smith, R. M.; Martell, A. E.; Motekaitis, R. J. NIST Critically Selected Stability Constants of Metal Complexes Database. Standard Reference Data Program, National Institute of Standards and Technology, U.S. Dept. of Commerce: Gaithersburg, MD, 2004.

19. Hansch, C.; Leo, A.; Taft, R. W. A Survey of Hammett Substituent Constants and Resonance and Field Parameters. *Chem. Rev.* **1991**, *91* (2), 165-195.

20. Albert, A.; Goldacre, R.; Phillips, J. 455. The Strength of Heterocyclic Bases. *J. Chem. Soc.* **1948**, (0), 2240-2249.

21. Deleers, M.; Servais, J. P.; Delaveleye, F.; Wulfert, E., Effect of Lipid-Composition Changes on Carbocyanine Dye Fluorescent Response. *Biochem. Biophys. Res. Commun.* **1984,** *123* (1), 178-185.

22. Hu, K. H.; Friede, R. L. Topographic Determination of Zinc in Human Brain by Atomic Absorption Spectrophotometry. *J. Neurochem.* **1968**, *15* (7), 677-685.

23. Sandstead, H. H.; Frederickson, C. J.; Penland, J. G. History of Zinc as Related to Brain Function. *J. Nutr.* **2000**, *130* (2), 496S-502S.

24. Sheldrick, G. M. SHELXT - Integrated Space-Group and Crystal-Structure Determination. *Acta Crystallogr. A* **2015**, *71*, 3-8.

25. Sheldrick, G. M. Crystal Structure Refinement with SHELXL. *Acta Crystallogr. C* **2015,** *71*, 3-8.

26. Gans, P.; O'Sullivan, B. GLEE, a New Computer Program for Glass Electrode Calibration. *Talanta* **2000**, *51* (1), 33-37.

CHAPTER 4

AFFINITY MISMATCH: TUNING THE AFFINITY OF EMISSION-RATIOMETRIC FLUORESCENT PROBES USING INTERCHANGEABLE METAL-BINDING LIGANDS FOR PROBING KINETICALLY EXCHANGEABLE INTRACELLULAR ZN(II)

4.1 Introduction

The physiological regulation of Zn(II) entails a complex array of endogenous Zn(II)-binding ligands, including membrane-localized transporters, cytoplasmic metal-binding proteins, and low-molecular-weight biomolecules that tightly regulate the storage, import/export, and subcellular localization of the metal ion to ensure proper cellular function. The miscellany of these Zn(II)-binding molecules gives rise to a broad range of affinities that spans several orders of magnitudes. The corresponding affinities of these ligands are manifested by their chemical diversity, which encompasses not only the coordination environment but also the molecular location of the bound metal ion (i.e. whether the metal ion is surface-exposed or buried within the molecule), thus the chemical nature of these Zn(II)-binding sites dictates whether the metal ions are freely exchangeable between ligands or are hindered by a large kinetic barrier for exchange.

As discussed in Chapter 1, human metallothioneins (MT), which contain ~ 20 conserved cysteine residues that participate in binding up to seven Zn(II) ions per protein, constitute a prominent example of one Zn(II)-binding protein that may play a central role in intracellular zinc regulation. Metallothionein displays a range of Zn(II) affinities that spans four orders of magnitude, which is made possible through two chemically distinct

Zn(II) cluster binding sites of the two subunits of the protein.[1-3] One of the binding sites results in the formation of a Zn_4S_{11} cluster with an average apparent log*K* of 11.8, corresponding to a picomolar dissociation constant.[4] One the other hand, the second cluster, denoted as the Zn_3S_9 cluster, is characterized by weaker affinities, with one Zn(II) ion coordinating with an apparent log*K* of 7.7 and the other two Zn(II) ions displaying two apparent log*K*'s of ~ 10 and 10.5. To establish the binding affinities of the weakly bound Zn(II) ions, fluorescent probes with varying affinities for Zn(II) were employed in competition titrations with thionein, the apo form of metallothionein, and evaluated through fluorimetric titrations. However, elucidating the binding affinity of the more-tightly bound Zn(II) ions required chelating ligands with tighter binding affinities, such as nitriloacetic acid (NTA), in order to compete with the MT for Zn(II) binding. These experimental observations suggest that the availability of Zn(II) for biological processes is dependent on not only the redox state of MT but also the thermodynamic and kinetic accessibilities, which in turn depend on the molecular structure of the ligands involved in metal exchange. Therefore, an associative exchange between various metal-binding ligands requires that the ligands participating in the metal-transfer equilibria boast similar dissociation constants.

To probe intracellular Zn(II) that exists in an environment with a higher thermodynamic stability, fluorescent indicators must be designed with sufficiently high binding affinities to be able to participate in associative exchanges with the endogenous ligands. At the same time, probing intracellular Zn(II) pools that are much more dynamic and labile requires fluorescent indicators with lower affinities. Tuning the affinity of fluorescent indicators to achieve a wide dynamic range of affinities, therefore, is critical for exploring highly dynamic and more static Zn(II)-transfer equilibria involved in regulating the complex trafficking and homeostasis processes in cells.

Experimentally determining the dissociation constants that result from tuning the affinity of fluorescent indicators demands the employment of Zn(II)-chelating ligands with matching affinities to compete with the fluorescent indicators for the metal analyte. If the binding affinity of the chelating ligand is well-characterized, competition titrations, in which the solution containing the preformed metal complex of the fluorescent indicator is supplemented with the competing ligand, can be performed, and the data can be analyzed computationally to establish the binding affinity of the fluorescent indicator. Important criteria, however, include not only the availability of a suitable competing reference ligand but that also the coordination chemistry, protonation constants, and binding affinity of the ligand have been well-established.

4.1.1 Affinity Standards for Determining the Stability Constants of Zn(II)-Responsive Fluorescent Probes

The most commonly employed of the available affinity standards for Zn(II) are presented in Table 4.1. With the exception of TEDTA, all ligands are commercially available in analytically pure grades, and protonation constants and absolute stability constants for Zn(II) have been well-established. Although the most commonly reported intracellular pH is 7.2,[5] the experimentally determined cytosolic pH ranges between 6.8 and 7.4,[6-15] thus a neutral pH of 7 corresponds to a representative average for characterizing the stability constants of fluorescent indicators. Considering an ionic background of $I = 0.1$ M (K^+ ion), the pH-independent stability constants of the affinity standards can be converted into apparent stability constants at pH 7.0 using the corresponding protonation constants tabulated in Table 4.1.

Table 4.1: Thermodynamic properties of affinity standards for Zn(II) at 25°C.[a]

Ligand	pK_{a4}	pK_{a3}	pK_{a2}	pK_{a1}	logβ	logβ'[b]	K_d'[b]
DTPA	10.50	8.50	4.28	2.70	18.2	13.0	0.1 pM
EDTA	10.19	6.13	2.69	2.00	16.5	13.1	79 fM
EGTA	9.40	8.79	2.70	1.90	12.6	8.2	6.3 nM
HEDTA	9.87	5.38	2.62	1.60	14.6	11.6	2.5 pM
TEDTA	9.31	8.37	2.68	2.00	13.4	9.5	0.32 nM
TMDTA	10.30	7.90	2.63	2.09	15.2	10.7	20 pM
TPEN	7.12	4.81	3.30	2.88	15.4	15.0	1 fM

[a] All values are acquired from reference [21]. [b] pH 7.0, 25°C, 0.1 M ionic background. Acronyms: DTPA = diethylenetriaminepentaacetic acid; EDTA = ethylenediaminetetraacetic acid; EGTA = ethylene glycol-bis(2-aminoethylether)-*N*,*N*,*N*′,*N*′-tetraacetic acid; HEDTA = *N*-(2-hydroxyethyl)ethylenediamine-*N*,*N*′,*N*′-triacetic acid; TEDTA = thiobis(ethylenenitrilo)tetraacetic acid; TMDTA = trimethylenediaminetetraacetic acid; TPEN = *N*,*N*,*N*',*N*'-tetrakis(2-pyridylmethyl)ethylenediamine

As illustrated in Figure 4.1A, the Zn(II) stability constants of the affinity standards span a dynamic range of affinities of nearly six orders of magnitude between logβ = 12.6 and 18.2. Because the stability constants do not consider protonation equilibria that may compete for metal binding to the ligand, the pH-dependent apparent stability constants are typically lower protonation equilibria will inherently result in an apparent stability constant that is lower, given that the pK_a's of most of these ligands reside above physiological pH.[16] For example, diethylenetriaminepentaacetic acid (DTPA) boasts an absolute logβ of 18.2; however, due to the presence of two pK_a's above pH 7.0, the apparent stability constant decreases a dramatic five logarithmic units to 13.0 at pH 7.0, corresponding to a nearly 160,000-fold decrease in the dissociation constant from 0.63 aM to 0.1 pM (Figure 4.1B). Interestingly, despite the nearly two-logarithmic-unit decrease in the logβ of EDTA compared to DTPA, the presence of only one pK_a above pH 7.0 results in a 0.1-logarithmic-unit increase in the apparent stability constant, corresponding to a 1.3-fold lower binding affinity for DTPA relative to EDTA. This ordering is reversed, however, when the pH

is increased from 7.0 to 7.4, a commonly referenced physiological pH of eukaryotic cells.[9] At pH 7.4, DTPA has a 0.2-logarithmic-unit increase in the apparent stability constant, corresponding to a 1.6-fold lower affinity for EDTA relative to DTPA (Figure 4.1C). Because the solution pH can dramatically affect the stability constants for these affinity standards, it is important to ensure that the pH is effectively controlled throughout the competition titration; this can be accomplished using a sufficient concentration (10 - 20 mM) of a non-complexing buffer[17] with a buffer capacity at or near the pH of choice, as well as verifying the pH of the solution at the beginning and end of the competition titration. In addition, when determining the apparent stability constant of the fluorescent indicator at the pH of interest, once an approximate binding affinity has been determined through a preliminary titration, it is to validate the apparent stability constant using an affinity standard whose dissociation constant is within the dynamic range (± 1 logarithmic unit) of the dissociation constant of the indicator to ensure robust data fitting to the corresponding equilibrium model.

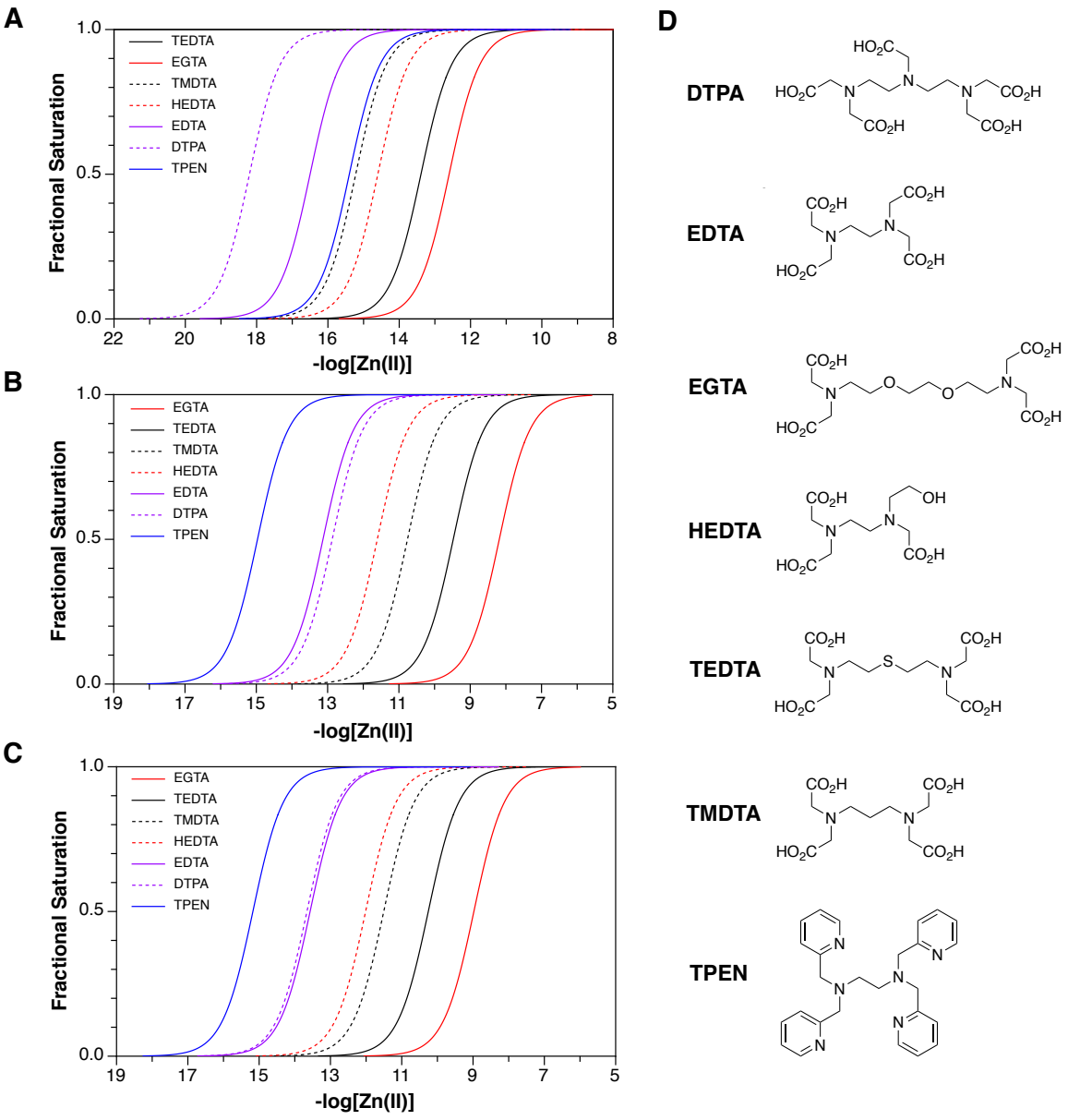

Figure 4.1: Affinity standards for determining Zn(II)-binding affinities and the effect of competing protonation equilibria on their Zn(II) dynamic range. Binding isotherms depicting the dynamic range for Zn(II) binding are presented as absolute stability constants (A), not factoring in protonation constants) and as apparent stability constants at pH 7.0 (B) and at pH 7.4 (C). D) Chemical structures with corresponding acronyms of the affinity standards shown in A-C.

4.1.2 Tuning the Affinity of Non-Centrosymmetric Donor-Acceptor Emission-Ratiometric Fluorescent Probes

As evidenced by the three-logarithmic-unit difference in the stability constants between fluorophores **3.3b** and chromis-2, the modularity of the 2-thiazolyl fluorophore core derived from the aldehyde functionality developed in Chapter 3 enabled facile affinity tuning via the reductive coupling of various chemically diverse metal-chelating ligands with the fluorophore. This chapter entails the design and synthesis of several Zn(II)-binding ligands that, once coupled to the 2-thiazolyl fluorophore core, led to the development of a series of fluorescent indicators offering a broad dynamic range of binding affinities spanning several orders of magnitude for exploring the thermodynamic and kinetic barriers availability of labile Zn(II) pool in biological systems.

4.2 Development of a Low-Affinity Fluorescent Probe for Accessing Dynamic Labile Zn(II) Pools buffered in the Pico- to Nanomolar Concentration Range

The intricate cellular machinery, such as the metallothionein/thionein couple and other endogenous proteins, that helps regulate the cytoplasmic “labile” Zn(II) pool in the picomolar regime results in an environment that is nearly devoid of free Zn(II) present as the aquo-complex. Nonetheless, Zn(II) may accumulate at much higher concentrations within subcellular structures. To probe this Zn(II) pool, fluorescent probes with significantly lower affinity are required, thus demanding a new ligand system that would coordinate Zn(II) much weaker compared to the previously employed pyridine or pyrimidine-based ligands. Considering the substitution of a carboxylate group with a hydroxyl group results in a two-logarithmic-unit decrease in the stability constant of HEDTA relative to EDTA,

hydroxyl groups represented a promising modification for designing ligands with weaker Zn(II) affinity. The search for potential ligands incorporating a secondary amine and hydroxyl groups led to investigating the use of commercially available diethanolamine as a ligand offering a low affinity for Zn(II). The result of this design approach was the synthesis and characterization of probe **4.1**.

*4.2.1 Synthesis of Probe **4.1***

As shown in Scheme 4.1, the synthesis of **4.1a** was accomplished in one step by coupling commercially available bis(2-hydroxyethyl)amine to aldehyde **3.16** through a reductive amination using sodium cyanoborohydride ($NaCNBH_3$) in MeOH. Previous reductive aminations to synthesize various fluorophores in Chapters 2 and 3 were successful using sodium triacetoxyborohydride ($Na(OAc)_3BH$) in 1,2-dichloroethane, as the reduced reactivity of the triacetoxyborohydride reagent helps to prevent reduction of the aldehyde to the corresponding alcohol; however, the reactivity of $Na(OAc)_3BH$ has proven to be very inconsistent in protic solvents[18], and given the presence of the hydroxyl groups of bis(hydroxyethyl)amine, it is possible that these functional groups could have an influence on the stability of the hydride reagent.

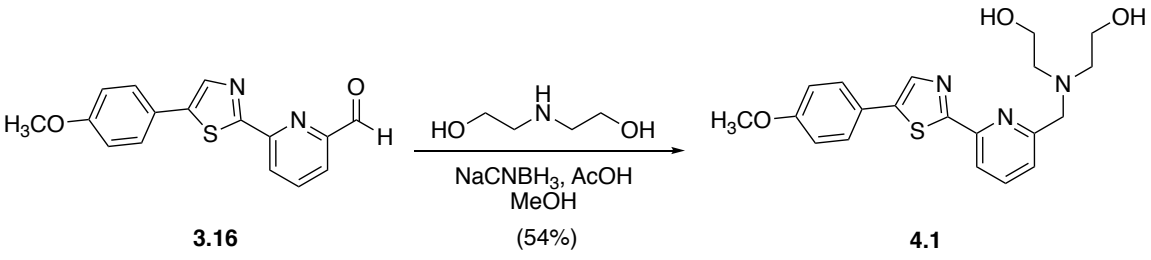

Scheme 4.1: Synthesis of the bis(hydroxyethyl)amine-containing fluorophore **4.1**.

The reaction of the bis(hydroxyethyl)amine with aldehyde **3.16** to form the corresponding iminium intermediate had the susceptibility to undergo a reversible, intramolecular acyl-like substitution reaction to generate the corresponding oxazolidine ring intermediate, which inhibits reduction of the intermediate by the hydride reagent (Scheme 4.2). To overcome this challenge, one equivalent of AcOH was added to promote the elimination of the alcohol, reforming the iminium intermediate, and to increase the reactivity of the cyanoborohydride, as the reduction of imines are much faster at weakly acidic to neutral pH's.[19] Despite these precautions, the synthesis of **4.1** was accomplished with only a 54% yield, suggesting that the equilibrium to form the iminium intermediate was not favorable enough to permit isolation of the product in high yield.

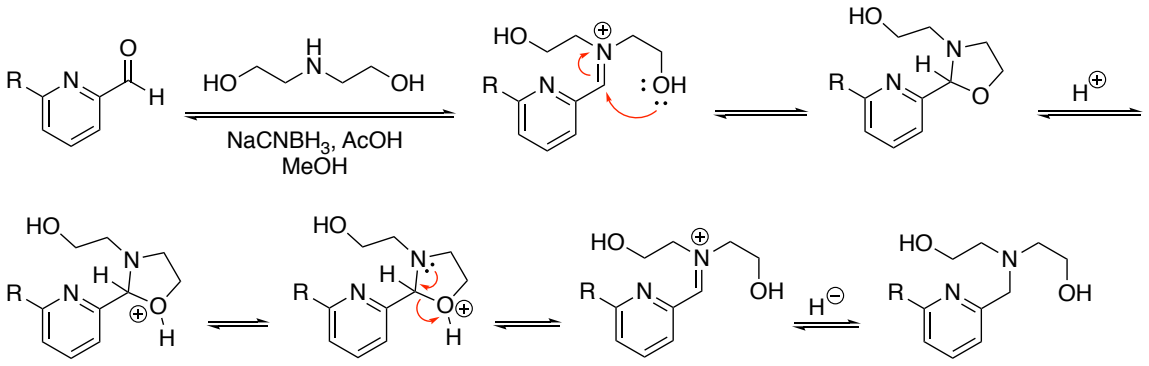

Scheme 4.2: Proposed mechanism for the formation of the oxazolidine intermediate, which can reversibly undergo elimination in the presence of a weak acid to reform the iminium intermediate that is reactive towards [H^-].

*4.2.2 Probe **4.1** Binds Zn(II) with Low Micromolar Affinity*

As detailed in Chapter 1, Zn(II) has an intermediate hard/soft acidic character, thus the nature of the ligands used for selective complexation of Zn(II) in aqueous solution tend to be nitrogenous bases, such as imidazole and pyridine, given their analogous borderline hard/soft basic character. The presence of the bis(hydroxyethyl)amine ligand coupled to

the donor-acceptor fluorophore introduces two hard Lewis bases as donors for coordinating Zn(II), which was expected to significantly lower the affinity for Zn(II), while still maintaining a 1:1 binding stoichiometry through the formation of a trigonal bipyramidal geometry from the five available donor atoms. Before the stability constant of **4.1** for Zn(II) could be determined, a fluorimetric, metal-addition titration was performed to establish whether the probe would bind Zn(II) with near unity fractional saturation, thus permitting a molar ratio titration to be performed. However, the metal-addition titration confirmed a substantially lower affinity compared to **3.3b**, thus determination of the stability constant was performed through a fluorimetric metal-addition titration by **4.1** (20 μM) with $ZnSO_4 \cdot 7H_2O$ from 0-220 μM. Non-linear least-squares fitting of the fluorimetric data yielded a uniform apparent stability constant of $\log K_{Zn(II)L} = 5.34 \pm 0.04$ at pH 7.0 and 0.1 M KCl ionic background, corresponding to an apparent dissociation constant of 4.6 ± 0.4 μM (Figure 4.2).

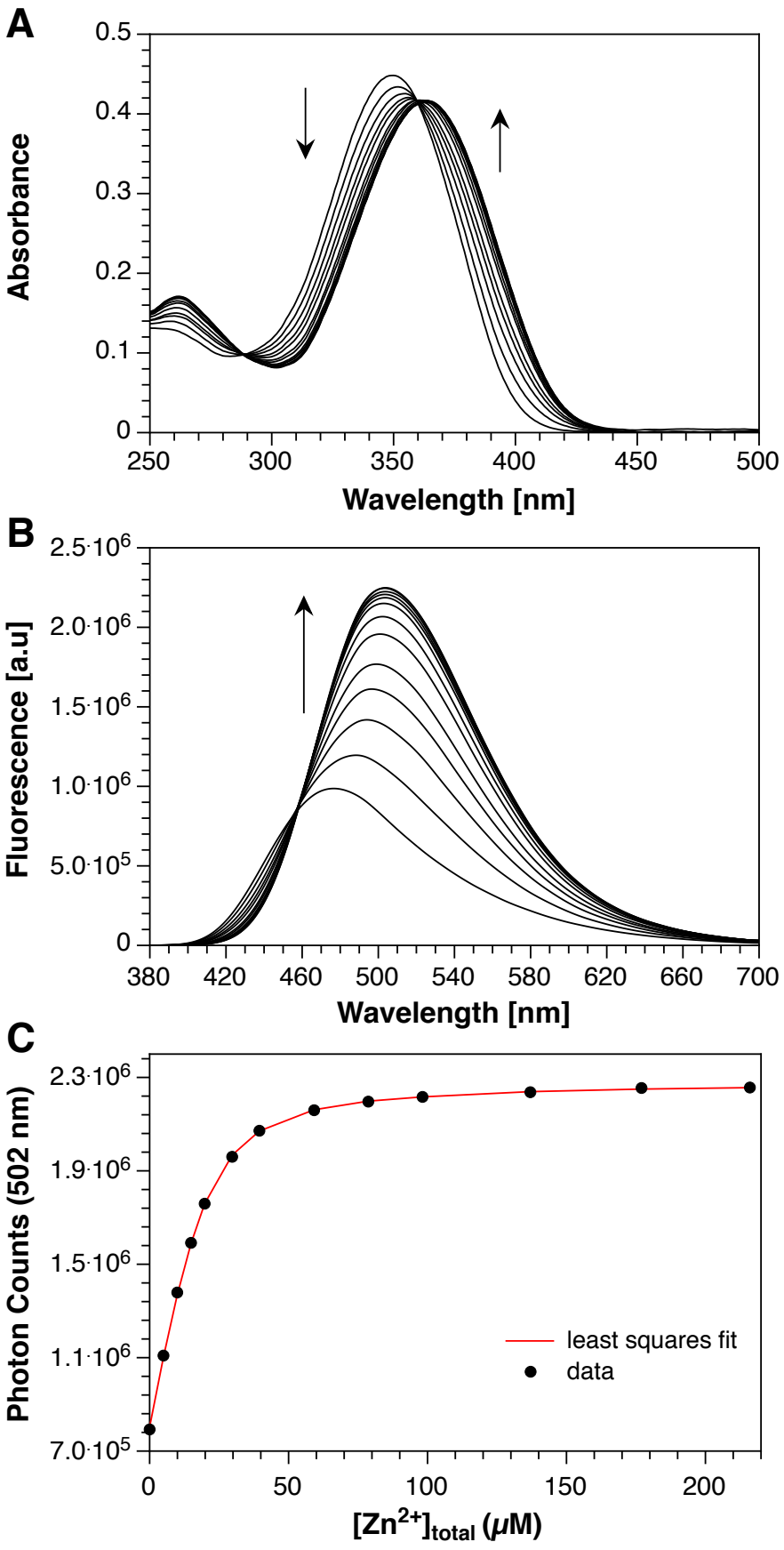
A
Absorbance
0.5
0.4
0.3
0.2
0.1
0
250
300
350
400
450
500
Wavelength [nm]
B
Fluorescence [a.u]
2.5·10^6
2.0·10^6
1.5·10^6
1.0·10^6
5.0·10^5
0
380
420
460
500
540
580
620
660
700
Wavelength [nm]
C
Photon Counts (502 nm)
2.3·10^6
1.9·10^6
1.5·10^6
1.1·10^6
7.0·10^5
0
50
100
150
200
[Zn2+]total (μM)
least squares fit
data

Definition of Equilibrium System:

Species	Zn(II)	**4.1**	H	logβ'
Zn(II)	1	0	0	0.0
4.1	0	1	0	0.0
[(**4.1**)Zn(II)]	1	1	0	*5.34 ± 0.04*

Figure 4.2: Fluorimetric determination of the Zn(II) stability constant of **4.1** by a direct, metal-addition titration. Probe **4.1** (20 μM) was equilibrated in chelexed aqueous buffer (10 mM PIPES, 0.1 M KCl, pH 7.0, 25ºC) and titrated with $ZnSO_4 \cdot 7H_2O$ from 0-220 μM. The fluorescence spectra (excitation: 360 nm) were analyzed by non-linear least squares fitting to give an average apparent $\log K_{Zn(II)L}$ of 5.34 ± 0.04 (n = 3) at pH 7.0, μ = 0.1 M (KCl). B) Change in fluorescence response at 502 nm with corresponding fit to the equilibrium system model described above.

*4.2.3 Absorbance and Fluorescence Properties of Probe **4.1***

The discovery of the micromolar affinity of **4.1** for Zn(II), manifested by the lack of a linear emission increase upon incremental addition of Zn(II), revealed weaker chromatic shifts in both the absorption and emission compared to chromis-2 (**3.4**). Upon complete saturation, **4.1** underwent a 14-nm bathochromic shift in the absorbance maximum from 350 nm (ε = 22,400 $M^{-1} \cdot cm^{-1}$) to 364 nm (ε = 20,800 $M^{-1} \cdot cm^{-1}$) (Table 4.2). The presence of two clean isosbestic points at 289 and 360 nm, in addition to the tight correlation of the fluorimetric titration data to the corresponding equilibrium model, are indicative of a well-defined equilibrium between the free- and Zn(II)-saturated species with a 1:1 binding stoichiometry.

Comparably, the fluorescence emission of the free- and Zn(II)-saturated **4.1** revealed a weaker bathochromic emission shift of only 27 nm from 475 nm to 502 nm, nearly half that of chromis-2 and probe **3.3b**. Interestingly, the quantum yield of free **4.1** only increased from 0.25 to 0.29, with Zn(II)-saturated **4.1** decreasing from 0.69 to 0.65, relative to **3.3b**, despite the lack of the bispicolylamine moiety to foster an ESPT that can lead to a fluorescence quenching. However, the two hydroxyl groups of the chelating moiety of **4.1** likely influence the pK_a of the tertiary nitrogen due to sigma donation from the oxygen

lone pairs, resulting in an increase in the pK_a to a value that is near or above physiological pH, which is evident when comparing the emission response of **4.1** in deuterated and non-deuterated buffer (Figure 4.3).

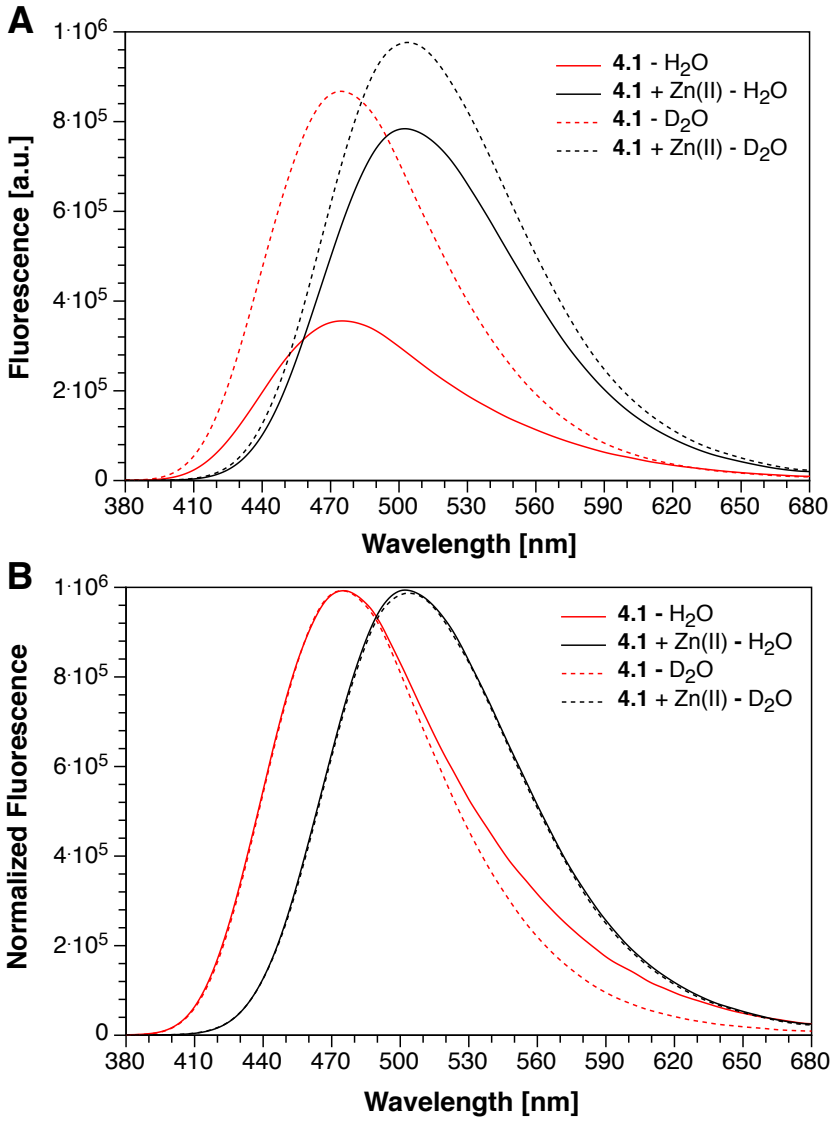

Figure 4.3: A) Solvent deuterium isotope effect of probe **4.1** (5 μM) in deuterated versus non-deuterated buffer (10 mM PIPES, 100 mM KCl, pH/D 7.0, 25°C). B) Normalization of the fluorescence spectra of free and Zn(II)-bound **4.1** as shown in (A).

Table 4.2: Photophysical properties of probe **4.1**[a]

	4.1	**[(4.1)Zn(II)]**
Absorbance λ_{max} (nm)[b]	350	364
ε (10^4 $M^{-1}cm^{-1}$)[c]	2.24	2.0
Emission λ_{max} (nm)[d]	475	502
Φ_F [e]	0.29	0.65
δ_{max} (GM)[f]	n.d.	n.d.
λ_{max} (nm)[g]	n.d.	n.d.

[a]10 mM PIPES, 0.1 M KCl, 25°C. [b]lowest-energy band of the one-photon absorption spectrum. [c]molar extinction coefficient at λ_{max}. [d]maximum fluorescence emission. [e]fluorescence quantum yield, referenced to quinine sulfate (Φ_F = 0.546).[20] [f]maximum two-photon absorption. [g]two-photon absorption cross section. n.d. = not determined.

*4.2.4 Exploring the Performance of Probe **4.1** in Mouse Fibroblast Cells*

To explore whether **4.1** can be utilized to follow dynamic fluctuations of endogenous free Zn(II) pools, adherent NIH 3T3 fibroblast cells grown under basal conditions were incubated with the probe (10 μM) and imaged by TPEM over the course of 30 minutes before supplementing the incubation medium with zinc pyrithione. However, treatment of the NIH 3T3 cells with the probe induced acute cytotoxicity that resulted in uniform cell death, which prevented the monitoring of basal Zn(II) levels.

4.3 Development of a Non-Phototoxic, Low-Affinity Fluorescent Probe for Zn(II)

The unpredicted cytotoxicity of **4.1** precluded its use as a fluorescent indicator in live cells. Because the structural deviation between chromis-2 and probe **4.1** is evident only in the chelator group, it was hypothesized that the presence of the diethanolamine chelator was responsible for its phototoxicity. Although the substitution of one of the ethanolamine arms of the diethanolamine chelator with a pyridine moiety would increase its

affinity for Zn(II), it was expected that the remaining, weakly donating hydroxyl group would maintain an affinity at or near that of chromis-2. This presumption led, first, to the synthesis of a new chelating ligand, which was then incorporated into the synthesis of a new fluorescent probe (**4.2a/b**) for imaging dynamically exchangeable Zn(II) in cells.

*4.3.1 Synthesis of Probe **4.2b***

The conception of a chelator whose binding affinity would theoretically lie between that of the bis(hydroxyethyl)amine-containing probe **4.1** and probe **3.3b** stimulated the design of a hybrid chelator, whose structure featured an asymmetric secondary amine, with one arm incorporating an isonicotinic acid methyl ester moiety and the other arm incorporating a hydroxyethyl moiety. The asymmetry of the new hybrid chelator demanded the synthesis of a new isonicotinic acid derivative that could be easily scaled up for future synthesis of diverse chelators without the need for conversion to a hydrogen halide salt, as in the synthesis of bromide **2.10**. Given the chemical versatility of the reductive amination reaction, the design of an aldehyde-containing isonicotinate derivative, that could be employed as a chemical foundation for the preparation of ligands of varying affinities, was conceived.

The synthesis of the aldehyde building block benefited from the already-established chemistry used in the synthesis of alcohol **2.9**, and preparation proceeded through a double esterification of 2,4-pyridinedicarboxylic acid to generate the corresponding dimethyl ester **4.5** (Scheme 4.3), which crystallized as pure white crystals significantly more easily than the analogous diethyl ester prepared in the synthesis of the metal-binding ligand of chromis-1. The esterification was accomplished by refluxing the dicarboxylic acid in MeOH using TMSCl as a catalyst, generating HCl *in situ* from the reaction of methanol with TMSCl, rather than the conventional concentrated H_2SO_4 or HCl. The reductive

chemistry used to synthesized alcohol **2.9** was adopted for use in preparation of methyl 2-(hydroxymethyl)isonicotinate **4.6**; however, reduction of the *o*-methyl ester of **4.5** using $NaBH_4$ (1.0 equivalent) in MeOH was completed in less than 40 minutes, whereas the analogous reduction of **2.8** to the corresponding alcohol **2.9** required 2.5 hours for complete conversion. Despite TLC confirmation that complete conversion occurred without the formation of any side products, in addition to the added lipophilicity of the *p*-methyl ester, the isolated yield of **4.6** was only 69%, most likely due to the incomplete extraction by virtue of the hydrophilic nature of the 2-pyridinemethanol unit. Finally, oxidation of the benzylic alcohol to the corresponding aldehyde was accomplished by refluxing **4.6** with 5.0 equivalents of precipitated active MnO_2, which selectively oxidizes benzylic alcohols to aldehydes, in toluene. A literature substructure survey of MnO_2 oxidations demonstrated the use of solvents such as acetone or chloroform with reaction times between 14-24 hours due to the solvents' low boiling points; however, the use of toluene as the solvent permitted complete conversion to aldehyde **4.7** in only 1.5 hours without the formation of any side products and with a yield after recrystallization of 91%.

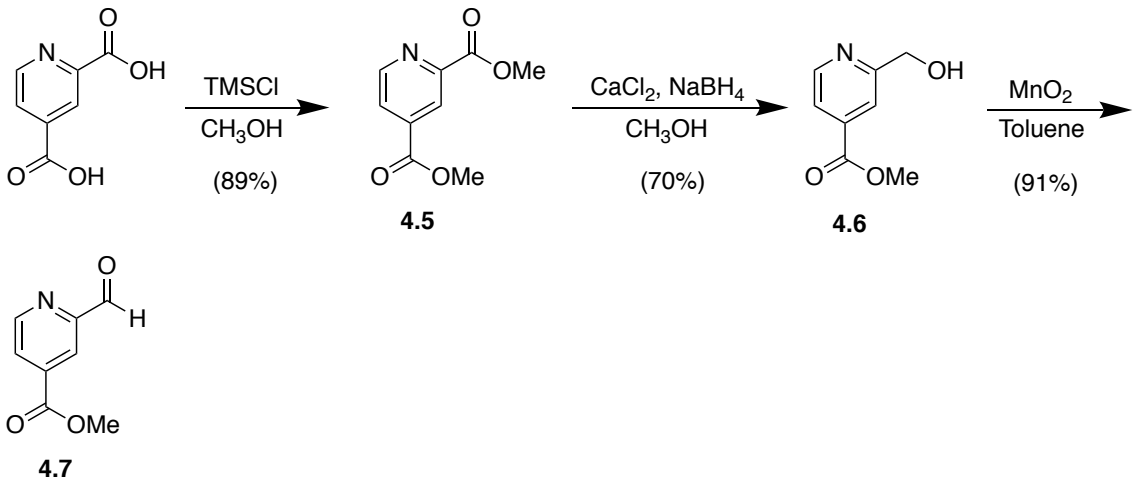

Scheme 4.3: Synthesis of methyl 2-formylisonicotinate **4.7**.

To promote the addition of only one molecule of 2-aminoethanol to aldehyde **4.7**, a solution of aldehyde **4.7** in MeOH was supplemented with 3.0 equivalents of the primary amine and left to react overnight, thereby building up the imine intermediate, which, upon the addition of $NaCNBH_3$, was reduced to the corresponding secondary amine (**4.8**) within 20 minutes at room temperature (Scheme 4.4). Despite TLC confirmation that the reaction had completed, purification by flash column chromatography on silica gel revealed an overall yield of only 40%.

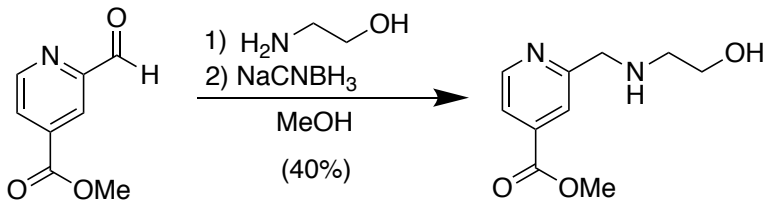

4.7 **4.8**

Scheme 4.4: Synthesis of metal-binding ligand **4.8.**

Using similar chemistry employed in the preparation of **4.1**, amine **4.8** was reacted with aldehyde **3.16** using $NaCNBH_3$ as the reducing agent to furnish fluorophore **4.2a**. Unfortunately, the substitution of one hydroxyethyl "arm" of bis(2-hydroxylethyl)amine with a methyl isonicotinate group did not observe an improved yield in the preparation of **4.2a** compared to **4.1**, despite addition of AcOH to prevent the potential formation of a potential oxazolidine intermediate. Nonetheless, probe **4.2a** was successfully prepared with a yield of 39%, and upon purification, a portion of the pure material was saponified by refluxing with 1.5 equivalents of NaOH(*aq*) in MeOH to afford the corresponding pure sodium carboxylate salt **4.2b** in high yield (91%), which was isolated by crystallization from and subsequent filtration of a MeOH:EtOH mixture upon cooling to room temperature.

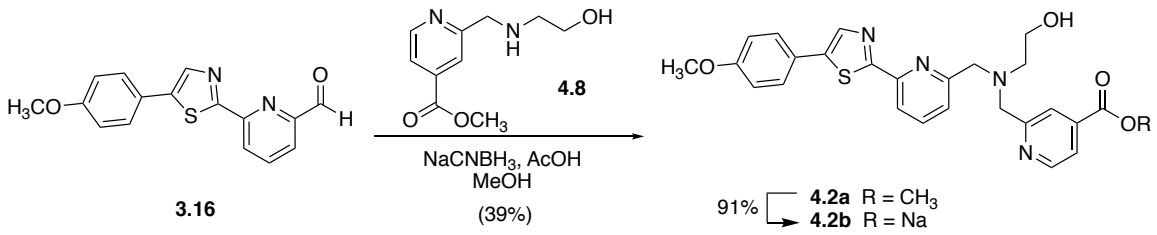

Scheme 4.4: Synthesis of probes **4.2a and 4.2b**.

*4.3.2 Absorption and Fluorescence Properties of Probe **4.2b***

Consistent with coordination of Zn(II) to the pyridyl acceptor of the fluorophore, **4.2b** also underwent a 14-nm bathochromic absorbance shift from a λ_{max} of 349 nm (ε = 22,200 $M^{-1}\cdot cm^{-1}$) to 363 nm (ε = 20,500 $M^{-1}\cdot cm^{-1}$) for the Zn(II)-saturated form (Table 4.3). The presence of two clean isosbestic points at 286 and 359 nm, in addition to an equimolar saturation of the probe with metal, are indicative of a well-defined equilibrium between the free- and Zn(II)-saturated species with a 1:1 binding stoichiometry (Figure 4.4A). Not surprisingly, the substitution of one of the hydroxyethyl arms with an isonicotinate moiety had a profound effect on the fluorescence quantum yield of the free form of **4.2b**, down 10% from 0.25 to 0.15 relative to probe **4.1**. Analysis of the structure of **4.2b** suggests that the hydroxyl group of the chelator could participate in the transfer of a proton from the chelator pyridine to the pyridyl acceptor of the fluorophore, a process that may be more efficient than an intermolecular, water-mediated transfer, thus resulting in a greater fluorescence quenching of the free form. The fluorescence emission of free **4.2b** revealed a similar emission maximum (467 nm) to chromis-2 and **3.3b**, which underwent a 38-nm emission shift to 505 nm for the Zn(II)-saturated form, while boasting a more-than-4-fold increase in the fluorescence quantum yield to from 0.15 to 0.65 (Figure 4.4B).

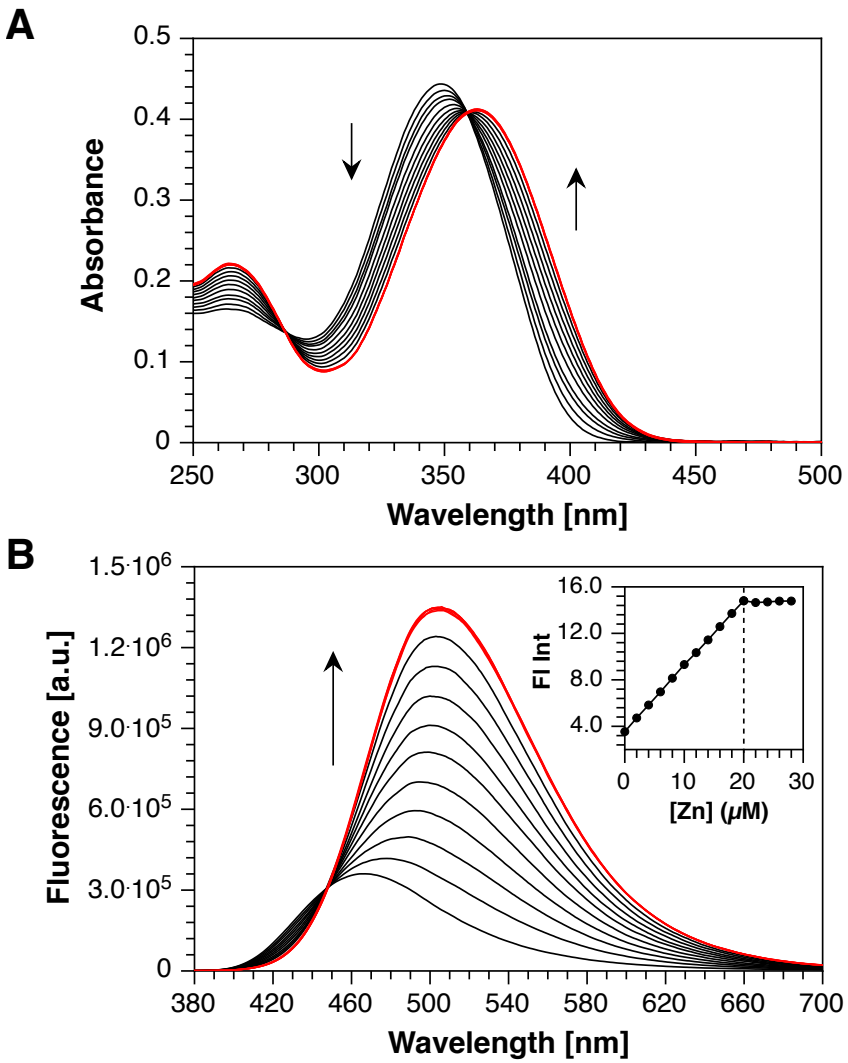

Figure 4.4: Spectral changes of **4.2b** in neutral aqueous buffer (10 mM PIPES, 100 mM KCl, 25°C) at pH 7.0 upon stepwise saturation of Zn(II). (A) Absorption (UV-Vis) spectral changes upon saturation with Zn(II). (B) Fluorescence emission response upon saturation with Zn(II) (excitation at 359 nm). The red curves indicate the spectra after complete saturation (1.0 eq.) with Zn(II) is achieved. Inset: fluorescence integration over the entire spectral window as a function of molar equivalents of Zn(II).

Table 4.3: Photophysical properties of probe **4.2b**[a]

	4.2b	**[(4.2b)Zn(II)]**
Absorbance λ_{max} (nm)[b]	349	363
ε (10^4 $M^{-1}cm^{-1}$)[c]	2.22	2.05
Emission λ_{max} (nm)[d]	467	505
Φ_F [e]	0.15	0.65
δ_{max} (GM)[f]	n.d.	n.d.
λ_{max} (nm)[g]	n.d.	n.d.

[a]10 mM PIPES, 0.1 M KCl, 25°C. [b]lowest-energy band of the one-photon absorption spectrum. [c]molar extinction coefficient at λ_{max}. [d]maximum fluorescence emission. [e]fluorescence quantum yield, referenced to quinine sulfate (Φ_F = 0.546 in 1N H_2SO_4).[20] [f]maximum two-photon absorption. [g]two-photon absorption cross section. n.d. = not determined.

*4.3.3 Zn(II)-Binding Affinity Measurements of Probe **4.2b***

In contrast to probe **4.1**, a molar ratio titration of probe **4.2b** that demonstrated a linear emission increase, along with a sharp, equimolar saturation point indicative of tight Zn(II) binding, permits the determination of a reliable stability constant through spectroscopic titrations of the probe with a competing ligand whose protonation and stability constants are well established. Substitution of a hydroxyl group with a pyridine in the structure of the chelator was expected to increase the stability constant of **4.2b** by a few orders of magnitude over **4.1**, thus EGTA as the lowest-affinity, commercially available Zn(II) chelator with a 1:1 binding stoichiometry was employed as a competing ligand to measure the affinity of **4.2b**. Attempts to determine the affinity in neutral aqueous buffer (10 mM PIPES, 100 mM KCl, pH 7.0, 25°C) using EGTA revealed a sharp decrease in the fluorescence intensity upon addition of 1.0 equivalent of EGTA. After further supplementation of EGTA to complete the competition titration within the 10-90% fractional saturation window, fitting of the fluorimetric titration data to the 1:1 binding equilibrium model resulted in a poor data

fit with a less-than-ideal standard deviation (Figure 4.5A, B), which was likely due to an affinity mismatch between probe **4.2b** and EGTA at pH 7.0 that resulted in a ~ 50% fractional saturation of the probe after equimolar addition of the competing ligand.

By virtue of the two protonation constants of EGTA that reside above 7, decreasing the pH by 0.5 logarithmic units translated to an apparent affinity for Zn(II) that is one logarithmic unit lower than at pH 7.0, as a higher percentage of protonated EGTA inevitably decreases its affinity for binding the metal. Therefore, the fluorimetric competition titration with **4.2b** was performed at pH 6.5 rather than pH 7.0, thereby engendering a better affinity match between the two components of the equilibrium. Non-linear, least-squares fitting of the fluorimetric data from the competition titration performed at pH 6.5 afforded an apparent stability constant of $\log K_{Zn(II)L}' = 7.75 \pm 0.06$, corresponding to an apparent dissociation constant of $K_d' = 18 \pm 3$ nM and yielding a more robust fit with a lower standard deviation (Figure 4.5C,D).

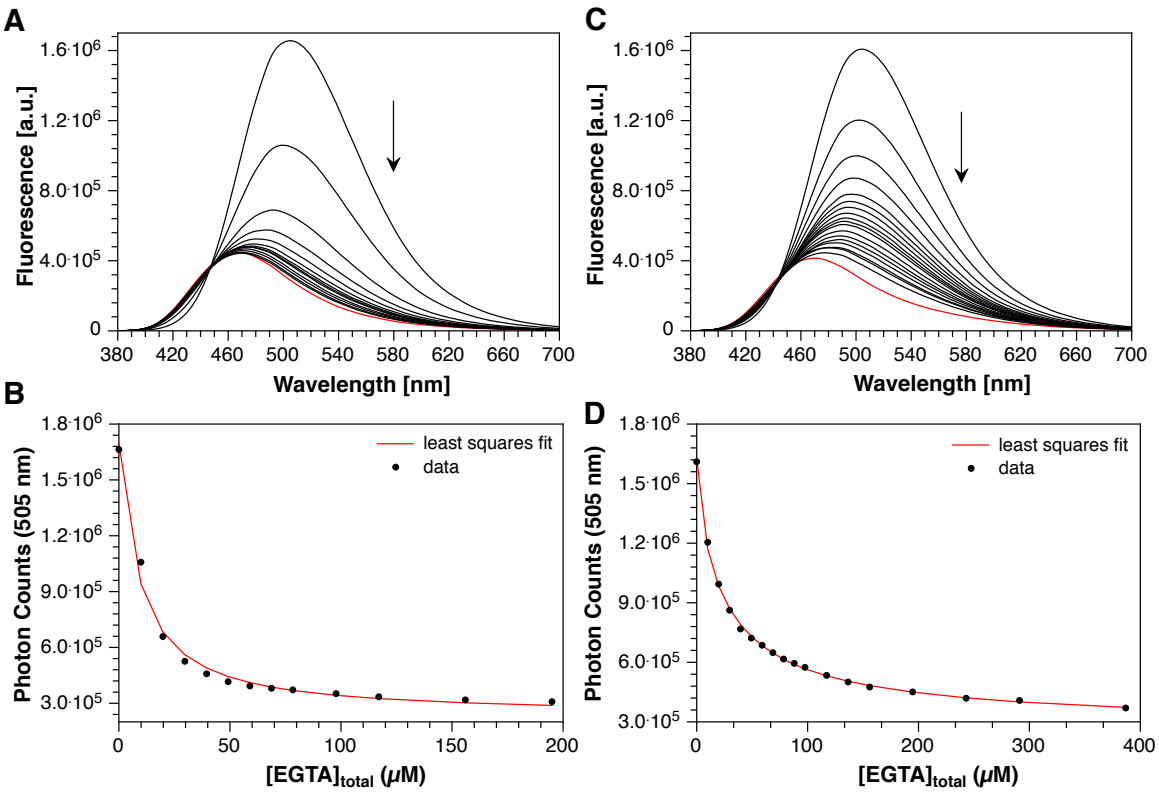

Definition of Equilibrium System:

Species	Zn(II)	EGTA	**4.2b**	H	log β
Zn(II)	1	0	0	0	0
EGTA	0	1	0	0	0
4.2b	0	0	1	0	0
EGTA(H)	0	1	0	1	9.51
EGTA(H_2)	0	1	0	2	18.41
EGTA(H_3)	0	1	0	3	21.22
[(EGTA)Zn(II)]	1	1	0	0	12.6
[(**4.2b**)Zn(II)]	1	0	1	0	*7.75 ± 0.06*

Figure 4.5: A) Fluorimetric determination of the Zn(II) stability constant of **4.2b** via competition with EGTA at pH 7.0 and 6.5. Probe **4.2b** (10 μM) was equilibrated with $ZnSO_4 \cdot 7H_2O$ (10 μM) in chelexed aqueous buffer (10 mM PIPES, 0.1 M KCl, pH 7.0, 25ºC) and titrated with EGTA from 0-400 μM. The fluorescence spectra (excitation: 359 nm) were analyzed by non-linear least squares fitting to give an average apparent $\log K_{Zn(II)L}$ of 7.75 ± 0.06 (n = 3) at pH 6.5, μ = 0.1 M (KCl). B) Change in fluorescence response at 505 nm with corresponding fit to the equilibrium system model described above.

*4.3.4 Metal-Ion Selectivity of Probe **4.2b***

As illustrated in Figure 4.6, the metal-ion selectivity of probe **4.2b** was evaluated in the presence of the excess of biologically relevant divalent metal ions. Identical to the methods for evaluating the metal-ion selectivity of the previous Zn(II)-binding fluorescent probes, the fluorescence response to probe **4.2b** was measured in the presence of 4.0 and 8.0 equivalents of the biologically relevant divalent metal ions to completely saturate both the fluorescent probe and the EDTA that was introduced to sequester any adventitious metal ions in solution. As expected, Mg(II) and Ca(II) had no influence on the fluorescence response of the probe (Figure 4.6A&B), whereas all divalent transition metal ions, except Zn(II) and Mn(II), completely quenched the fluorescence (Figure 4.6C-H). However, the quenching did not translate into a ratiometric readout that would otherwise interfere with ratiometric imaging.

Therefore, to evaluate the selectivity of **4.2b**, the ratiometric response was measured in the presence of 0.8 molar equivalents (80% fractional saturation of the probe) of the interfering metal ion (Figure 4.7, black bars), yielding an average ratio (R_{avg}) = 0.39 ± 0.02. The remaining 20% of the available probe was then saturated with Zn(II), which elicited a ratiometric response (R_{avg} = 1.46 ± 0.05), consistent with the emission response of the Zn(II)-saturated **4.2b** observed in the absence of any interfering metal ion (Figure 4.7, red patterned bars). Therefore, the quenching of the probe's fluorescence in the presence of the interfering metal ions render does not affect the ratiometric readout of **4.2b** when saturated with Zn(II).

Supplementation of millimolar concentrations of Mg(II) to **4.2b** did not elicit a change in fluorescence, as expected (Figure 4.8A). On the other hand, addition of millimolar Ca(II) led to a substantial 39% increase in the fluorescence response, along with a

6-nm shift in the emission maximum, indicating that the hydroxyl group engages in binding of Ca(II) at higher (millimolar) concentrations (Figure 4.8B). However, even in the presence of a 400-fold excess of Ca(II), supplementation of 1.0 Zn(II) shifts the emission response to that of the [(**4.2b**)Zn(II)] complex in the absence of any interfering metals. All other divalent transition metals, excluding Zn(II) and Mn(II), exhibited a stoichiometric fluorescence quenching behavior consistent with the previously tested Zn(II)-responsive fluorescent probes (Figure 4.8C-G). Comparable to chromis-2, the nanomolar affinity of **4.2b** for Zn(II), manifested by the hydroxyethyl moiety of the metal-binding ligand, resulted in a non-quantitative fluorescence quenching when supplemented with Mn(II). Although the Mn(II)-induced fluorescence quenching indicated a binding, albeit weak, interaction with the probe, Mn(II) was immediately outcompeted by supplementation of 1.0 equivalent of Zn(II) to restore the emission response to that of the [(**4.2b**)Zn(II)] complex observed in the molar ratio titration. Furthermore, addition of Ni(II) to the solution containing probe **4.2b** led to a time-dependent fluorescence quenching that reached equilibrium after ~ 10 minutes (Figure 4.8G, inset), consistent with chromis-2 observations.

As a consequence of a non-quantitative binding of Mn(II) to **4.2b**, a fluorimetric, metal-addition titration was performed to determine the stability constant for the formation of the [(**4.2b**)Mn(II)] complex. Fitting of the fluorimetric titration data from the metal-addition titration yielded a Mn(II) stability constant of $\log K_{Mn(II)L}' = 5.21 \pm 0.008$ (Figure 4.9), corresponding to an apparent dissociation constant of $K_d' = 6.17\ \mu M$ at pH 7.0, which is half a logarithmic unit lower than the Mn(II) stability constant of chromis-2.

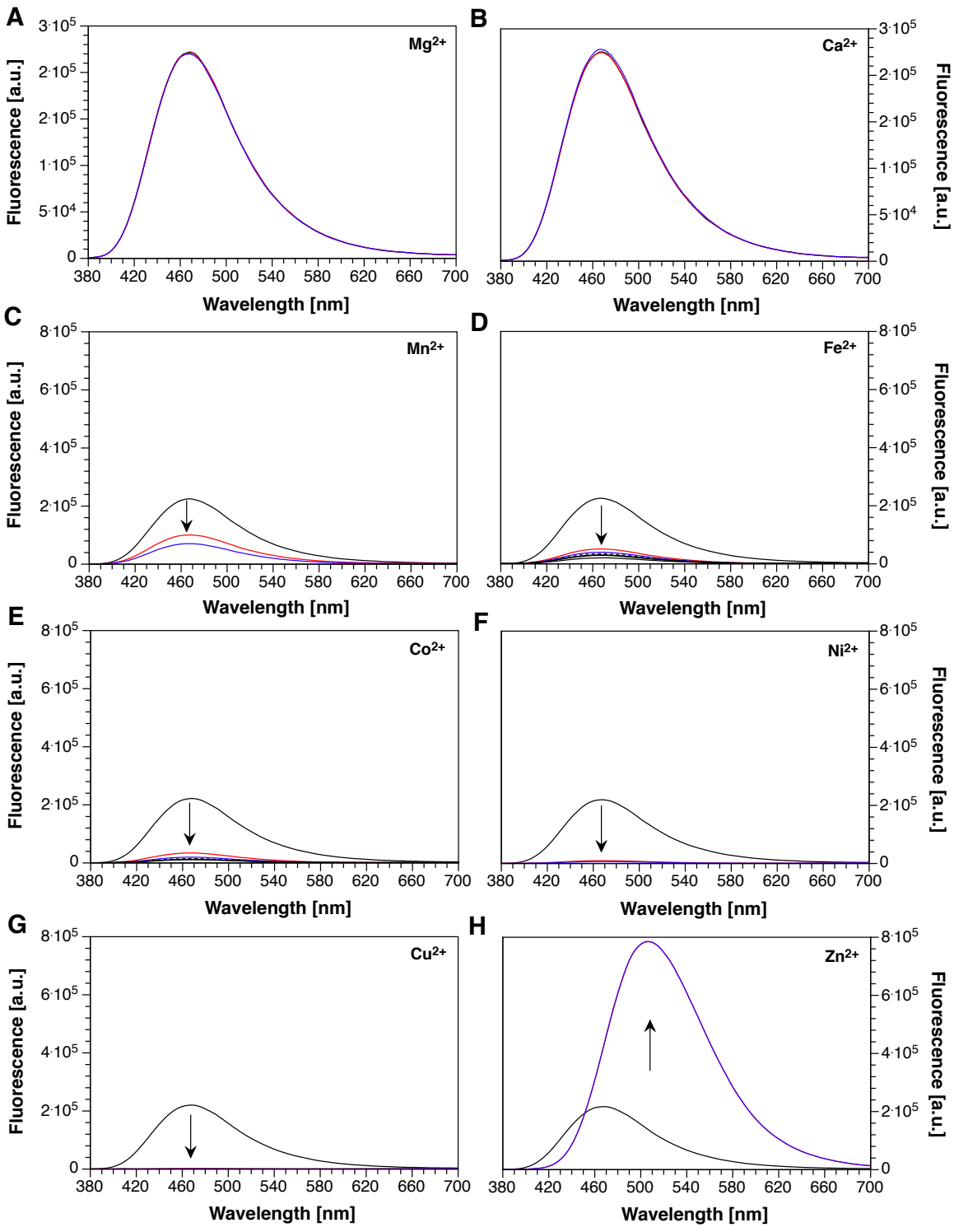

Figure 4.6: Fluorescence response of **4.2b** in the presence of 4.0 and 8.0 equivalents of interfering divalent metal ions. A-H) Blue traces represent free **4.2b** (5 μM) in pH 7.0 buffer (10 mM PIPES, 0.1 M KCl, 25°C) supplemented with 10 μM EDTA. Red and blue traces represent the addition of 20 μM and 40 μM, respectively, of interfering divalent transition metals. Excitation: 355 nm.

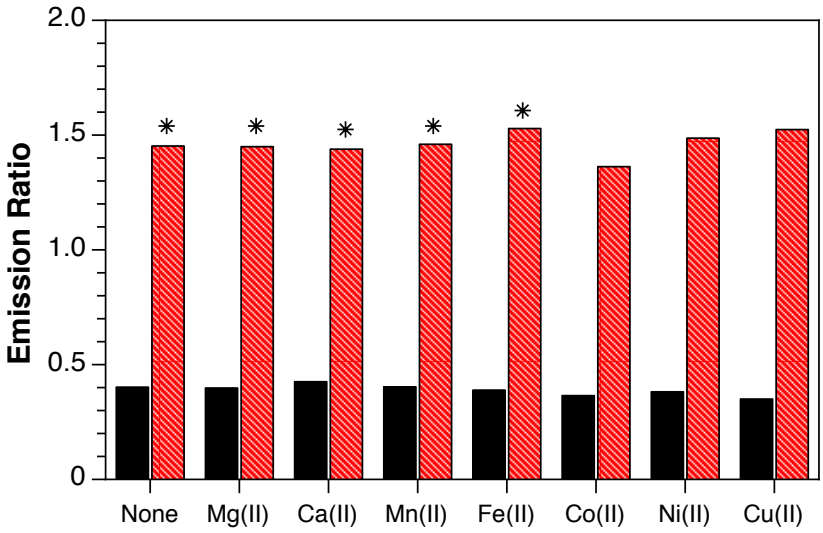

Figure 4.7: Emission-ratiometric response of **4.2b** (5 μM) towards selected divalent metal cations at 80% fractional saturation (calculated based on ratio of the integrated fluorescence intensity between 510-570 nm (channel 2) and 440-495 nm (channel 1)). The red bars represent the ratio at 80% fractional saturation, and the corresponding red patterned bars represent the ratio after saturating the remaining 20% of free fluorophore with Zn(II). Asterisks denote that the ratio was calculated after the addition of 5 μM Zn(II) rather than 1 μM (20%) Zn(II). Excitation: 359 nm.

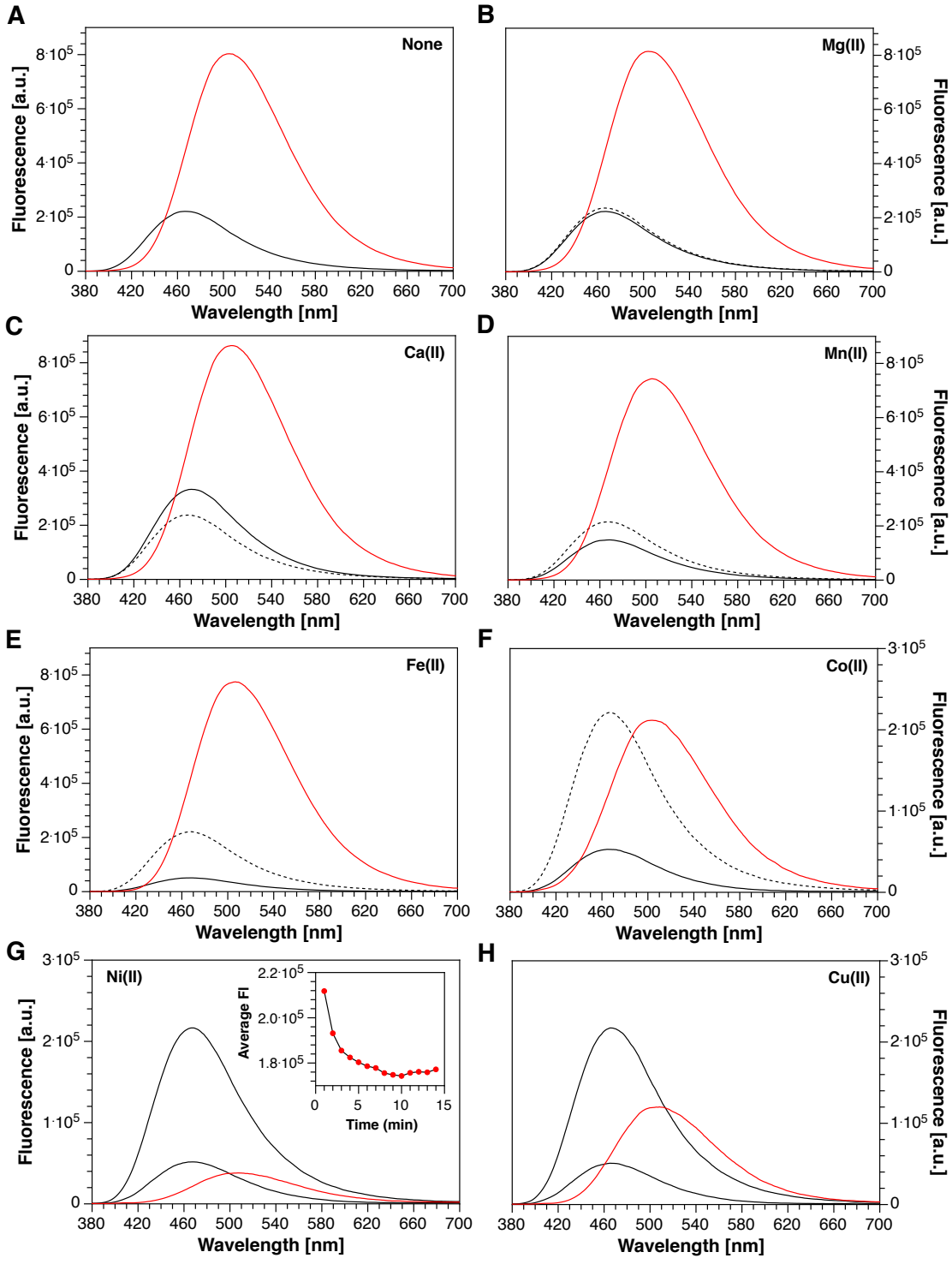

Figure 4.8: Emission spectral response of **4.2b** (5 μM) towards selected divalent metal cations at 80% fractional saturation. A&B) Fluorescence response of **4.2b** in pH 7.0 buffer (10 mM PIPES, 100 mM KCl, 25°C) in the presence of 2 mM alkaline earth metals, with corresponding saturation of probe with 1.0 eq. Zn(II). C-H) Fluorescence response of **4.2b** in the presence of 80% fractional saturation (solid black curves) of interfering divalent metal ions, with corresponding saturation of remaining 20% probe with Zn(II) (red curves). Inset: Kinetics of equilibration of **4.2b** with Ni(II). Excitation: 355 nm.

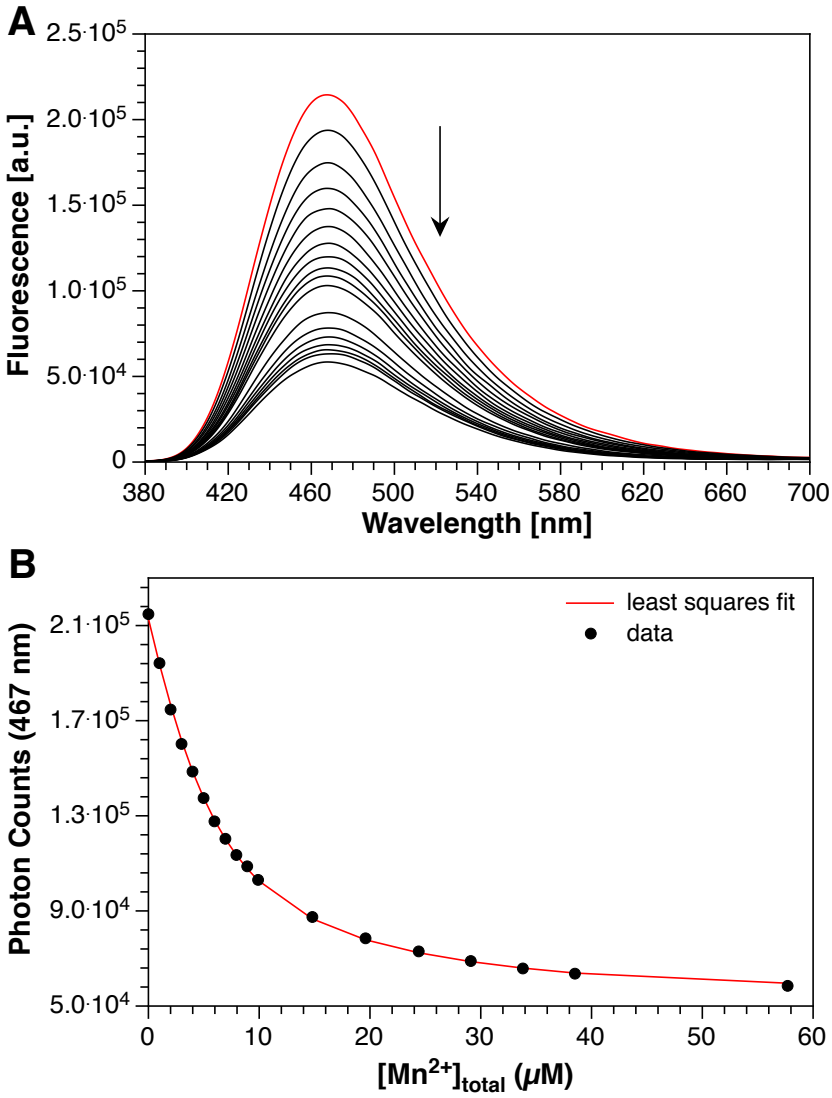

Definition of Equilibrium System:

Species	Mn(II)	**4.2b**	H	log β
Zn(II)	1	0	0	0.0
4.2b	0	1	0	0.0
[(**4.2b**)Mn(II)]	1	1	0	*5.21 ± 0.008*

Figure 4.9: A) Fluorimetric determination of the Mn(II) stability constant of **4.2b** via a direct, metal-addition titration. Probe **4.2b** (5 μM) was equilibrated in aqueous buffer (10 mM PIPES, 100 mM KCl, pH 7.0, 25ºC) treated with Chelex and titrated with $MnSO_4 \cdot H_2O$ from 0-60 μM, and a fluorescence spectrum was acquired after the addition of each aliquot of Mn(II). The red curve indicates free chromis-1 before supplementation with Mn(II). Emission spectra were analyzed by non-linear least squares fitting to provide a stability constant of $\log K_{Mn(II)L} = 5.21 \pm 0.008$ ($n = 1$). B) Change in fluorescence response at 467 nm with corresponding fit to the equilibrium system model.

4.4 Gleaning from the Arsenal of Zn(II) Affinity Standards: Development of a High-Affinity Ratiometric Fluorescent Probe for Zn(II)

The widespread prevalence of ethylenediamine bridges in the structures of various Zn(II)-binding ligands, including EDTA, TPEN, HEDTA, and DTPA, all of which boast Zn(II)-binding stability constants of 12.6 and above, demonstrates the utility of this bidentate unit for developing high-affinity ligands for binding Zn(II). However, altering the structure of the fluorophore core to increase the affinity for Zn(II) could alter its photophysical properties. To achieve a higher Zn(II)-binding affinity than **3.3b**, a new metal-binding ligand featuring an ethylenediamine unit coupled to the secondary amine of the bispicolylamine chelator employed in **3.3b** was synthesized and incorporated into the structure of a new high-affinity, Zn(II)-binding fluorescent probe intended for detecting less dynamic Zn(II) fluxes in the cell. This led to the development of fluorophores **4.3a** and the corresponding water-soluble disodium salt of **4.3b**.

*4.4.1 Synthesis of Probe **4.3b***

To incorporate the ethylenediamine bridge into the structure of a new chelator, commercially available *N*-boc-*N*-methylethylenediamine underwent a double reductive amination with methyl 2-formylisonicotinate (**4.7**) to afford the corresponding *N*-boc-*N*-methyl-*N*',*N*'-bis(2-pyidylmethyl)ethylenediamine **4.9** (Scheme 4.5). The presence of the methyl group on the carbamate nitrogen of the boc group led to the observation of two distinct conformers that were not freely interchangeable at room temperature on the NMR timescale, similar to what was observed with the characterization of several Fmoc-protected intermediates in the synthesis of chromis-1 (Chapter 2). To corroborate this observation, characterization of **4.9** in DMSO-d6 at various elevated temperatures (60°C, 80°C and

100°C), demonstrated the convergence of the two conformers as the temperature was incrementally increased. To remove the boc protecting group, **4.9** was reacted with freshly distilled trifluoroacetic acid (TFA) in anhydrous dichloromethane to prevent the saponification of the methyl esters by residual water, affording the deprotected secondary amine **4.10** in high yield (97%). The available secondary amine was then used immediately after characterization in order to prevent intermolecular polymerization reactions of the amine with the methyl esters.

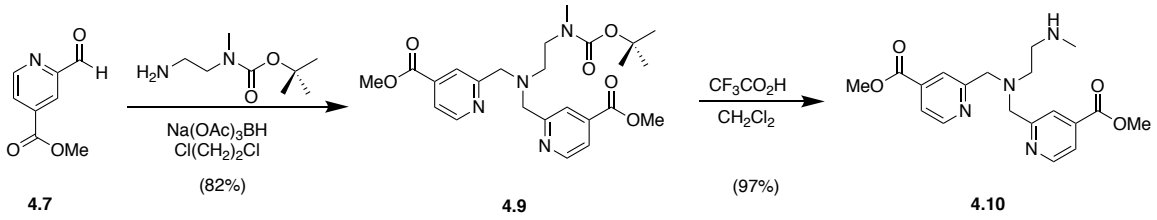

Scheme 4.5: Synthesis of metal-binding ligand **4.10** used to synthesize fluorophore **4.3a**.

Using the newly synthesized *N*-methylethylenediamine bispicolylamine chelator **4.10**, synthesis of fluorophore **4.3a** proceeded through a reductive amination with aldehyde **3.16** at room temperature using sodium triacetoxyborohydride ($Na(OAc)_3BH$) in anhydrous 1,2-dichloroethane (Scheme 4.6). After column purification, a portion of the material was saponified by refluxing with NaOH(*aq*) in MeOH, followed by dilution with EtOH and crystallization upon cooling to room temperature, to afford pure **4.3b** as the disodium dicarboxylate salt in high yield (93%).

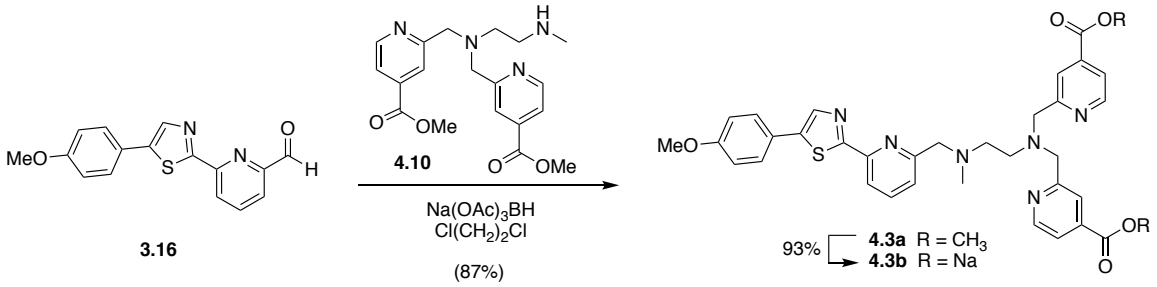

Scheme 4.6: Synthesis of probes **4.3a** and **4.3b**.

*4.4.2 Absorption and Fluorescence Properties of Probe **4.3b***

In comparison to **3.3b**, the additional ethylenediamine bridge between the fluorophore and the bispicolylamine chelating moiety was employed to increase the affinity of the metal-binding fluorophore and results in a weaker bathochromic shift in both the absorption and emission. Upon coordination of Zn(II) to the metal-acceptor moiety, **4.2b** underwent a 16-nm bathochromic shift in the absorption from a λ_{max} of 351 nm (ε = 21,200 $M^{-1}\bullet cm^{-1}$) to 367 nm (ε = 22,500 $M^{-1}\bullet cm^{-1}$) for the Zn(II)-saturated form (Table 4.4). The presence of two clean isosbestic points at 288 and 355 nm, in addition to an equimolar saturation of the probe with Zn(II), are indicative of a well-defined equilibrium between the free- and Zn(II)-saturated species with a 1:1 binding stoichiometry (Figure 4.10A). In addition, comparison of the UV-Vis spectra of **4.3b** to the preceding 2-thiazolyl fluorophores (**3.3b**, chromis-2, **4.1**, and **4.2b**) revealed an increase in the molar absorptivity (ε) of **4.3b** upon Zn(II) binding relative to the free form, whereas the others realized a decrease in the molar absorptivity of the Zn(II)-bound species.

Comparably, the fluorescence emission maximum of **4.3b** was red-shifted from 474 nm to 500 nm upon Zn(II) binding, corresponding to a modest 26 nm (Figure 4.10B). The installation of the ethylenediamine bridge led to a slight (4%) increase in the fluorescence quantum yield of the free form, from 0.25 to 0.29 relative to **3.3b**, whereas the

quantum yield of the Zn(II)-bound form of **4.3b** was reduced from 0.69 to 0.57. Interestingly, the fluorescence profiles of the free and metal-bound species revealed balanced emission intensities between the two species, which may indicate a less favorable ESPT process.

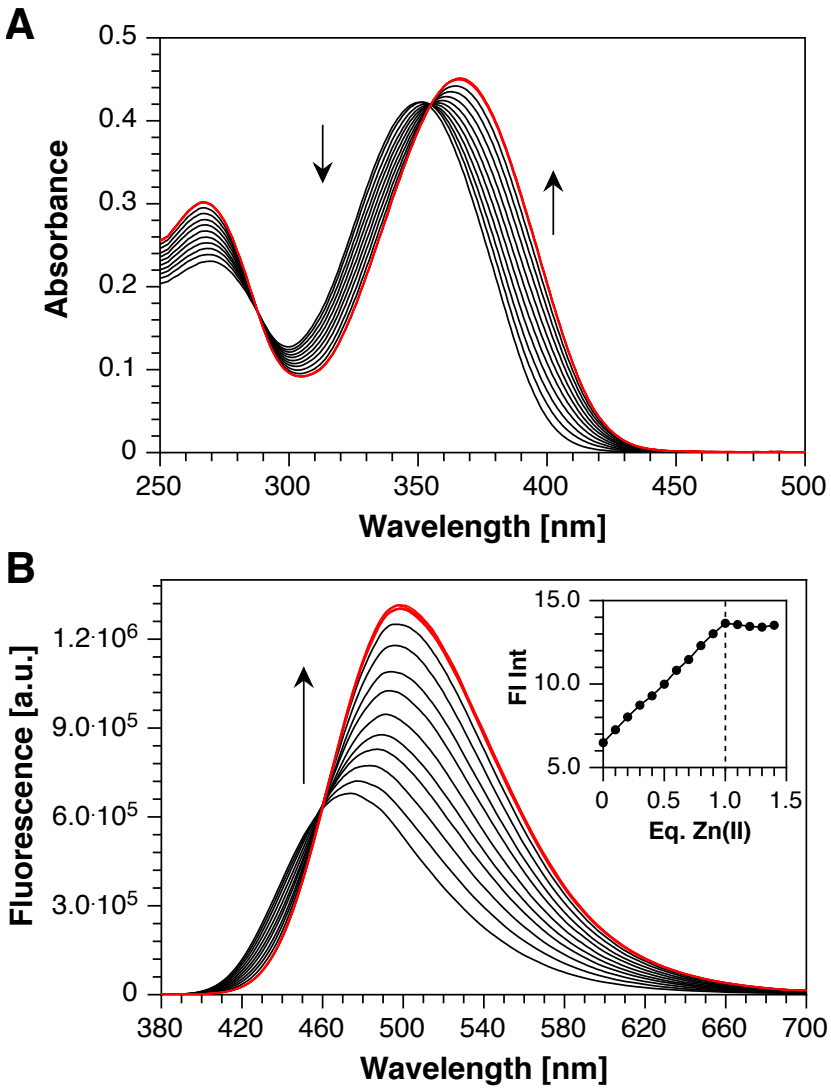

Figure 4.10: Spectral changes of **4.3b** (20 μM) in neutral aqueous buffer (10 mM PIPES, 100 mM KCl, 25°C) at pH 7.0 upon stepwise addition of Zn(II). (A) Absorption (UV-Vis) spectral changes upon saturation with Zn(II). (B) Fluorescence emission response upon saturation with Zn(II) (excitation at 355 nm). Red curves indicate the spectra after complete saturation (1.0 eq.) with Zn(II) is achieved. Inset: fluorescence integration over the entire spectral window as a function of molar equivalents of Zn(II).

Table 4.4: Photophysical properties of probe **4.3b**[a]

	4.3b	**[(4.3b)Zn(II)]**
Absorbance λ_{max} (nm)[b]	351	367
ε (10^4 $M^{-1}cm^{-1}$)[c]	2.12	2.25
Emission λ_{max} (nm)[d]	474	500
Φ_F [e]	0.29	0.57
δ_{max} (GM)[f]	n.d.	n.d.
λ_{max} (nm)[g]	n.d.	n.d.

[a]10 mM PIPES, 0.1 M KCl, 25°C. [b]lowest-energy band of the one-photon absorption spectrum. [c]molar extinction coefficient at λ_{max}. [d]maximum fluorescence emission. [e]fluorescence quantum yield, referenced to quinine sulfate (Φ_F = 0.546).[20] [f]maximum two-photon absorption. [g]two-photon absorption cross section. n.d. = not determined.

*4.4.3 Probe **4.3b** Binds Zn(II) with Low Femtomolar Affinity*

The addition of the *N*-methylethylenediamine bridge between the fluorophore and the bispicolylamine chelator moiety was expected to increase the affinity of **4.3b** compared to its ethylenediamine bridge-less analog **3.3b** ($\log K_{Zn(II)L}$ = 10.8), which demanded a stronger competing ligand for determination of the fluorophore's Zn(II) stability constant. As described in Section 4.1, examination of the Zn(II)-binding ligands that have been extensively characterized for their formation and protonation constants, EDTA (ethylenediaminetetraacetic acid) and DTPA (diethylenetriaminepentaacetic acid) were the two ligands with the best matching apparent affinities ($\log K_{Zn(II)L}'$ = 13.13, 12.87, respectively) at pH 7.0 relative to the expected apparent affinity of **4.3b**. Preliminary attempts at determining the kinetics of equilibration upon addition of both EDTA and DTPA (500 μM) to solutions containing the preformed Zn(II) complex of **4.3b** (20 μM) observed an associative exchange that reached equilibrium after ~ 15 hours for EDTA (Figure 4.11A) and ~ 18 hours for DTPA (Figure 4.11B) at 25°C. Because spectroscopic titrations to determine the stability constant for a metal-binding ligand ideally requires 10-15 data points for calculating

a reliable value with a robust fit to its corresponding equilibrium binding model, it was not readily feasible to titrate EDTA or DTPA in successive aliquots of increasing concentration into one solution of the preformed Zn(II) complex of **4.3b**.

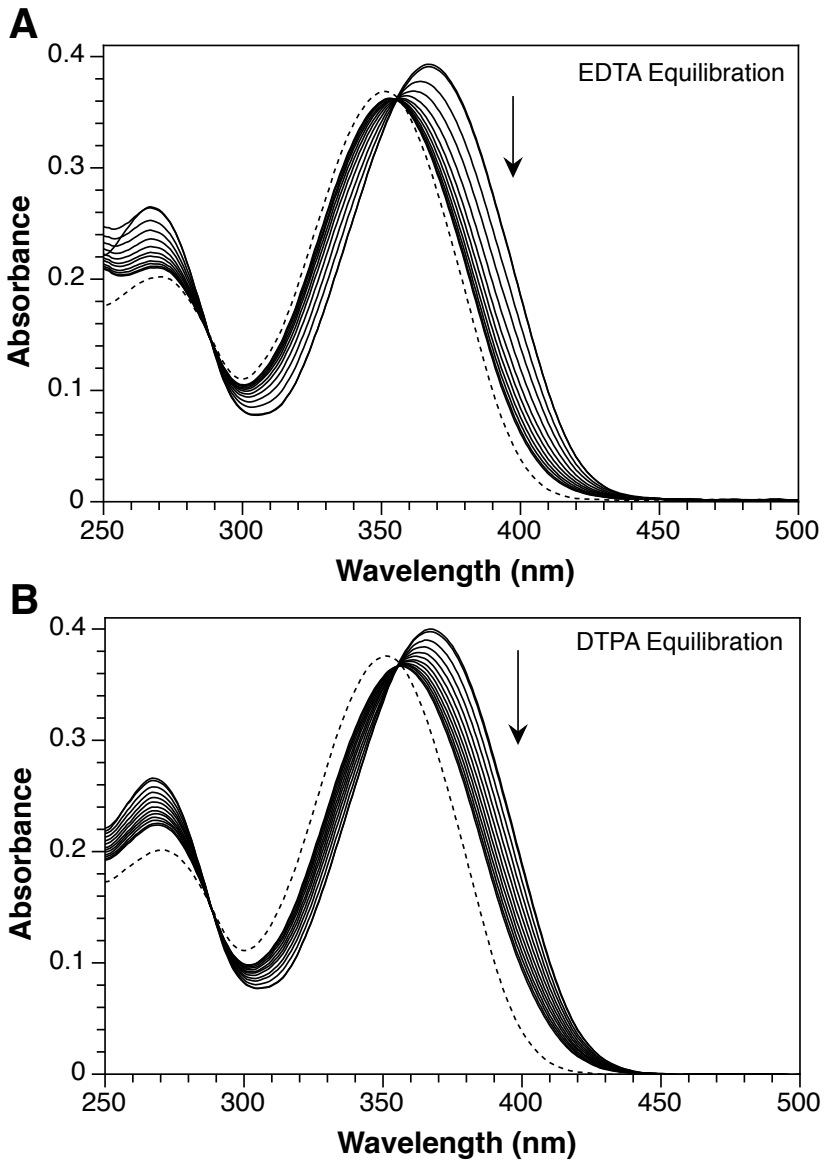

Figure 4.11: Spectrophotometric determination of the kinetics of equilibration of [(**4.3b**)Zn(II)] (20 μM) in the presence of 500 μM EDTA (A) and DTPA (B) in pH 7.0 aqueous buffer (10 mM PIPES, 100 mM KCl, 25°C). EDTA required ~ 15 hours to reach equilibrium, whereas DTPA required ~ 18 hours to reach equilibrium. Dotted line represents the absorbance spectrum of free **4.3b** before saturation with Zn(II).

Because of the slow kinetics of equilibration, a buffer method was attempted, by which a working solution of the [(**4.3b**)Zn(II)] complex was prepared in pH 7.0 aqueous buffer (10 mM PIPES, 100 mM KCl) and aliquoted into vials that were then supplemented with various, predetermined concentrations of EDTA. Fluorescence spectra were acquired of each solution after a 17-hour equilibration at 25°C, and the spectra were fitted to an equilibrium model with EDTA as the competing ligand in order to determine the stability constant of **4.3b**. Non-linear, least-squares fitting of the fluorimetric data yielded an apparent stability constant of $\log K_{Zn(II)L}' = 14.0 \pm 0.1$, corresponding to an apparent dissociation constant of $K_d' = 10 \pm 3$ fM (Figure 4.12).

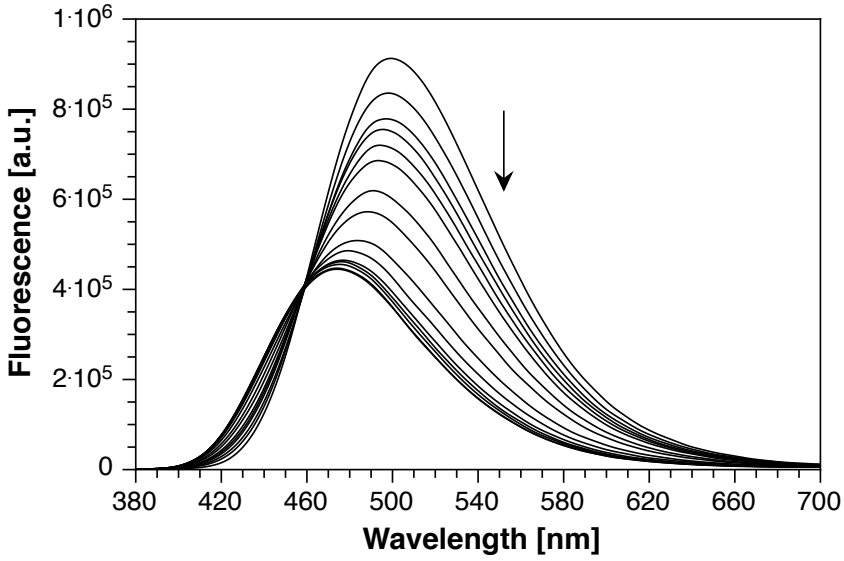

Definition of Equilibrium System:

Species	Zn(II)	EDTA	**4.3b**	H	logβ
Zn(II)	1	0	0	0	0
EDTA	0	1	0	0	0
4.3b	0	0	1	0	0
EDTA(H)	0	1	0	1	10.30
EDTA(H_2)	0	1	0	2	6.24
EDTA(H_3)	0	1	0	3	2.80
[(EDTA)Zn(II)]	1	1	0	0	16.50
[(**4.3b**)Zn(II)]	1	0	1	0	*14.0 ± 0.1*

Figure 4.12: A) Fluorimetric determination of the Zn(II) stability constant of **4.3b** via a competition titration with EDTA. The preformed [(**4.3b**)Zn(II)] complex (10 μM) in aqueous buffer (10 mM PIPES, 0.1 M KCl, pH 7.0, 25ºC) was aliquoted into multiple vials and supplemented with various aliquots of EDTA that ranged from 0-900 μM. After a 17-hour equilibration, the fluorescence spectra (excitation: 355 nm) were analyzed by non-linear least squares fitting to yield an average apparent log$K_{Zn(II)L}$ of 14.0 ± 0.1 (n = 2) at pH 7.0, μ = 0.1 M (KCl). B) Change in fluorescence response at 500 nm with corresponding fit to the equilibrium system model described above.

*4.4.4 Metal-Ion Selectivity Measurements of Probe **4.3b***

As expected, the additional ethylenediamine bridge of **4.3b** did not adversely affect the Zn(II) selectivity of the fluorophore, serving only as an additional donor to engage in coordination of both Zn(II) and interfering divalent metals. Although EDTA is capable of undergoing exchange reactions with the probe, the slow kinetics of exchange did not affect

the use of EDTA (10 μM) as a Zn(II) sequestrant prior to addition of **4.3b** (5 μM) to the buffer solution. As expected, addition of 20 and 40 μM (4.0 and 8.0 equivalents) of Mg(II) and Ca(II) did not affect the fluorescence response of **4.3b** (Figure 4.123&B), whereas supplementation of the probe with the same concentrations of interfering divalent transition metal ions resulted in the complete fluorescence quenching of the fluorescence response (Figure 4.13C-G), including Mn(II). Consistent with the 80-20 fractional saturation method to measure the selectivity of the previously synthesized ligands, the ratiometric response of **4.3b** was evaluated in the presence of 0.8 molar equivalents (80% fractional saturation) of the interfering metal ion, leading to a uniform average emission ratio (R_{avg}) of 0.46 ± 0.007 (Figure 4.14, black bars). The quenching by the interfering metals does not result in a ratiometric readout and only leads to a masking effect that reduces the amount of probe availability of the probe for binding Zn(II). Therefore, the emission ratio of the remaining 20% of free probe was unaffected by any of the interfering divalent metal ions (Figure 4.14, red patterned bars), producing a ratiometric response comparable to the [(**4.3b**)Zn(II)] complex observed in the absence of any interfering metal, with an average ratio of R_{avg} = 1.17 ± 0.06 upon saturation with Zn(II). The individual spectra for the fluorescence responses addition of all eight divalent metal ions tested is provided in Figure 4.3.

Interestingly, supplementation of **4.3b** with millimolar concentrations (2 mM) of both Mg(II) and Ca(II) did not elicit a change in the fluorescence response, which deviates from analogous measurements of chromis-2, **3.3b**, and **4.2b** in the presence of millimolar Mg(II) and Ca(II) (Figure 4.15A&B). Although Mn(II) stoichiometrically quenched the fluorescence of the probe in the same capacity as the other interfering divalent transition metal ions, supplementation of the *in situ*-generated [(**4.3b**)Mn(II)] complex with 1.0 equivalent of Zn(II) immediately outcompeted Mn(II) for binding to the fluorophore and restored

the fluorescence profile and the corresponding emission ratio to that of the [(**4.3b**)Zn(II)] complex both in the presence and absence of interfering divalent metals (Figure 4.155D). Consistent with selectivity measurements of the other ligands in response to interfering divalent metal ions, binding of Ni(II) to the probe led to a time-dependent fluorescence quenching that plateaued after ~ 10 minutes (Figure 4.15G, inset), indicating that, while the coordination of Ni(II) results in quantitative quenching of the fluorophore, the kinetics of association are slower than the other divalent metals tested.

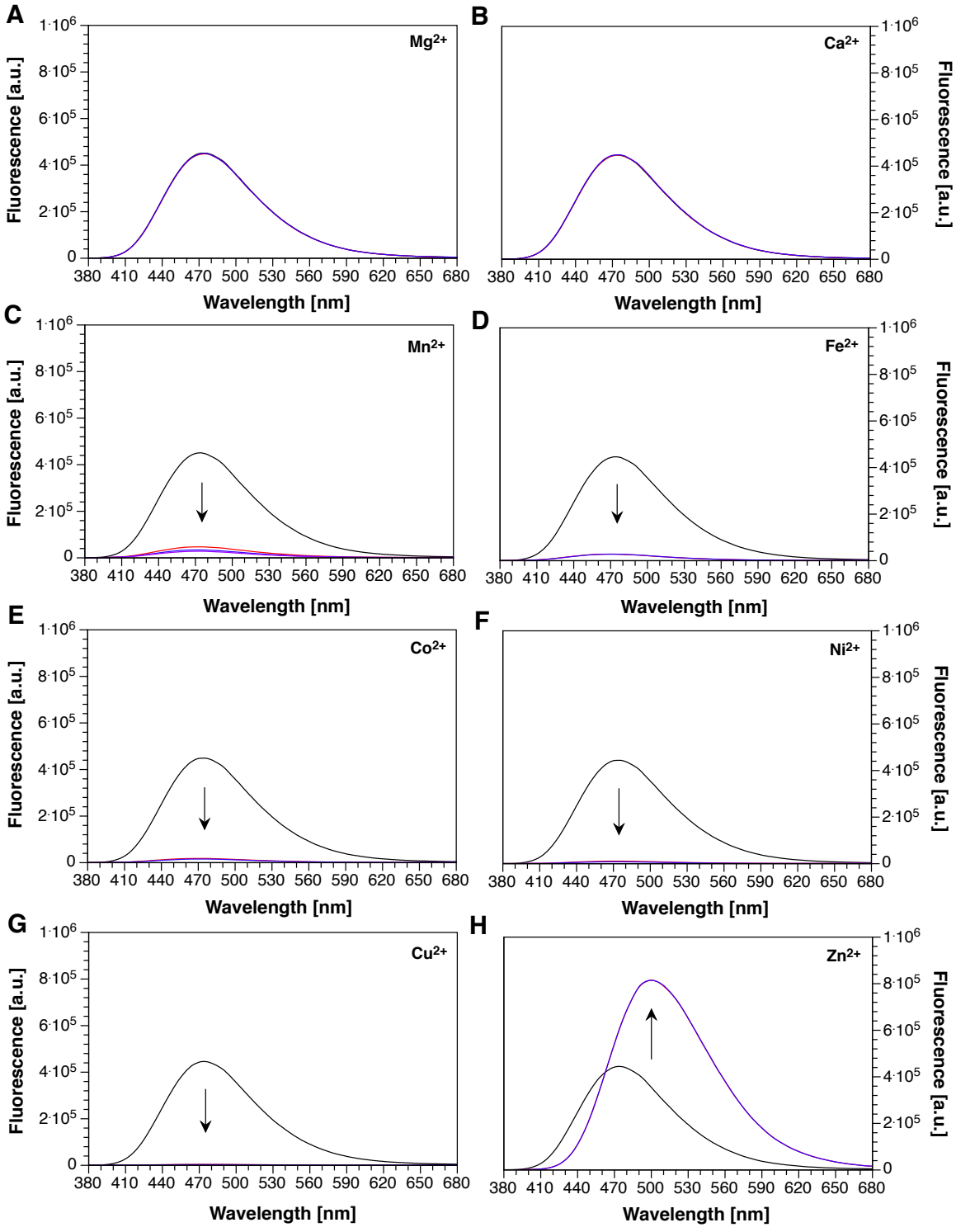

Figure 4.13: Fluorescence response of **4.3b** in the presence of 4.0 and 8.0 equivalents of interfering divalent metal ions. A-H) Blue traces represent free **4.3b** (5 μM) in pH 7.0 buffer (10 mM PIPES, 0.1 M KCl, 25°C) supplemented with 10 μM EDTA. Red and blue traces represent the addition of 20 μM and 40 μM, respectively, of interfering divalent transition metals. Excitation: 355 nm.

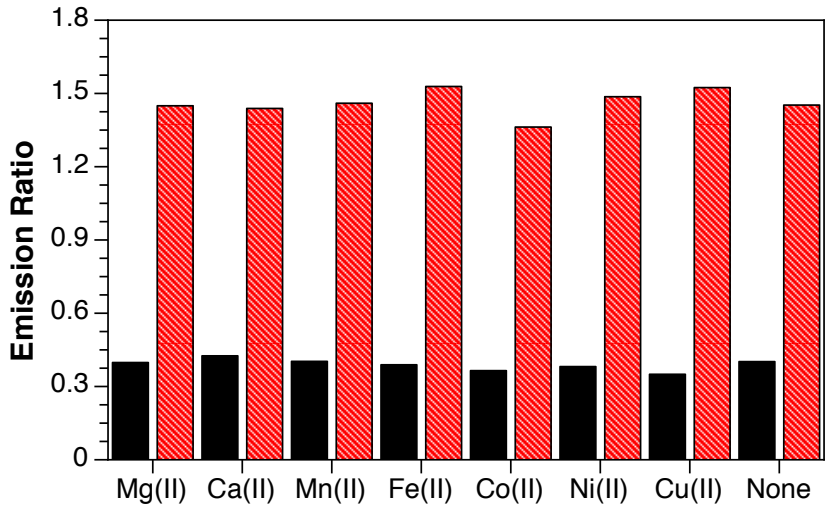

Figure 4.14: Emission-ratiometric response of probe **4.3b** (5 μM) towards selected divalent metal cations at 80% fractional saturation (calculated based on ratio of the integrated fluorescence intensity between 510-570 nm (channel 2) and 440-495 nm (channel 1)). The red bars represent the ratio at 80% fractional saturation, and the corresponding red patterned bars represent the ratio after saturating the remaining 20% of free fluorophore with Zn(II). Excitation: 355 nm.

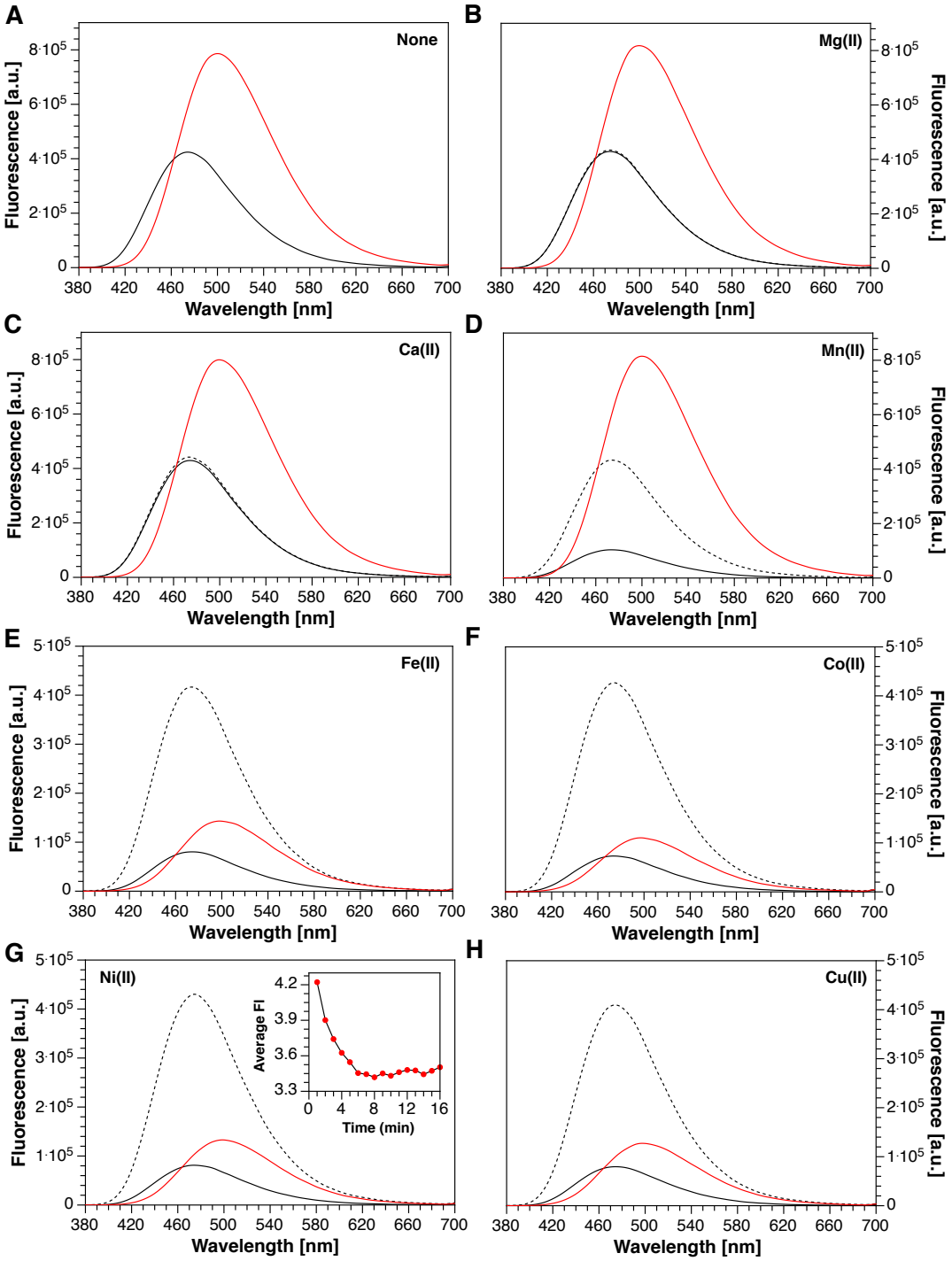

Figure 4.15: Emission spectral response of **4.3b** (5 μM) towards selected divalent metal cations at 80% fractional saturation. A-B) Fluorescence response of **4.3b** in pH 7.0 buffer (10 mM PIPES, 100 mM KCl, 25°C) to 2 mM alkaline earth metals, with corresponding saturation of probe with 1.0 eq. Zn(II). C-H) Fluorescence response of **4.3b** in the presence of 80% fractional saturation (solid black curves) of interfering divalent metal ions, with corresponding saturation of remaining 20% probe with Zn(II) (red curves). Inset: Kinetics of equilibration of **4.3b** with Ni(II). Excitation: 355 nm.

4.5 Exploiting the Structure-Derived Femtomolar Affinity of TPEN for the Development of a High-Affinity Zn(II)-Selective Fluorescent Probe

Analysis of the stability constants of **4.1**, **4.2b**, **3.3b**, and **4.3b** revealed an approximate trend in the influence of pyridine on the Zn(II)-binding affinity, demonstrating that the substitution of a hydroxyl group with an isonicotinate group yielded a ~ three-logarithmic-unit increase in the stability constant. Given the pervasive use of TPEN as a high-affinity chelator for sequestering Zn(II) in biological imaging, it became evident that the similarities between the structure of the metal receptor ligand of probe **4.3b** and the structure of TPEN supported the incorporation of an additional pyridine group into probe **4.3b** to generate a new Zn(II)-binding fluorophore whose metal-binding ligand resembles the structure of TPEN. Taking advantage of the trend to increase the affinity of a ligand by the addition of a pyridine moiety, the new Zn(II)-responsive fluorescent probe (**4.4b**), which was expected to boast an even higher affinity than **4.3b**, was developed.

4.5.1 Synthesis of Probe 4.4b

In order to incorporate a TPEN-like chelator into the design of a fluorescent probe with comparable affinity to TPEN, the chemistry used to synthesize the chelator of **4.3** was adopted and modified to permit the incorporation of a third pyridine group. However, the presence of the methyl group of *N*-boc-*N*-methyl-*N*',*N*'-bis(2-pyidylmethyl)ethylenediamine (**4.9**) that was used to synthesize **4.10** results in a secondary amine once deprotected, thereby impeding both the installation of a third pyridine moiety and coupling the chelator to the fluorophore's aldehyde functionality. To overcome this hurdle, aldehyde **4.7** underwent a double reductive amination with *N*-boc-ethylenediamine to afford the in-

termediate *N*-boc-*N*',*N*'-bis(2-pyridylmethyl)ethylenediamine (**4.11**) under identical conditions, including purification procedures, compared to the preparation of **4.9** (Scheme 4.7). The lack of a methyl group on the carbamate nitrogen circumvented the unexpected conformational rotation barrier observed when characterizing **4.11**, thus NMR characterization of the compound was performed in $CDCl_3$ under standard conditions. Deprotection of the boc group using anhydrous TFA in anhydrous CH_2Cl_2 to provide the primary amine **4.12** was performed under identical conditions as in the preparation of **4.9**. Coupling of **4.12** with aldehyde **4.7** to yield the secondary amine **4.13** was then performed using an excess (1.5 equivalents) of the amine relative to the aldehyde to prevent a double reductive amination that otherwise would have yielded a tetracarboxylated TPEN derivative and resulted in a lower yield of the desired **4.13**.

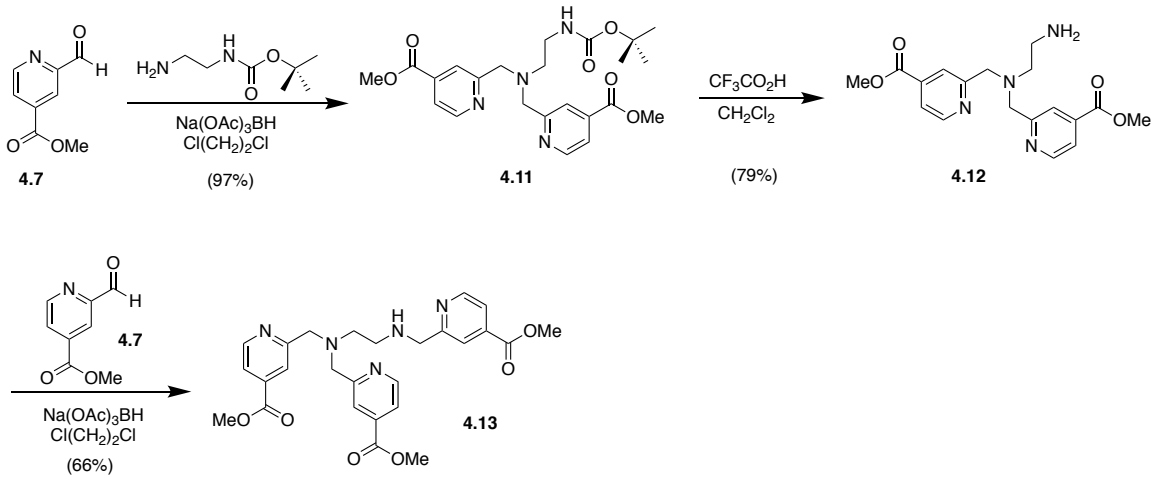

Scheme 4.7: Synthesis of metal-binding ligand **4.13**.

Reductive amination of secondary amine **4.13** with the aldehyde functionality of the fluorophore core afforded fluorophore **4.4a** in surprisingly lower yield (63%) compared

to the preparation of **4.3a**, and a portion of the product underwent saponification by refluxing the trimethyl ester with 3.5 equivalents of NaOH (*aq*) in MeOH to provide the corresponding water-soluble sodium tricarboxylate salt with a 96% yield (Scheme 4.8).

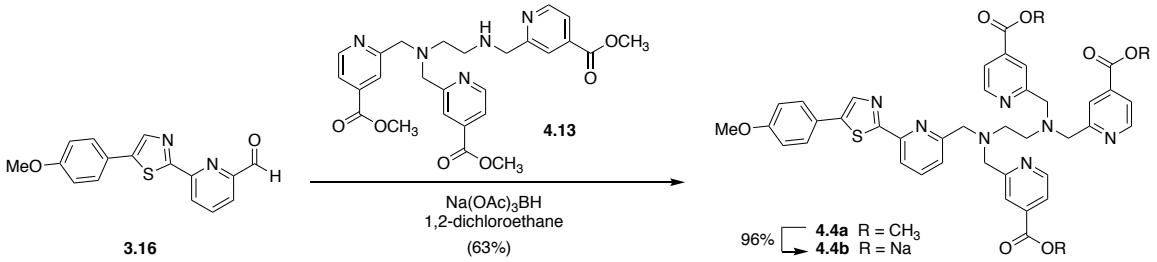

Scheme 4.8: Synthesis of probes **4.4a** and **4.4b**.

*4.5.2 Absorption and Fluorescence Properties of Probe **4.4b***

Not surprisingly, the structural variation between the N-methylethylenediamine functionality of **4.3b** and the *N*-pyridylmethylethylenediamine functionality of **4.4b** did not influence the magnitude of the bathochromic shift in the absorption, with the free form undergoing a consistent 16-nm red shift from 351 nm (ε = 21,200 $M^{-1}\cdot cm^{-1}$) to 367 nm (ε = 19,600 $M^{-1}\cdot cm^{-1}$) upon saturation with Zn(II) (Table 4.5). Consistent with the other Zn(II)-binding fluorescent probes developed, the presence of two clean isosbestic points at 290 and 362 nm, in addition to an equimolar saturation of the probe with Zn(II), are indicative of a well-defined equilibrium between the free- and Zn(II)-saturated species with a 1:1 binding stoichiometry (Figure 4.16A). The emission maximum of the free form of **4.4b** is also red-shifted 34 nm from 471 nm to 505 nm upon binding Zn(II), corresponding to an 8-nm larger shift than its predecessor **4.3b** (Figure 4.16B). Excitation at the absorption's isosbestic point ensured that the emission intensities are a direct reflection on the quantum yield, which increased more than three-fold from 0.24 to 0.73 upon saturation with Zn(II).

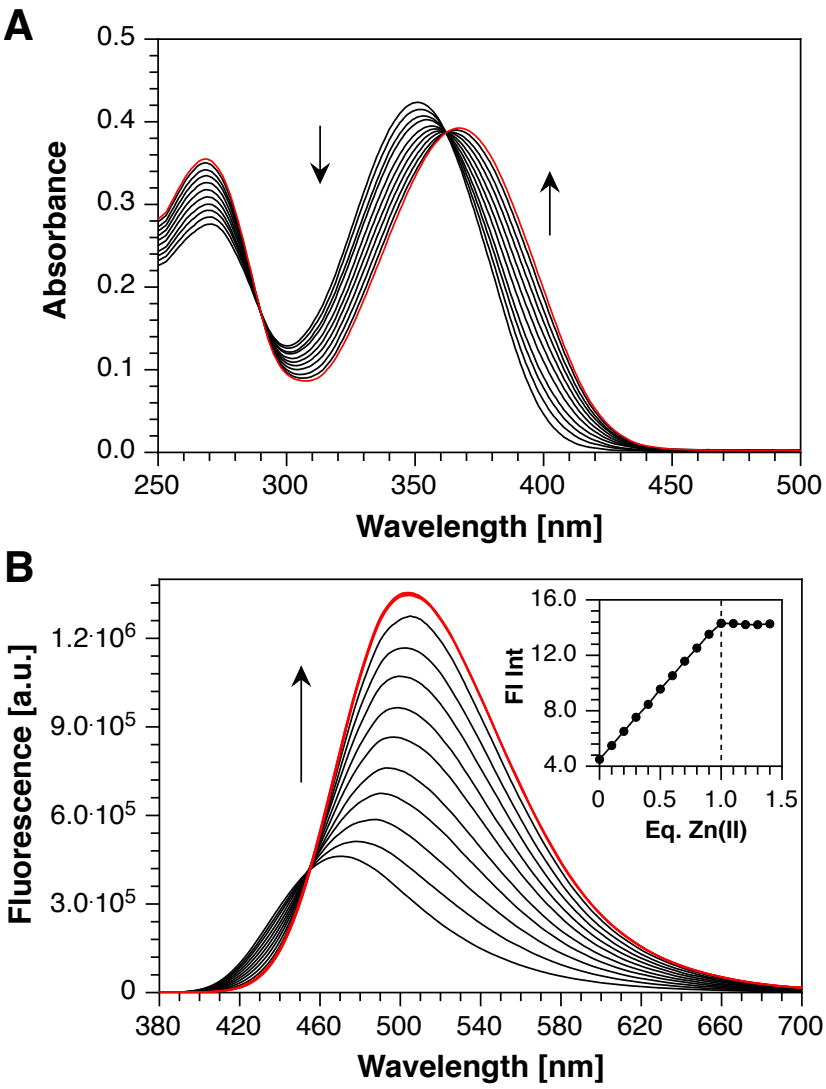

Figure 4.16: Spectral changes of **4.4b** (20 μM) in neutral aqueous buffer (10 mM PIPES, 100 mM KCl, 25°C, pH 7.0) upon the stepwise saturation with Zn(II). (A) Absorption (UV-Vis) spectral changes upon saturation with Zn(II). (B) Fluorescence emission response upon saturation with Zn(II) (excitation at 362 nm). Red curves indicate the spectra after complete saturation (1.0 eq.) with Zn(II) is achieved. Inset: fluorescence integration over the entire spectral window as a function of molar equivalents of Zn(II).

Table 4.5: Photophysical properties of probe **4.4b**[a]

	4.4	**[(4.4)Zn(II)]**
Absorbance λ_{max} (nm)[b]	351	367
ε (10^4 $M^{-1}cm^{-1}$)[c]	2.12	1.96
Emission λ_{max} (nm)[d]	471	505
Φ_F [e]	0.24	0.73
δ_{max} (GM)[f]	n.d.	n.d.
λ_{max} (nm)[g]	n.d.	n.d.

[a]10 mM PIPES, 0.1 M KCl, 25°C. [b]lowest-energy band of the one-photon absorption spectrum. [c]molar extinction coefficient at λ_{max}. [d]maximum fluorescence emission. [e]fluorescence quantum yield, referenced to quinine sulfate (Φ_F = 0.546).[20] [f]maximum two-photon absorption. [g]two-photon absorption cross section. n.d. = not determined.

*4.5.3 Determination of the Zn(II)-Binding Affinity of Probe **4.4b***

The substitution of the *N*-methylethylenediamine unit of the chelator of **4.3b** with an *N*-pyridylmethylethylenediamine unit in **4.4b** was expected to further increase the binding affinity compared to its predecessor by ~ two orders of magnitude, based on the trends observed during the determination of the stability constants of the previous affinity-tuned probes. A two logarithmic-unit increase in the affinity over **4.3b** would demand the employment of a competing ligand whose apparent affinity at pH 7.0, μ = 0.1 M is a minimum of one logarithmic unit higher than EDTA. Surveying the inventory of ligands with an apparent affinity higher than EDTA led to the application of TPEN (*N*,*N*,*N*',*N*'-tetrakis(2-pyridylmethyl)ethylenediamine; $\log K_{TPEN \cdot Zn(II)}$ = 14.96 ± 0.06, K_d = 1 fM at pH 7.0 μ = 0.1 M)[21] as a competing ligand with matching affinity relative to the hypothesized binding affinity of **4.4b**. Fluorimetric and spectrophotometric titrations were performed in the presence of both **4.4b** and TPEN (30 μM) with incremental supplementation of Zn(II), and non-linear, least-squares fitting of the spectroscopic data yielded a uniform apparent stability constant

of $\log K_{\mathbf{4.4b}\cdot Zn(II)}' = 15.1 \pm 0.06$, corresponding to an apparent dissociation constant of $K_d' =$ 37 fM at pH 7.0, $\mu = 0.1$ M (Figure 4.17).

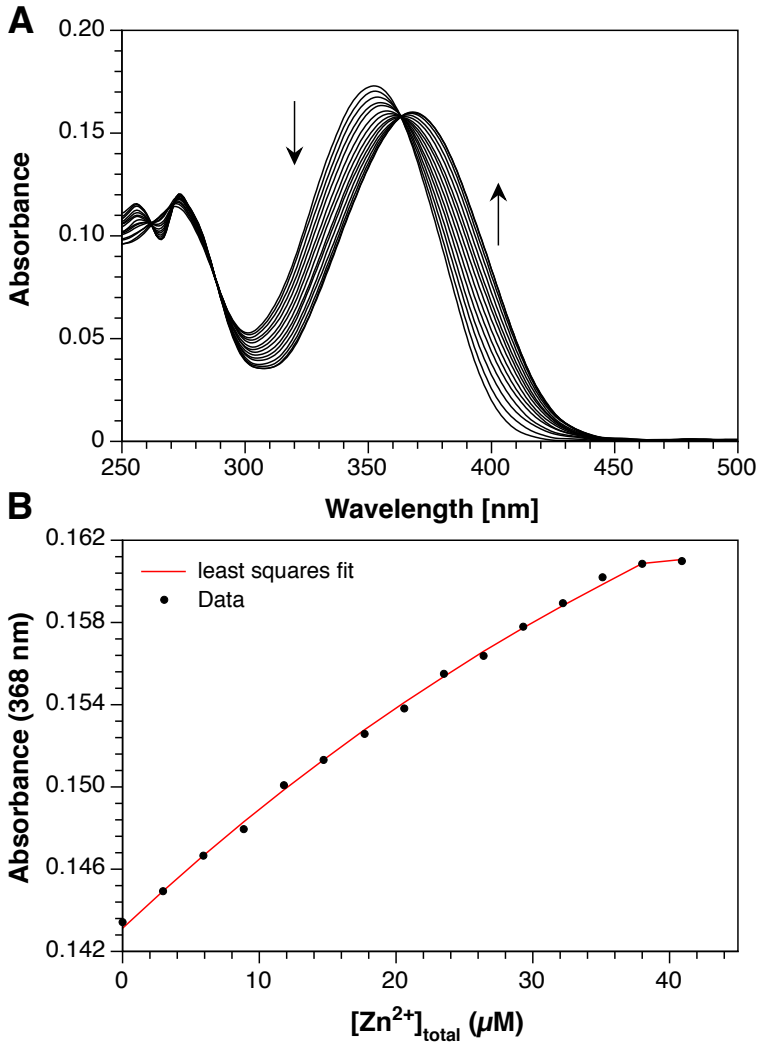

Definition of Equilibrium System:

Species	Zn(II)	TPEN	**4.4b**	H	logβ
Zn(II)	1	0	0	0	0
TPEN	0	1	0	0	0
4.4b	0	0	1	0	0
TPEN(H)	0	1	0	1	7.23
TPEN(H_2)	0	1	0	2	12.15
TPEN(H_3)	0	1	0	3	15.56
[(TPEN)Zn(II)]	1	1	0	0	15.4
[(**4.4b**)Zn(II)]	1	0	1	0	*15.1 ± 0.06*

Figure 4.17: A) Spectrophotometric determination of the Zn(II) stability constant of **4.4b** via a Zn(II)-addition titration in the presence of TPEN as a competing ligand. Probe **4.4b** (10 μM) was equilibrated in aqueous buffer (10 mM PIPES, 100 mM KCl, pH 7.0, 25°C) supplemented with TPEN (30 μM), and the probe solution was titrated with $ZnSO_4 \cdot 7H_2O$ from 0-40 μM, with an absorbance spectrum acquired after the addition of each aliquot of Zn(II). Spectra were analyzed by non-linear least squares fitting to provide a $\log K_{Zn(II)L} = 15.1 \pm 0.06$ ($n = 3$). B) Change in fluorescence response at 467 nm with corresponding fit to the equilibrium system model.

*4.5.4 Metal-Ion Selectivity Measurements of Probe **4.4b***

Compared to probe **4.3b**, the additional pyridine ring did not affect the Zn(II) selectivity of the fluorophore, despite the additional donor serving to engage in coordination of both Zn(II) and interfering divalent metals. As expected, addition of 20 and 40 μM (4.0 and 8.0 equivalents, respectively) of Mg(II) and Ca(II) did not affect the fluorescence response of **4.4b** (Figure 4.18A,B), whereas the supplementation of the probe with the same concentrations of interfering divalent transition metal ions resulted in the complete fluorescence quenching of the probe (Figure 4.18C-G), including Mn(II), which could not be reversed upon the addition of Zn(II). Consistent with the 80-20 fractional saturation method to determine the selectivity of the previously synthesized probes, the ratiometric response of **4.4b** was evaluated in the presence of 0.8 molar equivalents (80% fractional saturation) of the interfering metal ion (Figure 4.19, black bars), leading to a uniform average emission ratio (R_{avg}) of 0.49 ± 0.04. Under these conditions, the emission ratio of the remaining 20% of free probe was unaffected by any of the quenching metal ions (Figure 4.19, red patterned bars), yielding an average ratio of R_{avg} = 1.40 ± 0.04 upon saturation of Zn(II), which is consistent with the [(**4.4b**)Zn(II)] complex observed in the absence of any interfering metal. The spectral data for these selectivity measurements are displayed in Figure 4.20.

Comparable to the other fluorophores, except **4.3b,** whose selectivities were measured under identical conditions, supplementation of **4.4b** with millimolar concentrations of Mg(II) did not elicit a change in the fluorescence profile (Figure 4.20A), whereas addition of millimolar Ca(II) resulted in a 77% increase in the fluorescence intensity but yielded a negligible 15% increase in the emission ratio (Figure 4.20B). The higher affinity

of **4.4b** compared to the other affinity-tuned probes manifested a greater degree of fluorescence quenching in response to the all interfering divalent transition metals, which could not be reversed by the addition of Zn(II), even for Mn(II) and Fe(II). Furthermore, supplementation of the probe with Ni(II) also demonstrated an expected time-dependent fluorescence quenching because of slow binding kinetics, which was observed with all previously characterized Zn(II)-binding fluorescent probes.

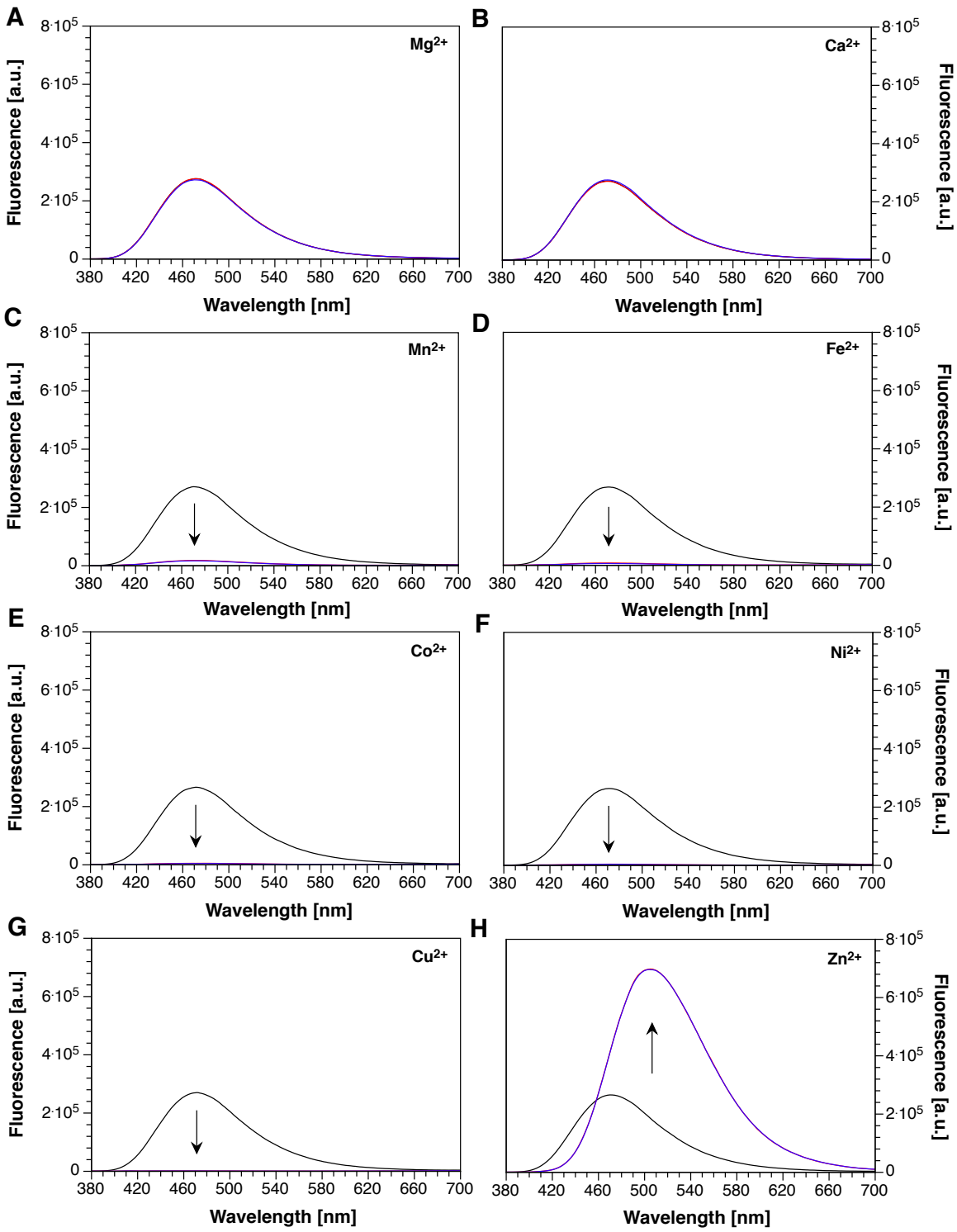

Figure 4.18: Fluorescence response of **4.4b** in the presence of 4.0 and 8.0 equivalents of interfering divalent metal ions. A-H) Blue traces represent free **4.4b** (5 μM) in pH 7.0 buffer (10 mM PIPES, 0.1 M KCl, 25°C) supplemented with 10 μM EDTA. Red and blue traces represent the addition of 20 μM and 40 μM, respectively, of interfering divalent transition metals. Excitation: 362 nm.

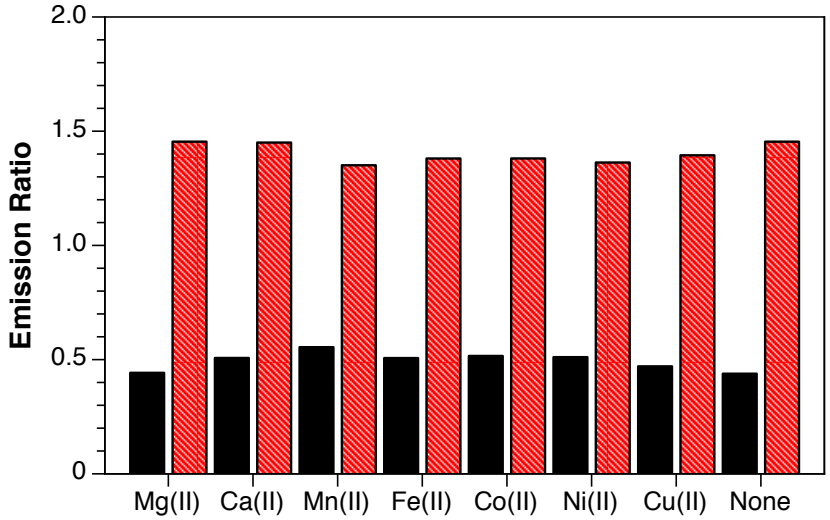

Figure 4.19: Emission-ratiometric response of probe **4.4b** (5 μM) towards selected divalent metal cations at 80% fractional saturation (calculated based on ratio of the integrated fluorescence intensity between 510-570 nm (channel 2) and 440-495 nm (channel 1)). The black bars represent the ratio at 80% fractional saturation, and the corresponding patterned red bars represent the ratio after saturating the remaining 20% of free probe with Zn(II). Excitation: 362 nm.

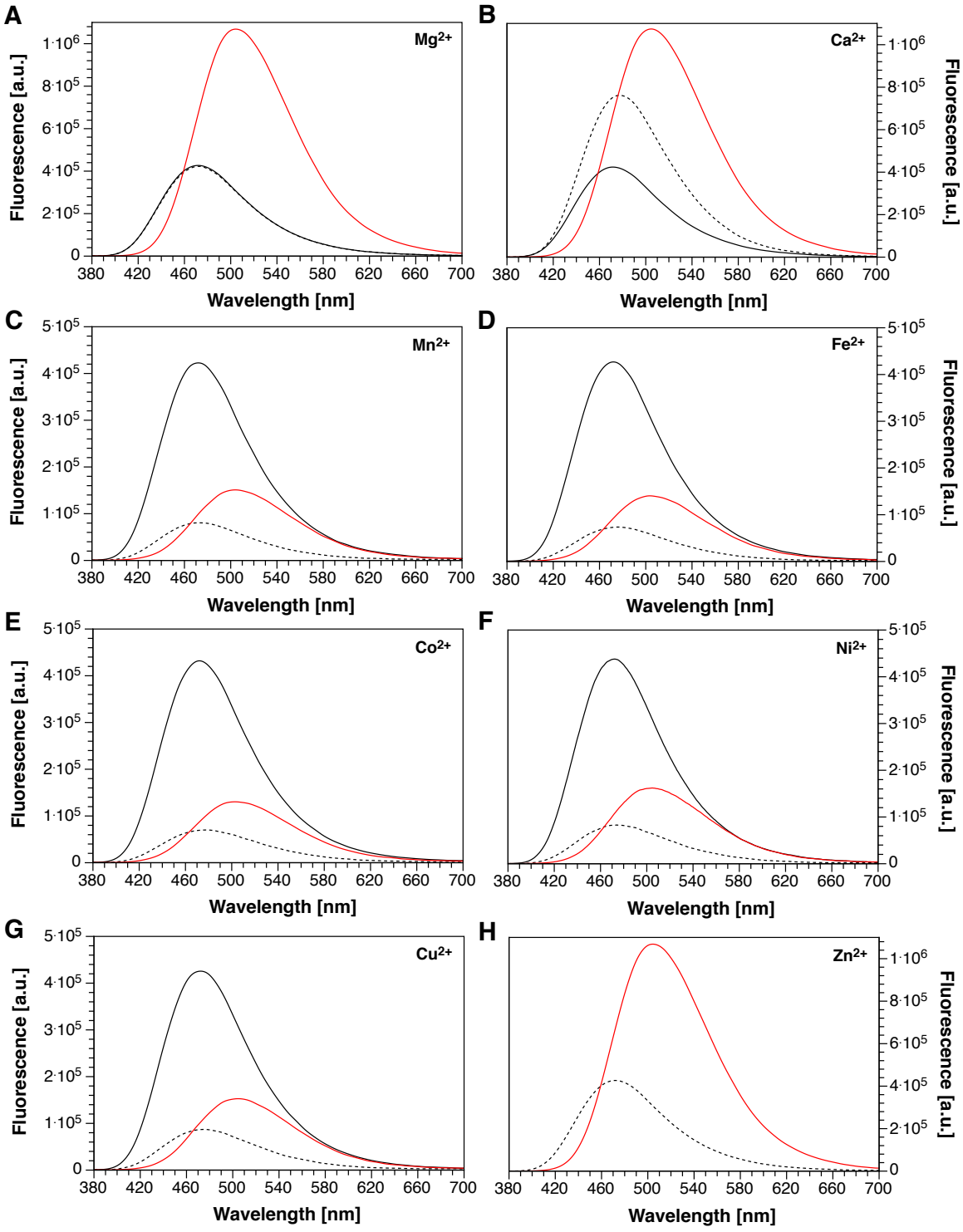

Figure 4.20: Emission spectral response of **4.4b** (5 μM) towards selected divalent metal cations at 80% fractional saturation. A,B) Fluorescence response of **4.4b** in pH 7.0 buffer (10 mM PIPES, 100 mM KCl, 25°C) in the presence of 2 mM alkaline earth metals, with corresponding saturation of probe with 1.0 eq. Zn(II). C-H) Fluorescence response of **4.4b** in the presence of 80% fractional saturation (solid black curves) of interfering divalent metal ions, with corresponding saturation of remaining 20% probe with Zn(II) (red curves). Excitation: 362 nm.

4.6 Conclusions

The highly complex regulation of intracellular Zn(II) that entails endogenous ligands displaying Zn(II)-binding affinities spanning many orders of magnitude demands the development and application of fluorescent indicators that cover the intrinsic dynamic range of the Zn(II)-transfer equilibria between endogenous ligands with which the indicators can compete. Utilizing the donor-acceptor fluorophore core developed for probe **3.3b** and chromis-2, a series of fluorescent probes, whose binding affinities for Zn(II) span nearly 10 orders of magnitude from 5.4 to 15.1 (Figure 4.21), were developed using a knowledge-driven application of metal-ligand coordination chemistry tailored towards Zn(II). Using the 90:10 fractional saturation window[16], this dynamic range increases by one logarithmic unit to provide a biologically relevant window of affinities that spans 11 orders of magnitude for sensing varying concentrations of intracellular Zn(II). By exploiting the inherent modularity of the fluorophore's aldehyde functionality, the metal-binding fluorophores were synthesized through facile reductive amination reactions with chelating ligands boasting secondary amines to which the pyridine acceptor of the fluorophore can be coupled.

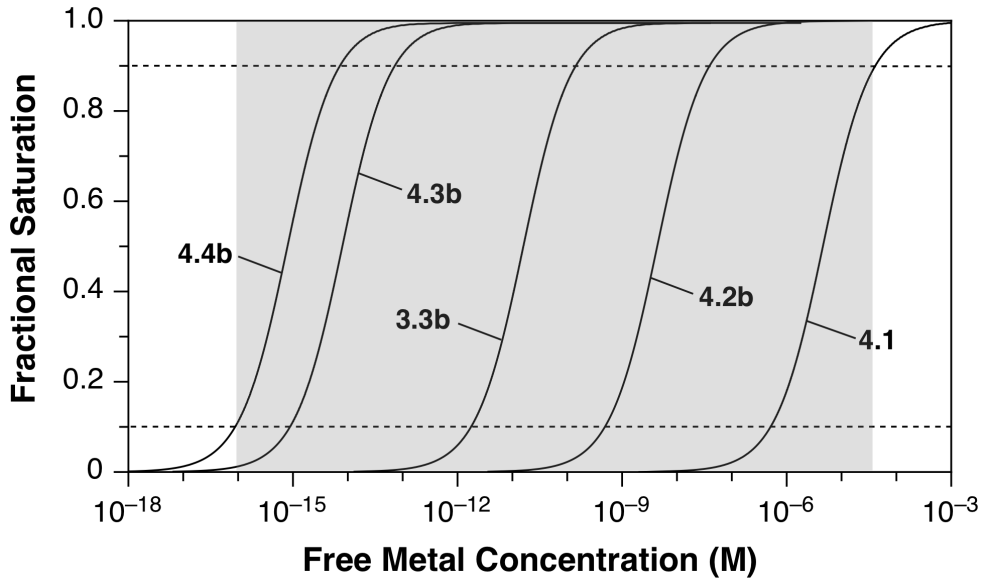

Figure 4.21: Binding isotherms illustrating the dynamic range for affinity-tuned fluorescent probes **4.1**, **4.2b**, **4.3b**, **4.4b** based on their apparent stability constants determined at pH 7.0, μ = 0.1 M KCl. The grey box represents the ~ 11-logarithmic-unit dynamic range of the series of affinity-tuned fluorescent probes within the 90:10 fractional saturation window.

Including probe **3.3b**, the water-soluble fluorescent probes whose affinities span ten logarithmic units within the biologically relevant regime display very comparable photophysical properties. As illustrated in Figure 4.22A, the absorbance spectra of the metal-free fluorophores display notable differences in the UV region below 300 nm, while the region above 300 nm reveals nearly identical spectra with absorbance maxima that demonstrate only a 3-nm span. In the emission, the corresponding fluorescence spectra display a slightly larger range of emission maxima of 9 nm from 465 to 474 nm. Consistent with Zn(II) coordination to the pyridyl acceptor of the fluorophore, the absorbance maxima shift to higher wavelength with an average absorbance maximum of 366 nm upon saturation with Zn(II), and the profiles of the absorbance spectra below 300 nm become more similar compared to the Zn(II)-free spectra, which is characteristic of the formation of ordered metal-ligand complexes (Figure 4.22B). Comparably, the fluorescence spectra of the Zn(II)-saturated fluorophores display bathochromic shifts of the emission maxima to

an average wavelength of 505 nm with a 15-nm range from 500 to 515 nm, and the emission profiles are much more uniform compared to corresponding Zn(II)-free emission spectra. Interestingly, while Zn(II)-free **3.3b** presents the most blue-shifted emission spectrum, saturation with Zn(II) results in an emission spectrum that is signficiantly more red-shifted than the other fluorophores. Nevertheless, these fluorescent probes, upon binding Zn(II), exhibit large shifts in both the absorption and emission, the latter of which is an essential prerequisite for performing quantitative ratiometric imaging analysis using TPEM (Figure 4.22C).

Each of these fluorescent indicators, including probe **3.3b**, is the product of innovative design strategies to tune the affinity of Zn(II)-responsive fluorophores through the development of metal-binding ligands that take advantage of widely-investigated Zn(II) coordination chemistry. Although the metal-binding ligands that are tethered to the acceptor moiety of the fluorophore utilize either pyridine moieties, which incorporate anionic carboxylate groups to increase water-solubility, or aliphatic hydroxyl groups, these affinity-tuning strategies can be applied to the design of pyrimidine- and pyrazine-containing, Zn(II)-binding ligands to overcome the issue of ESPT that can interfere with ratiometric imaging. While pyrimidine and pyrazine chemistries are more difficult to perform because of the higher electron-withdrawing nature of the aromatic rings compared to pyridine, exploration of ligands incorporating these heteroaromatic groups can be advantageous for cell imaging using either one- or two-photon excitation microscopy by expanding the availability of fluorescent sensors that are pH-insensitive yet provide a broad range of affinities.

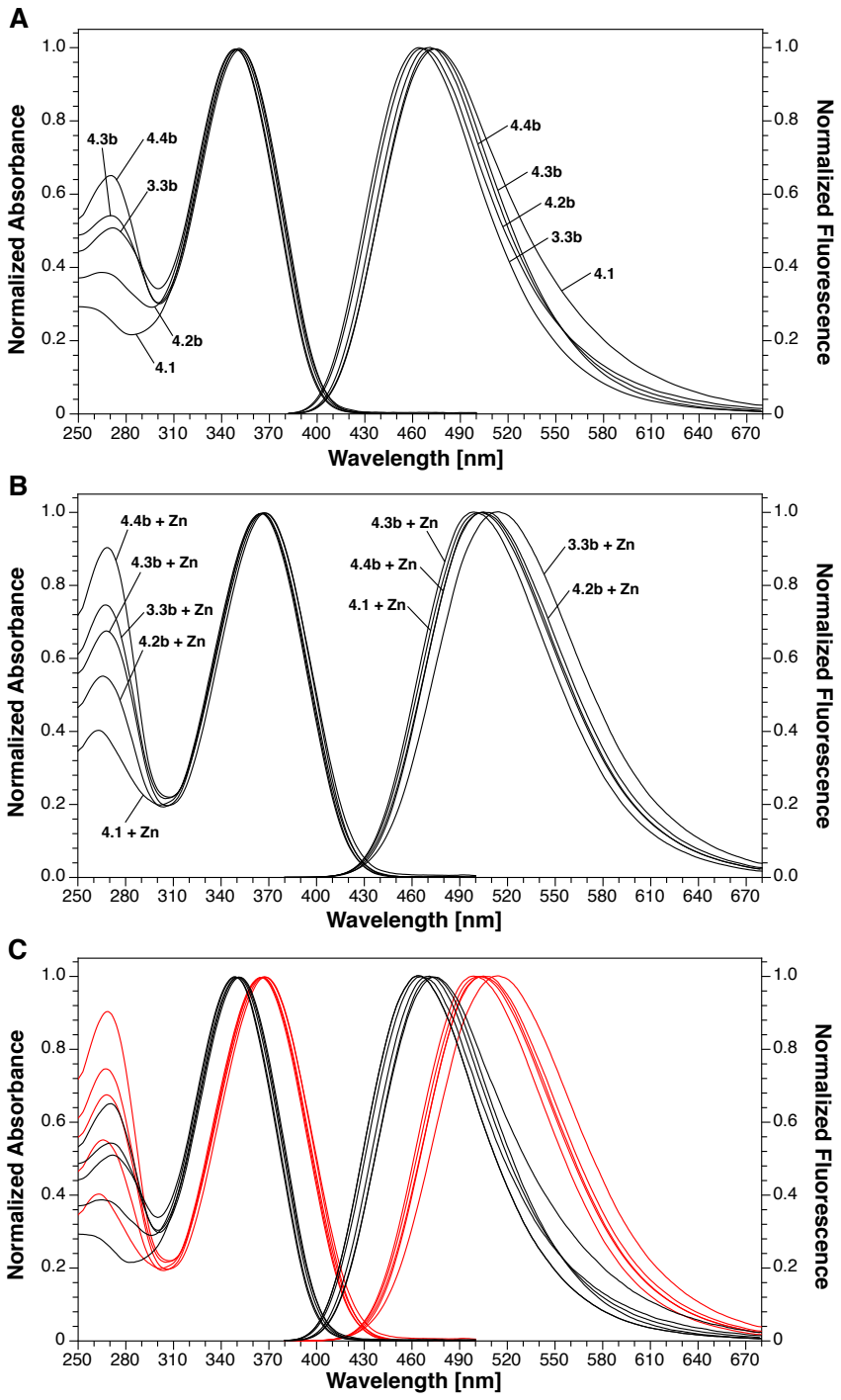

Figure 4.22: Normalized absorption and emission spectra of the affinity-tuned, Zn(II)-responsive fluorescent probes developed for probing labile Zn(II). A) Normalized absorption and emission spectra for the metal-free probes **4.1**, **4.2b**, **3.3b**, **4.3b**, and **4.4b**. B) Normalized absorption and emission spectra for the Zn(II)-bound probes. C) Overlay of the normalized absorption and emission spectra shown in (A) and (B), with the black lines representing the metal-free species, and the red lines representing the Zn(II)-bound species. Probes were excited at their respective absorption isosbestic points.

4.7 Experimental Section

4.7.1 Synthesis

Materials and Reagents. 2,4-pyridinedicarboxylic acid (Alfa Aesar), diethanolamine (Fisher Scientific), 2-aminoethanol (TCI), *tert*-butyl 2-aminoethylcarbamate (Matrix Scientific), *N*-boc-(2-aminoethyl)-*N*-methylamine (Ark Pharm, Inc.), methyl 2-pyrimidinecarboxylate (Ark Pharm, Inc.), and 2-pyrazinecarboxylic acid (Chem-Impex Int', Inc.) were purchased commercially and used without further purification. Flash chromatography purification was performed on general purpose silica gel (60 Å pore size, 250 mesh, Sorbent Technologies). NMR: ^{1}H NMR spectra were recorded at 400 MHz at ambient temperature (20-23°C), unless state otherwise, and referenced to an internal TMS standard (0 ppm) for all solvents except D_2O, which was referenced to externally added sodium 3-trimethylsilylpropionate-2,2,3,3-d_6 (0.0 ppm). ^{13}C spectra were acquired at 100 MHz and referenced to the known chemical shift of the solvent peak ($CDCl_3$: 77.0 ppm; DMSO-d_6: 39.5 ppm; CD_3OD: 49.0 ppm), excluding D_2O, which was referenced to sodium 3-trimethylsilylpropionate-2,2,3,3-d_6 (0.0 ppm). The ^{13}C spectrum of compound **4.4b**, however, was acquired at 125 MHz for improved sensitivity. NMR Spectra are provided in Appendix A2. Mass spectra were recorded by the Georgia Tech Mass Spectrometry Facility.

Bis(2-hydroxyethyl)amine fluorophore (4.1). To an oven-dried 10-mL round bottom flask equipped with a stir bar was added aldehyde **3.16** (1 eq., 0.270 mmol, 80 mg), diethanolamine (2 eq., 0.540 mmol, 56.8 mg), and $NaCNBH_3$ (1.5 eq., 0.405 mmol, 25.5 mg). Upon dissolution with anhydrous methanol (1 mL), glacial acetic acid (0.2 eq., 0.054 mmol, 3.1 μL) was pipetted into the solution, and the solution was stirred overnight. The reaction was quenched with 1 M citric acid (1 mL) by stirring for ~20 minutes. The mixture was made basic by the addition of 30% (w/v) K_2CO_3 (1 mL), and the aqueous layer was

extracted with dichloromethane (3 x 5 mL). The combined organic layers were dried over $MgSO_4$, filtered, and concentrated to a pale yellow oil residue. The residue was redissolved in 1:1 EtOAc:EOH, heated to boiling, and while cooling to room temperature, concentrated HCl (2.0 eq, 52 μL) was added. The product was left to crystallize overnight at 4ºC, collecting the bright yellow crystals by suction filtration and drying under a steady argon stream, as the hydrochloride product is hygroscopic and deliquesces in the presence of moisture from the air. Note: the product was isolated as the pure dihydrochloride. Yield: 55 mg (0.120 mmol, 45%). ^{1}H NMR ($CDCl_3$, 400 MHz) δ 2.91 (t, J = 5.2 Hz, 4H), 3.66 (t, J = 5.2 Hz, 4H), 3.85 (s, 3H), 3.96 (s, 2H), 6.94 (d, J = 8.9 Hz, 2H), 7.26 (d, J = 8.5 Hz, 1H), 7.58 (d, J = 8.9 Hz, 2H), 7.77 (t, J = 7.8 Hz, 1H), 7.97 (s, 1H), 8.09 (d, J = 8.5 Hz, 1H). ^{13}C NMR ($CDCl_3$, 100 MHz) δ 55.4, 57.3, 59.1, 59.7, 114.4, 118.2, 123.1, 123.9, 128.2, 137.9, 138.7, 141.9, 151.5, 159.5, 159.9, 166.4. ESI-MS *m/z* 386 ($[M+H]^+$, 100%), 221 (20%). ESI-HRMS *m/z* calc'd for $C_{20}H_{24}N_3O_3S$ ($[M+H]^+$) 386.1533, found 386.1531.

Methyl 2,4-pyridinedicarboxyate (4.5). To a 500-mL round bottom flask charged with 2,4-pyridinedicarboxylic acid (1 eq., 59.8 mmol, 10.0 g) was added methanol (200 mL), followed by trimethylsilyl chloride (TMSCl, 3 eq., 180 mmol, 22.9 mL). The reaction mixture was vigorously stirred under reflux for 12 hours, after which the majority of the methanol was removed by gentle evaporation to azeotropically remove water. The solution was diluted with additional methanol, and the reaction was stirred under reflux for another 12 hours. The methanol was then removed under reduced pressure, the corresponding residue was taken up in dichloromethane (200 mL), and washed with 100 mL of saturated $NaHCO_3$ solution. The aqueous phase was extracted with dichloromethane (2 x 100 mL), and the combined organic layers were dried over Na_2SO_4, filtered, concentrated under reduced pressure, and dried under vacuum to afford **4.5** as pure white crystals. Yield: 10.4 g (53.0 mmol, 89%). ^{1}H NMR ($CDCl_3$, 400 MHz) δ 4.01 (s, 3H), 4.06 (s,

3H), 8.06 (dd, *J* = 4.9, 1.6 Hz, 1H), 8.67 (dd, *J* = 1.6, 0.9 Hz, 1H), 8.92 (dd, *J* = 4.9, 0.8 Hz). ^{13}C NMR ($CDCl_3$, 100 MHz) δ 52.9, 53.1, 124.3, 126.0, 138.6, 148.9, 150.6, 164.6, 164.5. EI-MS *m/z* 195 ($[M]^+$, 5%), 165 (18%), 137 (100%), 136 (30%), 123 (28%), 81 (27%), 77 (24%), 69 (48%), 51 (29%). EI-HRMS *m/z* calc'd for $C_9H_9NO_4$ 195.0532, found 195.0531.

2-(hydroxymethyl)isonicotinic acid methyl ester (4.6). In a 250-mL round bottom flask equipped with a stir bar was added dimethyl ester **4.5** (1 eq., 51.2 mmol, 10.0 g), anhydrous $CaCl_2$ (1 eq., 51.2 mmol, 5.69 g as a finely crushed powder), and methanol (100 mL). The flask was lowered into an ice bath containing saturated NaCl, and after equilibrating for ~ 20 minutes, $NaBH_4$ (1 eq., 51.2 mmol, 1.94 g) was added in small portions over the course of 2 minutes. The reaction mixture was vigorously stirred at 0°C for 40 minutes, after which it was quenched with 12.1 N HCl (1 eq., 4.23 mL) and stirred for another ~ 10 minutes at room temperature. The methanol was removed under reduced pressure, and the solid residue was reconstituted in dichloromethane (100 mL). The dichloromethane was washed with water, and 1 M disodium citrate (prepared from citric acid and trisodium citrate dihydrate) to solubilize any borate ester salts. The aqueous layer was extracted with dichloromethane (2 x 100 mL), heating gentle under warm water to help partition the product into the organic layer. The combined organic layers were dried over $MgSO_4$, filtered, and concentrated to a light yellow oil that crystallized while drying under vacuum. The product was recrystallized from boiling cyclohexane, filtered, and dried under vacuum to afford **4.6** as a white crystalline solid. Yield: 6.02 g (36.0 mmol, 70%). ^{1}H NMR ($CDCl_3$, 400 MHz) δ 3.97 (s, 3H), 4.85 (s, 2H), 7.77 (d, *J* = 4.7 Hz, 1H), 7.87 (s, 1H), 8.70 (d, *J* = 5.1 Hz, 1H). ^{13}C NMR ($CDCl_3$, 100 MHz) δ 52.8, 64.3, 119.9, 121.6, 138.1, 149.3, 160.5, 165.4. EI-MS *m/z* 167 ($[M]^+$, 70%), 166 (100%), 138 (50%),

136 (37%), 78 (38%), 51 (38%). EI-HRMS *m/z* calc'd for $C_8H_9NO_3$ 167.0582, found 167.0581.

Methyl 2-formylisonicotinate (4.7). Methyl 2-(hydroxymethyl)isonicotinate **4.8** (1 eq., 32.9 mmol, 5.50 g) and manganese dioxide (MnO_2, 5 eq., 164.5 mmol, 14.3 g) were added to a 250 mL round bottom flask equipped with a stir bar. Toluene (100 mL) was added, and the mixture was vigorously stirred under reflux for 1.5 hours. After cooling to room temperature, the mixture was filtered through a bed of celite, the inside of the flask was washed with hot toluene and ethyl acetate (50 mL each), and the resulting filtrate was gently removed under reduced pressure to provide off-white crystals that formed after the flask cooled to room temperature. The solid was then recrystallized from boiling cyclohexane, collected by suction filtration, and dried under vacuum to afford aldehyde **4.7** as a white crystalline solid. Yield: 4.63 g (29.8 mmol, 91%). ^{1}H NMR ($CDCl_3$, 400 MHz) δ 4.02 (s, 3H), 8.10 (dd, *J* = 4.9, 1.7 Hz), 8.47 (dd, *J* = 1.6, 0.9 Hz, 1H), 8.97 (dd, *J* = 4.9, 0.8 Hz, 1H), 10.15 (s, 1H). ^{13}C NMR ($CDCl_3$, 100 MHz) δ 52.9, 120.7, 126.7, 138.6, 150.9, 153.5, 164.5, 192.3. EI-MS *m/z* 165 ($[M]^+$, 22%), 137 (100%), 134 (25%), 122 (23%), 106 (34%), 78 (39%), 51 (37%). EI-HRMS *m/z* calc'd for $C_8H_7NO_3$ 165.0426, found 165.0428.

Methyl 2-(((2-hydroxyethyl)amino)methyl)isonicotinate 4.8. To a 16- mL vial with a PTFE-lined screw cap containing a stir bar was added aldehyde **4.7** (1 eq., 3.03 mmol, 500 mg) and ethanolamine (3 eq., 9.09 mmol, 555 mg), and both starting materials were dissolved in anhydrous methanol (6 mL). Upon dissolution, glacial acetic acid (1 eq., 3.03 mmol, 174 μL) was pipetted into the solution, and the reaction was stirred overnight at room temperature to build up the formation of the iminium ion intermediate. The next day, $NaCNBH_3$ (2 eq., 6.06 mmol, 381 mg) was added to the stirring solution in small portions over the course of ~ 2 minutes. After vigorously stirring for 20 minutes, TLC

analysis (4:1 EtOAc: MeOH) confirmed the complete consumption of the starting aldehyde, so the reaction was quenched with 1 M citric acid (1 mL), followed by 2 mL of saturated Na_2CO_3(*aq*). The aqueous layer was extracted with dichloromethane (3 x 10 mL), and the combined organic layers were dried over $MgSO_4$, filtered, and concentrated to a light purple-colored oil residue. The residue was purified by column chromatography (silica gel, 4:1 EtOAc:MeOH) to afford the free base of **4.8** as a pale yellow oil. Yield: 256 mg (1.22 mmol, 40%). ^{1}H NMR ($CDCl_3$, 400 MHz) δ 2.86 (t, *J* = 5.2 Hz, 2H), 3.10 (s, br., 1H), 3.70 (t, *J* = 5.1 Hz, 2H), 3.97 (s, 3H), 4.04 (s, 2H), 7.74 (dd, *J* = 5.1, 1.5 Hz, 1H), 7.85 (s, 1H), 8.71 (dd, *J* = 5.1, 0.7 Hz, 1H). ^{13}C NMR ($CDCl_3$, 100 MHz) δ 50.9, 52.7, 54.2, 60.8, 121.3, 121.5, 137.9, 150.1, 160.6, 165.6. ESI-HRMS *m/z* calc'd for $C_{10}H_{15}N_2O_3$ ($[M+H]^+$) 211.1077, found 211.1077.

Fluorophore 4.2a. A 4-mL vial complete with a septum-sealed cap was charged with aldehyde **3.16** (1 eq., 0.34 mmol, 100 mg), secondary amine **4.8** (1.3 eq., 0.44 mmol, 92 mg), $NaBH_3CN$ (1.5 eq., 0.51 mmol, 32 mg) and a stir bar. The vial was sealed, evacuated under high vacuum, and backfilled with argon. The reagents were dissolved in anhydrous MeOH (2 mL), and the solution was supplemented with glacial AcOH (0.2 eq., 0.07 mmol, 3.85 μL) and stirred overnight at 35°C. The following day, the reaction was quenched with 1 M citric acid and diluted further with EtOAc (1 mL). The EtOAc was decanted, and the aqueous layer was extracted further with EtOAc (2 x 2 mL). The combined organic layers were dried over $MgSO_4$, filtered, and concentrated under reduced pressure to a yellow oil residue. The residue was purified by flash column chromatography (silica, 19:1 EtOAc:MeOH) to afford **4.2a** as a pure pale yellow oil. Yield: 65 mg (0.133 mmol, 39%). ^{1}H NMR ($CDCl_3$, 400 MHz) δ 2.96 (t, *J* = 5.1 Hz, 2H), 3.73 (t, *J* = 5.1 Hz, 2H), 3.83 (s, 3H), 3.86 (s, 3H), 3.99 (s, 2H), 4.07 (s, 2H), 6.96, (d, *J* = 8.8 Hz, 2H), 7.29 (dd, *J* = 7.6, 0.9 Hz, 1H), 7.60 (d, *J* = 8.8 Hz, 2H), 7.67-7.71 (m, 2H), 7.89 (s, 1H), 7.98 (s, 1H),

8.01 (dd, J = 7.9, 0.9 Hz, 1H), 8.70 (dd, J = 5.1, 1.1 Hz, 1H). ^{13}C NMR ($CDCl_3$, 100 MHz) δ 52.6, 55.4, 56.8, 59.5, 59.7, 59.9, 114.5, 117.7, 121.4, 122.3, 123.6, 124.1, 128.1, 137.4, 137.9, 138.6, 141.6, 149.9, 151.1, 159.0, 159.9, 160.7, 165.6. ESI-MS *m/z* 491 ($[M+H]^+$, 100%), 282 (17%). ESI-HRMS *m/z* calc'd for $C_{26}H_{27}N_4O_4S$ ($[M+H]^+$) 491.1748, found 491.1743.

Fluorophore 4.2b. In a 10-mL round-bottom flask equipped with a stir bar, fluorophore **4.2a** (1 eq., 0.092 mmol, 45 mg) was dissolved in MeOH (2 mL). NaOH (1.5 eq., 0.14 mmol, 27.6 μL of a 20% (w/v) solution in H_2O) was pipetted into the stirred solution, which was then vigorously stirred under reflux for 2 hours. The solution was diluted with isopropanol (iPrOH), and the precipitated product was then recrystallized from the MeOH:iPrOH mixture, filtered by suction filtration, and dried under vacuum to afford **4.2b** as pale yellow crystals. Yield: 43 mg (0.086 mmol, 94%). ^{1}H NMR (MeOD, 400 MHz) δ 2.82 (t, J = 5.8 Hz, 2H), 3.71 (t, J = 5.8 Hz, 2H), 3.84 (s, 3H), 3.93 (s, 2H), 3.98 (s, 2H), 7.00 (d, J = 8.9 Hz, 2H), 7.58 (dd, J = 7.7, 0.8 Hz, 1H), 7.63 (d, J = 8.9 Hz, 2H), 7.70 (dd, J = 5.1, 1.6 Hz, 1H), 7.83 (t, J = 7.8 Hz, 1H), 7.95 (dd, J = 7.8, 0.8 Hz, 1H), 8.02 (s, 1H), 8.03 (s, 1H), 8.51 (dd, J = 5.1, 0.7 Hz, 1H). ^{13}C NMR (MeOD, 100 MHz) δ 55.9, 57.8, 60.7, 61.0, 61.3, 115.7, 118.6, 123.2, 124.4, 125.0, 125.4, 129.1, 138.9, 139.3, 143.1, 148.5, 149.7, 151.6, 160.9, 161.0, 161.7, 168.7, 172.7. ESI-MS *m/z* 475 ($[M+H]^+$, 100%), 281 (33%). ESI-HRMS *m/z* calc'd for $C_{33}H_{31}N_6O_5S$ ($[M+H]^+$) 475.1445, found 475.1440.

***N*-methyl-*N*-boc-protected bispicolylamine 4.9**. Aldehyde **4.7** (2.2 eq., 6.06 mmol, 1.00 g), *t*-butyl-*N*-methyl(2-aminoethyl)carbamate (1 eq., 2.75 mmol, 480 mg), and $Na(OAc)_3BH$ (2.5 eq., 6.88 mmol, 1.46 g) were added to a 50 mL round bottom flask equipped with a stir bar. The flask was fitted with a rubber septum, evacuated under high vacuum to remove moisture, and backfilled with argon. Through the rubber septum was added anhydrous 1,2-dichloroethane (20 mL), and the mixture was allowed to stir at room

temperature overnight. The mixture was diluted with CH_2Cl_2 (20 mL), quenched with diH_2O (5 mL), the organic layer was removed. The aqueous layer was extracted with CH_2Cl_2 (2 x 50 mL), and the combined organic layers were dried over $MgSO_4$, filtered, and concentrated to a yellow oil. The residue was purified via column chromatography (silica gel, neat EtOAc). The combined column fractions were concentrated to a pale yellow oil residue, and the product was crystallized by heating in 2,2,4-trimethylpentane followed by cooling to room temperature overnight, affording the boc-protected *N*-methylbispicolylamine **4.9** as a white solid. Yield: 1.09 g (2.38 mmol, 82%). Note: ^{1}H characterization of **4.9** in $CDCl_3$ at room temperature showed the presence of two conformers, so the ^{1}H spectrum was acquired in DMSO-d6 at elevated temperatures (60, 80, 100°C). These conformational isomers precluded acquiring a ^{13}C NMR spectrum. ^{1}H NMR (DMSO-d6, 400 MHz, 100°C) δ 1.30 (s, 9H), 2.72 (s, 3H), 3.30 (t, *J* = 6.6 Hz, 2H), 3.90 (s, 6H), 3.94 (s, 4H), 7.63 (dd, *J* = 5.0, 1.6 Hz, 2H), 7.89 (s, 2H), 8.65 (dd, *J* = 5.0, 0.8 Hz, 2H). EI-MS *m/z* 472 ($[M]^+$, 3%), 328 (74%), 179 (46%), 177 (44%), 151 (52%), 150 (25%), 137 (50%), 97 (20%), 95 (22%), 83 (24%), 81 (22%), 69 (37%), 57 (100%). EI-HRMS *m/z* calc'd for $C_{24}H_{32}N_4O_6$ 472.2322, found 472.2321.

***N*-methyl-ethylenediamine bispicolylamine 4.10**. Boc-protected *N*-methylbispicolylamine **4.9** (1 eq., 1.97 mmol, 932 mg) was added to a 25 mL round bottom flask and dissolved in anhydrous dichloromethane (1 mL). Under a gentle stream of argon was added freshly distilled trifluoroacetic acid (TFA, 3 mL), and the flask was fitted with a glass frit to allow gas effusion. The solution was stirred for 20 minutes, transferred to an Erlenmeyer flask, diluted with dichloromethane (50 mL), and while stirring, saturated Na_2CO_3 was slowly pipetted into the flask to neutralize the remaining TFA and make the aqueous layer basic. The aqueous layer was then extracted with dichloromethane (2 x 50 mL), and the combined organic layers were dried over Na_2SO_4, filtered, and concentrated under

reduced pressure to reveal **4.10** as an amber-colored oil. The free base was used synthetically without further purification. Yield: 714 mg (1.92 mmol, 97%). ^{1}H NMR ($CDCl_3$, 400 MHz) δ 2.47 (s, 3H), 2.82-2.93 (m, 4H), 3.96 (s, 6H), 3.98 (s, 4H), 5.03 (s, br., 1H), 7.70 (dd, *J* = 5.1, 1.6 Hz, 2H), 7.91 (s, 2H), 8.68 (dd, *J* = 5.1, 0.7 Hz, 2H). ^{13}C NMR ($CDCl_3$, 100 MHz) δ 35.2, 48.7, 52.7, 53.3, 60.2, 121.3, 122.2, 137.8, 149.9, 160.4, 165.5. EI-MS *m/z* 372 ($[M]^+$, 8%), 329 (30%), 328 (100%), 322 (36%), 191 (20%), 179 (62%), 177 (85%), 151 (88%), 150 (43%), 92 (30%), 64 (22%). EI-HRMS *m/z* calc'd for $C_{19}H_{24}N_4O_4$ 372.1798, found 372.1783.

Fluorophore 4.3a. Aldehyde **3.16** (1 eq., 0.270 mmol, 80 mg), secondary amine **4.10** (1.5 eq., 0.404, 151 mg), $Na(OAc)_3BH$ (2 eq., 0.540 mmol, 115 mg), and a magnetic stirring bar were added to a 10 mL round bottom flask that was sealed with a rubber septum. The flask was evacuated under high vacuum to remove moisture and backfilled with argon. Anhydrous 1,2-dichloroethane (2 mL) was added through the septum, and the mixture was allowed to stir overnight. The reaction was quenched by the addition of 1 M citric acid, and after ~10 minutes of vigorous stirring, the mixture was made basic by the addition of saturated Na_2CO_3. The organic layer was decanted, the aqueous layer was extracted with dichloromethane (2 x 10 mL), and the combined organic layers were dried over Na_2SO_4, filtered, and concentrated to a yellow oil residue. The residue was purified by flash column chromatography (silica gel, 20:1 EtOAc:MeOH) to afford the pure **4.3a** as a yellow oil. Yield: 153 mg (0.234 mmol, 87%). ^{1}H NMR ($CDCl_3$, 400 MHz) δ 2.29 (s, 3H), 2.74 (t, *J* = 6.7 Hz, 2H), 2.85 (t, *J* = 6.7 Hz, 2H), 3.73 (s, 2H), 3.86 (s, 3H), 3.92 (s, 6H), 3.98 (s, 4H), 6.95 (d, *J* = 8.9 Hz, 2H), 7.42 (dd, *J* = 7.7, 1.0 Hz, 1H), 7.55 (d, *J* = 8.9 Hz, 2H), 7.66 (dd, *J* = 5.1, 1.6 Hz, 2H), 7.70 (t, *J* = 7.8 Hz, 1H), 7.95 (s, 1H), 7.99 (d, *J* = 7.7 Hz, 1H), 8.07 (s, 2H), 8.64 (dd, *J* = 5.1, 0.7 Hz, 2H). ^{13}C NMR ($CDCl_3$, 100 MHz) δ 42.9, 52.4, 52.6, 55.4, 55.5, 60.7, 63.6, 114.5, 117.3, 121.1, 122.2, 123.4, 124.2, 128.0, 137.2,

137.8, 138.5, 141.3, 149.8, 150.7, 159.6, 159.8, 161.1, 165.7, 167.5. EI-MS *m/z* 652 ($[M]^+$, 10%), 502 (26%), 328 (70%), 324 (100%), 282 (73%), 281 (46%), 191 (23%), 177 (45%), 151 (42%), 150 (24%). EI-HRMS *m/z* calc'd for $C_{35}H_{36}N_6O_5S$ 652.2468, found 652.2440.

Fluorophore 4.3b. To a 10 mL round bottom flask containing fluorophore **4.3a** (1 eq., 0.191 mmol, 125 mg) and a stir bar was added methanol (3 mL). While stirring, NaOH (2.5 eq., 0.479 mmol, 96 µL of a 20% (w/v) aqueous solution) was pipetted into the solution, and the mixture was refluxed for 2 hours. Upon completion of the saponification, the methanol was removed under reduced pressure, and the product was recrystallized from boiling ethanol to give the dicarboxylate disodium salt **4.3b** as a light yellow solid. Yield: 119 mg (0.178 mmol, 93%). ^{1}H NMR (MeOH, 400 MHz) δ 2.00 (s, 3H), 2.64-2.81 (m, 4H), 3.55 (s, 3H), 3.84 (s, 3H), 3.89 (s, 4H), 7.02 (d, *J* = 8.9 Hz, 2H), 7.35 (dd, *J* = 7.6, 0.9 Hz, 1H), 7.62-7.66 (m, 4H), 7.86-7.90 (m, 3H), 7.96 (dd, *J* = 7.9, 0.9 Hz, 1H), 8.15 (s, 1H), 8.41 (dd, *J* = 5.1, 0.8 Hz, 2H). ^{13}C NMR (MeOH, 100 MHz) δ 42.5, 52.7, 55.9,56.1, 61.5, 63.7, 115.8, 120.2, 123.2, 124.5, 124.7, 125.6, 129.2, 139.6, 139.7, 143.3, 148.4, 150.4, 151.7, 160.3, 161.9, 167.5, 172.5. ESI-MS *m/z* 623 ($[M+H]^+$, 100%), 535 (22%). ESI-HRMS *m/z* calc'd for $C_{33}H_{31}N_6O_5S$ ($[M+H]^+$) 623.2082, found 623.2084.

2,2'-(((2-((*tert*-butoxycarbonyl)amino)ethyl)azanediyl)bis(methylene))diisonicotinic acid dimethyl ester (4.11). Aldehyde **4.7** (2.2 eq., 5.71 mmol, 943 mg), *tert*-butyl-*N*-(2-aminoethyl)carbamate (1 eq., 2.60 mmol, 416 mg), and $Na(OAc)_3BH$ (2.5 eq., 6.49 mmol, 1.38 g) were added to a 50-mL round bottom flask equipped with a stir bar. The flask was fitted with a rubber septum, evacuated under high vacuum to remove moisture, and backfilled with argon. Through the rubber septum was added anhydrous 1,2-dichloroethane (20 mL), and the mixture was allowed to stir at room temperature overnight. The mixture was diluted with CH_2Cl_2 (20 mL), quenched with diH_2O (5 mL), and the organic

layer removed. The aqueous layer was extracted with CH_2Cl_2 (2 x 50 mL), and the combined organic layers were dried over $MgSO_4$, filtered, and concentrated to a yellow oil. The residue was purified via column chromatography (silica gel, neat EtOAc). The combined column fractions were concentrated to a pale yellow oil residue. Yield: 1.12 g (2.44 mmol, 97%). ^{1}H NMR ($CDCl_3$, 400 MHz) δ 1.42 (s, 9H), 2.76 (t, *J* = 5.8 Hz, 2H), 3.25 (q, *J* = 5.7 Hz, 2H), 3.96 (s, 10H), 5.65 (s, br, 1H), 7.72 (dd, *J* = 5.1, 1.6 Hz, 2H), 7.93 (s, 2H), 8.72 (dd, *J* = 5.1, 0.7 Hz, 2H). ^{13}C NMR ($CDCl_3$, 100 MHz) δ 28.4, 38.5, 52.7, 53.8, 60.0, 78.9, 121.4, 122.3, 137.9, 150.0, 156.1, 160.3, 165.6. EI-MS *m/z* 458 ([M]$^+$, 8%), 385 (28%), 329 (29%), 328 (100%), 308 (37%), 252 (40%), 220 (27%), 206 (30%), 191 (27%), 177 (54%), 165 (20%), 151 (58%), 150 (36%), 92 (24%), 57 (40%). EI-HRMS *m/z* calc'd for $C_{23}H_{30}N_4O_6$ 458.2165, found 458.2157.

2,2'-(((2-aminoethyl)azanediyl)bis(methylene))diisonicotinic acid dimethyl ester (**4.12**). Boc-protected amine **4.11** (1 eq., 2.22 mmol, 1.02 g) was added to a 25-mL round bottom flask and dissolved in anhydrous dichloromethane (2 mL). Under a gentle stream of argon was added freshly distilled trifluoroacetic acid (TFA, 5 mL), and the flask was fitted with a glass frit to allow gas effusion. The solution was stirred for 20 minutes, transferred to an Erlenmeyer flask, diluted with dichloromethane (25 mL), and while stirring, saturated Na_2CO_3 was slowly pipetted into the flask to neutralize the remaining TFA and make the aqueous layer basic (pH ~ 9). The aqueous layer was then extracted with dichloromethane (2 x 25 mL), and the combined organic layers were dried over Na_2SO_4, filtered, and concentrated under reduced pressure to yield **4.12** as a light amber-colored oil. The pure primary amine as the free base was used synthetically without further purification. Note: for ^{1}H/^{13}C NMR characterization, a portion of the compound was converted to the hydrochloride salt upon the slow addition of 3 eq. of TMSCl to a solution of **4.12** in EtOAc:EtOH. Yield (free base): 628 mg (1.92 mmol, 79%). ^{1}H NMR (MeOH, 400 MHz) δ

3.12 (t, *J* = 6.0 Hz, 2H), 3.33 (t, *J* = 6.0 Hz, 2H), 4.04 (s, 6H), 4.43 (s, 4H), 8.36 (dd, *J* = 5.9, 1.6 Hz, 2H), 8.47 (d, *J* = 0.9 Hz, 2H), 9.01 (d, *J* = 5.9 Hz, 2H). ^{13}C NMR (MeOH, 100 MHz) δ 37.7, 53.4, 54.2, 57.4, 126.4, 127.6, 146.0, 146.2, 155.5, 164.3. ESI-MS *m/z* 359 ([M+H]$^+$, 20%), 282 (100%). ESI-HRMS *m/z* calc'd for $C_{18}H_{23}N_4O_4$ ([M+H]$^+$) 359.1714, found 359.1712.

Secondary amine (4.13). Primary amine **4.12** (1.5 eq., 1.38 mmol, 496 mg), aldehyde **4.7** (1 eq., 0.923 mmol, 152 mg) and $Na(OAc)_3BH$ (1.5 eq., 1.38 mmol, 293 mg) were added to a 25-mL round bottom flask equipped with a stir bar. The flask was evacuated under high vacuum and backfilled with argon through a rubber septum. Through the septum was added anhydrous 1,2-dichloroethane (12 mL), and the mixture was stirred overnight at room temperature. The reaction was quenched by the addition of diH_2O (4 mL), followed by the addition of saturated $NaHCO_3$ (4 mL). The organic layer was decanted, and the aqueous layer was extracted with dichloromethane (3 x 15 mL). The combined organic layers were dried over $MgSO_4$, filtered, and concentrated to a brown oily residue that was purified via flash column chromatography (silica gel, 9:1 CH_2Cl_2:MeOH) to afford the pure secondary amine as a light amber-colored oil. Yield: 466 mg (0.918 mmol, 66%). ^{1}H NMR ($CDCl_3$, 400 MHz) δ 3.93 (s, 6H), 3.95 (s, 3H), 3.97 (s, 4H), 4.00 (s, 2H), 7.69 (dd, *J* = 5.1, 1.6 Hz, 2H), 7.73 (dd, *J* = 5.0, 1.5 Hz, 1H), 7.89 (s, 1H), 7.97 (s, 2H), 8.67 (dd, *J* = 5.1, 0.6 Hz, 2H), 8.69 (dd, *J* = 5.1, 0.7 Hz, 1H). ^{13}C NMR ($CDCl_3$, 100 MHz) δ 46.6, 52.6, 52.6, 53.7, 54.1, 60.2, 121.2, 121.3, 121.5, 122.2, 137.7, 137.8, 149.8, 150.0, 160.5, 165.5(0), 165.5(1). ESI-MS *m/z* 508 ([M+H]$^+$, 100%), 342 (32%). ESI-HRMS *m/z* calc'd for $C_{26}H_{30}N_5O_6S$ ([M+H]$^+$) 508.2191, found 508.2179.

Fluorophore 4.4a. A 10-mL round bottom flask equipped with a stir bar was charged with aldehyde **3.16** (1 eq., 0.25 mmol, 75 mmol), secondary amine **4.13** (1.2 eq., 0.31 mmol, 155 mg), and $Na(OAc)_3BH$ (1.5 eq., 0.38 mmol, 81 mg). The flask was sealed

with a rubber septum, evacuated under high vacuum, and backfilled with argon. Under an argon atmosphere, the reagents in the flask were dissolved in anhydrous 1,2-dichloroethane (2 mL), and the reaction mixture was stirred vigorously at room temperature overnight. The following day, the reaction was quenched with 1 M citric acid (1 mL), and then the aqueous layer was made basic using saturated Na_2CO_3(*aq*). The aqueous layer was extracted with dichloromethane (3 x 10 mL), and the combined organic layers were dried over $MgSO_4$, filtered, and concentrated to an amber-colored oil residue. The residue was then purified by flash column chromatography (silica gel, 1:1 DCM:acetone) to afford pure **4.4a** as a light amber-colored oil. Yield: 127 mg (0.161 mmol, 63%). ^{1}H NMR ($CDCl_3$, 400 MHz) δ 2.89 (s, 4H), 3.86 (s, 5H), 3.87 (s, 3H), 3.90 (s, 6H), 3.91 (s, 6H), 3.94 (s, 2H), 6.95 (d, *J* = 8.8 Hz, 2H), 7.42 (dd, *J* = 7.7, 0.9 Hz, 1H), 7.55 (d, *J* = 8.8 Hz, 2H), 7.63 (dd, *J* = 5.1, 1.7 Hz, 2H), 7.66 (dd, *J* = 5.1, 1.6 Hz, 1H), 7.70 (t, *J* = 7.8 Hz, 1H), 7.95 (s, 1H), 7.97-8.00 (m, 4H), 8.60 (dd, *J* = 5.1, 0.8 Hz, 2H), 8.64 (dd, *J* = 5.1, 0.8 Hz, 1H). Note: due to the high molecular weight and the chemical similarity of the carbons in **4.4a**, only 30 distinct signals were observed in the ^{13}C NMR spectrum acquired instead of the 32 theoretical signals. ^{13}C NMR ($CDCl_3$, 100 MHz) δ 52.2, 52.3, 52.6, 55.4, 60.1, 60.6(0), 60.6(2), 77.2, 105.0, 114.5, 117.4, 121.1, 122.1, 123.4, 124.2, 128.0, 137.3, 137.7, 138.5, 141.4, 149.7, 150.7, 159.3, 159.8, 160.8, 161.0(5), 161.1, 165.6(5), 165.7, 167.7. ESI-MS *m/z* 788 ($[M+H]^+$, 100%), 473 (7%), 422 (100%), 346 (45%), 272 (20%). ESI-HRMS *m/z* calc'd for $C_{42}H_{42}N_7O_7S$ ($[M+H]^+$) 788.2861, found 788.2850.

Fluorophore 4.4b. In a 10-mL round bottom flask equipped with a stir bar, fluorophore **4.4a** (1 eq., 0.095 mmol, 75 mg) was dissolved in MeOH (2 mL). While stirring, the solution was supplemented with NaOH (3.5 eq., 0.33 mmol, 67 μL of a 20% (w/v) solution in H_2O), and the solution was stirred under reflux for 2 hours. The solution was concentrated under a gentle stream of argon and then diluted with a minimal amount of EtOH,

after which the mixture was heated to boiling until the solid redissolved, and upon cooling, crystallization was initiated by the addition of a few drops of MTBE. The crystals were collected by suction filtration and dried under vacuum to afford **4.4b** as a pale yellow crystalline solid. Yield: 74 mg (0.091 mmol, 96%). ^{1}H NMR (MeOD, 400 MHz) δ 2.71-2.77 (m, 4H), 3.46 (s, 2H), 3.62 (s, 4H), 3.70 (s, 2H), 3.86 (s, 3H), 7.07 (d, *J* = 8.9 Hz, 2H), 7.28 (dd, *J* = 7.5, 0.8 Hz, 1H), 7.51 (dd, *J* = 5.1, 1.4 Hz, 1H), 7.57 (dd, *J* = 5.0, 1.1 Hz, 2H), 7.65 (s, 1H), 7.67 (s, 2H), 7.75 (d, *J* = 8.9 Hz, 2H), 7.86 (t, *J* = 7.7 Hz, 1H), 7.92 (dd, *J* = 7.8, 0.8 Hz, 1H), 8.28-8.33 (m, 4H). ^{13}C NMR (MeOD, 125 MHz) δ 51.9, 52.0, 55.9(1), 55.9(5), 59.1, 60.4, 61.3, 115.9, 120.6, 123.1, 123.2, 124.3, 124.5, 124.7, 125.6, 129.4, 139.8, 140.0, 143.4, 148.2, 150.96, 151.01, 151.7, 160.0(3), 160.0(7), 160.1, 162.0, 167.1, 172.5. ESI-MS *m/z* 744 ([M+H]$^{+}$, 100%), 700 (25%), 281 (10%). ESI-HRMS *m/z* calc'd for $C_{39}H_{34}N_7O_7S$ ([M+H]$^{+}$) 744.2246, found 744.2242.

4.7.2 Steady-State Absorption and Fluorescence Spectroscopy

4.7.2.1 General Spectroscopic Methods

All buffers and stock solutions used for spectroscopic measurements were prepared using either HPLC-grade water (JT Baker) or 18.2 MΩ•cm Mili-Q water and filtered through a 0.2 μm filter to remove interfering dust particles or fibers. UV-Vis measurements were performed on a Varian Cary Bio50 spectrophotometer with a constant temperature accessory (Peltier) at 25°C. Fluorescence measurements were performed with a PTI fluorimeter equipped with a 75 W xenon arc lamp excitation source and a photomultiplier detection system (PMT voltage was 1100 V for all experiments). Fluorescence spectra were corrected for the spectral response of the detection system and for the spectral irradiance of the excitation source (via a calibrated photodiode). For all experiments, both

UV-Vis and fluorescence, a 1-cm path length quartz cuvette was used, except for quantum yield determinations, which were performed with a 10-cm path length quartz cuvette for absorbance measurements.

4.7.2.2 Determination of Fluorescence Quantum Yields

Fluorescence quantum yields of **4.1**, **4.2b**, **4.3b**, and **4.4b** were determined in aqueous buffer (10 mM PIPES, 0.1 M KCl) treated with Chelex (1% (w/v), Biorad) at pH 7.0 by a 4-point measurement over an OD range of 0.1-0.4 using a 10-cm cuvette, with fluorimeter excitation at 365 nm. For all probes, including **4.3b** and **4.4b**, the solutions containing the free forms were supplemented with 20 μM EDTA (from a 30 mM stock solution in diH_2O) to sequester adventitious Zn(II), whereas to determine the Zn(II)-bound forms, the solutions were supplemented with 20 μM $ZnSO_4 \cdot 7H_2O$ to ensure complete saturation of the fluorophore. Fluorescence quantum yields for all fluorophores were determined using quinine sulfate (Φ_F = 0.546 in 1.0 N H_2SO_4) as a fluorescence standard.[20]

4.7.2.3 Solvent Deuterium Isotope Effect of Probe **4.1** by Fluorescence

Comparison of the fluorescence intensities of probe **4.1** was conducted in deuterated and non-deuterated buffer (10 mM PIPES, 100 mM KCl, pH/D 7.0, 25°C). A 3.0-mL solution of aqueous buffer was supplemented with 10 μM of the probe (from 3 mM stock solutions in H_2O), and after thorough mixing via magnetic stirring, a fluorescence spectrum of **4.1** was acquired over the spectral window of 380-700 nm with excitation at 360 nm. To saturate the fluorescent probe, the solution was supplemented with 300 μM $ZnSO_4 \cdot 7H_2O$ (from a 500 mM stock solution in H_2O), and another fluorescence spectrum was acquired. This was repeated in deuterated buffer, and the spectra were compared graphically.

4.7.2.4 Molar Ratio Titrations

Molar ratio titrations were performed via spectrophotometric and fluorimetric titrations to determine the stoichiometries of the fluorescent probes. For probes **4.2b**, **4.3b**, and **4.4b**, 20 μM solutions of each in pH 7.0 aqueous buffer (3.0 mL, 10 mM PIPES, 0.1 M KCl, 25°C) were prepared in a fluorescence quartz cuvette with a 1-cm pathlength, and the probes were titrated with $ZnSO_4 \cdot 7H_2O$ (from a 3 mM aqueous stock solution) in 2 μM (0.1 eq.) increments. After each aliquot, the solutions were equilibrated for 30 seconds by magnetic stirring, and absorbance (spectral window: 250-500 nm) and fluorescence spectra (spectral window: 380-700 nm, with excitation at 359 nm (**4.2b**), 355 nm (**4.3b**), and 361 nm (**4.4b**)) were acquired.

4.7.2.5 Analyte Selectivities of Probes **4.2b**, **4.3b**, and **4.4b**

A 5 μM solution (40 mL) of each probe was prepared in pH 7.0 aqueous buffer (10 mM PIPES, 100 mM KCl, 25°C) that had been previously treated with Chelex (1% (w/v), Biorad) and filtered through a 0.2 μm filter. An aliquot (2.0 mL) of the solution was transferred to a quartz cuvette with a 1-cm path length, and a fluorescence spectrum was acquired over the emission range of 380-700 nm with excitation at the wavelengths described in the previous protocol. Under magnetic stirring, the solution was supplemented with each divalent metal cation (4 μM for transitions metals, corresponding to 80% fractional saturation of the probe; 2 mM for Ca(II) and Mg(II)) under rapid magnetic stirring, and a fluorescence spectrum was immediately acquired. The solution was then supplemented with $ZnSO_4 \cdot 7H_2O$ (from a 1 mM stock solution in H_2O) to a final concentration of 1 μM (for solutions containing Co(II), Ni(II), and Cu(II)) or 5 μM (for solutions containing

all other metals: Mg(II), Ca(II), Mn(II), Fe(II)), and a fluorescence spectrum was immediately acquired. For probe **4.3b**, the solution containing Mn(II) was supplemented only with 1 μM Zn(II) to saturate the probe, and for probe **4.4b**, the solutions containing both Mn(II) and Fe(II) were supplemented with 1 μM Zn(II), The emission spectra corresponding to the addition of 80% fractional saturation with the interfering metal ions, as well as the addition of Zn(II) were integrated over the ranges of 440-495 nm (CH1) and 510-570 nm (CH2), and the resulting intensities were computed as a ratio of CH2/CH1. Metal cations were supplied as aqueous stock solutions of the following salts: Mg(II), Ca(II) as chlorides (1 M stocks); Co(II) as the nitrate salt (1 μM stock); Mn(II), Fe(II), Cu(II), and Zn(II) as sulfates (1 μM stocks). To avoid aerial oxidation of Fe(II), the stock solution was freshly prepared in 10 mM H_2SO_4 before use.

To measure the fluorescence response of the probes upon complete saturation of the probe, the working solutions that were prepared in aqueous buffer (10 mM PIPES, 100 mM KCl, 25°C, pH 7.0) were supplemented with 2.0 equivalents (10 μM, from a 30 mM stock solution in H_2O) of EDTA. A fluorescence spectrum was acquired of the free probe over the spectral window of 380-700 nm with excitation at the wavelengths corresponding to each probe as previously mentioned. The probe solution was then supplemented with interfering divalent metal ions (from 30 mM stocks solutions of each metal in H_2O) to final concentrations of 20 and 40 μM, with a fluorescence spectrum acquired immediately after the addition of each aliquot.

4.7.2.6 Determination of the Zn(II)-Binding Affinity of Probe **4.1**

The Zn(II) stability constant of **4.1** was determined through a both a spectrophotometric and fluorimetric metal-addition titration. In a quartz fluorescence cuvette with a 1-cm pathlength, a 20 μM solution of **4.1** (from a 3 mM stock solution in DMSO) in 3.00 mL

of aqueous buffer (10 mM PIPES, 0.1 M KCl, pH 7.0) at 25°C was titrated with $ZnSO_4 \cdot 7H_2O$ (from 5 and 60 mM analytical stock solutions in H_2O) from 0-220 μM. After the addition of each aliquot of Zn(II), the solution was equilibrated by magnetic stirring, and both an absorbance spectrum over the spectral window of 250-500 nm and a fluorescence spectrum over the spectra window of 380-700 nm, with excitation at 360 nm, were acquired. The spectroscopic data were analyzed by non-linear least-squares fitting using the Specfit[22] software suite.

4.7.2.7 Determination of the Zn(II)-Binding Affinity of Probe **4.2b**

The Zn(II) stability constant of **4.2b** was determined through a both a spectrophotometric and fluorimetric metal-addition titration. In a quartz fluorescence cuvette with a 1-cm pathlength, a 20 μM solution of **4.2b** (from a 3 mM stock solution in DMSO) in 3.00 mL of aqueous buffer (10 mM PIPES, 0.1 M KCl, pH 7.0) at 25°C was titrated with $ZnSO_4 \cdot 7H_2O$ (from 5 and 60 mM analytical stock solutions in H_2O) from 0-220 μM. After the addition of each aliquot of Zn(II), the solution was equilibrated by magnetic stirring, and both an absorbance spectrum over the spectral window of 250-500 nm and a fluorescence spectrum over the spectra window of 380-700 nm, with excitation at 360 nm, were acquired. The spectroscopic data were analyzed by non-linear least-squares fitting using the Specfit software suite.

4.7.2.8 Determination of the Zn(II)-Binding Affinity of Probe **4.3b**

The Zn(II) stability constant of **4.3b** was determined through a fluorimetric titration using EGTA as the competing ligand. A 10 μM solution (40 mL) of the probe was diluted from a 3 mM stock solution in H_2O prepared into pH 7.0 aqueous buffer (10 mM PIPES, 100 mM KCl, 25°C) that had been previously treated with Chelex (1% (w/v), Biorad) and

filtered through a 0.2 μm filter. The probe was saturated with Zn(II) by supplementing the solution with 10 μM $ZnSO_4 \cdot 7H_2O$ (from a 60 mM analytical stock solution in H_2O). The working solution containing the preformed [(**4.3b**)Zn(II)] complex was aliquoted into 15 separate 4-mL vials complete with PTFE-lined caps to prevent solvent evaporation, and each vial was supplemented with EDTA (from 6 and 60 mM analytical stock solutions in H2O) in various concentrations over the range of 0-900 μM. The vials were sealed and placed in a shaking incubator at 25°C for 17 hours to ensure complete equilibration. After the complete equilibration period, the solutions were transferred to a quartz fluorescence cuvette with a 1-cm pathlength, and an emission spectrum of each solution was acquired over the spectral range of 380-700 nm with excitation at 355 nm. The titration data were analyzed by non-linear least-squares fitting using the Specfit software suite.

4.7.2.9 Determination of the Zn(II)-Binding Affinity of Probe **4.4b**

The Zn(II) stability constant of **4.4b** was determined through a spectrophotometric titration using TPEN as the competing ligand. In a quartz cuvette with a 1-cm pathlength, a 10 μM solution of **4.4b** (from a 3 mM stock solution in H_2O) was prepared in 3.00 mL of aqueous buffer (10 mM PIPES, 0.1 M KCl, pH 7.0) at 25°C containing 30 mM TPEN (from a 3 mM stock solution in pH 5.0 aqueous buffer containing 10 mM PIPBS and 100 mM KCl. An absorption spectrum was acquired over the spectral window of 250-500 nm. The solution was titrated with $ZnSO_4 \cdot 7H_2O$ (from a 5 mM analytical stock solution in H_2O) from 0-42 μM. After the addition of each aliquot of Zn(II), the solution was equilibrated by magnetic stirring for 30 minutes, and an absorption spectrum was acquired over the spectral window of 250-500 nm. The spectrophotometric data were analyzed by non-linear least-squares fitting using Specfit.

4.8 References

1. Maret, W. The Function of Zinc Metallothionein: a Link Between Cellular Zinc and Redox State. *J. Nutr.* **2000**, *130* (5), 1455S-1458S.

2. Maret, W. Redox Biochemistry of Mammalian Metallothioneins. *J. Biol. Inorg. Chem.* **2011**, *16* (7), 1079-1086.

3. Coyle, P.; Philcox, J. C.; Carey, L. C.; Rofe, A. M. Metallothionein: The Multipurpose Protein. *Cell. Mol. Life Sci.* **2002**, *59* (4), 627-647.

4. Krezel, A.; Maret, W. Dual Nanomolar and Picomolar Zn(II) Binding Properties of Metallothionein. *J. Am. Chem. Soc.* **2007**, *129* (35), 10911-10921.

5. Casey, J. R.; Grinstein, S.; Orlowski, J. Sensors and Regulators of Intracellular pH. *Nat. Rev. Mol. Cell Biol.* **2010**, *11* (1), 50-61.

6. Chaloupka, R.; Sureau, F.; Kocisova, E.; Petrich, J. W. Hypocrellin A Photosensitization Involves an Intracellular pH Decrease in 3T3 Cells. *Photochem. Photobiol.* **1998**, *68* (1), 44-50.

7. Civan, M. M.; Williams, S. R.; Gadian, D. G.; Rozengurt, E. P-31 NMR Analysis of Intracellular pH of Swiss Mouse 3T3-Cells - Effects of Extracellular Na+ And K+ and Mitogenic Stimulation. *J. Membr. Biol.* **1986**, *94* (1), 55-64.

8. Gillies, R. J.; Martinezzaguilan, R. Regulation of Intracellular pH In BALB/c 3T3 Cells - Bicarbonate Raises pH via $NaHCO_3$/HCl Exchange and Attenuates the Activation of Na+/H+ Exchange by Serum. *J. Biol. Chem.* **1991**, *266* (3), 1551-1556.

9. Madshus, I. H. Regulation of Intracellular pH in Eukaryotic Cells. *Biochem. J.* **1988**, *250* (1), 1-8.

10. Gillies, R. J.; Martinezzaguilan, R.; Martinez, G. M.; Serrano, R.; Perona, R. Tumorigenic-3T3 Cells Maintain an Alkaline Intracellular pH Under Physiological Conditions. *Proc. Natl. Acad. Sci. U. S. A.* **1990**, *87* (19), 7414-7418.

11. Han, J. Y.; Burgess, K. Fluorescent Indicators for Intracellular pH. *Chem. Rev.* **2010**, *110* (5), 2709-2728.

12. Schuldiner, S.; Rozengurt, E. Na+/H+ Antiport in Swiss 3T3 Cells: Mitogenic Stimulation Leads to Cytoplasmic Alkalinization. *Proc. Natl. Acad. Sci. U.S.A* **1982**, *79* (24), 7778-7782.

13. Schwartz, M. A.; Both, G.; Lechene, C. Effect of Cell Spreading on Cytoplasmic pH in Normal and Transformed Fibroblasts. *Proc. Natl. Acad. Sci. U.S.A.* **1989**, *86* (12), 4525-4529.

14. Szwergold, B. S.; Brown, T. R.; Freed, J. J. Bicarbonate Abolishes Intracellular Alkalinization in Mitogen-Stimulated NIH 3T3 Cells. *Ann. N.Y. Acad. Sci.* **1988**, *551*, 277-279.

15. Wei, L. Y.; Stutts, M. J.; Hoffman, M. M.; Roepe, P. D. Overexpression of the Cystic-Fibrosis Transmembrane Conductance Regulator in NIH 3T3 Cells Lowers Membrane Potential and Intracellular pH and Confers a Multidrug-Resistance Phenotype. *Biophys. J.* **1995**, *69* (3), 883-895.

16. Fahrni, C. J., Probing Biological Trace Metals with Fluorescent Indicators. In *Metals in the Brain*, 1 ed.; White, A. R., Ed. Humana Press: 2017; pp 71-107.

17. Yu, Q. Y.; Kandegedara, A.; Xu, Y. P.; Rorabacher, D. B. Avoiding Interferences from Good's Buffers: a Contiguous Series of Noncomplexing Tertiary Amine Buffers Covering the Entire Range of pH 3-11. *Anal. Biochem.* **1997**, *253* (1), 50-56.

18. Abdel-Magid, A. F.; Mehrman, S. J. A Review on the Use of Sodium Triacetoxyborohydride in the Reductive Amination of Ketones and Aldehydes. *Org. Process Res. Dev.* **2006**, *10* (5), 971-1031.

19. Borch, R. F.; Bernstein, M. D.; Durst, H. D. Cyanohydridoborate Anion as a Selective Reducing Agent. *J. Am. Chem. Soc.* **1971**, *93* (12), 2897-2904.

20. Brouwer, A. M. Standards for Photoluminescence Quantum Yield Measurements in Solution (IUPAC Technical Report). *Pure Appl. Chem.* **2011**, *83* (12), 2213-2228.

21. Smith, R. M.; Martell, A. E.; Motekaitis, R. J. NIST Critically Selected Stability Constants of Metal Complexes Database. Standard Reference Data Program, National Institute of Standards and Technology, U.S. Dept. of Commerce: Gaithersburg, MD, 2004.

22. Binstead, R. A., Zuberbühler, A. D. *SPECFIT Global Analysis System*, 2001.

CHAPTER 5

EVALUATING THE PHOTOPHYSICAL AND THERMODYNAMIC PROPERTIES OF MONOVALENT COPPER-SELECTIVE FLUORESCENT PROBES IN LIPOSOMES: ELUCIDATING THE FLUORESCENCE DEPENDENCE ON POLARITY

All experiments and data encompassing this chapter were conducted by the author unless state otherwise and have either been published (reference 22) or are in preparation for publication (reference 29)

The design of cation-selective fluorescent probes for use as analytical tools in elucidating metal-ion biochemistry requires a detailed understanding of not only the photophysical properties governing the signal transduction that occurs upon binding of the metal analyte but also how these properties compare between spectroscopic characterization and cellular imaging studies. The dichotomous environment of the cell, featuring lipid-rich regions, such as plasma membranes and lipid vacuoles, and the aqueous cytosol and internal fluids of organelles that solubilize the hydrophilic components, demands probes bearing structural features that enable both passive diffusion across plasma membranes as well as water-solubility. However, characterization of fluorescent probes that are lipophilic enough to diffuse across the cell membrane can be challenging due to aggregation in aqueous buffer, which often affects the photophysical properties, including the brightness and emission wavelength of the probes.[1]

The delivery of small molecules into the cell to reach their cellular targets is an important goal in biological research. At present, most fluorescent probes are considerably lipophilic to ensure diffusion across cellular membranes, but their poor water-solubility

requires dilution from concentrated stock solutions of the probes at millimolar concentrations, that are typically prepared in organic solvents, into the incubation buffer. Upon dilution of the concentrated stock solution into aqueous buffer, often to final probe concentrations in the micromolar range, the appearance of a homogeneous solution does not necessarily preclude the formation of nanoparticles of the aggregated fluorescent probe with sizes residing below the diffraction limit. The discrepancies in the emission response of fluorescent probes between aqueous buffer and the cellular environment often go unnoticed due to the lack of awareness of aggregation, which can be deceiving, in part, due to the absence of solution turbidity when working at micromolar concentrations.

To overcome this issue, the characterization of lipophilic fluorescent probes can be performed in the presence of liposomes as model membranes in order to predict their fluorescence spectral behaviors by providing a medium in which to dissolve the probe all while conducting the characterization in aqueous buffer. Even if a fluorescent probe bears water-solubilizing functional groups to preclude aggregation at micromolar concentrations or higher, its emission response should still be evaluated in the presence of liposomes in case there are any lipid-mediated fluorescence enhancements or spectral shifts of the fluorescence that are independent of the metal analyte. This chapter focuses on evaluating of the fluorescence dependence on the polarity environment through the characterization, in liposomes, of Cu(I)-selective fluorescent probes that are widely employed for detecting labile Cu(I) changes in various cell and tissue types. Beforehand, however, it is important to establish the current state of affairs in the development of Cu(I)-responsive fluorescent indicators for probing monovalent copper biological systems.

5.1 Current State of Affairs in Cu(I)-Responsive Fluorescent Probes

5.1.1 The Hurdles Associated with Detecting Intracellular Cu(I)

Synthetic fluorescent probes represent powerful tools with high sensitivity for the *in situ* detection of metal ions, including monovalent copper, which is the predominant oxidation state of copper in cells[2]. In comparison to Zn(II) and Fe(II), the concentration of cellular copper is roughly one order of magnitude lower, amounting to 3 ~ 5 femtograms of total copper, for example, in 3T3 mouse fibroblast cells.[3] The resulting total copper within a single cell, therefore, resides below the limit of detection for customarily used analytical instrumentation used in trace metal analysis, such as Inductively coupled plasma mass spectrometry (ICP-MS) or atomic emission spectroscopy (AES).[4] On the other hand, designing fluorescent probes for detecting Cu(I) is much more challenging than other non-redox-active metals, such as Zn(II), Mg(II), or Ca(II), because of interfering quenching pathways that involve metal-to-ligand or ligand-to-metal charge-transfer states, leading to rapid intersystem crossing to produce non-fluorescent triplet states in the excited state.[5] In addition, at micromolar concentrations, Cu(I), has the propensity to spontaneously disproportionate into Cu(0) and Cu(II) in acidic aqueous solution, whereas at neutral or basic pH, Cu(I) can precipitate as cuprous oxide (Cu_2O); these reaction pathways only add to the difficulty of designing fluorescent sensors for the selective detection of aqueous Cu(I).

5.1.2 Cu(I)-Selective Fluorescent Probes Currently Available

Presumably due to the difficulty in designing fluorescent indicators for probing monovalent copper, only few fluorescent probes have been reported in the literature.[6] Of those currently available (a selection with corresponding structures is provided in Figure

5.1), the majority utilize a PET (photoinduced electron transfer) mechanism for signaling the association of the metal with the probe and enables the discrimination of the metal-bound probe from the metal-free probe. The PET reaction is an electron-transfer reaction by which an electron is moved from a donor group to an electronically decoupled acceptor group in the excited state. The donor group, which undergoes a facile a one-electron oxidation, is covalently linked to the fluorophore unit through an sp^3-hybridized spacer, permitting the transfer of an electron from the donor moiety to the acceptor fluorophore in the excited-state and results in a non-radiative $S_1 \rightarrow S_0$ transition, thereby quenching the fluorescence.[7] However, binding of a metal cation can obstruct the one-electron oxidation process, thus significantly reducing the rate of PET and producing a fluorescence "turn-on" response. Of the probes shown in Figure 5.1, fluorescence contrast ratios (fluorescence enhancement factors), which are the ratios of the fluorescence intensity of the Cu(I)-saturated probe to the fluorescence intensity of the metal-free probe, range between 9.6 (probe **5.7**) and 75 (**5.4**: CS3). For fluorescence turn-on probes, the contrast ratio is an important component of their photophysical properties, as the increase in fluorescence upon binding of the metal cation is what discriminates it from its metal-free counterpart. Thus, the higher the contrast ratio, the more useful it will serve when probe Cu(I) in live cells.

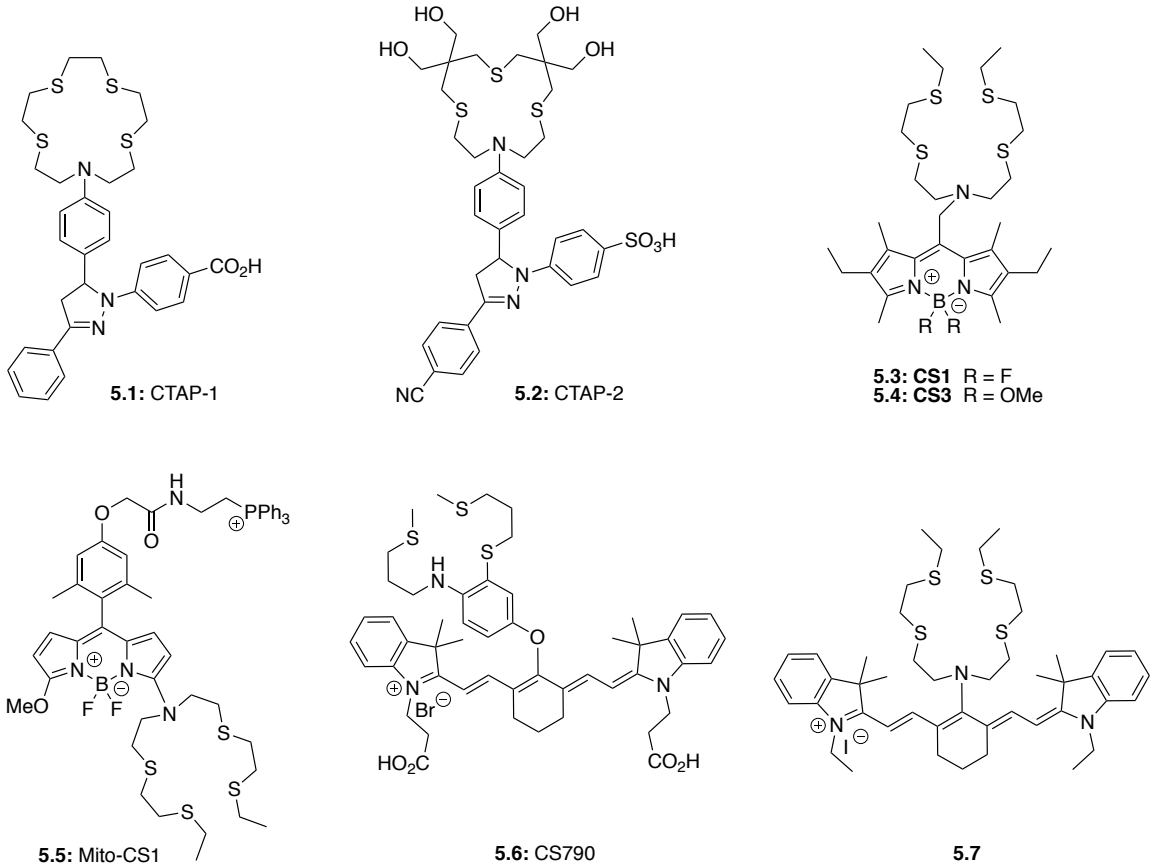

Figure 5.1: Structures of selected fluorescent probes for sensing monovalent copper

Table 5.1: Photophysical properties of selected fluorescent sensors for probing Cu(I) shown in Figure 5.1

Cu(I) Probe	Abs λ_{max} (nm)	Em λ_{max} (nm)	Φ_F [a]	f_e [b]	Buffer, pH	Mechanism [c]
CTAP-1 (**5.1**)[8]	365	485	0.14	4.6	PIPES, 7.2[d]	PET
CTAP-2 (**5.2**)[1]	396	508	0.083	65	MOPS, 7.2	PET
CS1 (**5.3**)[9-10]	540	561	0.13	10	HEPES, 7.0[d]	PET
CS3 (**5.4**)[11]	540	548	0.40	75	HEPES, 7.0[d]	PET
Mito-CS1 (**5.5**)[12]	550	558	0.05	10	PBS, 7.4[d]	ICT
CS790 (**5.6**)[13]	760	790	0.072	15	HEPES, 7.0[d]	PET
5.7[14]	750	792	n.d.	9.6	PBS, 10% EtOH, 7.0[e]	ICT

[a]Fluorescence quantum yield of the Cu(I)-saturated species; [b]fluorescence enhancement factor (contrast ratio) between the Cu(I)-saturated metal-free species; [c]PET: photoinduced electron transfer, CT: charge-transfer; [d]probe stock solution prepared in and diluted in aqueous buffer; [e]probe prepared in ethanol and diluted into aqueous buffer; n.d. = not determined. Table adapted from reference [5] with permission from author.

The very first synthetic fluorescent turn-on probe for detecting Cu(I) in aqueous solution was CTAP-1 (copper triarylpyrazoline 1, **5.1**), developed by Fahrni and coworkers.[8] CTAP-1 utilizes PET as a fluorescence quenching mechanism, which is suppressed upon binding of Cu(I), resulting in a nearly 5-fold fluorescence enhancement factor in aqueous buffer at pH 7.2. Despite the presence of a carboxylic acid to promote water-solubility, CTAP-1 required DMSO in order to prepare concentrated stock solutions necessary for dilution into the incubation buffer for cellular and photophysical characterization. In addition, Yang and coworkers observed significant colocalization of the probe with the elemental copper topography provided by preforming X-ray fluorescence microscopy (micro-XRF).[8] In order to suppress the production of colloidal aggregates, as well as improve the water-solubility, optimization of the structure of CTAP-1 led to the development of CTAP-2 (**5.2**), in which the thiocrown receptor unit was functionalized with four hydroxyl groups, and the pyrazoline fluorophore was functionalized with a sulfonic acid. The improved water-solubility permitted the preparation of stock solutions of CTAP-2 at millimolar concentrations in water without the need of organic cosolvents. In addition, the optimization of the thiocrown receptor unit and pyrazoline unit led to a 65-fold fluorescence enhancement upon binding of Cu(I) compared to a 4.6-fold enhancement for CTAP-1, as well as a 10-fold increase in the binding affinity at pH 7.2.

Based on an entirely different fluorophore architecture, the boron-dipyrromethene (BODIPY)-based CS1 (coppersensor-1, **5.3**) exhibited a 10-fold fluorescence enhancement upon binding Cu(I) to the metal-cation receptor, which is composed of a thioether-rich acyclic 3,6,12,15-tetrathia-9-monoazaheptadecane ligand.[9-10] The significant lipophilicity of the BODIPY fluorophore makes it membrane-permeant and thus allows for facile internationalization of the probe into cells for imaging labile Cu(I) pools using fluorescence microscopy. In order to improve the photophysical properties of CS1, most

importantly the turn-on response,[6] substitution of the fluorines with more electron-rich methoxy substituents afforded coppersensor-3 (CS3, **5.4**), which was reported to boast a 75-fold fluorescence enhancement upon saturation with Cu(I), in addition to a three-fold increase in the quantum yield of the Cu(I)-bound form.[11] Interestingly, substitution of the fluorines with methoxy groups provided a nearly two logarithmic-unit increase in the apparent stability constant of CS3 ($\log K_{Cu(I)L}$ = 13.1) compared to CS1 ($\log K_{Cu(I)L}$ = 11.4) at pH 7.2, despite the presence of identical tetrathioether-containing Cu(I) chelators.

The BODIPY fluorophore platform of CS1 and CS3 was also used as a chemical foundation to develop a Cu(I)-selective fluorophore, mito-CS1, for detecting labile Cu(I) pools in localized subcellular compartments, such as mitochondria, by the conjugation of a synthetic localization tag to the BODIPY fluorophore.[12] In addition, Cu(I)-selective fluorescent probes based on the cyanine 7 fluorophore platform have been developed for application in two-photon and near-infrared imaging of Cu(I) in tissues and whole animals, demonstrating the versatility of designing Cu(I)-responsive fluorescent probes for employment in various types microscopy.[6, 13-14]

5.2 Evaluating the Fluorescence Response of Cu(I)-Selective Fluorescent Probes in the Presence of Liposomes

5.2.1 Assessing the Fluorescence Dependence of Coppersensor-3 (CS3) on the Polarity Environment

Despite the formation of colloidal aggregates in aqueous solution, the employment of CS3 (**5.2**, Figure 5.1) for cellular imaging has been quite pervasive throughout the literature for use in detecting labile Cu(I) in a wide variety of organisms.[11-12, 15-20] To verify the

formation of colloidal aggregates, dynamic light scattering (DLS) measurements with CS1 and CS3 (5 μM each) in aqueous buffer (10 mM MOPS/K^+, pH 7.2, 25°C) indicated the formation of probe nanoparticles with average sizes equal to 49 nm and 67 nm, respectively.[1] As previously mentioned, the formation of colloidal aggregates may alter the photophysical properties of the metal-free probe in the aggregated form relative to the monomeric form, including a shift in the maximum emission wavelength or an increase or decrease in the fluorescence intensity. To determine whether CS3 undergoes aggregation-induced fluorescence quenching, the photophysical properties of both metal-free and Cu(I)-saturated CS3 were evaluated in the presence of liposomes and compared to those in aqueous buffer.

Although CS3 was reported to undergo a 75-fold fluorescence enhancement upon saturation with Cu(I) in aqueous buffer,[11] only fluorescence contrast ratios up to ~ 13 were achieved, despite rigorous column purification, as well as supplementation with MCL-1[21], a water-soluble high-affinity Cu(I) chelator that would sequester adventitious Cu(I) from the buffer (Figure 5.2A). To compare the signaling response of CS3 in aqueous buffer with the fluorescence response in the presence of liposomes, the fluorescence emission of CS3 was evaluated in the presence of 100 μM 1,2-dimyristoyl-*sn*-glycero-3-phosphorylcholine (DMPC) as model membranes.

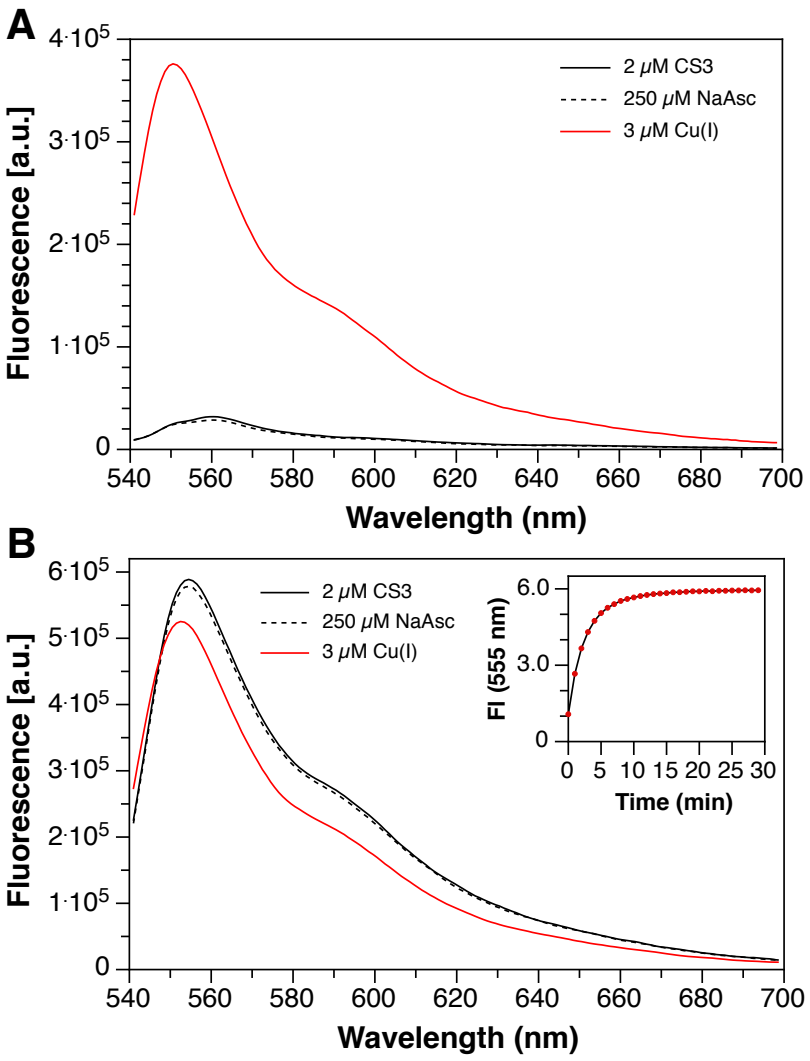

Figure 5.2: Comparison of the fluorescence response of CS3 (2 μM) upon saturation with Cu(I) in the presence (A) and absence (B) of DMPC liposomes (100 μM) pH neutral aqueous buffer (10 mM PIPES, 100 mM KCl, pH 7.0, 25°C). Inset: time-dependent fluorescence change at 555 nm prior to saturation of Cu(I). Excitation: 530 nm.

In support of a slow kinetics of dissolution of the aggregated form into the bilayer of the liposomes[20], CS3 displayed a time-dependent fluorescence increase in the presence of buffer containing 100 μM DMPC liposomes, reaching its maximum fluorescence intensity after approximately 20 minutes depending on the rate of stirring (Figure 5.2B, inset). Addition of Cu(I), produced by *in situ* reduction of $CuSO_4 \cdot 5H_2O$ by excess sodium ascorbate (NaAsc) as a reducing agent led to a 15% decrease in the emission intensity of

CS3, in sharp contrast to the 12-fold increase in the fluorescence intensity upon saturation with Cu(I) in buffer containing no liposomes. In addition, CS3 underwent a blue shift of 5 nm towards shorter wavelength upon binding to Cu(I) in both the presence and absence of DMPC-containing liposomes. These observations indicate that metal-free CS3 undergoes an aggregation-induced fluorescence quenching, which, upon deaggregation into its monomeric form, results in a liposome-mediated turn-on response, even in the absence of Cu(I) binding.

Given the varied mixture of phospholipids present in cellular membranes across organisms, giving rise to deviations in the surface charge density as a consequence of the phospholipid head groups, the fluorescence response of CS3 was evaluated in a liposome mixture comprising neutral DMPC and anionic sodium 1,2-dimyristoyl-*sn*-glycero-3-phosphorylglycerol (DMPG) in a 4:1 ratio to model the surface charge density of cellular membranes. Both lipids have similar phase transition temperatures and, as a consequence of their fully saturated fatty acid chains, are stable towards lipid peroxidation. To compare the size of newly prepared 4:1 DMPC:DMPG liposomes to that of the 100% DMPC liposomes used in previous experiments with CS3, the freshly extruded liposomes measured by tunable resistive pulse sensing (TRPS) displayed an average diameter of 120 nm, with the size distribution peaking at 100 nm (Figure 5.3).

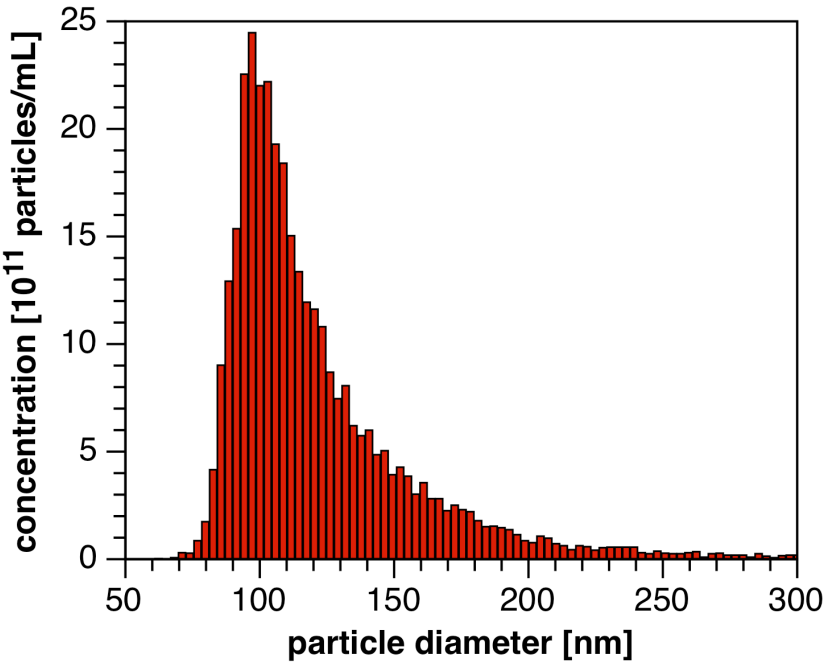

Figure 5.3: Size distribution of 4:1 DMPC/DMPG liposomes prepared in 10 mM PIPES buffer (pH 7.0, 0.1 M $KClO_4$, 25°C) through mechanical extrusion (200 nm pore size polycarbonate membrane). The average diameter of the liposomes is 120 nm and the size distribution peaks at a diameter of 100 nm. Figure and caption reproduced with permission from reference [22].

Incubation of CS3 (2 μM) in aqueous buffer (10 mM PIPES, 100 mM $KClO_4$, pH 7.0) at 25°C supplemented with a 4:1 DMPC:DMPG liposomes mixture (100 μM) displayed a time-dependent fluorescence increase consistent with observations in liposomes composed of 100% DMPC lipids (Figure 5.4). However, the equilibrium between the aggregated form and the monomeric form displayed significantly slower kinetics of dissolution and required nearly five hours to fully reach its maximum fluorescence intensity once fully dissolved in the lipid bilayer (Figure 5.4, inset). The Cu(I)-saturated CS3 displays a 3-nm hypsochromic shift in the emission, as well as a ~ 40% decrease in the fluorescence intensity, suggesting that the net negative charge of the liposomes influences the signaling

response of Cu(I)-CS3. Interestingly, the liposome-mediated fluorescence turn-on response of Cu(I)-free CS3 is nearly 50% stronger than the fluorescence response of Cu(I)-saturated CS3 in buffer containing no liposomes.

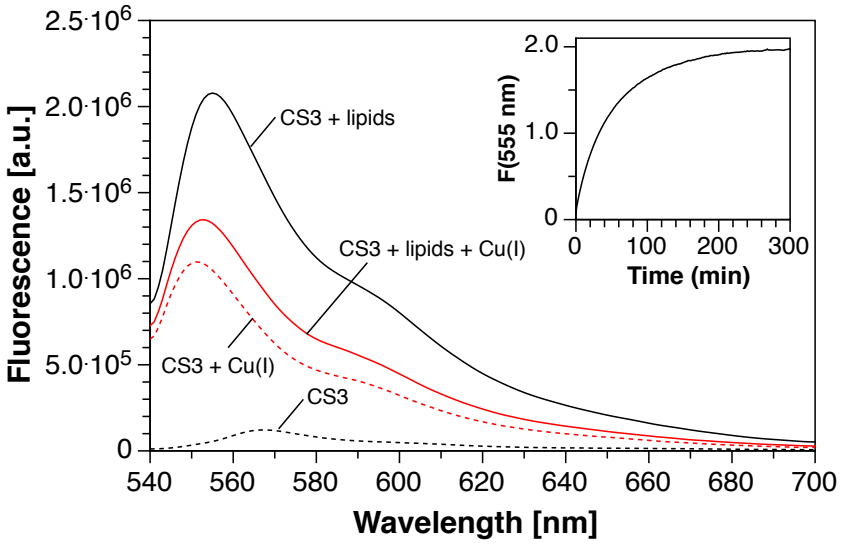

Figure 5.4: Fluorescence response of CS3 (2 μM) upon saturation with Cu(I) in the presence and absence of 4:1 DMPC:DMPG liposomes (100 μM) in pH 7.0 aqueous buffer (10 mM PIPES, 100 mM $KClO_4$, 100 nM MCL-1, 25°C). Inset: time-dependent evolution of the fluorescence intensity at 555 nm prior to the addition of Cu(I). Solid lines represent measurements of CS3 in liposomes, whereas the dashed lines represent measurements of CS3 in aqueous buffer with no liposomes. Excitation: 530 nm. Figure adapted with permission from reference [22].

To corroborate the discrepancies in the signaling response of CS3 in liposomes versus aqueous buffer, the fluorescence response of the lipophilic Cu(I) probe was compared in MeOH and octanol. As illustrated in Figure 5.5 (dashed lines), CS3 undergoes a 6-fold increase in fluorescence upon saturation with Cu(I). However, analogous measurements in octanol, a solvent of much lower polarity, demonstrated a very minimal change in the fluorescence response upon saturation with Cu(I) (Figure 5.5, solids lines), suggesting that in more polar organic solvents such as MeOH, the Cu(I)-induced fluorescence increase is accompanied by a deaggregation of the probe.

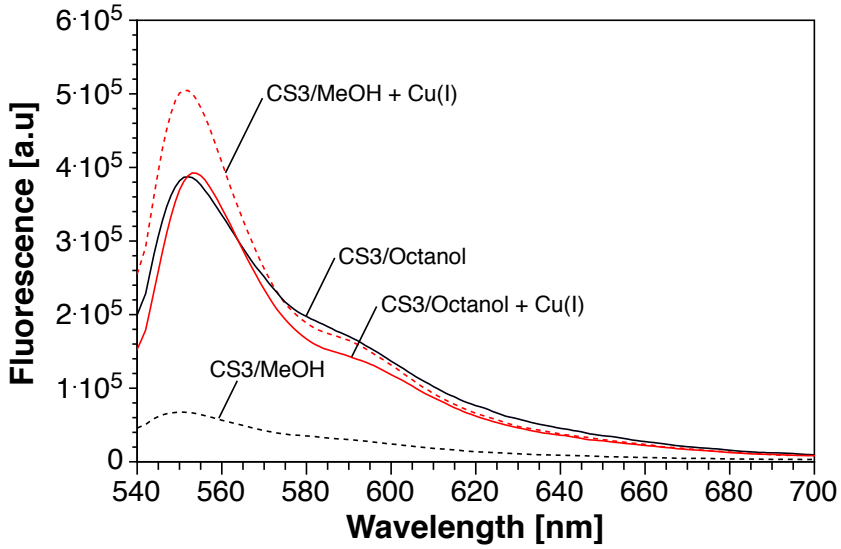

Figure 5.5: Comparison of the fluorescence response of CS3 (2 μM) upon saturation with $CuPF_6$ in MeOH and Octanol. Solid lines represent measurements of CS3 in octanol, whereas the dashed lines represent measurements of CS3 in octanol. Excitation: 530 nm.

5.2.2 CTAP-2 is a Water-Soluble Fluorescent Probe that Interacts with Lipid Bilayers

Dynamic light scattering measurements with CTAP-1 analogous to those performed with CS1 and CS3 revealed nanoparticle formation with an average hydrodynamic radius of approximately 63 nm, despite the presence of the carboxylic acid on the 1-aryl ring of the pyrazoline unit to promote water-solubility.[1] The development of CTAP-2, therefore, included installation of additional water-solubilizing groups to increase the solubility in aqueous buffer at millimolar concentrations and prevent the formation of colloidal aggregates. When diluted from an aqueous concentrated stock solutions into the identical buffer used for CS3 measurements, CTAP-2 underwent a ~ 60-fold fluorescence enhancement upon saturation with Cu(I) with an emission maximum at 512 nm (Figure 5.6, dashed lines), consistent with the 65-fold fluorescence enhancement reported by Morgan *et al.*[1] However, upon addition of CTAP-2 to aqueous buffer supplemented with a 4:1 DMPC:DMPG liposome mixture (100 μM), CTAP-2 exhibited a strong blueshift of 26 nm

relative to metal-free CTAP-2 in aqueous buffer without liposomes, indicating a strong interaction with the lipid bilayer of the liposomal vesicles (Figure 5.6, solid black line). Interestingly, upon saturation of lipid-solvated CTAP-2 with Cu(I), the emission spectrum underwent a 26-nm redshift (Figure 5.6, solid red line) to match that of the Cu(I)-saturated CTAP-2 spectrum in aqueous buffer devoid of liposomes, suggesting that the Cu(I)-bound form does not significantly interact with the liposomes.

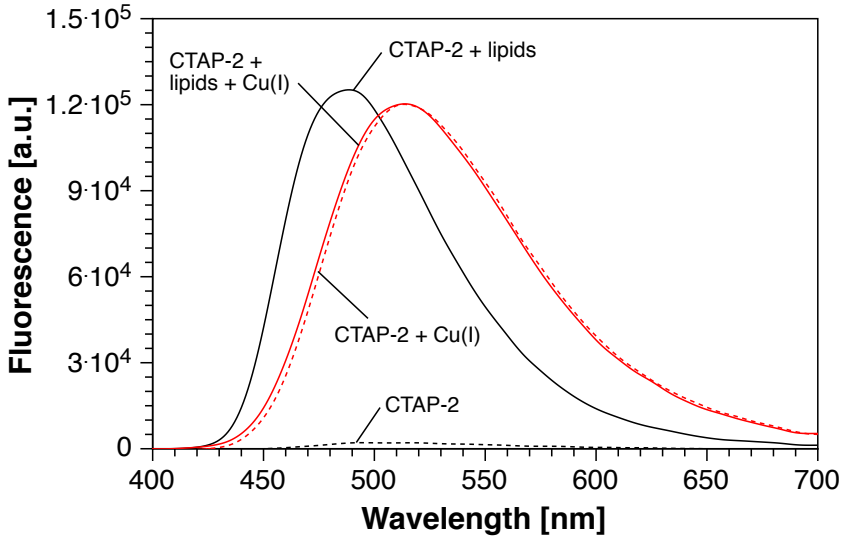

Figure 5.6: Fluorescence response of CTAP-2 (2 μM) upon saturation with Cu(I) in the presence and absence of 4:1 DMPC:DMPG liposomes (100 μM mixture) in pH 7.0 aqueous buffer (10 mM PIPES, 100 mM $KClO_4$, 100 nM MCL-1, 25°C). Solid lines represent measurements of CTAP-2 in liposomes, whereas the dashed lines represent measurements of CTAP-2 in aqueous buffer with no liposomes. Excitation: 380 nm. Figure adapted with permission from reference [22].

5.3 Characterization of a Water-Soluble, Lipid-Compatible Fluorescent Probe for Cu(I) with Sub-Part-Per-Trillion Sensitivity

As previously observed with CS3 and CTAP-2, de-aggregation of lipophilic fluorophore colloids upon partitioning into the lipid phase of liposomes can induce a metal cation-independent fluorescence increase, rendering the interpretation of staining patterns challenging when imaging the probes in live cells. The development of CTAP-2 was realized with an effort to improve the fluorescence contrast ratio (f_e = 4.6) and modest fluorescence quantum yield (Φ_F = 0.14) of CTAP-1 in aqueous buffer while increasing the water-solubility without compromising cell-membrane permeability. While the optimization led to a 14-fold improvement in the fluorescence contrast ratio, the decrease in the fluorescence quantum yield to 8% limited its detection sensitivity. In addition, the metal cation-independent fluorescence increase of CTAP-2 in the presence of liposomes was likely a structural consequence of the 3-aryl ring of the pyrazoline fluorophore. Therefore, further optimization of the structure of CTAP-2 to improve the photophysical properties in aqueous buffer, while permitting interactions with liposomes that do not result in analyte-dependent fluorescence increases, led to the development of CTAP-3 (**5.8**, Figure 5.7) as a water-soluble, lipid-compatible, Cu(I)-selective fluorescent sensor for probing labile Cu(I) in biological samples.[22] The following subsection describes the photophysical characterization of CTAP-3 in aqueous buffer in the presence and absence of liposomes.

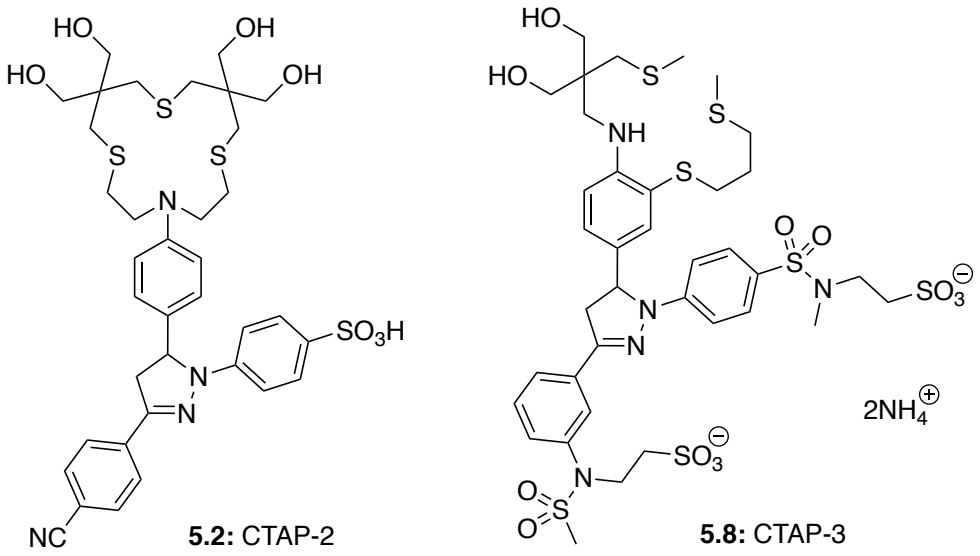

Figure 5.7: Structural comparison between CTAP-2 (**5.2**) and CTAP-3 (**5.8**)

5.3.1 Steady-State Absorption and Emission Properties of CTAP-3 in the Presence and Absence of Liposomes

Similar to CTAP-2, the water-solubilizing ammonium sulfonate groups on the pyrazoline core permitted direct preparation of concentrated stock solutions at millimolar concentrations without the need for organic cosolvents. The molar absorptivity coefficients at the peak absorption of the free and Cu(I)-bound CTAP-3 remained relatively the same, however, the addition of Cu(I) shifted the absorbance maximum of the free form 3 nm towards shorter wavelength from 367 to 364 nm (Table 5.2). Although PET renders the free form of CTAP-3 essentially non-fluorescent, titration with Cu(I) did not shift the 455-nm emission maximum, which plateaued at 1.0 equivalent of Cu(I) relative to the probe, consistent with a 1:1 binding stoichiometry. The saturation of CTAP-3 with Cu(I) resulted in an astounding 180-fold fluorescence enhancement factor, reaching a maximum fluorescence quantum yield of 0.41.[22]

Table 5.2: Photophysical properties of CTAP-3 (**5.8**) in aqueous buffer at pH 7.0.[a]

	– Liposomes		+ Liposomes[b]	
	CTAP-3[c]	[(CTAP-3)Cu(I)]	CTAP-3[c]	[(CTAP-3)Cu(I)]
Absorbance λ_{max} (nm)[d]	367	364	n.d.	n.d.
ε (10^4 $M^{-1}cm^{-1}$)[e]	3.05	3.15	n.d.	n.d.
Emission λ_{max} (nm)[f]	455	455	443	455
Φ_F [g]	–	0.41	n.d.	n.d.

[a]10 mM PIPES, 0.1 M $KClO_4$, 25°C. [b]buffer supplemented with 100 μM liposomes (4:1 DMPC:DMPG). [c]supplemented with 1 μM MCL-2 to sequester adventitious Cu(I). [d]lowest-energy band of the one-photon absorption spectrum. [e]molar extinction coefficient at λ_{max}. [f]maximum fluorescence emission. [g]fluorescence quantum yield, referenced to norharmane (Φ_F = 0.58).[23] n.d. = not determined.

Incubation of CTAP-3 in pH-neutral aqueous buffer supplemented with the 4:1 DMPC:DMPG liposome mixture resulted in a slight blueshift of 12 nm for the emission spectrum of CTAP-3 compared to the corresponding emission maximum of CTAP-3 in the absence of liposomes, which was expected for a fluorescent probe in a lower-polarity environment (Figure 5.8). However, the association with the lipid bilayer effected only a slight increase in the baseline fluorescence intensity compared to CTAP-3 in neat buffer, and upon saturation with Cu(I), CTAP-3 displayed a more-than-60-fold fluorescence enhancement in the presence of liposomes. As observed with CTAP-2, the presence of liposomes did not affect the emission spectrum of Cu(I)-bound CTAP-3, producing a nearly identical emission spectrum compared to Cu(I)-bound CTAP-3 in neat buffer. Interestingly, control measurements of CTAP-3 in liposomes containing 100% DMPC demonstrated a similar 60-fold fluorescence enhancement upon saturation with Cu(I), suggesting that weakness of the interaction with the liposomes cannot be attributed exclusively to the electrostatic repulsion between the anionic liposomes and the dianionic charge of the CTAP-3.

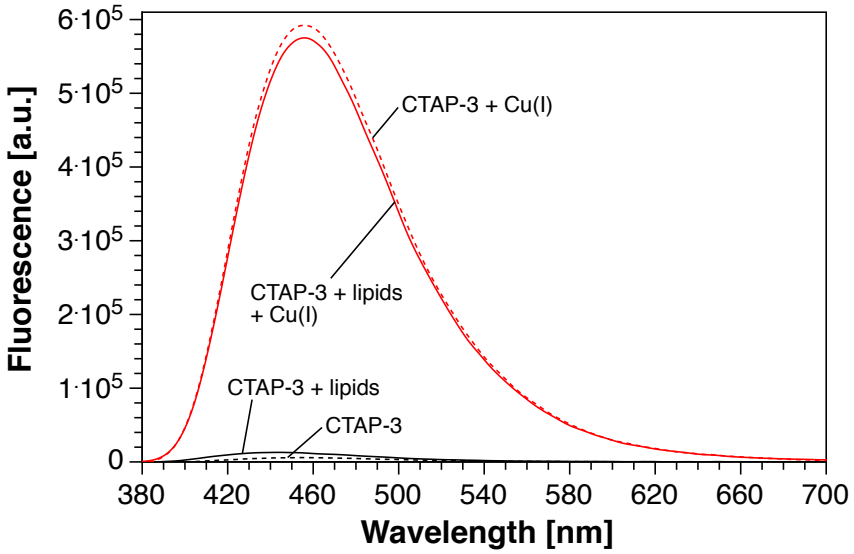

Figure 5.8: Fluorescence response of CTAP-3 (2 μM) upon saturation with Cu(I) in the presence and absence of 4:1 DMPC:DMPG liposomes (100 μM mixture) in pH 7.0 aqueous buffer (10 mM PIPES, 100 mM $KClO_4$, 100 nM MCL-1, 25°C). Solid lines represent measurements of CTAP-3 in liposomes, whereas the dashed lines represent measurements of CTAP-3 in aqueous buffer with no liposomes. Excitation: 365 nm. Figure adapted with permission from reference [22].

5.3.2 Determination of the Protonation Constants of CTAP-3

The presence of the *N*-arylthiaza ligand receptor of CTAP-3 renders the aniline nitrogen susceptible to protonation at lower pH, which would result in a protonation-induced fluorescence increase by inhibiting photoinduced electron transfer from the donor group to the pyrazoline fluorophore. To determine the protonation constant for the aniline nitrogen of CTAP-3, the change in the fluorescence response of the probe in 0.1 M KCl was measured as a function of decreasing pH. As illustrated in Figure 5.9, the fluorescence emission of CTAP-3 remained quenched over the pH range of 7.0 to 4.0, after which the fluorescence intensity increased as a consequence of protonation of the aniline nitrogen. Acidification below pH 1.5 ensued quenching of the fluorescence, suggesting the presence of a second protonation equilibrium most likely associated with the pyrazoline

ring of the fluorophore unit. Nonetheless, non-linear, least squares fitting of the fluorimetric data over the entire pH range of the titration yielded protonation constants (pKa's) of 2.00 ± 0.01 and 1.32 ± 0.01 for the two protonation equilibria.

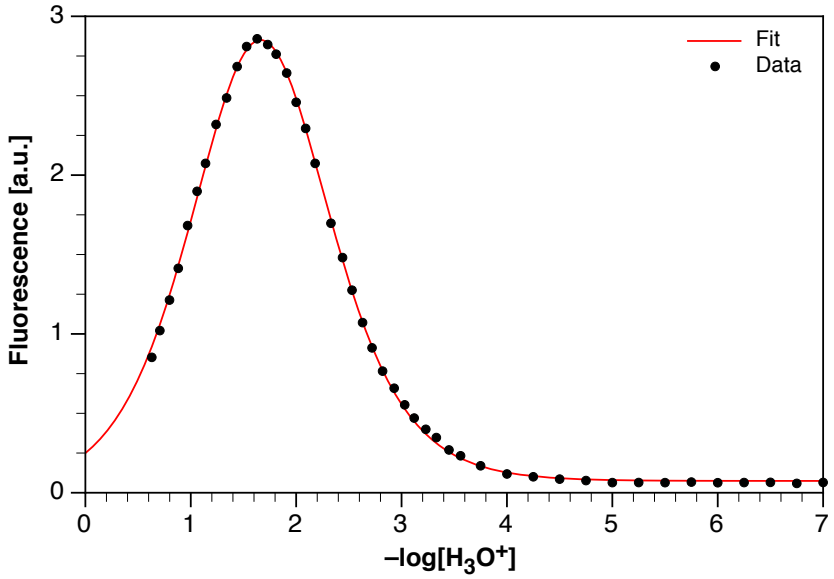

Figure 5.9: Fluorimetric pH titration of CTAP-3 at 25 °C in 0.1 M KCl. The fluorescence intensity at λ_{max} = 455 nm was recorded as a function of pH_c (–log[H_3O^+]), and the data were analyzed by non-linear least-squares fitting using equation 5-1 in Section 5.6.6 to yield the average pK_a values of pK_{H1} = 1.99 ± 0.01, and pK_{H2} = 1.32 ± 0.01. Figure and caption were adapted with permission from reference [22].

5.3.3 Determination of the Cu(I) Stability Constant of CTAP-3

The transition from the NS_4-thiazacrown of CTAP-1 to the NS_3-thiaza ligand receptor of CTAP-2 led to a one log-unit increase in the apparent binding affinity, from 10.4 to 11.4, respectively. Despite the presence of an NS_3-thiaza ligand receptor in CTAP-3, optimization of the PET-driving force to increase in the fluorescence contrast ratio of CTAP-2 let to the fusion of the thioether-containing receptor ligand to the aniline ring of the donor moiety of CTAP-3, thus decreasing the conformational flexibility of the receptor ligand, which was expected to increase fluorescence turn-on response. This structural change was also expected to influence the affinity for binding Cu(I). Taking advantage of

a series of robust Cu(I) affinity standards developed by Fahrni and coworkers,[21] MCL-2 served as a Cu(I)-selective ligand to compete with CTAP-3 for Cu(I) with matching affinity. To determine the apparent stability constant of CTAP-3, fluorimetric titrations of CTAP-3 with the tripodal MCL-2 affinity standard were performed by first saturating CTAP-3 with the Cu(I) complex of MCL-2, followed by titration with metal-free MCL-2 ligand over a 90-10% fractional saturation window in aqueous buffer (10 mM MES, 100 mM $KClO_4$, 25°C) at pH 6.0 to prevent precipitation of cuprous oxide at micromolar concentrations. Non-linear, least squares fitting of the fluorimetric titration data yielded a uniform apparent stability constant of $\log K_{Cu()\cdot CTAP\text{-}3} = 10.29 \pm 0.06$ (Figure 5.10). Given a pK_a of 2.0 for the aniline nitrogen, the apparent affinity of CTAP-3 for Cu(I) is expected to remain constant above pH 4.0.

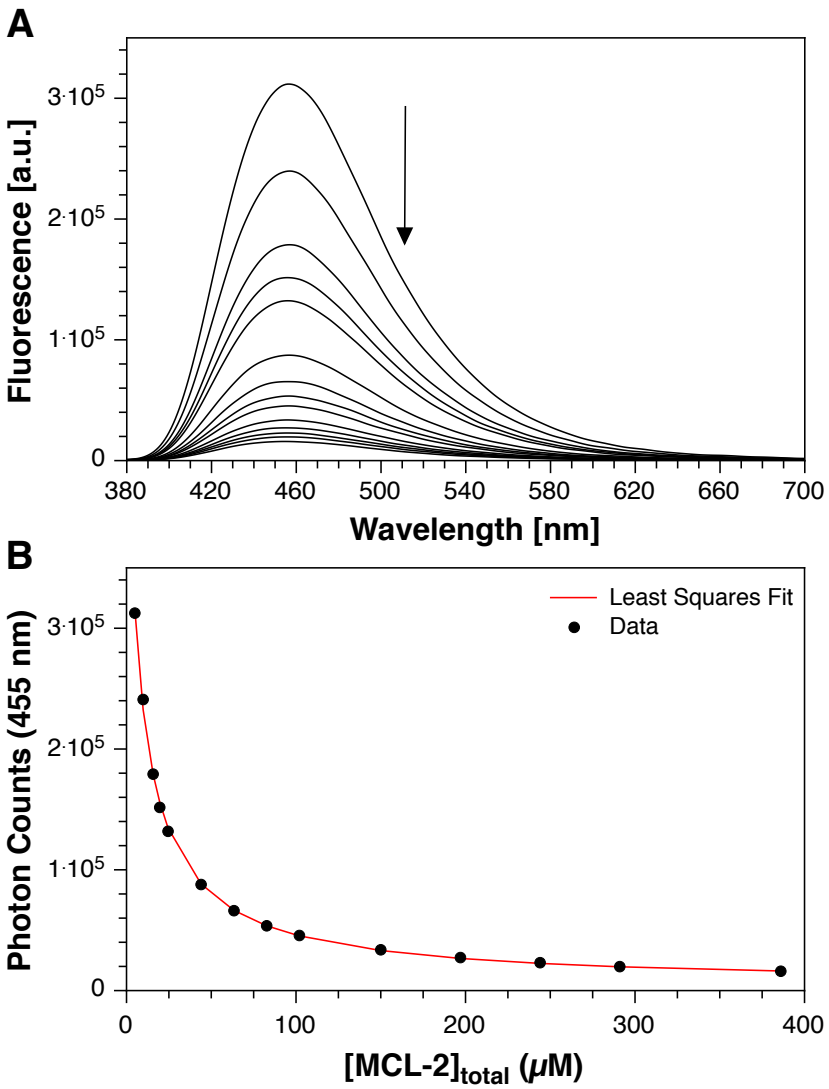

Definition of Equilibrium System:

Species	Cu(I)	MCL-2	CTAP-3	H	logβ
Cu(I)	1	0	0	0	0
MCL-2	0	1	0	0	0
CTAP-3	0	0	1	0	0
MCL-2(H)	0	1	0	1	9.09
[(MCL-2)Cu(I)]	1	1	0	0	13.08
[(CTAP-3)Cu(I)]	1	0	1	0	*10.29 ± 0.06*

Figure 5.10: A) Fluorimetric determination of the stability constant of CTAP-3 (**5.8**) via a competition titration with MCL-2[21]. A solution of [(MCL-2)Cu]Na_3PF_6•7.5H_2O (5 μM) and CTAP-3 (5 μM) was equilibrated in MES buffer at pH 6.0 (10 mM, 0.1 M $KClO_4$, 25°C) and then titrated with MCL-2 to a final concentration of 0.4 mM. The fluorescence traces (A) were analyzed by non-linear least squares fitting over the entire spectral range to yield an average log$K_{Cu(I)L}$ of 10.29 ± 0.06 (n = 3). B) Fluorescence intensity change and corresponding fit to equilibrium model at 455 nm. Figure and caption were adapted with permission from [22].

5.4 Characterization in Liposomes of an Emission-Ratiometric Fluorescent Probe for Monovalent Copper

Previous attempts at microinjecting the Cu(I) complex of CTAP-3 into NIH 3T3 mouse fibroblast cells to monitor fluctuations in labile Cu(I) using fluorescence microscopy revealed bursts of fluorescence followed by rapid decreases in the fluorescence intensity, indicating a swift demetallation of Cu(I)-bound CTAP-3 via the association with an endogenous ligand that sequesters Cu(I) from the probe.[24] Present at millimolar concentrations in the cytosol, glutathione (GSH), a sulfur-containing, non-ribosomal tripeptide, is known to rapidly reduce Cu(II) to Cu(I) and is believed to function in the transport of intracellular Cu(I), in addition to functioning as a redox buffer[25] and antioxidant for impeding oxidative stress from the production of reactive oxygen species (ROS). Because of its high concentrations and propensities to coordinate Cu(I), it was hypothesized that GSH might have been responsible for stripping the Cu(I) ion from CTAP-3, leading to the rapid decrease in fluorescence. The implication of this observation is that the binding affinities of current Cu(I) probes in the literature, including CTAP-3, are not high enough to compete with GSH for Cu(I) binding. A series of spectrophotometric and potentiometric titrations performed by Fahrni and coworkers to establish a robust thermodynamic model for the GSH-Cu(I) equilibrium system indicated that GSH buffers intracellular Cu(I) at sub-femtomolar concentrations,[26] which is consistent with buffered Cu(I) values based on the most recent determinations of the binding affinities of cellular Cu(I) chaperones.[27-28] Therefore, in order to detect cellular Cu(I) that is buffered at attomolar concentrations, a fluorescent probe with a Cu(I) binding affinity in the attomolar range or lower is required.

5.4.1 Probing Subfemtomolar Cellular Cu(I) Concentrations by Utilizing Phosphines and Phosphine Sulfides as Innovative Donors for Cu(I) Ligands

To overcome the thermodynamic barrier for competing with GSH for Cu(I), both fluorescent probes and Cu(I) chelators needed to be redesigned to engage in stronger coordination with Cu(I), which entailed a complete overhaul of conventional synthetic ligands to coordinate the soft metal cation. Previous Cu(I)-selective ligands with 1:1 binding stoichiometries that employ amine-thioether combinations as donors for binding Cu(I) typically provide affinities in the picomolar to femtomolar range, with the tightest binder providing an affinity of $\log K \sim 16$. In comparison to these conventional donors, phosphines provide stronger coordination to soft metal cations, such as Cu(I), but have the propensity to undergo oxidation when exposed to air.

To achieve a higher binding affinity using phosphines as stronger donors without undergoing aerial oxidation, phosphine sulfides, which boast a polarized P-S bond that was expected to increase the donor strength compared to thioethers while remaining unsusceptible to aerial oxidation, in combination with phosphines, were employed in the development of PSP-2, an EDTA-like chelator that was expected to bind Cu(I) with significantly higher affinity than MCL-1 (Figure 5.11). Molar-ratio titrations by Morgan *et al.* of PSP-2 against the preformed Cu(I) complex of BCA (2,2'-bicinchoninic acid) confirmed a 1:1 binding stoichiometry.[29] In addition, competition titrations with PSP-2 in the presence of excess BCS (disodium bathocuproine disulfonate) revealed an apparent stability constant of $\log K_{Cu(I)\cdot PSP\text{-}2} = 20.02 \pm 0.06$ for the 1:1 complex, corresponding to an apparent dissociation constant of K_d = 10 zM (zeptomolar), categorizing the ligand as one of the tightest Cu(I)-binding synthetic ligand available to date.[29]

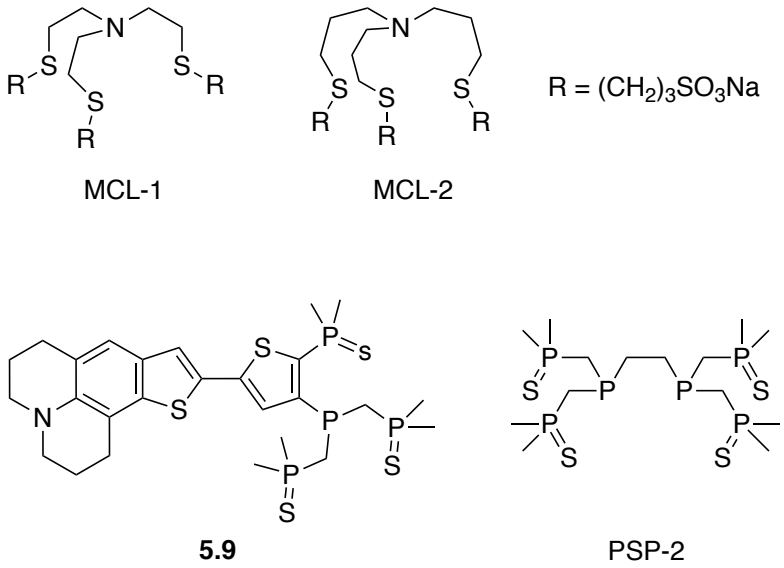

Figure 5.11: Structures of MCL-1, MCL-2, PSP-2, and fluorescent probe **5.9**

Despite the extraordinary affinity for Cu(I) that exceeds the affinity range of cytosolic metallochaperones, such as Atox1, PSP-2 did not interact with other divalent *3d* transitions metals with biological relevance, including Zn(II), Fe(II), and Mn(II), even at concentrations of 1 mM (Figure 5.12). In addition, by virtue of its non-basic phosphines and phosphine sulfides, PSP-2 did not show any evidence of protonation at a pH as low as 1 (100 mM $HClO_4$); therefore, the affinity for Cu(I) is expected to remain constant, irrespective of the pH.

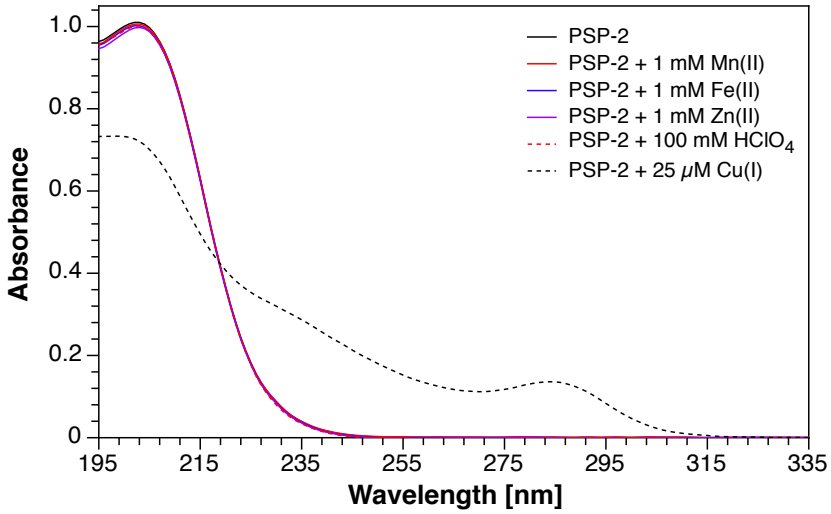

Figure 5.12: Absorption spectral changes of PSP-2 (25 μM) in response to Cu(I), acidification, and millimolar concentrations of selected divalent transitions metals.

The electron-withdrawing capacities and donor strength of both phosphines and phosphine sulfides when electronically coupled to aromatic rings provided rationale for integrating the ligand motif into the design of a noncentrosymmetric dipolar donor-acceptor fluorophore whose fluorophore core is similar to chromis-1 and 2. In contrast to ratiometric fluorophores, the employment of turn-on fluorescent probes for probing biological copper inhibits the reliable quantification of cellular metal-ion concentrations, which is important for understanding intracellular copper homeostasis given its health implications. Taking advantage of the strategies for designing emission-ratiometric non-centrosymmetric D-A fluorophores discussed in Chapter 1, in addition to synthetic developments in redox-stable phosphine sulfide chemistry as substitutes for conventional thioethers for coordinating Cu(I), the following subsections discuss the characterization of the emission-ratiometric fluorescent probe (**5.9**, Figure 5.9) with a Cu(I)-binding motif that was adopted from the high-affinity PSP-2 ligand.

*5.4.2 Absorption and Fluorescence Properties of Probe **5.9***

Despite the presence of substantially polarized P-S bonds from the phosphine sulfides that increase its water solubility, all characterizations were initially performed in methanol to avoid interferences in the fluorescence properties due to potential aggregation in aqueous buffer as a consequence of the lipophilicity of the fluorophore moiety. Morgan *et al* established that saturation of **5.9** with [(MCL-2)Cu(I)]PF_6 in an air-equilibrated, 95% MeOH (5% water) solution yielded a 24-nm shift in the absorption from 410 nm (ε = 27,200 $M^{-1}\cdot cm^{-1}$) to 434 nm (ε = 27,300 $M^{-1}\cdot cm^{-1}$) for the Cu(I)-saturated form (Figure 5.13A). Similarly, in the emission, a molar-ratio titration of **5.9** with [(MCL-2)Cu(I)]PF_6 in MeOH produced a 52-nm shift from 581 nm to 633 nm in the emission (Figure 5.13B). Clean isosbestic points at 421 nm in the absorption and 634 nm in the emission, in addition to a sharp saturation at 1.0 molar equivalent of Cu(I) relative to probe, signified an unambiguous, single-coordination equilibrium between free **5.9** and its corresponding Cu(I) complex with a 1:1 binding stoichiometry.

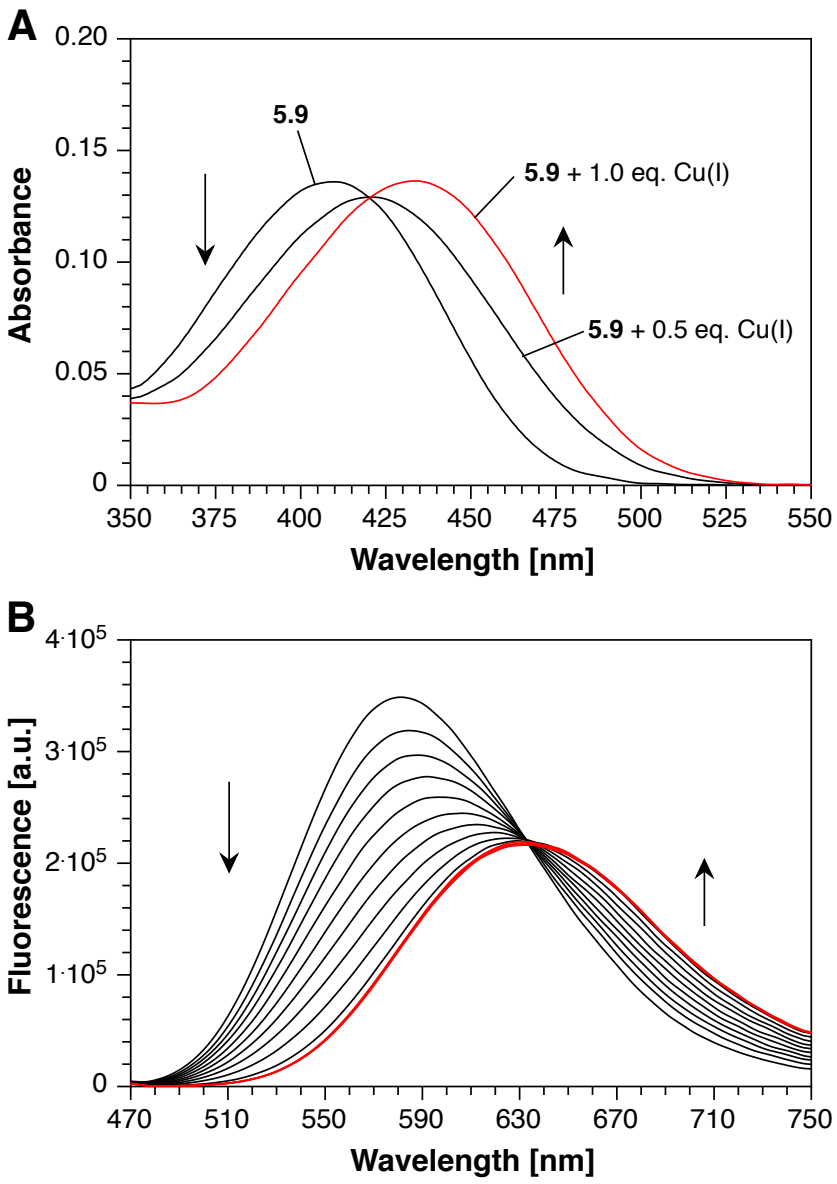

Figure 5.13: Spectral changes of **5.9** (5 μM) upon incremental addition of Cu(I) in MeOH. A) Selected absorbance spectra of upon addition of [(MCL-2)Cu(I)]PF_6 to the probe in MeOH. B) Fluorimetric titration of **5.9** with [(MCL-2)Cu(I)]PF6 from 0-1.3 μM in 0.1 μM aliquots. Excitation: 460 nm. Red traces indicate the absorption and fluorescence spectra of Cu(I)-saturated **5.9**. *Data acquired by M. Thomas Morgan, Ph.D., but figure was prepared by the author.*

After observing that probe **5.9** engages in coordination to Cu(I) with a 1:1 metal-ligand stoichiometry, in addition to exhibiting a red shift of both the excitation and emission spectra, characterization of the fluorescent probe in aqueous buffer supplemented with liposomes served to provide a biologically relevant comparison to cellular imaging studies.

The transition from liposomes comprising 100% DMPC to a 4:1 DMPC:DMPG mixture served to provide a lipid mixture with a more biologically relevant charge density as observed in the lipid bilayer of cell membranes. However, cellular membranes also comprise myriad phospholipids with varying degrees of saturation to enable fluidity. This understanding directed the characterization of the fluorescence properties of **5.9** in an even more biologically relevant lipid composition containing 1-palmitoyl-2-oleoyl-*sn*-glycero-3-phosphocholine (POPC) and sodium 1-palmitoyl-2-oleoyl-*sn*-glycero-3-phospho-rac-glycerol (POPG) in a 4:1 ratio. However, the presence of an unsaturated fatty acid chain in both POPC and POPG led to the slow peroxidation of the oleoyl chain of the phospholipids, despite storing the liposome concentrate at 4°C in deoxygenated buffer prior to extrusion to prevent decomposition of the lipids. The peroxide formation led to the *in situ* oxidation of the probe, which was manifested by a decrease in the fluorescence intensity and a broadening of the emission spectrum of the free form of **5.9**, leading to a change in the emission ratio. Supplementation of a freshly prepared liposome concentrate with the antioxidant α-Tocopherol (1 mol %), which was intended to prevent peroxidation of the fatty acid chains, still led to decomposition of the phospholipids over time. However, oxidation of the probe within the cell should not be an issue, as the cell contains complex chemical machinery to ensure a proper redox balance for maintaining homeostasis.

To overcome the propensity for oxidation of the fluorophore, the liposome composition was switched back to the 4:1 DMPC:DMPG mixture for probe characterization. Upon dilution from a concentrated stock solution in DMSO into aqueous buffer supplemented with 4:1 DMPC:DMPG liposomes (100 μM), probe **5.9** underwent a 59-nm red-shift in the emission from 556 nm to 615 nm, with corresponding fluorescence quantum yields of 0.21 and 0.54 for the metal-free and Cu(I)-bound species (Table 5.3), respectively, when referenced to coumarin 153 (Φ_F = 0.544 in EtOH).[30] However, the stepwise

saturation of **5.9** with Cu(I) performed in aqueous buffer supplemented with liposomes revealed the presence two isosbestic points that formed over the course of the molar-ratio titration, alluding to the presence of multiple species in solution (Figure 5.14).

Interestingly, the addition of the first aliquot (0.1 mol eq.) of Cu(I) to **5.9** observed a significantly larger change in the emission compared to the successive aliquots. Furthermore, the addition of 0.5 molar equivalents of Cu(I) displayed a larger change in the fluorescence, in addition to the formation of a second isosbestic point. While the clean isosbestic point observed in the molar ratio titration of **5.9** in MeOH precluded the formation of multiple metal-ligand complex equilibria, the divergent behavior of the probe in the presence of liposomes is likely due to the ability for **5.9**, once dissolved in the lipid bilayer, to become exposed to a membrane-impermeable Cu(I) source.

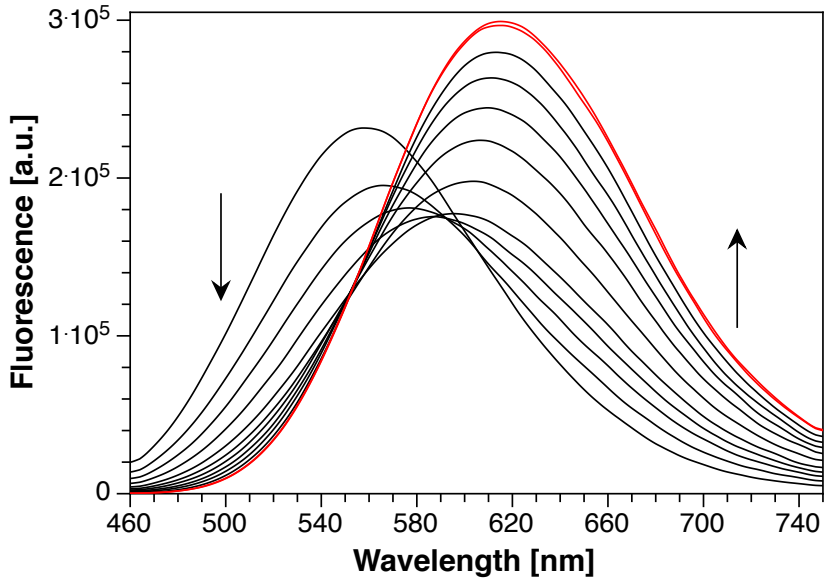

Figure 5.14: Fluorescence spectral changes of **5.9** upon incremental addition of Cu(I). Probe **5.9** (2 μM) was incubated in aqueous buffer (10 mM PIPES, 100 mM KCl, pH 7.0, 25°C) supplemented with 4:1 DMPC:DMPG liposomes (100 μM) and titrated with [(MCL-2)Cu(I)] from 0-1.2 μM in 0.1 μM aliquots. Excitation: 450 nm.

Table 5.3: Photophysical properties of ratiometric probe **5.9** in MeOH and in aqueous buffer at pH 7.0[a].

	MeOH		Buffer + Liposomes[b]	
	5.9[c]	[(**5.9**)Cu(I)]	**5.9**[c]	[(**5.9**)Cu(I)]
Absorbance λ_{max} (nm)[d]	410	434	406	440
ε (10^4 $M^{-1}cm^{-1}$)[e]	2.72	2.73	2.15	2.22
Emission λ_{max} (nm)[f]	581	633	556	615
Φ_F [g]	n.d.	n.d.	0.21	0.54

[a]10 mM PIPES, 0.1 M KCl, 25°C. [b]buffer supplemented with 100 μM liposomes (4:1 DMPC:DMPG). [c]supplemented with 1 μM PSP-2 to sequester adventitious Cu(I). [d]lowest-energy band of the one-photon absorption spectrum. [e]molar extinction coefficient at λ_{max}. [f]maximum fluorescence emission. [g]fluorescence quantum yield, referenced to coumarin 153 (Φ_F = 0.544 in EtOH).[30]

It was hypothesized that the divergent behavior is a result the thermodynamic barrier for transverse diffusion of the probe between the two leaflets of the lipid bilayer being too high to allow the probe to diffuse from the inner leaflet of the liposomes to the outer leaflet, thus preventing exposure of the probe to Cu(I) and resulting in the formation of multiple metal-ligand species. It is possible that the dramatic change in the emission spectrum in the early stages of the molar ratio titration was due to an intramembrane association between two probe molecules and one Cu(I) ion, and upon addition of 0.5 molar equivalents of Cu(I), the formation of a species with a 1:1 stoichiometry emerged, thus manifesting a second isosbestic point. Nevertheless, incremental addition of Cu(I) led to the saturation of **5.9** at equimolar concentrations, despite alluding to the presence of three separate species in solution. Molar ratio titrations of **5.9** in liposomes were not performed in the absorption, as the molar absorptivity coefficient of the probe is not large enough to provide a decent signal-to-noise ratio at a probe concentration of 2 μM.

To ensure that protonation of the julolidine nitrogen would not interfere with the ratiometric readout of the probe during both spectroscopic characterization and cellular staining experiments, given a pK_a of aniline around 4.6,[31] emission spectra of the free and

metal-bound probe were acquired in aqueous buffer pH 7.0 and 5.0 supplemented with the 4:1 DMPG:DMPC liposomes. Comparison of the emission spectra indicated only a minimal narrowing of the emission response of the metal-free form at pH 5 compared to pH 7, whereas the Cu(I)-saturated form revealed a slightly high fluorescence intensity and wider profile on the red edge at pH 5 compared to 7 (Figure 5.15).

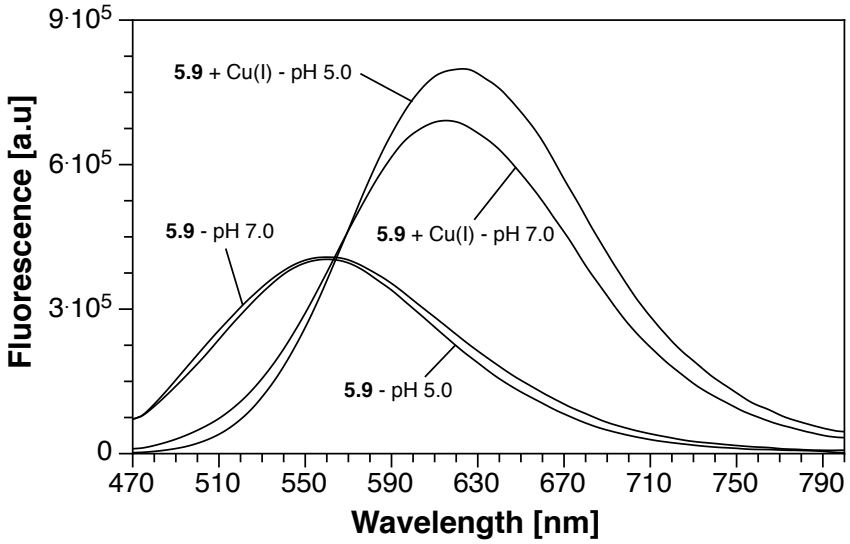

Figure 5.15: Fluorescence dependence of probe **5.9** on pH. Probe **5.9** was equilibrated in aqueous buffer (10 mM PIPES, 100 mM KCl, 25°C) at pH 7.0 and 5.0, both supplemented with 4:1 DMPC:DMPG liposomes (100 μM each), and saturated with MCL-2-Cu(I). Excitation: 450 nm.

*5.4.3 Metal-Ion Selectivity Measurements of Probe **5.9***

Fluorescent probe **5.9** displayed excellent selectivity for Cu(I) in the presence of other biologically relevant divalent transition metal ions. In the presence of 5 equivalents (10 μM) of selected divalent metal ions, probe **5.9** demonstrated no change in its emission-ratiometric response compared to free probe (Figure 5.16). The interfering divalent metal ions did, however, result in a negligible decrease in the fluorescence intensity (Figure 5.16, solid black lines) but manifested no change in the emission ratio as a result, yielding an

average ratio of $R = 6.00 \pm 0.003$ (Figure 5.17, orange bars). Moreover, saturation of the probe with Cu(I) led to a ratiometric readout consistent with the formation of the [(**5.9**)Cu(I)] complex without any interfering divalent metal ions present in solution, with a uniform average ratio of $R = 3.97 \pm 0.07$ (Figure 5.17, green bars).

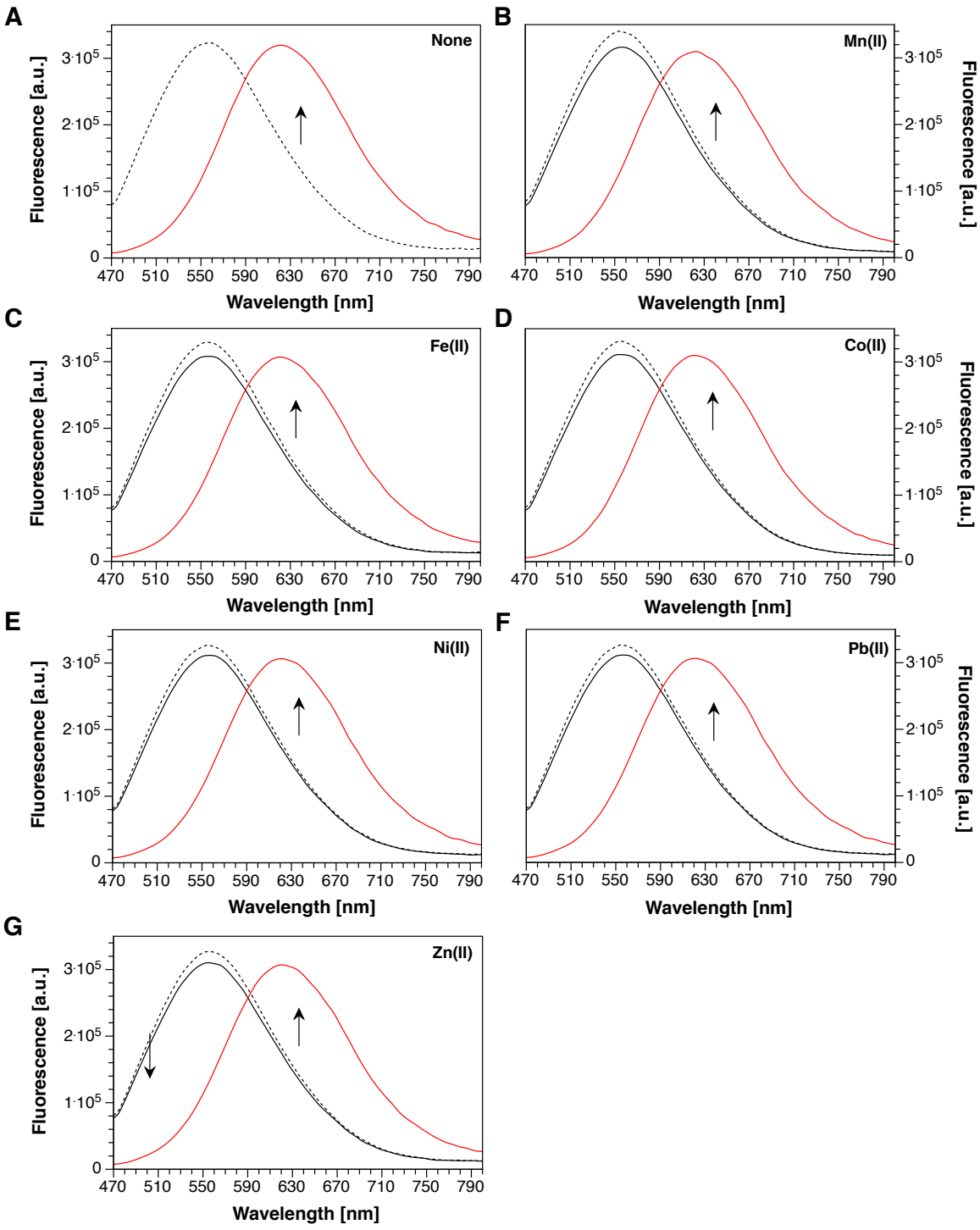

Figure 5.16: Fluorescence response of **5.9** (2 μM) in the presence of 5.0 equivalents of selected divalent transition metal ions in pH 7.0 aqueous buffer (10 mM PIPES, 100 mM KCl, 25°C) supplemented with 100 μM 4:1 DMPC:DMPG liposomes. Black dashed curves represent the fluorescence spectrum of **5.9** in the absence of interfering metal, the solid black curves represent the spectrum in the presence of interfering metals, and the red solid curves represent saturation of the probe with Cu(I). Excitation: 450 nm.

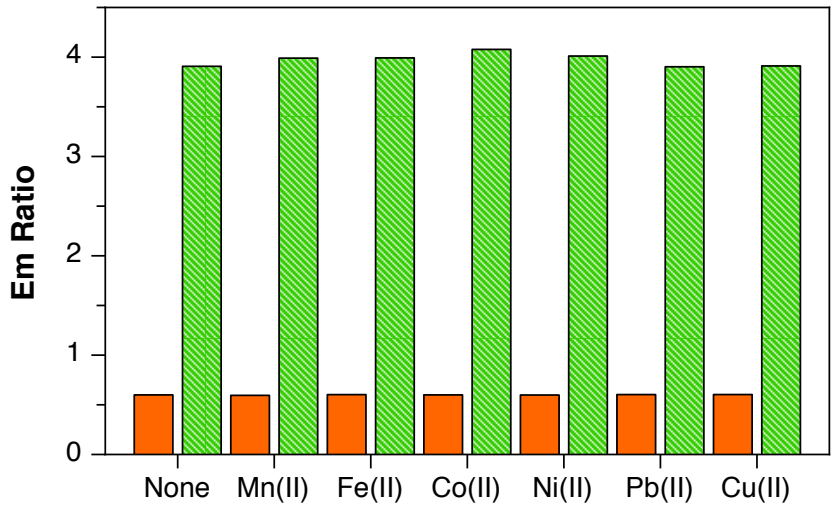

Figure 5.17: Fluorescence response of **5.9** (2 μM) towards selective divalent transitions metals and comparison to Cu(I) based on the intensities calculated from data provided in Figure 5.16. Responses were calculated based on ratio of the integrated fluorescence intensity between 590-750 nm (channel 2) and 480-580 nm (channel 1)). The orange bars represent the ratio in the presence of 5 equivalents of interfering transition metals, and the corresponding green bars represent the ratio after saturating fluorescent probe with Cu(I). Excitation: 450 nm.

*5.4.4 Probe **5.9** Boasts an Attomolar Binding Affinity for Cu(I)*

Incorporation of the phosphine-phosphine sulfide ligand motif of PSP-2 demanded the use of a Cu(I)-selective chelator with well-characterized thermodynamics properties as an affinity standard for determining the apparent stability constant of **5.9**. Of the affinity standards to Cu(I) available as tools to elucidate the thermodynamic properties of the fluorescent probe, MCL-1 possessed the best matching affinity to the expected binding affinity of **5.9** within the 90:10 fractional saturation window. After incubation of the probe (2 μM) in aqueous buffer supplemented with 4:1 DMPC:DMPG liposomes, addition of [(MCL-1)Cu(I)] and subsequent titration of MCL-1 from 0 to 640 μM afforded fluorescence spectral data that, upon non-linear least squares fitting, yielded an apparent stability constant of 17.0 ± 0.2, corresponding to an apparent dissociation constant of K_d = 10 ± 5 aM (Figure 5.18).

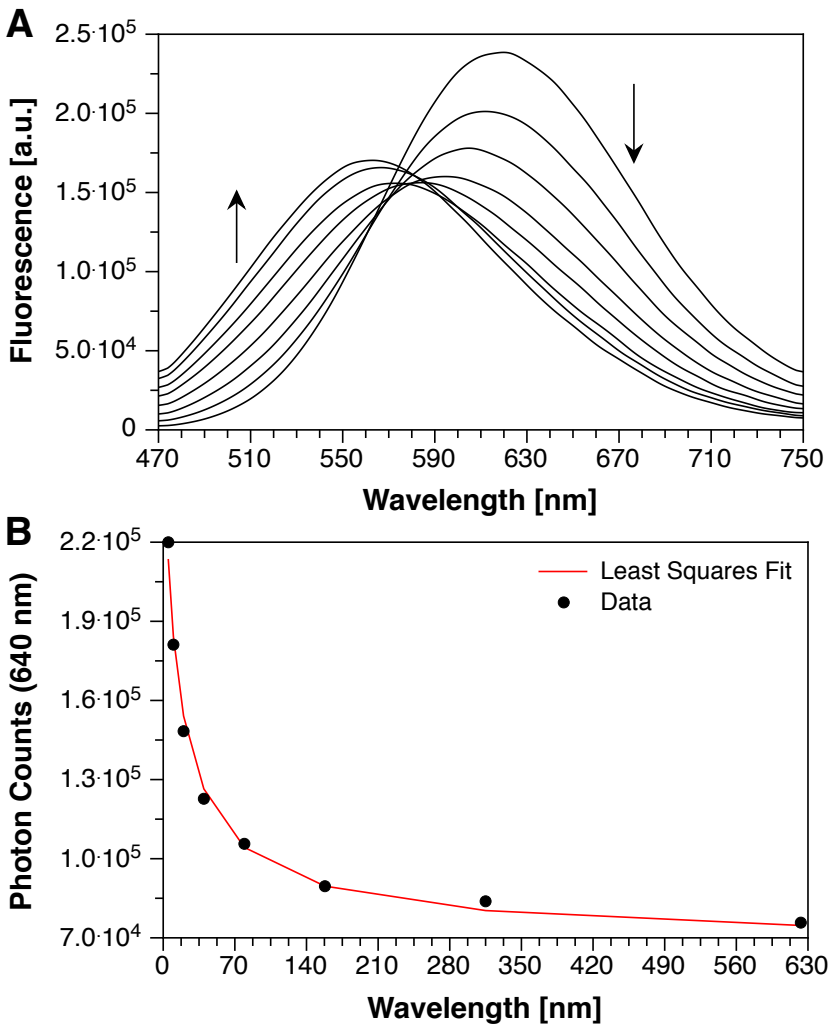

Definition of Equilibrium System:

Species	Cu(I)	MCL-2	**5.9**	H	log β
Cu(I)	1	0	0	0	0
MCL-2	0	1	0	0	0
5.9	0	0	1	0	0
MCL-1(H)	0	1	0	1	7.11
[(MCL-1)Cu(I)]	1	1	0	0	16.33
[(**5.9**)Cu(I)]	1	0	1	0	*17.0 ± 0.2*

Figure 5.18: A) Fluorimetric determination of the Cu(I) stability constant of probe **5.8** via a competition titration with MCL-1[21]. A solution of probe **5.9** (2 μM) was equilibrated in PIPES buffer at pH 7.0 (10 mM, 100 mM KCl, 25°C) supplemented with 4:1 DMPG:DMPC liposomes. The probe was saturated with [(MCL-1)Cu(I)] and titrated with MCL-1 from 0-640 μM. The fluorescence traces (A) were analyzed by non-linear least squares fitting over the entire spectral range to yield an average $\log K_{Cu(I)L}$ of 17.0 ± 0.2 (n = 3). B) Fluorescence intensity change and corresponding fit to equilibrium model at 640 nm.

5.5 Conclusions

Previously developed Cu(I)-responsive fluorescent probes that have become the cornerstone of copper biochemistry by serving as chemical tools for the cost-effective detection of Cu(I) in biological samples[4, 32] have been based on hydrophobic, thioether-rich receptor ligands that are linked to uncharged fluorophore units, which tend to aggregate when diluted into aqueous solution. Although it is crucial that these small-molecule fluorescent probes be lipophilic enough to passively diffuse across cellular membranes, it is also important that they be sufficiently water-soluble to prevent aggregation that may promote hydrophobic interaction-induced changes in the fluorescence response, independent of the metal analyte. Two of the earliest fluorescent sensors for probing monovalent copper, CTAP-1 and Coppersensor-1 (CS1), both aggregate in aqueous solution, which was discovered through dynamic light scattering experiments.[1] Even the presence of the carboxylic acid group of CTAP-1 did not provide enough ionizable character to prevent aggregation.

Modifications to the structures of the two fluorescent probes to promote increased water-solubility and improve the photophysical properties, such as increasing the fluorescence enhancement factor, afforded the second-generation fluorescent probes CTAP-2 and Coppersensor-3 (CS3). While polyhydroxylation of the thiazacrown ligand receptor and installation of a sulfonic acid group on the fluorophore unit achieved water-solubility in the millimolar concentration regime in aqueous solution, CTAP-2 displayed a liposome-mediated fluorescence enhancement that yielded a fluorescence intensity nearly identical to that of the Cu(I)-bound form of CTAP-2 in the absence of liposomes, as well as a substantial lipid-mediated blue shift compared to aqueous buffer. Moreover, metal-free CS3 also displayed a liposome-mediated fluorescence turn-on response that was 2-fold higher

than the intensity of the Cu(I)-bound form in the absence of liposomes, and upon saturation with Cu(I), the fluorescence intensity of CS3 in the presence of liposomes decreased roughly 40%. This observation significantly deviates not only from the 75-fold enhancement originally reported but also from the ~ 12-fold enhancement that was observed when comparing the fluorescence responses of CS3 to CTAP-2 at equimolar concentrations in liposome-free aqueous buffer.

Both CTAP-2 and CS3 represented innovative advancements in the development of molecular tools for probing Cu(I) biochemistry, but the weak fluorescence quantum yield of CTAP-2 limited its detection senstivity, and CS3's lipid-mediated fluorescence turn-on response that decreases upon binding Cu(I) contradicts the cellular staining patterns observed in mammalian cells. Therefore, there exist vacancies in the availability of biologically useful fluorescent probes for Cu(I). To overcome this, drastic improvements in the reduction of the PET driving force of the triarylpyrazoline unit present in both CTAP-1 and CTAP-2 led to the development of CTAP-3, which offered a nearly 5-fold increase in the fluorescence quantum yield, as well as a profound 180-fold contrast ratio in free aqueous buffer and a more-than-60-fold contrast ratio in the presence of liposomes. Despite the knowledge-driven approach to developing a water-soluble and lipid-compatible fluorescent probe for Cu(I), its picomolar affinity for Cu(I) and its membrane-impermeability by virtue of its two sulfonic acid groups limits its application in biological imaging.

The transition from the optical turn-on response of CTAP-3 to the emission-ratiometric fluorescence response of probe **5.9** enabled the ability to obtain meaningful quantitative data from cellular imaging studies with the probe. Moreover, the redesign of the metal-acceptor ligand provided a nearly six logarithmic-unit increase in the stability constant, which enables the probe to effectively compete with endogenous GSH for free Cu(I). However, the lack of water-solubilizing groups demanded photophysical characterization

to be performed in the presence of liposomes, which hampered the metal-binding equilibrium by allowing homoleptic ternary complex formation, despite methanolic characterization alluding to an unambiguous 1:1 binding equilibrium. Nonetheless, probe **5.9** represents the first example of an emission-ratiometric fluorescent probe for Cu(I) that boasts a high-enough affinity to compete with endogenous GSH.

While the supplementation of fluorescent probes with water-solubilizing groups can significantly increase hydrophilicity and preclude aggregation, a drastic change in the photophysical properties of the fluorophore, such as the quantum yield or enhancement factor, can result, which may demand further optimization. Instead, to ensure that the solution chemistry is representative of the behavior in cells, photophysical characterization of lipophilic probes should be performed in aqueous buffer that is supplemented with liposomes as model membranes to mimic the dichotomous environment of the cell. Moreover, even if the structure of a fluorescent probe has been supplemented with hydrophilic groups, its lipid compatibility should be investigated extensively to ensure that the fluorescence response in the cuvette matches its fluorescence behavior in the cell.

5.6 Experimental Section

5.6.1 General Spectroscopic Methods

All buffers and probe stock solutions were prepared using JT Baker HPLC-grade water or 18.2 MΩ•cm Mili-Q water. Nevertheless, an increased background fluorescence due to traces of adventitious copper was frequently observed. It was therefore necessary to add a small amount of the high affinity Cu(I) ligand MCL-1 as a sequestrant in most experiments as described in detail below. Deoxygenation, where specified, was achieved

by bubbling with argon. Initial detection limit experiments indicated that the brass gas regulator could serve as an additional source of copper contamination, which was prevented by passing the argon through a 5 μM filter. UV-vis absorption spectra were acquired at 25°C with a Varian Cary Bio50 spectrophotometer with constant temperature accessory. Fluorescence spectra were recorded with a PTI fluorimeter equipped with a 75 W xenon arc lamp excitation source and model 814 photomultiplier detection system (PMT voltage 1100 V for all measurements). The fluorescence spectra were corrected for the spectral response of the detection system and for the spectral irradiance of the excitation source (via a calibrated photodiode). The path length was 1 cm for absorbance and fluorescence spectra and 10 cm for absorbance measurements for determining the fluorescence quantum yields.

5.6.2 Preparation of Liposomes

A 2 mM solution of a 4:1 mixture of 1,2-dimyristoyl-*sn*-glycero-3-phosphocholine (DMPC): 1,2-dimyristoyl-*sn*-glycero-3-phospho-(1'-rac-glycerol) (DMPG) was prepared according to the thin-film hydration method.[33] After dissolving DMPC (32.3 mg) and DMPG (8.21 mg) in 4:1dichloromethane:methanol (20 mL), the solvent was evaporated under reduced pressure (Rotavap) to produce a thin film of the lipid. Remaining solvent traces were removed by drying under high vacuum for 2 hours. The lipid film was then hydrated by addition of 29.8 mL of aqueous buffer (10 mM PIPES, 0.1 M $KClO_4$, 100 nM MCL-1, pH 7.0) that had been deoxygenated by purging with argon. The resulting solution was sonicated for 5 min and passed 21 times through an extruder (LiposoFast, Avestin) equipped with a polycarbonate membrane (200 nm pore size). The freshly extruded DMPC liposomes were immediately used for the experiments described below. For experiments conducted in 100% DMPC liposomes, DMPC lipids (13.56 mg) were dissolved

in dichloromethane (10 mL), and the dichloromethane was removed under reduced pressure to produce a thin film. The film was then dried under high vacuum for 2 hours and then hydrated in the buffer described above. The remaining procedure is identical compared to the 4:1 DMPC:DMPG liposomes.

5.6.3 Liposome Size Distribution

Liposome diameters were measured based upon the Tunable Resistive Pulse Sensing (TRPS) principle using an Izon qNano particle analyzer (Izon Science Ltd., Burnside, New Zealand). The instrument was calibrated with monodisperse carboxylated polystyrene particles (200-nm diameter) in deionized water (Izon) following the manufacturer's recommendations. The membrane pore size used for these measurements was 150-300 nm. Calibration and particle analysis runs were conducted with a 46-mm nanopore stretch, an electric potential of 0.44 V, and an applied pressure of 10 mm Hg (variable pressure module). Each measurement was performed by detecting a minimum of 1000 particles. The data were analyzed using the Izon Control Suite 2.1 software to determine the mean diameter and size distribution of the liposomes.

5.6.4 Fluorescence Response of CS3 in DMPC liposomes and Comparison to MeOH and Octanol

The fluorescence response of CS3 upon addition of Cu(I) in the presence of DMPC liposomes was measured in aqueous buffer at pH 7.0 (10 mM PIPES, pH 7.0, 0.1 M $KClO_4$, 100 nM MCL-1). A freshly prepared 2-mM DMPC liposome concentrate in 10 mM PIPES (pH 7.0, 0.1 M $KClO_4$) was diluted into PIPES buffer and mixed gently to yield a 500 μM liposome solution, which was extruded immediately prior to use. In a quartz cuvette with a 1-cm pathlength, PIPES buffer (2.40 mL) was diluted with the 500 μM extruded liposome

solution (600 μL), and after equilibrating at 25°C for 10 minutes by magnetic stirring, CS3 was added (from a 3 mM stock solution in DMSO) to a final concentration of 2 μM. After equilibrating for 30 minutes, the solution was supplemented with 250 μM sodium ascorbate as reducing agent, which was directly diluted into the cuvette from a 250 mM stock solution (diH_2O). To the solution was added $CuSO_4$ (from a 6 mM stock solution (diH_2O) to yield final concentration of 3 μM. A fluorescence emission spectrum was acquired over the spectral range from 540-700 nm with excitation at 530 nm before and after addition of $CuSO_4$. The fluorescence response of CS3 towards Cu(I) in octanol and MeOH was assessed under the same conditions described above.

5.6.5 Fluorescence Response of CS3, CTAP-2, and CTAP-3 Towards Cu(I) in the Presence of DMPC:DMPG (4:1) Liposomes

The fluorescence response of CTAP-3 upon addition of Cu(I) (prepared by *in situ* reduction of $CuSO_4$) in the presence of 4:1 DMPC:DMPG liposomes was measured in PIPES buffer at pH 7.0 (10 mM, pH 7.0, 0.1 M $KClO_4$, 100 nM MCL-1). A freshly prepared 500 μM DMPC:DMPG (4:1) liposome stock solution in 10 mM PIPES (pH 7.0, 0.1 M $KClO_4$) was diluted into PIPES buffer and mixed by gentle inversion to yield a final liposome concentration of 100 μM. The resulting solution (3.0 mL) was transferred to a fluorescence cuvette (1 cm pathlength) and CTAP-3 was added (300 μM stock solution in diH_2O) to a final concentration of 2 μM. Furthermore, the solution was supplemented with 250 μM sodium ascorbate as reducing agent, which was directly diluted into the cuvette from a 250 mM stock solution (diH_2O). The resulting solution was equilibrated for 30 min and $CuSO_4$ was added from a 6 mM stock solution (diH_2O) to yield final concentration of 3 μM. A fluorescence emission spectrum was acquired over the spectral range from 380-700 nm with excitation at 365 nm before and after addition of $CuSO_4$. The fluorescence

response of CTAP-2 and CS3 towards Cu(I) was assessed under the same conditions described above for CTAP-3, except that CTAP-2 was diluted into the PIPES buffer from a 5 mM stock solution in diH_2O, and CS3 was diluted into the PIPES buffer from a 2 mM stock solution in DMSO. Fluorescence spectra for CTAP-2 were acquired over a spectral window of 400-700 nm with an excitation at 380 nm, and fluorescence spectra for CS3 were acquired over a spectral window of 540-700 nm with excitation at 530 nm.

5.6.6 Determination of the Protonation Constants of CTAP-3

A 5 μM solution of CTAP-3 in aqueous 0.1 M KCl was prepared and the solution pH was adjusted to 6.0. To remove interfering dust particles or fibers, the solution was passed through a 0.2 μm membrane filter. A combined potentiometric and fluorimetric titration was carried out in a quartz cuvette with 1 cm pathlength by addition of HCl to adjust the pH between 6.0 and 0.5 (constant temperature accessory set to 25°C). After addition of each aliquot acid, the solution equilibrated, the potential was recorded (in mV), and the fluorescence intensity was measured at 455 nm with excitation at 365 nm. The data were analyzed by non-linear least-squares fitting using equation 5.1 below:

$$F = \frac{F_{max}K_{a1}[H_3O^+] + F_{min}K_{a1}K_{a2}}{[H_3O^+]^2 + [H_3O^+]K_{a1} + K_{a1}K_{a2}} \quad (5\text{-}1)$$

where F is the measured fluorescence intensity at $pH_c = -\log[H_3O^+]$, F_{max} and F_{min} are the limiting fluorescence intensities, and K_{a1} and K_{a2} correspond to the first and second protonation constants, respectively.

5.6.7 Determination of the Cu(I)-Binding Affinity of CTAP-3

The Cu(I) stability constant for CTAP-3 was determined through a fluorimetric titration using the affinity standard MCL-2 as competing ligand. A solution of [(MCL-2)Cu]Na_3PF_6•7.5 H_2O (5 μM) and CTAP-3 (5 μM) in aqueous buffer (pH 6.0, 10 mM MES, 0.1 M $KClO_4$, 25°C) was equilibrated and then titrated with MCL-2 (3 mM stock solution in water) from 10-400 μM. After the addition of each aliquot, a fluorescence emission spectrum was acquired with excitation at 365 nm over the range of 380-700 nm. The data were analyzed by non-linear least squares fitting using Specfit.[34] Based on the MCL-2 formation constant of logβ = 13.08 and a pK_a of 8.98 (corrected upward by 0.11 units to account for 0.1 M ionic strength)[35], an average log$K$ of 10.29 ± 0.06 was obtained.

5.6.8 Analyte Selectivity of PSP-2

In a quartz fluorescence cuvette with a 1-cm path length, a 25 μM solution of PSP-2 (from a 3 mM stock solution in acetonitrile) was prepared in H_2O (3.00 mL). The solution was supplemented with divalent transition metal ions (from 500 mM stock solutions of each metal in H_2O) to a final concentration of 1 mM. An absorbance spectrum was acquired from 195 to 350 nm before and after addition of each divalent metal cation tested (2 mM). Divalent metal cations (Zn(II), Fe(II), and Mn(II)) were supplied as sulfate salts and prepared immediately before use. To test the response of PSP-2 under acid conditions, absorbance spectra of the free chelator were acquired in aqueous $HClO_4$ (10 and 100 mM). For measurement of the Cu(I) complex of PSP-2, the ligand solution was supplemented with [(MCL-2)Cu(I)]Na_3PF_6•7.5 H_2O (from a 3 mM stock solution in H_2O) to a final concentration of 25 μM, and an absorbance spectrum was acquired from 195-350 nm.

*5.6.9 Molar Ratio Titration of Probe **5.9***

The fluorescence response of **5.9** upon addition of [(MCL-2)Cu(I)]Na_3PF_6•7.5 H_2O in the presence of 4:1 DMPC:DMPG liposomes was measured in aqueous buffer at pH 7.0. A freshly extruded 500 μM DMPC:DMPG (4:1) liposome stock solution in aqueous buffer (10 mM PIPES, 0.1 M KCl, 25°C) at pH 7.0 was diluted into PIPES buffer (2.40 mL) in a fluorescence quartz cuvette with a 1-cm pathlength to yield a final liposome concentration of 100 μM. The resulting solution (3.0 mL) was supplemented with probe **5.9** (1 mM stock solution in H_2O) to a final concentration of 2 μM, and the solution was equilibrated for 30 minutes. A fluorescence spectrum was acquired over the spectra window of 460-750 nm with excitation at 450 nm. The solution was supplemented with [(MCL-2)Cu(I)]Na_3PF_6•7.5 H_2O (from a 3 mM stock solution in H_2O) in 0.2-μM aliquots from 0-2.2 μM, with equilibrations of 1 minute each, and fluorescence spectra were recorded after each aliquot addition.

*5.6.10 Fluorescence Response of Probe **5.9** at pH 7.0 and 5.0*

The fluorescence response of **5.9** upon addition of [(MCL-2)Cu(I)]Na_3PF_6•7.5 H_2O in the presence of 4:1 DMPC:DMPG liposomes was compared in aqueous buffer at pH 7.0 and pH 5.0. A freshly extruded 500 μM DMPC:DMPG (4:1) liposome stock solution in aqueous buffer (10 mM PIPES, 0.1 M KCl, 25°C) at pH 7.0 was diluted into PIPES buffer (2.40 mL) in a fluorescence quartz cuvette with a 1-cm pathlength to yield a final liposome concentration of 100 μM. The resulting solution (3.0 mL) was supplemented with probe **5.9** (1 mM stock solution in H_2O) to a final concentration of 2 μM, and the solution was equilibrated for 30 minutes. A fluorescence spectrum was acquired over the spectra window of 470-800 nm with excitation at 450 nm. The solution was supplemented with 3 μM

[(MCL-2)Cu(I)]Na_3PF_6•7.5 H_2O (from a 3 mM stock solution in H_2O), and a fluorescence spectrum was acquired. The procedure was repeated with the 4:1 DMPC:DMPG liposomes prepared in aqueous buffer (10 mM PIPES, 100 mM KCl, 25°C) at pH 5.0.

*5.6.11 Analyte Selectivity of Fluorescent Probe **5.9***

A 100 μM solution (12 mL) of 4:1 DMPC:DMPG liposomes were prepared by dilution of the 2 mM liposome concentrate into buffer (10 mM PIPES-K^+, pH 7.0). While mechanically stirring for 15 minutes at 25°C, PSP-2 was added (1 mM stock solution in DMSO) to the buffered liposomes to afford a concentration of 500 nm in order to sequester an adventitious Cu(I). After equilibration, the liposomes were supplemented with **5.9** (2 μM) by direct dilution from a 1 mM stock solution in DMSO, followed by a 30-min equilibration to ensure complete dissolution in the liposomes. An aliquot (1.5 mL) of the resulting solution was transferred to a quartz cuvette (1 cm path length) and supplemented with each interfering divalent metal cation (10 μM), diluting directly from a 5 mM stock solution of each metal in H_2O. A fluorescence spectrum was acquired over the emission range of 470 to 800 nm with 450 nm excitation after a 1-minute equilibration. To ensure true selectivity for Cu(I), each interfering metal solution was supplemented with Cu(I) (4 μM) as the MCL-2-Cu(I)•7.5H_2O complex by diluting from a 3 mM stock solution in H_2O. The metal cations were supplied as aqueous solutions from the following salts: Co(II), Ni(II), and Pb(II) as nitrates; Mn(II), Fe(II), and Zn(II) as sulfates. To prevent oxidation of Fe(II), the stock solution was prepared immediately before use.

*5.6.12 Determination the Cu(I) Stability Constant of Probe **5.9***

The Cu(I) stability constant for **5.9** was determined through a fluorimetric titration using the affinity standard MCL-1 as competing ligand. A solution of **5.9** (2 μM) in aqueous buffer (pH 7.0, 10 mM PIPES, 0.1 M KCl, 25°C) containing 100 μM freshly extruded 4:1 DMPC:DMPG liposomes (from a 500 μM liposome stock solution) was equilibrated for 30 minutes. The solution was supplemented with 2 μM [(MCL-1)Cu(I)] (from a 3 mM stock solution in H_2O) and then titrated with MCL-1 (from a 3 mM stock solution in H_2O) from 0-640 μM. After the addition of each aliquot, a fluorescence emission spectrum was acquired with excitation at 450 nm over the range of 470-750 nm. The data were analyzed by non-linear least squares fitting using Specfit.[34]

5.7 References

1. Morgan, M. T.; Bagchi, P.; Fahrni, C. J. Designed To Dissolve: Suppression of Colloidal Aggregation of Cu(I)-Selective Fluorescent Probes in Aqueous Buffer and In-Gel Detection of a Metallochaperone. *J. Am. Chem. Soc.* **2011**, *133* (40), 15906-15909.

2. Go, Y. M.; Jones, D. P. Redox Compartmentalization in Eukaryotic Cells. *Biochim. Biophys. Acta - Gen. Subj.* **2008**, *1780* (11), 1271-1290.

3. McRae, R.; Lai, B.; Fahrni, C. J. Copper Redistribution in Atox1-Deficient Mouse Fibroblast Cells. *J. Biol. Inorg. Chem.* **2010**, *15* (1), 99-105.

4. McRae, R.; Bagchi, P.; Sumalekshmy, S.; Fahrni, C. J. In Situ Imaging of Metals in Cells and Tissues. *Chem. Rev.* **2009**, *109* (10), 4780-4827.

5. Fahrni, C. J. Synthetic Fluorescent Probes for Monovalent Copper. *Curr. Opin. Chem. Biol.* **2013**, *17* (4), 656-662.

6. Cotruvo, J. A.; Aron, A. T.; Ramos-Torres, K. M.; Chang, C. J. Synthetic Fluorescent Probes for Studying Copper in Biological Systems. *Chem. Soc. Rev.* **2015**, *44* (13), 4400-4414.

7. Morgan, M. T. Molecular Tools for Elucidating Copper Biochemistry: Water-Soluble Fluorescent Probes and Robust Affinity Standards. Ph.D. Dissertation, Georgia Institute of Technology, 2013.

8. Yang, L. C.; McRae, R.; Henary, M. M.; Patel, R.; Lai, B.; Vogt, S.; Fahrni, C. J. Imaging of the Intracellular Topography of Copper with a Fluorescent Sensor and by Synchrotron X-ray Fluorescence Microscopy. *Proc. Natl. Acad. Sci. U.S.A.* **2005**, *102* (32), 11179-11184.

9. Miller, E. W.; Zeng, L.; Domaille, D. W.; Chang, C. J. Preparation and Use of Coppersensor-1, a Synthetic Fluorophore for Live-Cell Copper Imaging. *Nat. Protoc.* **2006**, *1* (2), 824-827.

10. Zeng, L.; Miller, E. W.; Pralle, A.; Isacoff, E. Y.; Chang, C. J. A Selective Turn-On Fluorescent Sensor for Imaging Copper in Living Cells. *J. Am. Chem. Soc.* **2006**, *128* (1), 10-11.

11. Dodani, S. C.; Domaille, D. W.; Nam, C. I.; Miller, E. W.; Finney, L. A.; Vogt, S.; Chang, C. J. Calcium-Dependent Copper Redistributions in Neuronal Cells Revealed by a Fluorescent Copper Sensor and X-ray Fluorescence Microscopy. *Proc. Natl. Acad. Sci. U.S.A.* **2011**, *108* (15), 5980-5985.

12. Dodani, S. C.; Leary, S. C.; Cobine, P. A.; Winge, D. R.; Chang, C. J. A Targetable Fluorescent Sensor Reveals That Copper-Deficient SCO1 and SCO2 Patient Cells

Prioritize Mitochondrial Copper Homeostasis. *J. Am. Chem. Soc.* **2011**, *133* (22), 8606-8616.

13. Hirayama, T.; Van de Bittner, G. C.; Gray, L. W.; Lutsenko, S.; Chang, C. J. Near-Infrared Fluorescent Sensor for in vivo Copper Imaging in a Murine Wilson Disease Model. *Proc. Natl. Acad. Sci. U.S.A.* **2012**, *109* (7), 2228-2233.

14. Cao, X. W.; Lin, W. Y.; Wan, W. Development of a Near-Infrared Fluorescent Probe for Imaging of Endogenous Cu+ in Live Cells. *Chem. Commun.* **2012**, *48* (50), 6247-6249.

15. Dodani, S. C.; Firl, A.; Chan, J.; Nam, C. I.; Aron, A. T.; Onak, C. S.; Ramos-Torres, K. M.; Paek, J.; Webster, C. M.; Feller, M. B.; Chang, C. J. Copper is an Endogenous Modulator of Neural Circuit Spontaneous Activity. *Proc. Natl. Acad. Sci. U.S.A.* **2014**, *111* (46), 16280-16285.

16. Ouml; hrvika, H.; Nose, Y.; Wood, L. K.; Kim, B. E.; Gleber, S. C.; Ralle, M.; Thiele, D. J. Ctr2 regulates Biogenesis of a Cleaved Form of Mammalian Ctr1 Metal Transporter Lacking the Copper- and Cisplatin-Binding Ecto-Domain. *Proc. Natl. Acad. Sci. U.S.A.* **2013**, *110* (46), E4279-E4288.

17. Polishchuk, E. V.; Concilli, M.; Iacobacci, S.; Chesi, G.; Pastore, N.; Piccolo, P.; Paladino, S.; Baldantoni, D.; van Ijzendoorn, S. C. D.; Chan, J.; Chang, C. J.; Amoresano, A.; Pane, F.; Pucci, P.; Tarallo, A.; Parenti, G.; Brunetti-Pierri, N.; Settembre, C.; Ballabio, A.; Polishchuk, R. S. Wilson Disease Protein ATP7B Utilizes Lysosomal Exocytosis to Maintain Copper Homeostasis. *Dev. Cell* **2014**, *29* (6), 686-700.

18. Huang, C. P.; Fofana, M.; Chan, J.; Chang, C. J.; Howell, S. B. Copper Transporter 2 Regulates Intracellular Copper and Sensitivity to Cisplatin. *Metallomics* **2014**, *6* (3), 654-661.

19. Lin, X. S., X.; Manorek, G.; Fofana, M.; Howell, S. B. Integrin AlphaV Modulates the Cellular Pharmacology of Copper and Cisplatin by Regulating Expression of the Influx Transporter CTR1. *Oncoscience* **2014**, *1* (3), 185-195.

20. Hong-Hermesdorf, A.; Miethke, M.; Gallaher, S. D.; Kropat, J.; Dodani, S. C.; Chan, J.; Barupala, D.; Domaille, D. W.; Shirasaki, D. I.; Loo, J. A.; Weber, P. K.; Pett-Ridge, J.; Stemmler, T. L.; Chang, C. J.; Merchant, S. S. Subcellular Metal Imaging Identifies Dynamic Sites of Cu Accumulation in Chlamydomonas. *Nat. Chem. Biol.* **2014**, *10* (12), 1034-1042.

21. Bagchi, P.; Morgan, M. T.; Bacsa, J.; Fahrni, C. J., Robust Affinity Standards for Cu(I) Biochemistry. *J. Am. Chem. Soc.* **2013**, *135* (49), 18549-18559.

22. Morgan, M. T.; McCallum, A. M.; Fahrni, C. J. Rational Design of a Water-Soluble, Lipid-Compatible Fluorescent Probe for Cu(I) with Sub-Part-Per-Trillion Sensitivity. *Chem. Sci.* **2016**, *7* (2), 1468-1473.

23. Pardo, A.; Reyman, D.; Poyato, J. M. L.; Medina, F. Some Beta-Carboline Derivatives as Fluorescence Standards. *J. Lumines.* **1992**, *51* (5), 269-274.

24. Microinjection Experiments with the Cu(I) Complex of CTAP-3 were performed by Daisy M. Bourassa and M. Thomas Morgan, Georiga Institute of Technology, 2013.

25. Schafer, F. Q.; Buettner, G. R. Redox Environment of the Cell as Viewed Through the Redox State of the Glutathione Disulfide/Glutathione Couple. *Free Radical Bio. Med.* **2001**, *30* (11), 1191-1212.

26. Morgan, M. T.; Nguyen, L. A. H.; Hancock, H. L.; Fahrni, C. J. Glutathione Sequesters Copper to Sub-Femtomolar Concentrations Through Cooperative Assembly of a Tetranuclear Cluster. *J. Biol. Chem.*, *submitted for publication.*

27. Xiao, Z. G.; Brose, J.; Schimo, S.; Ackland, S. M.; La Fontaine, S.; Wedd, A. G. Unification of the Copper(I) Binding Affinities of the Metallo-Chaperones Atx1, Atox1, and Related Proteins: Detection Probes and Affinity Standards. *J. Biol. Chem.* **2011**, *286* (13), 11047-11055.

28. Allen, S.; Badarau, A.; Dennison, C. Cu(I) Affinities of the Domain 1 and 3 Sites in the Human Metallochaperone for Cu,Zn-Superoxide Dismutase. *Biochemistry* **2012**, *51* (7), 1439-1448.

29. Morgan, M. T.; Yang, B.; Nabatilan, A. M. M.; Sun, F.; Bourassa, D. M.; McCallum, A. M.; Harankhedkar, S. A.; Wu, R.; Forest, C.; Fahrni, C. J. Stabilization of Aliphatic Phosphines by Phosphine sulfides: A Ligand Design Strategy Offering Zeptomolar affinity and Unprecedented Selectivity for Monovalent Copper. *In preparation*

30. Rurack, K.; Spieles, M. Fluorescence Quantum Yields of a Series of Red and Near-Infrared Dyes Emitting at 600-1000 nm. *Anal. Chem.* **2011**, *83* (4), 1232-1242.

31. Bryson, A. The Effects of M-Substituents on the pKa Values of Anilines, and on the Stretching Frequencies of the N-H Bonds. *J. Am. Chem. Soc.* **1960**, *82* (18), 4858-4862.

32. Domaille, D. W.; Que, E. L.; Chang, C. J. Synthetic Fluorescent Sensors for Studying the Cell Biology of Metals. *Nat. Chem. Biol.* **2008**, *4* (3), 168-175.

33. Bangham, A. D.; Standish, M. M.; Watkins, J. C. Diffusion of Univalent Ions Across the Lamellae of Swollen Phospholipids. *J. Mol. Biol.* **1965**, *13* (1), 238-52.

34. Binstead, R. A.; Zuberbühler, A. D. *SPECFIT Global Analysis System*, 3.0.27; Spectrum Software Associates, Marlborough MA 01752: 2001.

35. Martell, A. E.; Smith, R. M. *Critical Stability Constants*. Plenum Press: New York, 1974.

CHAPTER 6

CONCLUSIONS AND FUTURE DIRECTION

All the work described in this thesis is the product of strategic objectives that were aimed at addressing some of the key, fundamental issues regarding the tools currently available for elucidating zinc biochemistry in biological systems. These issues are: 1) the status of suitable Zn(II)-responsive fluorescent probes designed for sensing labile Zn(II) in cells, and 2) the methods to characterize the photophysical and thermodynamic properties of the fluorescent probes whose application in cells is intended to yield both qualitative and quantitative data. Regarding the status of suitable fluorescent indicators for detecting labile Zn(II) pools, the issues that plague the fluorescent probe field entail a lack of knowledge about the fundamental photophysical and thermodynamic properties of metal-binding probes and how these properties must be tailored for the particular imaging modality used to investigate the subtle changes in buffered Zn(II) levels in cells. Furthermore, the lack of awareness of how the signaling responses of fluorescent probes in the cellular environment compare to their solution characterization often translates into misleading interpretations of cellular data upon processing of the micrographs acquired from the fluorescence microscope. As the fluorescent probes become more-routinely employed in multifarious biological imaging applications, these misleading interpretations often become perpetuated. Considering these issues and the potential means to circumvent them, the quest for developing biologically applicable Zn(II)-responsive fluorescent probes optimized for TPEM led to the knowledge-driven design and optimization of a noncentro-

symmetric dipolar donor-π-acceptor fluorophore platform whose photophysical and thermodynamic properties enabled the generation of quantitative data from which reliable buffered Zn(II) concentrations could be calculated.

6.1 Emission-Ratiometric Fluorescent Probes for Detecting Kinetically Labile Zn(II) Pools

6.1.1 Optimizing the Photophysical Properties of Emission-Ratiometric Fluorescent Probes for TPEM

Despite the difficult in designing emission-ratiometric fluorescent probes that undergo shifts in the emission spectra upon binding of the metal cation, the development of the first emission-ratiometric probe[1] for Zn(II) paved the way for a new fluorophore platform that offers large two-photon cross sections and elicits large chromatic shifts in both the excitation and emission spectra upon coordination of Zn(II), both of which are necessary for robust imaging capabilities using TPEM. However, this probe served only as a proof of concept because the region for which the free and metal-bound species exhibited balanced 2PA cross sections resided below the excitation range of the Ti:sapphire lasers of two-photon fluorescence microscopes. By substituting the oxazole bridge with a thiazole bridge, the balanced two-photon cross section window was shifted into the range accessible by the two-photon lasers, which gave rise to chromis-1, the emission-ratiometric, Zn(II)-selective fluorescent probe that enabled practical applications in biological imaging instead of remaining a proof of concept.

The incorporation of hydrophilic groups into the structure of chromis-1 facilitated water-solubility while averting aggregation in the aqueous buffer in which the probe was

characterized. Chromis-1 displayed a large 37-nm shift in the emission wavelength maximum, as well as a more-than-two-fold increase in the 2PA cross section, upon binding Zn(II), which are two properties necessary for effective TPEM imaging. In addition, chromis-1 displayed excellent selectivity towards Zn(II) and a stability constant for the formation of the corresponding Zn(II) complex in the low picomolar regime. Chromis-1 ester, which served as the derivative of the probe used in biological imaging, enabled a reliable estimation of intracellular buffered Zn(II) concentrations between 50-100 pM based on an independent *in situ* calibration with the probe in live cells and the Zn(II) stability constant of the probe determined in liposomes as model membranes. This estimated concentration range agrees well with previously reported buffered Zn(II) levels using genetically encoded fluorescent probes.[2]

6.1.2 Suppressing Excited-State Proton Transfer

During the photophysical characterization of chromis-1 acid, it was evident that the pyridyl acceptor of the fluorophore core was undergoing an excited-state protonation, even at neutral pH in aqueous solution, which led to a fluorescence quenching and red-edge broadening of the fluorescence profile of the free form. Literature precedent for remedying this phenomenon led to the rearrangement of the acceptor pyridine, which reduced the propensity for undergoing protonation in the excited state. Incorporation of this newly optimized design into a metal-binding fluorophore, however, did not render the ESPT phenomenon eradicated, but instead required tuning of the basicity of the metal-binding ligand that was discovered to facilitate an excited-state intramolecular proton transfer to the fluorophore pyridine. Further refinement of the photophysical properties of the 2-thiazolyl metal-binding fluorophore led to the incorporation of a brand-new metal-binding ligand, albeit with significantly reduced basicity compared to pyridine, into the structure of the

probe, giving rise to chromis-2 as the next generation Zn(II)-responsive, emission-ratiometric fluorescent probe for imaging labile Zn(II) in mammalian cells and tissue. In addition, a control compound that does not bind Zn(II) yet still demonstrates a nearly identical emission response compared to the metal-free form of chromis-2 was developed to ensure that the fluorescence response of chromis-2 inside the cell was not the product of artifacts produced by the interaction of the probe with the lipid-rich environment of biological membranes and lipid droplets.

6.1.3 Tuning the Zn(II)-Binding Affinity of Emission-Ratiometric Fluorescent Probes

The chemical identity of the metal-binding ligands that are tethered to the electron-deficient acceptor moiety of the donor-acceptor fluorophore dictate the intrinsic binding affinity of the metal-binding fluorescent probe. This was exploited in the design of the 2-thiazolyl fluorophore core, which featured an aldehyde functionality to which any primary or secondary amine-containing ligand could be coupled, thereby demonstrating a modular synthetic approach. This led to the development of a series of affinity-tuned fluorescent probes with Zn(II) stability constants that span a 10 logarithmic-unit range between log$K$ of 5.35 and 15.1. However, as is the case with any associative metal-ligand exchange equilibrium, there exist both thermodynamic and kinetic barriers for metal exchange; therefore, a higher Zn(II)-binding affinity does not necessarily translate to the capability of detecting tightly bound or unavailable Zn(II) if the kinetic component of the equilibrium precludes the exchange reaction at a reasonable rate. Nonetheless, affinity tuning of fluorescent probes represents a step in the right direction in terms of better understanding the changes in buffered Zn(II) levels and Zn(II) redistribution in the cellular environment.

6.1.4 Fluorescence Dependence on the Polarity Environment

Although the majority of this work was devoted to the development and optimization of Zn(II)-responsive fluorescent probes, many of the strategies discussed throughout this thesis can be translated to the development of chemical tools for the detection of biologically relevant monovalent copper, the predominant species present inside the cell. The presence of interfering quenching pathways by virtue of the rich redox chemistry of Cu(I) limited the number of fluorescent probes available for probing the metal ion, of which all utilized a fluorescence intensity-based signaling mechanism. In addition, due to the highly lipophilic nature of these fluorescent probes, characterization of the photophysical and thermodynamic properties demonstrated divergent behavior in comparison to the corresponding signaling responses inside the cell.

To remedy this issue, the fluorescence behavior of several fluorescence turn-on probes were re-evaluated in the presence of liposomes that served to mimic the dichotomous environment of cell. The result was the demonstration of analyte-independent, lipid-mediated increases in the fluorescence intensity of two Cu(I) probes, CS3 and CTAP-2, both of which deviated significantly from their fluorescence responses in aqueous buffer without liposomes. The successor to CTAP-2, CTAP-3, did not display a lipid-mediate fluorescence increase and responded with a more-than-60-fold fluorescence enhancement in the presence of liposomes. The modest Cu(I)-binding affinity, however, prohibited its use for detecting biologically relevant Cu(I), which is believed to be buffered in the sub-femtomolar regime due to the presence of endogenous glutathione (GSH). This, in addition to the lack of quantitative analysis capabilities, prompted the development of probe **5.9** as the first ratiometric Cu(I) probe. The overall lipophilic properties of the probe demanded the presence of liposomes for solubility to ensure proper characterization, which

rendered the fluorescence behavior of the probe inconsistent between measurements. Despite its lipophilic nature, probe **5.9** was the first ratiometric fluorescent probe capable of detecting labile Cu(I) in the cell, its development constitutes a pivotal advancement in the design of fluorescent probes for imaging labile cellular Cu(I).

6.2 Future Direction

Despite its overwhelming advantages, the utilization of two-photon excitation microscopy in biological imaging has a few limitations, one of which is a lack of availability at most research centers because of its high cost. The high photon flux required to increase the probability of simultaneous two-photon excitation renders the optical equipment, including lasers, very expensive, and for that reason, two-photon microscopes are not as pervasive as wide-field and confocal fluorescence microscopes, both of which utilize less advanced lasers that enable one-photon excitation. The wavelength of excitation of the lasers in wide-fields and confocal microscopes are most often 405, 458, and 476 nm, as well as a few others of longer wavelength, which are significantly red-shifted compared to the wavelength of excitation (720 nm for two-photon) of the ratiometric fluorescent probes are presented in this work. Therefore, to broaden the availability of Zn(II)-responsive, emission-ratiometric fluorescent probes for biological imaging in a wide variety of applications, it would be advantageous to develop derivatives of these probes with red-shifted wavelengths of excitation while still retaining many of the intrinsic photophysical and thermodynamic properties that overwhelmingly make these probes far superior compared to the Zn(II)-binding fluorescent probes currently available.

There are several strategies for shifting the wavelength of excitation to longer wavelength. One such strategy is to increase the strength of the electron-rich donor. While the anisole donor of the chromis series, including the affinity-tuned analogs, serves

as a pH-insensitive donor group, the decreased donor strength of oxygen compared to nitrogen, for example, can limit the degree of charge delocalization throughout the π-system. Therefore, substituting the anisole for an *N*-alkylated aniline group to provide a stronger electron donor will enable a shift of the wavelength of excitation further into the visible range. Another strategy is to increase the length of π-conjugation, as more extended conjugated systems boast longer wavelengths of absorption due to smaller energy transitions between the HOMO and LUMO. This can be accomplished either through the implementation of a new fluorophore structure, such as the use of a coumarin platform, or through the incorporation of additional π-bonds into the π-conjugated bridge of the donor-acceptor architecture, such as an additional thiophene or heteroaromatic group. Depending on the degree of wavelength shift desired, the implementation of both strategies could prove advantageous for the development of a new Zn(II)-responsive, emission-ratiometric fluorophore suitable for either one-photon or two-photon microscopy, provided the photophysical properties, including the brightness, are sufficient for either imaging modality.

6.3 References

1. Sumalekshmy, S.; Henary, M. M.; Siegel, N.; Lawson, P. V.; Wu, Y.; Schmidt, K.; Bredas, J. L.; Perry, J. W.; Fahrni, C. J. Design of Emission Ratiometric Metal-Ion Sensors with Enhanced Two-Photon Cross Section and Brightness. *J. Am. Chem. Soc.* **2007**, *129* (39), 11888-11889.

2. Maret, W. Analyzing Free Zinc(II) Ion Concentrations in Cell Biology with Fluorescent Chelating Molecules. *Metallomics* **2015**, *7* (2), 202-211.

APPENDIX A

A.1 X-Ray Crystallographic Data

Table A.1: Crystal data and structure refinement for the Zn(II) complex of ligand **2.1b** [Zn(II)-(**2.1b**)]$_2$Ca(DMF)(H_2O)$_6$

Empirical formula	$C_{63}H_{65}CaCl_2N_{11}O_{17}S_2Zn_2$	
Formula weight	1554.16	
Temperature	100(2)	
Wavelength	MoKα (λ = 0.71073)	
Crystal system	Triclinic	
Space group	P-1	
Unit cell dimensions	a = 11.8106(6) Å	α = 79.625(4)°
	b = 13.3625(6) Å	β = 81.802(4)°
	c = 22.2111(11) Å	γ = 77.504(4)°
Volume	3346.7(3) Å^3	
Z	2	
Density (calculated)	1.542 g/cm^3	
Absorption coefficient	1.014 mm^{-1}	
F(000)	1604.0	
Crystal size	0.218 × 0.093 × 0.028 mm	
Theta range for data collection	1.580 to 24.712°	
Index ranges	-13 ≤ h ≤ 13, -15 ≤ k ≤ 15, -26 ≤ l ≤ 26	
Reflections collected	27927	
Independent reflections	11181 [R_{int} = 0.1247, R_{sigma} = 0.1227]	
Refinement method	Full-matrix least-squares on F^2	
Data / restraints / parameters	11181/836/911	
Goodness-of-fit on F^2	1.063	
Final R indices [I > 2σ(I)]	R_1 = 0.0899, wR_2 = 0.1820	
R indices (all data)	R_1 = 0.1502, wR_2 = 0.2195	
Largest diff. peak and hole	1.552/-0.762 e•Å^{-3}	

Table A.2: Selected bond lengths and bond angles for the Zn(II) complex of ligand **2.1b** $[Zn(II)\text{-}(\mathbf{2.1b})]_2Ca(DMF)(H_2O)_6$.

	2.1b	**2.1b-B**
Zn1-Cl1	2.266(2)	2.252(2)
Zn1-N1	2.101(7)	2.098(7)
Zn1-N2	2.088(7)	2.116(7)
Zn1-N3	2.097(7)	2.095(7)
Zn1-N4	2.254(7)	2.244(7)
N1-Zn1-Cl1	98.9(2)	103.6(2)
N1-Zn1-N2	117.8(3)	117.3(3)
N1-Zn1-N3	115.0(3)	114.6(3)
N1-Zn1-N4	77.0(3)	76.4(3)
N2-Zn1-Cl1	104.8(2)	101.9(2)
N2-Zn1-N3	112.9(3)	112.2(3)
N2-Zn1-N4	77.3(3)	76.1(3)
N3-Zn1-Cl1	104.7(2)	105.1(2)
N3-Zn1-N4	77.4(3)	77.0(3)
N4-Zn1-Cl1	175.69(2)	177.66(2)

Table A.3: Atomic coordinates (x 10^4) and equivalent isotropic displacement parameters ($Å^2$ x 10^3) for the Zn(II) complex of ligand **2.1b** [Zn(II)-(**2.1b**)]$_2$Ca(DMF)(H_2O)$_6$. U(eq) is defined as one third of the trace of the orthogonalized U^{ij} tensor.

Atom Label	x	y	z	U(eq)
Zn1	7283.9(9)	8179.9(8)	7512.0(5)	15.4(2)
Cl1	8452(2)	8238.4(17)	8225(1)	20.9(5)
S1	3496(2)	4311.5(18)	8531.2(10)	19.1(5)
O2	3693(6)	13138(5)	7350(3)	22.9(14)
O4	11592(6)	5793(5)	5424(3)	25.6(12)
O1	-177(6)	993(5)	9318(3)	23.9(13)
N2	6382(6)	9704(5)	7305(3)	16.1(12)
N5	4458(7)	4373(6)	9490(3)	18.4(14)
N1	6346(6)	7080(5)	8022(3)	16.4(11)
O5	10219(6)	6392(7)	4783(3)	44(2)
N3	8434(6)	7671(5)	6769(3)	16.6(11)
N4	6062(6)	8041(5)	6852(3)	16.0(8)
C3	5074(7)	5556(6)	8604(4)	15.0(12)
C25	7980(8)	7282(7)	6358(4)	17.4(14)
C16	5035(8)	7738(7)	7228(4)	16.9(12)
C8	3118(8)	3523(7)	9202(4)	18.9(14)
C18	5722(8)	9903(7)	6839(4)	16.0(12)
C10	2205(8)	2337(7)	8768(4)	20.1(16)
C9	2280(8)	2845(7)	9249(4)	19.1(14)
C27	9848(8)	6855(7)	5787(4)	18.5(14)
C29	9590(8)	7685(7)	6679(4)	19.1(13)
C1	5382(7)	6962(6)	7792(4)	14.4(13)
C4	6031(8)	5714(7)	8841(4)	18.0(16)
C14	1495(8)	2728(7)	9784(4)	20.7(16)
C6	4403(8)	4777(7)	8910(4)	18.2(12)
C17	5802(8)	9062(6)	6464(4)	15.4(12)
C7	3703(8)	3691(7)	9649(4)	21.9(17)
C22	6355(8)	10444(7)	7642(4)	20.3(18)
C21	5626(8)	11431(7)	7537(4)	18.5(17)
C23	4147(8)	12682(7)	6906(4)	18.6(15)
C26	8661(8)	6896(7)	5857(4)	19.3(16)
C13	666(8)	2109(7)	9826(4)	20.2(16)
C12	610(8)	1606(7)	9328(4)	19.5(15)

C20	4964(8)	11645(7)	7046(4)	17.0(15)
C2	4756(8)	6211(7)	8057(4)	17.9(13)
C11	1404(8)	1708(7)	8807(4)	18.3(15)
C5	6664(8)	6456(6)	8548(4)	15.5(14)
C19	5023(8)	10872(7)	6689(4)	15.8(13)
C28	10313(8)	7281(7)	6196(4)	20.2(16)
C24	6707(7)	7221(7)	6491(4)	17.1(12)
C30	10604(8)	6309(7)	5276(4)	22.4(16)
C15	-1121(9)	1028(8)	9785(5)	28(2)
Zn1B	11584.5(9)	6663.3(8)	2113.6(5)	14.8(2)
Cl1B	12897.7(19)	7214.3(17)	1358.1(10)	21.1(5)
S1B	8408(2)	2794.1(18)	1476.5(10)	19.8(5)
O3B	13995(5)	4067(5)	4816(3)	20.9(13)
O2B	15635(5)	4503(5)	4311(3)	24.1(14)
N1B	10897(6)	5635(5)	1725(3)	16.3(14)
N5B	8515(6)	4144(6)	498(3)	17.1(13)
N4B	10333(6)	6060(5)	2880(3)	13.5(12)
O1B	4755(6)	-183(5)	1024(3)	27.7(14)
N3B	10393(7)	8010(5)	2297(3)	18.6(14)
N2B	12630(6)	6019(5)	2840(3)	14.7(13)
C3B	9670(7)	4408(7)	1274(4)	15.9(14)
C16B	10338(8)	4999(6)	2782(4)	14.4(16)
C4B	10301(8)	5069(7)	879(4)	19.6(16)
C1B	10290(8)	4990(6)	2113(4)	15.7(15)
C17B	10763(7)	6061(6)	3464(4)	13.5(13)
C5B	10887(8)	5667(7)	1117(4)	17.2(15)
C6B	8912(8)	3856(7)	1039(4)	17.3(12)
C2B	9683(8)	4367(7)	1903(4)	16.6(14)
C18B	12075(7)	5791(7)	3410(4)	14.8(12)
C20B	13890(8)	5066(7)	3824(4)	15.7(14)
C25B	9413(8)	7859(7)	2663(4)	15.7(15)
C10B	5981(8)	2189(7)	534(4)	21.9(14)
C21B	14454(8)	5340(7)	3246(4)	18.1(16)
C8B	7569(8)	2771(7)	905(4)	17.7(12)
C23B	14579(8)	4509(7)	4364(4)	17.5(13)
C14B	6897(8)	1134(7)	1393(4)	22.1(17)
C22B	13805(8)	5808(7)	2762(4)	16.7(15)
C9B	6803(8)	2019(7)	945(4)	16.9(14)

C13B	6203(8)	430(8)	1408(5)	25.7(19)
C12B	5375(8)	593(7)	985(4)	20.3(16)
C27B	8838(8)	9680(7)	2733(4)	16.8(15)
C7B	7757(8)	3559(7)	423(4)	20.2(17)
C29B	10591(8)	8976(7)	2124(4)	19.9(17)
C19B	12678(8)	5308(7)	3905(4)	16.4(13)
C30B	8056(8)	10579(7)	3010(4)	21.1(17)
C26B	8615(8)	8680(7)	2898(4)	16.3(15)
C11B	5261(8)	1483(7)	542(4)	23.9(18)
C28B	9832(7)	9823(7)	2335(4)	17.0(15)
C24B	9213(7)	6762(6)	2814(4)	15.7(12)
C15B	3750(9)	31(8)	693(5)	32(2)
O1S	1857(9)	10389(7)	4663(4)	58(2)
N1S	1925(13)	8902(10)	4299(6)	74(3)
C2S	2317(14)	9489(11)	4597(6)	61(3)
C3S	2580(15)	7839(12)	4235(8)	82(4)
C4S	797(17)	9264(15)	4083(10)	108(7)
Ca1	13006.3(16)	4466.0(14)	5757.5(8)	17.6(4)
O6W	12390(5)	4873(5)	6773(3)	19.0(12)
O1W	7110(6)	13337(5)	3083(3)	25.0(15)
O2W	2713(7)	11156(5)	5554(3)	37.9(19)
O3W	4735(7)	11855(7)	5001(4)	57(2)
O4W	6582(9)	11989(6)	4096(4)	62(3)
O5W	11832(5)	3248(5)	5667(3)	22.1(13)
O3	3969(6)	12979(5)	6350(3)	28.0(15)
O4B	8257(6)	11461(5)	2790(3)	29.4(15)
O5B	7263(6)	10366(5)	3433(3)	27.8(14)

Table A.4: Crystal data and structure refinement for the Zn(II) complex of ligand **3.3c**: [(**3.3c**)Zn(II)]$(ClO_4)_2(H_2O)$

Empirical formula	$C_{28}H_{27}Cl_2N_5O_{10}SZn$	
Formula weight (g/mol)	761.87	
Temperature (K)	100(2)	
Wavelength (nm)	MoKα (λ = 0.71073)	
Crystal system	monoclinic	
Space group	$P2_1/c$	
Unit cell dimensions	a = 12.6948(4) Å	α = 90°
	b = 16.2339(5) Å	β = 91.625(3)°
	c = 15.1941(4) Å	γ = 90°
Volume	3130.03(16) $Å^3$	
Z	4	
Density (calculated)	1.617 g/cm^3	
Absorption coefficient	1.088 mm^{-1}	
F(000)	1560.0	
Crystal size	0.40 × 0.37 × 0.18 mm	
Theta range for data collection	2.414 to 30.508°	
Index ranges	$-18 \le h \le 18$, $-23 \le k \le 23$, $-21 \le l \le 21$	
Reflections collected	27117	
Independent reflections	9537 [R_{int} = 0.0367, R_{sigma} = 0.1483]	
Refinement method	Full-matrix least-squares on F^2	
Data / restraints / parameters	9537/251/465	
Goodness-of-fit on F^2	1.035	
Final R indices [I>2sigma(I)]	R_1 = 0.0523, wR_2 = 0.1271	
R indices (all data)	R_1 = 0.0717, wR_2 = 0.1368	
Largest diff. peak and hole	1.238/-0.538 $e.Å^{-3}$	

Table A.5: Selected bond lengths and bond angles for the Zn(II) complex of ligand **3.3c**: [(**3.3c**)Zn(II)]$(ClO_4)_2(H_2O)$

	3c
N1-Zn1	2.044(2)
N2-Zn1	2.1218(19)
N3-Zn1	2.246(2)
N4-Zn1	2.037(2)
N5-Zn1	2.039(2)
	3c
N1-Zn1-N4	117.03(8)
N1-Zn1-N5	123.19(8)
N4-Zn1-N5	109.57(8)
N1-Zn1-N2	78.99(8)
N2-Zn1-N4	112.37(8)
N2-Zn1-N5	111.70(8)
N1-Zn1-N3	76.83(8)
N3-Zn1-N4	81.01(8)
N3-Zn1-N5	80.33(8)
N2-Zn1-N3	155.72(8)

Table A.6: Fractional atomic coordinates (x 10^4) and equivalent isotropic displacement parameters ($Å^2$ x 10^3) for the Zn(II) complex of ligand **3.3c**: [(**3.3c**)Zn(II)]$(ClO_4)_2(H_2O)$. U(eq) is defined as one third of the trace of the orthogonalized U_{ij} tensor.

Atom	x	y	z	U_{eq}
Zn1	3348.3(2)	5252.6(2)	7736.3(2)	15.51(8)
Cl2B	8006.4(18)	5947.8(17)	8573.7(18)	23.1(2)
O6B	8577(4)	5285(3)	9014(3)	29.2(7)
O7B	8745(3)	6469(3)	8126(3)	31.1(6)
O8B	7467(3)	6432(2)	9224(2)	28.8(7)
O9B	7248(3)	5610(2)	7949(2)	36.9(7)
S1	4563.6(5)	6333.6(4)	5235.8(4)	17.93(13)
O1	9632.3(15)	5977.8(12)	4153.2(12)	25.9(4)
N2	4338.5(16)	5560.6(12)	6683.6(12)	15.5(4)
N1	2291.4(17)	5792.4(13)	6875.9(13)	18.0(4)
N3	1837.7(17)	5223.2(13)	8469.8(13)	18.9(4)
N4	3223.2(17)	4012.8(13)	7910.1(13)	19.0(4)
N5	3846.8(16)	5789.7(12)	8887.1(12)	16.0(4)
C6	3812(2)	6005.4(14)	6083.4(14)	15.9(4)
C8	5372(2)	5475.5(14)	6479.4(14)	16.1(4)
C7	5659.3(19)	5855.6(14)	5712.5(14)	15.9(4)
C5	2679(2)	6171.3(14)	6169.5(14)	16.9(4)
C4	2047(2)	6650.3(16)	5614.9(16)	21.2(5)
C3	984(2)	6726.9(17)	5815.5(17)	24.9(5)
C2	584(2)	6316.2(17)	6539.1(17)	23.8(5)
C1	1274(2)	5846.4(15)	7063.4(16)	19.5(5)
C16	944(2)	5334.3(17)	7843.6(17)	23.1(5)
C17	1836(2)	4414.2(16)	8916.8(17)	22.9(5)
C18	2429(2)	3763.9(15)	8420.4(16)	20.8(5)
C19	2200(2)	2932.0(17)	8530.7(18)	27.9(6)
C20	2815(3)	2348.2(17)	8128.6(18)	31.1(7)
C21	3648(3)	2602.9(17)	7619.1(18)	28.5(6)
C22	3824(2)	3439.9(16)	7521.7(16)	22.4(5)
C23	1951(2)	5908.4(16)	9099.2(16)	20.4(5)
C24	3075(2)	5976.9(15)	9450.4(15)	17.7(5)
C25	3306(2)	6265.6(16)	10296.5(16)	22.3(5)
C26	4348(2)	6392.6(17)	10558.1(16)	23.8(5)
C27	5134(2)	6223.2(16)	9973.3(16)	22.4(5)
C28	4860(2)	5914.6(15)	9146.6(15)	18.6(5)

C9	6692(2)	5900.1(14)	5296.0(14)	16.8(4)
C14	7484(2)	5320.8(14)	5510.5(16)	19.5(5)
C13	8459(2)	5370.4(15)	5125.0(16)	21.0(5)
C12	8659(2)	5991.9(16)	4510.8(15)	19.3(5)
C11	7885(2)	6575.9(16)	4300.0(15)	20.2(5)
C10	6914(2)	6525.2(15)	4692.1(15)	19.5(5)
C15	9911(2)	6651(2)	3589.0(18)	30.4(6)
Cl1B	3211(3)	7941(3)	7905(2)	19.14(16)
O2B	3703(6)	8741(3)	7876(5)	37.5(8)
O3B	2831(6)	7769(4)	8773(3)	36.2(7)
O4B	3964(5)	7312(4)	7685(5)	30.2(7)
O5B	2332(5)	7897(4)	7283(4)	32.4(6)
O10	711(2)	8685.6(15)	6393.1(17)	41.5(6)
Cl1A	3133.5(14)	7906.5(12)	7865.3(11)	19.14(16)
O2A	3338(3)	8758.7(16)	7662(2)	37.5(8)
O3A	3266(3)	7751(2)	8797.1(14)	36.2(7)
O4A	3854(3)	7383(2)	7404(2)	30.2(7)
O5A	2069.2(19)	7687(2)	7597(2)	32.4(6)
Cl2A	8093(4)	5920(4)	8534(4)	23.1(2)
O6A	8729(9)	5371(7)	9080(7)	29.2(7)
O7A	8754(8)	6567(7)	8197(8)	31.1(6)
O8A	7277(7)	6282(6)	9056(6)	28.8(7)
O9A	7618(8)	5464(5)	7810(5)	36.9(7)

Table A.7: Crystal data and structure refinement for the Zn(II) complex of chromis-2 (**3.4**): [(chromis-2)Zn(II)]$(BF_4)_2(H_2O)_2$.

Empirical formula	$C_{26}H_{27}B_2F_8N_7O_3SZn$	
Formula weight	756.59	
Temperature	100(2)	
Wavelength	CuKα (λ = 0.154184)	
Crystal system	monoclinic	
Space group	$P2_1/c$	
Unit cell dimensions	a = 9.86710(10) Å	α = 90°
	b = 19.3141(2) Å	β = 100.6150(10)°
	c = 16.4920(2) Å	γ = 90°
Volume	3089.16(6) $Å^3$	
Z	4	
Density (calculated)	1.627 g/cm^3	
Absorption coefficient	2.564 mm^{-1}	
F(000)	1536.0	
Crystal size	0.265 × 0.246 × 0.206 mm	
Theta range for data collection	7.12 to 144.336°	
Index ranges	$-12 \le h \le 11$, $-23 \le k \le 23$, $-20 \le l \le 20$	
Reflections collected	19414	
Independent reflections	5977 [R_{int} = 0.0241, R_{sigma} = 0.0223]	
Refinement method	Full-matrix least-squares on F^2	
Data / restraints / parameters	5977/6/450	
Goodness-of-fit on F^2	1.049	
Final R indices [I>2sigma(I)]	R_1 = 0.0295, wR_2 = 0.0765	
R indices (all data)	R_1 = 0.0316, wR_2 = 0.0777	
Largest diff. peak and hole	0.63/-0.66 e.$Å^{-3}$	

Table A.8: Selected bond lengths and bond angles for the Zn(II) complex of chromis-2 (**3.4**): [(chromis-2)Zn(II)]$(BF_4)_2(H_2O)_2$.

	Chromis-2 (3.4)
N1-Zn1	2.1137(13)
N2-Zn1	2.1690(14)
N3-Zn1	2.3520(13)
N4-Zn1	2.1009(13)
N5-Zn1	2.0937(13)
O2-Zn1	2.1096(11)
	Chromis-2 (3.4)
N2-Zn1-N4	105.19(5)
N2-Zn1-N5	108.78(5)
N3-Zn1-N4	77.10(5)
N3-Zn1-N5	76.56(5)
N1-Zn1-N2	76.23(5)
N1-Zn1-N3	75.53(5)
N1-Zn1-N4	101.78(5)
N1-Zn1-N5	93.13(5)
N2-Zn1-O2	91.10(5)
N3-Zn1-O2	117.38(5)
N4-Zn1-O2	86.95(5)
N5-Zn1-O2	85.42(5)
N1-Zn1-O2	166.08(5)
N2-Zn1-N3	151.51(5)
N4-Zn1-N5	145.27(5)

Table A.9: Fractional atomic coordinates (x 10^4) and equivalent isotropic displacement parameters ($Å^2$ x 10^3) for the Zn(II) complex of chromis-2 (**3.4**): [(chromis-2)Zn(II)]$(BF_4)_2(H_2O)_2$. U(eq) is defined as one third of the trace of the orthogonalized U_{ij} tensor.

Atom	x	y	z	U_{eq}
Zn1	3933.2(2)	5072.8(2)	2388.5(2)	11.39(7)
S1	6470.1(4)	4422.8(2)	4870.4(2)	14.30(9)
F2	5035.0(11)	7215.1(6)	2646.6(6)	26.4(2)
F7	654.1(10)	5987.2(5)	-264.9(6)	23.6(2)
F4	5510.6(11)	6988.9(6)	4017.6(6)	29.4(2)
F3	7247.9(11)	7043.5(6)	3293.7(7)	31.2(3)
O2	4951.7(12)	5928.2(6)	1977.3(7)	18.2(2)
F1	6098.3(13)	8023.8(6)	3527.4(9)	38.9(3)
F6	-300.4(13)	6749.5(7)	514.9(9)	40.7(3)
O1	11913.0(12)	6249.3(6)	6735.4(8)	22.7(3)
F8	1997.2(13)	6542.6(7)	793.7(9)	42.7(3)
O3	7385.4(12)	5706.5(7)	1568.1(8)	22.7(3)
F5	1049.2(17)	7132.8(6)	-368.8(10)	50.3(4)
N1	3391.5(13)	4165.7(7)	2971.0(8)	12.9(3)
N2	5455.3(13)	5017.5(7)	3517.7(8)	13.7(3)
N3	1904.1(13)	4683.8(7)	1530.5(8)	13.7(3)
N5	4662.3(13)	4517.2(7)	1466.7(8)	13.6(3)
N4	2443.7(13)	5778.9(7)	2638.9(8)	12.8(3)
N6	81.7(14)	6088.1(7)	2414.5(8)	15.1(3)
N7	4063.2(14)	4124.1(8)	87.7(9)	18.9(3)
C18	1133.1(15)	5706.0(8)	2255.6(9)	13.0(3)
C9	8442.8(15)	5476.8(8)	5173.5(9)	13.8(3)
C7	7239.8(16)	5186.2(8)	4629(1)	14.0(3)
C10	9126.7(16)	5110.1(8)	5861.3(10)	14.6(3)
C11	10277.0(16)	5380.6(9)	6369.9(10)	15.4(3)
C12	10773.3(16)	6029.7(9)	6198.4(10)	15.9(3)
C23	3766.8(16)	4423.0(8)	762.2(10)	14.4(3)
C6	5291.2(16)	4475.1(8)	3968.6(9)	13.5(3)
C19	2732.6(16)	6292.1(8)	3193.7(10)	14.8(3)
C5	4179.7(15)	3977.9(8)	3693.4(9)	13.9(3)
C14	8955.6(16)	6127.2(8)	5014.1(10)	16.9(3)
C20	1713.2(17)	6718.5(8)	3387.6(10)	17.3(3)
C24	5944.5(16)	4266.9(9)	1515.6(10)	17.6(3)
C4	3930.5(17)	3383.0(9)	4108.3(10)	18.5(3)

C1	2344.7(15)	3771.5(8)	2627.9(10)	14.2(3)
C21	376.2(17)	6584.9(8)	2983(1)	17.6(3)
C8	6548.2(16)	5418.2(8)	3883.1(10)	14.1(3)
C2	2003.8(17)	3171.7(9)	3019.6(10)	18.7(3)
C17	777.0(16)	5171.4(9)	1584.2(10)	16.5(3)
C22	2320.0(16)	4697.2(9)	714.4(10)	15.8(3)
C13	10116.1(17)	6403.2(9)	5515.6(10)	18.1(3)
C16	1597.9(16)	3972.2(8)	1777.5(10)	17.2(3)
C3	2798.1(18)	2980.3(9)	3763.1(11)	21.3(3)
C26	5349.7(18)	3886(1)	138.1(11)	22.8(4)
C25	6331.4(17)	3933.2(9)	855.2(11)	21.8(4)
C15	12411(2)	6932.7(10)	6611.1(13)	28.4(4)
B1	5990(2)	7328.8(10)	3382.4(12)	18.6(4)
B2	835(2)	6613.0(11)	165.6(14)	24.9(4)
Zn1	3933.2(2)	5072.8(2)	2388.5(2)	11.39(7)
S1	6470.1(4)	4422.8(2)	4870.4(2)	14.30(9)
F2	5035.0(11)	7215.1(6)	2646.6(6)	26.4(2)
F7	654.1(10)	5987.2(5)	-264.9(6)	23.6(2)
F4	5510.6(11)	6988.9(6)	4017.6(6)	29.4(2)
F3	7247.9(11)	7043.5(6)	3293.7(7)	31.2(3)
O2	4951.7(12)	5928.2(6)	1977.3(7)	18.2(2)
F1	6098.3(13)	8023.8(6)	3527.4(9)	38.9(3)
F6	-300.4(13)	6749.5(7)	514.9(9)	40.7(3)

A.2 ^{1}H and ^{13}C NMR Spectra

^{1}H NMR (DMSO-d6, 400 MHz)

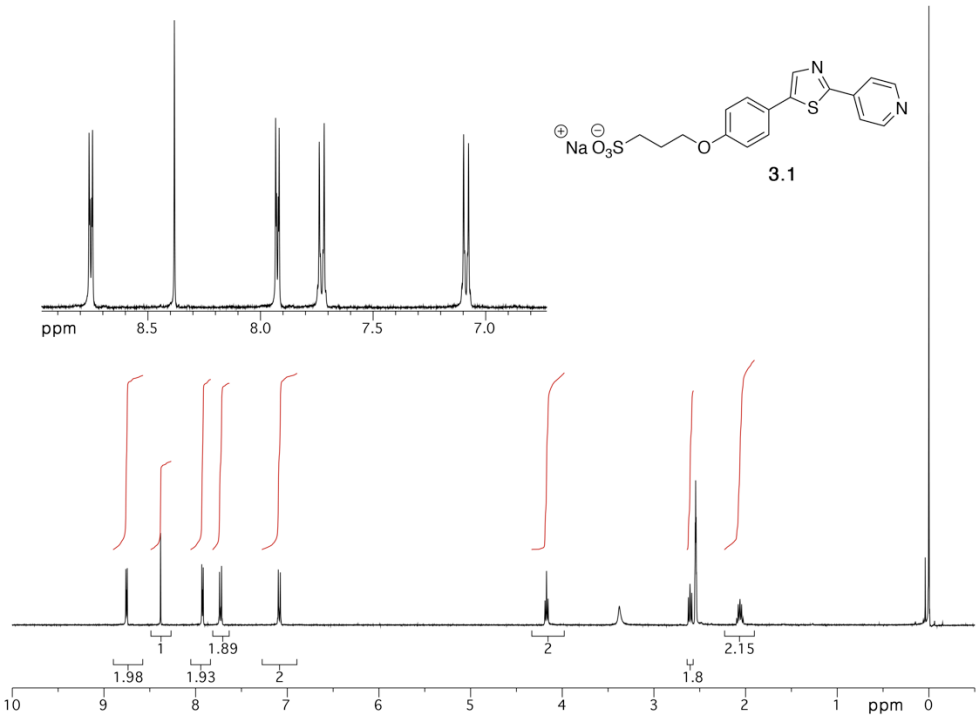

^{13}C NMR (DMSO-d6, 100 MHz)

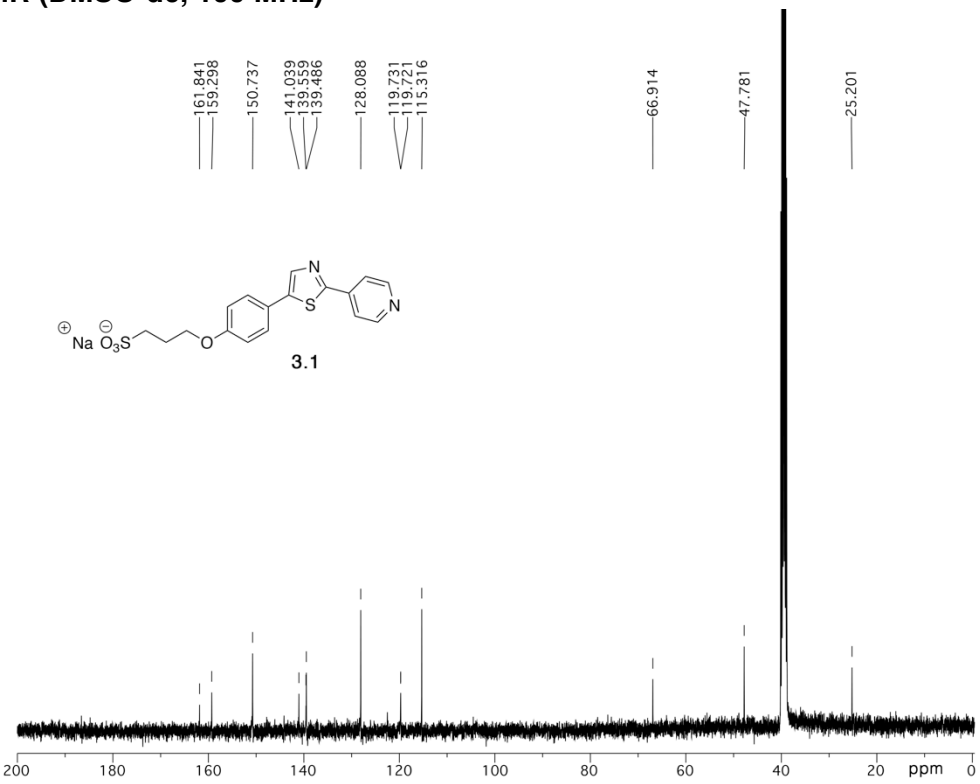

^{1}H NMR (DMSO-d6, 400 MHz)

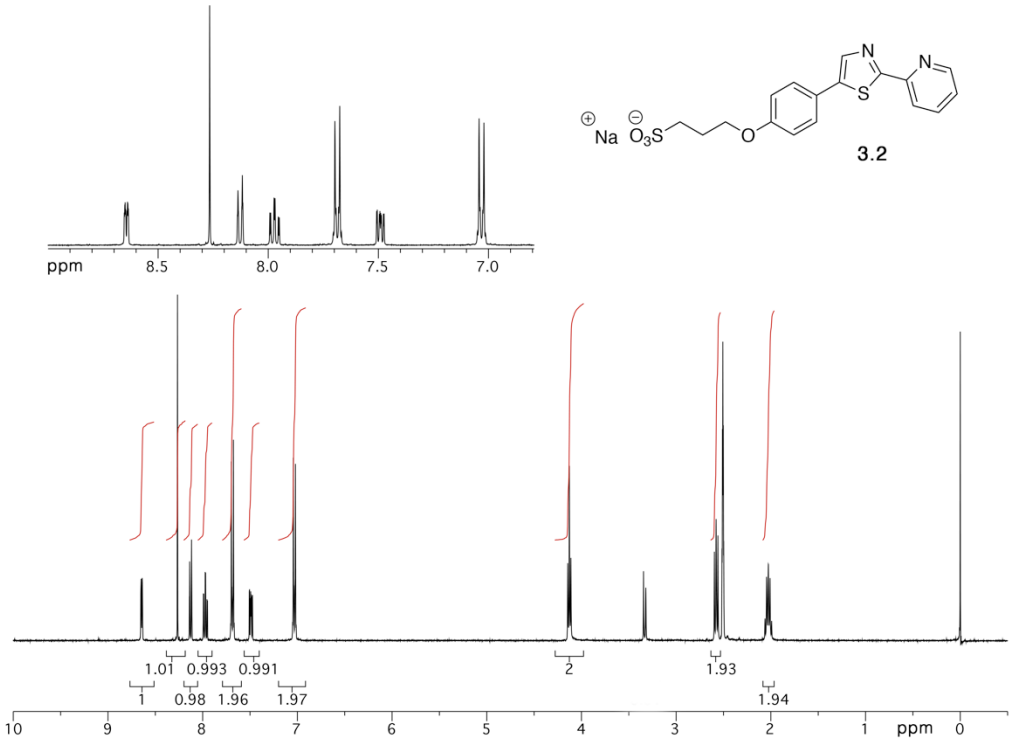

^{13}C NMR (DMSO-d6, 100 MHz)

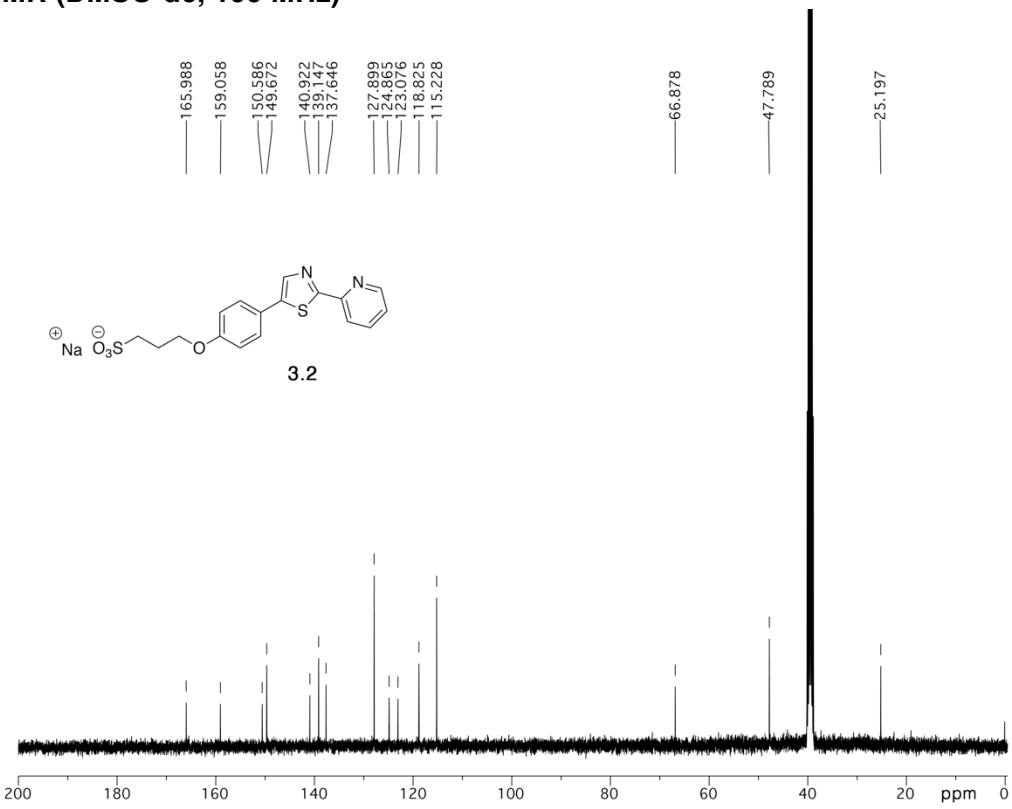

^{1}H NMR ($CDCl_3$, 400 MHz)

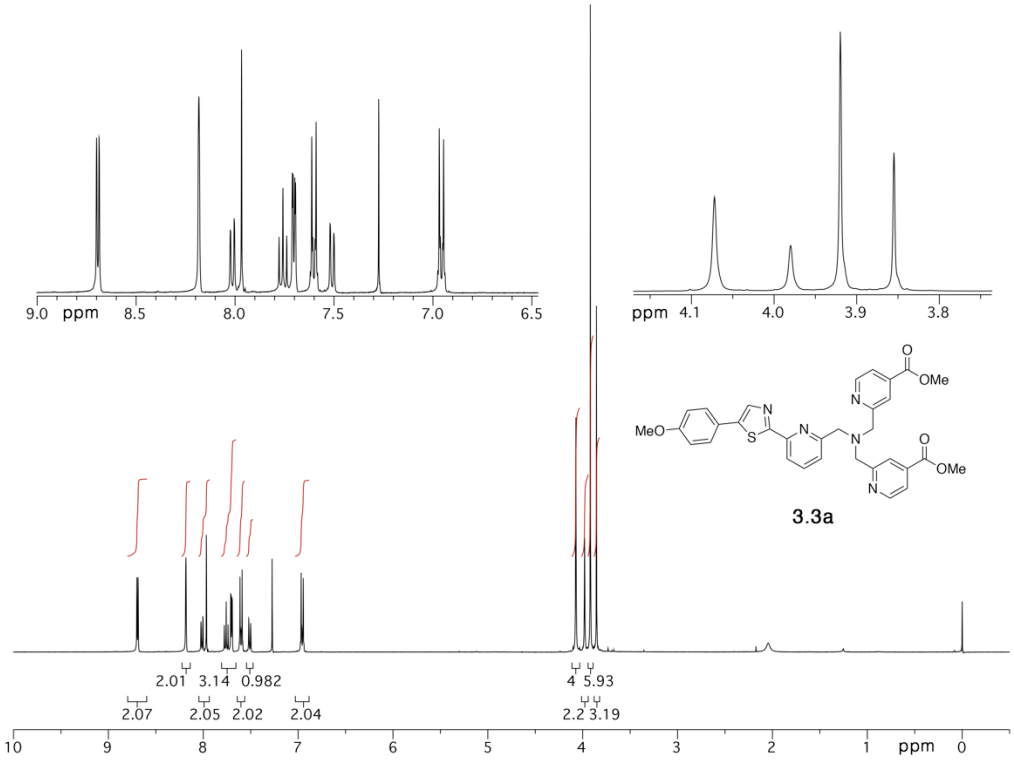

^{13}C NMR ($CDCl_3$, 100 MHz)

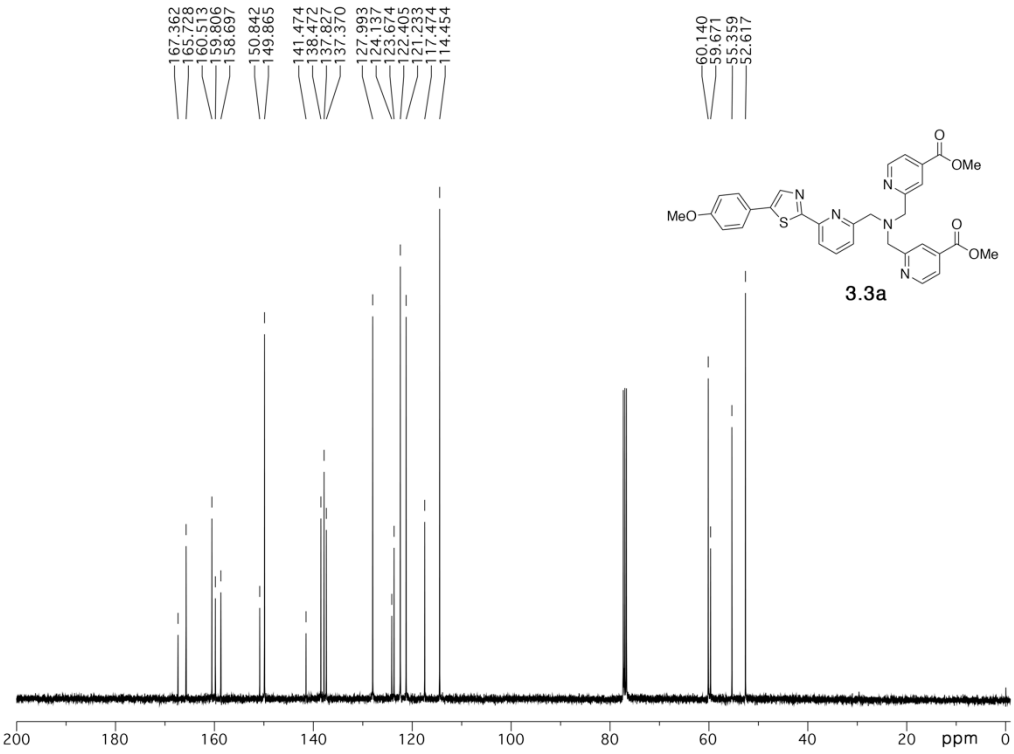

^{1}H NMR (MeOD, 400 MHz)

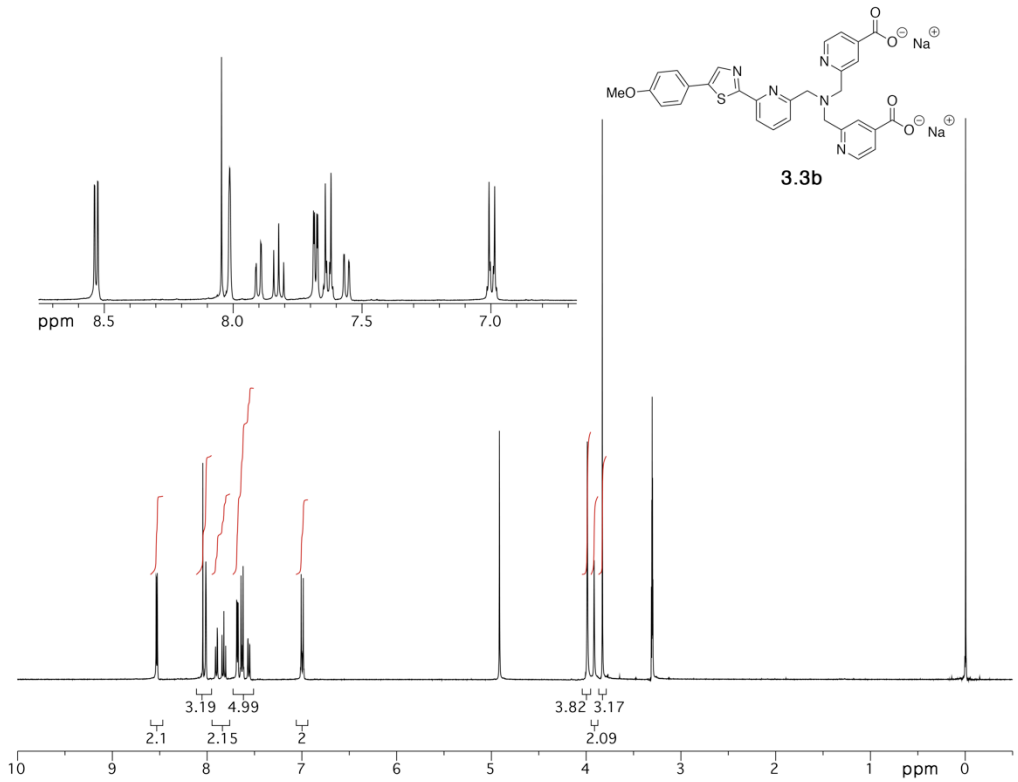

^{13}C NMR (MeOD, 100 MHz)

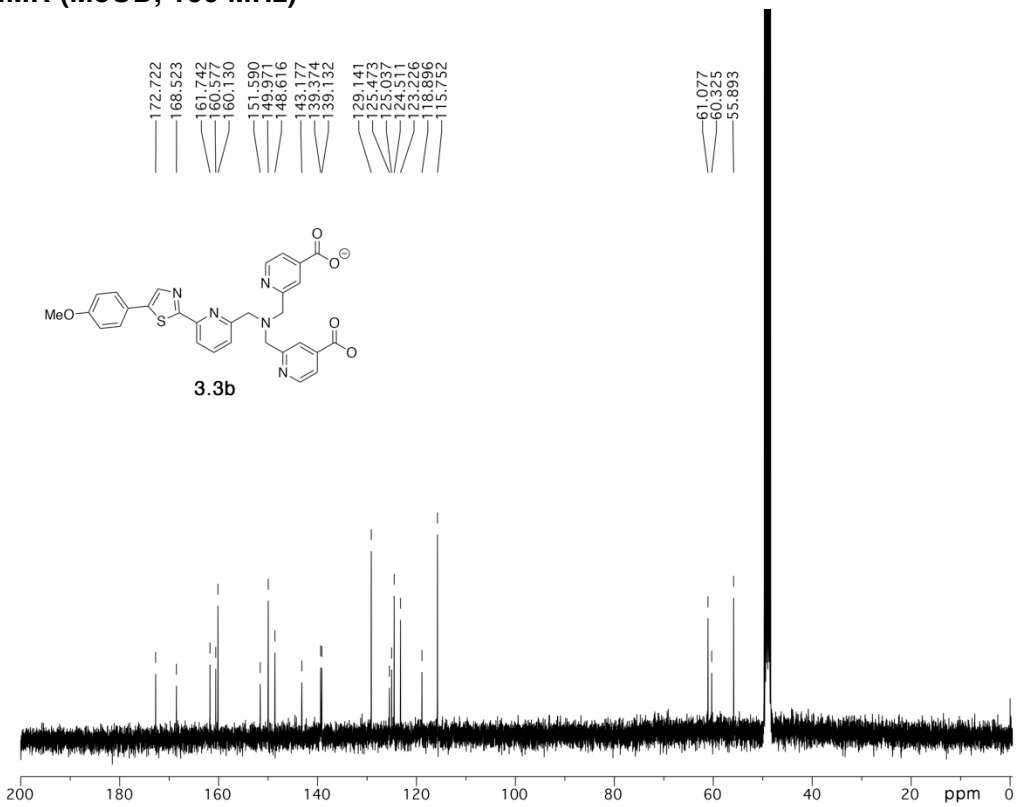

^{1}H NMR ($CDCl_3$, 400 MHz)

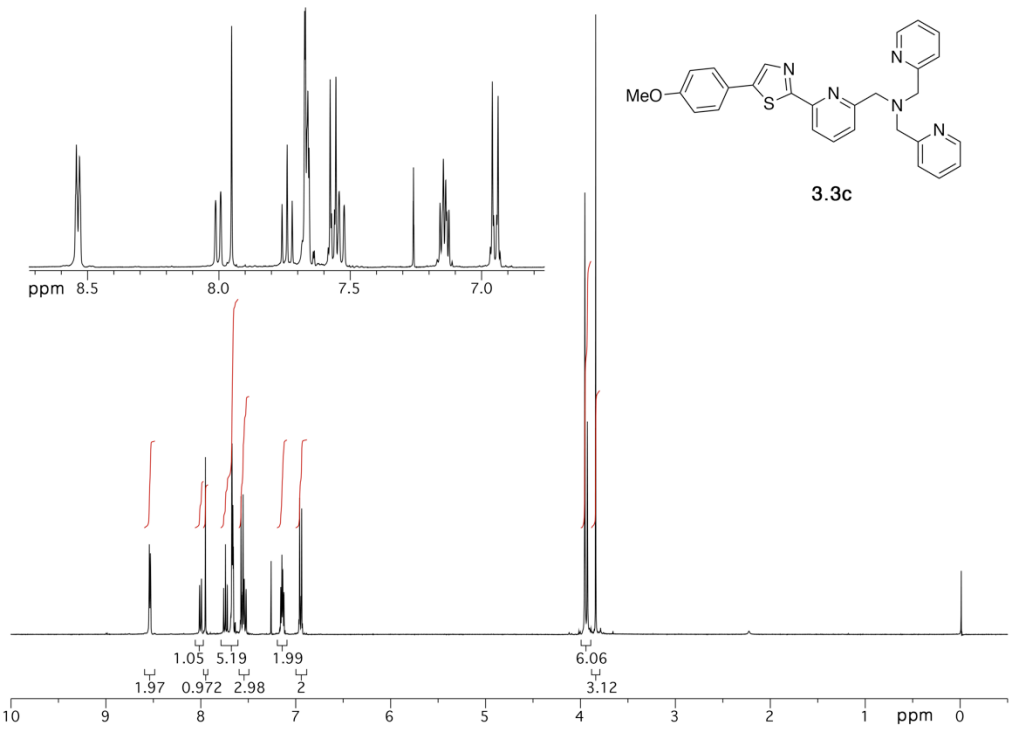

^{13}C NMR ($CDCl_3$, 100 MHz)

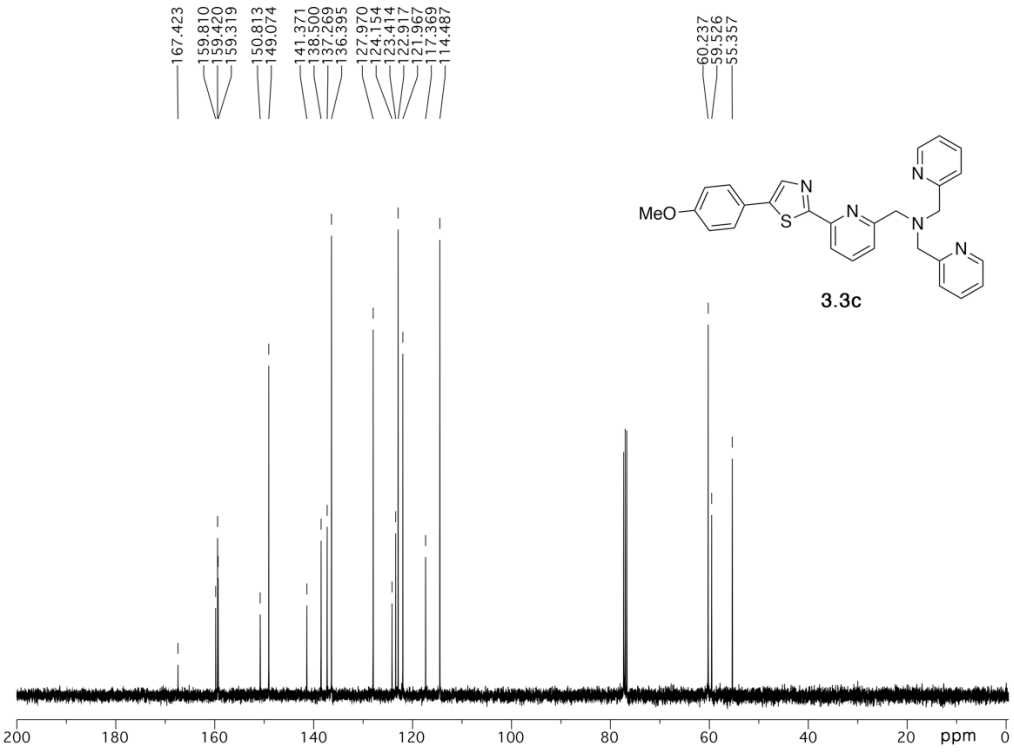

^{1}H NMR ($CDCl_3$, 400 MHz)

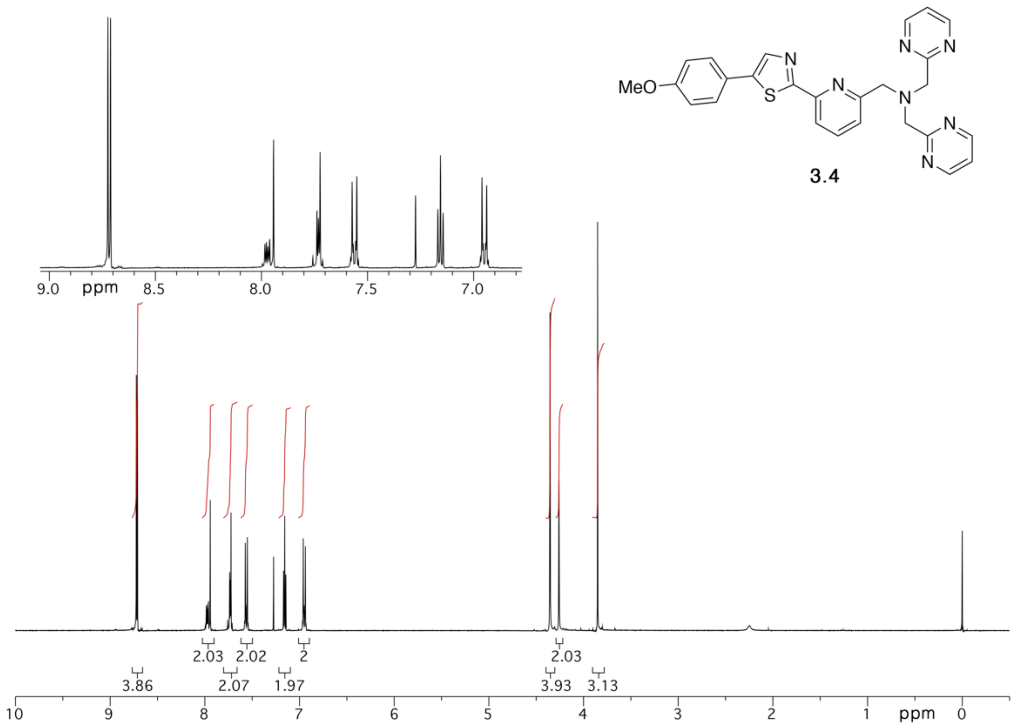

^{13}C NMR ($CDCl_3$, 100 MHz)

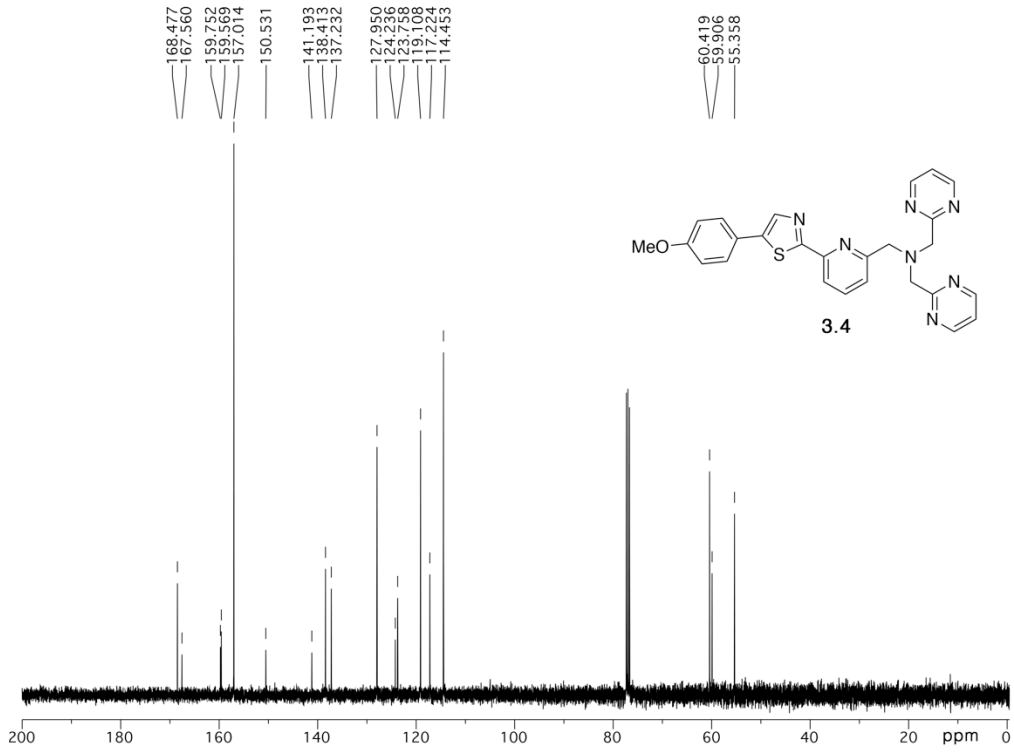

^{1}H NMR ($CDCl_3$, 400 MHz)

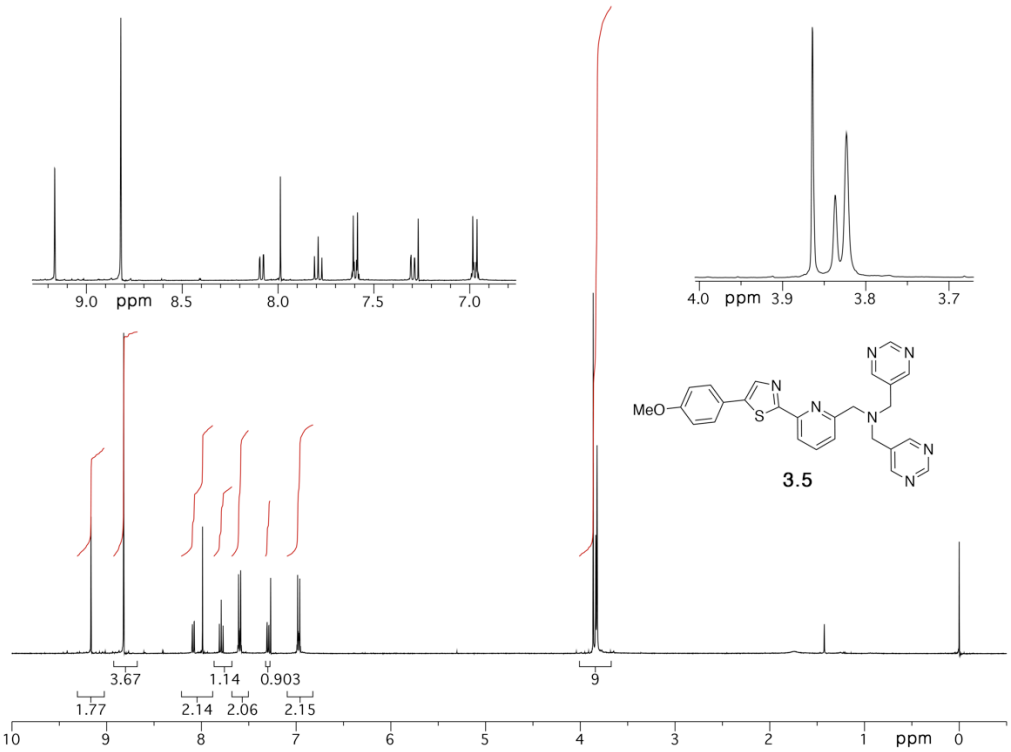

^{13}C NMR ($CDCl_3$, 100 MHz)

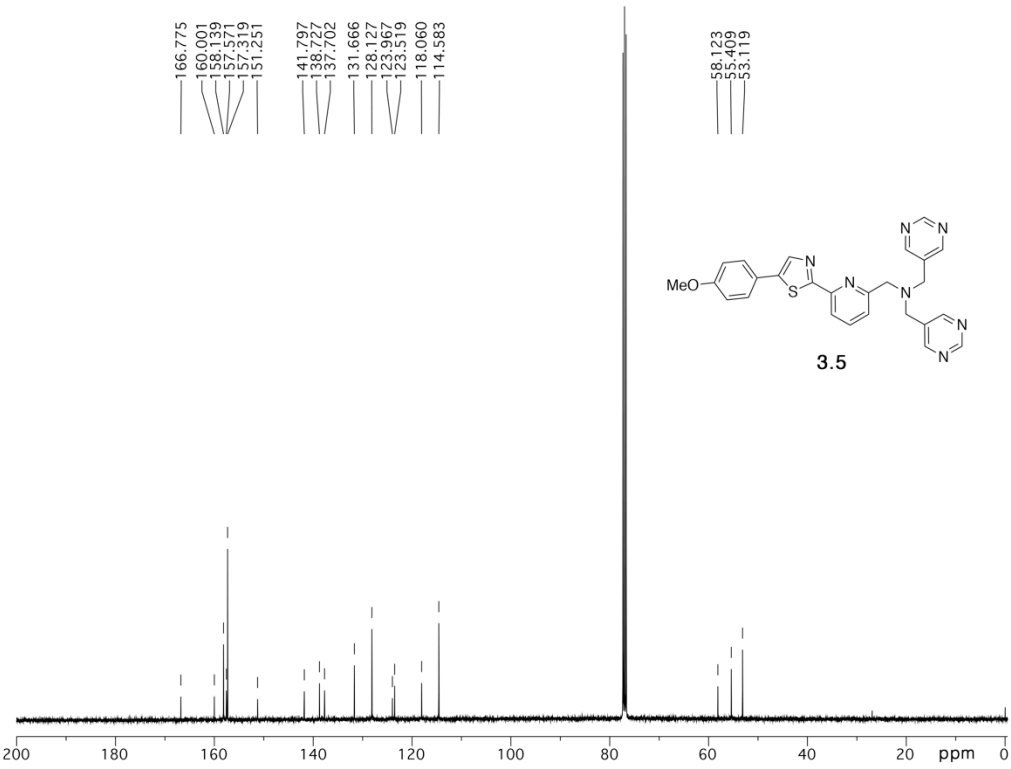

^{1}H NMR ($CDCl_3$, 400 MHz)

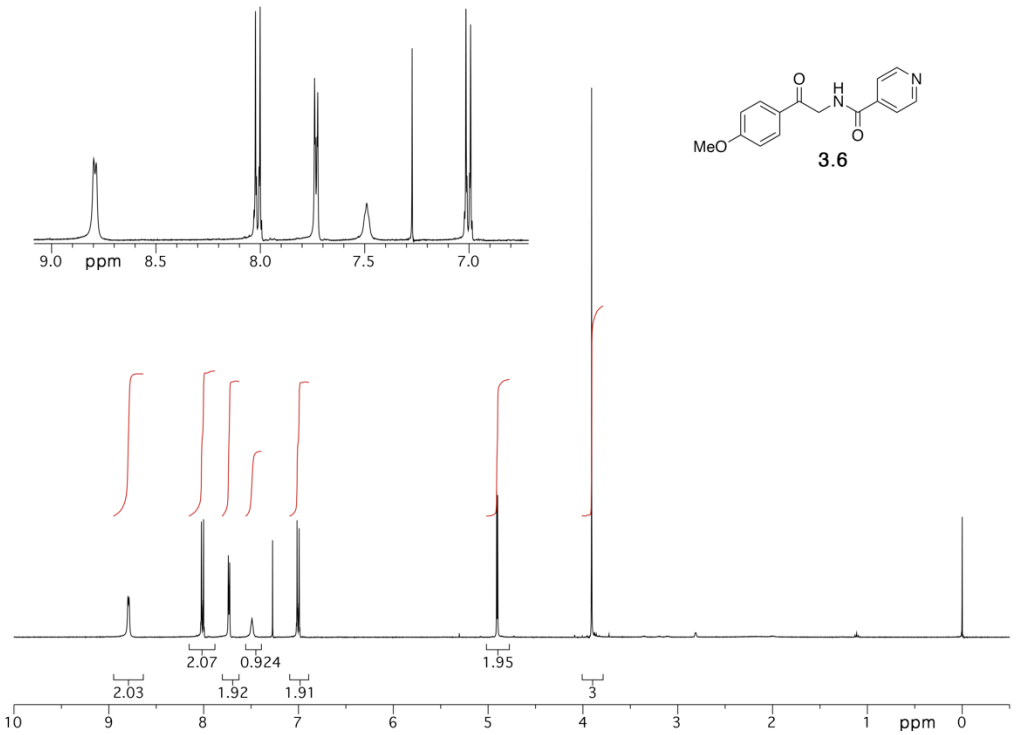

^{13}C NMR ($CDCl_3$, 100 MHz)

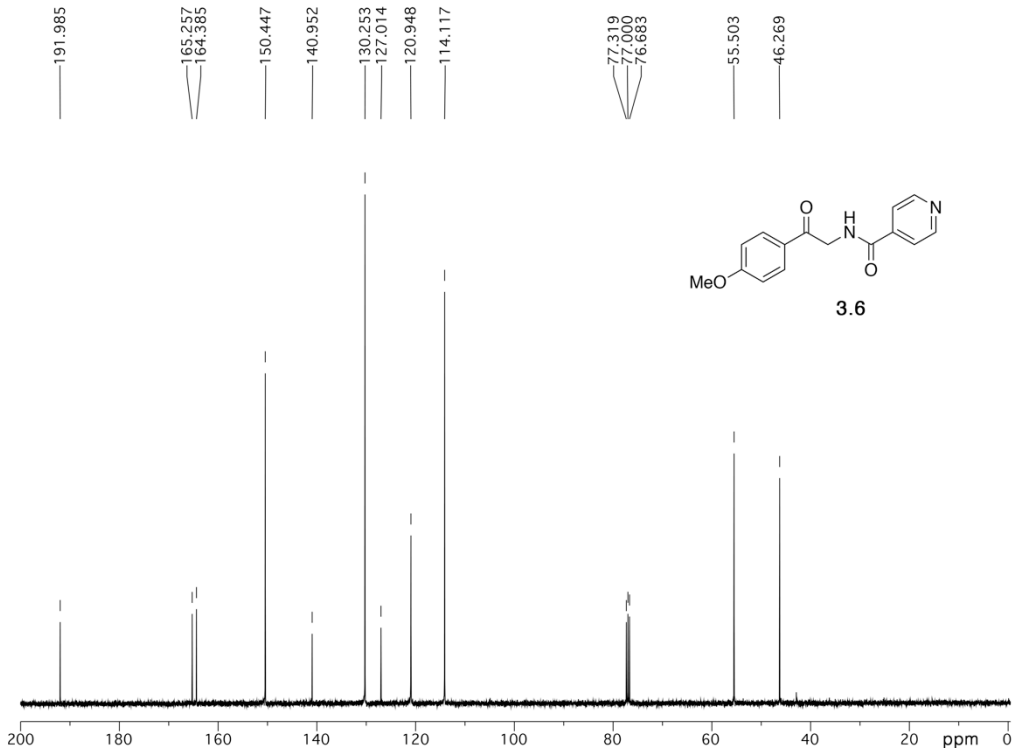

^{1}H NMR ($CDCl_3$, 400 MHz)

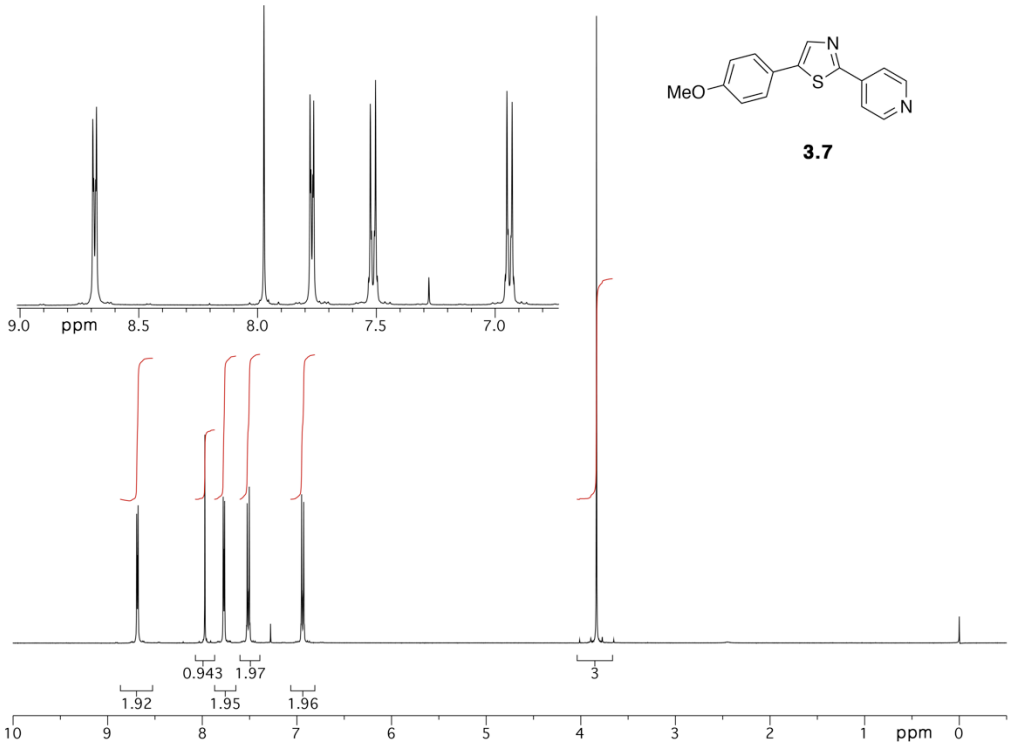

^{13}C NMR ($CDCl_3$, 100 MHz)

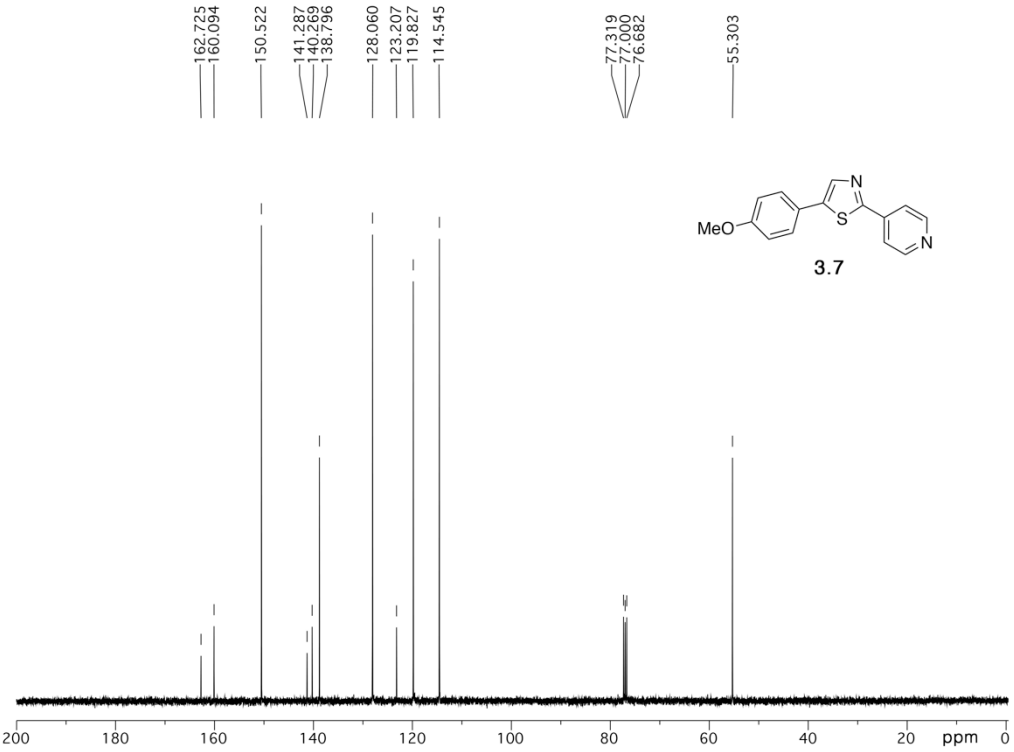

^{1}H NMR (DMSO-d6, 400 MHz)

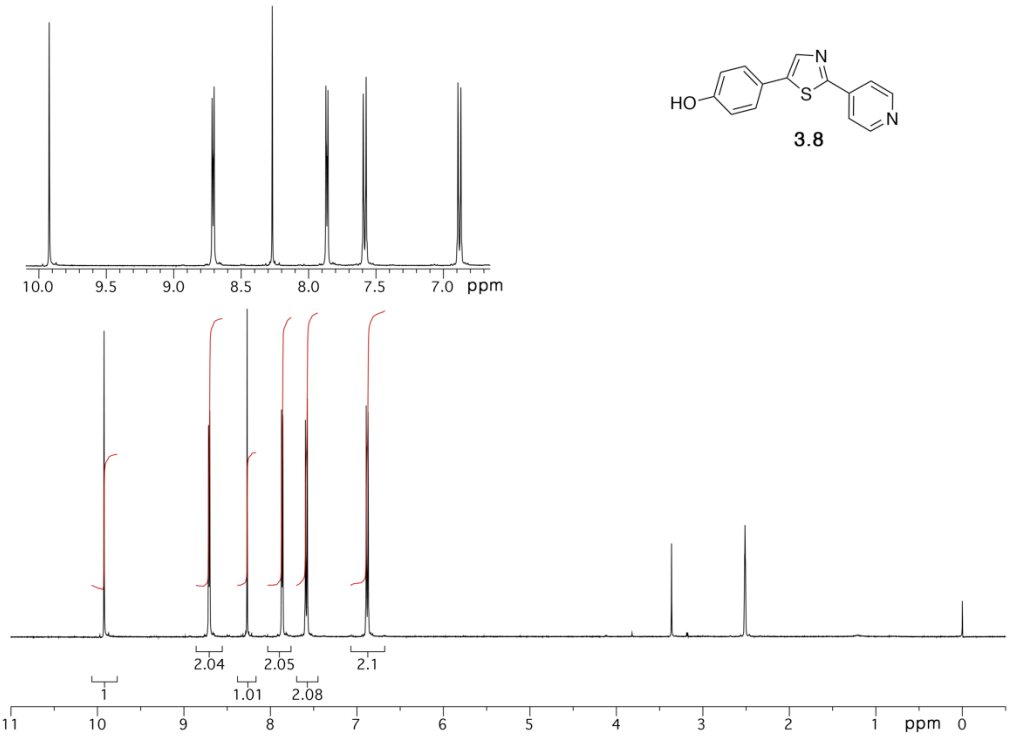

^{13}C NMR (DMSO-d6, 100 MHz)

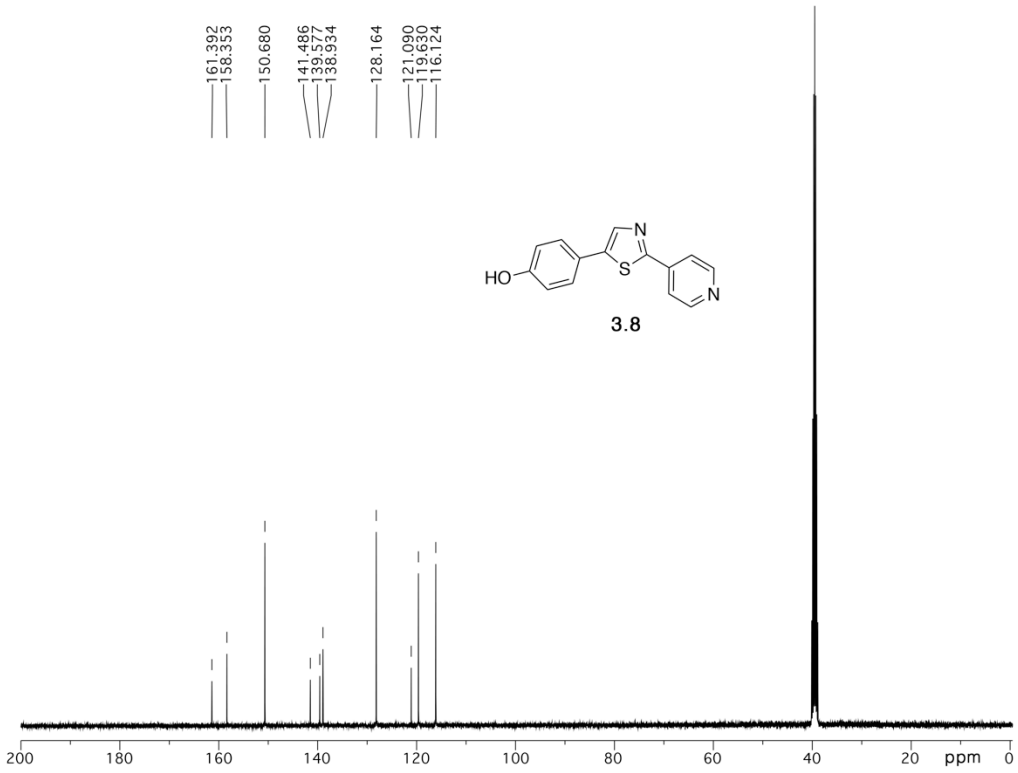

^{1}H NMR ($CDCl_3$, 400 MHz)

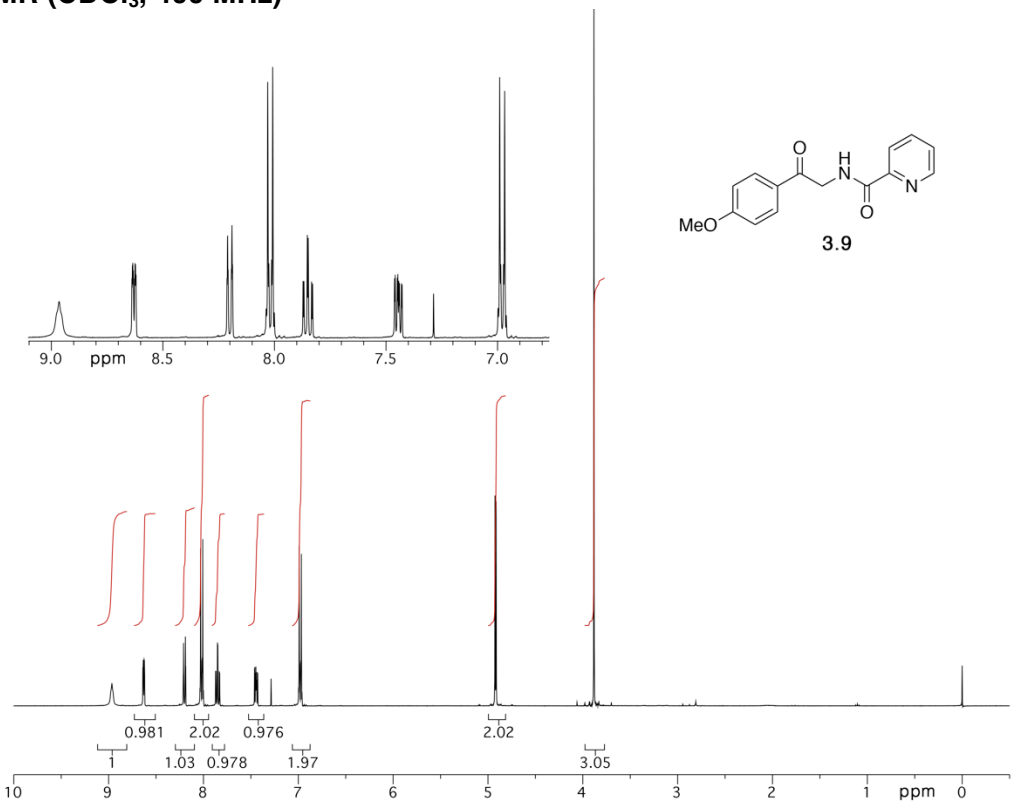

^{13}C NMR ($CDCl_3$, 100 MHz)

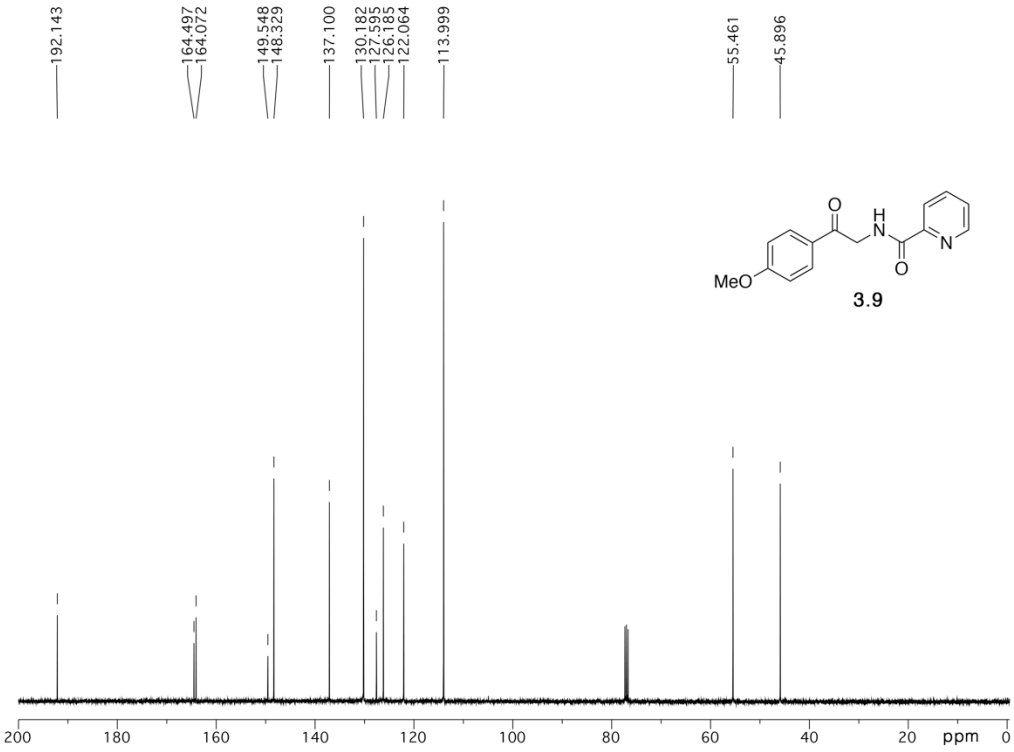

^{1}H NMR ($CDCl_3$, 400 MHz)

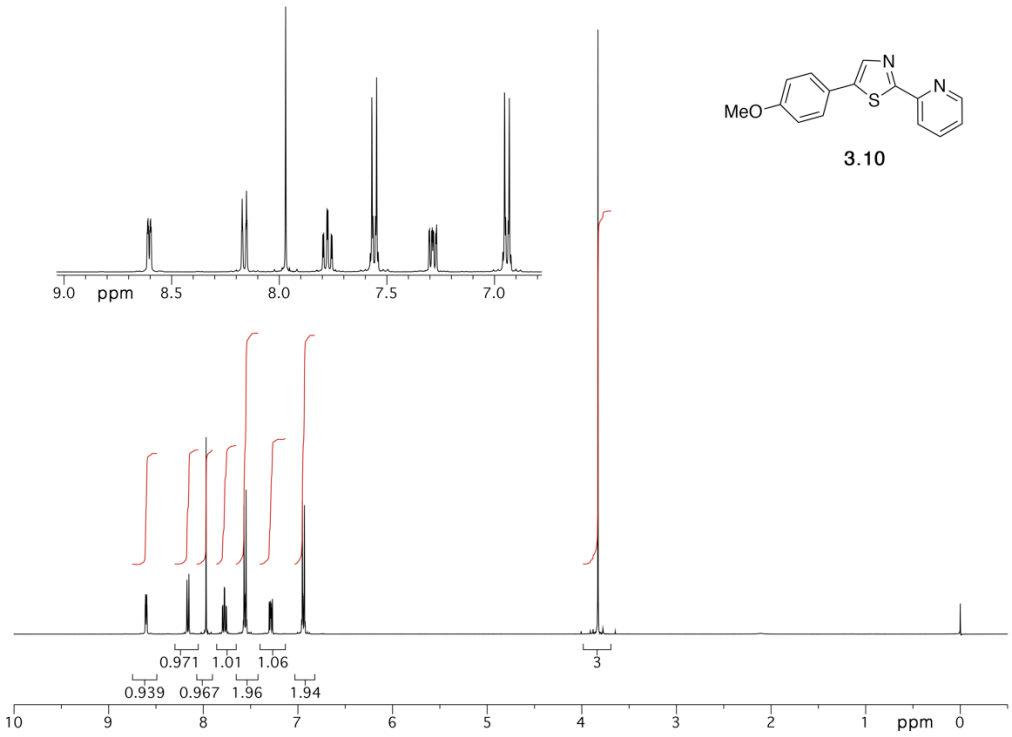

^{13}C NMR ($CDCl_3$, 100 MHz)

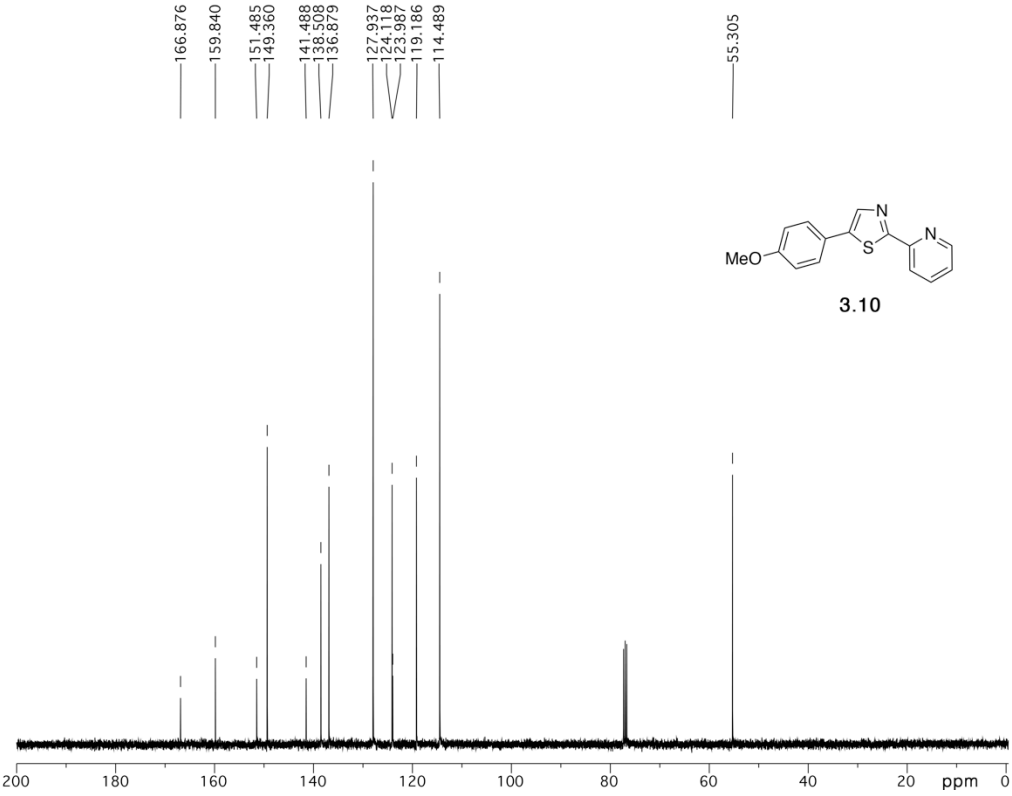

^{1}H NMR (MeOD, 400 MHz)

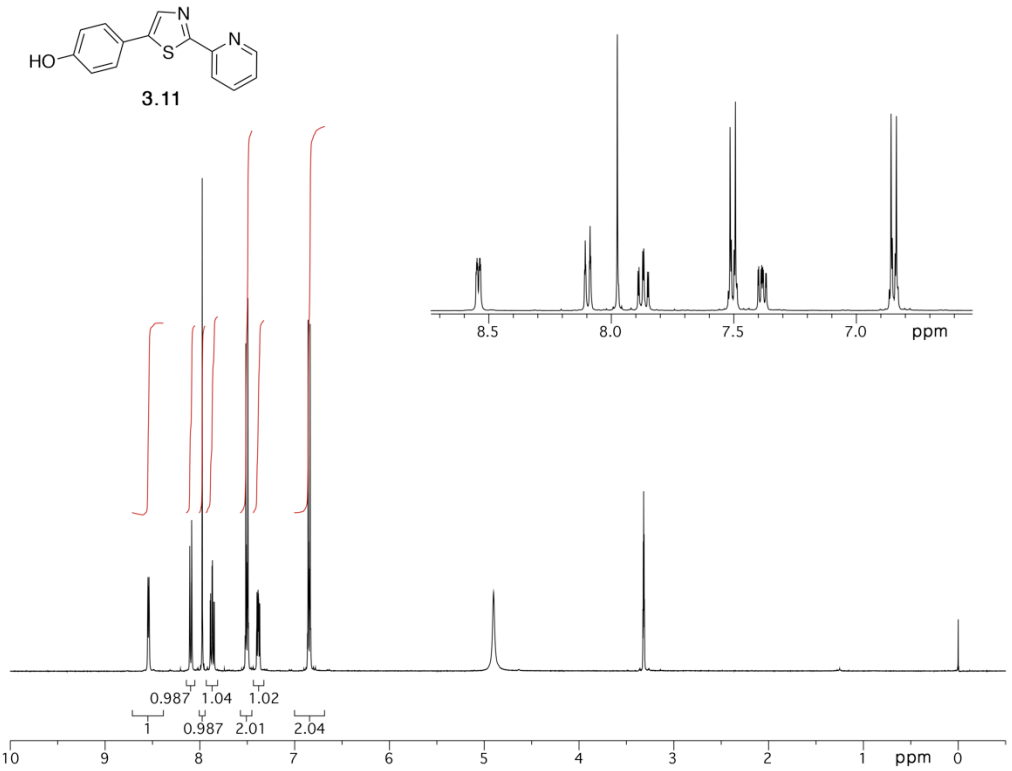

^{13}C NMR (MeOD, 100 MHz)

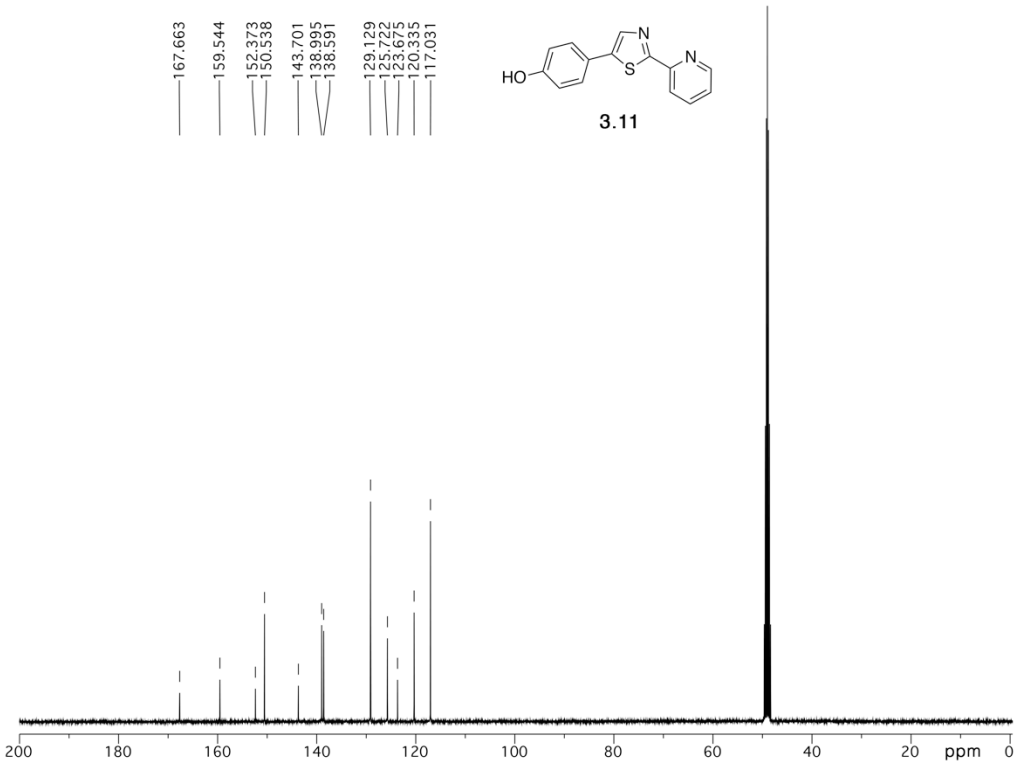

^{1}H NMR ($CDCl_3$, 400 MHz)

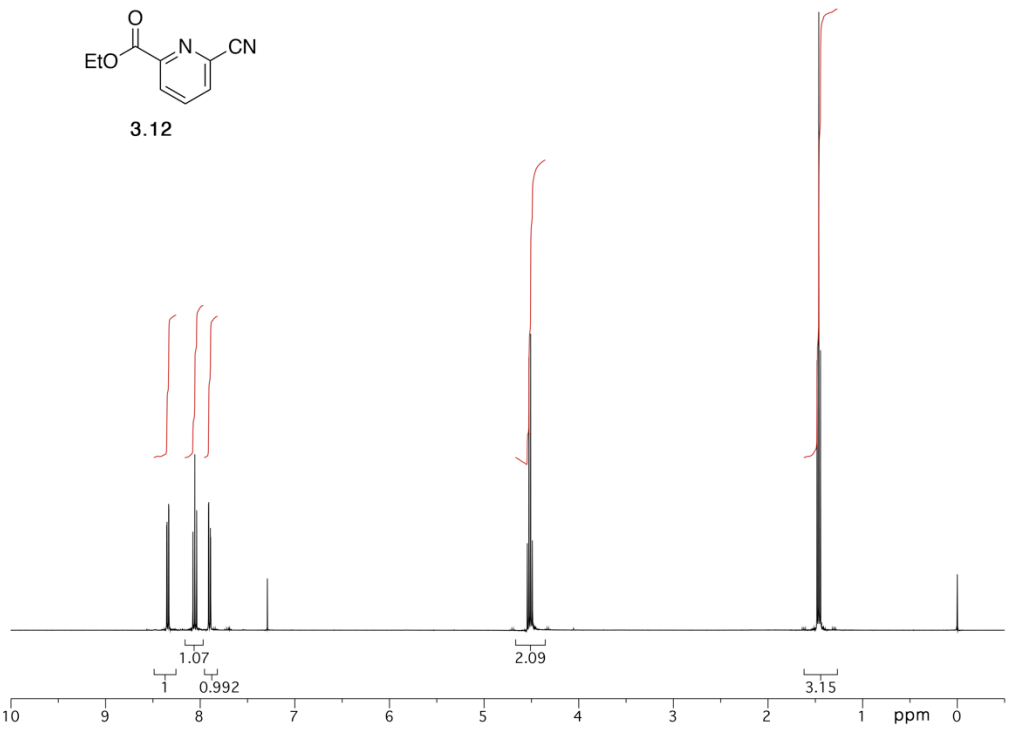

^{13}C NMR ($CDCl_3$, 100 MHz)

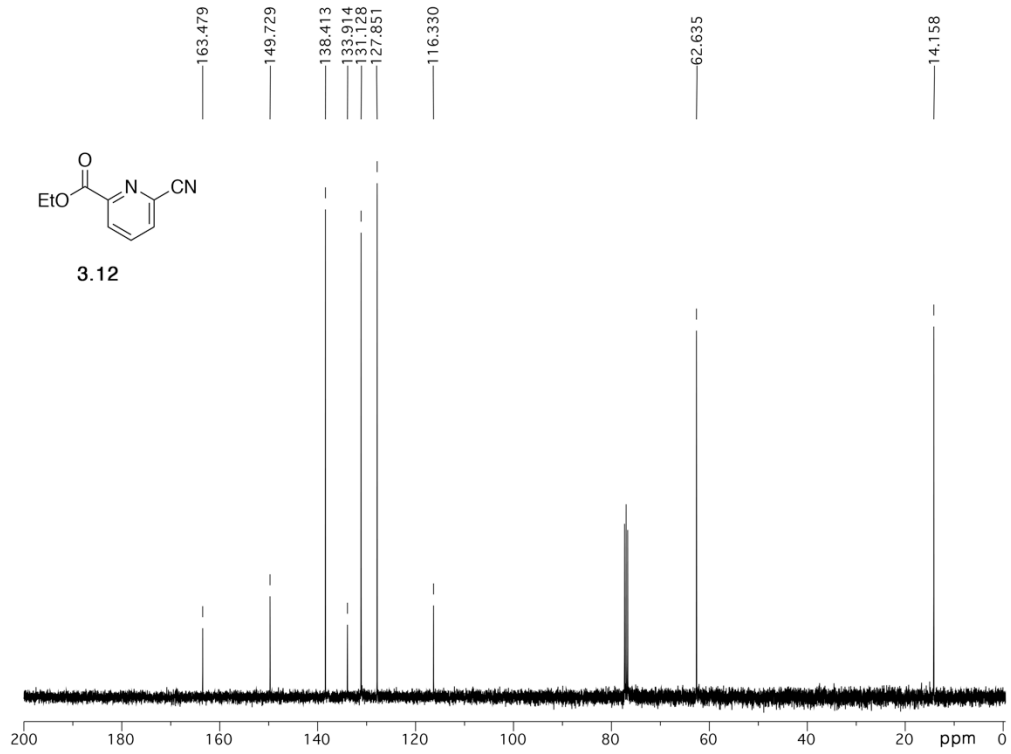

^{1}H NMR (Acetone-d6, 400 MHz)

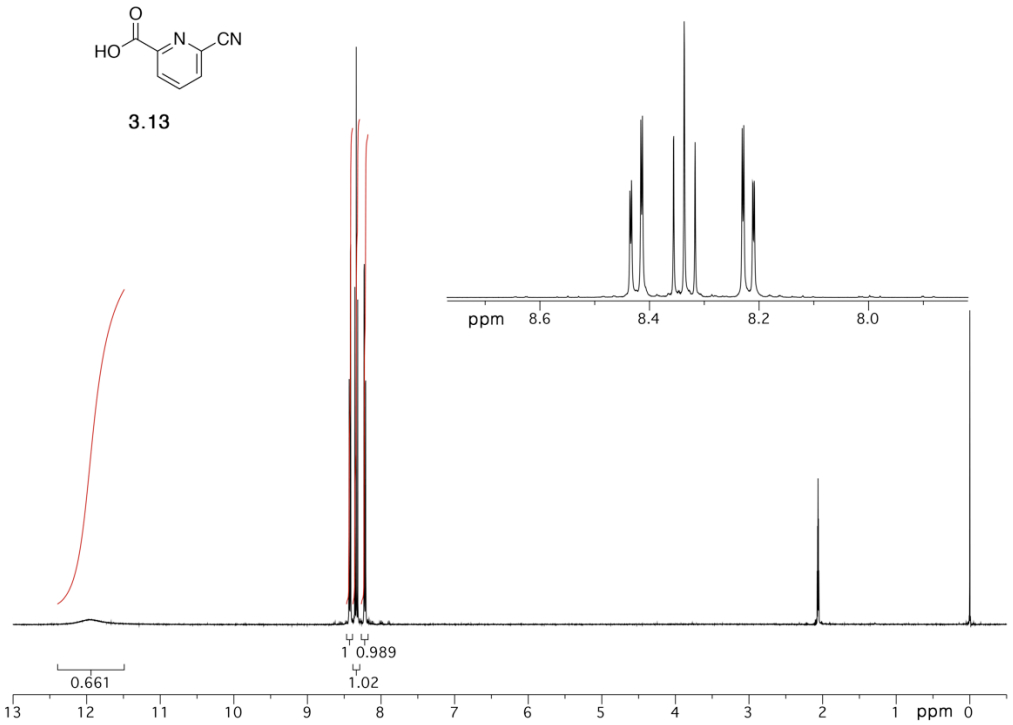

^{13}C NMR (Acetone-d6, 100 MHz)

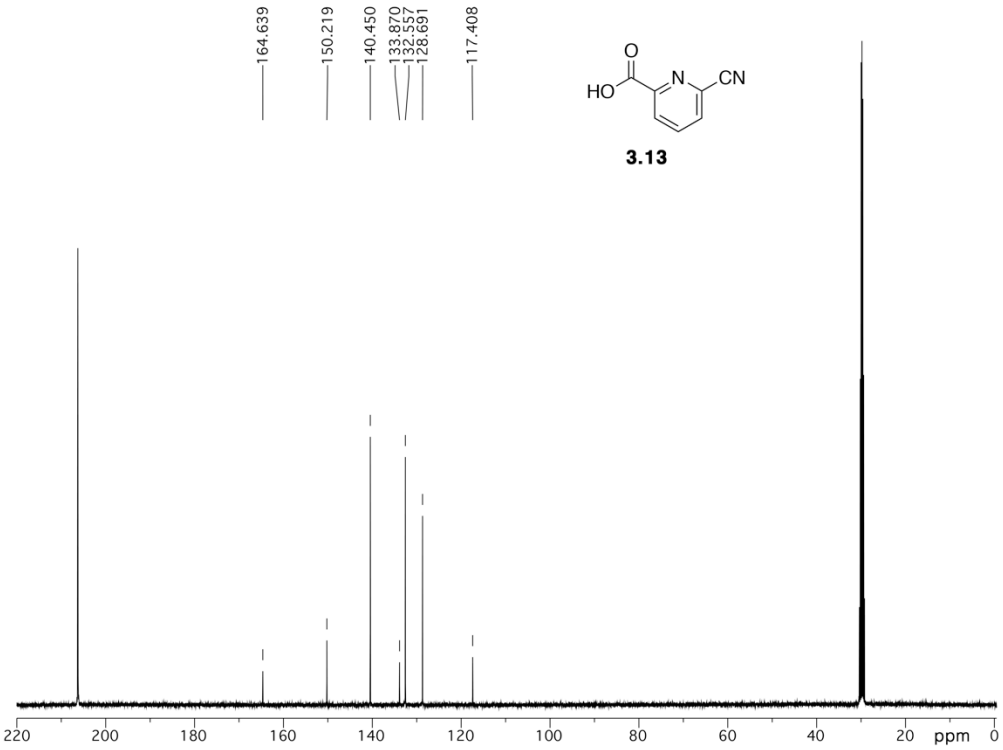

^{1}H NMR ($CDCl_3$, 400 MHz)

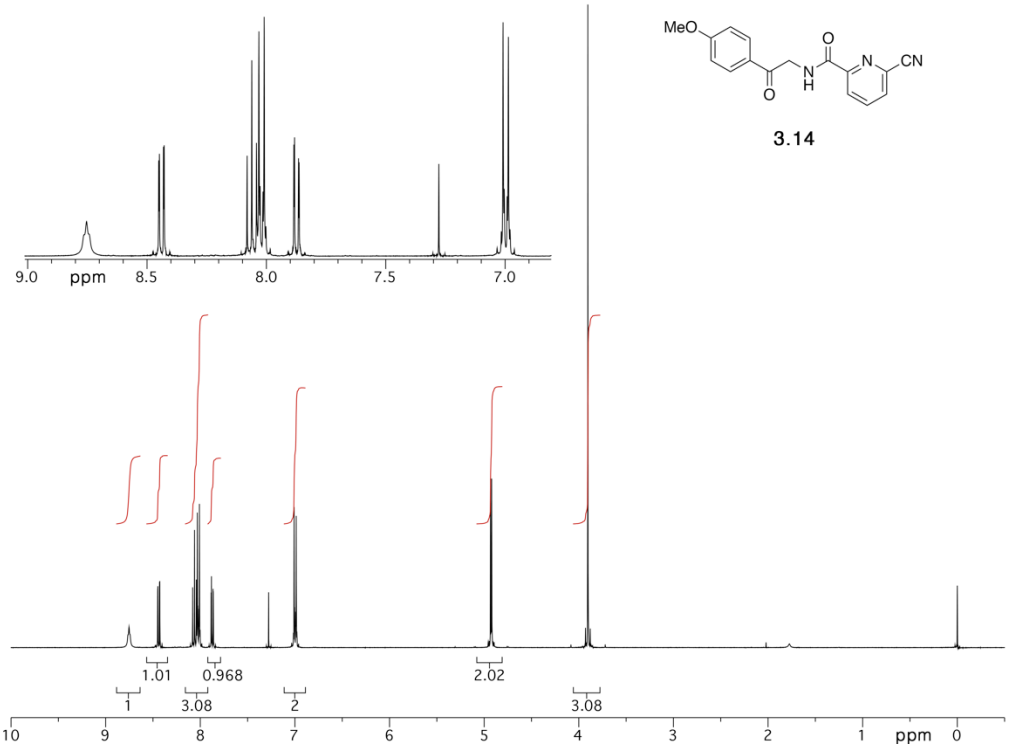

^{13}C NMR ($CDCl_3$, 100 MHz)

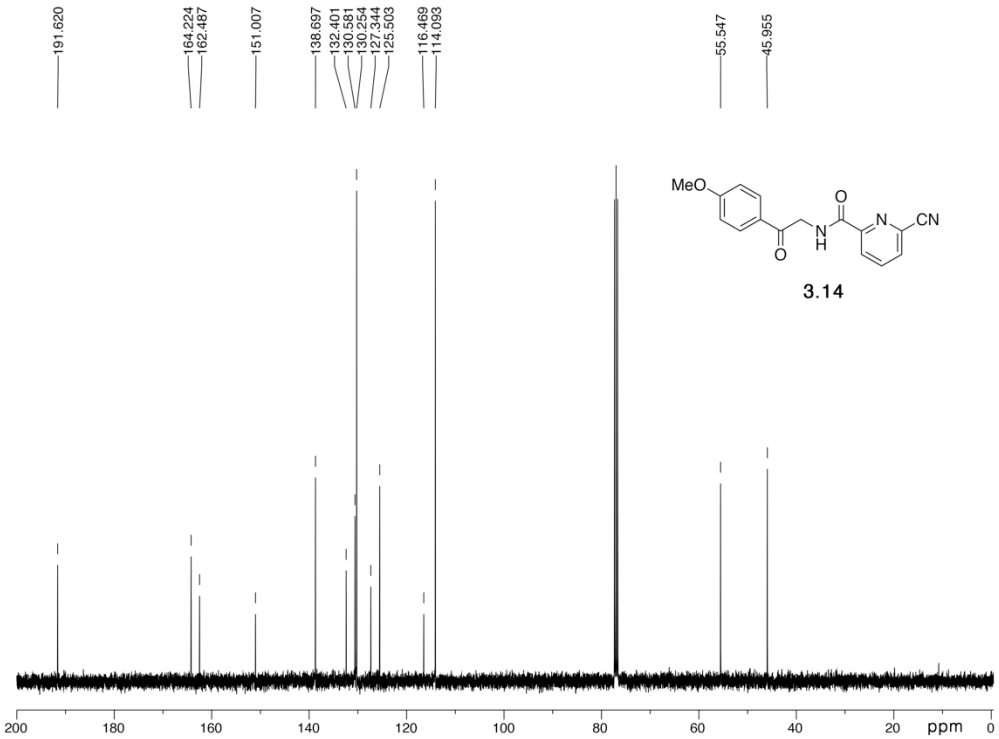

^{1}H NMR ($CDCl_3$, 400 MHz)

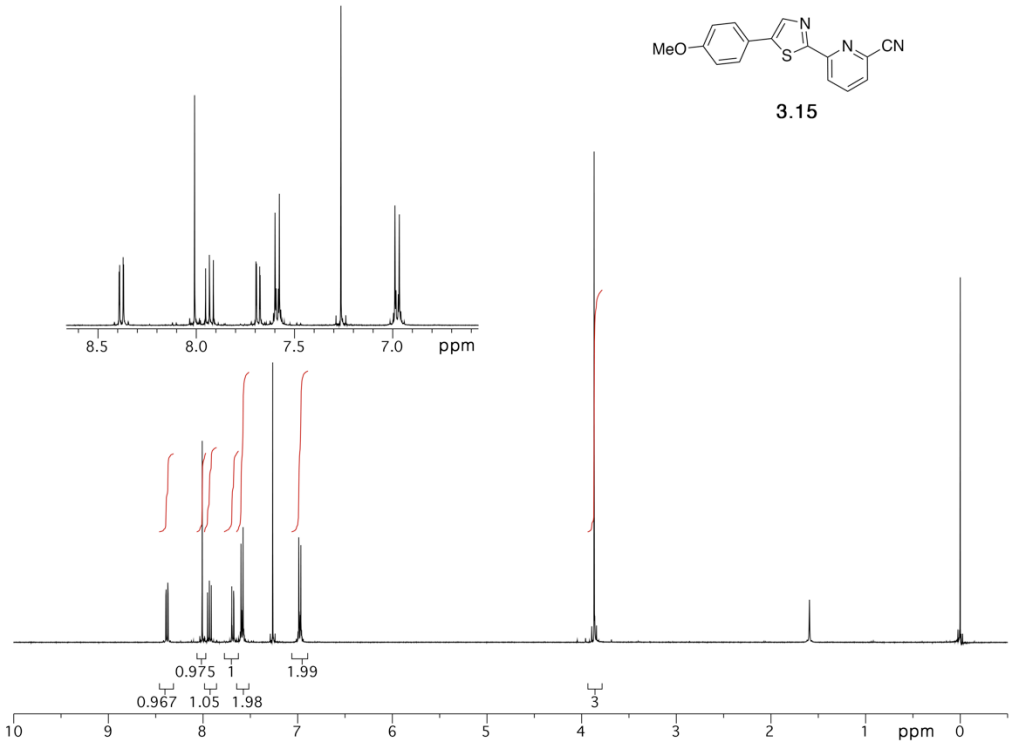

^{13}C NMR ($CDCl_3$, 100 MHz)

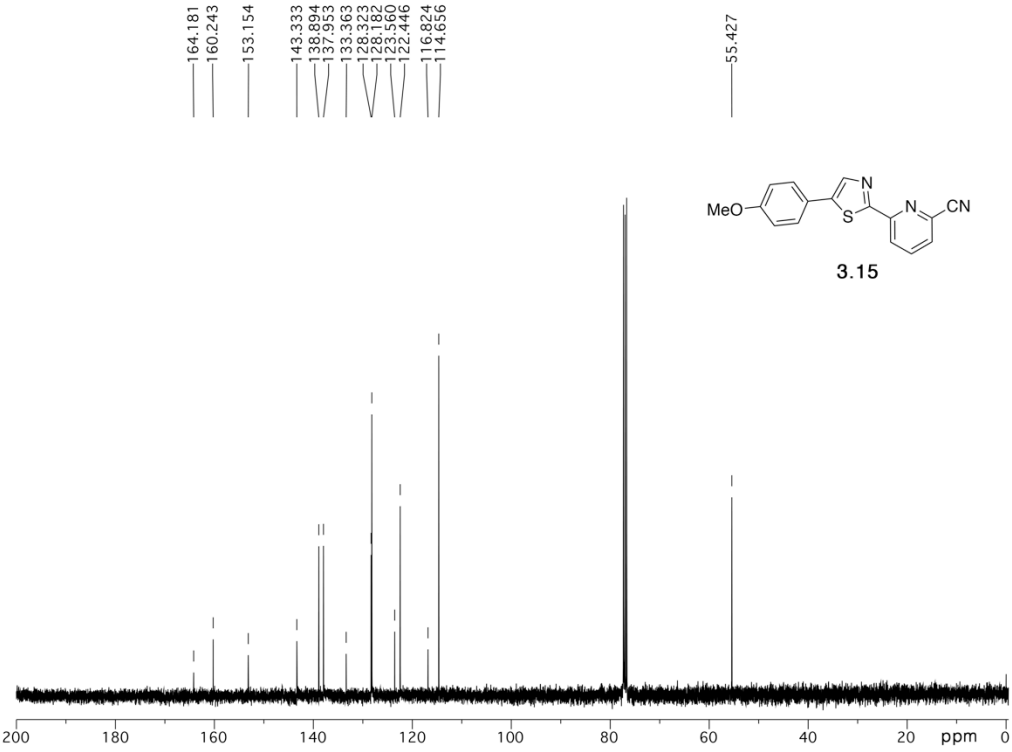

^{1}H NMR ($CDCl_3$, 400 MHz)

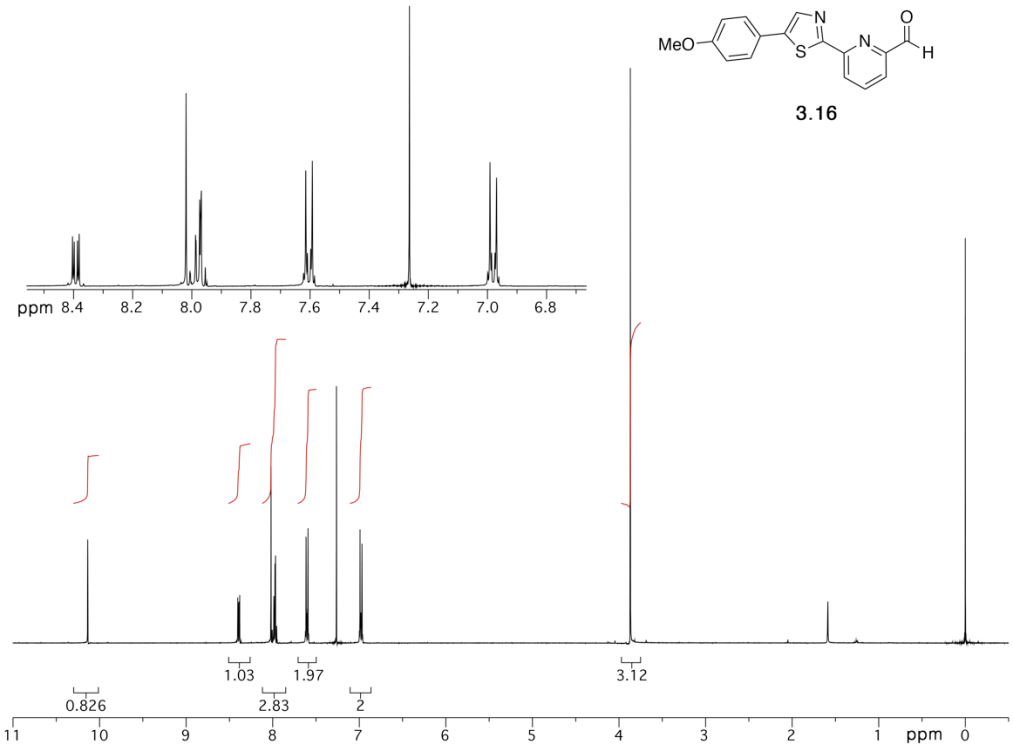

^{13}C NMR ($CDCl_3$, 100 MHz)

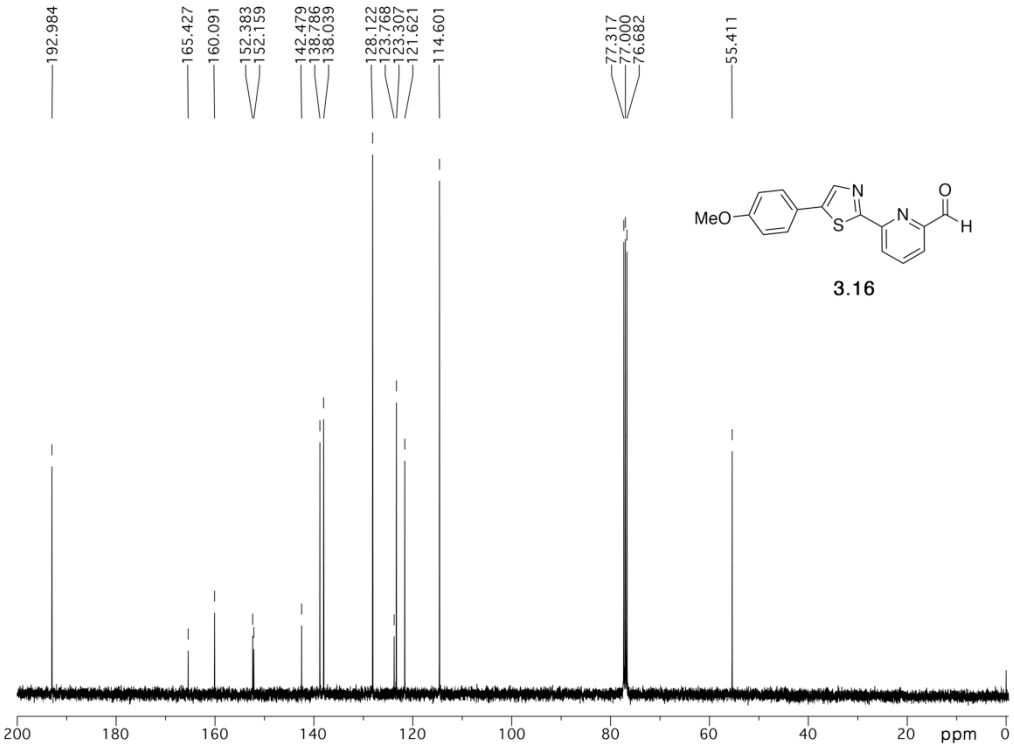

^{1}H NMR (D_2O, 400 MHz)

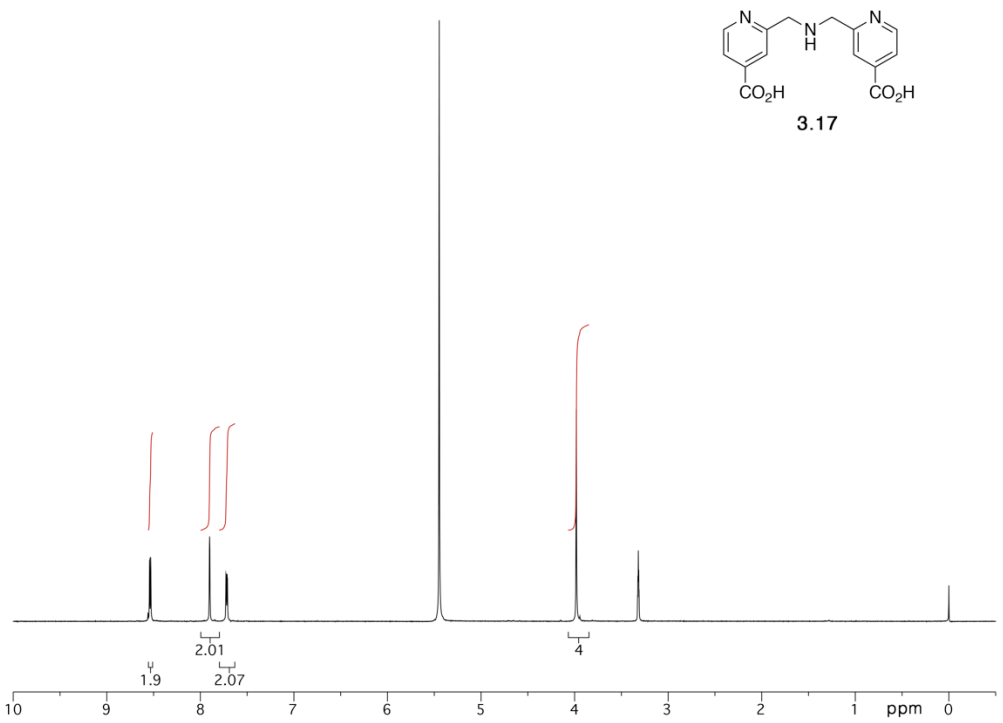

^{13}C NMR (D_2O, 100 MHz)

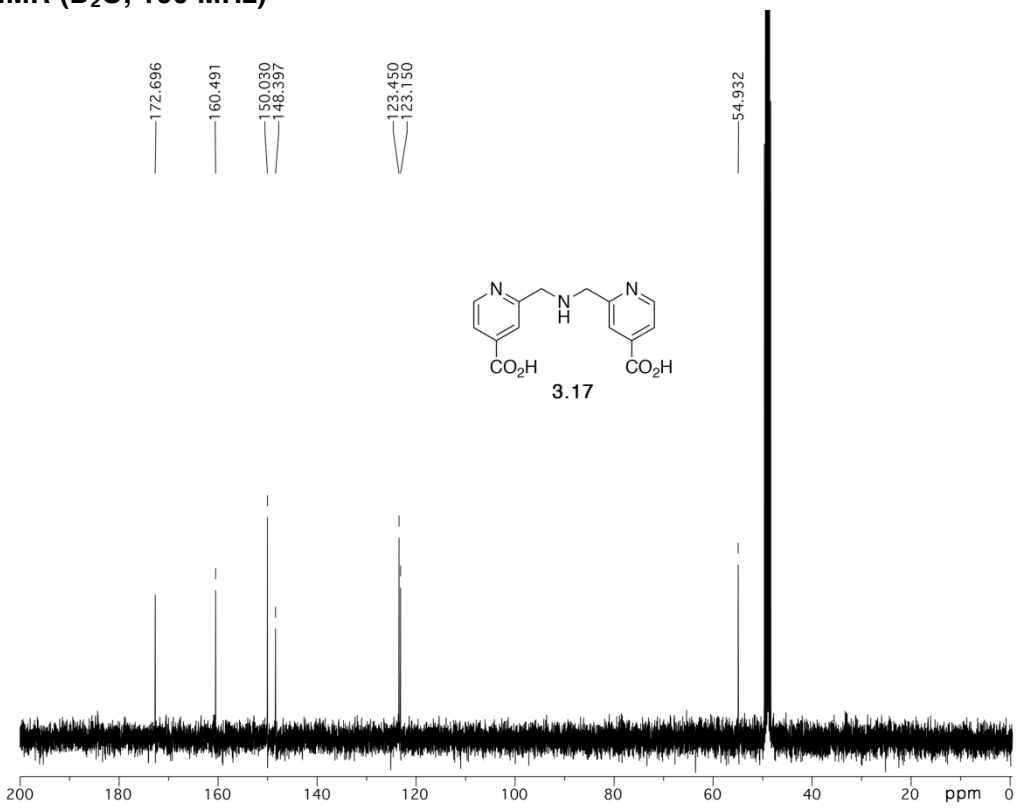

^{1}H NMR ($CDCl_3$, 400 MHz)

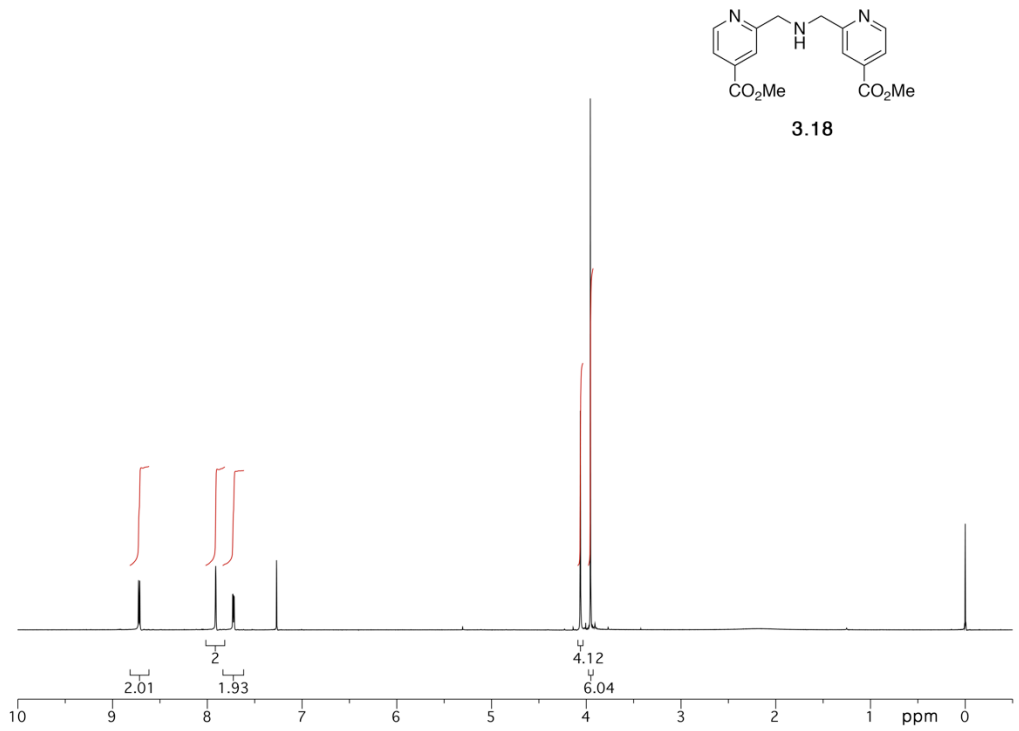

^{13}C NMR ($CDCl_3$, 100 MHz)

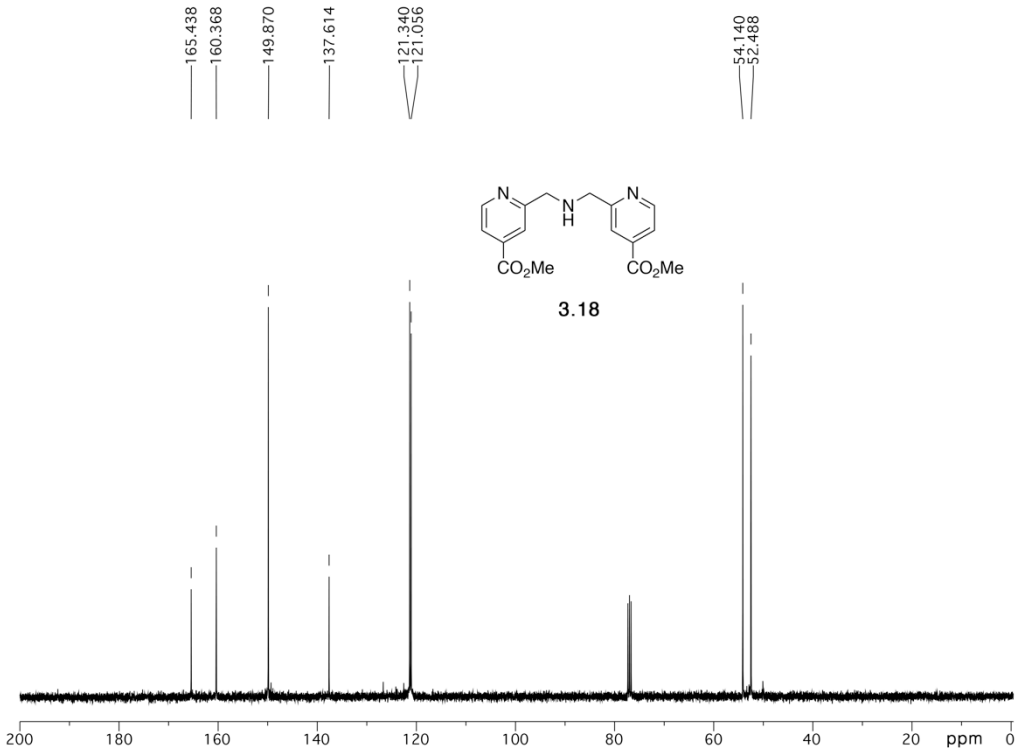

^{1}H NMR (D_2O, 400 MHz)

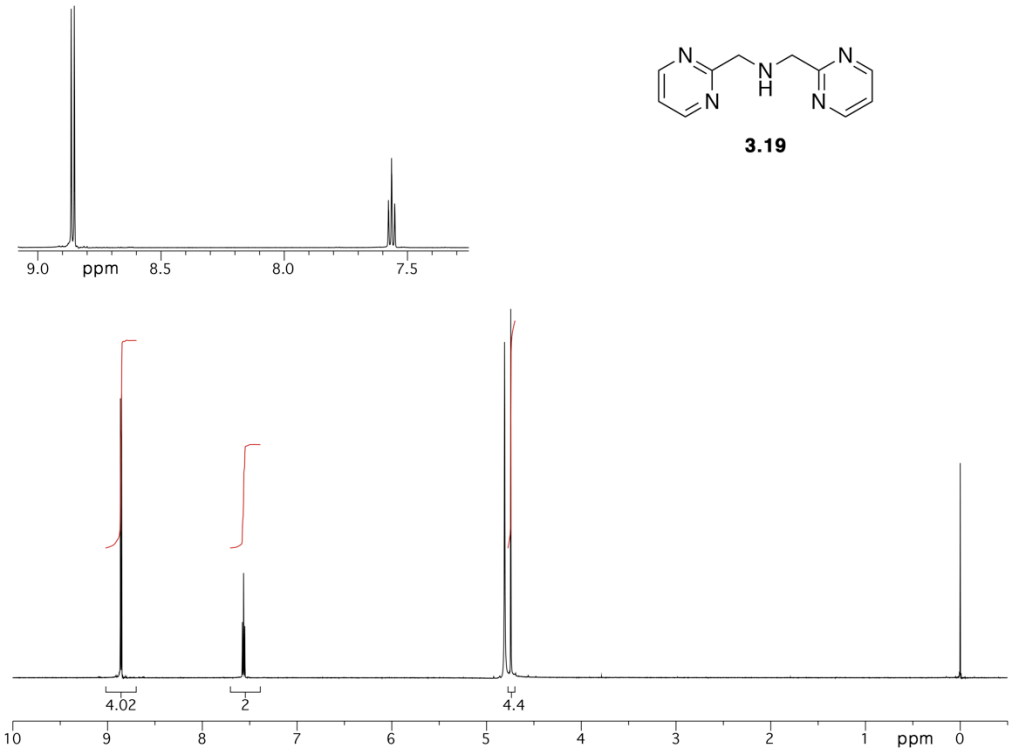

^{13}C NMR (D_2O, 100 MHz)

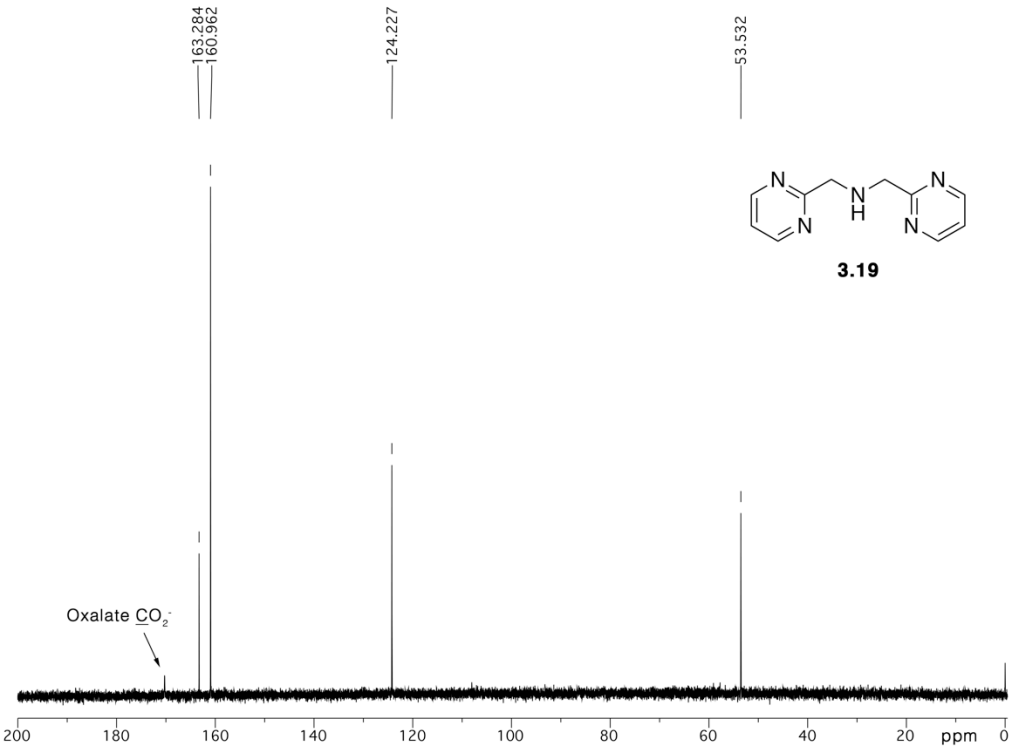

^{1}H NMR ($CDCl_3$, 400 MHz)

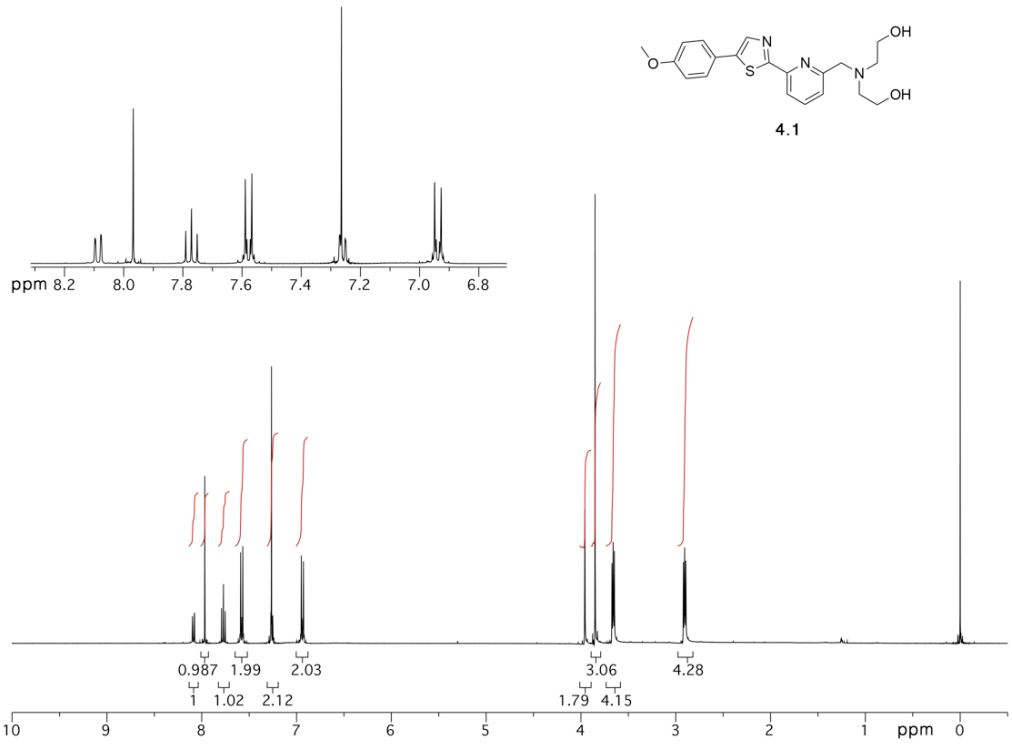

^{13}C NMR ($CDCl_3$, 100 MHz)

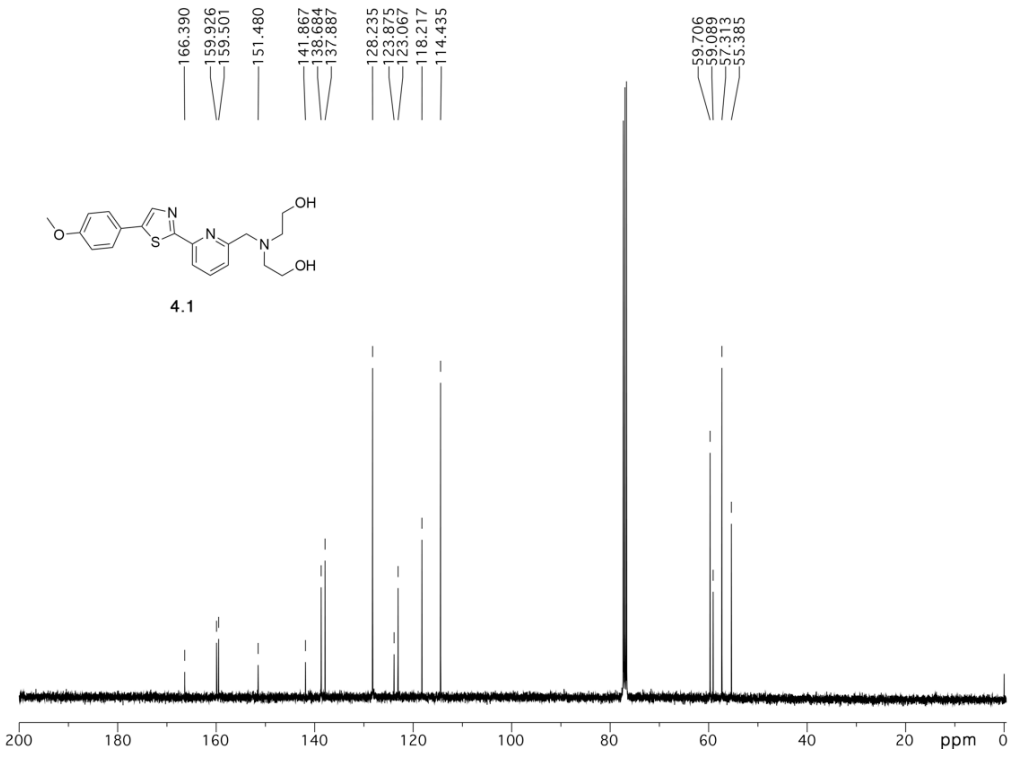

^{1}H NMR ($CDCl_3$, 400 MHz)

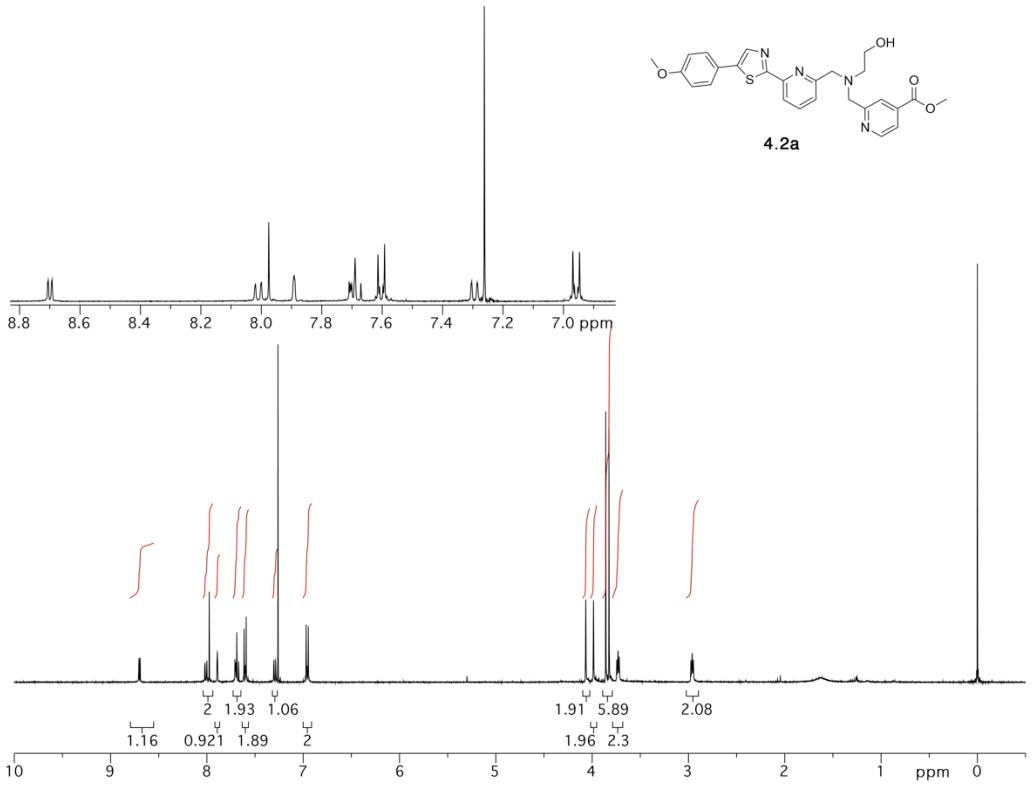

^{13}C NMR ($CDCl_3$, 100 MHz)

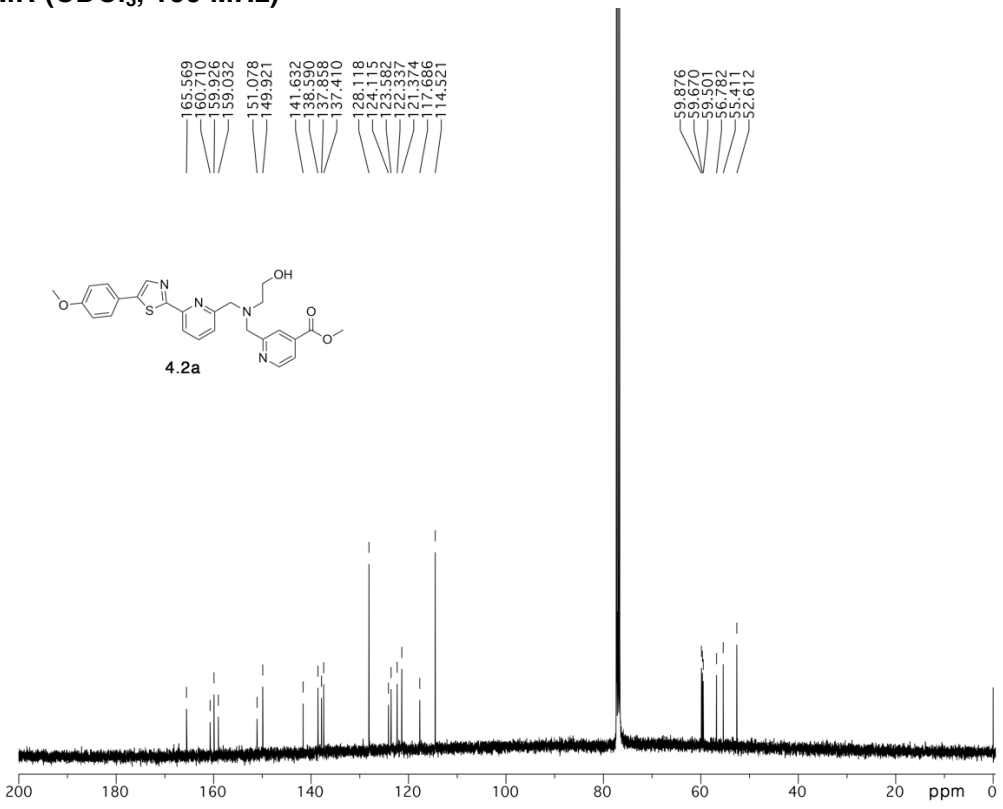

^{1}H NMR (MeOD, 400 MHz)

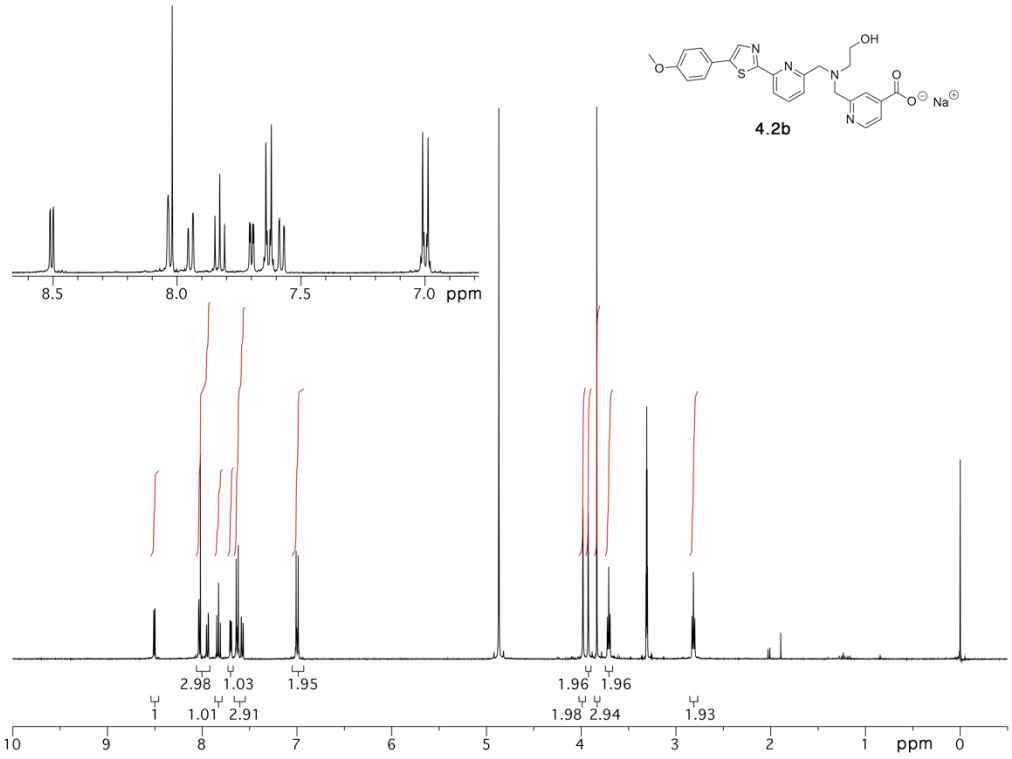

^{13}C NMR (MeOD, 100 MHz)

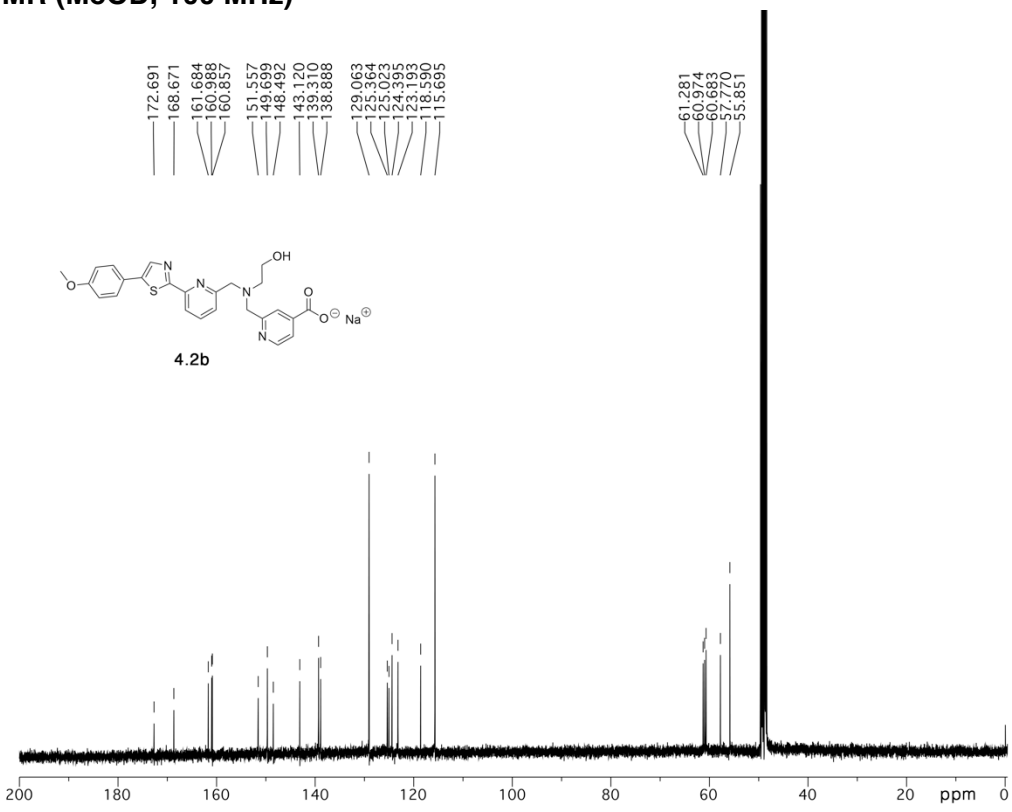

^{1}H NMR ($CDCl_3$, 400 MHz)

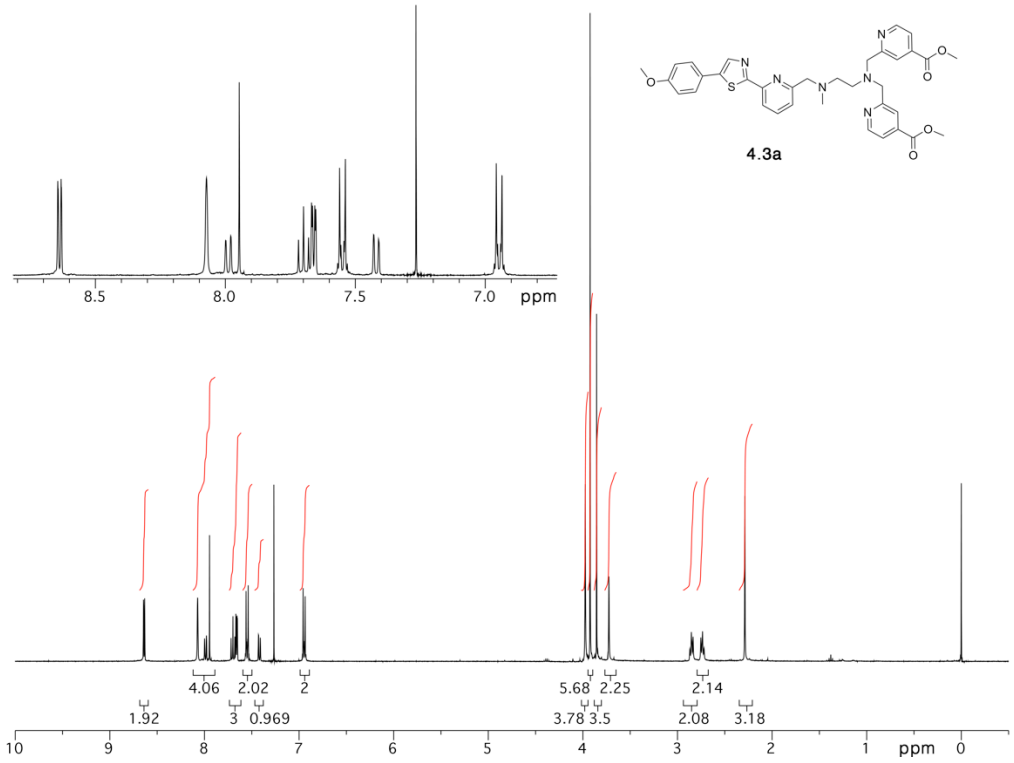

^{13}C NMR ($CDCl_3$, 100 MHz)

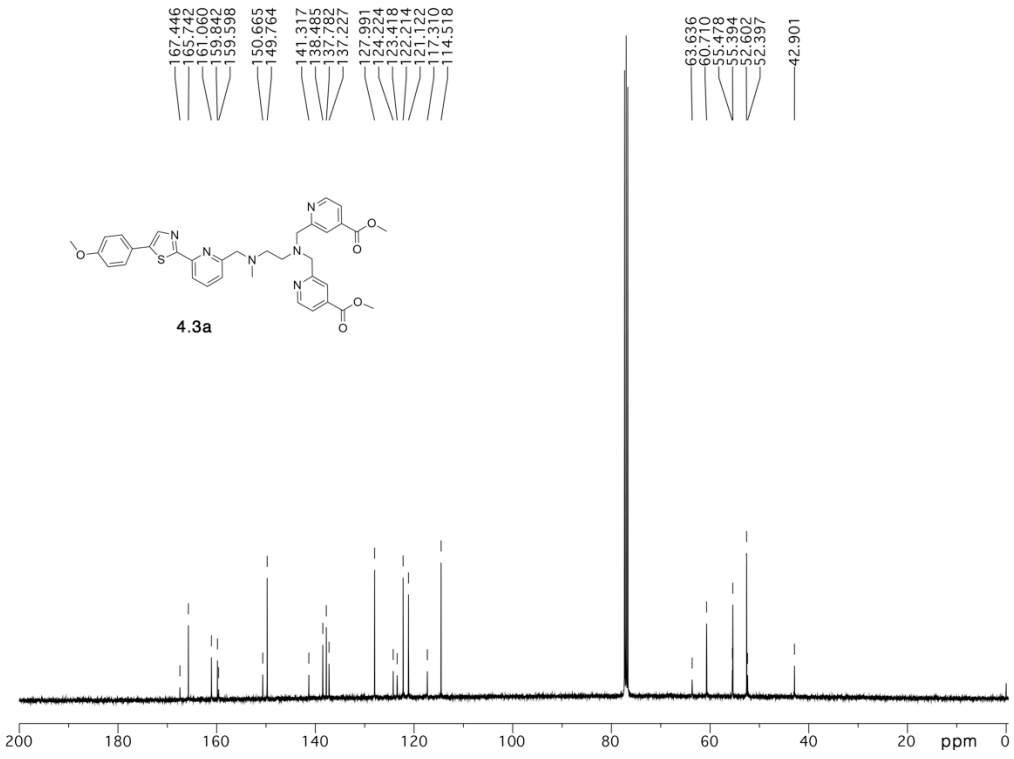

^{1}H NMR (MeOD, 400 MHz)

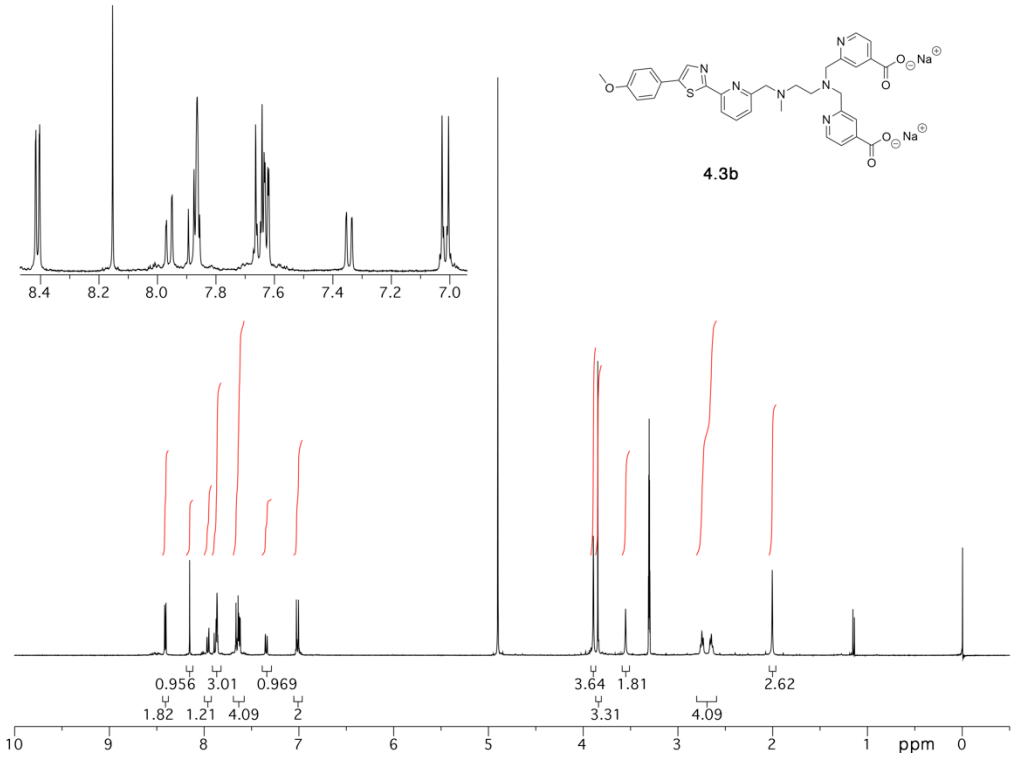

^{13}C NMR (MeOD, 100 MHz)

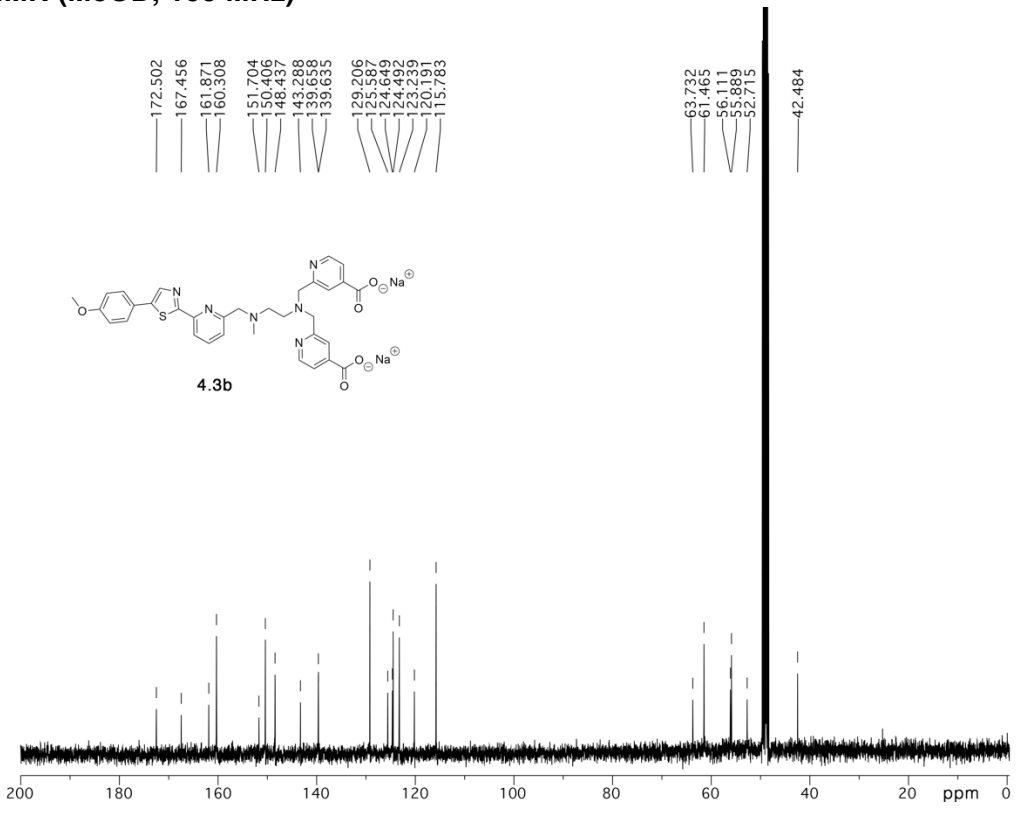

^{1}H NMR ($CDCl_3$, 400 MHz)

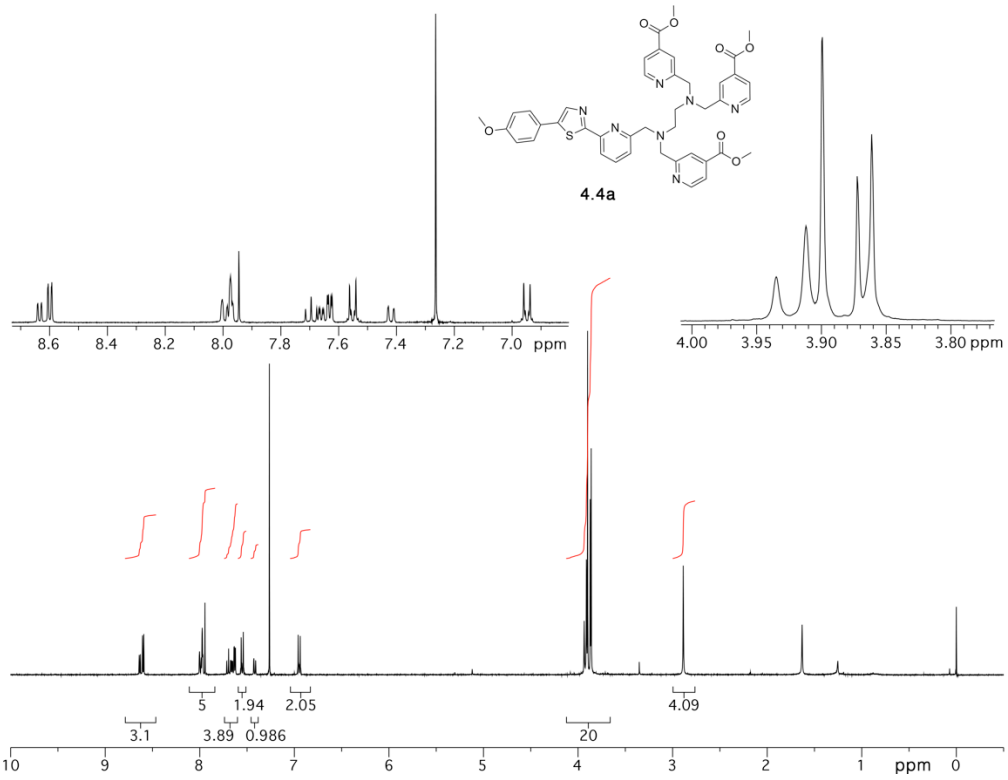

^{13}C NMR ($CDCl_3$, 100 MHz)

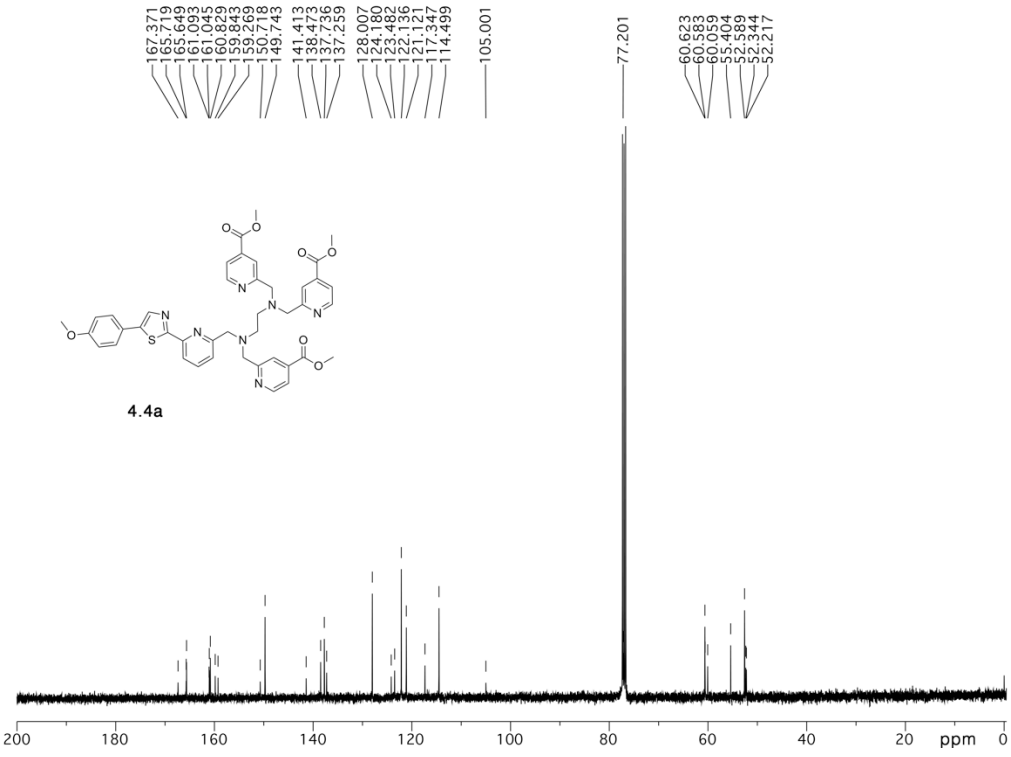

^{1}H NMR (MeOD, 400 MHz)

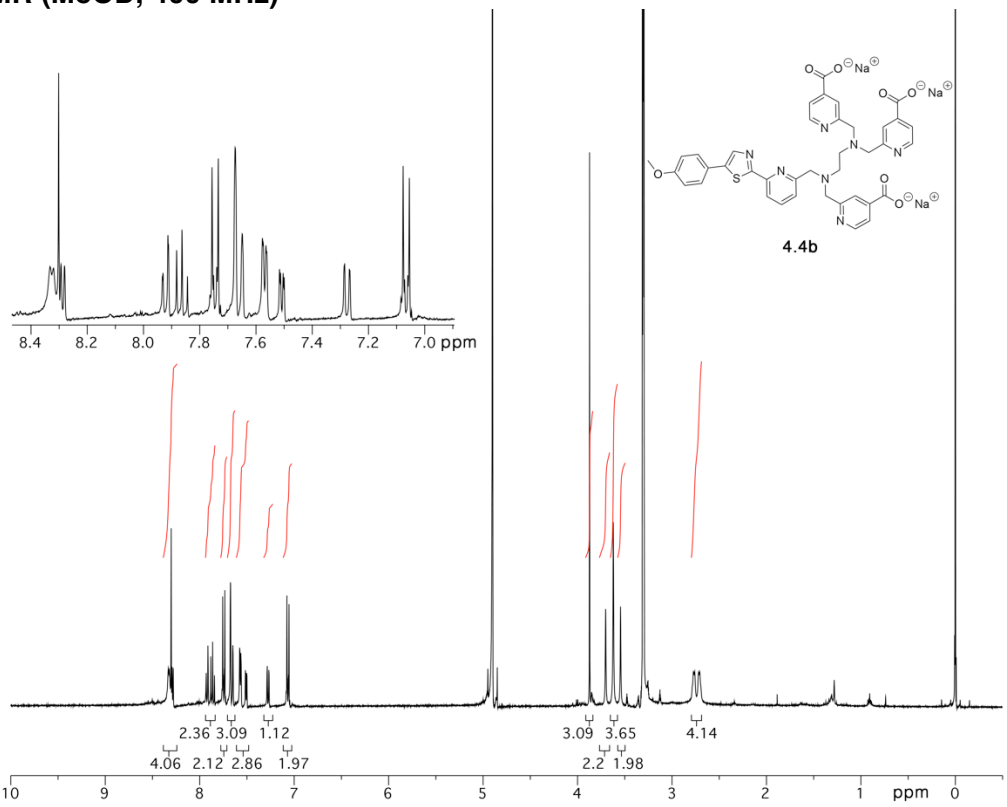

^{13}C NMR (MeOD, 125 MHz)

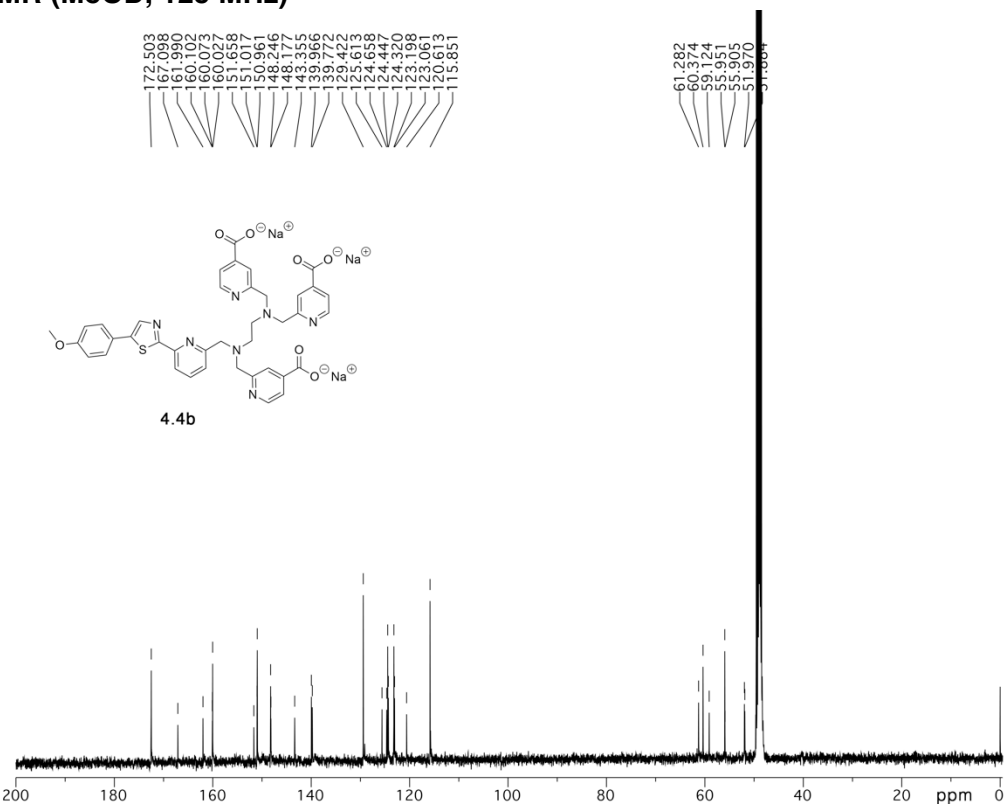

^{1}H NMR ($CDCl_3$, 400 MHz)

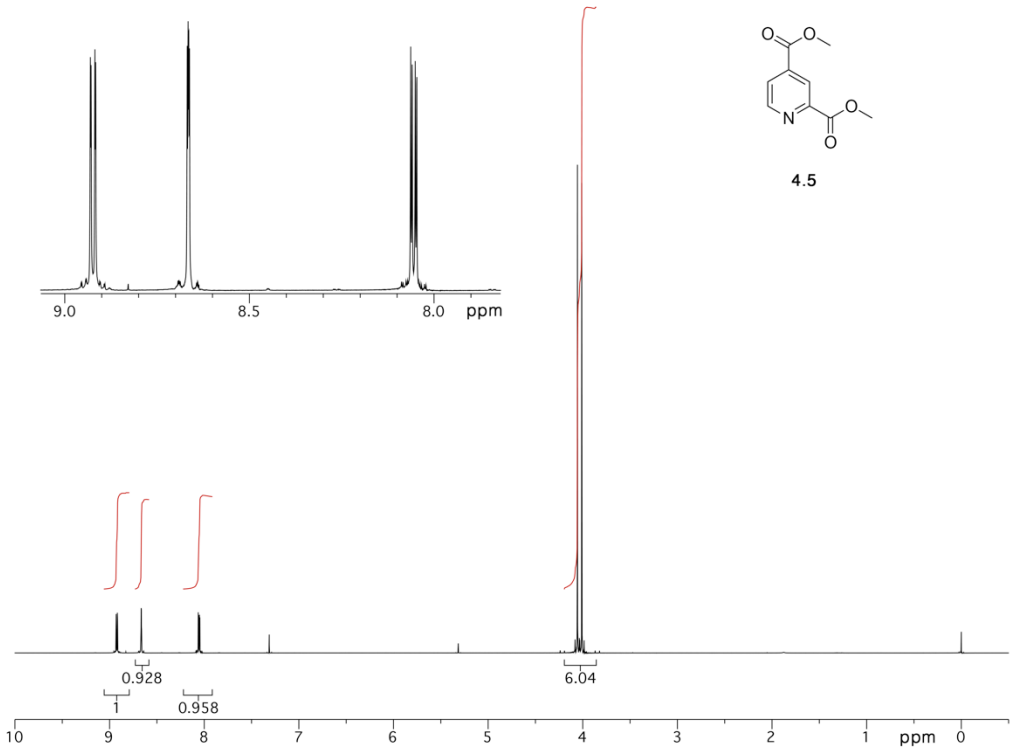

^{13}C NMR ($CDCl_3$, 100 MHz)

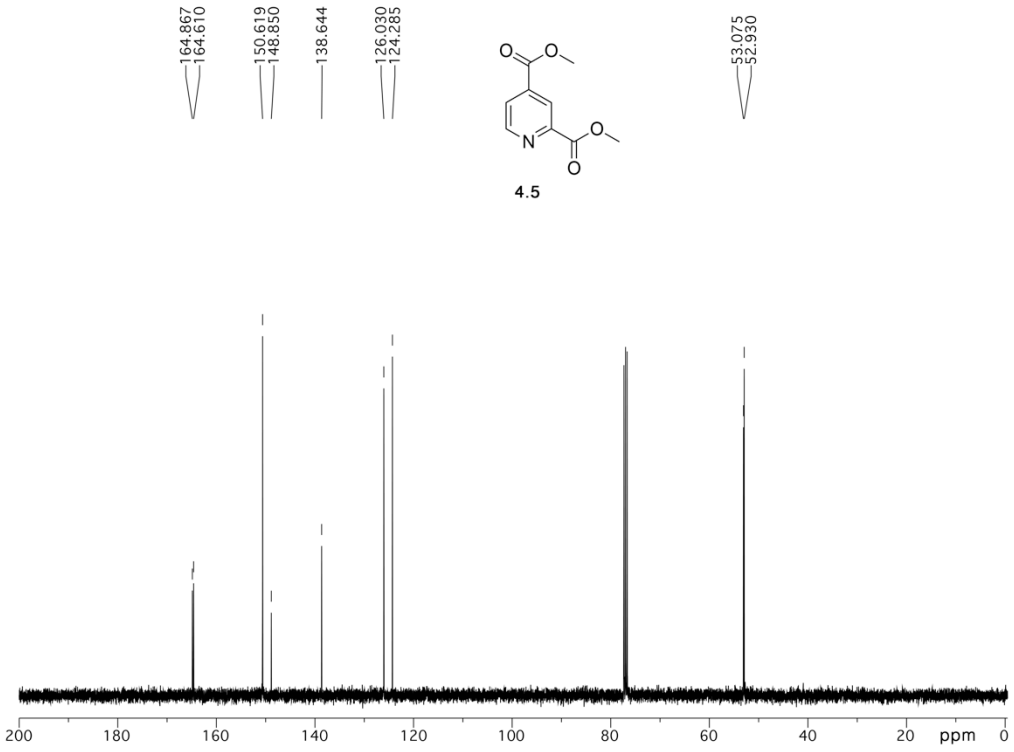

^{1}H NMR ($CDCl_3$, 400 MHz)

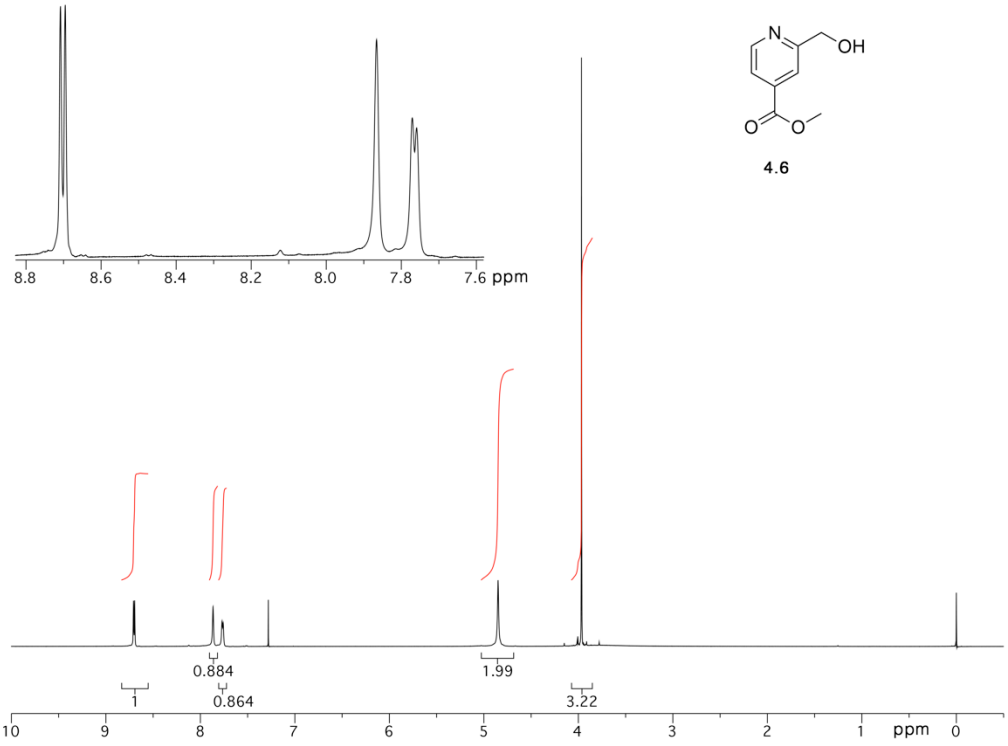

^{13}C NMR ($CDCl_3$, 100 MHz)

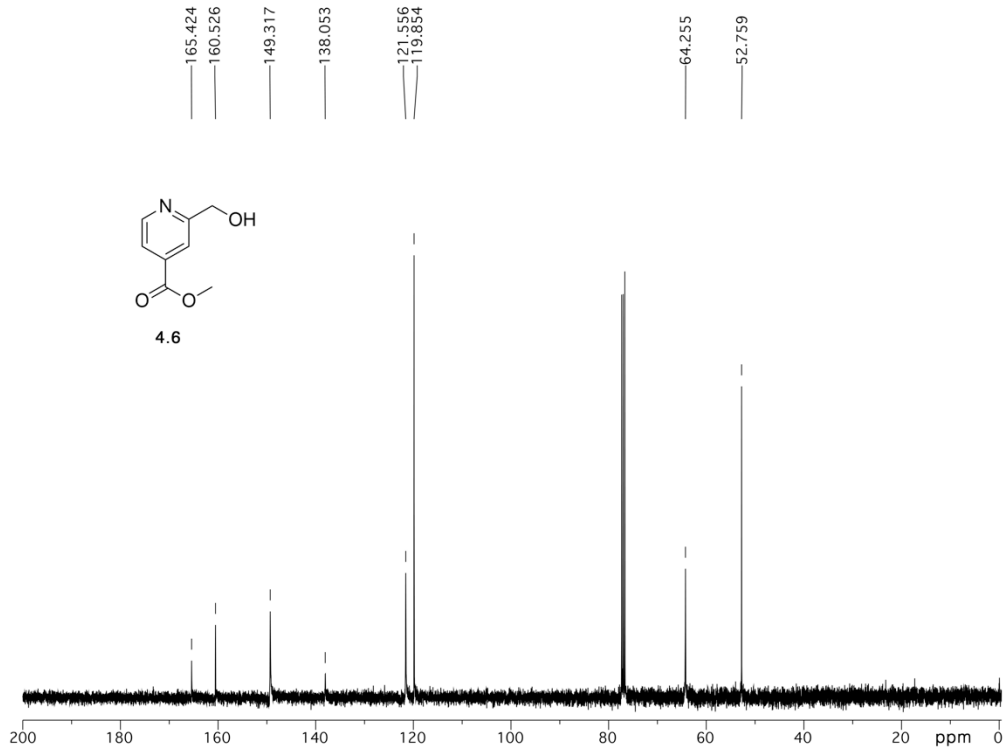

^{1}H NMR ($CDCl_3$, 400 MHz)

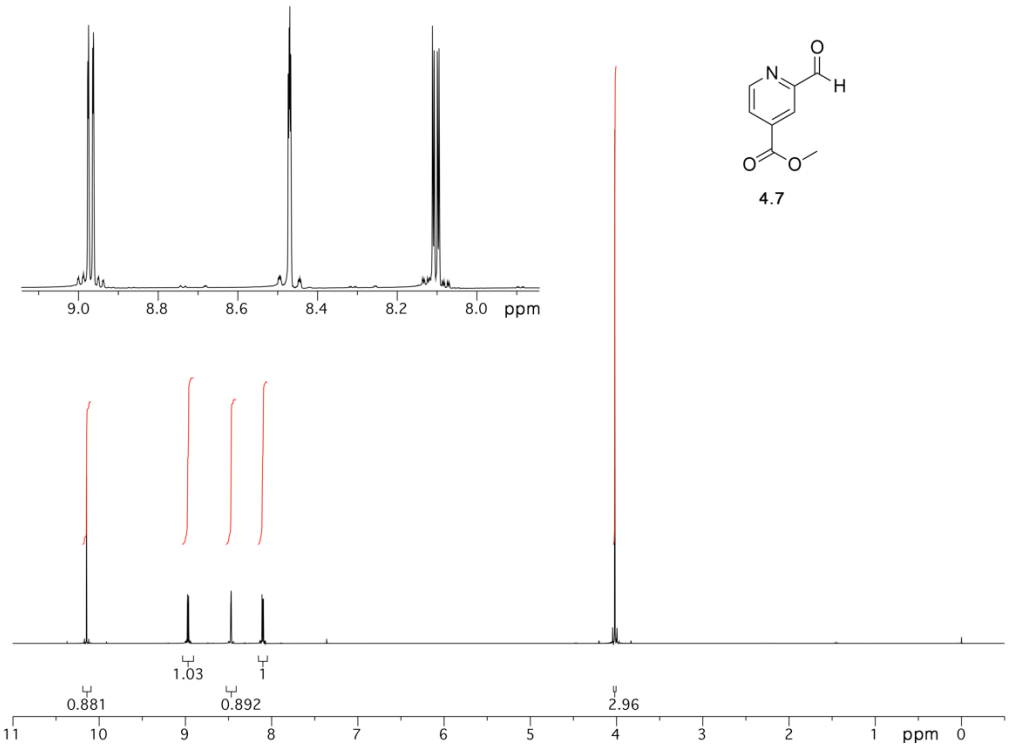

4.7

^{13}C NMR ($CDCl_3$, 100 MHz)

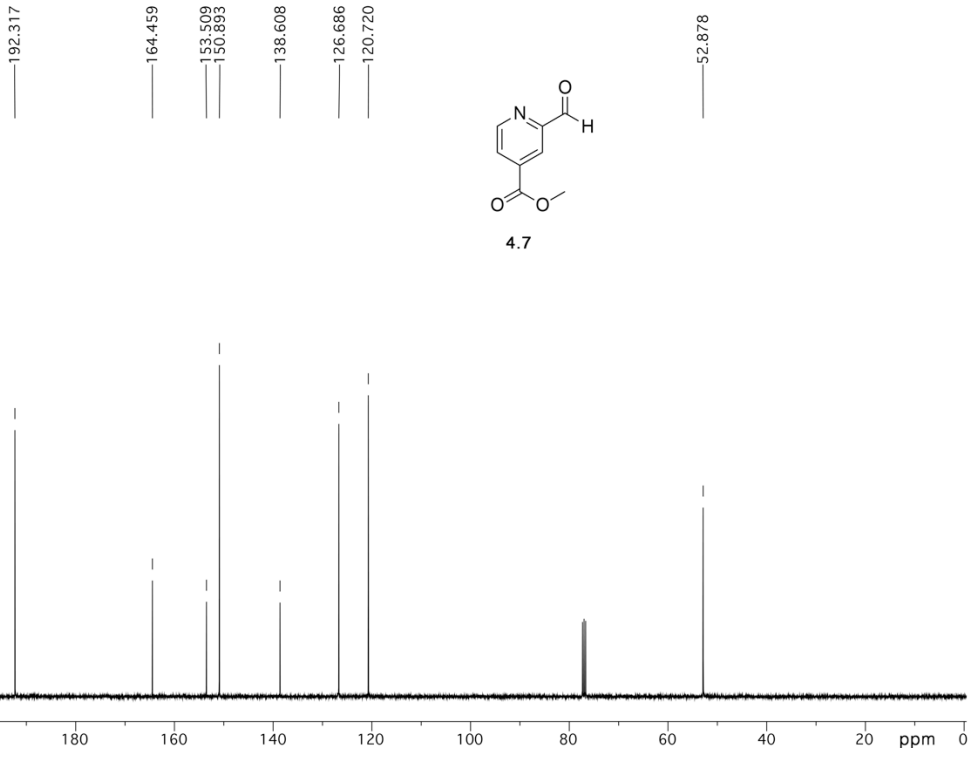

4.7

^{1}H NMR ($CDCl_3$, 400 MHz)

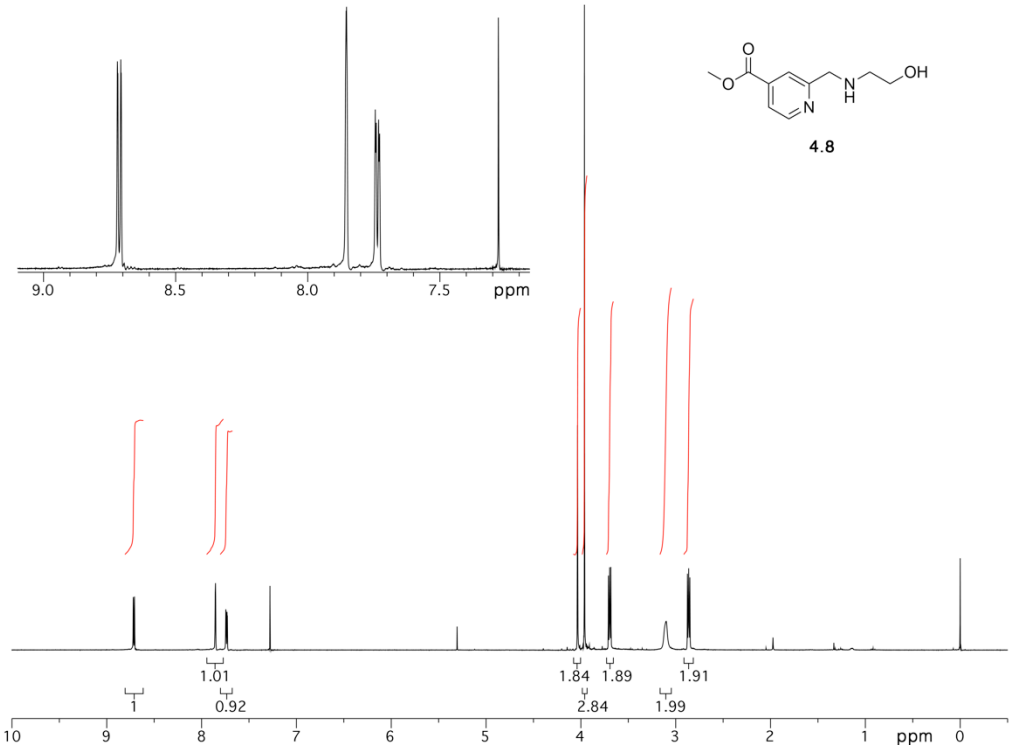

^{13}C NMR ($CDCl_3$, 100 MHz)

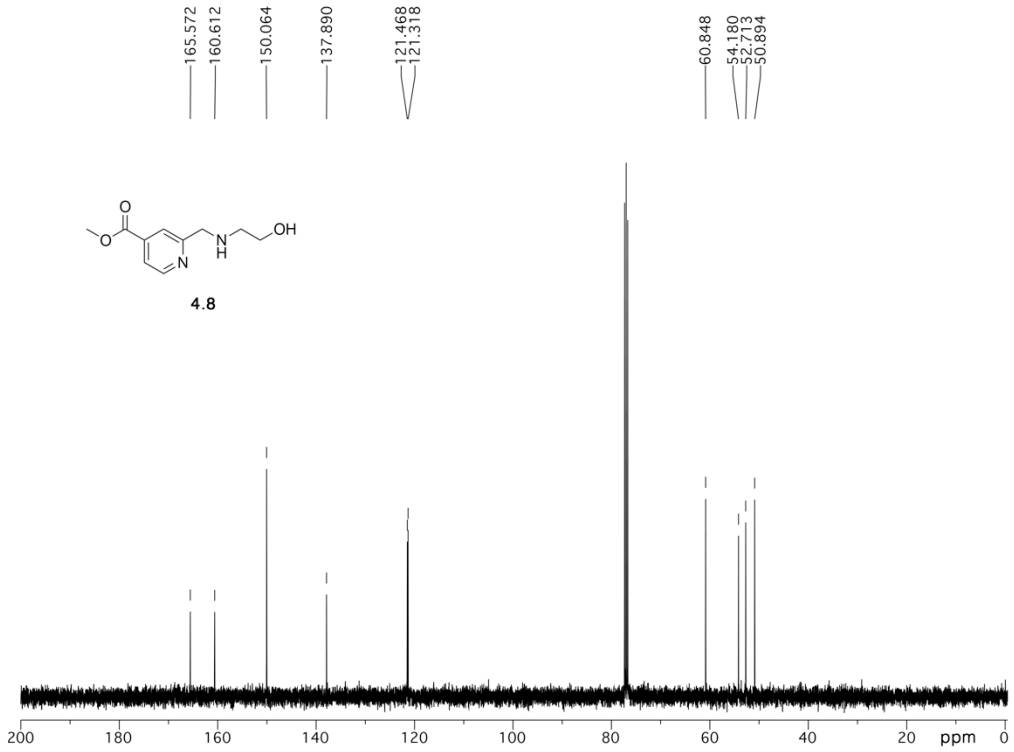

^{1}H NMR (DMSO, 400 MHz, 398K)

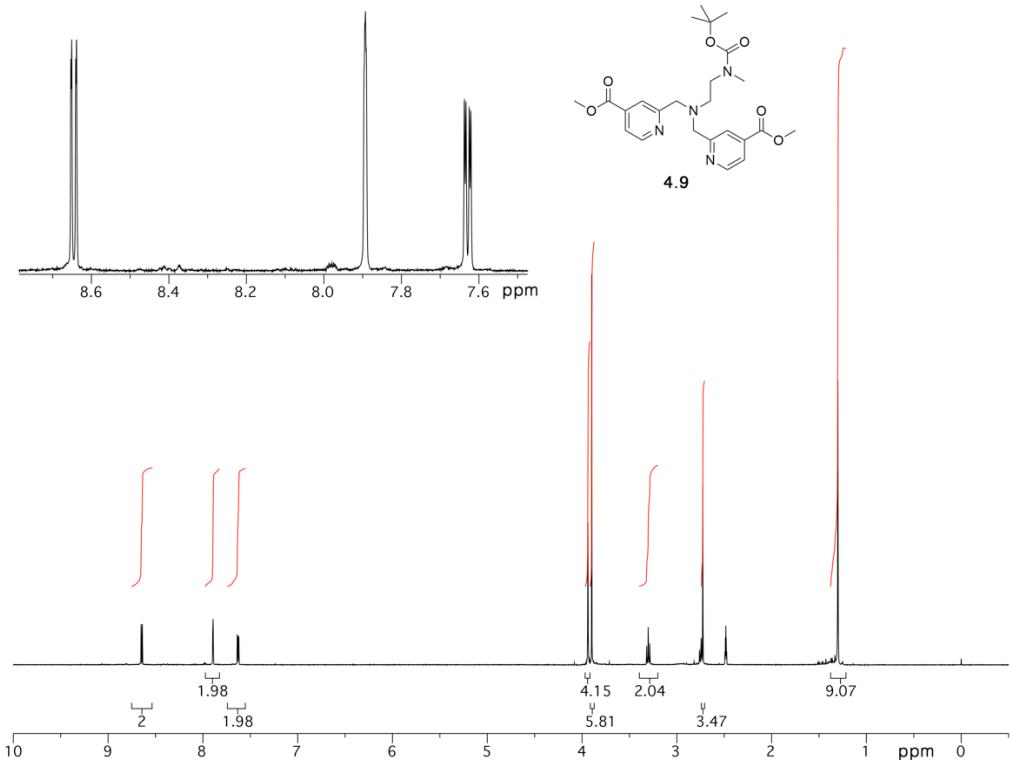

^{1}H NMR ($CDCl_3$, 400 MHz)

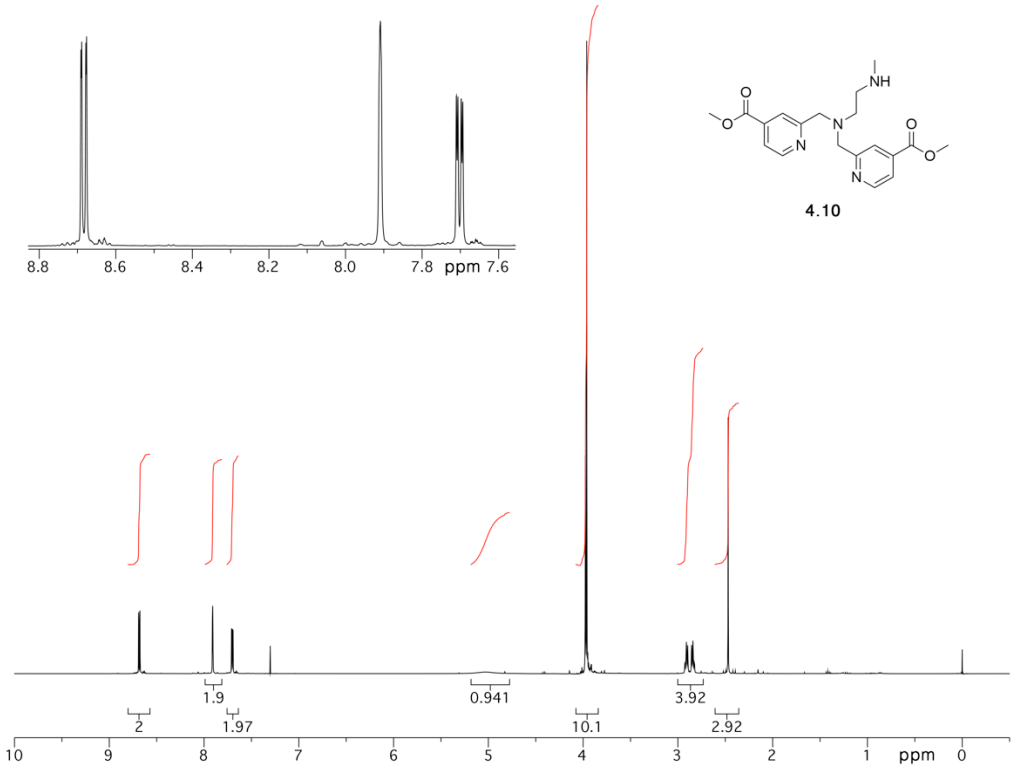

^{13}C NMR ($CDCl_3$, 100 MHz)

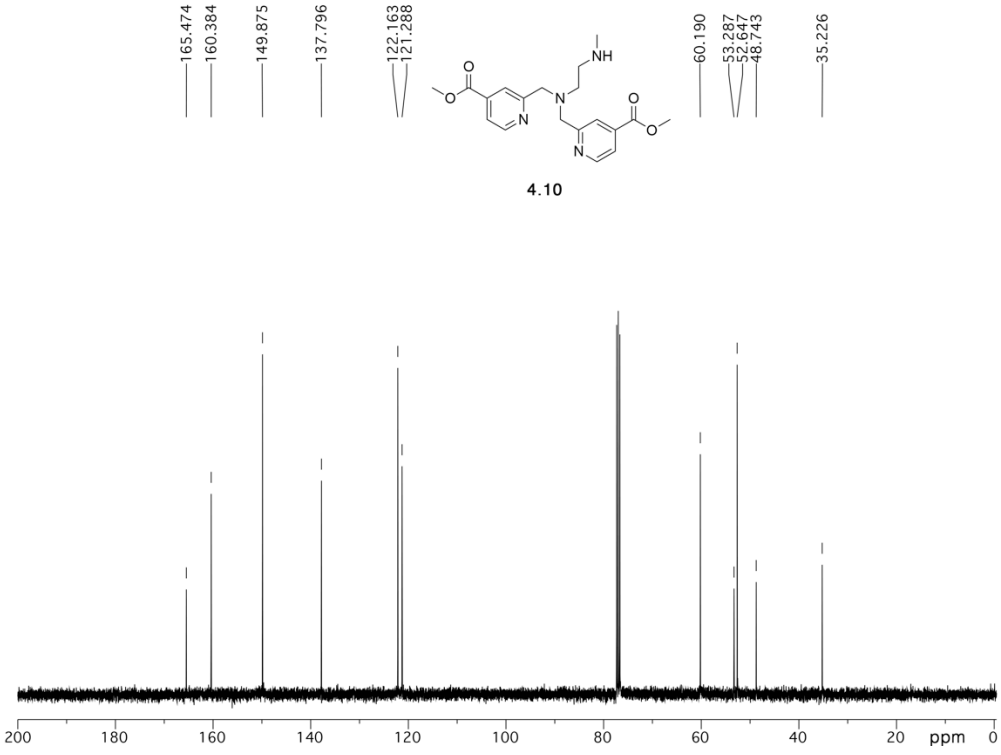

^{1}H NMR ($CDCl_3$, 400 MHz)

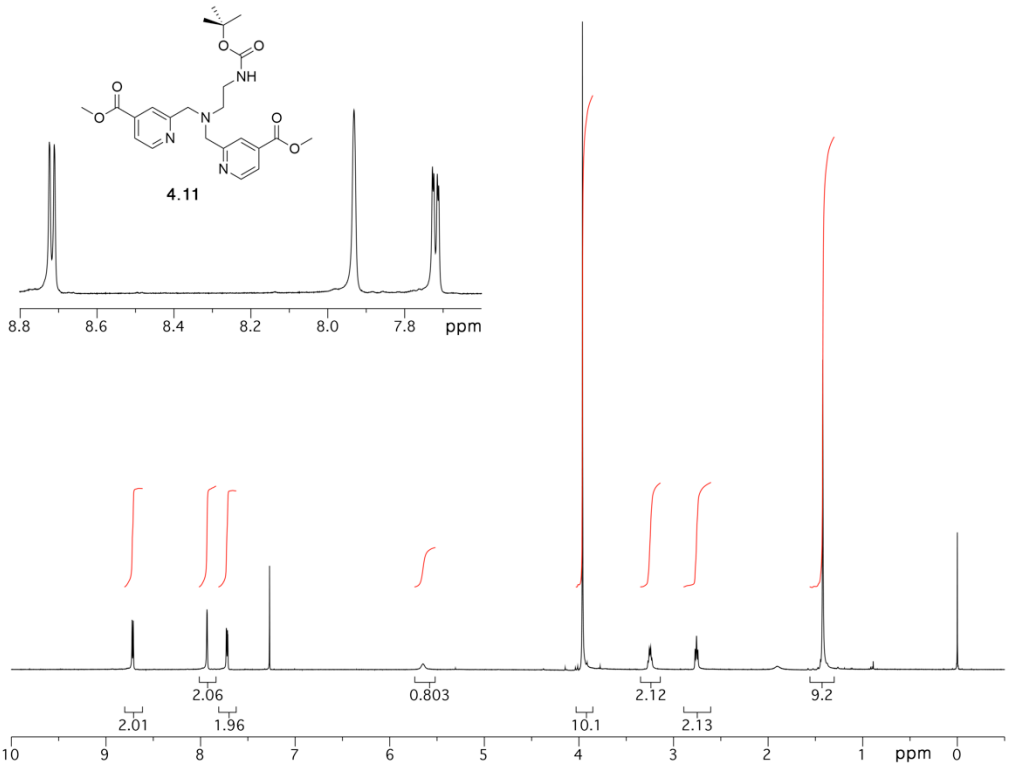

^{13}C NMR ($CDCl_3$, 100 MHz)

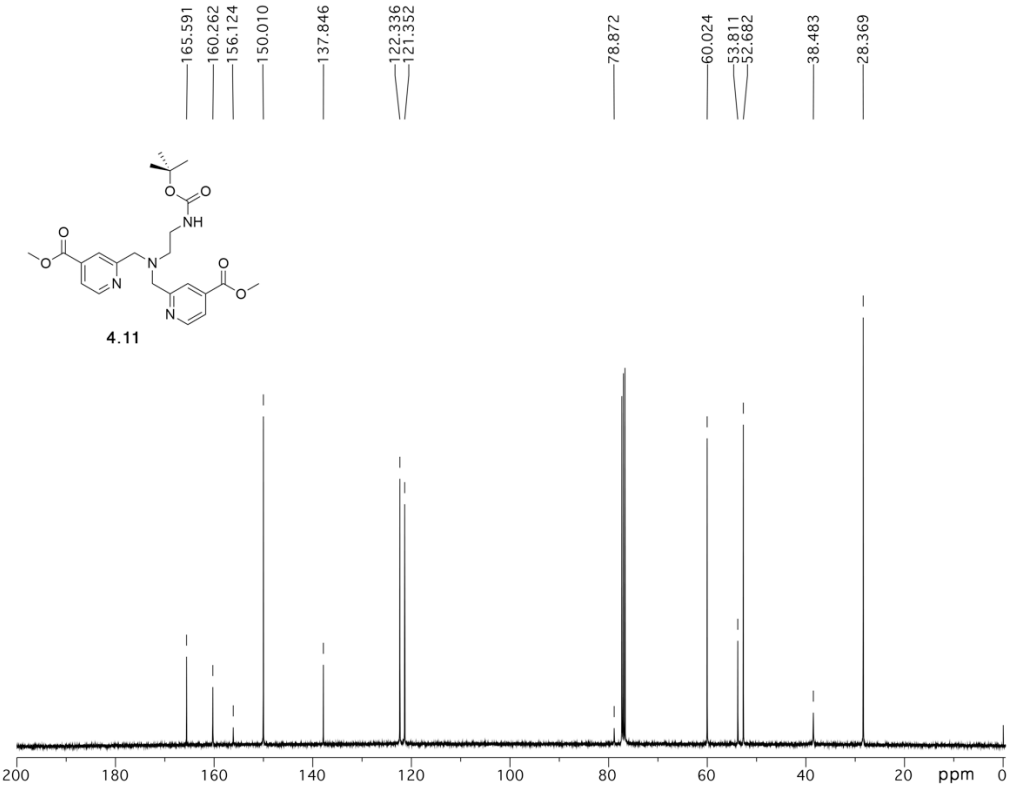

^{1}H NMR (MeOD, 400 MHz)

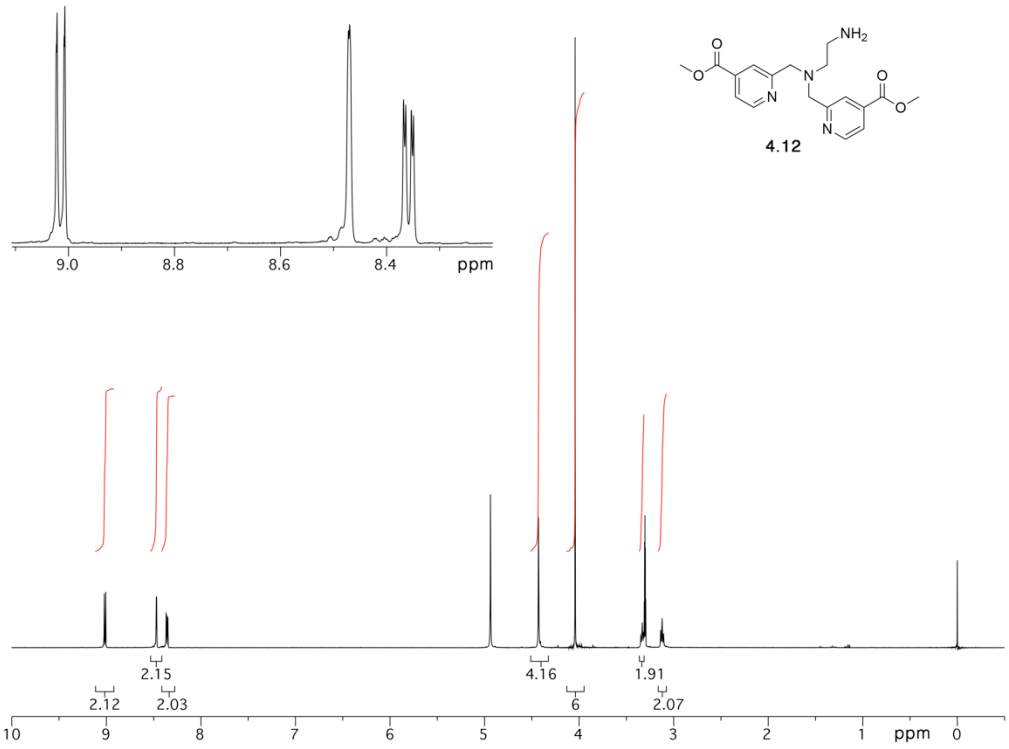

^{13}C NMR (MeOD, 100 MHz)

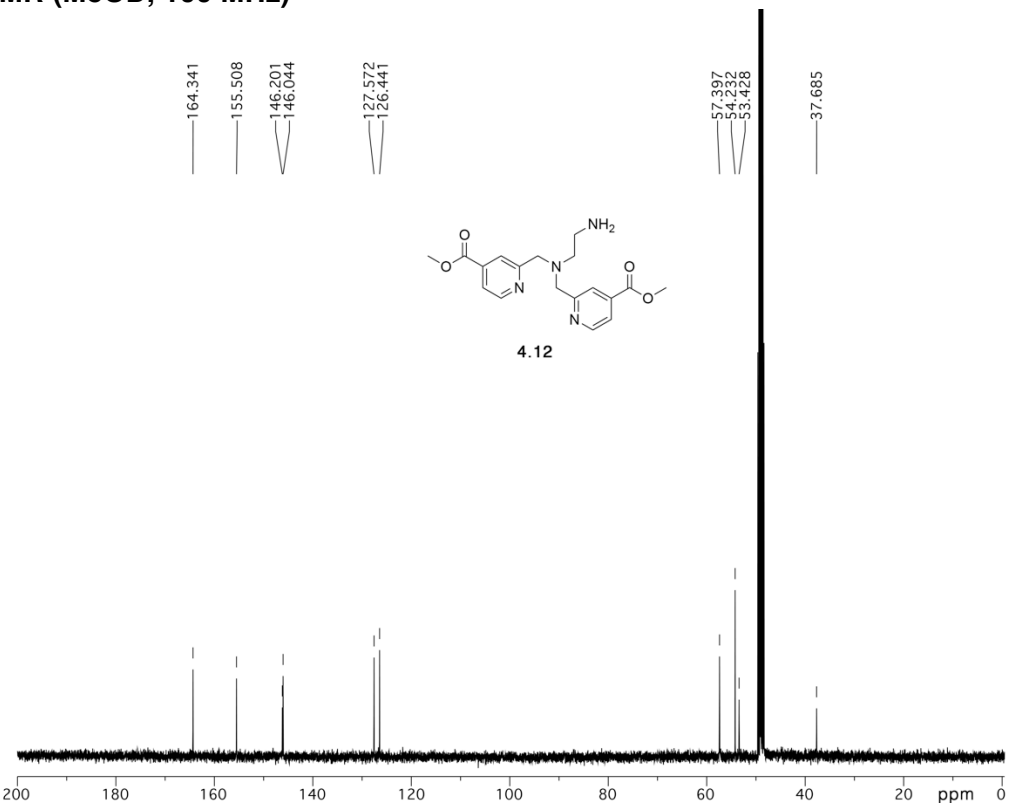

^{1}H NMR ($CDCl_3$, 400 MHz)

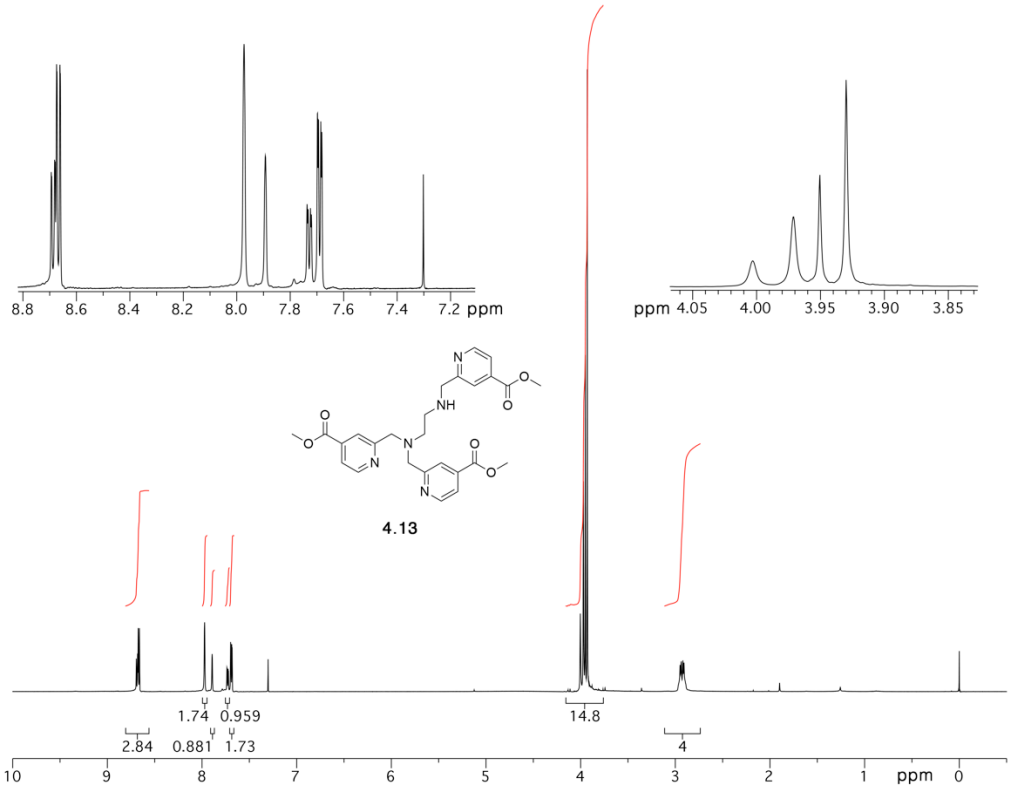

^{13}C NMR ($CDCl_3$, 100 MHz)